Transactions of the ASME®

Technical Editor
H. L. JULIEN (1998)

Associate Technical Editors
Advanced Energy Systems
M. J. MORAN (1999)
Gas Turbine
D. COOKE (1999)
H. NELSON (1999)
J. PETERS (1999)
J. N. SHINN (1996)
Internal Combustion Engines
D. ASSANIS (1999)
Power
D. LOU (1998)

BOARD ON COMMUNICATIONS
Chairman and Vice President
R. MATES

OFFICERS OF THE ASME
President, **R. J. GOLDSTEIN**
Executive Director, **D. L. BELDEN**
Treasurer, **J. A. MASON**

PUBLISHING STAFF
Managing Director, Engineering
CHARLES W. BEARDSLEY
Director, Technical Publishing
PHILIP DI VIETRO
Managing Editor, Technical Publishing
CYNTHIA B. CLARK
Managing Editor, Transactions
CORNELIA MONAHAN
Production Coordinator
VALERIE WINTERS
Production Assistant
MARISOL ANDINO

Transactions of the ASME, Journal of Engineering for Gas Turbines and Power (ISSN 0742-4795) is published quarterly (Jan., April, July, Oct.) for $175.00 per year by The American Society of Mechanical Engineers, 345 East 47th Street, New York, NY 10017. Periodicals postage paid at New York, NY and additional mailing offices. POSTMASTER: Send address changes to Transactions of the ASME, Journal of Engineering for Gas Turbines and Power, c/o THE AMERICAN SOCIETY OF MECHANICAL ENGINEERS, 22 Law Drive, Box 2300, Fairfield, NJ 07007-2300.
CHANGES OF ADDRESS must be received at Society headquarters seven weeks before they are to be effective. Please send old label and new address.
PRICES: To members, $40.00, annually: to nonmembers, $175.00. Add $30.00 for postage to countries outside the United States and Canada.
STATEMENT from By-Laws. The Society shall not be responsible for statements or opinions advanced in papers or . . . printed in its publications (B7.1, par. 3).

COPYRIGHT © 1997 by The American Society of Mechanical Engineers. Authorization to photocopy material for internal or personal use under circumstances not falling within the fair use provisions of the Copyright Act is granted by ASME to libraries and other users registered with the Copyright Clearance Center (CCC) Transactional Reporting Service provided that the base fee of $3.00 per article is paid directly to CCC, Inc., 222 Rosewood Dr., Danvers, MA 01923. Request for special permission or bulk copying should be addressed to Reprints/Permission Department.

INDEXED by Applied Mechanics Reviews and Engineering Information, Inc. Canadian Goods & Services Tax Registration #126148048

Journal of Engineering for Gas Turbines and Power

Published Quarterly by The American Society of Mechanical Engineers

VOLUME 119 • NUMBER 2 • APRIL 1997

TECHNICAL PAPERS

Gas Turbines: Aircraft

265 **Non-Random Adaptive Grid Method for High-Speed Optimization of Highly Dimensional, Badly Behaving Real Time Functions** (94-GT-487)
K. E. Shahroudi

Gas Turbines: Ceramics

273 **Dynamic Fatigue Testing of Candidate Ceramic Materials for Turbine Engines to Determine Slow-Crack-Growth Parameters** (95-GT-235)
N. R. Osborne, G. A. Graves, and M. K. Ferber

279 **Thermal Cycling Effects on Dynamic Mechanical Properties and Crystallographic Structures of Silicon Nitride-Based Structural Ceramics**
S. Yang, R. F. Gibson, G. M. Crosbie, and R. L. Allor

Gas Turbines: Coal, Biomass, and Alternative Fuels

285 **Economic Scales for First-Generation Biomass-Gasifier/Gas Turbine Combined Cycles Fueled From Energy Plantations** (96-GT-540)
E. D. Larson and C. I. Marrison

291 **Modeling Sulfur Dioxide Capture in a Pulverized Coal Combustor** (96-GT-112)
R. B. Nair and S. Yavuzkurt

298 **Next-Generation Integration Concepts for Air Separation Units and Gas Turbines** (96-GT-144)
A. R. Smith, J. Klosek, and D. W. Woodward

Gas Turbines: Combustion and Fuels

305 **An Experimental and Computational Study of Swirling Hydrogen Jet Diffusion Flames** (95-GT-307)
M. S. Anand, F. Takahashi, M. D. Vangsness, M. D. Durbin, and W. J. Schmoll

315 **Optimization of Multiple Jets Mixing With a Confined Crossflow** (95-GT-313)
Th. Doerr, M. Blomeyer, and D. K. Hennecke

322 **The Effects of Different Sulfur Compounds on Jet Fuel Oxidation and Deposition** (95-GT-222)
R. E. Kauffman

328 **An Experimental and Numerical Study of the Isothermal Flowfield Behind a Bluff Body Flameholder** (95-GT-102)
C. N. Raffoul, A. S. Nejad, R. D. Gould, and S. A. Spring

340 **Combustion Oscillation Control by Cyclic Fuel Injection** (95-GT-224)
G. A. Richards, M. J. Yip, E. Robey, L. Cowell, and D. Rawlins

344 **Hydrocarbon Fuel Cooling Technologies for Advanced Propulsion** (95-GT-226)
D. R. Sobel and L. J. Spadaccini

352 **Differential Mass and Energy Balances in the Flame Zone From a Practical Fuel Injector in a Technology Combustor** (95-GT-112)
D. L. Warren and P. O. Hedman

Gas Turbines: Controls and Diagnostics

362 **Numerical Simulation of Blade Fault Signatures From Unsteady Wall Pressure Signals** (94-GT-289)
V. Dedoussis, K. Mathioudakis, and K. D. Papailiou

370 **The Negative Information Problem in Mechanical Diagnostics** (96-GT-35)
D. L. Hall, R. J. Hansen, and D. C. Lang

378 **Multivariable Trend Analysis Using Neural Networks for Intelligent Diagnostics of Rotating Machinery**
S. Zhang and R. Ganesan

Gas Turbines: Industrial and Cogeneration

385 **Split Stream Boilers for High-Temperature/High-Pressure Topping Steam Turbine Combined Cycles** (95-GT-29)
I. G. Rice

(Contents continued on p. 492)

Downloaded 03 Jun 2010 to 171.66.16.159. Redistribution subject to ASME license or copyright; see http://www.asme.org/terms/Terms_Use.cfm

(Contents continued)

Gas Turbines: Pipelines

395 **Preliminary Estimation of Antisurge Valve Carrying Capacity**
S. Savitsky

Gas Turbines: Structures and Dynamics

397 **"Snapping" Torsional Response of an Anisotropic Radially Loaded Rotor** (95-GT-396)
D. E. Bently, P. Goldman, and A. Muszynska

404 **A Numerical Method for the Prediction of Bladed Disk Forced Response** (94-GT-293)
M. Berthillier, M. Dhainaut, F. Burgaud, and V. Garnier

411 **Energy Analysis to the Design of Rotor-Bearing Systems** (95-GT-314)
W. J. Chen

418 **Nonlinear Vibrations and Stability of a Rotor-Bearing System With Nonsymmetric Clearances**
R. Ganesan

425 **Comparison of the Rotor Dynamic and Structure Dynamic Calculation of Compressors** (95-CTP-51)
M. Hohlrieder and H. Irretier

430 **Synchronous Dynamics of a Coupled Shaft/Bearing/Housing System With Auxiliary Support From a Clearance Bearing: Analysis and Experiment** (95-GT-216)
J. L. Lawen, Jr., and G. T. Flowers

436 **Modeling and Simulation Methods for MDOF Structures and Rotating Machinery With Impact Dampers** (95-GT-397)
J. M. McElhaney, A. Palazzolo, and A. Kascak

447 **Dynamic Response of a Cracked Rotor With Some Comments on Crack Detection** (94-GT-29)
G. Meng and E. J. Hahn

456 **Balanced Model Reduction and Control of Rotor-Bearing Systems**
J. T. Sawicki and W. K. Gawronski

464 **Optimization of Bearing Locations for Rotor Systems With Magnetic Bearings** (95-GT-217)
S. Srinivasan, E. H. Maslen, and L. E. Barrett

469 **Wave-Rotor-Enhanced Gas Turbine Engines**
G. E. Welch, S. M. Jones, and D. E. Paxson

Power

478 **An Investigation of the Effects of Flue Gas Injection on Natural Draft Cooling Tower Performance**
T. V. Eldredge, D. J. Benton, and J. W. Hodgson

485 **A Tabular Taylor Series Expansion Method for Fast Calculation of Steam Properties**
K. Miyagawa and P. G. Hill

ANNOUNCEMENTS

278 **Change of address form for subscribers**

Inside back cover Information for authors

Downloaded 03 Jun 2010 to 171.66.16.159. Redistribution subject to ASME license or copyright; see http://www.asme.org/terms/Terms_Use.cfm

Non-Random Adaptive Grid Method for High-Speed Optimization of Highly Dimensional, Badly Behaving Real Time Functions

K. E. Shahroudi
Department of Aerospace Engineering, Aircraft Design and Flight Mechanics Group, Delft University of Technology, Delft, The Netherlands

The majority of optimization methods lose their applicability when solving highly dimensional functions. The required calculation effort usually becomes enormous as dimensions increase, regardless of the elegance of the method. Most methods concern themselves with finding a single optimum that satisfies the required accuracy, but that provides no quantitative measure (i.e., probability of correctness) indicating whether the true optimum is found. Furthermore, there is usually no exact measure of the calculation effort prior to starting the procedure. There is always an unavoidable coupling (i.e., relation) between the accuracy, probability, and calculation effort of an optimization method, but the exact form of this relation is dependent on the procedures followed to reach optimum. Ideally, an optimization method should facilitate the statement of required accuracy, required probability, and the required calculation effort separately and the method should take care of the rest (i.e., total decoupling of the three requirements). Although this ideal case is generally not possible, it is possible to move toward it by finding procedures that reduce the strength of this unwanted coupling. This report derives simple analytical relations between the required accuracy, probability, and calculation effort of a general multidimensional adaptive grid non-gradient guided (NGG) search method where the search points are generated either decisively or randomly. It is then shown that any adaptive method based on reducing the total solution space is heavily penalized. Further, it is analytically illustrated that if the adaptive grid is randomly generated, it is far less successful than the non-random adaptive grid, because the amount of grid adaptation is less decisive at every step, due to the randomness. As with many optimization techniques, the dimensionality problem limits the application of this method to cases where the function evaluation is real time (~milliseconds) and dimensions are lower than say 25, which occurs in conceptual/preliminary design systems such as CAGED (Shahroudi, 1994b). This method is also particularly useful for problems in which the number of optima is known in advance. In this case the required probability can be set to its minimum value, which is required in order to distinguish an absolute optimum from a known (or likely) number of optima. The coupling relations derived in this report will then provide the minimum calculation effort necessary to satisfy accuracy and probability requirements.

1 Introduction

Non-gradient guided search techniques are traditionally restricted to optimization of functions that are not "well behaved" or for locating a significant region for further optimization by gradient-guided methods. For moderately dimensional (i.e., <25) problems, however, it is not at all clear that gradient-guided approach is advantageous regarding the calculation effort necessary to satisfy the required accuracy and the required probability of finding the true optimum.

The NGG search possesses several very attractive features as opposed to gradient-guided search, namely,

1 The search strategy is function call intensive rather than procedure call intensive.
2 It is possible to determine the calculation effort, before starting procedure, which satisfies the accuracy and probability requirements.
3 The number and complexity of constraint functions do not significantly add to calculation effort.

Increasing computing speeds have in recent years generated much interest in high-speed simulation of large and complex systems. Sugiyama (1990) reports a "real time or faster than real time simulation of gas turbine engines" with the aid of specially designed computer hardware and software. High-speed modeling (order of milliseconds calculation times) provides a very effective tool for natural design and real time optimization of complex systems such as gas turbines. The Computer-Aided General Engine Design System (CAGED) uses high-speed modeling techniques to aid in the conceptual and preliminary phases of gas turbine design (see Shahroudi, 1994a).

In this high-speed modeling domain, NGG techniques become very appealing because of their first quality mentioned

Contributed by the International Gas Turbine Institute and presented at the 39th International Gas Turbine and Aeroengine Congress and Exposition, The Hague, The Netherlands, June 13–16, 1994. Manuscript received by the International Gas Turbine Institute March 21, 1994. Paper No. 94-GT-487. Associate Technical Editor: E. M. Greitzer.

Copyright © 1997 by ASME
Downloaded 02 Jun 2010 to 171.66.16.105. Redistribution subject to ASME license or copyright; see http://www.asme.org/terms/Terms_Use.cfm

above, i.e., the calculation time to evaluate the functions is very small compared to the calculation time to follow an elaborate procedure. Further, since the relationship or the coupling between accuracy, probability, and calculation effort is available, minimal information about the function to be optimized (F) will lead to large reduction in wastage of calculation effort. For example, suppose it is known that F is not likely to have more than two optima. So a probability of larger than 50 percent in solution will give us enough certainty to determine the true optimum. The coupling will then provide us with the minimum calculation effort that will result in this required probability for a given error, thereby avoiding wastage.

This report is concerned with deriving the coupling between accuracy, probability, and calculation effort for a general adaptive grid NGG technique, where after each step, the total multidimensional space occupied by the grids is being reduced in size while at the same time the grid lines are concentrated near the optimum region. The coupling relations will show that for a general F (i.e., the case where F is not a special case), the search strategy is heavily penalized if the total search volume is reduced, i.e., search points must be generated in the total solution space, but they can tend to be more concentrated near the best region.

Further, the difference between definitive and random grid adaptation is explored. A break-even point is then found where the definitive adaptation of the grid will give better return on calculation effort.

For brevity, only basic ideas are given that are necessary to derive the coupling relations. The reader is referred to Shahroudi (1994b) for full derivations.

2 Some Fundamental Distinctions

The accuracy or error ϵ, probability P, and calculation effort E of a solution method are fundamentally separate but related concepts:

1. P indicates the probability that the found optimum is a true and global optimum.
2. ϵ indicates that if the true optimum is found, then the real position of O cannot be farther than ϵ.
3. E is the calculation effort spent to arrive at O. For the types of NGG techniques considered in this report, E can be represented by the total number of function evaluations required to complete search.

If ϵ is specified as the dimensionless error along each independent variable, then there is a range of values outside of which probability loses its meaning:

$$P_{\max} = 1 - \epsilon^d; \quad P_{\min} = \epsilon^d$$

$$\text{meaningful range is } \epsilon^d \leq P \leq 1 - \epsilon^d \qquad (1)$$

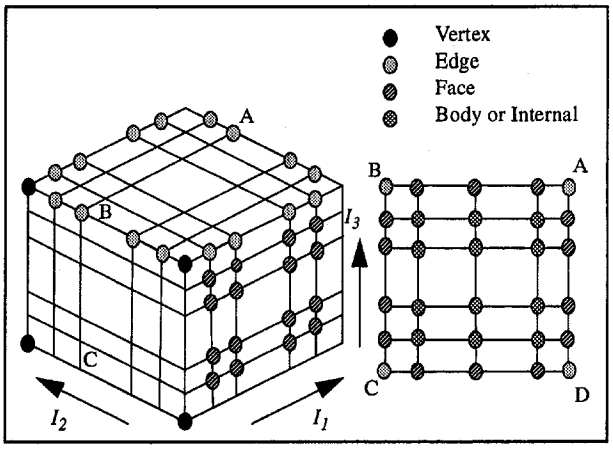


Fig. 1 Three-dimensional version of the basic grid system with definition of vertex, face, edge, and internal points. The total volume of the grid system represents the solution space. The small hypercubes generated by the intersection of grid plane are called subregions.

where the lower and upper bounds represent impossible and unavoidable events, respectively. Further, it is not meaningful to compare two probability values that have a difference of less than ϵ^d.

Coupling is a quantitative relationship between E, ϵ, and P, which depends on the search strategy and is possible to derive for exhaustive search and the adaptive grid search.

For example, non-adaptive non-random grid method (this is an exhaustive search) with N equispaced grid lines along each dimension,

$$P_{\text{Non-Adaptive Non-Random}} = 1 - \frac{1}{(N-1)^d} = 1 - \epsilon^d$$

$$E_{\text{Non-Adaptive Non-Random}} = \text{Number of grid points} \times \text{Number of steps} = N^d \times N_s \qquad (2)$$

e.g., for $d = 5$, $\epsilon = 0.01$, the relations yield $P = 0.999999999$, $N = 101$, and $E = 1.0510e^{10}$. The calculation effort is already enormous for a low dimensional problem.

The adaptive grid search is fundamentally different from the exhaustive search. The latter tries to hit O directly, and is successful after many tries in the whole of the solution space. The former tries to achieve total success in the final step, hence minimizing the time spent in insignificant parts of the solution space.

Nomenclature

A = gridded subspace of S
d = dimensionality of F
Def1 = definition of step success used to estimate Def2
Def2 = robust definition of step success
E = calculation effort
ϵ = required inaccuracy or error in each independent variable. Note: all independent variables vary between 0 and 1 and ϵ is nondimensional based on this unit range
F = multidimensional function to be optimized
f = shrinkage factor of A per step
I_K = kth independent variable
J = step index
k = dimension index
N = number of grid lines in each dimension
NGG = non-gradient guided search techniques based on function evaluation only and not gradients
N_S = number of steps
old & new = grid positions before and after beam transformation
O = optimum region of size ϵ^d
O_1, O_2 . . . etc. = local optima other than O
P_{grid} = contribution of gridding to step success
$P_{\max}$ = maximum meaningful value of probability
$P_{\min}$ = minimum meaningful value for P
P_{step} = probability of step being successful
S = total solution space
SR = significant region of solution S

Downloaded 02 Jun 2010 to 171.66.16.105. Redistribution subject to ASME license or copyright; see http://www.asme.org/terms/Terms_Use.cfm

3 Search Strategies

In order to provide a basis for comparison between the various methods, a universal grid system is defined that will remain the same in all methods. The difference between the methods is then found by comparing how the grids adapt their positions with each step.

Figure 1 shows this grid and differentiates between vertex, face, edge, and body points. This differentiation is necessary because the numbers of subregions affected by various points are different. Full accounting of number of points and their subregions is as follows:

$$\underbrace{\left\{\begin{array}{c} N_{\text{Grid Points}} = N^d \\ N_{\text{Vertex}} = 2^d \\ N_{\text{Edge}} = d2^{d-1}(N-2) \\ N_{\text{Body}} = (N-2)^d \\ N_{\text{Face}} = N_{\text{Grid Points}} - N_{\text{Vertex}} - N_{\text{Edge}} - N_{\text{Body}} \\ \quad = N^d - 2^d - d2^{d-1}(N-2) - (N-2)^d \end{array}\right\}}_{\text{Number of Points}},$$

$$\underbrace{\left\{\begin{array}{l} N_{\text{Subregions}_{\text{Vertex}}} = 1 \\ N_{\text{Subregions}_{\text{Edge}}} = 2 \\ N_{\text{Subregions}_{\text{Body}}} = 2^d \\ N_{\text{Subregions}_{\text{Face}}} = 2^{d-1} \end{array}\right\}}_{\text{Number of Affected Subregions}}, \quad (3)$$

For convenience in comparison, the calculation effort will be estimated by the number of function calls only (i.e., the number of times the optimization function F will be evaluated) and grid calculation efforts will be neglected. So,

$$E_{\text{All Methods}} = N^d \times N_s \quad (4)$$

It will be shown that reducing the search volume is very counterproductive regarding *RoI*. If search volume is constant, then the bounding grids are not moving, and the vertex points and the edges remain fixed in position. Also to delay dimensionality explosion, function is not evaluated at face and edge points, but calculated from values at vertex points (i.e., by interpolation). Hence the calculation effort becomes,

$$E_{\text{Constant Volume}} = 2^d + N_{\text{Body}}N_s = 2^d + (N-2)^d N_s \quad (5)$$

3.1 The Non-Adaptive Random Search. Here all the N^d search points are generated randomly and it is hoped that at least one of the search points will hit the subregion of size ϵ^d that contains the optimum point. In this method the information that comes from a point hitting a significant region (SR) is totally ignored and the next search point is independently generated. A significant region is the region in the solution space, which, when hit by a search point, will lead the search to the optimum O.

Gottfried and Weisman (1973) derive the following coupling:

$$P_{\text{Non-Adaptive Random}} = 1 - (1 - \epsilon^d)^{N^d \times N_s} \quad (6)$$

3.2 The Non-Random Adaptive Grid Search

3.2.1 The Basic Search Strategy. The underlying principles are very simple. A subspace A of solution space S is selected (Fig. 2). A is itself subdivided into $(N-1)^d$ subregions by N grid planes cutting each of the d dimensions. The strategy is as follows:

1 Start with A equal to S.
2 Grid the space enclosed by A. The initial order of the grid planes need not be regular, i.e., the subregions of A do not have to be equal sizes to begin with.
3 Evaluate F at all the grid points and select the best point. This implies that we have selected a number of best subregions that surround this point. The exact number of subregions affected depends on the type of best point as given in Eq. (3).
4 Adapt the position of the grid planes toward this best point. This implies that after grid adaptation, both the volume of A and of the affected subregions are reducing.
5 Repeat steps (2) and (3) until the grid planes are so close together that the size of the best subregions is equal or less than ϵ^d. The optimum is now found to within an error radius of ϵ^d.

Note: In step (5), if search volume is constant (i.e., vertex points and edges are fixed in space) and if d is high, then in order to delay the dimensionality explosion, re-evaluate function *only* at body points. The rest of the points can then be evaluated by interpolation using the function values at body and vertex points.

3.2.2 The Coupling Relations for the Non-Random Adaptive Grid Method. It is possible to derive the coupling relations if we have a robust definition for stepwise success of each adaptation step. Our definition will be robust if on the basis of this definition, it can be required that every step be successful to arrive at final true optimum.

Consider the following definition:

- Def1: A step is successful if and only if "the optimum O is located in one of the affected subregions of the selected best point *and* remains there after these subregions have been shrunk by the grid adaptation."

Accepting Def1 for a moment, it can be seen that every step need not be successful for overall success of the method. If the optimum O is not located in the affected subregions of the selected best point, it is possible that grid adaptation of this step will cause success in some future step.

The following definition of success has ultimate robustness:

- Def2: A step is successful if the selected best point hits a significant region (SR) of the function to be optimized. Significant regions are locations in the solution space, which will drive the search strategy to the true optimum, by the time the final step is completed.

In other words, Def2 says that if a step is 100 percent successful, then true optimum will be found after the final step is completed

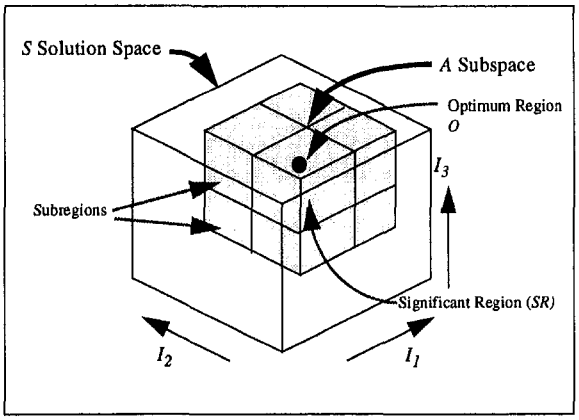


Fig. 2 Division of the solution space into the gridded region *A* and nongridded region. *A* decreases in size by a constant factor *F* after every step. *A* is subdivided into $(N-1)^d$ subregions (SR) of generally unequal size, where *N* is number of grid planes cutting each dimension.

Downloaded 02 Jun 2010 to 171.66.16.105. Redistribution subject to ASME license or copyright; see http://www.asme.org/terms/Terms_Use.cfm

(note: not vice versa). Let P_{step} represent the probability of success in the context of Def2. The overall search fails if step 1 *and* step 2 *and* . . . *and* step N_S fail. If we find a good estimate for P_{step} and consider each step to be an independent Bernouli trial then we can use the binomial distribution and the following logic to estimate probability of success after completion of the last step,

$$\therefore P_{\text{Adaptive Grid}} = 1 - \text{Prob (Zero Success After } N_s \text{ Steps)}$$
$$= 1 - (1 - P_{step})^{N_s} \quad (7)$$

If P_{step} is not constant in every step then,

$$P_{\text{Adaptive Grid}} = 1 - (1 - P_{\text{step}_1}) \times (1 - P_{\text{step}_2}) \times \ldots \times (1 - P_{\text{step}_{N_s}}) \quad (8)$$

If no prior information is available about F and O, then conditions of Def2 cannot be tested. Instead Def1 is used to estimate the success of Def2, realizing that the resulting relations underestimate *RoI*. The resulting step success is then (fully derived by Shahroudi, 1994b):

$$P_{\text{step}_J} = f^J \times P_{\text{grid}} \times K \quad (9)$$

where $P_{\text{grid}} = \{2^d(1 - 2^{d-1}) + d2^d(N - 2)(1 - 2^{d-2}) + 2^{d-1}(N - 2)^d + 2^{d-1}N^d\} + \{(N^d(N - 1)^d\}$ is the gridding term, $K = (\epsilon(N - 1))^{d/N_S}$ is the shrinkage factor of the best subregion, f is constant shrinkage factor of gridded subspace A, and J is the step index.

Equations (4), (8), and (9) define the coupling fully for a general adaptive grid search where the gridded search volume is reducing in size and the best subregions are shrunk. Variations on the search method are produced by setting particular values to some terms, e.g.,

- Setting $K = 1$ represents a shrinking A method where the best subregions are not given bias.
- When $N = 2$, the middle term becomes unity. Setting $K = 1$ and $N = 2$ represents a method where the search volume (which is not subdivided into subregions) is shrinking.
- Setting $f = 1$ represents a method where the search volume remains as large as the total solution space.

For $N = 5$, $d = 5$, $\epsilon = 0.01$, $f = 0.9$, $N_S = 40$, the relations above yield $K = 0.6687$, $P_{\text{grid}} = 0.01565$. The first term (RHS of Eq. (9)) is the contribution of reducing the size of the search volume A. Like all three terms, its effect is to reduce the success of the each step; however it becomes more and more penalizing as the search continues (i.e., as the value of J increases). In the sample case, although the starting value of f is quite high, after 30 steps its magnitude reduces to 0.0424. The increasing penalization then accumulates, resulting in very low overall probability of success for a given N_S and N. The only way to counteract this effect is to use a value of f close to unity, implying that the search points must be generated in *all* of the solution space in each step. Therefore,

- Any NGG technique based on reducing search volume is doomed!

This conclusion, however, does not hinder the possibility of increasing the concentration of search points in a particular region, as long as enough search points are generated to cover the total solution space.

The middle term is the contribution of the gridding to the stepwise success, P_{Grid}. Evaluating P_{Grid} for various values of d and N gives the perhaps surprising result that P_{Grid} increases as the number of grid lines N decreases! The reason is that the adaptive grid tries to find the optimum in the final step and not immediately in one go. The less the grid lines, the larger the affected subregions of the selected best point, and therefore the smaller the chance that the selected best point will miss the SR. Setting f to unity in Eq. (9) makes the step success constant for every step. Using this in Eq. (7) gives a measure of the overall success for the general adaptive grid method,

$$\boxed{P_{\text{Adaptive Grid}} = 1 - \{1 - P_{\text{grid}}K\}^{N_S}} \quad (10)$$

If the grid is randomly generated (rather than decisively) then there is no guarantee that the required shrinkage will be achieved, and more steps will be needed to reach solution. See section 3.5 for definition of the break-even point.

3.3 Grid Adaptation Using Imaginary Flexible Beam. For a given grid system and calculation effort (i.e., given N, d, and N_S), the only way to influence the overall success is through the shrinkage factor K. For simplicity in derivation of Eq. (10), K was assumed to remain constant with steps. The resulting coupling relation (10) is then independent of the actual way in which the grids are adapted.

It can be argued (Shahroudi, 1994b) that for best *RoI*

- Grid adaptation should be relatively slow during the early and final steps of the search. It can then be relatively faster in the intermediate stages to make up for lost time, given N_S.

Deflection properties of an imaginary flexible beam are used to adapt the grid positions conforming to the above rule (see Fig. 3). The deflected shape of the beam is calculated by superimposing two sinosoidal curves and a straight line. Shahroudi (1994b) gives the grid adaptation equation (or the "beam equation") for the Jth step and the kth dimension:

$$I_{k_{\text{new}}} = I_{k_{\text{old}}} + J\frac{1 - \epsilon(N - 1)}{\pi N_S}\left[S_1 l \sin\left(\frac{\pi}{l} I_{k_{\text{old}}}\right) + S_2(1 - l)\sin\left(\pi\left(\frac{I_{k_{\text{old}}} - l}{1 - l} + 1\right)\right)\right] \quad (11)$$

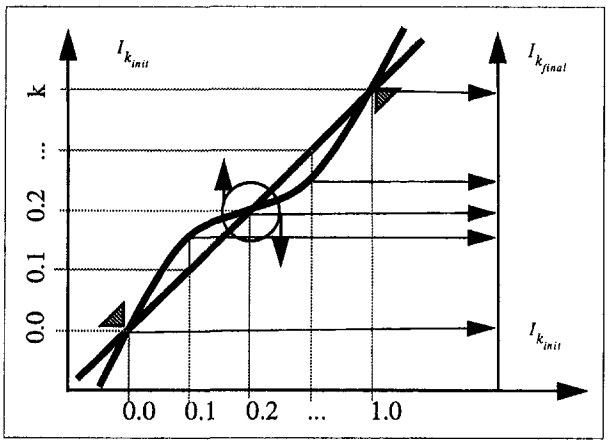


Fig. 3 Concentration of grid lines near a favored point. An imaginary, straight, and weightless flexible beam is used along each independent direction in the solution space in order to define the relation between old and new grid positions. At a favored point where it is required that the grid lines be closer together, a couple is applied to the beam. The resulting deflection of the beam is immediately calculated from the imaginary "beam equations." The deflected beam is then used to get new grid positions.

Downloaded 02 Jun 2010 to 171.66.16.105. Redistribution subject to ASME license or copyright; see http://www.asme.org/terms/Terms_Use.cfm

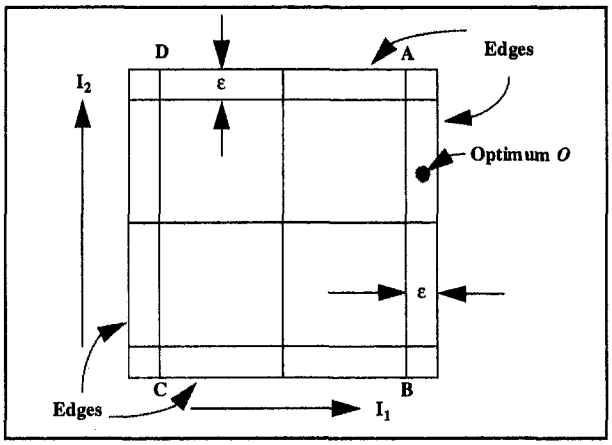


Fig. 4 A two-dimensional view of the minimum gridding. The starting position of the gridding is significant. Suppose optimum *O* falls between the edge and the preceding grid line. If best point is chosen on the edge grid of I_1 then the preceding grid line can adapt and move toward *O*. If the best point is chosen on the *AB* line, then *AB* and the edge cannot get closer due to the "beam equations." Therefore the grid line *AB* is initially placed a distance ϵ from the edge.

$$\text{where} \quad S_1 = \begin{cases} 1, & \text{If } (0.0 \le I_{k_{\text{old}}} \le l) \\ 0, & \text{If } (l \le I_{k_{\text{old}}} \le 1.0) \end{cases} \quad \text{and} \quad S_2 = !S_1.$$

3.4 Practical Issues. Basically a choice of N and N_S must be made such that the calculation effort E will be a minimum to satisfy the required probability and accuracy for optimization of a d dimensional function F. Equation (4) suggests that for large d, calculation effort is extremely sensitive to N as opposed to N_S.

Given (N, ϵ, d), N_S can be increased in order to increase P (Eq. (10)). However there is a maximum meaningful value of N_S beyond which all the grid lines have converged and cannot converge further, thereby limiting the maximum achievable P. Stated simply,

- Minimum calculation effort is achieved by choosing minimum N, as long as the necessary N_S remains meaningful.

Further there is a minimum value for N that is still meaningful. If the total search volume is to remain constant then we need two grid lines at $I_k = 0$ and $I_k = 1$ along each dimension k that will not move.

Then at least two more grid lines are necessary to contain the optimum in each dimension. So the basic minimum number of grid lines necessary to give adaptation meaning is,

$$N_{\min} = 4 \tag{12}$$

Note: For low values of d (e.g., 5), it is possible to use a higher number of grid lines (i.e., $N = 5$) before dimensionality explosion sets in.

The starting position of the grid lines is also important. Initially a grid line is placed at a distance of ϵ from each edge, to avoid grid adaptation failure in case O is very close to the edge, as shown in Fig. 4. Further, there is a minimum limit on N_S below which the grid adaptation is too fast in the beginning and final steps, i.e., $N_{S_{\min}} < N_S < N_{S_{\max}}$. (Shahroudi, 1994b, quantifies the bounds on N_S).

$$N_{S_{\min}} = \frac{1+\sqrt{1-H}}{2H}, H = 2 \times \left(1 - \frac{1}{\left(1+\epsilon^{2/3}\left(\frac{\pi^2}{6}\right)^{1/3}\right)^2}\right)$$

$$N_{S_{max}} = \frac{1+\sqrt{1-H}}{2H}, H = 2 \times \left(1 - \frac{1}{\left(1+\frac{\epsilon^{0.61458}}{4.6281}\right)^2}\right) \tag{13}$$

3.5 The Effect of Randomness on Adaptation (Break-Even Point). In the adaptive random search, the search points are generated randomly and initially equally distributed in the solution space (S). Then a best point is chosen and the next set of search points is more likely to fall near the old best point. A new best point is then selected and the procedure continued until the concentration of search points near the best point is high enough to satisfy the accuracy requirements.

If we keep N and N_S the same between the random and non-random grid generation, then the adaptive random search can be considered fundamentally the same as the non-random adaptive search with the exception that the search points are randomly generated and it is not possible to achieve shrinkage K decisively. In other words, the search points are likely to follow shrinkage as desired; however, this is not guaranteed and some points may fall outside of the desired subregion. Hence the coupling relations for the non-random method can be used with substitution of K_{EX} (expected shrinkage) instead of the required shrinkage K. Further, if the shrinkage is different, then the final best subregion will not have the required size ϵ^d, which needs to be taken into account. K_{EX} and ϵ_{EX} are derived by Shahroudi (1994b):

$$K_{EX} = \frac{m}{M} \frac{\left(\frac{M \times \epsilon^d}{m}\right)^{1/N_S} (N-3)^d}{(1-\epsilon)^d}, \quad \epsilon_{EX} = \frac{K_{EX}^{N_S/d}}{N-1} \tag{14}$$

giving

$$P_{\text{Random Adaptive Grid}} = [1 - (1 - P_{\text{Grid}} K_{EX})^{N_S}] \times \left(\frac{\epsilon}{\epsilon_{EX}}\right)^d \tag{15}$$

The term m/M accounts for the degree of randomness in generation of search points and varies in the range (see Shahroudi, 1994b):

$$\left.\frac{m}{M}\right|_{\text{Fully Random}} \le \frac{m}{M} \le \left.\frac{m}{M}\right|_{\text{Minimum Random}} \rightarrow$$

$$\frac{2^d}{(N-2)^d} \le \frac{m}{M} \le \frac{2}{(N-2)} \tag{16}$$

It is now possible to derive the break-even point between the random and the non-random cases by equating the shrinkage factors of the two methods, and extracting the break-even value of N_S,

$$K_{EX} = K = \{\epsilon(N-1)\}^{d/N_S} \tag{17}$$

Substituting for K_{EX} from Eq. (12) and rearranging gives:

$$N_{S_{\text{Break Even}}} = \frac{\log\left((N-1)^d \frac{m}{M}\right)}{\log\left(\frac{m}{M}\frac{(N-3)^d}{(1-\epsilon)^d}\right)} \tag{18}$$

Above this break-even point, the non-random adaptive grid is advantageous as compared with its random opponent. Simulations have shown that $N_{S_{\text{Break Even}}}$ is usually very low (e.g., ~3), far less than $N_{S_{\min}}$. Small values of N_S represent very low values of probability. Therefore,

- If any significant measure of probability is required, then the non-random adaptive grid gives much better return (or probability) on investment (or calculation effort) for a given required accuracy.

Downloaded 02 Jun 2010 to 171.66.16.105. Redistribution subject to ASME license or copyright; see http://www.asme.org/terms/Terms_Use.cfm

4 Variations of the Basic Theme

4.1 Inclusion of Constraints in the Search Strategy. Inclusion of any type of inequality constraint (e.g., linear, nonlinear, constraints on independent and/or dependent variables) is very simple to include since the strategy here is a NGG search. In order to include any kind of inequality constraints, it is sufficient to state,

- The best point is the best grid point that offers the best F and that does not violate any constraints.

Another variation is to set up penalty relations for not satisfying the constraints, then selecting the grid point where the least penalty might eventually lead to optimum,

- If none of the grid points currently satisfy the constraints, then the current best point will be the least offender.

In practice, equality constraints can always be transformed into inequality constraints because in the physical world, there is usually a sense in which the equality is meant.

4.2 Multiple Optima. Having found the true optimum O of function F, the rest of the optima (O_1, O_2, . . . etc.) are found by repeating the same procedure as above with the following addition to the rule:

- The 2^d points immediately surrounding O are not allowed to be selected as the best point, because their selection will lead to O.

Once O and O_1 have been found, the procedure can be continued, but this time the points immediately surrounding O and O_1 are not allowed to be selected as best point, and so on.

If the number or the likely number of optima (N_{optims}) is known in advance, then the required probability can be set to the minimum value, which is just sufficient to distinguish O from O_1, O_2, . . . , $O_{N\text{optims}-1}$. In general,

$$P_{\text{Min Required}} = \epsilon^d + \frac{N_{\text{optim}} - 1}{N_{\text{optim}}} \tag{19}$$

The ϵ^d term is the minimum meaningful value for probability (Eq. (1)).

4.3 Independent Runs to Improve RoI. In cases where it is not important to estimate the *RoI* prior to starting the procedure, and particular knowledge exists that F is relatively simple (i.e., not very deceptive to search strategy), then it is possible to significantly increase *RoI* by running the non-random adaptive grid search with very low values of N_S, several times, independently, until at least two of the optima are the same.

If two or more independent runs yield the same optimum, then the probability that the true optimum is found is improved, namely,

$$P_{\text{Coalesce}} = 1 - (1 - P_{\text{independent}})^{N_{\text{Coalesce}}} \tag{20}$$

e.g., if two independent optima coalesce with individual $P = 0.90$, then the probability that solution is correct is heavily increased; if $P = 0.90$, then the combined value is $P = 1 - (1 - 0.90)^2 = 0.99$. This approach requires that the starting positions of the grids be totally independent between separate runs.

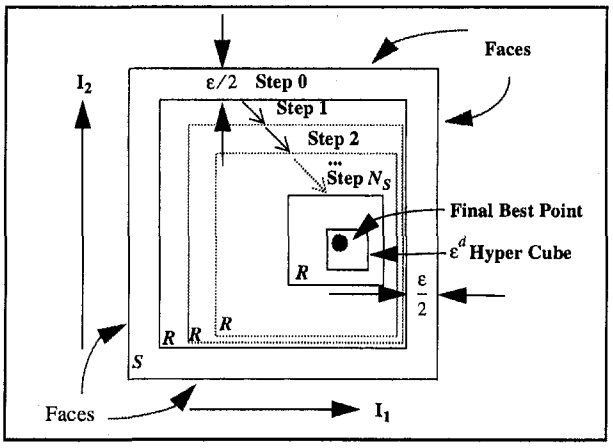


Fig. 5 In the random adaptive grid the search points are initially distributed equally in the solution space S. But as the search goes on, the distribution of the search points become more and more concentrated in some area. This can be visualized by imagining the maximum likelihood hypercube R to be decreasing in size as shown. R is the region where search points are $(1 - \epsilon)^d$ likely to fall.

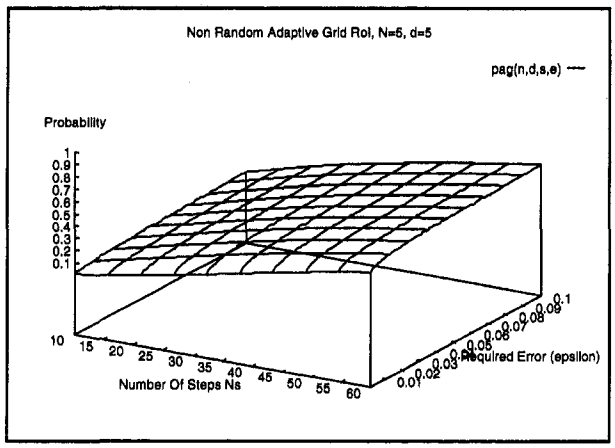


Fig. 6 The *RoI* for the non-random adaptive grid increases with number of steps and the required error

5 Results

It is very difficult to find a practical basis for comparison of various optimization techniques. If we take a sample multidimensional function F and show that the non-random adaptive grid offers orders of magnitude better *RoI*, then it can always be argued that F was a special case, resulting in no general conclusions. Conclusive practical proof would need a large number of significantly different F's, which is beyond this report.

General theoretical comparisons are also difficult because many popular optimization techniques do not provide a measure of *RoI*. The relations developed above provide basis for comparison between the random and the non-random adaptive grid.

Figure 6 shows the obvious that certainty in the optimum found improves as more calculation effort is spent and as the required accuracy diminishes.

The adverse effect of increasing dimensionality is illustrated in Fig. 7. Increasing the dimension of F from 5 to 15 increases the calculation effort by 100.

Figure 8 shows that the non-random adaptive grid is orders of magnitude superior to the random adaptive grid if any significant certainty in the found optimum is required.

The minimum number of grid lines in each dimension is 4 (Eq. (4)). For problems with relatively low dimensions, higher values of N can be used to increase confidence, without adding too much to the calculation effort. Although the relations already give an indication of how good the optimum is (i.e., a P value), we recognize that the relations are approximate and any increase in confidence is appreciated. Figures 9 and 11 show the effect of using different numbers of grid lines.

The allowable range of values for N_S decreases as the required accuracy decreases (Fig. 10). The upper bound on N_S (Eq.

Downloaded 02 Jun 2010 to 171.66.16.105. Redistribution subject to ASME license or copyright; see http://www.asme.org/terms/Terms_Use.cfm

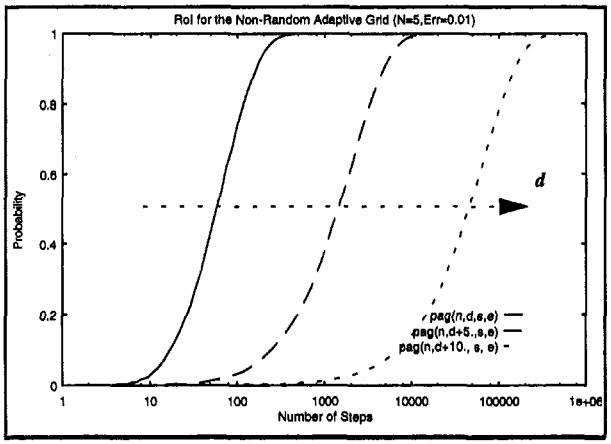


Fig. 7 The effect of dimensionality on *RoI* for the non-random adaptive grid

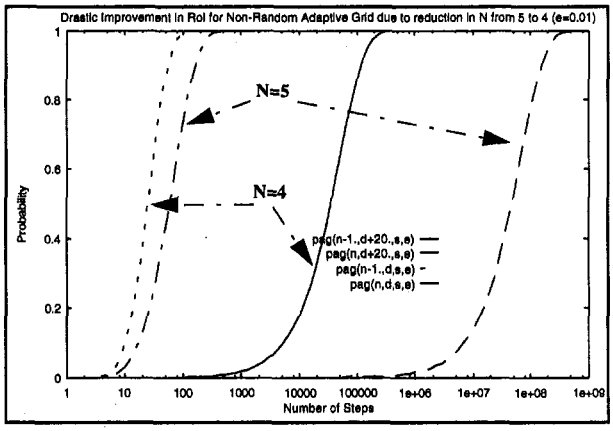


Fig. 9 Effect of *d* and *N* on *RoI*

(13)) is not a serious constraint and can be violated, as long as the starting positions of the grid lines are adjusted so that the grid lines do not become fully concentrated before the final steps are reached. For example, suppose $N_S = 50$ is necessary with $\epsilon = 0.01$. Figure 10 shows that this N_S value is too high. However, $N_S = 50$ is allowed if the starting position of the *AB* and *CD* grid lines (Fig. 4) is 0.002 from the edges instead of 0.01.

6 Discussion

Def2 forms the basis of the relations derived. At first sight it may falsely appear that it is a "circular" definition or that success of each step depends on the success of the previous step. If step successes are interdependent then they cannot be considered as Bernouli trials, making the derivations false.

The key here is the definition of step success. A step is 100 percent successful if the selected best point falls in a SR. If the selected best point does fall in a SR, there is no guarantee/implication that the best point chosen during the next step will also fall in a SR. The only implication or guarantee is that solution will be found in the final step. SR or SRs could be of any size or shape and could be anywhere in the solution space.

So the event considered here is the event of a selected best point falling in a SR. Step success is the probability of this event. These successive events are in general totally independent of each other. The event of selected best point falling in a SR gets no influence from the grid adaptation mechanism that relates successive steps. Of course grid adaptation in one step influences the position of the grids in the following step, but this does not imply anything about grid points falling in SR in this step that follows, because no information is known about function behavior prior to solution.

100 percent step success is a special case. Here the probability of success of the following steps becomes insignificant, because final solution is guaranteed, i.e., when a selected best point falls in a SR, it is not important whether the following points will also fall in SR during the next step.

Unfortunately, it is impossible to quantify step success as defined by Def2. Here then the condition in Def1 is used to estimate the value of step success in Def2. So the logic behind the derivations is Def2. The consequence of using Def1 to estimate step success is to get a conservative estimate of overall P. In other words, the overall success of the method is better than that given by the coupling relations.

It is natural to think that behavior of constraints or functions will affect the probability of overall success of a search method. This is usually true for iterative and/or gradient-based methods, which can either be totally fooled by the behavior of function and/or constraints or will require a longer time (i.e., larger number of steps) before they home in onto the solution. In the adaptive grid methods, however, this is the wrong way to think because the number of steps is fixed in advance and the search method could not care less how badly the function and constraints behave, as long as the function and constraints can be evaluated.

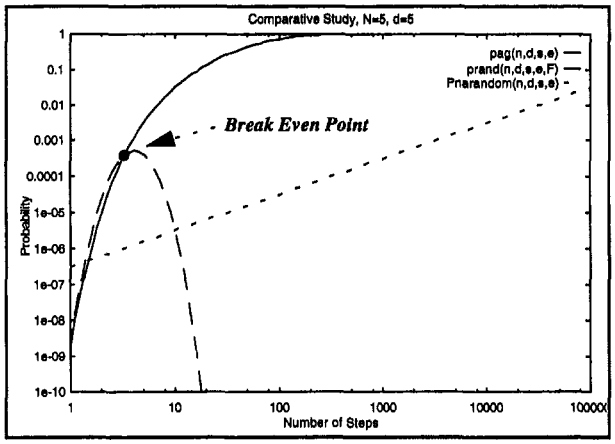


Fig. 8 Comparison of *RoI* between the non-random adaptive grid (solid), the adaptive random (dashed), and the simple random (dotted) search techniques

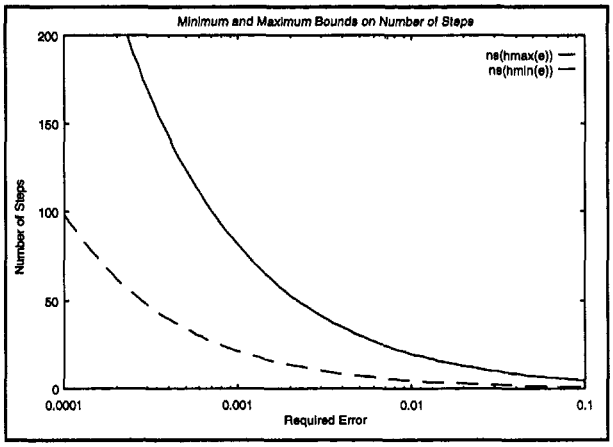


Fig. 10 Maximum (solid) and minimum (dashed) constraints on the number of steps as function of required error

Downloaded 02 Jun 2010 to 171.66.16.105. Redistribution subject to ASME license or copyright; see http://www.asme.org/terms/Terms_Use.cfm

7 Conclusion

The return of investment (*RoI*) (i.e., the coupling between probability, accuracy, and calculation effort) is a big issue in optimization in general. In developing modern, high-speed design, analysis, or modeling systems where all the various tasks are carefully matched and tuned to give a high-speed overall system, it is extremely important to have a quantitative measure of this coupling prior to starting the solution procedure, if optimization is an "in the loop" event.

It is possible to derive the full *RoI* relations analytically for the non-random adaptive grid search and further modify them to represent random adaptive grid with various degrees of randomness. The following conclusions can be drawn from this theoretical study:

1. Reduction of search volume (e.g., in the simplex approach) increasingly penalizes step success as solution proceeds and therefore heavily reduces the overall *RoI*.
2. Any degree of randomness in generation of search points causes the shrinkage of the best region to occur less decisively. This translates to very poor *RoI*.
3. Grid adaptation should be relatively slow during the early and final steps of the search. It can then be relatively faster in the intermediate stages to make up for lost time.
4. Deflection properties of flexible beam can be used to adapt grid position complying with previous step.
5. The analytical relations for the break-even number of steps suggest, that if any significant level of probability is required, then the non-random adaptive grid gives orders of magnitude better *RoI* than the random adaptive grid.

NGG search techniques have gathered a bad reputation in the past regarding calculation effort, because they were usually based on reduction of search volume and/or random generation of search points. The non-random adaptive grid search provides a fresh alternative to traditional NGG search and becomes especially appealing in cases . . .

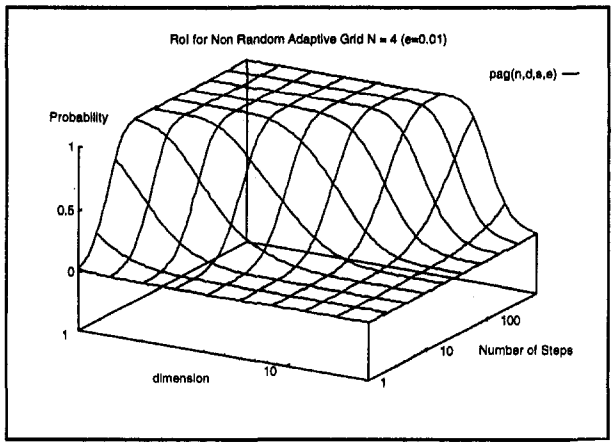


Fig. 11 ***RoI*** **for the non-random adaptive grid with** $N = 4$ **instead of 5**

- where the computation time to evaluate F is very small, so that NGG search is far less time consuming than following an elaborate gradient guided or direction set search.

References

Gottfried, B. S., and Weisman, J., 1973, *Introduction to Optimization Theory,* Prentice Hall, Englewood Cliffs, NJ.

Press, W. H., Flannery, B. P., Teukilsky, S. A., and Vetterling, W. T., 1989, *Numerical Recipes in Pascal: The Art of Scientific Computing,* Cambridge University Press, Cambridge, United Kingdom.

Shahroudi, K. E., 1994a, "A Modern Computer-Aided Approach to Conceptual/Preliminary Design of Gas Turbines," ASME Paper No. 94-GT-458.

Shahroudi, K. E., 1994b, "Development and Validation of a Computer Assisted Design Methodology for Gas-Turbine-Based Aircraft Engines," PhD Thesis, Delft University Press, ISBN 90-407-1070-8.

Sugiyama, 1990, "Generalized High-Speed Simulation of Gas Turbine Engines," ASME Paper No. 90-GT-270.

Downloaded 02 Jun 2010 to 171.66.16.105. Redistribution subject to ASME license or copyright; see http://www.asme.org/terms/Terms_Use.cfm

N. R. Osborne

G. A. Graves

Metals and Ceramics Division,
University of Dayton Research Institute,
Dayton, OH 45469

M. K. Ferber
High Temperature Materials Laboratory,
Oak Ridge National Laboratory,
Oak Ridge, TN 37831

Dynamic Fatigue Testing of Candidate Ceramic Materials for Turbine Engines to Determine Slow-Crack-Growth Parameters

The purpose of this study was to evaluate the mechanical strength and slow-crack-growth parameter values for two commercially available silicon nitrides, SN-88 and NT164, at three high-temperature conditions. Weibull analysis and dynamic fatigue slow-crack-growth parameters were used to characterize the material strength and resistance to slow crack growth at high temperatures for use in life prediction models. Although both materials are commercially available Si_3N_4, their high-temperature behavior was found to be significantly different.

Introduction

Over the past few decades silicon-based ceramic materials, such as silicon nitride and silicon carbide, have shown promise as potential candidates for advanced heat engine application. These materials have high strength, and good oxidation and thermal shock resistance. The use of these materials offers a number of advantages including higher temperature operation, decreased weight, greater efficiency, lower life-cycle cost, and reduced dependency on the use of strategic materials.

Many companies have been involved in the development of improved Si_3N_4 materials. Because of limited characterization information, these materials have found limited application as structural components in the hot section of prototype and demonstration engines. For silicon nitride to become a reality for its intended applications, a number of requirements must be met, namely, the development of reliable overall life-prediction methodology, appropriate test methods, and demonstration of feasibility for ceramic component design.

Background

Under applied stress, brittle materials exhibit a wide variability in strength. When macroscopic applied stresses reach critical values at crack tips, rapid and catastrophic failure will occur. The strength of brittle components can thereby be related to the flaw populations that are distributed on tensile surfaces, within the bulk, or along the edges of ceramic parts.

The Weibull two-parameter distribution is most often used to characterize the strength distribution of brittle materials [1]. The two physical constants determined using the Weibull model are the scale parameter, σ_o, and the Weibull modulus, **m**. The scale parameter is used to perform a normalizing function, and the Weibull modulus reflects the degree of variability in strength—the higher the **m** the less variability in the strength. Values of 5 to 20 for **m** are typical for ceramic materials [2].

The two-parameter Weibull model is determined using the maximum likelihood method. The maximum likelihood approach provides a means of determining the statistical error values for the test parameters and is somewhat less conservative than a linear regression technique [3].

Many brittle materials are susceptible to slow crack growth, or static fatigue, while under tensile load in a corrosive environment. The crack growth rate can be expressed as a power law relationship with the stress intensity level, K_I, described by

$$v = v_0\left(\frac{K_I}{K_{Ic}}\right)^n = AK_I^n \tag{1}$$

where v_0 and A are material constants, and $K_{Ic} = Y\sigma_a c^{1/2}$. For semicircular flaws located at the surface of a brittle component, $Y = 2.24/\pi^{1/2}$. The constant n is a measure of the stress corrosion susceptibility of the material and is determined from the slope of the ln stressing rate versus ln median strength plot

$$n = \left(\frac{1}{\text{slope}}\right) - 1 \tag{2}$$

and B, the alternative second crack growth parameter, is given by

$$B = \frac{2}{(n-2)AY^2K_{Ic}^{(n-2)}}. \tag{3}$$

To determine the dynamic fatigue, strength measurements at two or more constant stress rates combined with a knowledge of the intrinsic strength are needed for the evaluation of n and B. The variability in n depends on the fatigue resistance of the material, and large n values generally represent materials with greater fatigue resistance [4].

Experimental Procedure

Two sets of 150 test-ready flexure bars of each material were supplied to the University of Dayton Research Institute (UDRI) by Oak Ridge National Laboratory for dynamic fatigue testing. The materials, SN-88 and NT164, were produced by NGK, Nagoya, Japan, and Norton Advanced Ceramics, St. Gobain/Norton Industrial Ceramics, East Granby, CT, respectively. The test specimens were used to characterize the flexural strength of the materials based on the results of experimental evaluation of four groups of ten specimens at each of four stressing rates for three different test temperatures.

The flexural strength was measured using SiC four-point bend fixtures in a universal testing machine[1] following ASTM C1161-

Contributed by the International Gas Turbine Institute and presented at the 40th International Gas Turbine and Aeroengine Congress and Exhibition; Houston, Texas, June 5–8, 1995. Manuscript received by the International Gas Turbine Institute March 2, 1995. Paper No. 95-GT-235. Associate Technical Editor: C. J. Russo.

[1] Instron model 1123A with 1000 pound load cell and 500 pound range, Instron Corp., Canton, MA.

Copyright © 1997 by ASME

Downloaded 02 Jun 2010 to 171.66.16.105. Redistribution subject to ASME license or copyright; see http://www.asme.org/terms/Terms_Use.cfm

Table 1 Flexural strength measured for NGK SN-88

Test Temperature °C	Crosshead Speed in/min	Atmosphere	Number of Tests	Weibull Modulus *m*	Weibull Scale Parameter σ_o	Median Strength σ_m	Dynamic Fatigue Shape Parameter n	Dynamic Fatigue Scale Parameter B ($secMPa^2$)
20	0.2	Air	30	23	838	922		
1038	0.2	Air	10	25	703	693	-202.0	-7×10^{30}
	0.02	Air	10	26	682	672		
	0.002	Air	10	38*	699	692		
	0.0002	Air	10	42	721	715		
1150	0.2	Air	10	21	697	685	392.3	9.8×10^{-50}
	0.02	Air	10	16	671	656		
	0.002	Air	10	23	679	669		
	0.0002	Air	10	25	679	669		
1350	0.2	Air	10	42	641	635	-51.8	-1×10^{13}
	0.02	Air	10	23	667	656		
	0.002	Air	10	18	741	726		
	0.0002	Air	10	28	735	725		

90 (MIL-STD-1942 (MR)). Measurements at 1038°C, 1150°C, and 1350°C were conducted in a high-temperature furnace[2] adapted for use in the testing machine. The test specimens were 3 mm × 4 mm × 50 mm with the tensile surfaces ground and the long edges of the tensile surfaces rounded to minimize failures initiated by edge chips. Specimens were loaded at machine crosshead speeds of 2×10^{-1}, 2×10^{-2}, 2×10^{-3}, and 2×10^{-4} in/min (8.4×10^{-5}, 8.4×10^{-6}, 8.4×10^{-7}, and 8.4×10^{-8} m/s).

The Weibull parameter, **m**, and median strength, σ_m, were determined for each test condition, and dynamic fatigue was characterized by ln-ln plots of fracture strength σ_f versus loading rate ($\dot{\sigma}$), which is expressed by the relationship

$$\sigma_f = A'\dot{\sigma}^{(1/(n+1))} \tag{4}$$

where A' and n are material constants.

[2] ATS model 3320, Applied Test Systems Inc., Butler, PA.

Results and Discussion

The values determined for the Weibull parameter **m** and scale parameter, σ_o, using maximum likelihood regression for SN-88 are found in Table 1. The Weibull plots for the four stressing rates at each of the three temperatures used in this study are shown in Figs. 1–3. The dynamic fatigue plots for SN-88 generated from the Weibull results are shown in Fig. 4. Similar information for NT164 is found in Table 2 and Fig. 5–8. A comparison of the median strengths of the materials for all four machine crosshead speeds at the three test temperatures is shown in Fig. 9.

The Weibull modulus, **m**, for both materials was higher than expected. This may be attributed to the small number of specimens (10) tested for each temperature/loading rate condition. It is generally accepted that at least 30 specimens must be tested at each test condition before the results are considered statistically reliable.

The fast fracture strength of SN-88 from 20 to 1350°C decreased as the temperature increased. At 1038 and 1150°C SN-

Table 2 Flexural strength measured for Norton NT164

Test Temperature °C	Crosshead Speed in/min	Atmosphere	Number of Tests	Weibull Modulus *m*	Weibull Scale Parameter σ_o	Median Strength σ_m	Dynamic Fatigue Shape Parameter n	Dynamic Fatigue Scale Parameter B ($secMPa^2$)
20	0.1	Air	10	14	1134	1106		
1038	0.2	Air	10	15	768	749	405.5	1.5×10^{-70}
	0.02	Air	10	8	710	680		
	0.002	Air	10	17	760	744		
	0.0002	Air	10	25	724	713		
1150	0.2	Air	10	23	781	769	34.5	0.371
	0.02	Air	10	21	733	721		
	0.002	Air	10	28	688	659		
	0.0002	Air	10	17	645	631		
1350	0.2	Air	10	21	647	635	17.8	9.61
	0.02	Air	10	16	559	546		
	0.002	Air	10	12	500	486		
	0.0002	Air	10	20	432	424		

Downloaded 02 Jun 2010 to 171.66.16.105. Redistribution subject to ASME license or copyright; see http://www.asme.org/terms/Terms_Use.cfm

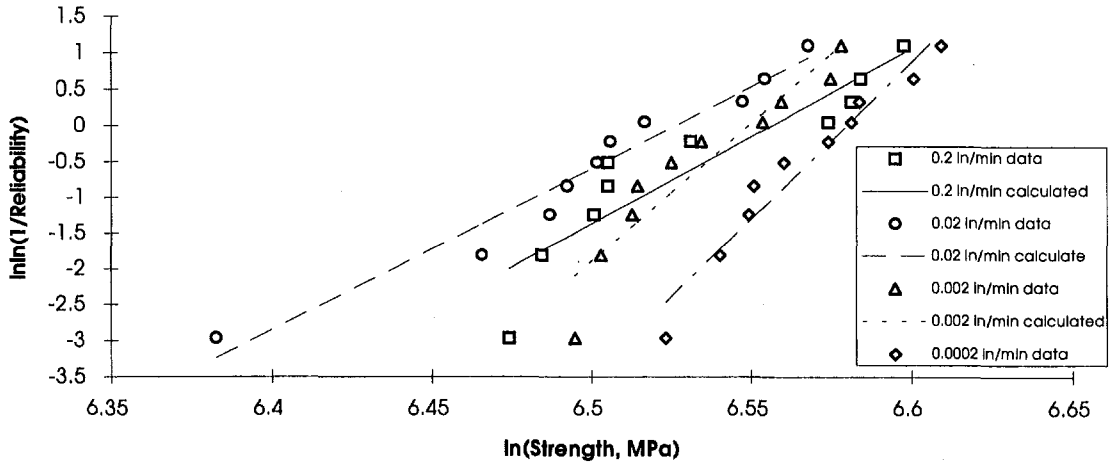


Fig. 1 SN-88 maximum likelihood probability plots for strengths measured at all four displacement rates and 1038°C

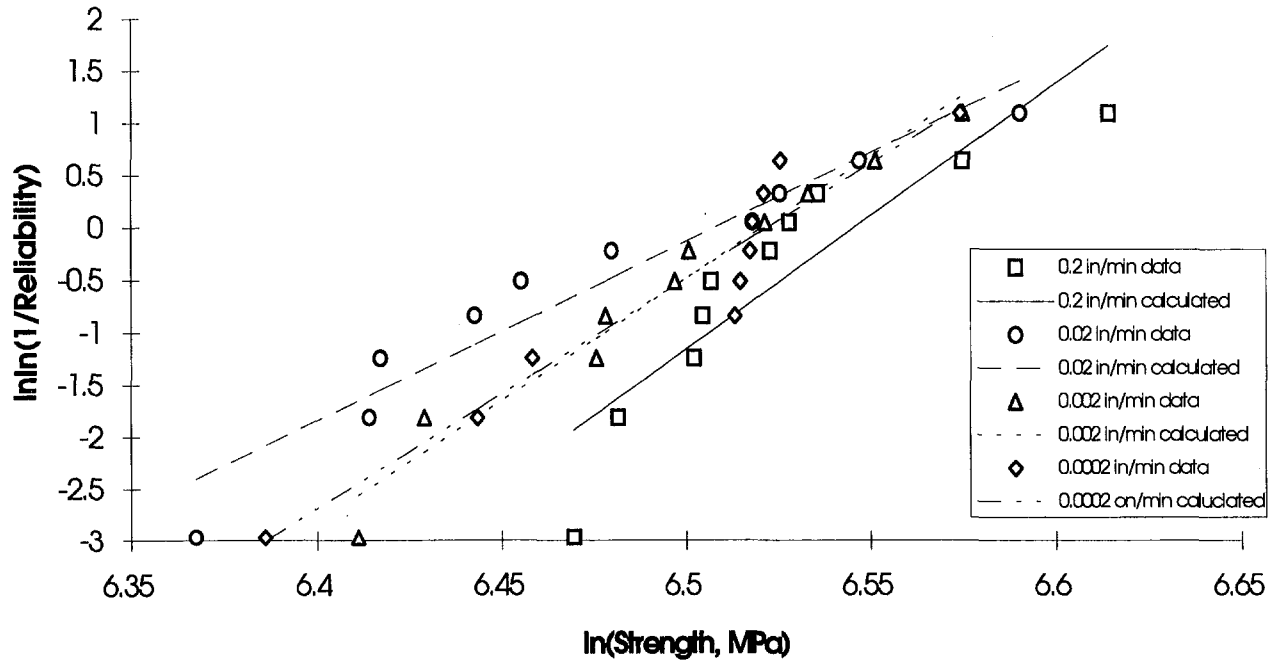


Fig. 2 SN-88 maximum likelihood probability plots for strengths measured at all four displacement rates and 1150°C

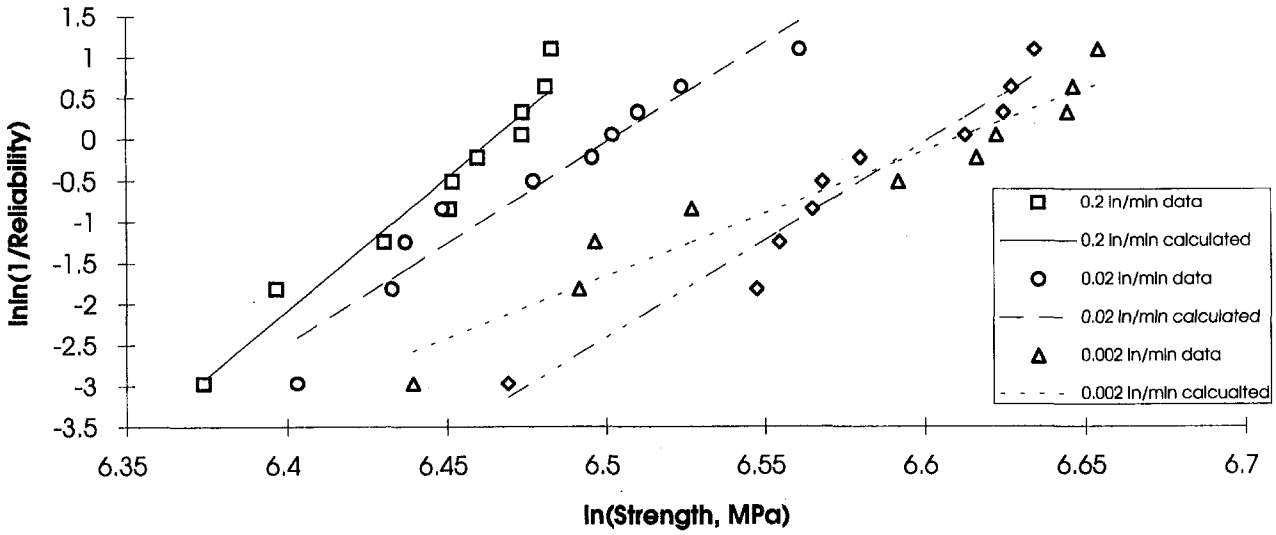


Fig. 3 SN-88 maximum likelihood probability plots for strengths measured at all four displacement rates and 1350°C

Downloaded 02 Jun 2010 to 171.66.16.105. Redistribution subject to ASME license or copyright; see http://www.asme.org/terms/Terms_Use.cfm

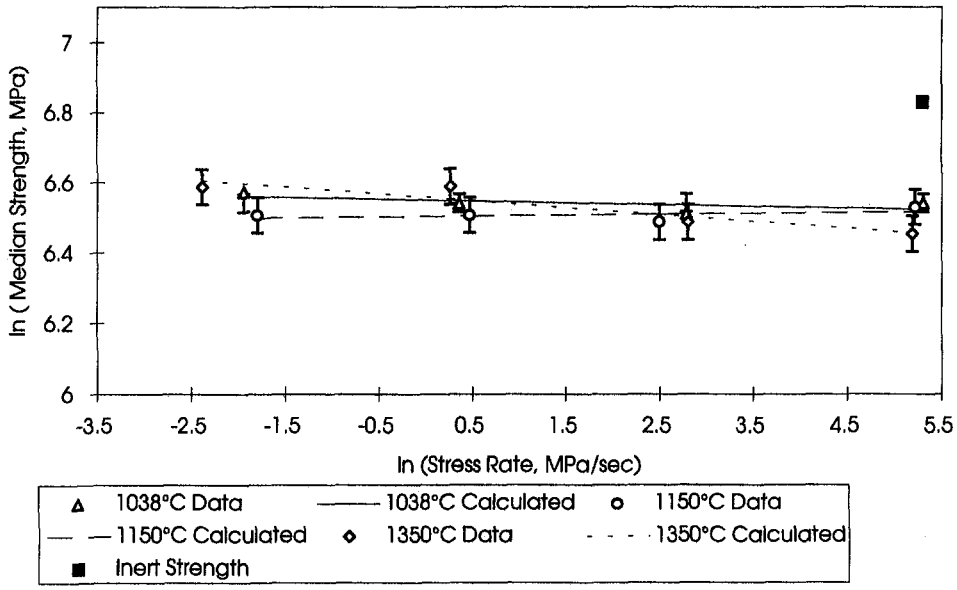


Fig. 4 SN-88 dynamic fatigue plots at all three test temperatures

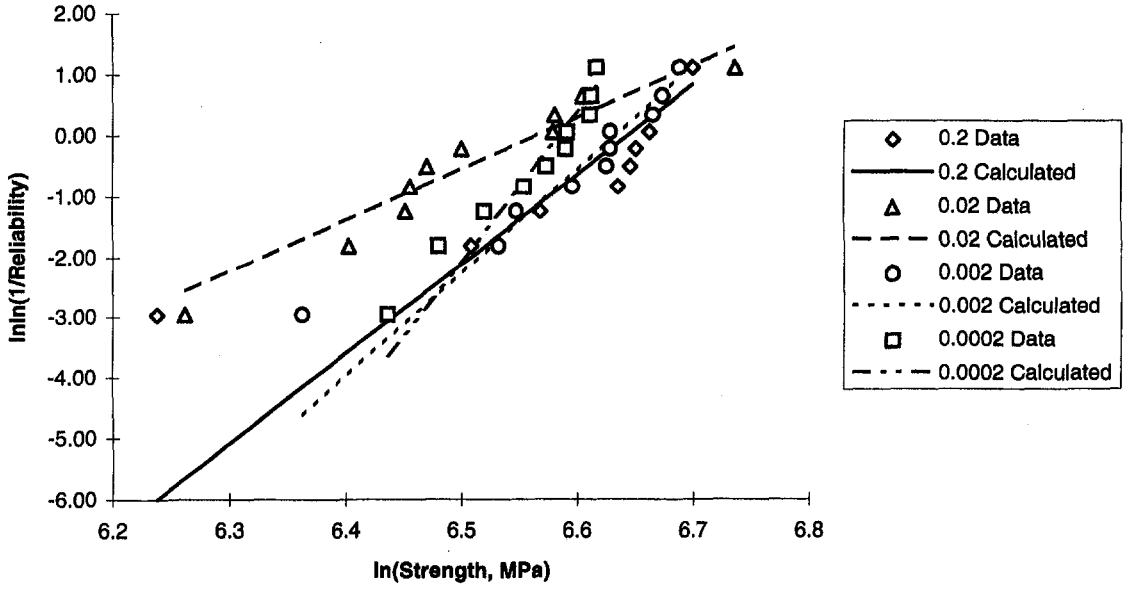


Fig. 5 NT164 maximum likelihood probability plots for strengths measured at all four displacement rates and 1038°C

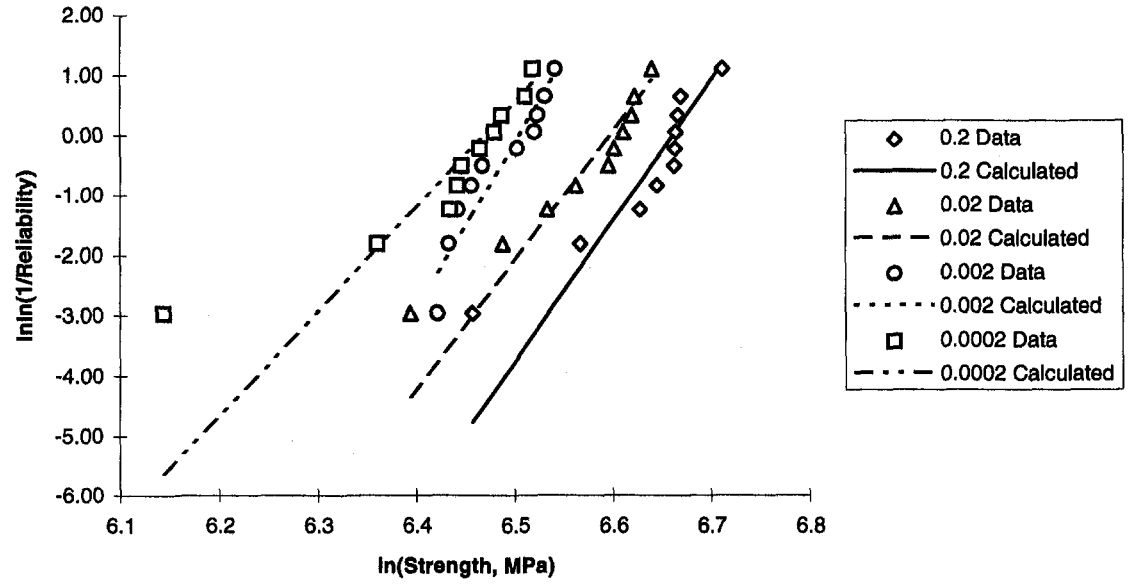


Fig. 6 NT164 maximum likelihood probability plots for strengths measured at all four displacement rates and 1150°C

Downloaded 02 Jun 2010 to 171.66.16.105. Redistribution subject to ASME license or copyright; see http://www.asme.org/terms/Terms_Use.cfm

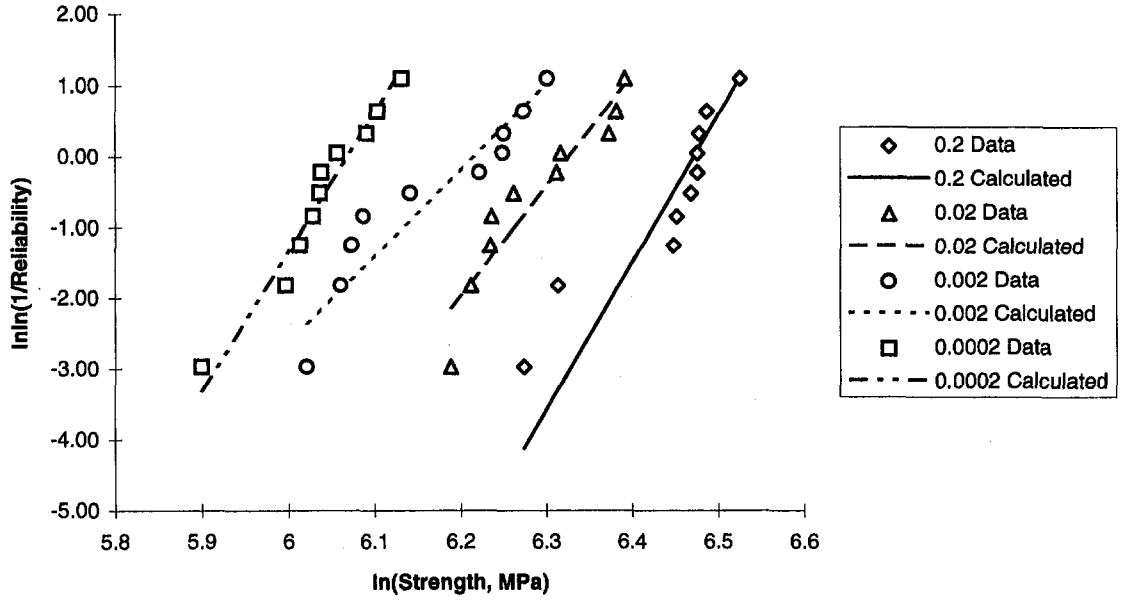


Fig. 7 NT164 maximum likelihood probability plots for strengths measured at all four displacement rates and 1350°C

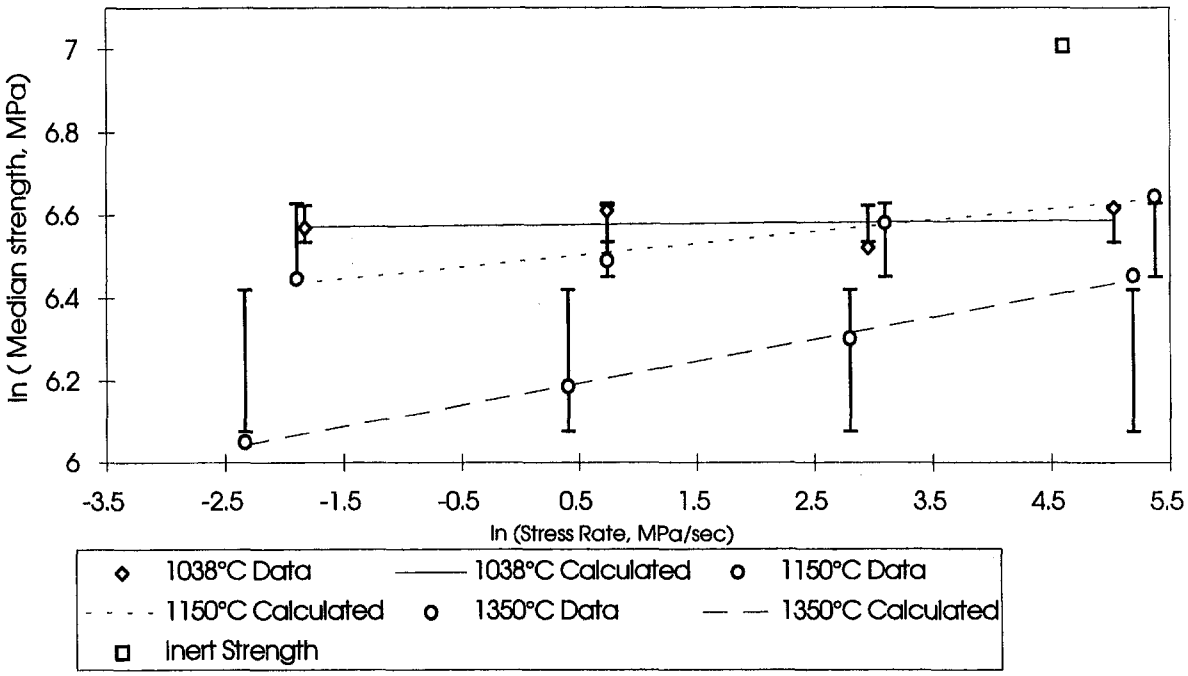


Fig. 8 NT164 dynamic fatigue plots at all three test temperatures

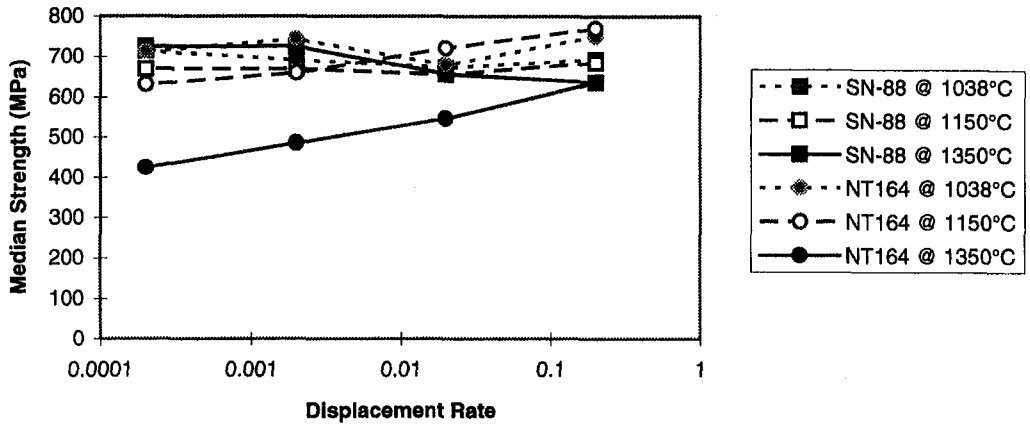


Fig. 9 Comparison of median strength for NT164 and SN-88

Downloaded 02 Jun 2010 to 171.66.16.105. Redistribution subject to ASME license or copyright; see http://www.asme.org/terms/Terms_Use.cfm

88 was not subject to slow crack growth. At 1350°C strength actually increased as the stressing rate decreased. Additions to this material produces an intergranular glassy phase, which may act to redistribute applied stress as it softens at the higher temperatures. This would account for both the negative n values and the relatively high median strengths found at the lower stressing rates.

Ritter et al. [5] suggest that variability in the values of n and B depends on the total number of samples tested, the stressing rate range, the Weibull parameter, and the fatigue resistance of the material. The statistical uncertainty in n can be very large for samples sizes much smaller than 100. It is recommended that before meaningful conclusions can be drawn regarding the effect of a test variable on n as measured by the dynamic fatigue data, the statistical reproducibility of n should be evaluated.

A significant drop in strength with increasing temperature was observed in NT164, and no effects of dynamic fatigue were seen at 1038 and 1150°C. At 1350°C a dramatic decrease in strength with decreased loading rate was observed. This was in sharp contrast with the SN-88 whose strength increased with decreasing loading rate.

Ongoing studies at UDRI indicate that the SN-88 material has much higher creep rates under identical conditions than the NT164. A fractographic evaluation of the materials at 1350°C at the lowest loading rate might provide the necessary information concerning the behavior of the two materials.

Conclusions

SN-88 was not subject to slow crack growth at 1038 and 1150°C. At 1350°C and above the material behavior indicated some type of stress relief. Stress redistribution due to softening of a glassy grain boundary phase might be occurring.

At 1150 and 1350°C NT164 was subject to slow crack growth behavior, while fast fracture strength from room temperature to 1350°C decreased as temperature increased. Although both materials are commercially available Si_3N_4, their high-temperature behavior is significantly different.

References

1 Weibull, W. "A Statistical Distribution Function of Broad Applicability." ASME *Journal of Applied Mechanics,* Vol. 18, 1951, pp. 293–297.

2 Davidge, R. W., *Mechanical Behavior of Ceramic: Cambridge Solid State Science Series.* Cambridge University Press, 1979.

3 Berens, A., personal communication, 1994.

4 Evans, A. G., "Fracture Mechanics Determinations," *Fracture Mechanics of Ceramics,* R. C. Grandt, ed., Vol. 4, Plenum Press, New York, 1978.

5 Ritter, J. E., Bandyopadhyay, N., and Jakus, K., "Statistical Reproducibility of the Crack Propagation Parameter N in Dynamic Fatigue Test," *J. Amer. Ceram. Soc.,* Vol. 62, No. 9–10, 1900, pp. 542–543.

Downloaded 02 Jun 2010 to 171.66.16.105. Redistribution subject to ASME license or copyright; see http://www.asme.org/terms/Terms_Use.cfm

S. Yang
Research Associate.
Assoc. Mem. ASME

R. F. Gibson
Professor.
Fellow ASME

Advanced Composites Research Laboratory,
Department of Mechanical Engineering,
Wayne State University,
Detroit, MI 48202

G. M. Crosbie
Research Scientist.

R. L. Allor
Research Engineer.

Ford Research Laboratory,
Ford Motor Company,
Dearborn, MI 48202

Thermal Cycling Effects on Dynamic Mechanical Properties and Crystallographic Structures of Silicon Nitride-Based Structural Ceramics

Thermal cycling effects on dynamic mechanical properties of hot pressed silicon nitride (HPSN) based structural ceramics were investigated in a simulated thermal cycling environment from room temperature up to 1100°C. Two monolithic silicon nitrides and two silicon nitride composites reinforced with silicon carbide whiskers were studied in such an environment. Experiments show that the dynamic mechanical properties of the tested materials are influenced by thermal cycle. The materials stiffened slightly while damping capacity decreased slightly during each thermal cycle. X-ray diffraction (XRD) was subsequently used to examine the corresponding crystallographic alterations. The XRD patterns show that the amorphous glass phases in the silicon nitride matrix were partially crystallized during thermal cycling.

Introduction

Silicon nitride is one of the most promising materials for high-temperature structural applications. Silicon nitride-based ceramics exhibit excellent mechanical properties, high wear resistance and oxidation resistance, and good thermal shock behavior at both room temperature and high temperature. These properties have made silicon nitride structural materials strong candidates for many applications in extreme conditions. Examples include automotive engine components and gas turbine components.

For gas turbine applications, silicon nitride seems to offer performance that is superior to that of silicon carbide, which is another candidate for high-temperature structural applications. Compared with silicon nitride, silicon carbide has better heat resistance, and also maintains its strength up to higher temperatures. However, silicon carbide has a low fracture toughness and is very brittle. Even though silicon nitride is slightly inferior to silicon carbide in terms of heat resistance, it has a higher fracture toughness and is less brittle. In addition, silicon nitride has better thermal shock resistance because its elastic modulus and thermal expansion coefficient are lower than that of silicon carbide (Hoffmann and Petzow, 1993; Matsui, 1993).

In the efforts to improve the mechanical properties of structural ceramics, fracture toughness, strength, and heat resistance are the three major properties that many researchers have tried to improve. Due to the high-temperature, vibratory environment in engine and gas turbine applications, dynamic mechanical properties of silicon nitride or other structural ceramics should be of great interest. Dynamic mechanical properties usually refer to dynamic modulus and damping capacity of a material. Dynamic modulus strongly affects vibration frequencies and damping capacity strongly influences noise and vibration levels for structures or structural components under vibration. The authors have conducted considerable research on dynamic mechanical properties of silicon nitride-based structural ceramics (Yang et al., 1997). Based on this previous research, this study reports on thermal cycling effects on dynamic mechanical properties of these structural ceramics. The experiments were carried out in a laboratory environment. Thermal cycling was simulated from room temperature up to 1100°C. Dynamic modulus and damping capacity were measured as a function of temperature during each cycle up to three cycles. Finally, the XRD patterns of thermal cycled samples and uncycled samples were compared to examine corresponding crystallographic alterations and thermal cycling effects.

Materials

The excellent thermal and mechanical properties of silicon nitride are mainly attributed to its chemical structure. Silicon nitride consists of materials with $[SiN_4]$ and $[(Si, Al)\ (N, O)_4]$ as fundamental building units. One particular feature of silicon nitride ceramics is that the Si—N bond is highly covalent in nature with extremely low diffusivity of both Si and N even at very high temperatures. It is this structural feature that leads to the superior behavior of silicon nitride ceramics to metals and superalloys. However, the highly covalent nature also makes the densification of silicon nitride by solid-state diffusion impossible. Silicon nitride usually has to be densified with sintering aids. Alumina, yttria, and other rare earth oxides are typical sintering additives.

The densification of silicon nitride from initial α-powders is a liquid phase sintering process. The liquid phase is created by the addition of sintering aids, which forms a low melting eutectic liquid with a surface layer of silicon nitride powder. At higher temperatures, silica, which is usually located at the surface of the silicon nitride particles, reacts with the oxides to form an oxide melt, then results in an oxynitride by dissolving silicon nitride with increasing temperature. β-silicon nitride particles are precipitated while the α-powders dissolve and supersaturate the liquid phase. The β-silicon nitride grains have an elongated hexagonal rod morphology. These rod-shaped grains form an interlocking microstructure, which is highly desired for excellent mechanical properties. However, due to the presence of the sintering aids, the liquid phase can also form a glassy grain boundary phase during cooling. This remaining glass phase can soften grain boundary regions at certain high tempera-

Contributed by the International Gas Turbine Institute for publication in the JOURNAL OF ENGINEERING FOR GAS TURBINES AND POWER. Manuscript received at ASME Headquarters July 18, 1996. Associate Technical Editor: H. L. Julien.

Copyright © 1997 by ASME

Downloaded 02 Jun 2010 to 171.66.16.105. Redistribution subject to ASME license or copyright; see http://www.asme.org/terms/Terms_Use.cfm

tures. Therefore, glassy phases in these structural ceramics are usually considered to be degrading factors for mechanical properties in structural applications (Yang et al., 1996).

Four hot pressed silicon nitride (HPSN) based ceramics and composites were tested in this research. The first two are KemaNord silicon nitrides with and without silicon carbide whiskers, and hence are identified by KNw/SiC and KNw/oSiC, respectively. The third and fourth are UBE silicon nitride with and without silicon nitride whiskers, and hence are identified by UBEw/SiC and UBEw/oSiC, respectively. The KemaNord materials are processed from moderate purity matrix powders while the UBE materials are made from high purity matrix powders. The whiskers are randomly distributed in the matrix and with a 5 percent volume fraction for each of the reinforced composites (those with whiskers). The sintering additives for all of the four silicon nitrides were 6 percent by weight of alumina and 3 percent by weight of yttria.

Samples and Experiments

The dynamic mechanical properties during thermal cycling were measured on rectangular beam samples in a cantilever boundary configuration. The impulse-frequency response technique and the half power band width method were used to measure the dynamic modulus and damping loss factor (Suarez and Gibson, 1987). The samples of the four materials were made to the same dimensions, with a free end length of 156 mm, a width of 12.7 mm, and a thickness of 1.524 mm. In each cycle, the samples were heated from room temperature to 1100°C by a quartz lamp heater and then cooled to room temperature. The measurements were taken during the heating part of the cycle to 1100°C. At each measuring point, temperature was maintained for about 4 to 5 minutes so as to have the sample reach thermal equilibrium. The tests were conducted in air, not in vacuum, due to the fact that these materials will not be used in vacuum conditions in combustion engines and other structural applications. The experimental details are discussed in a previous publication (Yang et al., 1997).

The dynamic mechanical properties of the samples tested were found to be affected by the repeated thermal heating, but the micromechanical mechanisms for these changes required that a different test method be used. Hence, the XRD technique was used to examine the crystallographic structures of the materials before and after thermal cycling. The XRD samples were prepared from the beam samples by breaking them into small pieces with unequal side lengths from 1 mm to 3 mm. The surfaces of the beam samples that experienced heating were first ground by silicon carbide sand papers to remove the gray-white colored oxidation layer. These XRD samples were divided into two groups, one following three thermal cycles, one without thermal cycling.

Experimental Results

Dynamic Mechanical Properties Under Thermal Cycling. Thermal cycling effects on dynamic modulus and damping capacity of the materials tested were observed by repeatedly heating the samples from room temperature to 1100°C, and then cooling to room temperature. Figures 1–8 demonstrate the effects of up to three thermal cycles for all four materials. Each odd-numbered figure shows the damping loss factor, and the even-numbered figure shows the dynamic storage modulus. The numerical data of dynamic mechanical properties (resonant frequency, f_n, damping loss factor, η, and storage modulus, E) at room temperature and at the damping peak temperatures (approximately 900°C) are listed in Tables 1 and 2, respectively. The statistical values in the two tables are based on 16 tests for each of the materials. These results show that all of the materials seem to be stiffened, with higher natural frequencies, larger storage moduli, and smaller damping loss factors, following each thermal cycle.

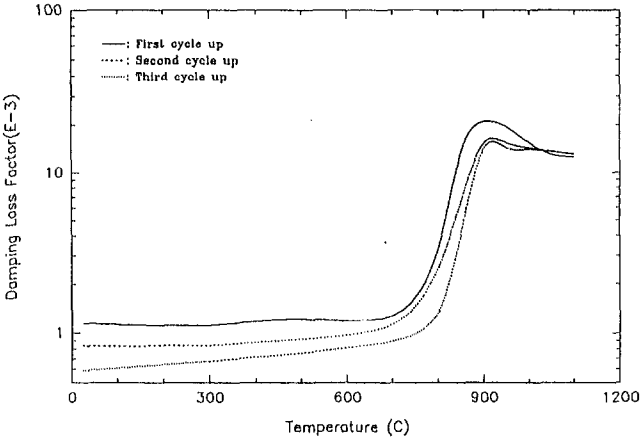


Fig. 1 Damping of KNw/SiC samples versus temperature for three thermal cycles

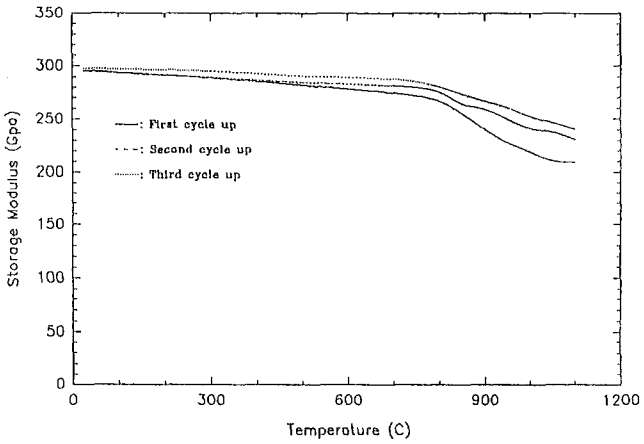


Fig. 2 Dynamic modulus of KNw/SiC samples versus temperature for three thermal cycles

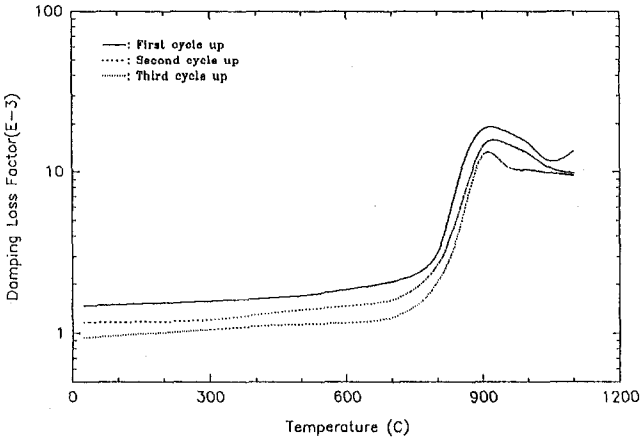


Fig. 3 Damping of KNw/oSiC samples versus temperature for three thermal cycles

Two possible mechanisms may be responsible for the thermal cycling influence on the stiffness and damping capacity of these materials. The first one is that microcracks within the silicon nitride matrix may be partially "healed" as a result of the viscoelastic flow at high temperatures. The second is that

Downloaded 02 Jun 2010 to 171.66.16.105. Redistribution subject to ASME license or copyright; see http://www.asme.org/terms/Terms_Use.cfm

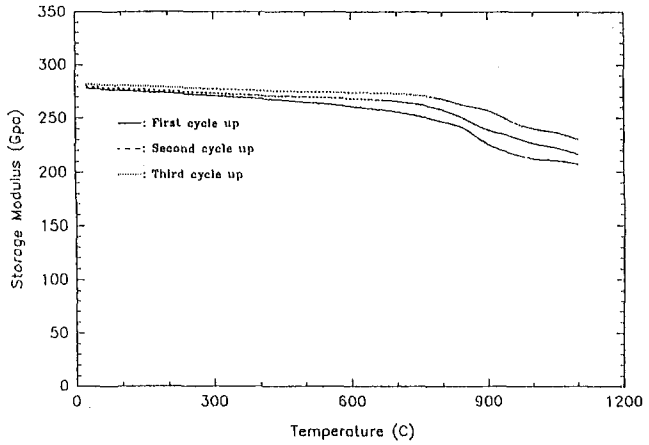


Fig. 4 Dynamic modulus of KNw/oSiC samples versus temperature for three thermal cycles

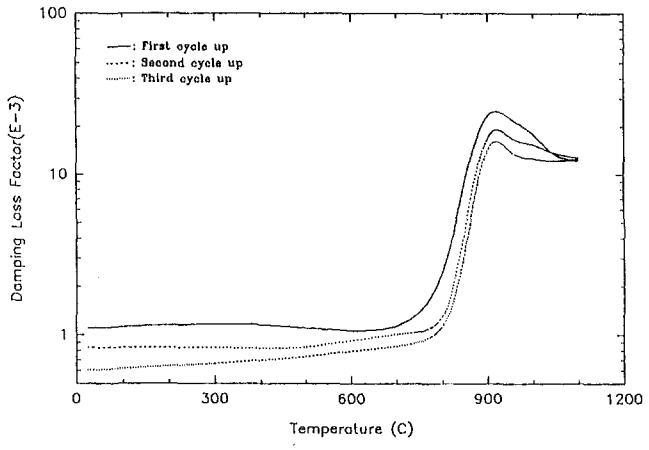


Fig. 5 Damping of UBEw/SiC samples versus temperature for three thermal cycles

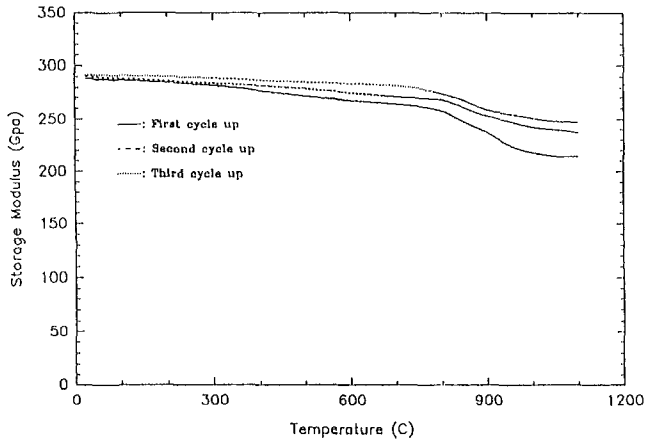


Fig. 6 Dynamic modulus of UBEw/SiC samples versus temperature for three thermal cycles

changes in structural compositions such as the devitrification or crystallization of the glass phase and the grain boundary glassy phase may result in the stiffening of the materials. The "crack healing" mechanism is not believed to be a main factor here. If the crack healing is to be significant, then there must be many microcracks in the materials. This means that the initial room temperature damping should have been much larger due

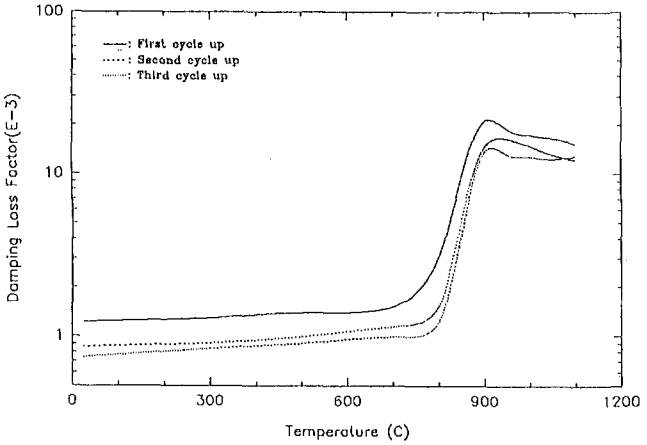


Fig. 7 Damping of UBEw/oSiC samples versus temperature for three thermal cycles

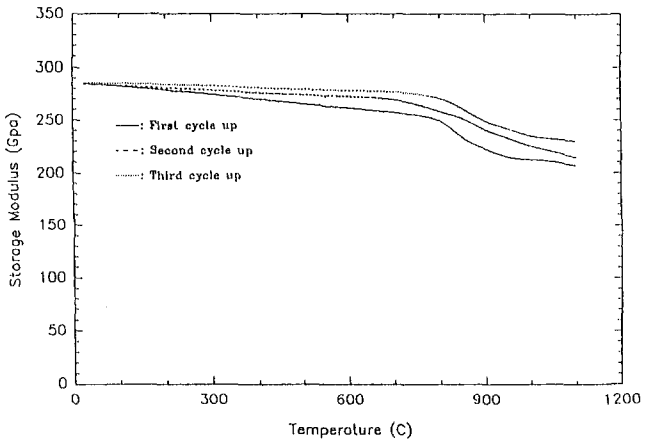


Fig. 8 Dynamic modulus of UBEw/oSiC samples versus temperature for three thermal cycles

Table 1 Experimental results at room temperature

Material	No. of Cycles	f_n (Hz) Mean	E' (Gpa) Mean	η Max (10^{-3})	η Min (10^{-3})	η Mean (10^{-3})	η Std. Dev (10^{-3})
KNw/SiC	1	119.63	295.37	0.897	1.324	1.147	0.062
	2	119.80	296.17	0.653	1.012	0.842	0.056
	3	120.10	297.61	0.612	0.322	0.587	0.071
KNw/oSiC	1	116.18	278.55	1.598	1.224	1.486	0.066
	2	116.50	280.09	1.321	0.857	1.166	0.041
	3	116.92	282.15	1.007	0.759	0.940	0.047
UBEw/SiC	1	118.15	288.13	1.218	0.797	1.105	0.067
	2	118.57	290.13	1.084	0.706	0.836	0.069
	3	118.90	291.79	0.864	0.447	0.605	0.054
UBEw/oSiC	1	117.26	283.76	1.386	1.102	1.220	0.072
	2	117.43	284.40	1.132	0.754	0.869	0.057
	3	117.70	285.84	0.886	0.534	0.746	0.055

Table 2 Experimental results at 900°C

Material	No. of Cycles	f_n (Hz) Mean	E' (Gpa) Mean	η Max (10^{-3})	η Min (10^{-3})	η Mean (10^{-3})	η Std. Dev (10^{-3})
KNw/SiC	1	108.02	240.60	21.95	20.38	21.01	0.545
	2	112.15	259.59	16.20	14.72	15.26	0.410
	3	113.78	267.17	14.64	13.15	14.01	0.368
KNw/oSiC	1	104.62	225.87	20.35	17.42	18.44	0.723
	2	107.60	238.92	14.66	13.86	12.35	0.274
	3	111.63	257.18	13.36	12.37	11.92	0.314
UBEw/SiC	1	107.79	239.54	24.01	22.72	23.51	0.448
	2	110.91	253.65	17.62	16.58	17.31	0.260
	3	112.12	259.18	14.78	13.96	14.46	0.294
UBEw/oSiC	1	103.99	223.18	21.97	20.33	20.38	0.500
	2	108.14	241.37	17.16	15.88	16.33	0.403
	3	110.01	249.76	14.33	12.56	13.41	0.471

Downloaded 02 Jun 2010 to 171.66.16.105. Redistribution subject to ASME license or copyright; see http://www.asme.org/terms/Terms_Use.cfm

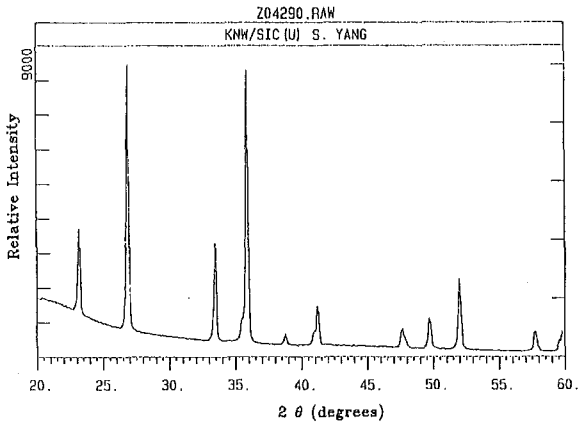


Fig. 9 XRD pattern of KNw/SiC sample before thermal cycle

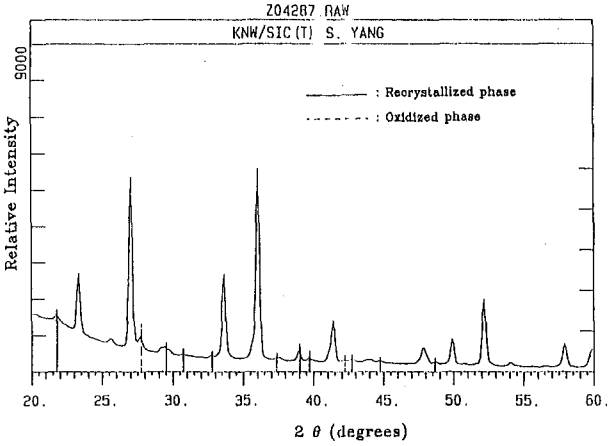


Fig. 10 XRD pattern of KNw/SiC sample after three thermal cycles

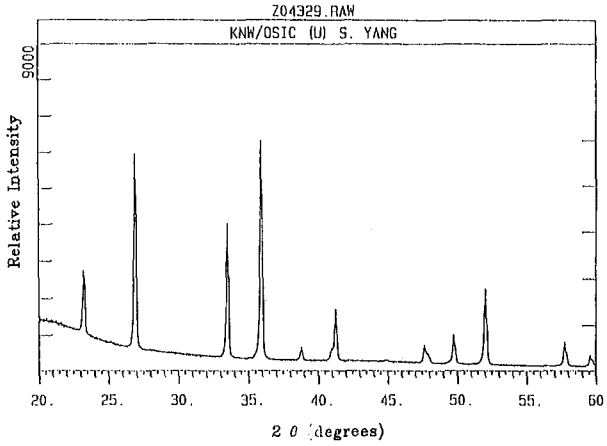


Fig. 11 XRD pattern of KNw/oSiC sample before thermal cycle

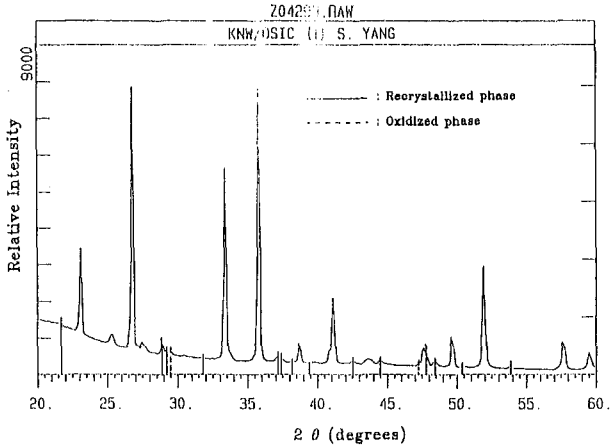


Fig. 12 XRD pattern of KNw/oSiC sample after three thermal cycles

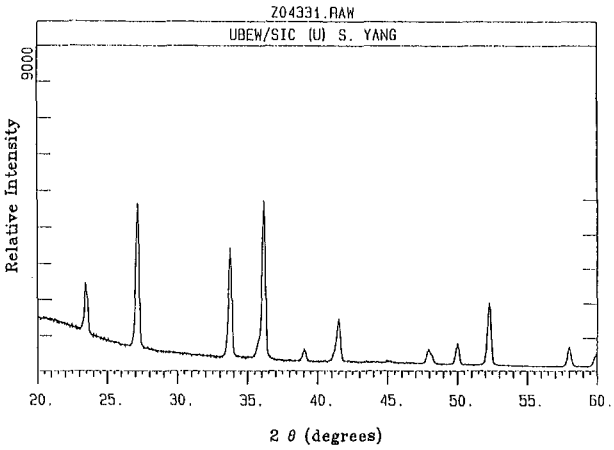


Fig. 13 XRD pattern of UBEw/SiC sample before thermal cycle

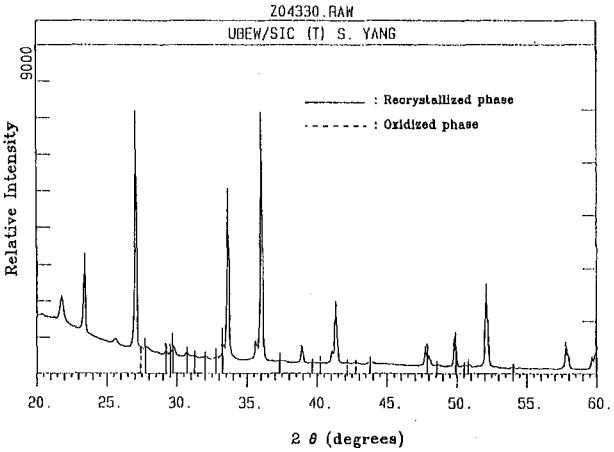


Fig. 14 XRD pattern of UBEw/SiC sample after three thermal cycles

to the friction damping at crack interfaces. The experimental results showed, however, the initial room temperature damping is not very large. Thus, XRD was applied to compare the crystallographic structure changes of the samples before and after thermal cycling.

The XRD Crystallographic Analysis. The X-ray diffraction patterns for the ceramic samples investigated here are shown in Figs. 9–16 in the form of relative X-ray intensity versus double diffraction angles, 2θ (Azaroff, 1968). Each odd-numbered figure represents the results before thermal cycling and each even-numbered figure represents the results after three thermal cycles. By comparing each pair of diffraction patterns before and after thermal cycling, the difference between them is clear. The patterns for the thermally cycled samples have several peaks that are not present in the patterns for the samples before heating. These new peaks (marked by vertical lines in the corresponding figure), even though some of them are very small, indicate different crystalline phases in the materials. The further comparison of these new peaks against the standard

Downloaded 02 Jun 2010 to 171.66.16.105. Redistribution subject to ASME license or copyright; see http://www.asme.org/terms/Terms_Use.cfm

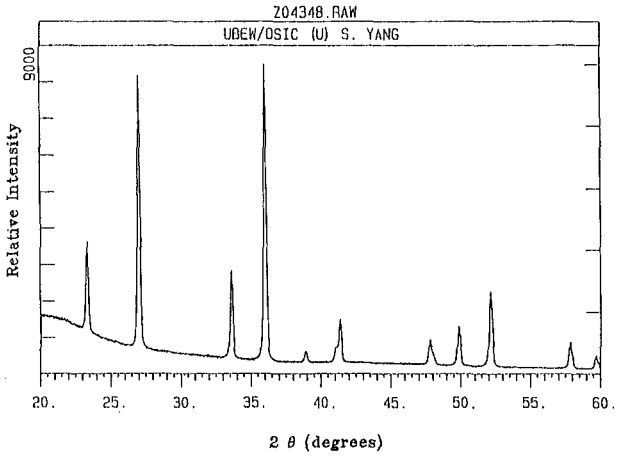


Fig. 15 XRD pattern of UBEw/oSiC sample before thermal cycling

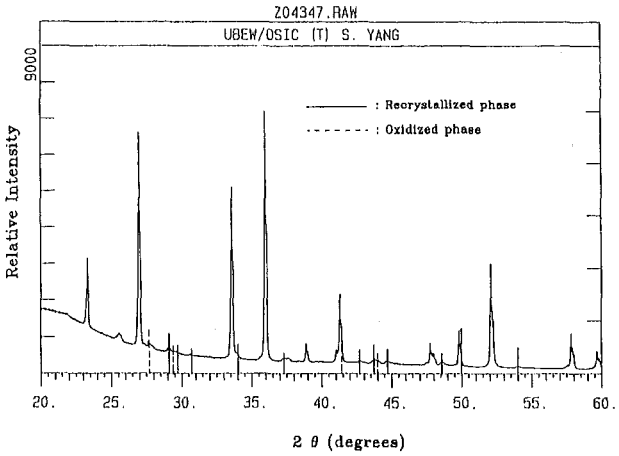


Fig. 16 XRD pattern of UBEw/oSiC sample after three thermal cycles

referenced patterns indicates that the newly generated phases are yttrium silicate ($Y_2Si_2O_7$), and yttrium silicon oxide nitrides ($Y_8Si_4N_4O_{14}$, $Y_2Si_3N_4O_3$, $Y_{20}N_4Si_{12}O_{48}$, $YSiO_2N$). The yttrium silicate phase (dashed lines in the patterns) is an oxidation phase caused by the high-temperature heating during testing, but the yttrium silicon oxide nitride phases (solid lines in the patterns) are crystalline phases that are crystallized from the grassy phases in the materials. The transformation from a vitreous phase to a nonvitreous phase is also called crystallization. Table 3 gives numerical data on the double diffraction angles and the corresponding compositions for the newly generated phases after thermal cycling.

The oxidation of the ceramic samples should not account for increases in the stiffness and reductions in the damping capacity of the materials, since oxidation would be expected to degrade the stiffness of the materials (Bolz and Tuve, 1980). This side effect can be avoided by testing in an inert atmosphere, but this is not practical for engines or engine components in real working environments.

From this consideration, it appears that crystallization of the glassy phases is a factor in the alteration of the dynamic mechanical properties of the samples. The crystallized phases usually have higher elasticity than the corresponding amorphous glassy phases. Intuitively, a crystalline material can be imaged as a truss bridge with uniform beam elements, but a glassy material can be imaged as a truss bridge made of disorganized triangles of unequal length sides. The rigidity of a nonuniform truss bridge is, of course, less than that of a regular one (Ashby and Jones, 1986). Hence, the stiffness was increased with more

Table 3 New phase compositions and double diffraction angles

Figure	Material	Double Diffraction Angle of New Phases (°)				
		Oxidized	Nonvitreous			
		$Y_2Si_2O_7$	$Y_8Si_4N_4O_{14}$	$Y_2Si_3N_4O_3$	$Y_{20}N_4Si_{12}O_{48}$	$YSiO_2N$
6	KNw/SiC	27.69 42.24	32.71 39.62 44.62	37.38 56.78	21.66 39.82 48.71	29.56 37.32
8	KNw/oSiC	29.47 47.43	29.16 39.42	31.96 37.38 38.13	42.57 44.42 48.38	47.92 50.32 53.92
10	UBEw/SiC	27.39 40.17 42.24	27.86 30.62 39.62	37.31 43.81	30.21 42.13 49.96	32.71 50.36
12	UBEw/oSiC	27.69 29.47 44.05	29.16 30.60 34.21	37.38 43.82 53.92	42.57 48.71 49.96	29.76 43.80

nonvitreous phases, and furthermore, the damping capacity was reduced with less glassy phases after thermal cycling. This phenomenon also confirms that the glassy phases play an important role in the viscoelastic properties of the ceramic materials tested at high temperatures.

Discussion

The exact amount of the glassy phases that have been crystallized under each thermal cycling was not determined at the moment. High-temperature damping (see Figs. 1, 3, 5, and 7) and low-temperature dynamic moduli (see Figs. 2, 4, 6, and 8) seem to indicate that this glassy phase crystallization may finally reach equilibrium. Contrarily, low-temperature damping and high-temperature moduli do not show this tendency obviously. Even though it is reasonable to anticipate that the crystallization of the glassy phases will finally reach a balance under more thermal cycles due to their limited remaining amount. The dynamic mechanical properties of the monolithic silicon nitrides (KNw/oSiC and UBEw/oSiC) and composite silicon nitrides (KNw/SiC and UBEw/SiC) are compared here (see Tables 1 and 2). The comparison shows that the composite silicon nitrides have smaller damping at room temperature, but larger damping at elevated temperatures, than the corresponding monolithic silicon nitrides. This might mean that the damping in the monolithics and the composites is dominated by different mechanisms. For example, one of the possibilities for the higher damping of the reinforced silicon nitride at elevated temperatures is the extra friction of the silicon carbide whiskers in melt glassy phases. The comparison also indicates that the reinforced composites are stiffer than the corresponding monolithics, due to the higher modulus of silicon carbide whiskers (Chawla, 1993). However, the comparison shows no obvious difference of the effects of thermal cycling on the monolithic and the composite silicon nitrides. This might be because the 5 percent volume fraction of SiC whiskers in the composite silicon nitrides is small. Finally, it is of interest to compare the influence of thermal cycling on damping and dynamic modulus separately. The damping curves clearly reflect the thermal cycling influence even at room temperature. However, the dynamic modulus curves just show the obvious influence at high temperatures. This verifies that damping may be more sensitive to crystallographic changes. Damping measurements have a long history of being used as a means of monitoring microstructural damage and changes (Mosher et al., 1976; Tsai and Raj, 1980; Nishiyama et al., 1990). However, thermal cycling induced microstructural alterations and subsequent XRD crystallographic phase identification, as an explanation for the corresponding changes in damping and stiffness, have not been observed in the literature.

The stiffening of the tested silicon nitride-based structural ceramics due to repeatitive thermal cycling has been shown by measurement of increased dynamic stiffness and reduced damping capacity. This alteration of mechanical properties and crystalline structures results in opposite conclusions for differ-

Downloaded 02 Jun 2010 to 171.66.16.105. Redistribution subject to ASME license or copyright; see http://www.asme.org/terms/Terms_Use.cfm

ent considerations. For example, it is good for the purpose of generating higher stiffness and greater creep resistance of ceramic materials, but is not desirable for the purpose of improving damping capacities of ceramic materials. Special consideration must be given for different uses of ceramics and ceramic composites.

The thermal cycling condition can be considered to be a simplified simulation of an engine working environment, except for the heating rate and the numbers of cycles. So, it is hoped that this research has revealed some of the features of mechanical behavior of silicon nitride-based structural materials, or engine and turbine components made from these materials, under high temperatures and vibratory loads.

Concluding Remarks

A thermal cycling environment was simulated and corresponding effects on stiffness and damping capacity of some silicon nitride-based monolithic and composite ceramics were investigated. Dynamic measurements indicate that materials were stiffened with increasing numbers of thermal cycles. XRD patterns show that glassy phases or glassy grain boundary phases in silicon nitride matrix were recrystallized under cyclic thermal loads. It will be of interest to see if similar crystallographic alterations will occur in engine or turbine components made from the same materials under actual combustion conditions.

References

Ashby, M. F., and Jones, D. R., 1986, *Engineering Materials 2: An Introduction to Microstructures, Processing, and Design,* Pergamon Press, Oxford.

Azaroff, L. V., 1968, *Elementary of X-Ray Crystallography,* McGraw-Hill, New York.

Bolz, R. E., and Tuve, G. L., 1980, *CRC Handbook of Tables for Advanced Engineering Science,* 2nd ed., CRC Press, Boca Raton, FL.

Chawla, K. K., 1993, *Ceramic Matrix Composites,* 1st ed., Chapman & Hall.

Hoffmann, M. J., and Petzow, G., 1993, "Microstructural Design of Si_3N_4 Based Ceramics," *Silicon Nitride Ceramics, Scientific and Technological Advances,* Symposium Proceedings, Vol. 287, Materials Research Society, pp. 3–14.

Matsui, M., 1993, "Status of Research and Development on Materials for Ceramic Gas Turbine Components," *Silicon Nitride Ceramics, Scientific and Technological Advances,* Symposium Proceedings, Vol. 287, Materials Research Society, pp. 173–188.

Mosher, D. R., Raj, R., and Kossowsky, R., 1976, "Measurement of Viscosity of the Grain-Boundary Phase in Hot-Pressed Silicon Nitride," *Journal of Materials Science,* Vol. 11, pp. 49–53.

Nishiyama, K., Yamanaka, M., Omori, M., and Umekawa, S., 1990, "High Temperature Dependence of the Internal Friction and Modulus Change of Tetragonal ZrO_2, Si_3N_4 and SiC," *Journal of Materials Science Letters,* Vol. 9, pp. 526–528.

Suarez, S. A., and Gibson, R. F., 1987, "Improved-Frequency Response Techniques for Measurement of Dynamic Mechanical Properties of Composite Materials," *Journal of Testing and Evaluation,* Mar., pp. 114–121.

Tsai, R. L., and Raj, R., 1980, "The Role of Grain-Boundary Sliding in Fracture of Hot-Pressed Si_3N_4 at High Temperatures," *The American Ceramic Society Bulletin,* Vol. 63, pp. 513–517.

Yang, S., Gibson, R. F., Crosbie, G. M., and Allor, R. L., 1996, "Measurement of Dynamic Mechanical Properties of Advanced Ceramics and Ceramic Matrix Composites at Temperatures Above 1000°C," *Experimental Techniques,* Vol. 20, No. 3, pp. 20–23.

Yang, S., Gibson, R. F., Crosbie, G. M., and Allor, R. L., 1997, "Dynamic Mechanical Properties of Ceramics and Ceramic Composites at Elevated Temperatures," ASME JOURNAL OF ENGINEERING FOR GAS TURBINES AND POWER, Vol. 119, pp. 15–19.

Downloaded 02 Jun 2010 to 171.66.16.105. Redistribution subject to ASME license or copyright; see http://www.asme.org/terms/Terms_Use.cfm

Economic Scales for First-Generation Biomass-Gasifier/Gas Turbine Combined Cycles Fueled From Energy Plantations

E. D. Larson

C. I. Marrison[1]

Center for Energy and Environmental Studies,
School of Engineering and Applied Science,
Princeton University,
Princeton, NJ 08544

This paper assesses the scales at which commercial, first-generation biomass integrated-gasifier/gas turbine combined cycle (BIG/GTCC) technology is likely to be most economic when fueled by plantation-derived biomass. First-generation BIG/GTCC systems are likely to be commercially offered by vendors beginning around 2000 and will be based on either pressurized or atmospheric-pressure gasification. Both plant configurations are considered here, with estimates of capital and operating costs drawn from published and other sources. Prospective costs of a farm-grown energy crop (switchgrass) delivered to a power plant are developed with the aid of a geographic information system (GIS) for agricultural regions in the North Central and Southeast US in the year 2000 and 2020. A simplified approach is applied to estimate the cost of delivering chipped eucalyptus from an existing plantation in Northeast Brazil. The "optimum" capacity (MW_{opt}), defined as that which yields the minimum calculated cost of electricity (COE_m), varies by geographic region due to differences in delivered biomass costs. With pressurized BIG/GTCC plants, MW_{opt} is in the range of 230–320 MW_e for the sites considered, assuming most of the land around the power plant is farmed for energy crop production. For atmospheric-pressure BIG/GTCC plants, MW_{opt} ranges from 110 to 142 MW_e. When a lower fraction of the land around a plant is used for energy farming, values for MW_{opt} are smaller than these. In all cases, the cost of electricity is relatively insensitive to plant capacity over a wide range around MW_{opt}.

Introduction

Biomass integrated-gasifier/gas turbine combined cycle (BIG/GTCC) power plant technology is presently the focus of ten or more major demonstration projects worldwide. Commercial systems are likely to be offered beginning around 2000. The high efficiency and expected competitive capital costs for these systems hold forth the promise of competitive busbar costs, even when using biomass grown on dedicated farms, which will be more costly than residue biomass, the predominant biomass fuel source for existing steam-rankine power plants. This paper assesses the effects of BIG/GTCC power plant configuration and scale on the prospective costs of producing electricity from farm-grown switchgrass in the North Central and Southeast US and from eucalyptus plantations in the state of Bahia, Brazil. Only stand-alone electric power production is considered. A similar analysis could be carried out for cogeneration applications.

A unique feature of farm or plantation-based biomass power production is that the feedstock must be gathered from a wide area around the power plant. For a small facility, transport costs will be relatively low, but capital cost per unit of output will be high. For a large facility, transport costs will be high, but capital costs will be relatively low. At some intermediate scale, the total cost of energy should reach a minimum. A quantitative assessment of this tradeoff is made here by marrying region-specific biomass supply cost estimates with BIG/GTCC power plant capital and operating cost estimates.

Status of BIG/GTCC Technology Development

The biomass integrated-gasifier/gas turbine combined cycle (BIG/GTCC) concept involves sizing and drying of the feedstock, feeding to a gasifier, gasification, gas cooling, gas cleanup, and firing in a gas turbine, with steam raised in a heat recovery steam generator for use in a steam bottoming cycle (Fig. 1). A variety of equipment configurations have been proposed for BIG/GTCC systems, and key technology issues (Consonni and Larson, 1996a) are being addressed in ten or more commercially oriented demonstration projects ongoing worldwide. It is probable that BIG/GTCC systems will be offered commercially by the year 2000.

The first BIG/GTCC system to be built is a 6 MW_e plus 9 MW_{th} (20 MW biomass input) combined-cycle district-heating cogeneration facility in Varnamo, Sweden, by Bioflow, a joint venture of Sydkraft, Sweden's largest privately owned and second largest electric utility, and A. Ahlstrom Corp., a Finnish boiler and gasifier manufacturer that was recently acquired by Foster-Wheeler Boilers. The plant is built around a modified European Gas Turbine Typhoon gas turbine, and includes an air-blown pressurized circulating fluidized-bed gasifier and ceramic filters for gas cleanup at elevated temperature (Stahl et al., 1993). Shakedown testing of individual components began in 1994, and the plant operated for the first time in fully-integrated mode in early October, 1995 (Sydkraft, 1995).

A 30 MW_e BIG/GTCC demonstration is proceeding at a site in Northeast Brazil, backed by a $30 million grant from the Global Environment Facility (Elliott and Booth, 1993), and comparable equity investments from project participants that include Shell Brasil (an affiliate of the Shell International Petroleum Company) and Electrobras (the federal electric utility in Brazil). The project is led by the Hydroelectric Company of Sao Francisco (CHESF), the utility that serves Northeast Brazil. CHESF has identified some 200 GW of potential BIG/GTCC capacity that could be supported from future energy plantations in their service territory (Carpentieri et al.,

[1] Present address: Oliver, Wyman & Company, LLC, 666 Fifth Ave., New York, NY 10103.

Contributed by the International Gas Turbine Institute and presented at the 41st International Gas Turbine and Aeroengine Congress and Exhibition, Birmingham, United Kingdom, June 10–13, 1996. Manuscript received at ASME Headquarters February 1996. Paper No. 96-GT-540. Associate Technical Editor: J. N. Shinn.

Copyright © 1997 by ASME

Downloaded 02 Jun 2010 to 171.66.16.105. Redistribution subject to ASME license or copyright; see http://www.asme.org/terms/Terms_Use.cfm

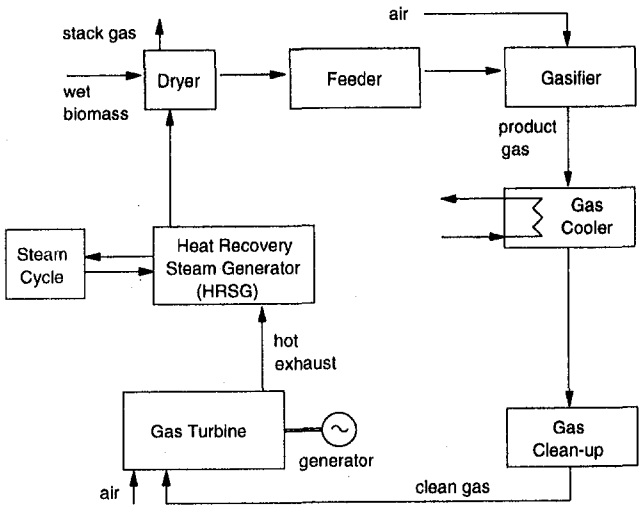


Fig. 1 Block diagram for biomass integrated-gasifier/gas turbine combined cycle (BIG/GTCC) technology

1993). Construction of the demonstration plant is slated to begin in 1997. The selected design is one proposed by TPS, a Swedish gasifier development company and is built around General Electric's LM2500. It includes an air-blown atmospheric-pressure circulating fluid-bed gasifier, followed by a separate catalytic reactor for reforming the heavy hydrocarbon (tar and oil) fraction of the gas, gas cooling, and wet scrubbing (TPS, 1995; Blackadder et al., 1994). Wood chips from an existing eucalyptus plantation will be the fuel. A pilot-scale (2 MW_{th}) TPS gasifier and gas cleanup system has been extensively tested, and two commercial scale gasifiers (15 MW_{th} each) have been successfully demonstrated for the production of boiler fuel at a site in Italy (Barducci et al., 1995).

Three demonstration projects are ongoing with financial support from the THERMIE program of the Directorate General for Energy of the European Commission (Maniatis and Ferrero, 1995). All three projects have in common the use of air-blown gasification, EGT's modified Typhoon gas turbine, and feedstock that will be derived from short-rotation forestry crops. Construction will begin in 1997 in all three cases. One project in Italy (11.9 MW_e) will utilize a Lurgi atmospheric-pressure circulating fluidized-bed gasifier, followed by a wet scrubbing system. A Lurgi CFB bark gasifier has been operating commercially for several years to supply fuel to a pulp mill's lime kiln in Austria (Herbert et al., 1988). A second project in the UK (8 MW_e) will use the TPS gasifier design, coupled with a catalytic tar cracker and wet scrubbing for gas cleanup. The third project in Denmark will be a district heating cogeneration system (7 MW_e, 8.2 MW_{th}) utilizing the pressurized fluidized-bed gasification technology of Enviropower of Finland, with ceramic filter hot gas cleaning. A pilot-scale Enviropower gasifier (rated at 10 MW coal input) has been extensively tested at Tampere, Finland, beginning in late 1991. Modifications were completed in late 1992 to permit operation on biomass (Bodlund et al., 1993), and nearly 1000 hours of testing with biomass were completed successfully in 1993, including tests with ceramic hot gas filters (Anon., 1994). Subsequently, 2100 tonnes of paper mill waste were gasified in 1995 at the pilot plant to provide data for design of a 50 MW_e combined cycle based on GE's Frame 6B turbine that is under consideration for a large paper mill in Finland (Horvath, 1995).

Another European demonstration project is in planning for the province of North Holland, The Netherlands (DWEB, 1994). The equipment configuration under consideration is similar to that selected for the Brazilian project, and the proposed fuel is biomass waste.

Two projects are ongoing in the United States, both co-financed by the Department of Energy. The Pacific International Center for High Technology Research is leading a project in Hawaii to demonstrate air-blown pressurized, bubbling fluidized-bed gasification of bagasse for gas turbine power production or (in the longer term with oxygen blowing) for methanol synthesis. The gasifier is the Renugas design originally developed at the Institute of Gas Technology (IGT) in Chicago, with which extensive pilot-scale operating experience exists (Lau et al., 1993). Construction of the 100 tonne per day gasifier is complete, and preliminary tests have been run using bagasse, the residue of sugarcane milling (Kinoshita, 1995). The gasifier will be used to test hot gas cleanup systems developed by Westinghouse (Wiant et al., 1995). Coupling to a gas turbine of 3–5 MW_e output is anticipated after 1997.

The second project is a 200 dry tonnes per day biomass (45 MW_{th}) demonstration at the McNeil wood-fired power station in Burlington, Vermont, of the indirectly heated gasifier design developed by the Battelle Columbus Laboratory (BCL) (Paisley and Farris, 1995). The BCL design is an atmospheric-pressure twin, entrained-flow system, in which a combustor unit provides heat to a separate gasification unit via circulating sand. Residual char from the gasifier provides the fuel for the combustor. Product gas is recirculated as the fluidizing agent, along with some steam. The indirect-heating produces a gas undiluted with nitrogen without using costly oxygen. The technology has been extensively evaluated at pilot scale (500 kg/h capacity) (Feldman et al., 1988). A 200 kW_e Solar Spartan gas turbine was successfully operated during 1994/95 on gas from the pilot unit. A catalytic hot gas conditioning system is under development by Battelle for use in a BIG/GT configuration (Paisley and Gebhard, 1995). The first phase of the Vermont project—construction and test operation of the gasifier—is being carried out during 1996/97. Addition of hot gas conditioning and gas turbine are planned for the second phase.

Analytical Approach and Assumptions

In this paper costs are estimated as a function of scale for (*i*) biomass delivered to a conversion facility and (*ii*) for conversion of biomass to electricity. On the basis of these estimates, the total cost for electricity is calculated as a function of scale.

Costs for Delivered Biomass. Costs are estimated here for growing and harvesting biomass and transporting it to a power plant site. Three geographic regions are considered, since costs can vary significantly depending on climate, soil quality, land rent, labor costs, and other regional parameters. Also, transportation costs will depend on the layout of the local road system, among other factors.

North Central and Southeast United States. Development of energy crops in the United States is focused on short-rotation woody crops for some regions and on perennial herbaceous crops for others (Hohenstein and Wright, 1994). Switchgrass is a primary candidate energy crop for the North Central (NC) and Southeast (SE) regions. Projected switchgrass costs are relatively high in the former region and low in the latter. To develop specific cost estimates for growing switchgrass in these regions, a four-county farming region in south-central Iowa, where there is intense interest in biomass energy farming (Cooper, 1995), was selected for detailed analysis. The relative soil qualities and road layout at this site were assumed to represent an agricultural region in the North Central US (which includes Iowa), as well as in the Southeast.

The selected area in Iowa includes the adjoining counties of Appanoose, Lucas, Monroe, and Wayne and covers approximately 5100 km^2, over 90 percent of which is farmed today. Road maps (USGS, 1986) and soil maps (at one-acre [0.4 hectare] resolution) (IGS, 1973) were input to a geographic information system (GIS), which was used to facilitate cost calculations (Marrison, 1995; Marrison and Larson, 1995a). The cost of growing and harvesting biomass on each acre was input as a function of the soil type, and the road map was used to calculate the cost of transporting the biomass to a power plant assumed to be located near the center of the four-county region. Switchgrass production costs for year-2000 and year-2020 farming systems were developed based on

Downloaded 02 Jun 2010 to 171.66.16.105. Redistribution subject to ASME license or copyright; see http://www.asme.org/terms/Terms_Use.cfm

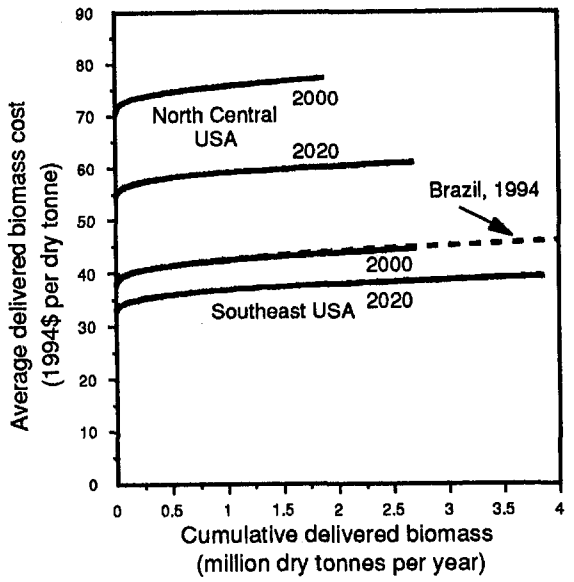


Fig. 2 Average cost for delivered biomass versus cumulative delivered tonnage for year 2000 and 2020 switchgrass farming in the North Central and Southeast regions of the USA and for present industrial eucalyptus plantations in Southern Bahia state, Brazil. Costs rise with tonnage supplied due to increasing transport distances and/or decreasing soil productivities. Assumed discount rates are 6.5 percent for the US (as suggested by Walsh and Graham, 1995) and 10 percent for Brazil. Additional details are provided by Marrison and Larson (1995a, 1995b).

projections by Walsh and Graham (1995). (Marrison and Larson, 1995a, give details.)

Biomass transport costs in $/tonne are typically expressed as a fixed cost (e.g., truck loading and unloading) plus a cost that varies with distance. Based on a review of several studies (see Marrison and Larson, 1995a), the following baseline relationship for transport of switchgrass bales was selected:

$$\$/\text{dry tonne delivered} = [3 + 0.18 \cdot (\text{one-way distance in km})]/0.9 \quad (1)$$

The 0.9 accounts for an assumed 10 percent post-harvest loss (UMinn, 1994) (assumed to occur during storage at the power plant site). [All costs in this paper have been converted to 1994 dollars using the U.S. GDP deflator (Council of Economic Advisors, 1995).]

Summing the production and transportation costs for each acre of land gives the total cost of biomass delivered to the conversion facility from that acre. Figure 2 shows average production cost plotted against cumulative biomass tonnage delivered from up to a maximum radius of 32 km (the limit of the four-county area examined[2]), assuming 94 percent of the area is used for switchgrass production. This percentage excludes primarily towns and lakes, and thus represents the maximum possible production. Costs are lowest in the Southeast region.

Southern Bahia State, Brazil. For comparison with US regions, a similar analysis was carried out for an existing industrial eucalyptus plantation in southern Bahia state, Brazil. To avoid data- and time-intensive GIS analysis, a simplified approach was developed for estimating delivered biomass costs and verified against a GIS analysis (Marrison and Larson, 1995b; Marrison, 1995). The maximum assumed land coverage was 80 percent, as Brazilian law requires at least 20 percent of the area of a plantation to be left in natural vegetation. Costs for delivered eucalyptus chips from present-day industrial plantations in Brazil are comparable to projected year-2000 costs for delivered switchgrass bales in the Southeast US (Fig. 2).

BIG/GTCC Performance and Cost Characteristics. Overall cost and performance parameters for BIG/GTCC systems are needed for the analysis here. Given the precommercial status of these systems, uncertainties are inherent in such parameters, but extensive ongoing design and demonstration efforts provide a relatively sound basis for estimation. The estimates described here are based on published literature, contact with developers and vendors, and other sources. Costs are estimated assuming commercially mature technology, i.e., after development costs are recovered.

Two basic BIG/GTCC configurations are considered, one using low-pressure (LP) air-blown gasification with wet scrubbing cleanup and one using air-blown pressurized (HP) gasification and hot-gas ceramic filter cleanup. Estimated costs and performance of commercial biomass/steam-rankine systems are also included for reference. The performance and cost characteristics described here for the BIG/GTCC systems can probably be achieved in the first generation of commercial BIG/GTCC systems. Some advanced cycle modifications that have already been identified are likely to improve performance and/or lower costs in the longer term. These include compressor intercooling (Consonni and Larson, 1996a) and steam-injection (Consonni and Larson, 1996b; Larson and Hughes, 1996).

Capital Costs. An expression for capital costs has been derived based on limited cost estimates for BIG/GT systems at different scales (see notes to Table 1). Because relatively few data points were available for this curve fitting process, a simple (three-parameter) form was chosen for the expression. Total installed unit capital

Table 1 Estimated unit capital costs, efficiencies, and operating and maintenance costs for biomass power plants at various capacities. All costs are in 1994$.

Power plant technology	Capacity (MW_e)[a]	Generating effic. (%)[b]	Capital cost ($/kW$_e$)	O&M ($/kWh)[c]
Low-pressure BIG/GTCC[d,e]	10	37	2577	0.008
	60	37	1288	0.008
	large	37	1200	0.008
Pressurized BIG/GTCC[e,f]	30	40	1800	0.008
	60	40	1425	0.008
	large	40	1100	0.008
Fluid-bed boiler/ steam cycle[g]	10	20	3510	0.0125
	50	n.r.[h]	1647	0.0125
	large	27	1200	0.0125

(a) The estimates for the "large" capacity units are discussed in the text.

(b) Net electricity out divided by the higher heating value of the biomass input.

(c) Assumed constant for all capacities.

(d) The source for the two lower-capacity capital cost estimates is from TPS [Lundberg, 1994]. TPS is actively working to commercialize biomass-gasifier/gas turbine combined cycles that would use their near-atmospheric pressure circulating fluidized-bed gasifier system that includes a secondary tar cracking reactor and wet scrubbing for gas cleanup. The efficiency is an estimate for a system of about 25 MW_e capacity that would use a General Electric LM2500 gas turbine [Elliott and Booth, 1993].

(e) The O&M cost estimate is based on two sources. One is the best "guesstimate" for a commercial, 25-30 MW_e BIG/GT facility in Brazil by industry experts involved in the development of the first commercial-scale BIG/GT demonstration project (to be built in Brazil). The "guesstimate" is 0.5 to 1.0 cents per kWh [Elliott, 1994]. Williams and Larson [1993] give estimates of O&M costs from 0.75 to 0.87 cents/kWh for 100-MW_e scale advanced BIG/GT systems.

(f) The capital cost estimates for the two lower-capacity units are from Puhakka [1994] and represent the low end of an estimated range at each capacity (see Consonni and Larson [1994b] for details). The estimates are for future commercial-level costs for a plant in Europe that would be based on the gasification design of Bioflow (see description in text). The indicated efficiency is for a system of 25-30 MW_e capacity that would use the General Electric LM2500 gas turbine [Elliott and Booth, 1993].

(g) From EPRI [1993b], except for capital cost and efficiency of the "large" unit. For the latter, see text.

(h) Not required for the analysis in this paper.

[2] The area is more or less rectangular, but the greatest transport distance used in the analysis was the minimum distance from the power plant (near the center of the area) to an outer edge of the area. This defined a 32-km radius circle.

Downloaded 02 Jun 2010 to 171.66.16.105. Redistribution subject to ASME license or copyright; see http://www.asme.org/terms/Terms_Use.cfm

cost (UC, in $ per unit of capacity) for a stand-alone power plant is assumed to vary with capacity, Cap, as follows:

$$UC = \mathbf{C} + \mathbf{D} \cdot (Cap)^{\mathbf{E}} \quad (2)$$

where **C**, **D**, and **E** are constants for a given configuration that are determined from available cost projections. **E** is a negative number, i.e., unit cost falls with increasing capacity. **C** corresponds to the unit cost that is reached asymptotically at large scale. Values for **C** can be assigned with somewhat greater confidence than the other parameters on the basis of several considerations (next paragraph). Cost estimates for two additional facilities with different capacities can then be used to determine values for **D** and **E**.[3]

Values for **C** were established as follows. For the BIG/GTCC systems, $1100 was selected for the HP system. Craig et al. (1994) give this as an estimate for a 148 MW_e system based on IGT's Renugas gasifier design and the Frame 6FA gas turbine. The value for the configuration using LP gasification ($1200/kW) is based on estimates provided by Lundberg (1994), together with a detailed analysis by Blackadder et al. (1994), suggesting that the total electricity production cost with a LP system would be lower than from a HP system up to scales of 50 to 80 MW_e. For the steam-rankine cycle, **C** ($1200/kW) is based on an extrapolation to 100 MW of a cost versus capacity relationship developed from reported total plant costs for 10 to 60 MW_e wood-fired circulating fluidized-bed combustion/steam rankine cycles (EPRI, 1993b). Also, $1200/kW is 10 to 15 percent less than the cost estimated by EPRI (1993a) for the least costly 300 MW coal-fired power plant with flue gas desulfurization. (Desulfurization would not be needed with biomass because of its low/zero sulfur content.)

The notes to Table 1 provide details as to the source of estimates for intermediate-sized facilities. The resulting equations used for calculations here are as follows:

$$\text{HP-BIG/GTCC: } \$/kW_e = 1100 + 110420 \cdot MW_e^{-1.42} \quad (3)$$

$$\text{LP-BIG/GTCC: } \$/kW_e = 1200 + 47198 \cdot MW_e^{-1.56} \quad (4)$$

$$\text{Steam cycle: } \$/kW_e = 1200 + 22195 \cdot MW_e^{-0.93} \quad (5)$$

It should be noted that the assumed form of the capital cost equation influences the final cost versus scale results. The particular form used here (Eq. (2)) was chosen because of the greater confidence in estimating the cost for a large plant (greater than about 100 MW_e). The expression is less accurate for very small scales. Equations (3)–(5) can be applied most confidently in the scale range that spans the point estimates shown in Table 1: 10–60 MW_e for the LP-BIG/GTCC, 30–60 MW_e for the HP-BIG/GTCC, and 10–50 MW_e for the steam cycle. The relationships are probably reasonable at plant sizes above these ranges, but high confidence in results much below the lower-capacity point estimates is unwarranted.

It should be noted that new cycle configurations for biomass that might be developed in the longer term could have very different capital cost characteristics than estimated here for combined cycles. Cycles have been examined that reduce the capacity of the steam bottoming plant [e.g., a combined cycle based on an intercooled gas turbine (Consonni and Larson, 1996b)] or that eliminate the bottoming steam turbine altogether without significant loss of efficiency [e.g., in a steam-injected (Larson and Hughes, 1996) or intercooled steam-injected configuration]. Such cycles are likely to be based on aeroderivative machines, in which case it may be feasible to maintain the relative scale insensitivity of unit capital costs down to smaller scales than for the GTCC systems considered here.

Fuel and Operating and Maintenance Costs. Fuel costs are determined by the efficiencies of the conversion systems. The efficiencies for LP and HP BIG/GTCCs are as estimated by Elliott and Booth (1993) for 25–30 MW_e facilities built around an LM2500 gas turbine (Table 1). The efficiencies for each of the two BIG/GTCC systems are considered to be fixed with capacity. This simplification underestimates efficiencies at larger scales and overestimates them at smaller scales, but does not qualitatively change the conclusions of the analysis. Because the steam-rankine technology is commercial today, cost-optimized efficiencies at different capacities are well established, and an equation having the same form as Eq. (2) was developed for efficiency versus scale.[4] Non-fuel operating and maintenance (O&M) costs per unit of output were assumed fixed regardless of scale for each technology (Table 1). Details regarding O&M cost estimates are provided in the notes to Table 1.

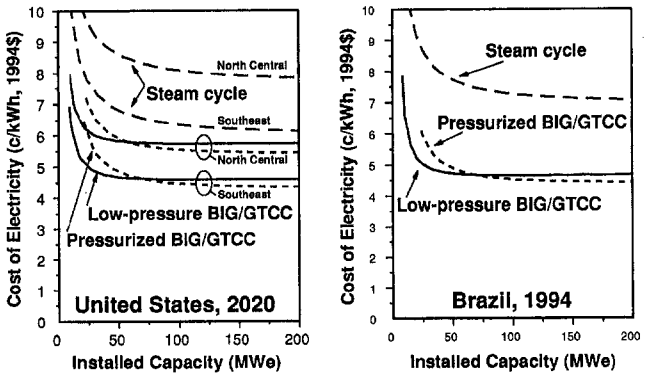


Fig. 3 Total levelized busbar electricity cost as a function of installed plant capacity for power plants using biomass from year-2020 switchgrass farms in the North Central (NC) and Southeast (SE) regions of the US and from present-day industrial eucalyptus plantations in Southern Bahia state, Brazil. In several cases, the minimum COE is reached off the right-end of the capacity scale (see Table 2).

Levelized Busbar Cost Results

The total levelized busbar cost of electricity was calculated by combining capital, feedstock, and O&M charges. The levelized cost of electricity (COE) in $/kWh is:

$$COE = (C_b \cdot 3.6)/(HHV \cdot \eta_e \cdot 1000) + UC \cdot CCR/(8766 \cdot CF) + OM \quad (6)$$

where C_b is the average delivered cost of biomass in $/dry tonne (from Fig. 2), HHV is the higher heating value of the fuel (18.44 GJ/dry tonne for switchgrass and 19.34 GJ/dry tonne for eucalyptus), η_e is the electricity generating efficiency (from Table 1 and footnote 4), UC is in $/kW from Eqs. (3)–(5), CCR is the capital charge rate,[5] 8766 is the average number of hours in a year, CF is the capacity factor (assumed to be 0.75), and OM is the O&M cost (Table 1). Results are presented for a baseline set of assumptions and for a sensitivity analysis focussing on some of the most important parameters.

Baseline Results. The capacity for which COE is a minimum (COE_m) is defined as the "optimal" capacity (MW_{opt}). For capacities up to MW_{opt}, falling unit capital costs for the conversion systems more than offset increasing biomass costs that arise from increased transportation costs (Fig. 3). For capacities larger than MW_{opt}, the COE rises gradually as transport

[3] Once a value for **C** is established, then $\mathbf{D} = (\text{UnitCost}_1 - \mathbf{C})/\text{Capacity}_1^{\mathbf{E}}$, where $\mathbf{E} = \{\log([\text{UnitCost}_1 - \mathbf{C}]/[\text{UnitCost}_2 - \mathbf{C}])\}/\{\log(\text{Capacity}_1/\text{Capacity}_2)\}$.

[4] For the steam-rankine cycle, η_e (percent) $= 100 \cdot [0.27 - 0.25 \cdot (MW_e)^{-0.56}]$, which assumes 20 percent efficiency at 10 MW_e (EPRI, 1993b) and 27 percent efficiency at "large" scale (100 MW_e wet wood chip combustion) (EPRI, 1993a).

[5] A capital charge rate of 0.101 is assumed, as suggested by EPRI (1993a) for a utility-financed renewable energy power plant with a 30-year life, 6.2 percent real pretax discount rate, and 38 percent income tax. Alternatively (e.g., for Brazil), a CCR of 0.101 would correspond to a 9.5 percent discount rate and 30-year plant life.

Downloaded 02 Jun 2010 to 171.66.16.105. Redistribution subject to ASME license or copyright; see http://www.asme.org/terms/Terms_Use.cfm

Table 2 Minimum cost of electricity (COE_m, 1994$) and related installed capacities for regions of US and Brazil

Electricity technology	Year[a]	COE_m (¢/kWh)	Installed Capacity (MW_e) for COE		
			= COE_m	≤ 1.01x COE_m	≤ 1.05x COE_m
NORTH CENTRAL USA					
Low-pressure BIG/GTCC	2000	6.6	114	60	27
	2020	5.7	127	61	30
Pressurized BIG/GTCC	2000	6.2	269	123	65
	2020	5.4	290	137	72
Steam cycle	2000	9.0	366	212	86
	2020	7.7	470	227	101
SOUTHEAST USA					
Low-pressure BIG/GTCC	2000	4.9	130	61	37
	2020	4.6	142	64	37
Pressurized BIG/GTCC	2000	4.6	285	140	85
	2020	4.3	319	154	91
Steam cycle	2000	6.5	424	214	99
	2020	6.0	519	244	111
SOUTHERN BAHIA STATE, BRAZIL					
Low-pressure BIG/GTCC	1994	4.8	110	60	35
Pressurized BIG/GTCC	1994	4.6	230	135	80
Steam cycle	1994	6.5	280	155	85

(a) Year in which the assumed biomass production costs are projected to be achievable.

Table 3 Results of sensitivity analysis for Southeast Region in 2020 showing values of COE_m (cents/kWh, 1994$) and corresponding MW

Parameter	LP-BIG/GTCC		HP-BIG/GTCC		Steam cycle	
	COE_m	MW	COE_m	MW	COE_m	MW
BASE CASE	4.57	142	4.33	319	6.05	520
Var. transp.[a] = $0.09/t-km	4.48	183	4.23	415	5.85	691
Var. transp.[a] = $0.36/t-km	4.71	100	4.50	208	6.39	304
Planting density[b] = 0.47	4.62	127	4.38	277	6.10	362
Planting density[b] = 0.094	4.76	87	4.59	121	6.80	75
Yield[c] = + 25% (t/ha/yr)	4.24	147	4.03	337	5.57	525
Yield[c] = - 25% (t/ha/yr)	5.10	123	4.83	301	6.83	447
Land rent[d] = + $123/ha/yr	5.00	142	4.73	319	6.66	520
Land rent[d] = - $123/ha/yr	4.13	142	3.93	319	5.43	520

(a) This is the coefficient multiplying distance in Eqn. 1. Baseline value is 0.18.

(b) The baseline value is 0.94.

(c) Baseline yield assumptions vary by soil type. See Marrison and Larson [1995a].

(d) Land rent represents an opportunity cost arising from choosing to grow energy crops instead of using the land for another purpose. A change in rent shifts the per-tonne cost of delivered biomass by a fixed amount regardless of tonnage delivered, so COE_m changes, but not MW_{opt} [Marrison and Larson, 1995a].

distances become increasingly more important. In all cases, the capacity at which COE_m is achieved (Table 2) is large compared to the size of biomass power plants operating today.

For a given technology, the considerably lower biomass costs projected for 2020 compared to 2000 or in the SE compared to the NC regions (Fig. 2), lead to lower COE_m and higher MW_{opt} in 2020 compared to 2000 and in the SE compared to the NC regions. At the Brazilian site, biomass costs, and correspondingly the values of COE_m, are somewhat higher than those for 2020 in the SE USA. However, for a given technology, MW_{opt} is smaller at the Brazilian site than in either of the US regions due primarily to the lower assumed maximum planting density (0.8 for Brazil versus 0.94 for the USA). Because of the flatness of the COE curves around the optimum, COE_m is actually approached at much smaller capacities than MW_{opt}: the capacity at which the COE falls to within 1 percent (5 percent) of COE_m is about half (one-quarter) of MW_{opt} (Table 2).

For the steam cycle, the capacities for being within 5 percent of COE_m (85-111 MW_e for the lowest-cost cases in Brazil and the USA) are larger than most biomass-fired steam-rankine power plants operating today. Most existing plants rely on low-cost biomass (e.g., residues of industrial processing), and their scales are set by the availability of feedstock, rather than by economies of scale.

The values of COE_m for BIG/GTCC cycles are approached at much smaller capacities than for steam cycles (COEs within 5 percent of COE_m at 27-91 MW_e—Table 2), because most of the capital cost scale economy gains come at smaller capacities with BIG/GTCCs.

At any scale, the higher efficiency and lower capital costs of the BIG/GT systems make them a significantly less costly source of electricity than steam-rankine cycles. With the costs in Table 2, BIG/GTs would be competitive with power from new coal-fired plants in the USA: coal-based electricity in 2000 and in 2020 is projected to cost 4.9¢/kWh and 5.2¢/kWh, respectively, in the NC region and 4.7¢/kWh and 4.9¢/kWh, respectively, in the SE region.[6] BIG/GTCC systems might become competitive in the NC region only when year-2020 targets are achieved with the system using HP gasification. In the SE region, BIG/GTCC systems would compete in year 2000 as well as 2020. In Brazil, the low COEs (assuming present biomass production technology) are likely to be competitive with a variety of other new power sources in the future, including new hydroelectric facilities (see Carpentieri et al., 1993).

Sensitivity Analysis. The sensitivity of the baseline results to four key input assumptions is illustrated using the year-2020 SE USA (Table 3). A particularly important parameter is planting density, i.e., the fraction of available land around the power plant that is used for biomass production. For the baseline case, it was assumed that all agriculturally suitable land in the selected area—94 percent of the area—was available to supply biomass. In practice, a diversity of crops would be planted. One initial bioenergy-crop strategy that has been proposed for Iowa (Brown, 1994) and other regions of the US is the use of lands currently under the Conservation Reserve Program for energy crop production.[7] For the specific four-county area considered in our analysis, 22 percent of agricultural land is held under CRP contracts. The average for Iowa as a whole is about 8 percent (Brown, 1994).

Reducing the planting density raises transport costs, resulting in somewhat higher COE_m and significantly lower MW_{opt}. For a planting density half that in the base case, COE_m is slightly higher than the baseline value. MW_{opt} drops by 10–15 percent for BIG/GTCC systems and by 30 percent for steam systems.

[6] These electricity costs are based on costs and performance estimates of EPRI (1993a) for 300 MW_e pulverized coal subcritical-steam plants with flue gas desulfurization in the East-West Central and Southeast regions (corresponding to the NC and SE regions in the analysis in this paper) and on electric utility steam-coal prices projected by the Department of Energy for the West-North Central and South Atlantic regions (EIA, 1995). For the NC region (in 1994$), the capital cost for the coal plant is $1662/$kW_e$, with fixed and variable O&M costs of $48.8/kW-yr and $0.0021/kWh, and a heat rate of 10.719 MJ/kWh. For the SE region, the figures are $1359/$kW_e$, $42.0/kW-yr, $0.0015/kWh, and 10.371 MJ/kWh. Assuming a continuation of DOE's projected growth rate between 2000 and 2010 in coal prices, coal in the NC region in 2000, 2010, and 2020 would cost $1.14/GJ, $1.27/GJ, and $1.40/GJ, respectively. For the SE region, the costs would be $1.56/GJ, $1.66/GJ, and $1.77/GJ.

[7] Under the CRP program, the US government rents environmentally sensitive lands from farmers for 10-year periods to keep the lands out of row-crop production and thereby to reduce soil erosion. Total CRP payments are currently some $1.8 billion per year in the U.S.

Downloaded 02 Jun 2010 to 171.66.16.105. Redistribution subject to ASME license or copyright; see http://www.asme.org/terms/Terms_Use.cfm

A planting density of 10 percent of the baseline value still does not increase COE_m dramatically, but MW_{opt} drops by 40–60 percent for BIG/GTCC technology and by over 85 percent for steam technology (Table 3).

Conclusions

This paper examined the impact of scale and technology configuration on prospective costs of electricity production from biomass integrated-gasifier/gas turbine combined cycle (BIG/GTCC) power plants fueled from energy plantations in the US and Brazil. Results are based on biomass production and BIG/GTCC costs that have not yet been commercially demonstrated, but that are best estimates based on pilot-scale and other relevant data. The most important conclusion is that for BIG/GTCC plants fueled from energy plantations, the capacity needed to achieve minimum busbar costs is large compared to conventional biomass power plant design practice, though there is a wide capacity range over which costs change relatively little. This scale insensitivity might be pushed to still smaller capacities by future cycle developments that reduce capital costs (e.g., through eliminating the steam bottoming cycle without significant efficiency loss). Nevertheless, large-scale units will also be economically viable.

Acknowledgments

For financial support of this research, the authors thank The Energy Foundation, The W. Alton Jones Foundation, The Geraldine R. Dodge Foundation, The Merck Fund, and the Research Institute of Innovative Technology for the Earth.

References

Anon., 1994, "Biomass Looks Good for Gasification Process," *Modern Power Systems,* Apr., pp. 61–65.

Barducci, G., Daddi, P., Polzinetti, G., and Ulivieri, P., 1995, "Thermic and Electric Power Production and Use From Gasification of Biomass and RDF: Experience at CFBG Plant at Greve in Chianti," *Proc. Second Biomass Conference of the Americas: Energy Environment, Agriculture, and Industry,* NREL/CP-200-8098, National Renewable Energy Lab, Golden, CO, pp. 565–575.

Blackadder, W. H., Lundberg, H., Rensfelt, E., and Waldheim, L., 1994, "Heat and Power Production via Gasification in the Range 5–50 MW_e," *Advances in Thermochemical Biomass Conversion,* A. V. Bridgwater, ed., Blackie Academic & Professional, London, pp. 449–75.

Bodlund, B., Bergman, J., and Lindman, N., 1993, "Power From Biomass in Sweden," *Proc. Strategic Benefits of Biomass and Waste Fuels,* Electric Power Research Institute, Palo Alto, CA.

Brown, R. C., 1994, *The Potential of Biomass Production and Conversion in Iowa,* Report from Iowa State Univ. to the Iowa Energy Center, ISU-ERI-Ames 95009, Ames, IA.

Carpentieri, A. E., Larson, E. D., and Woods, J., 1993, "Future Biomass-Based Power Generation in Northeast Brazil," *Biomass and Bioenergy,* Vol. 4(3), pp. 149–173.

Consonni, S., and Larson, E. D., 1996a, "Biomass-Gasifier/Aeroderivative Gas Turbine Combined Cycles Part B: Technologies and Performance Modeling," ASME JOURNAL OF ENGINEERING FOR GAS TURBINES AND POWER, Vol. 118, pp. 507–515.

Consonni, S., and Larson, E. D., 1996b, "Biomass-Gasifier/Aeroderivative Gas Turbine Combined Cycles Part B: Performance Calculations and Economic Assessment," ASME JOURNAL OF ENGINEERING FOR GAS TURBINES AND POWER, Vol. 118, pp. 516–525.

Cooper, J. T., 1995, "Agro-Energy: Redefining Energy and Agriculture in Iowa," *Proc. Second Biomass Conference of the Americas: Energy Environment, Agriculture, and Industry,* NREL/CP-200-8098, National Renewable Energy Lab, Golden, CO, pp. 1592–1600.

Council of Economic Advisors, 1995, *Economic Indicators,* USGPO, Washington, DC.

Craig, K. R., Mann, M. K., and Bain, R. L., 1994, "Cost and Performance Potential of Advanced Integrated Biomass Gasification Combined Cycle Systems," *Proc. Cogen Turbo Power '94,* ASME, New York, pp. 641–654.

DWEB (Dept. for Welfare, Economy, and Management), 1994, *Gasification of Biomass for Electricity Generations, Plan of Approach for the Construction of an Integrated 15-30 MW_e* System, Haarlem, Province of North Holland, The Netherlands, May.

EIA (Energy Information Administration), 1995, *Supplement to the Annual Energy Outlook 1995,* DOE/EIA-0554(95), USGPO, Wash. DC.

Elliott, P. (Shell International Petroleum Company, London), 1994, personal communication to R. Williams (Center for Energy and Environmental Studies, Princeton Univ., Princeton, NJ), Oct. 26.

Elliott, T. P., and Booth, R., 1993, *Brazilian Biomass Power Demonstration Project,* Special Project Brief, Shell International Petroleum Company, London.

EPRI (Electric Power Research Institute), 1993a, *TAG Technical Assessment Guide, Vol. 1, Electricit, Supply—1993 (Rev. 7),* TR-102275-V1R7, EPRI, Palo Alto, CA.

EPRI (Electric Power Research Institute), 1993b, *Strategic Analysis of Biomass and Waste Fuels for Electric Power Generation,* TR-102773, EPRI, Palo Alto, CA.

Feldmann, H. F., Paisley, M. A., Appelbaum, H. R., and Taylor, D. R., 1988, *Conversion of Forest Residues to a Methane-Rich Gas in a High-Throughput Gasifier,* PNL-6570, Pacific Northwest Lab, Richland, Washington.

Herbert, P. K., Baguss, I., and Loeffler, J. C., 1988, "Low-btu Gas From Bark and Waste Via CFB Gasification," *Proc. Energy From Biomass and Wastes XII,* Institute of Gas Technology, Chicago.

Hohenstein, W. G., and Wright, L. L., 1994, "Biomass Energy Production in the United States: an Overview," *Biomass and Bioenergy,* pp. 161–173.

Horvath, A. (Enviropower, Espoo, Finland), 1995, personal communication to E. Larson, Oct. 9.

IGS (Iowa Geological Survey), 1973, "Resource Development Land and Water Use Management, Eleven County Area South Central Iowa," Iowa City, Iowa.

Kinoshita, C. M., 1995, "Bagasse Gasification for Electricity Generation in Sugar/Alcohol Plants," presentation at the Workshop on Perspectives for Alcohol Fuel in Brazil, Univ. of Sao Paulo, Sao Paulo, Brazil, June 28–29.

Larson, E. D., and Hughes, W. E. M., 1996, "Performance Modeling of Aeroderivative Steam-Injected Gas Turbines and Combined Cycle Systems Fueled From Fixed or Fluid-Bed Biomass Gasifiers," ASME Paper No. 96-GT-89.

Lau, F. S., Carty, R. H., Onischak, M., and Bain, R. L., 1993, "Development of the IGT Renugas Process," *Proc. Strategic Benefits of Biomass and Waste Fuels,* Electric Power Research Institute, Palo Alto, CA.

Lundberg, H. (TPS, Stockholm, Sweden), 1994, personal communication to R. Williams (Center for Energy and Environmental Studies, Princeton Univ., Princeton, NJ), Oct. 29.

Maniatis, K., and Ferrero, G.-L., 1995, "The Thermie Targeted Projects on Biomass Gasification," *Proc. Second Biomass Conference of the Americas: Energy Environment, Agriculture, and Industry,* NREL/CP-200-8098, National Renewable Energy Lab, Golden, CO, pp. 576–585.

Marrison, C. I., 1995, *The Effect of Plant Size on the Economics of Producing Energy From Biomass,* Working Paper 133, Ctr. Energy & Environ. Studies, Princeton U., Princeton, NJ, June.

Marrison, C. I., and Larson, E. D., 1995a, "Cost Versus Scale for Advanced Plantation-Based Biomass Energy Systems in the U.S.," *Proc. Symposium on Greenhouse Gas Emissions and Mitigation Research,* US Environmental Protection Agency, Washington, DC.

Marrison, C. I., and Larson, E. D., 1995b, "Cost Versus Scale for Advanced Plantation-Based Biomass Energy Systems in the U.S.," *Proc. Second Biomass Conference of the Americas: Energy Environment, Agriculture, and Industry,* NREL/CP-200-8098, National Renewable Energy Lab, Golden, CO, pp. 1272–1290.

Paisley, M. A., and Farris, G., 1995, "Development and Commercialization of a Biomass Gasification/Power Generation System," *Proc. Second Biomass Conference of the Americas: Energy Environment, Agriculture, and Industry,* NREL/CP-200-8098, National Renewable Energy Lab, Golden, CO, pp. 553–564.

Paisley, M. A., and Gebhard, S. C., 1995, "Gas Cleanup for Combined Cycle Power Generation Using a Hot Gas Conditioning Catalyst," *Proc. Second Biomass Conference of the Americas: Energy Environment, Agriculture, and Industry,* NREL/CP-200-8098, National Renewable Energy Lab, Golden, CO, pp. 617–629.

Puhakka, M. (General Manager, Bioflow Ltd., Varkhaus, Finland), 1994, personal communication to E. Larson, Feb.

Stahl, K., Skog, E., and Lundqvist, R., 1993, "The Biomass IGCC Demonstration Power Plant, Varnamo, Sweden," *Proc. 12th Coal Gasification Conference,* Electric Power Research Institute, Palo Alto, CA.

Sydkraft AB, 1995, *Gas Operations Start Up at Sydkraft's Unique Biofueled Plant in Varnamo, Sweden,* press release, Malmo, Sweden, Oct. 5.

TPS, 1995, *Swedish Technology Selected for Prestigous BioEnergy Project in Brazil,* press release, Stockholm, Sweden, Sept. 7.

UMinn (Univ. of Minnesota), 1994, *Sustainable Biomass Energy Production, Vol. 1, Dedicated Feedstock Energy Supply,* for National Renewable Energy Lab., Golden, CO, Sept.

USGS (United States Geological Survey), 1986, *1:100000 scale topographic map,* Appanoose County, Lucas County, Monroe County, Wayne County.

Walsh, M. E., and Graham, R., 1995, *Biomass Feedstock Supply Analysis: Production Costs, Land Availability, Yields,* Biomass Feedstock Development Pgm., Oak Ridge National Laboratory, Oak Ridge, TN, 18 Jan.

Wiant, B. C., Bachovchin, D. M., Alvin, M. A., Onischak, M., Carty, R. H., and Knight, R. A., 1995, "Testing Status of the Biomass Gasification Hot Gas Cleanup Demonstration Program," paper presented at (but not in *Proceedings*) Second Biomass Conference of the Americas: Energy, Environment, Agriculture, and Industry, Portland, OR, Aug. 21–24.

Williams, R. H., and Larson, E. D., 1993, "Advanced Gasification-Based Biomass Power Generation," in *Renewable Energy: Sources for Fuels and Electricity,* T. B. Johansson, H. Kelly, A. K. N. Reddy, and R. H. Williams, eds., Island Press, Washington, DC, pp. 729–785.

Downloaded 02 Jun 2010 to 171.66.16.105. Redistribution subject to ASME license or copyright; see http://www.asme.org/terms/Terms_Use.cfm

Modeling Sulfur Dioxide Capture in a Pulverized Coal Combustor

R. B. Nair

S. Yavuzkurt

Center for Gas Turbines and Power,
Department of Mechanical Engineering,
The Pennsylvania State University,
University Park, PA

The formation and capture of sulfur dioxide in a pulverized coal combustor is investigated. A two-dimensional, steady, axisymmetric code, PCGC-2 (Pulverized Coal Gasification and Combustion—two Dimensional), originally developed at Brigham Young University, has been used to simulate combustion of the pulverized coal. This paper represents part of a project to investigate simultaneously enhancing sulfur capture and particulate agglomeration in combustor effluents. Results from the code have been compared to experimental data obtained from MTCI's (Manufacturing Technology and Conversion International) test pulse combustor, which generates sound pressure levels of ~180 dB. The overall goal behind the pulse combustor program at MTCI is to develop combustors for stationary gas turbines that use relatively inexpensive coal-based fuels. This study attempts to model the capture of sulfur dioxide when injected into a pulse combustor firing micronized coal. While this work does not presume to model the complex gas flow-field generated by the pulsating flow, the effects of the acoustic field are expressed by increased heat and mass transfer to the particles (coal/sorbent) in question. A comprehensive calcination-sintering-sulfation model for single particles was used to model the capture of sulfur dioxide by limestone sorbent. Processes controlling sulfation are external heat and mass transfer, pore diffusion, diffusion through the product layer of $CaSO_4$, sintering, and calcination. The model was incorporated into the PCGC-2 program. Comparisons of exit concentrations of SO_2 showed a fairly good agreement (within ~10 percent) with the experimental results from MTCI.

Introduction

With use of coal predicted to increase by the turn of the century (*The Economist,* June 1994), it has become imperative that the question of pollutants from coal-burning power plants be addressed. Some of the many polluting emissions from coal-fired utility boilers are sulfur oxides (SO_2 + SO_3), which have been found to be acid rain precursors. While natural emissions of sulfur have remained essentially constant, emissions from anthropogenic sources keep increasing. Stringent new regulations aim to reduce SO_2 emissions to 50 percent of their 1980 levels by the year 2000. Possible strategies for SO_2 control can be classified according to the stage of implementation, namely, before (physical beneficiation), during (atmospheric fluidized bed combustion or limestone sorbent injection multistage burning), and after combustion (wet or dry flue gas desulfurization). Wet scrubber systems (post-combustion) have been in use for some years; however, they are subject to drawbacks like corrosion, pressure drop through scrubber, and crystal deposits in the equipment. Hence, in-situ capture of sulfur dioxide by limestone sorbent is an attractive option, partly because limestone is cheap; further, the product ($CaSO_4$ in case of SO_2 capture) is inert. The limestone-based sorbent decomposes due to heating by hot gases and forms lime (CaO), which reacts further with SO_2 in the presence of excess O_2 to form $CaSO_4$. The reacted sorbents are then typically collected along with the fly-ash in a bag house or an electrostatic precipitator. A comprehensive sulfation model (Milne et al., 1990a, b, c) is used to describe the calcination, sintering, and sulfation processes.

Studies of pulverized coal combustion show that char combustion is the limiting factor in the overall burnout of coal in practical furnaces. This is primarily because in the later stages of combustion, the coal particle/agglomerate gets entrained in the bulk flow and as a result the effective Nusselt and Sherwood numbers reduce to the pure conduction values of 2.0. Theoretical investigations of acoustic enhancement of heat and mass transfer in the case of oscillating flow with and without a superimposed steady flow showed that relative slip velocity was maintained well into the later stages of coal burnout, and correlations for Nusselt and Sherwood numbers as a function of the ratio of the acoustic slip velocity to the steady slip velocity were developed (Ha and Yavuzkurt, 1993). The present study seeks to predict sulfur dioxide concentrations in a pulse combustor firing pulverized coal (Fig. 1). The effects of the acoustic fluctuations introduced by pulse combustion on the gas phase are not modeled, nor is the admittedly important interdependence of acoustic pressure fluctuation and combustion heat release accounted for. However, acoustic effects on the particles (both limestone and coal) are modeled using the correlation developed by Ha and Yavuzkurt (1993).

Modeling of Sulfation

Dry sorbent injection in pulverized coal boilers occurs at temperatures ranging from 1100–1500 K and the residence times range from 0.5–3.0 seconds. The sorbent initially calcines according to the following reaction before undergoing sulfation:

$$CaCO_{3(s)} \rightarrow CaO_{(s)} + CO_{2(g)} \quad (1)$$

The porous carbonate decomposes to a highly porous calcine of the same volume. Rapid initial sulfation of the newly formed CaO can occur in a high-temperature reactor in the presence of SO_2 and O_2 according to

$$CaO_{(s)} + SO_{2(g)} + 1/2O_{2(g)} \rightarrow CaSO_{4(s)} \quad (2)$$

However, it is important that the temperature be in the range for which pronounced sulfation can occur (1100–1500 K). Beyond 1500 K, the processes of grain sintering and decomposition of the $CaSO_4$ product occur, while below 1100 K, the kinetics of sulfation are too slow. The processes of calcination,

Contributed by the International Gas Turbine Institute and presented at the 41st International Gas Turbine and Aeroengine Congress and Exhibition, Birmingham, United Kingdom, June 10–13, 1996. Manuscript received at ASME Headquarters February 1996. Paper No. 96-GT-112. Associate Technical Editor: J. N. Shinn.

Copyright © 1997 by ASME

Downloaded 02 Jun 2010 to 171.66.16.105. Redistribution subject to ASME license or copyright; see http://www.asme.org/terms/Terms_Use.cfm

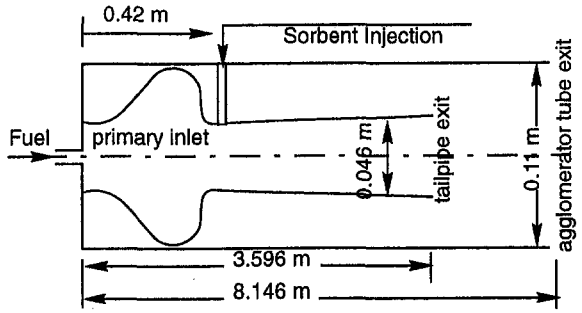


Fig. 1 MTCI pulse combustor schematic (not to scale)

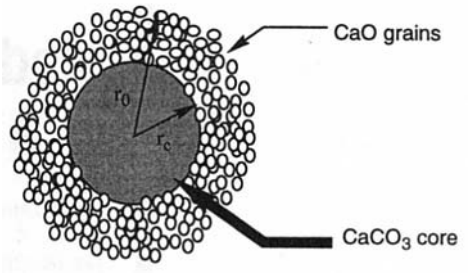


Fig. 2 Shrinking core model (Milne et al., 1990a)

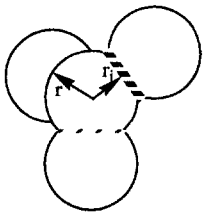


Fig. 3 Overlapping grain model (Lindner and Simonsson, 1981)

sintering, and sulfation occur simultaneously in a combustor. The following sections provide some particulars of each process. For more details refer to Milne et al. (1990a, b, c).

Calcination. The calcination process is described by a shrinking core model for a spherical particle. While this assumption may not always be true, especially at high heating rates, it is nevertheless useful as a simple approximation. Decomposition begins on the surface and proceeds inward symmetrically. Highly porous calcium oxide forms on the surface, and the radius of the unreacted core decreases as the reaction progresses. At the reaction interface, heat is absorbed and CO_2 diffuses out during calcination.

Mathematically, the shrinking core model can be represented as

$$\frac{dV_c}{dt} = -k_1(4\pi r_c^2) \tag{3}$$

However, in order to fit the calcination rate data from Hu et al. (1994) better, the following empirically modified equation was used:

$$x = 1 - \left(1 - \frac{k}{d_0^{0.55}}\, t\right)^3 \tag{4}$$

where x is the extent of calcination, k is a modified rate constant with properly adjusted units, d_0 is the initial diameter of the particle. The equation for k was the same as that used by Milne et al. (1990a), i.e.,

$$k = 10.303 \exp(-10980/T) \tag{5}$$

Sintering. The sintering model proposed by Lindner and Simonsson (1981), which approximated the calcine structure as a system of overlapping grains (Fig. 3) was used. The surface area and volume of a system of overlapping grains with n contacts per grain, r and r_i being the initial radius of the grain and the distance from the center of the grain to the plane of contact, respectively, were deduced from geometric considerations. Sintering influences both surface area and porosity. The model quantifying the loss of surface area is the one formulated by Milne et al. (1990b) as an empirical equation. Equation (6) accounts for the loss of surface area due to the presence of both water vapor and carbon dioxide, both of which are known to influence the phenomenon. Also, in the sintering model, the change in porosity is assumed to be proportional to the change in surface area.

$$\frac{dS_m}{dt} = \left.\begin{aligned} &-2450(1 + 50.7\, p_{H_2O}^{0.17} + 10.3\, p_{CO_2}^{0.67}) \\ &\times \exp\left(-\frac{29600}{T}\right)(S_m - 5000)^2 \end{aligned}\right\} \tag{6}$$

Sulfation. The process of sulfation is a complicated phenomenon, with structural changes occurring due to the increased molar volume of the product, $CaSO_4$ in comparison to that of

Nomenclature

a = pore radius, m
c = SO_2 concentration, kmol/m^3
d_0 = initial sorbent particle diameter, m
D_p = particle diameter, m
D_e = effective diffusivity, m^2/s
D_m = bulk diffusivity, m^2/s
D_K = Knudsen diffusivity in pores, m^2/s
D_s = product layer diffusivity, m^2/s
k = calcination rate constant for the modified shrinking core model, m$^{0.55}$/s
k_1 = calcination rate constant using the shrinking core model, kg/m^{2}s
M_{SO2} = molecular weight of SO_2, kg/kmol
Nu_0 = steady particle Nusselt number
Nu_t = acoustic particle Nusselt number
p_{CO2} = partial pressure of CO_2 in gas phase, kPa
p_{H2O} = partial pressure of H_2O in gas phase, kPa
r_c = radius of unreacted core of particle, m
r_0 = initial sorbent particle radius, m
Re = particle Reynolds number
Sh_0 = particle Sherwood number
Sh_t = acoustic particle Sherwood number
S = surface area per unit volume of particle, m^2/m^3
S_m = surface area per unit mass of particle, m^2/kg
S_r = diffusion surface area at radius r of particle, m^2
T = gas temperature, K
$\tilde{u}$ = Favre-averaged axial gas velocity, m/s
$\tilde{v}$ = Favre-averaged radial gas velocity/m/s
V_c = volume of unreacted core, m^3
$\tilde{Y}_i$ = Favre-averaged SO_2 mass fraction
Γ_Y = turbulent gas diffusivity for SO_2, m^2/s
ϵ = porosity of particle

Downloaded 02 Jun 2010 to 171.66.16.105. Redistribution subject to ASME license or copyright; see http://www.asme.org/terms/Terms_Use.cfm

CaO. The resulting swelling of the grain causes pore closure and hinders sulfation due to increased product layer thickness. Product layer (solid state) diffusion, pore diffusion, and external mass transfer (bulk gas phase diffusion) all play a part in sulfation. Diffusion through the product layer is modeled by assuming CaO grains to be spherical. Using a quasi-steady-state approximation and assuming constant product layer diffusivity, we get simply:

$$\frac{d}{dr}\left(S_r \frac{dc}{dr}\right) = 0 \tag{7}$$

Sulfation of the exposed CaO grain surface causes a monolayer of product ($CaSO_4$) to be formed, the process being considered instantaneous compared to the time scale of the transport processes. After formation of the monolayer, product layer diffusion is assumed to be limiting for the local rate of sulfation at the grain level. Details of the boundary conditions used and the formulation of the method used in solving this equation can be found in Milne et al. (1990b). The product layer diffusivity was expressed as the following Arrhenius type expression:

$$D_s = 4.10 \times 10^{-9} \exp\left(-\frac{12820}{T}\right) \tag{8}$$

The rate of sulfation of porous CaO is also limited by transport of SO_2 to the interior of the particle. Using a quasi-steady-state approximation, the differential equation for SO_2 diffusing through and reacting simultaneously in a porous sphere is given by:

$$\frac{d}{dr}\left(D_e r^2 \frac{dc}{dr}\right) + Gr^2 = 0 \tag{9}$$

where G is the rate of consumption of SO_2 per particle volume and D_e the effective pore diffusivity. The particle was now divided into shells of constant effective pore diffusivity, and the differential equation was integrated with the appropriate boundary conditions, thereby giving the SO_2 concentration profile in the particle. The effective pore diffusivity was calculated as:

$$D_e = \frac{\epsilon}{\tau}\left(\frac{1}{D_m} + \frac{1}{D_K}\right)^{-1},$$

where,

$$D_K = 97a(T/M_{SO_2})^{1/2} \tag{10}$$

D_K is the Knudsen diffusivity which is proportional to the pore radius, a given by $a = 2\epsilon/S$. The tortuosity, τ is assumed to be 1.47. Bulk diffusion, D_m is important for very large pores, and is calculated as the effective binary diffusivity of SO_2 in a multicomponent gas mixture as described by Bird et al. (1960).

For large particles ($\sim$100 μm), the rate of transport of SO_2 from the bulk gas phase to the surface of the particle becomes an important factor in capture by the sorbent. At very low particle Reynolds numbers (cases of low gas velocity, very small particles or complete entrainment of particles), the Sherwood and Nusselt numbers reduce to 2. However, this is not so for high particle Reynolds numbers.

Integration of Sulfation Model With PCGC-2

The PCGC-2 program is based on a two-dimensional comprehensive combustion model, which can solve the set of steady-state conservation equations for particle-laden, reacting gas flows in axisymmetric systems. The $k-\epsilon$ model is used for turbulence closure. Simulations also predict mean gas field properties and Lagrangian particle properties for steady-state, turbulent flames. A comprehensive description of the PCGC-2 code and the underlying models can be found in Smoot and Smith (1985), and Smoot et al. (1987). Steady-state, Eulerian, nonlinear, elliptic, partial differential equations describe the gas phase, while a Lagrangian framework is used to compute the particle trajectories that provide the source terms for the gas-phase equations. The effects of turbulent fluctuations in the gas phase on particle reaction rates is ignored.

PCGC-2 also assumes that the off-gas (gas evolved from the devolatilizing/burning coal particle) is of a constant elemental composition. Temperature gradients within coal (or sorbent) particles are assumed negligible. Further, the percentage of nitrogen and sulfur (that cause the formation of NO_x and SO_x respectively) in coal is very small (0.5–3 percent). Hence the resulting pollutant concentrations are small and will not significantly affect the velocity, density, or temperature fields. Therefore, the sorbent loading necessary is very light, and it does not affect the radiation fluxes in the energy equation; moreover, the sorbent particles injected into the combustor are small and do not cause changes in the mean gas velocities. Therefore, transport equations for polluting species can be decoupled from the main combustion model and solved following convergence of the combustion scheme. The principal advantage of this decoupling is the tremendous saving in computer resources. A transport equation for the SO_2 species can be written as:

$$\bar{\rho}\tilde{u}\left(\frac{\partial}{\partial x}\tilde{Y}_i\right) + \bar{\rho}\tilde{v}\left(\frac{\partial}{\partial r}\tilde{Y}_i\right) - \frac{\partial}{\partial x}\left(\Gamma_Y \frac{\partial \tilde{Y}_i}{\partial x}\right) - \frac{1}{r}\frac{\partial}{\partial r}\left(r\Gamma_Y \frac{\partial \tilde{Y}_i}{\partial r}\right) = \bar{W}_i \tag{11}$$

W_i is the mean chemical reaction source + sink term for the SO_2 species mass fraction. The source term for each Eulerian finite-difference cell is comprised of the sulfur released to the cell by reacting coal particles within the cell. The sink term is due to sulfur dioxide capture by the sorbent particles passing through the cell. The density and velocity fields and the turbulent diffusion coefficients are obtained from the converged coal combustion solution, which is solved prior to invoking the sorbent model. In order to solve Eq. (11), the following steps are taken: (1) First the reacting gas–coal particle flowfield is solved neglecting the effects of sorbent particles. The source term in Eq. (11) is calculated during this step. Sulfur release from the coal is assumed to occur at a rate proportional to the coal weight loss (similar to other elements) in PCGC-2. Local instantaneous equilibrium is assumed for all homogeneous chemical reactions except for NO_x. Thus, sulfur dioxide mass fractions can be computed from local equilibrium and the mass source term can be computed accordingly from the total mass of coal off-gas released by the reacting particles for each cell. (2) The Eulerian bulk number density for the particles is solved for next. The particle number density is necessary to calculate the so-called diffusive velocity of the sorbent particles during the Lagrangian tracking phase. (3) Once the number density is calculated, the Lagrangian equations of motion for the sorbent particle are solved. For each time step, the sorbent model (discussed in previous sections) is called and the sink terms (due to capture of sulfur dioxide by the sorbent during the sulfation process) are computed for each cell. (4) The net source/sink terms are now calculated and Eq. (11) is solved for the SO_2 mass fraction. Iteration of steps (3) and (4) is carried out till convergence.

The parameters for the simulation of the coal combustion are given in Table 1, and those for the sorbent particles are given in Table 2. Methane is used as a supplemental fuel for ease of ignition of the pulverized coal (primary fuel), and it has been taken into account in the combustion simulation. The pulse combustor is 3.596 m in length (including the tailpipe), and it is enclosed by a so-called "agglomerator tube" wherein the

Downloaded 02 Jun 2010 to 171.66.16.105. Redistribution subject to ASME license or copyright; see http://www.asme.org/terms/Terms_Use.cfm

Table 1 Parameters for coal combustion simulation

Parameter	Value
Air flow rate (kg/s)	0.2113
Methane flow rate (kg/s)	0.0027
Coal particle mass flow rate (kg/s)	0.0147
Mean particle diameter (μm)	49
Combustor tailpipe diameter (m)	0.0460
Combustor operating pressure (MPa)	3.0840
Combustor length (m)	3.5960
Combustor length including agglomerator tube (m)	8.1460

agglomeration of fly-ash particles has been observed. (MTCI Inc., 1994).

Acoustic Field Effects on Particles

As described by Rawson (1988), in a traveling wave acoustic field with a sound pressure of P_{rms} and acoustic impedance $\rho_g c_{\text{sound}}$, ρ_g being the density of the medium, and c_{sound} the speed of sound, the acoustic velocity amplitude is given by:

$$U_1 = \frac{\sqrt{2}P_{\text{rms}}}{\rho_g(\gamma R T_g)^{0.5}},$$

where

$$P_{\text{rms}} = 10^A, \quad \text{and} \quad A = (L_p - 94)/20 \tag{12}$$

L_p being the sound intensity in dB. When the Reynolds number of the flow over the particle is small, the entrainment factor η can be obtained by equating the particle drag and inertial forces for a smooth sphere as shown by Rawson (1988):

$$\eta = \frac{1}{(1 + \omega^2\tau_p^2)^{1/2}}, \quad \tau_p = \frac{\rho_p D_p^2}{18\,\mu} \tag{13}$$

where τ_p is the particle relaxation time, ω is the angular frequency of the acoustic wave, and μ the kinematic viscosity of the gas.

In order to implement the acoustic field in the PCGC-2 program, correlations developed by Ha (1990) using an unsteady, two-dimensional computer program for the heat and mass transfer over a spherical particle in the presence of an acoustic field were used. Since the sorbent (*or* coal) particles are more or less entrained in the gas flow, the steady relative velocity U_0 between the gas and the particle is close to zero. From Ha (1990), the dimensionless space and time-averaged, quasi-steady heat and mass transfer coefficients, normalized by their steady flow values, can be expressed as a function of the ratio

Table 2 Sorbent model parameters

Parameter	Value
Sorbent flow rate (kg/s)	0.0028
Particle diameter (μm)	10
BET surface area of carbonate (m^2/g)	10

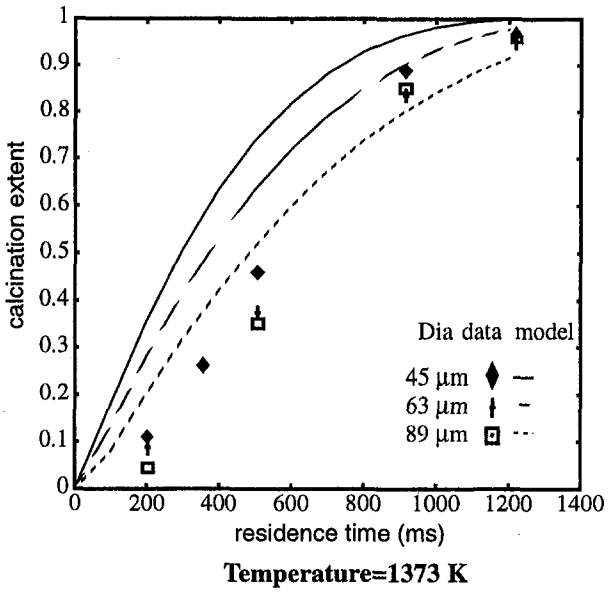


Fig. 4 Extent of calcination of limestone particles (comparison with experiments, Hu et al., 1994)

ξ ($=U_1/U_0$). The steady Reynolds number Re is given by Re $= \rho U_0 D_p/\mu$.

$$\frac{\text{Nu}_t - 2}{\text{Nu}_0 - 2}\left(\text{or}\ \frac{\text{Sh}_t - 2}{\text{Sh}_0 - 2}\right) = F(\xi) \tag{14}$$

where F is given by (Ha, 1990; Ha and Yavuzkurt, 1993) as:

$$F = 1.0 + 9.608 \times 10^{-3}\xi - 0.109608\,\xi^2 \quad \text{for } (0 \le \xi \le 1)$$

$$F = 0.7628\xi^{0.5} + 0.1372 \quad \text{for } \xi > 1 \tag{15}$$

where Nu_0 and Sh_0 are given by the following equations:

$$\text{Nu}_0 = 2.0 + 0.65\,\text{Re}^{1/2}\text{Pr}^{1/3} \tag{16}$$

$$\text{Sh}_0 = 2.0 + 0.65\,\text{Re}^{1/2}\text{Sc}^{1/3} \tag{17}$$

Results and Discussion

Model Validation. Figures 4 and 5 show a comparison of the experimental results obtained for the calcination and sulfation of different sized Linden Hall[1] carbonate particles. These experiments were conducted in an entrained flow reactor (EFR) consisting of a preheater, a side-heated sorbent injector, and a vertical reactor. The preheater, injector, and reactor were electrically heated to provide the desired gas preheating temperature and reactor temperature. The entrainment gas used was dry air that was preheated to same temperature as in the isothermal zone of the reactor. Experiments were carried out for temperatures of 1000°C and 1100°C. For the sulfation experiments, the SO_2 concentration was kept at 2000 ppm, by adjusting the flow rate via a mass flow controller. For further details on the experimental procedure, please refer to Hu et al. (1994). As is seen in Fig. 4, the model predicts extents of calcination in the later stages quite well, while it overpredicts during initial stages of calcination. However, for the purposes of inclusion in the PCGC-2 program in order to compute sulfur dioxide concentrations with and without sorbent, the time taken for calcination is but a small fraction of the overall residence time in the combustor, so the discrepancy does not significantly affect the simulation performance.

[1] Linden Hall is a trade name for a limestone quarried in Pennsylvania.

Downloaded 02 Jun 2010 to 171.66.16.105. Redistribution subject to ASME license or copyright; see http://www.asme.org/terms/Terms_Use.cfm

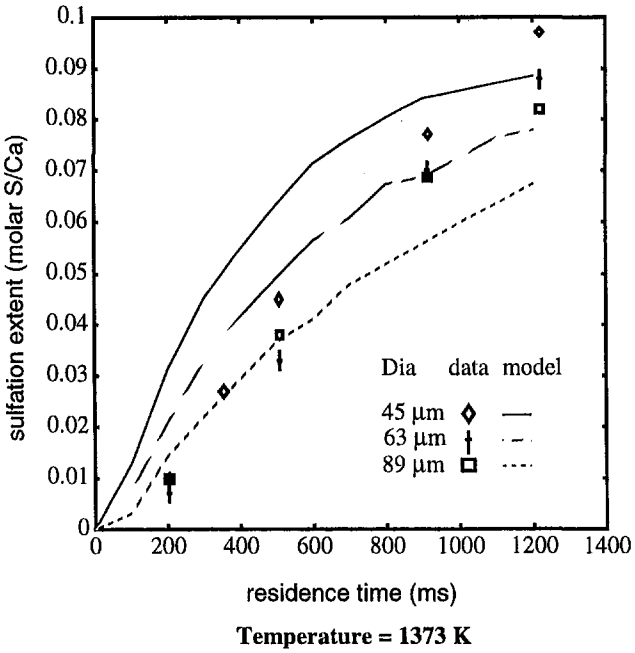


Fig. 5 Extent of sulfation of limestone particles (comparison with experiments, Hu et al., 1994)

Figure 5 shows a comparison of model results for sulfation of Linden Hall carbonate particles with experimental data from Hu et al. (1994). The results are seen to be within 20–30 percent for the most part, the maximum discrepancy occurring during the initial stages of sulfation. However, the discrepancy in the sulfation results is a consequence of that seen in the calcination results, since availability of fresh lime from calcination is necessary for subsequent sulfation. The overprediction in calcination in Fig. 4 thereby contributes to the overprediction in sulfation in Fig. 5.

Sulfur Dioxide Capture Predictions From PCGC-2. Figure 6 shows the representative trajectory of a sorbent particle injected through the side wall. The particles were injected with sufficient radial velocity to achieve penetration to at least three-fourths the diameter of the combustor. The particle then is seen to turn and get entrained in the primary flow and then finally leave the combustor. Since PCGC-2 is an axisymmetric code, side wall injection is modeled by a circumferential slit around the combustor.

Figure 7 shows the extent of sulfation and calcination of a typical sorbent particle that reacts to form $CaSO_4$, as it travels downstream in the combustor. As is seen from Fig. 7, calcination occurs fairly rapidly, and within ~1 m from the point of

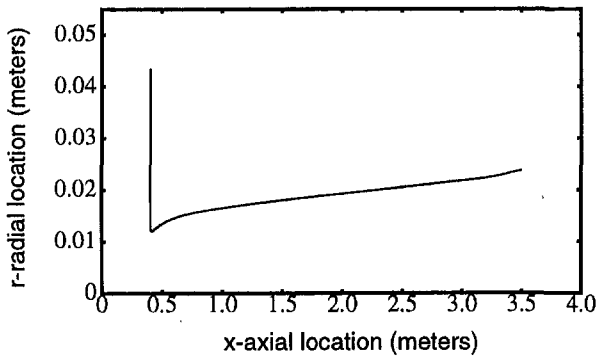


Fig. 6 Trajectory of 10 μm particle (with side wall injection)

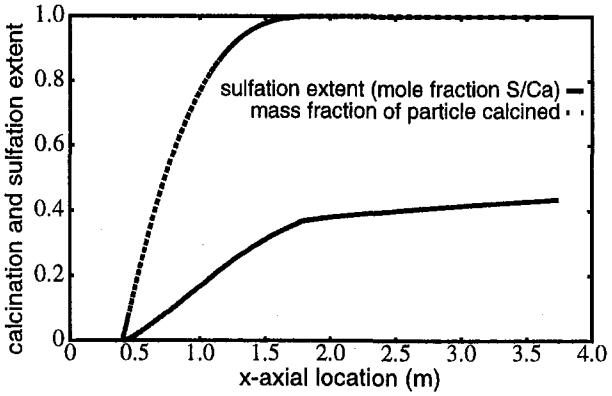


Fig. 7 Extent of sulfation of 10 μm particle (with side wall injection)

injection, the sorbent is completely calcined. It is also seen that the sulfation curve starts leveling off after the calcination is complete. This is because porosity and surface area start decreasing once the calcination is complete and sulfation is the only ongoing reaction. Hence, no fresh calcine is available to increase the porosity and specific surface area that aid in enhancing sulfation. Instead, the specific surface area and the porosity decrease due to sintering. The porosity also decreases because of pore closure, since the molar volume of the reaction product ($CaSO_4$) is 2.72 times that of the calcine (CaO).

Figure 8 shows the radial variation of the SO_2 concentration with and without sorbent, at different axial locations within the combustor for 10 μm sorbent particles injected through the side wall. The concentration of SO_2 decreases quite dramatically as one progresses along the combustor axis. The concentration of sorbent particles injected from the side wall is maximum in the concentric area ranging from $\sim\frac{1}{5}$ th of the combustor radius to $\sim\frac{1}{2}$ the combustor radius. This is seen from the concentration profiles of SO_2 shown in Figs. 8(a, b), which indicate a minimum around this concentric area and higher values near the walls and the centerline.

Since sidewall injection was modeled as a two-dimensional case because of restrictions of axisymmetric flow in PCGC-2, there is effectively an enhanced mixing and distribution of sorbent particles over a greater area than would be the case in an actual three-dimensional simulation. This would end up enhancing the capture of sulfur dioxide when compared to the actual simulation, and hence could be considered a drawback of two-dimensional axisymmetric simulations. For a more realistic picture, a three-dimensional simulation would be essential. However, most of the important phenomena can be explained using a two-dimensional axisymmetric model. Concentrations without sorbent injection are seen to be about 700 ppm throughout the combustor. With sorbent injection, the average radial concentration levels in the combustor drop to ~500 ppm at a distance of 0.765 m from the primary injector (0.362 m from the sidewall injector), ~130 ppm at the end of combustor tailpipe (x = 3.596 m) and ~105 ppm at the end of the agglomerator tube (x = 8.146 m). From the figures, it might seem that the mole fractions actually increase toward the exit, but this is primarily because diffusion from the walls tends to equalize the concentration gradient present upstream; further, there is no significant capture in the agglomerator tube.

Figure 9 shows the variation in amount of sulfur dioxide captured with change in the particle diameter. The percentage of total capture was computed by density-weighted integration of the SO_2 concentrations over the combustor volume. The integration was carried out over both the radial and axial directions in order to get a volume integrated capture. As expected, amount of sulfur dioxide captured by the sorbent decreases with increasing particle size. For 9 μm sorbent particles percentage capture

Downloaded 02 Jun 2010 to 171.66.16.105. Redistribution subject to ASME license or copyright; see http://www.asme.org/terms/Terms_Use.cfm

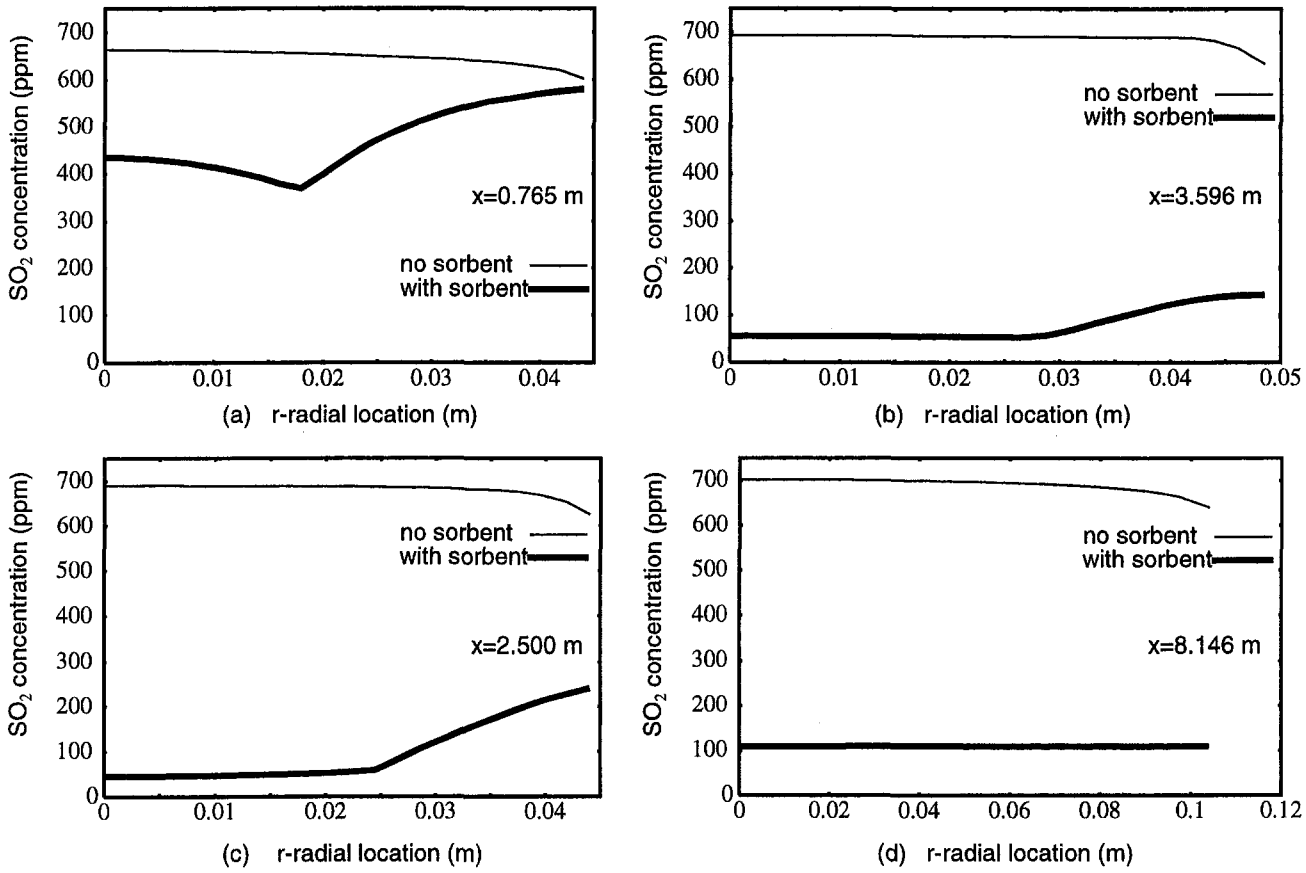


Fig. 8 Radial variation of SO_2 concentration at different axial locations along the combustor with and without sorbent

is as high as 85 percent while for 30 μm particles, capture falls to 33 percent.

Figure 10 shows radial variations of SO_2 concentration at the agglomerator tube exit when using different sorbent particle diameters. Again, using smaller particles gave lower exit concentrations. Hence, smaller sorbent sizes are definitely better from the viewpoint of enhanced sulfur dioxide capture, but the benefits obtained from this have to be weighed against the difficulty of capturing and disposing of the small sorbent particles in the flue gas.

Experimental tests were carried out by MTCI Inc.[2], for cases of combustion of pulverized coal with and without sorbent at ~180 dB, ~40 Hz. The tests were carried out for a mixture of methane and pulverized coal as indicated in Table 1. Methane was used as a supplemental fuel for ease of ignition. Comparisons to MTCI predictions revealed a fairly good match. MTCI reported SO_2 concentrations of ~711 ppm at the agglomerator tube exit without sorbent, which upon injection of sorbent fell to ~56 ppm. The conditions at which the MTCI test run was carried out were identical to the test case conditions reported earlier in this paper, in Tables 1 and 2.

Limitations of the Present Approach. The assumptions inherent in PCGC-2, for instance, that the release of sulfur from coal occurs at a rate proportional to its weight loss, can be considered limitations in the procedure used. Errors may be introduced due to the cumulative effect of this assumption and the fact that the sorbent model is invoked only after complete convergence of the main code. Further, the two-dimensional axisymmetric assumption introduces errors in predicting extent of sorbent mixing when used to simulate a realistic three-dimensional situation. This can lead to an overprediction compared to realistic cases.

Conclusions

A comprehensive sorbent model incorporating the effects of calcination, sintering, and sulfation has been incorporated into the PCGC-2 program. The model was first validated against experimental data for calcination and sulfation and seen to match within 20–30 percent of experimental data. Test cases were run for combustion of a mixture of methane and pulverized coal fuel. Gas properties, particle diameter, injection location, and the particle flow history can influence the overall capture by the sorbent. Optimum locations for sorbent injection can

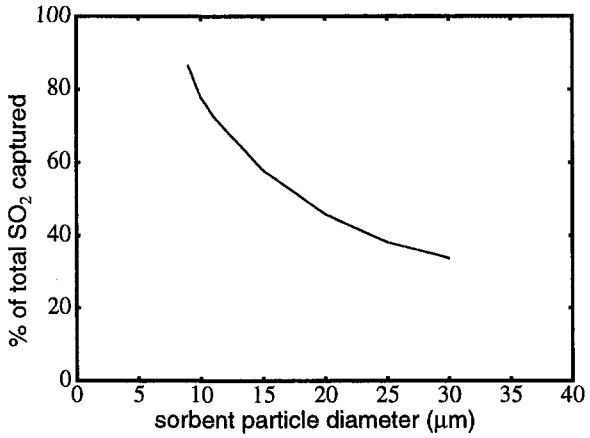


Fig. 9 Variation of percent SO_2 captured with increase in particle diameter

[2] Data were obtained as private communication from MTCI Inc., Columbia, MD.

Downloaded 02 Jun 2010 to 171.66.16.105. Redistribution subject to ASME license or copyright; see http://www.asme.org/terms/Terms_Use.cfm

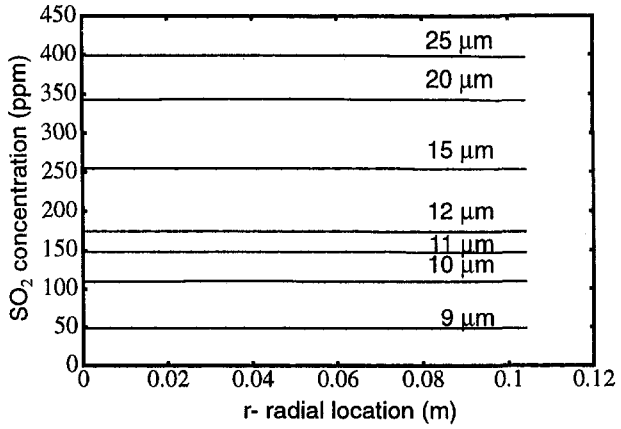


Fig. 10 SO_2 concentration at agglomerator tube exit—different particle diameter

also be identified using a comprehensive model such as the one used here. Results from the simulations show reasonable agreement with experimental test pulse combustor data for sulfur dioxide concentrations for both with and without sorbent injection (and also for other species, but they have not been presented here). Predicted exit concentrations of ~100 ppm with sorbent injection and ~700 ppm without sorbent compare well to data of 56 ppm and 711 ppm, with and without sorbent injection, respectively.

Acknowledgments

This work was partially sponsored by the DOE/METC and MTCI Inc. of Columbia, Maryland under subcontract No. 10038-04, Mod. 3. Their support is greatly appreciated.

References

Bird, R. B., Stewart, W. E., and Lightfoot, E. N., 1960, *Transport Phenomena,* Wiley, New York.

Borgwardt, R. H., 1985, "Calcination Kinetics and Surface Area of Dispersed Limestone Particles," *AIChE J.,* Vol. 31, pp. 103–111.

Borgwardt, R. H., Bruce, K. R., and Blake, J., 1987, "An Investigation of Product-Layer Diffusivity for CaO Sulfation," *Ind. Eng. Chem. Res.,* Vol. 26, pp. 1993–1998.

The Economist, 1994, "Power to the People," A Survey of Energy, June 18–24.

Ha, M. Y., 1990, "*A Theoretical Study of Augmentation of Particle Combustion Via Acoustic Enhancement of Heat and Mass Transfer,*" Ph.D. Thesis, The Pennsylvania State University, University Park, PA.

Ha, M. Y., and Yavuzkurt, S., 1993, "Heat Transfer Past Particles Entrained in an Oscillating Flow With and Without a Steady Velocity," *Int. J. Heat Mass Transfer,* Vol. 36, pp. 949–959.

Hu, N., Liu, Y., Miller, S. F., and Scaroni, A. W., 1994, "Experimental Investigation of High-Temperature, Short Residence-Time Calcination and Sulfation of Limestone and Dolostone Sorbents," *Proc. American Chemical Society National Meeting,* San Diego, p. 233.

Lindner, B., and Simonsson, D., 1981, "Comparison of Structural Models for Gas-Solid Reactions in Porous Solids Undergoing Structural Changes," *Chem. Eng. Sci.,* Vol. 36, pp. 1519–1527.

Miller, S. F., Hoffmann, T. L., Hu, N., Nair, R. B., Sharifi, R., Chen, W., Irwin, V., Miller, B. G., Koopmann, G. H., Yavuzkurt, S., and Scaroni, A. W., 1994, "Preliminary Demonstration of Acoustically-Enhanced Sulfur Capture and Bimodal Agglomeration," Final Report for Phase II, Work Performed for Subcontract No. 10038-04 Under DOE Contract No. DE-AC21-89MC26288.

Milne, C. R., Silcox, G. D., Pershing, D. W., and Kirchgessner, D. A., 1990a, "Calcination and Sintering Models for Application to High Temperature, Short-Time Sulfation of Calcium-Based Sorbents," *Ind. Eng. Chem. Res.,* Vol. 29, pp. 139–149.

Milne, C. R., Silcox, G. D., Pershing, D. W., and Kirchgessner, D. A., 1990b, "High Temperature, Short-Time Sulfation of Calcium-Based Sorbent. I. Theoretical Sulfation Model," *Ind. Eng. Chem. Res.,* Vol. 29, pp. 2192–2201.

Milne, C. R., Silcox, G. D., Pershing, D. W., and Kirchgessner, D. A., 1990c, "High Temperature, Short-Time Sulfation of Calcium-Based Sorbents. 2. Experimental Data and Theoretical Model Predictions," *Ind. Eng. Chem. Res.,* Vol. 29, pp. 2201–2214.

MTCI, Inc., 1994, Private Communication.

Rawson, S. A., 1988, "An Experimental Investigation of the Influence of High Intensity Acoustics on Heat and Mass Transfer Rates From Spheres as Related to Coal-Water Slurry Fuel Combustion Enhancement," M.S. Thesis, The Pennsylvania State University, University Park, PA.

Smoot, L. D., and Smith, P. J., 1985, *Coal Combustion and Gasification,* Plenum Press, New York, NY.

Smoot, L. D., Smith, P. J., and Brewster, B. S., 1987, "Revised User's Manual, *P*ulverized *C*oal *G*asification or *C*ombustion-*2* Dimensional," Vol. II, Final Report, Work Performed for the U.S. Department of Energy under Contract No. DE-AC21-85MC22059.

Silcox, G. D., Kramlich, J. C., and Pershing, D. W., 1989, "A Mathematical Model for the Flash Calcination of Dispersed $CaCO_3$ and $Ca(OH)_2$ particles," *Ind. Eng. Chem. Res.,* Vol. 28, pp. 155–160.

Smith, J. M., 1981, *Chemical Engineering Kinetics,* McGraw-Hill, New York, p. 647.

Downloaded 02 Jun 2010 to 171.66.16.105. Redistribution subject to ASME license or copyright; see http://www.asme.org/terms/Terms_Use.cfm

Next-Generation Integration Concepts for Air Separation Units and Gas Turbines

A. R. Smith

J. Klosek

D. W. Woodward

Air Products and Chemicals, Inc.,
Allentown, PA 18195

The commercialization of Integrated Gasification Combined Cycle (IGCC) power has been aided by concepts involving the integration of a cryogenic air separation unit (ASU) with the gas turbine combined-cycle module. Other processes, such as coal-based ironmaking and combined power/industrial gas production facilities, can also benefit from the integration. It is known and now widely accepted that an ASU designed for "elevated pressure" service and optimally integrated with the gas turbine can increase overall IGCC power output, increase overall efficiency, and decrease the net cost of power generation when compared to nonintegrated facilities employing low-pressure ASUs. The specific gas turbine, gasification technology, NO_x emission specification, and other site specific factors determine the optimal degree of compressed air and nitrogen stream integration. Continuing advancements in both air separation and gas turbine technologies offer new integration opportunities to improve performance and reduce costs. This paper reviews basic integration principles and describes next-generation concepts based on advanced high pressure ratio gas turbines, Humid Air Turbine (HAT) cycles and integration of compression heat and refrigeration sources from the ASU. Operability issues associated with integration are reviewed and control measures are described for the safe, efficient, and reliable operation of these facilities.

Introduction

Separation of air into its constituents is possible by employing adsorption, chemical, cryogenic or membrane technologies. For most oxygen production requirements in excess of 2500 Nm^3/h, the cryogenic process is the most efficient and cost-effective technology. Oxygen and nitrogen products can be produced from compressed air at high recoveries and purities using a conventional two distillation column process. Although operating at the opposite end of the temperature scale, gas turbines also require compressed air for supply of oxygen and for cooling the combustion process. A gas turbine that is designed for optimal performance with high-Btu fuels such as natural gas and distillate, may not perform optimally when fueled with medium and low-Btu fuels available from gasification processes. Because of design, manufacturing, and cost considerations, the major components in a gas turbine are usually not modified for a specific project. In contrast, the significantly lower cost and module design of an air separation unit makes it more amenable to project specific design changes. Project specific design of the ASU to accept air extracted from the gas turbine and provide injection of residual nitrogen into the turbine insures the gas turbine performs at maximum power output and high efficiency.

Air Products has supplied ASUs with no integration, nitrogen-only integration, and full air and nitrogen integration for gasification-based gas turbine combined cycle facilities. The degree of integration was determined by the gas turbine's operating characteristics at the specific ambient conditions for each project. The Demkolec facility in Buggenum, The Netherlands, employs a Siemens gas turbine that supplies all of the ASU's air flow by extracting a portion of the air from the turbine's air compressor discharge. All residual nitrogen from the ASU is compressed and mixed with the medium-Btu fuel prior to combustion. The Tampa Electric facility in Polk County, Florida, uses a General Electric gas turbine with no air extraction to the ASU, but injects all the residual nitrogen from the ASU into the gas turbine's combustors. Other studies have shown the potential benefits of partial air extraction combined with nitrogen injection into the gas turbine.

As gas turbine pressure ratios continue to increase, the ASU must be designed to accommodate higher air supply and nitrogen injection pressures. The approach to the critical pressure of air and nitrogen and the impact of higher operating pressure on separation efficiency and distillation column operation need to be factored into the selection of an ASU process to provide optimum facility economics.

Cryogenic Air Separation

A cryogenic air separation unit is characterized by a number of unit operations as shown in Fig. 1. Ambient air is compressed in an intercooled centrifugal or axial-centrifugal compressor. After the final stage of compression, an aftercooler reduces the air temperature and condenses some of the moisture in the air stream. Removal of the remaining water vapor, carbon dioxide, and certain hydrocarbon contaminants occurs at near-ambient temperature in the air pretreatment unit. This system uses adsorbents such as molecular sieve to remove impurities from the air stream, using a multiple bed, cyclical process. When the adsorbent in one bed becomes loaded, the air stream is switched to another bed to provide a continuous supply of treated air to the cryogenic unit. The off-line bed is regenerated by passing heated, dry nitrogen in countercurrent flow to drive the impurities from the adsorbent. After a period of time, the heating is stopped and the cool nitrogen returns the bed to normal operating temperature.

Following impurity removal, the air stream can be processed in the cryogenic unit. The first step is to cool the air in the main heat exchangers against cold, returning product streams. The cold air enters the distillation section where separation of the air into oxygen and nitrogen product streams occurs. Liquid products are sent to storage, if required. The gaseous products are warmed against incoming air and proceed to individual

Contributed by the International Gas Turbine Institute and presented at the 41st International Gas Turbine and Aeroengine Congress and Exhibition, Birmingham, United Kingdom, June 10–13, 1996. Manuscript received at ASME Headquarters February 1996. Paper No. 96-GT-144. Associate Technical Editor: J. N. Shinn.

Copyright © 1997 by ASME

Downloaded 02 Jun 2010 to 171.66.16.105. Redistribution subject to ASME license or copyright; see http://www.asme.org/terms/Terms_Use.cfm

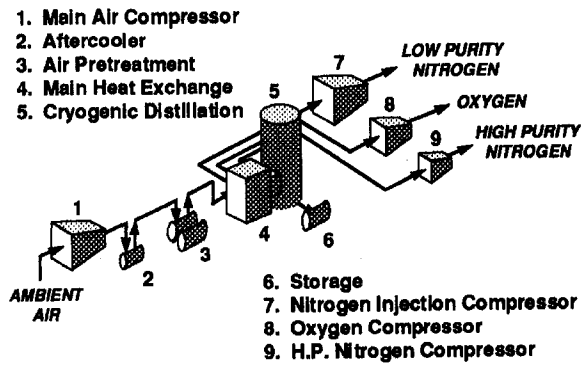


Fig. 1 Cryogenic unit operations

compressors. Oxygen purity in the range of 85–95 percent by volume is usually required for gasification processes. The gasification system usually requires some high-purity nitrogen with less than 0.1 percent oxygen by volume. Nitrogen for injection into the gas turbine usually contains from 1 to 4 percent oxygen by volume.

Figure 2 is a simplified flow diagram of the two-column cryogenic distillation process. Treated air enters the main exchanger and is cooled to near the dewpoint. A portion of the air is expanded and sent to the low-pressure column. This expansion provides the refrigeration to overcome heat leak, and produce liquids for reflux and storage. The major portion of the air stream enters the bottom of the high-pressure distillation column. As vapor flows upward, it becomes enriched in nitrogen. At the top of the column, nearly pure nitrogen is produced, and a portion is withdrawn as a gaseous product stream. Some of the nitrogen vapor is sent to the reboiler/condenser where it is condensed against boiling liquid oxygen. The liquefied nitrogen serves as reflux for both the high and low-pressure columns. The liquid flowing down the high-pressure column becomes enriched in oxygen, and forms a crude oxygen product in the sump. This liquid flows from the sump, is reduced in pressure, and flows to the middle of the low pressure distillation column. Final separation of oxygen from the remaining nitrogen occurs in this column. The pressure difference between the two columns is set by the need to maintain a temperature difference between condensing nitrogen and boiling oxygen in the reboiler/condenser. A given air supply pressure and nitrogen purity at the top of the high-pressure column determine the nitrogen condensing temperature. For a specified oxygen purity, there is a corresponding pressure at which the oxygen will boil and maintain an adequate temperature difference in the exchanger. Thus, air feed pressure determines the suction pressures to the product compressors or pumps.

Although the two-column, single reboiler process is adequate for many applications, there are alternative methods of heat integration that can reduce the power consumed by the ASU. Figure 3 shows the conventional two-column, single reboiler process; a two-column dual reboiler option; and a three-column multiple reboiler system. In the dual reboiler process (Fig. 3(b)), condensation of nitrogen from the top of the high-pressure column occurs higher up in the low-pressure column. As in the single reboiler process, the low-pressure column pressure is set by the need to maintain a temperature difference in the reboiler. Since the composition of the boiling liquid is richer in nitrogen higher up in the column, the corresponding equilibrium pressure will also be higher. Therefore, product compressor discharge pressures will be higher and power consumption will be lower compared to the single reboiler process. The bottom of the low-pressure column still requires a reboiler to generate vapor flow up the column. This duty is generated by condensing some of the feed air against boiling liquid oxygen. Liquefied air serves as intermediate reflux for the process. Figure 3(c) shows a more efficient process using three columns and multiple reboilers. This process is capable of producing up to half of the incoming nitrogen at pressures substantially higher than the single or dual reboiler processes. These are simplified examples of the numerous process cycles that can be developed for the cryogenic separation of air.

There are economic and thermodynamic limits on the operating pressures of the cryogenic process. As the operating pressure increases, the relative volatilities between oxygen, argon, and nitrogen decrease. This makes the separation process more difficult and requires more stages of distillation to produce the same purities and recoveries. As pressure increases, the difference in liquid and vapor densities decreases, making the physical separation of the two phases more difficult. A physical limit to the distillation of air is the critical pressure of nitrogen at about 3400 kPa. Two methods of using a source of air that is near or above the critical pressure of nitrogen are shown in Fig. 4. In Fig. 4(a) oxygen is removed as a liquid from the bottom of the low-pressure column, pumped to increase its pressure, and vaporized against the high-pressure air stream in the main heat exchangers. As in the reboiler, the pressure of the oxygen is set to maintain a close temperature approach to the condensing air stream. In this scheme about 30 percent of the feed air can be at high pressure. Figure 4(b) shows an option to include an expander to optimize the air feed pressure to the ASU. Varying amounts of high-pressure feed air can be expanded and the use of the oxygen pump is optional.

Basic Integration Principles

Unit integration will be discussed using the gasification combined cycle process as the example. The concepts can also be applied to other systems employing an ASU and gas turbine. Figure 5 shows a nonintegrated IGCC system employing a stand-alone ASU supplying oxygen and nitrogen to a gasifier, which in turn supplies syngas to a gas turbine. Since the majority of the feed air to the ASU is vented to atmosphere as reject nitrogen, the ASU operates at low pressure (LP ASU).

In Fig. 6 the residual nitrogen that is available after gasifier oxygen and nitrogen requirements have been met is compressed and sent to the gas turbine. Since all product streams are being compressed, the ASU air feed pressure is optimized to reduce the total power consumption and to provide a good match with available compressor frame sizes. Operating the ASU at feed air pressures resulting in product streams leaving the cryogenic unit at pressures above atmospheric is termed "elevated pressure" (EP ASU) operation. Some systems may require that some of the residual nitrogen is injected into the gas turbine and the remaining portion rejected to atmosphere. The amount of nitrogen to be rejected will determine whether an LP ASU or EP ASU with a nitrogen expander is chosen. Increasing the

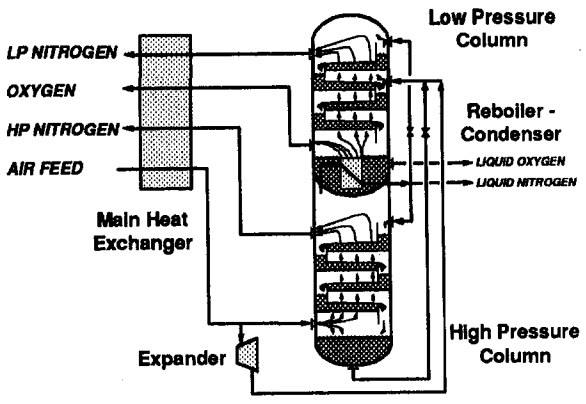


Fig. 2 Cryogenic distillation

Downloaded 02 Jun 2010 to 171.66.16.105. Redistribution subject to ASME license or copyright; see http://www.asme.org/terms/Terms_Use.cfm

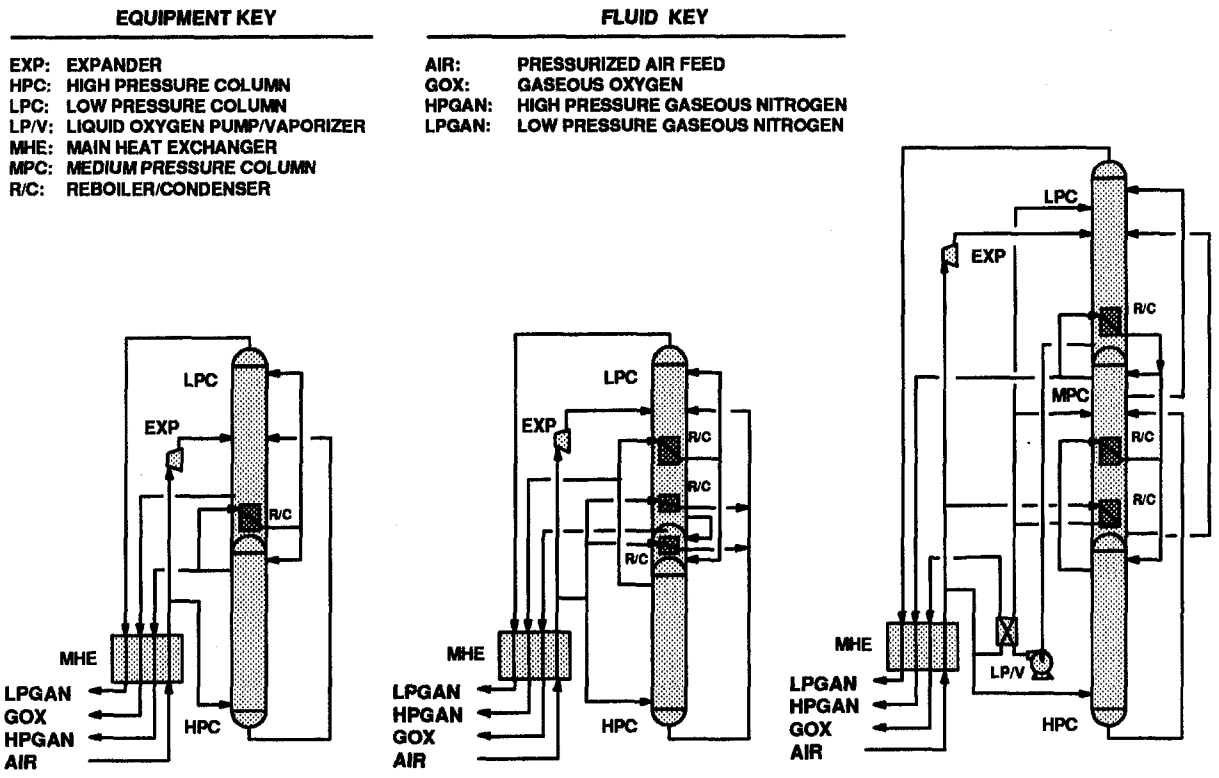


Fig. 3 Alternate ASU processes

diluent flow to the gas turbine can have a number of benefits, depending on the design of gas turbine:

- Increased diluent permits more syngas to be consumed, thus increasing the power output of the gas turbine while maintaining optimum firing temperatures. This is particularly beneficial for locations where the ambient temperature and/or elevation are high and the gas turbine would normally operate at reduced output.
- The diluent nitrogen reduces the formation of NO_x either by mixing with the syngas or injecting it directly into the combustor.

A higher degree of integration can be practiced by extracting some or all of the ASU's air requirement from the gas turbine, as shown in Fig. 7. Medium-Btu syngas streams result in a higher mass flow than natural gas to provide the same heat content to the gas turbine. Some gas turbine designs may need to extract air to maintain stable compressor or turbine operation in response to increased fuel flow rates. Other gas turbines may balance air extraction against injection of all of the available nitrogen from the ASU. Previous studies have shown optimum air extraction rates to be in the 25–50 percent range of the total ASU air flow. The amount of air extracted can also be varied as the ambient temperature changes at a given site to optimize year-round performance.

The degree of system optimization will take into account the following design targets and equipment constraints:

1 Maximize gas turbine power output at all ambient conditions.
2 Maintain optimum firing temperature for high efficiency.

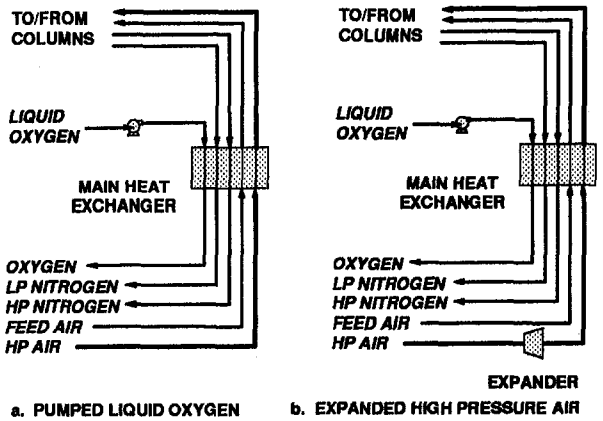


Fig. 4 High-pressure air processes

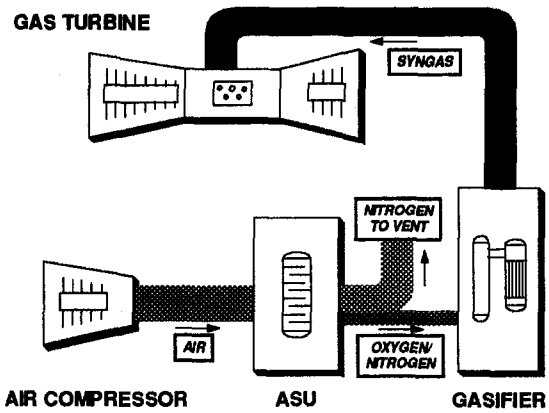


Fig. 5 Nonintegrated

Downloaded 02 Jun 2010 to 171.66.16.105. Redistribution subject to ASME license or copyright; see http://www.asme.org/terms/Terms_Use.cfm

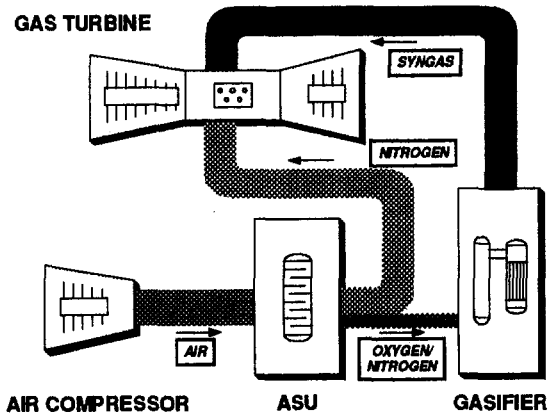


Fig. 6 Nitrogen integration

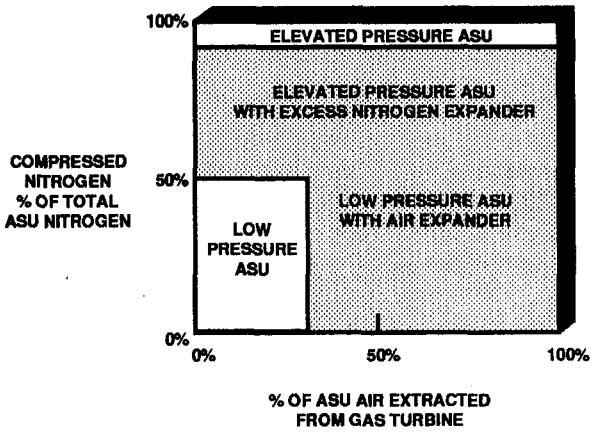


Fig. 8 ASU processes

3 Limit diluent flow to maintain combustion stability.
4 Account for gas turbine and ASU equipment operating limits.
5 Address start-up, ramping and stable operating points.

Optimal ASU Configurations

As noted in the previous section, different gas turbines have significantly different operating characteristics. The optimal ASU configuration will be determined by:

1 Pressure of the air supplied from the gas turbine.
2 Available air extraction rate.
3 Amount of injected nitrogen accepted by the gas turbine.
4 Oxygen and nitrogen supply pressures.

Figure 8 is a map of optimal ASU designs as a function of the amount of air extracted from the gas turbine and the amount of nitrogen injected into the gas turbine. This figure is applicable for "F" technology gas turbines with pressure ratios of about 14.

If the air extracted from the gas turbine is less than about 30 percent of the total ASU requirement and the nitrogen to be injected into the gas turbine is less than half of the total produced, a low-pressure ASU cycle is selected. The ASU incorporates pumping of liquid oxygen to take advantage of the partial flow of high pressure air or uses an air expander on the high pressure air feed. The air expander is useful if the amount or pressure of the extracted gas turbine air is expected to vary substantially due to ambient temperature effects or other operating conditions. As the air extraction rate increases, an LP ASU with expansion of a portion of the high-pressure air may be used if the percentage of injected nitrogen flow to the gas turbine remains low. As the percentage of injected nitrogen rises above 50 percent of the total available, an EP ASU will be selected. Any residual nitrogen can be expanded. The inlet temperature of air or nitrogen expanders is adjusted to provide the optimum amount of power recovery and thermal efficiency. If the inlet temperature is too high for the expansion ratio, the inlet stream is partially cooled against injection nitrogen or boiler feed water streams. Low inlet temperatures are raised by using low-level heat sources from the combined cycle or gasification processes.

Figure 9 is a generalized plot of a fully integrated ASU's power consumption versus air feed supply pressure to the ASU for a turbine with a pressure ratio of about 30. An air expander is used to reduce the pressure of the major portion of the feed air stream. The plot shows that there is an optimum ASU operating pressure for this system. As the ASU operating pressure continues to increase, the decrease in separation efficiency begins to outweigh the increasing product compressor suction pressures. This result can be expanded to produce a more definitive plot of ASU process selection as a function of gas turbine pressure ratio and percent of air extracted from the gas turbine, as shown in Fig. 10.

Advanced Integration Concepts

In addition to the basic integration concepts of single pressure air and nitrogen interchange between the ASU and the gas turbine, there are additional integration opportunities with both existing and advanced design gas turbines for the interchange of heat, refrigeration, and moisture.

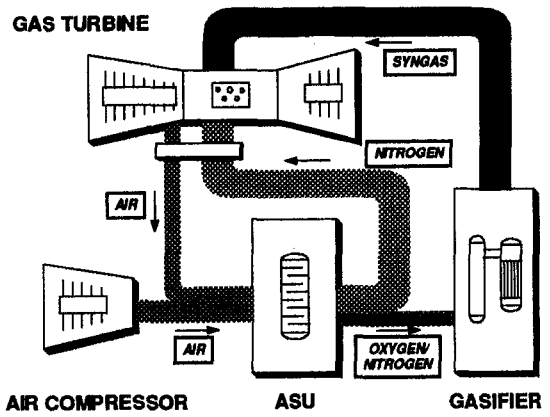


Fig. 7 Air and nitrogen integration

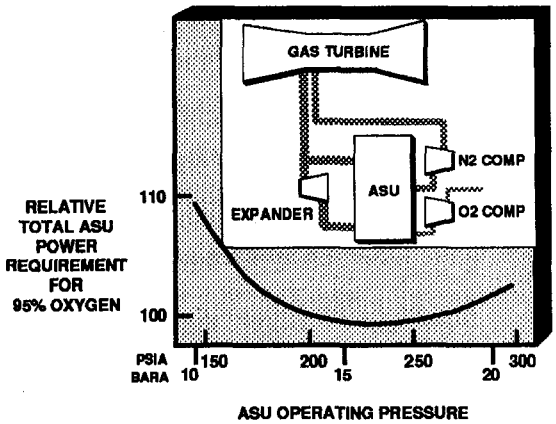


Fig. 9 Optimum ASU pressure

Downloaded 02 Jun 2010 to 171.66.16.105. Redistribution subject to ASME license or copyright; see http://www.asme.org/terms/Terms_Use.cfm

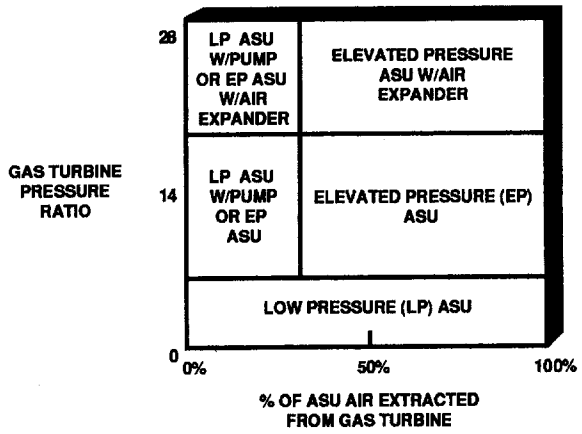


Fig. 10 Optimum ASU processes

Nitrogen Moisturization. For most modern gasification processes, the flame temperature of the produced syngas is too high to permit combustion with acceptable NO_x performance. Slurry feed gasification systems usually have sufficient low-level heat sources to permit moisturizing the syngas to control NO_x formation. Dry feed gasification systems usually have less low-level heat available and may have too high a heating value even after dilution with nitrogen from the ASU. Further dilution of the syngas can be achieved by moisturizing the nitrogen produced in the ASU. Moisturizing nitrogen rather than syngas results in fewer contaminants in the water leaving the saturation tower. A general nitrogen saturation and superheating scheme is shown in Fig. 11. Compressed nitrogen from the ASU enters a single or multiple-stage saturation tower where it contacts one or more streams of hot water. Hot water can be provided from low-level sources originating in the gasification or combined cycle systems. The amount and level of heat introduced into the saturator determines the degree of saturation that can be achieved. Adiabatic compression (no intercooling) of the nitrogen from the ASU can provide additional heat for saturation. The dry high-temperature nitrogen can be interchanged with saturated nitrogen and used to heat feed water to the tower. Up to 15–20 percent additional mass flow over the dry nitrogen rate can be generated by saturation. For reliable gas turbine operation, the wet nitrogen stream must be superheated. Extraction air from the gas turbine is a good source of heat, since this stream must be cooled prior to entering the ASU. It can be used to superheat the nitrogen and to heat water fed to the saturation tower. Higher levels of heating can be achieved by contact with hot boiler feed water from the combined cycle or heating directly in the heat recovery steam generator (HRSG).

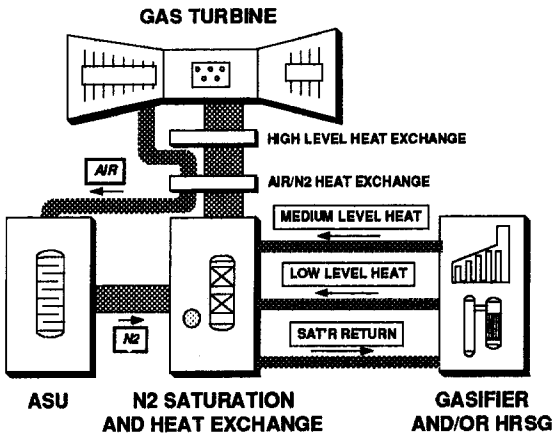


Fig. 11 Nitrogen moisturization

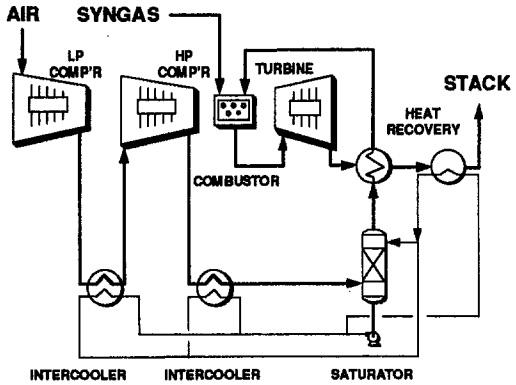


Fig. 12 HAT cycle

Humid (HAT) and Cascaded Humid Air Turbines (CHAT). HAT and CHAT power cycles are based on intercooled gas turbines incorporating turbine exhaust heat recovery and syngas saturation to eliminate the need for a separate steam turbine. The HAT cycle (Fig. 12) is based on an intercooled, two-stage air compressor linked to the turbine. The CHAT cycle employs a parallel air compression train with multiple pressure level combustors. In either cycle there are at least two pressure levels at which air can be extracted for use in the ASU. Similarly, there are several places in the cycles where nitrogen can be introduced from the ASU. A combination of about 70 percent low-pressure and 30 percent high-pressure air extraction to the ASU can result in a design requiring only a single-stage oxygen compressor to supply the gasifier, and no other ASU compression equipment. High-pressure air can be extracted after the first stage of gas turbine air compression, processed in an EP ASU, and nitrogen compressed to a pressure just above the extraction pressure for injection into the second stage of gas turbine air compression. Other opportunities for nitrogen injection include use as rotor and blade coolant, interstage turbine admittance, or injection into any of the combustors or to the saturator tower.

ASU Heat of Compression Recovery. Traditional compression equipment for ASUs have been centrifugal, cooling water intercooled units with stage pressure ratios generally less than two. The near-isothermal compression process requires the least amount of power and rejects nearly all the heat of compression to cooling water. After the final stage of compression, oxygen and nitrogen products need not be aftercooled so that some of the heat of compression is recovered in downstream processes. As noted in the section on nitrogen moisturization, adiabatic compression of the injection nitrogen stream can provide heat for the saturation process, or if no saturator is required the heat of compression will be recovered in the gas turbine combined cycle process. Studies have shown that overall IGCC cycle efficiency increases with the use of an adiabatic nitrogen compressor even though the shaft power is higher than for isothermal compression. Similar benefits can be achieved by compressing the oxygen to as high a temperature as practical before it is sent to the gasifier. Alternatively, recovery of the heat of compression in the form of boiler feed water or saturator tower water heating can be examined. Economic tradeoffs between shaft power, size of heat exchange equipment and level of heat to be recovered determine the optimum degree of heat recovery.

Cold Nitrogen and Chilled Water Integration. Dry nitrogen produced by the ASU can produce refrigeration either by expansion or by humidification. An LP ASU produces dry waste nitrogen at atmospheric pressure. The nitrogen can be sent to the bottom of a humidification tower and contacted against cooling water. As the dry nitrogen passes up through the tower,

Downloaded 02 Jun 2010 to 171.66.16.105. Redistribution subject to ASME license or copyright; see http://www.asme.org/terms/Terms_Use.cfm

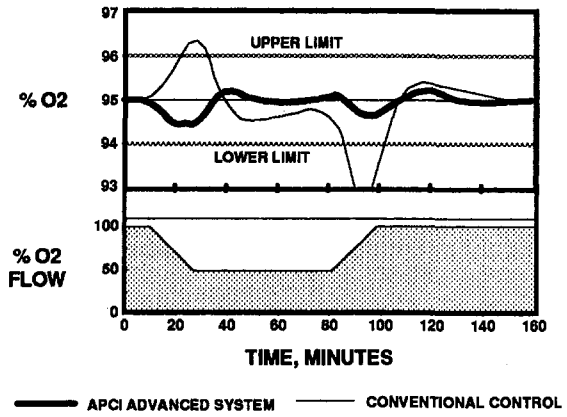


Fig. 13 Oxygen purity during ramping

water flowing down the tower evaporates into the gas stream. The release of the latent heat of water as it vaporizes cools the water flowing down the tower. The amount of chilled water produced is a function of the degree of chilling. The chilled water can be used for compressor intercooling in the ASU or exported for use in the combined cycle or gasification areas. The chilled water can be used in indirect contact with air entering the gas turbine or sprayed into the entering air flow to reduce the suction temperature and increase the mass flow through the gas turbine, resulting in increased power output on hot days. Pressurized nitrogen from an EP ASU can be expanded to produce even deeper levels of refrigeration. A study of splitting the pressurized nitrogen between compressed injection nitrogen to the gas turbine combustor and expanded nitrogen to the gas turbine suction showed a facility efficiency improvement compared to injecting all the nitrogen to the combustor. Refrigeration from either LP or EP nitrogen streams can be used in other parts of the facility such as in certain types of syngas cleanup systems that operate at subambient temperatures.

ASU Design and Operability

Higher degrees of unit integration obviously lead to more complexity in the transient and steady-state operation of any facility. A facility that is expected to operate full time at constant rates may be more amenable to the complexities of integration than a facility in peak shaving service or frequently changing load conditions. Changes in operating pressures or load have the most impact on the distillation system and product compressors in an ASU. LP or EP ASUs with their own source of air supply are the least affected by changes in other units in the facility. They can be started independently of the other units, ramped up in anticipation of other unit's requirements using feed-forward controls, ramped down at rates that maintain stable operation, and maintain operation while other units are recovering from a trip.

Air Integrated ASU Ramping. ASUs that are air integrated with the gas turbine are more complex, but with proper care in the design phase can accommodate the transient conditions encountered in IGCC facilities. The major complexity with air integration is the change in air pressure from the gas turbine as it changes load. As load drops from 100 to 50 percent of design, the air supply pressure may drop to about 65 percent of design. During a ramp down the following events occur in a conventionally designed ASU:

1 As the gas turbine power output decreases, syngas from the gasifier is reduced and causes less oxygen demand from the ASU. Air supply to the ASU is reduced in response to decreased oxygen demand.

2 Air supply pressure drops, causing a decrease in the high-pressure-column pressure. Low-pressure-column pressure must be reduced to maintain temperature approaches in the reboiler.

3 As column pressures are reduced, liquid inventory begins to boil and causes increased vapor flow. Increased boilup causes the oxygen concentration to increase in both the lower and upper sections of the low pressure column. The oxygen concentration of oxygen and injection nitrogen streams both increase and may go out of specification.

Upon ramping up from 50 percent of design, the increase in operating pressure tends to condense vapor inventory in the columns and produces the opposite result. Namely, the purity of oxygen to the gasifier drops below the specification. Figure 13 shows the change in oxygen concentration in the oxygen stream as a function of ramping, generated by dynamic computer analysis of a two column, single reboiler ASU. Also shown, is the trend for an ASU with an advanced control system and buffering equipment added to the process. As indicated, the ASU can be designed to maintain oxygen concentrations of ± 1 percent in the oxygen feed to the gasifier as the ASU is ramped down and back up to full production.

ASU Compressor Operation. Most ASU applications will be in a size range where air, nitrogen, and oxygen compression duties can be met by centrifugal machines. Occasionally, large single train sizes above 2500 tons per day of oxygen may require the use of an axial-centrifugal air compressor. A typical compressor map showing operating lines and guide vane settings as a function of relative pressure ratio and relative suction volumetric flow is contained in Fig. 14.

For ASUs with no gas turbine air integration, design and operation of the compression equipment are fairly straightforward. The design point is usually chosen to represent the conditions at which the ASU will operate for the most hours per year, or "Full Load" at a specified ambient. The design point may be moved slightly to accommodate a maximum volume flow case representing operation on a hot day. Off-design conditions are handled by guide vane adjustment to maintain efficient operation. Turndown below the minimum point is usually possible by suction throttling to reduce the pressure and thereby increase the relative volumetric flow. This increases the specific power consumption, since the pressure ratio will be increased. Too high a pressure ratio will move the machine toward surge. In general, stand-alone operation is characterized by moving along an operating line of fairly constant pressure ratio to "Part Load," changed only by system pressure drop variations as a function of system flow.

ASUs with partial gas turbine air extraction have significantly different compressor operating envelopes. As described in the section on ramping, gas turbine air pressure varies significantly

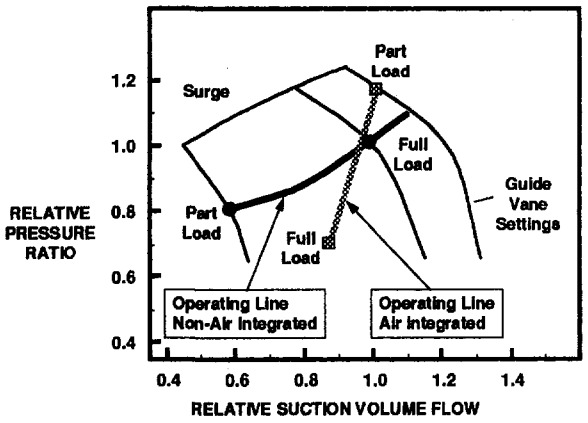


Fig. 14 Compressor map

Downloaded 02 Jun 2010 to 171.66.16.105. Redistribution subject to ASME license or copyright; see http://www.asme.org/terms/Terms_Use.cfm

as a function of load. At low load conditions, the following conditions exist relative to operation at the full load point:

1 The drop in air supply pressure reduces the required pressure ratio of the ASUs air compressor and reduces the suction pressures to all product machines.
2 To maintain as high a firing temperature as possible at reduced load, the gas turbine characteristics dictate sending additional extracted air to the ASU.
3 ASU air compressor operation is characterized by low pressure ratio and low flow operation compared to design.
4 Gasifier product pressures will often be maintained at constant pressure at reduced load, or if decreased, will not respond as quickly as the drop in ASU air supply pressure. Injection nitrogen pressure to the gas turbine will usually be decreased somewhat relative to design.
5 Product compressor operation is characterized by high pressure ratio and high volumetric flow rate compared to full-load operation.

As indicated in Fig. 14, the part-load case usually sets the maximum compressor design conditions and can result in machine designs with relatively lower efficiency at the design point than at turndown. If part-load operation is not required for a significant number of operating hours per year, the overall facility efficiency may be penalized due to the lowered compressor efficiencies at design rates.

Partial Air Integration Operation for High Efficiency. The following system design and operating approach are suggested to provide higher efficiencies at the expected full design rates and flexibility in ramping, at the expense of lowered efficiency at the less frequent part-load conditions. Establishing the degree of air integration is an iterative process between the gas turbine and ASU design teams, and needs to address full-load operation across the range of ambients encountered for a specific project. Upon establishing some preliminary air extraction rates, the following guidelines can be followed:

- Operation at the maximum ambient point will usually determine the maximum ASU air compressor flow, since gas turbine air flow decreases with increasing temperature. This operating point is located at the far right of the compressor map and determines the range of operation for the compressor. From the map, the minimum flow available can be determined and compared to operation at minimum ambient conditions when the gas turbine has excess air capacity and air extraction rates are usually increased. If operation at the minimum ambient is more critical to the project, then the ASU air compressor design is set by locating this operating point at the far left of the map with the resulting maximum air flow setting the limit on maximum ambient output.
- From the maximum ASU air compressor flow, the maximum amount of oxygen that can be produced with no gas turbine air extraction can be determined. This oxygen production determines a syngas flow rate, a corresponding gas turbine load point, air extraction pressure, and corresponding ASU compressor suction and discharge pressures. This will usually be a reasonable starting point for setting an efficient ASU design that will smoothly ramp up and down in capacity.
- Ramp down is characterized by reducing load while in an air integrated mode until the ASU air compressor can supply the flow required for stand-alone operation. At this point air extraction to the ASU ceases and the ASU begins constant pressure operation. Further reductions in oxygen output are accommodated by reducing ASU compressor air flow and adjusting compressor controls to maintain stable operation. Deep turndown may require venting of air or products if the ASU is required to operate on standby.
- Ramp up is characterized by increasing ASU air compressor and product flows as syngas flow is increased. At the maximum ASU stand-alone point, air pressure is matched to air extraction pressure from the gas turbine, air integration is commenced and production rate increased to produce the required syngas flow.

Conclusions

A gas turbine's design and performance characteristics will determine the feasibility and potential degree of integration with the ASU. IGCC facilities have been built and are operating with no integration, nitrogen injection from the ASU, and full gas turbine air and nitrogen injection integration. ASU processes can be tailored to fit the integration needs of current and next-generation gas turbines, including low, high, or mixed air pressure feeds. Additional facility benefits for certain gas turbines can be achieved by moisturization of the injection nitrogen stream using low, medium, or high levels of heat from the gasification or combined cycle units.

The design and operating characteristics of the ASU are dependent on the degree of integration with the gas turbine. Air integrated designs have special requirements for operating at varying air feed pressures and load conditions.

References

Anon., 1990, "A 500 MWe Coal Gasification Combined Cycle Power Plant to Give 46% Efficiency," *Modern Power Systems,* Nov.

Sorensen, J. C., Smith, A. R., and Wong, M., 1991, "Cost-Effective Oxygen for IGCC—Matching the Design to the Project," EPRI 10th Conference on Coal Gasification Power Plants, San Francisco, Oct. 16–18.

Smith, A., Alsandor, E., Doering, E., and Unger, P., 1994, "Improved IGCC Power Output and Economics Incorporating a Supplementary Gas Turbine," EPRI 13th Conference on Coal Gasification Power Plants, San Francisco, CA, Oct. 19–21.

Downloaded 02 Jun 2010 to 171.66.16.105. Redistribution subject to ASME license or copyright; see http://www.asme.org/terms/Terms_Use.cfm

M. S. Anand
Allison Engine Company,
Indianapolis, IN 46206

F. Takahashi

M. D. Vangsness

M. D. Durbin

W. J. Schmoll

University of Dayton Research Institute,
Dayton, OH 45469

An Experimental and Computational Study of Swirling Hydrogen Jet Diffusion Flames

Computations using the joint velocity-scalar probability density function (pdf) method as well as benchmark quality experimental data for swirling and nonswirling hydrogen jet diffusion flames are reported. Previous studies of diffusion flames reported in the literature have been limited to nonswirling flames and have had no detailed velocity data reported in the developing (near-nozzle) region of the flames. The measurements and computations reported herein include velocities (mean and higher moments up to fourth order) and temperature (mean and variance) near the burner exit and downstream locations up to 26.5 jet diameters. The velocities were measured with a three-component laser-Doppler velocimeter (LDV) and the temperature was measured using coherent anti-Stokes Raman spectroscopy (CARS). The joint pdf method offers significant advantages over conventional methods for computing turbulent reacting flow, and the computed results are in good agreement with data. This study serves to present data that can be used for model validation as well as to validate further the joint pdf method.

Introduction

Although jet diffusion flames have been studied extensively and reported in the literature (Magre and Dibble, 1988; Masri et al., 1988; Drake, 1988; Bilger, 1989; Chen and Kollmann, 1992; Barlow and Carter, 1994; Nandula et al., 1994, to name only a few), there are voids with respect to two key aspects. First, there are no detailed measurements, especially velocity measurements, in the developing regions of the flames, and second, the flames have been predominantly nonswirling. Swirl is widely used in practical combustion systems such as gas turbine combustors for flame stabilization and enhancing fuel–air mixing and combustion intensity. It is necessary that the turbulent combustion models be validated in detail in simpler flames incorporating the essential features of practical flows before they can be used with confidence to design practical combustion systems. In the present study, detailed velocity and temperature measurements are presented for swirling and nonswirling hydrogen jet diffusion flames in the developing region of the flames (<30 jet diameters in axial distance), and the measurements are used to further validate the joint velocity-scalar pdf method.

Several previous studies, reviewed by Pope (1990) as well as more recent works, have established the pdf method as the most suitable method for accurately computing the details of the flow and chemistry in complex turbulent reacting flows of practical interest. Ongoing work at Allison Engine Company has focused on the development and validation of the pdf method as the next-generation gas turbine combustor design and analysis tool. Unlike in the currently used turbulence models, the most important processes, namely convection by both mean and fluctuating velocities, reaction and turbulence/chemistry interactions appear in closed form in the joint velocity-scalar pdf method and need not be modeled (Pope, 1985). The joint pdf method has been applied to a number of reacting and nonreacting flows including several premixed and diffusion flames (e.g., Anand and Pope, 1987; Tiang et al., 1993; Norris and Pope, 1994), and two and three-dimensional recirculating flows (Anand et al., 1990; Haworth and El Tahry, 1991) to name only a few. Recently, computations of swirling flows with the pdf method were reported by Anand et al. (1993) and validated against benchmark data reported by Takahashi et al. (1992) for constant-density swirling flows from the same configuration used in the present study. The present computations of diffusions flames with the pdf method differ from previous computations in that for the first time: (*a*) swirling diffusion flames are being computed and (*b*) detailed comparison with data is made in the developing region of the flame.

Another notable feature of the measurements reported in this study is that the velocity correlations, as in Takahashi et al. (1992), are conditional upon the fluid originating from a given inlet stream, so errors due to velocity bias are avoided. These conditional quantities are readily computed in the pdf method without need for additional modeling, and serve as severe tests for the method's ability to predict the details of the individual streams and the transport processes between the streams.

Experimental Setup and Techniques

Figure 1 shows a schematic of the combustor system used. It consists of a central fuel tube (9.45 mm inner diameter [D], 0.2 mm lip thickness, 806 mm length) and a concentric annulus-air tube (26.92 mm inner diameter) centered in a vertical test section (150 × 150 mm square cross section with rounded corners, 486 mm length) through which external air is supplied. The test section is sided with four quartz windows for optical observations and diagnostics. A helical vane swirler unit can be placed in the annulus channel 96 mm upstream from the jet exit. Swirlers of vane angles 0 deg, 30 deg, and 45 deg were used in the present study.

The three-component LDV system, described in detail by Takahashi et al. (1994a), consists of the two segments of three-beam two-channel optics and two-beam one-channel optics. The former utilizes a 514.5 nm line of an argon-ion laser (Spectra Physics 171; 15W nominal output) and measures the velocity components in the directions of ±45 deg off the jet axis. The latter utilizes a 488.0 nm line of the laser and measures the tangential velocity component. The overlapping probe volume is approximately a 100-μm-dia sphere. The calculated fringe spacing is approximately 3.6 μm. Submicron-size zirconia

Contributed by the International Gas Turbine Institute and presented at the 40th International Gas Turbine and Aeroengine Congress and Exhibition, Houston, Texas, June 5–8, 1995. Manuscript received by the International Gas Turbine Institute March 16, 1995. Paper No. 95-GT-307. Associate Technical Editor: C. J. Russo.

Copyright © 1997 by ASME

Downloaded 02 Jun 2010 to 171.66.16.105. Redistribution subject to ASME license or copyright; see http://www.asme.org/terms/Terms_Use.cfm

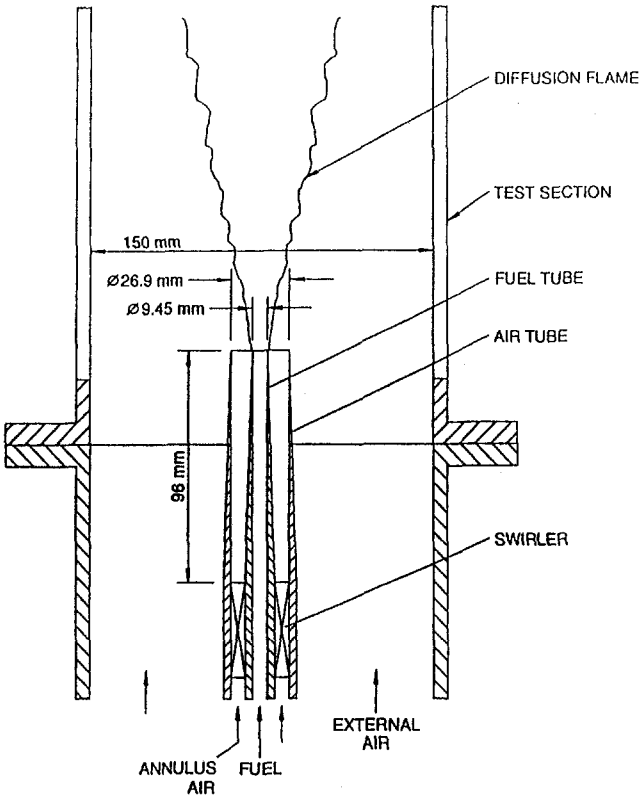


Fig. 1 Schematic of the swirling jet diffusion flame combustor test section

(ZrO_2) particles (97 percent < 1 μm) are used as the seed particles. A portion of the data was filtered out by the so-called $n - \sigma$ method (i.e., velocities whose deviation from the mean exceeded n times the standard deviation [σ] are eliminated). The coefficient $n = 4$ was employed because preliminary processing tests showed that $n = 3$ cut off some valid data and altered high moments considerably.

LDV measurements were made by seeding one stream at a time and completing all the axial and radical scans before seeding the next stream and repeating the scans. All the LDV measurements reported are conditional upon the fluid originating from either the jet annulus or the coflow.

The CARS system, described in detail by Takahashi et al. (1994b), consists of a pulsed Nd:YAG laser (Quanta Ray DCR-2A, 10 ns pulse width, 10 Hz repetition rate), dye laser optics, incident and collection optics, a $\frac{3}{4}$ m grating spectrometer, and an intensified charge-coupled device (CCD) camera (Princeton Instruments). The output from the laser is frequency doubled (532 nm, ~150 mJ) and divided into four beams of nearly equal intensity. Two of these serve as the pump beams, while the other two pump a dye laser oscillator and amplifier to provide a broadband Stokes beam centered at 607 nm. The Stokes beam and the two pump beams are then focused together in a folded BOXCARS configuration. The effective probe volume size is estimated at approximately 25 μm in diameter and 250 μm in length. Typically, 500 CARS signals are acquired at each location and processed by a microcomputer. The CARS measurements are based on nitrogen molecules originating in air. Unlike seed particles, which follow fluid elements, molecules diffuse among different species. Therefore, the CARS data are unconditional upon the origin of the fluid if they are mixed. In the jet-to-annulus fluid boundary zone near the jet exit, the determination of CARS temperature becomes difficult due to the interference by nonresonant background emission from hydrogen molecules. The accuracy of the temperature measurements is estimated to range between 10 percent near room temperature and 5 percent near the flame temperature, with the largest contribution to uncertainty from shot-to-shot variation in the Stokes-laser spectral distribution.

Computations

The Joint pdf Method. The pdf method used in the present study is the same as that used for the constant-density swirling flow study by Anand et al. (1993), except for the addition of the thermochemistry and molecular diffusion due to mean scalar gradient described later and, obviously, the variability of density. Only a brief overview is presented here; the reader is referred to Anand et al. (1993) for more details.

In the pdf method, the transport equations for the evolution of the joint pdf of velocity, viscous dissipation, and other scalars (four in the present study) are modeled and solved using a Lagrangian viewpoint. In the pdf transport equation, the terms to be modeled are those representing the effects of viscous dissipation, the fluctuating pressure gradient, and molecular mixing. All other processes are in closed form and need not be modeled. The solution is performed by a Monte Carlo algorithm.

In the boundary-layer (parabolic) algorithm used here, the joint pdf at each step in the x-direction (axial direction) is represented by a large number, N, of notional or modeled particles. At the axial position x, each particle has the position $\underline{x}^*(x)$, velocity $\underline{U}^*(x)$, the relaxation rate or frequency $\omega^*(x)$, and four scalar values $f^*(x)$, $\rho^*(f^*)$, $T^*(f^*)$, and $c^*(x)$. The scalar f^* is the mixture fraction (conserved scalar) used to model the thermochemistry. Its value changes due to turbulent and molecular mixing and molecular diffusion. The scalars ρ^* and T^* are density and temperature, respectively, and are derived from f^* based on the thermochemistry used. The scalar c^* is a passive scalar with no source terms (i.e., c^* is held constant), and is used to tag particles by their jet of origin.

In the general step from x to $x + \Delta x$, each particle evolves over a time interval Δt^* given by:

$$\Delta t^* = \Delta x / U_1 \tag{1}$$

The values of velocities, frequency, and mixture fraction vary during the time interval according to the following models described in greater detail by Anand et al. (1993). The velocities evolve according to the modified Langevin model (Pope, 1991), which includes the acceleration due to mean pressure gradient $(1/\rho^*)(\partial\langle P\rangle/\partial x_i)$ and models the effects of the fluctuating pressure gradient and viscous dissipation. The model constant C_o is set to 3.5 as in Anand et al. (1993) and other previous studies (e.g., Pope, 1991). The mean pressure gradients (both lateral and axial) are important, especially for swirling flows, and are calculated, as described by Anand et al. (1993), from the lateral momentum equation and the boundary-layer assumptions. An important observation regarding the acceleration due to mean pressure gradients is that particles of differing densities (e.g., burned and unburned particles) are accelerated by different amounts. This is the basis for the ability of the pdf method to compute turbulence/chemistry interaction phenomena automatically such as countergradient diffusion (see Anand and Pope, 1987) while conventional models require additional specialized modeling for such phenomena.

The evolution of the instantaneous turbulence frequency $\omega^*(\equiv\epsilon^*/\bar{k}$ where ϵ^* is the particle dissipation and $\bar{k}$ is the ω-weighted mean turbulent kinetic energy) is modeled by the stochastic dissipation model (Pope, 1991). The same model constants used by Anand et al. (1993), namely $C_{\omega 1} = 0.04$ and $C_{\omega 2} = 0.07$, are used in the present study. It should be noted that the stochastic model for velocity (Langevin model) uses the particle (instantaneous) dissipation rather than a mean dissipation value, thereby incorporating the effect of a range of turbulent time scales represented by the pdf of ω^* rather than a single time scale.

Downloaded 02 Jun 2010 to 171.66.16.105. Redistribution subject to ASME license or copyright; see http://www.asme.org/terms/Terms_Use.cfm

The turbulent mixing (i.e., turbulent convection) of the mixture fraction (f^*) is in closed form and need not be modeled. The molecular mixing is modeled using the improved mixing model (Pope, 1982) with the standard model constant $C_f = 2.0$. The molecular diffusion process is represented by Fick's Law. Typically, although it is in closed form, molecular diffusion due to mean scalar gradient is not explicitly included in the computations for high Reynolds number turbulent flows since turbulent mixing is dominant. However, in the present study, molecular diffusion is explicitly included since the stoichiometric surface lies at the outer edge of the shear layer (for most diffusion flames and especially for hydrogen flames due to the low value of the stoichiometric mixture fraction and the high diffusivity of hydrogen). In this region, the turbulent intensity is low and molecular diffusion plays an important role in the radial spread of the flame. The change in f^* due to molecular diffusion is given by:

$$\Delta f^* = \frac{\Delta t^*}{\rho^* r} \frac{\partial}{\partial r} \left(r \langle \rho \rangle D_f \frac{\partial \langle f \rangle}{\partial r} \right) \tag{2}$$

where $\langle \rho \rangle$ and $\langle f \rangle$ are the mean density and mixture fraction respectively, and D_f is the diffusivity taken as a function of $\langle f \rangle$ from Bilger (1982):

$$D_f = 0.26 + 257\langle f \rangle + 3.5 \times 10^8 \langle f \rangle^5 \ (\text{cm}^2/\text{s})$$

for $0 \leq \langle f \rangle \leq 0.0325$; and

$$D_f = 3.8 - 3.03\langle f \rangle + 27.5(1.0001 - \langle f \rangle)^{10} \ (\text{cm}^2/\text{s})$$

for $0.0325 < \langle f \rangle \leq 1.0$.

Means and other correlations are extracted from the solution at any desired axial station x by forming sums of particle properties within spatial bins in the lateral direction (r-direction) and fitting cubic B-splines to these sums. Typically density-weighted (Favre) means are calculated as is appropriate for reacting flows; however, means weighted by any desired quantity can be computed.

Thermochemistry. Due to the highly reactive nature of the fuel used, namely hydrogen, the thermochemistry in the present study is described using a fast one-step reaction in equilibrium. This allows the modeling of the diffusion flame using a single conserved scalar, the mixture fraction that is unity in the hydrogen stream and zero in the air streams. The reaction is completely described by the evolution of the mixture fraction. The temperature and density are then functions of mixture fraction alone and are determined from the equilibrium composition at the given value of f, using the heat of combustion, the specific heat at constant pressure (C_p) of the mixture as a function of temperature, and the ideal gas law. In the present study the equilibrium calculations were performed at different values of f prior to the pdf calculations and the values of specific volume (inverse of density) and temperature were tabulated for use (through linear interpolation) in the pdf calculations. The tables consisted of 21 points between $f = 0$ and the stoichiometric value $f_{st} = 0.0282$ and 51 points between f_{st} and $f = 1$ to provide sufficient accuracy for the pdf calculations.

Initial Conditions. Initial conditions for the computations are prescribed from experimental data. The first measurement station $x = 1.5$ mm ($x/D = 0.16$) is taken as the initial plane for the calculations. The initial velocity pdf is prescribed to be joint normal with the mean and covariances taken from linearly interpolated experimental data. The initial pdf of relaxation rate is taken to be log-normal, i.e., $\ln(\omega^*/\langle\omega\rangle)$ has a normal distribution with mean and variance $-\frac{1}{2}$ and 1, respectively, in accordance with the construction of the model. The initial profile of $\langle\omega\rangle$ is derived from experimental data using the following expression, as in Anand et al. (1993), based on the assumption of local equilibrium of the turbulence:

$$\langle\omega\rangle = 0.7\sqrt{C_\mu} \left| \left(\frac{\partial \langle U \rangle}{\partial r} \right)_{eq} \right| \tag{3}$$

where

$$\left[\frac{\partial \langle U \rangle}{\partial r} \right]_{eq} = \left[\left(\frac{\partial \langle U \rangle}{\partial r} \right)^2 + \left(\frac{\partial \langle W \rangle}{\partial r} - \frac{\langle W \rangle}{r} \right)^2 \right]^{1/2} \tag{4}$$

and $C\mu = 0.09$.

The initial profiles of the mean mixture fraction and its variance $\langle f'^2 \rangle$ are deduced from the measured mean and variance of temperature at the $x = 1.5$ mm location. The value of $\langle f \rangle$ is deduced from the tabulated values of temperature versus mixture fraction and the value of $\langle f'^2 \rangle$ is estimated by

$$\langle f'^2 \rangle = \frac{\overline{T'^2}}{T_{st}} f_{st} \tag{5}$$

where $\overline{T'^2}$ is the measured variance of temperature, and T_{st} (=2377 K) is the temperature at the stoichiometric mixture fraction f_{st}. The pdf of f is prescribed to be Gaussian with mean $\langle f \rangle$ and variance $\langle f'^2 \rangle$.

Results and Discussion

Experiments and computations were performed for the four cases listed in Table 1. The velocities U_j, U_a, and U_e are the nominal bulk-averaged axial velocities of the fuel jet, annular air jet, and the coflowing air stream, respectively. Two of the cases are nonswirling and two are swirling. For Case 2, the high-velocity nonswirling case, the lip thickness of the fuel tube used was 1.2 mm in order to anchor the flame and keep it from lifting. For all other cases, the tube walls were chamfered to form knife edges at the exit.

The nominal Reynolds number for the hydrogen jet based on U_j and the jet diameter (D) is 2208 for Case 1 and 8830 for the others, and the nominal Reynolds number for the annular air jet based on U_a and its hydraulic diameter is 8400 for Case 1 and 33,600 for the others. The swirl numbers for the annular jet, calculated from the measured axial and tangential velocities at the initial plane, are 0.382 for Case 3 and 0.516 for Case 4.

To be concise, only sample results from a nonswirling case (Case 2) and the two swirling cases in Table 1 will be presented here. Case 2 was selected to allow a more direct comparison between the nonswirling and swirling cases. Detailed tables and plots of the measured data for the four cases are reported in Takahashi et al. (1993a, b; 1994a, b, c, d), and the tabulated data are available on diskettes. Measurements have been made at axial stations $x/D = 0.16$ (initial plane), 1.06, 2.65, 5.29, 7.94, 15.9, and 26.5. Radial profiles of conditional mean velocities and velocity correlations up to fourth order as well as unconditional mean and variance of temperature have been reported.

The notation used to present the results for the velocity components is $\underline{U} \equiv (U, V, W) \equiv (\langle U \rangle + u, \langle V \rangle + v, \langle W \rangle + w)$. The notation for the temperature results is presented later. The

Table 1 Flow conditions

Case No.	U_j – m/s	U_a–m/s	U_e – m/s	Swirler angle – deg
1	25	4	1	0
2	100	20	4	0
3	100	20	4	30
4	100	20	4	45

Downloaded 02 Jun 2010 to 171.66.16.105. Redistribution subject to ASME license or copyright; see http://www.asme.org/terms/Terms_Use.cfm

measured mean axial velocity on the centerline at $x/D = 0.16$ denoted as $\langle U \rangle_{oc}$ is used to normalize the velocities and the temperature at the stoichiometric mixture fraction, T_{st} (=2377 K), is used to normalize temperatures. The values of $\langle U \rangle_{oc}$ are 132.8 m/s, 130.3 m/s, and 130.0 m/s for Cases 2, 3, and 4, respectively. The radial distance is normalized by the fuel jet radius R ($=D/2$).

Figure 2 shows the computed conditional and unconditional mean axial velocity profiles for the nonswirling case (Case 2) compared against measurements at various axial stations. The calculations are in good agreement with data. There are differences in the velocities of the fluids originating from the different streams as expected. The annulus air increases its axial velocity as it moves toward the central jet, but its axial velocity remains lower than that of the central jet. As the jets spread, the profiles become flatter and the differences get smaller at the downstream locations $x/D = 15.9$ and $x/D = 26.5$ (not shown). While the unconditional data cannot be deduced from the conditional data without additional measurement of the intermittency factor for the different streams, unconditional and conditional quantities of any order can be extracted from the pdf solution. The unconditional mean axial velocity in Fig. 2 lies between the conditional values as expected.

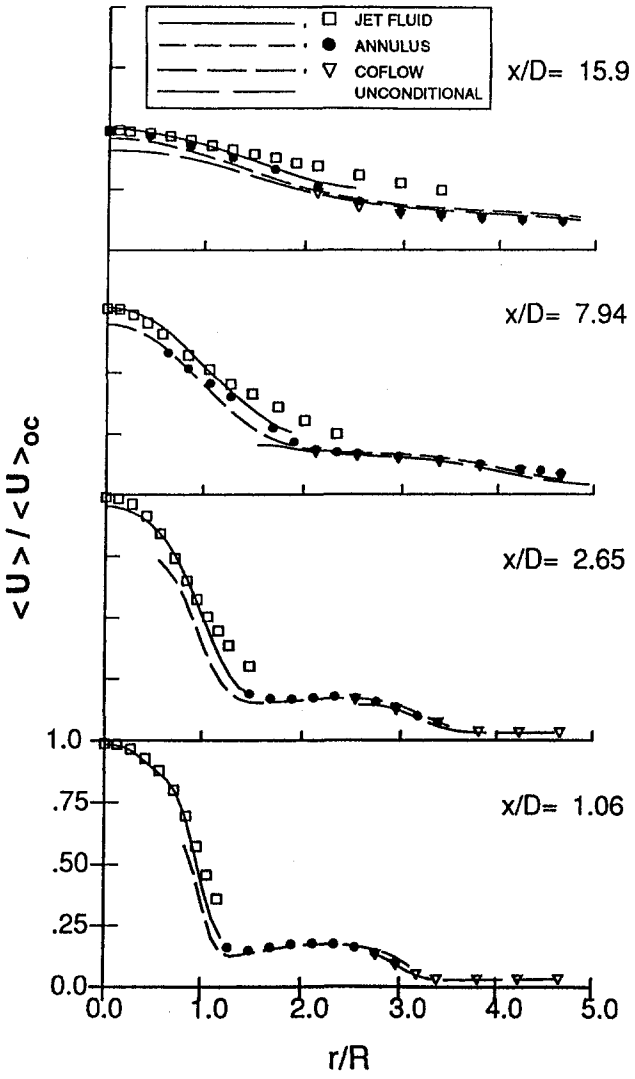


Fig. 2 Radial profiles of computed conditional and unconditional mean axial velocity (lines) compared against data (symbols) for the nonswirling case (Case 2)

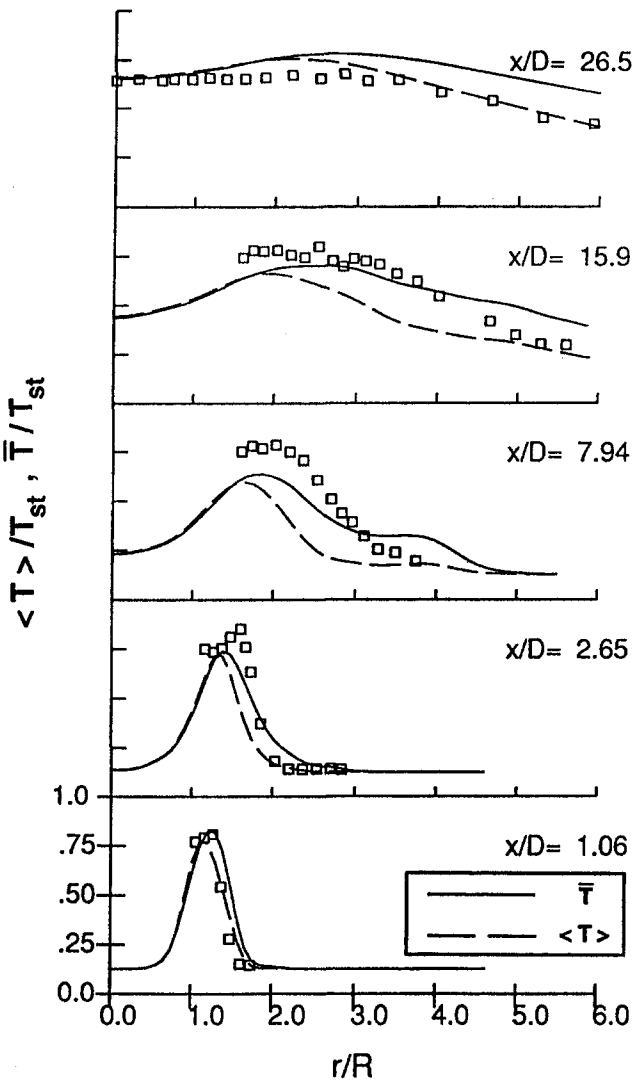


Fig. 3 Computed profiles of Favre-averaged mean temperature ($\langle T \rangle$) and Reynolds-averaged mean temperature ($\bar{T}$) compared against data (symbols) for the nonswirling case (Case 2)

Figure 3 shows the computed profiles of mean temperature for Case 2 compared against data. Both the Favre-averaged (density-weighted) mean temperature $\langle T \rangle$ and the Reynolds-averaged (volume-weighted or spatially averaged) mean temperature denoted by $\bar{T}$ are shown. The Favre average is lower in the flame's outer radial region where there is significant probability of both hot products and cold air, since the cold air is an order of magnitude denser (1.17 kg/m^3 at the inlet temperature of 298 K) and contributes more to the average than the hot rarer air (0.125 kg/m^3 at T_{st}), whereas on the inside of the flame the difference is negligible since the densities of cold unburned hydrogen (0.082 kg/m^3 at the inlet temperature of 298 K) and the burned products are of the same order of magnitude. Clearly, the spatial mean is much closer to the measured data, illustrating that the CARS measurement represents a spatial average and is not weighted by the mass flow into the measurement volume. This is an important observation and draws attention to the fact that although Favre averages are conventionally used in the computations of variable-density flows, one has to be careful to use the appropriate averaging while comparing with measurements. On the other hand, if the seeding of the flow is uniform, LDV measurements represent Favre means, and hence the Favre means are used while comparing velocity data. However, the velocity statistics computed using Reynolds

Downloaded 02 Jun 2010 to 171.66.16.105. Redistribution subject to ASME license or copyright; see http://www.asme.org/terms/Terms_Use.cfm

averaging were nearly identical to those computed using Favre averaging. This indicates that the velocity distributions of the high and low-density fluids in the mixture are nearly identical at any point in the flow.

The calculated profiles of (volume averaged) temperature in Fig. 3 show that the locations of the temperature peaks are well predicted; however, the peak values are lower than the measured values in the region between $x/D = 2.65$ and $x/D = 7.94$. At the further downstream locations $x/D = 15.9$ and $x/D = 26.5$, the calculated temperature is higher than the data at the outer radial locations.

Figure 4 shows the temperature variance for the nonswirling case (Case 2). Again, the Reynolds-averaged variance is in much better agreement with the data than the Favre average. The second peak of temperature variance on the inside (i.e., toward the centerline) seen in the calculations corresponds to the inner gradient of the temperature peak. Obviously, this is the region that lacks nitrogen and the CARS data are either not available or the measured temperature variance is expected to be low in this region.

The data as well as the computations in Figs. 2, 3, and 4 show that the flame lies at the outside edge of the shear layer between the fuel jet and the annulus jet as expected due to the low value of f_{st}.

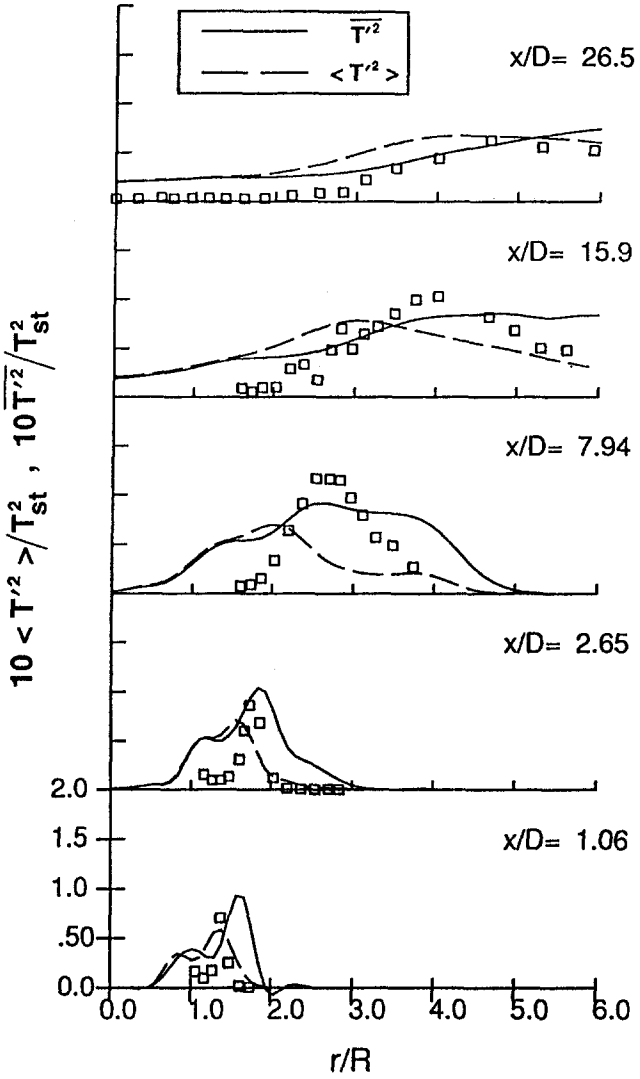


Fig. 4 Computed profiles of Favre-averaged temperature variance ($\langle T'^2 \rangle$) and Reynolds-averaged mean temperature ($\overline{T'^2}$) compared against data (symbols) for the nonswirling case (Case 2)

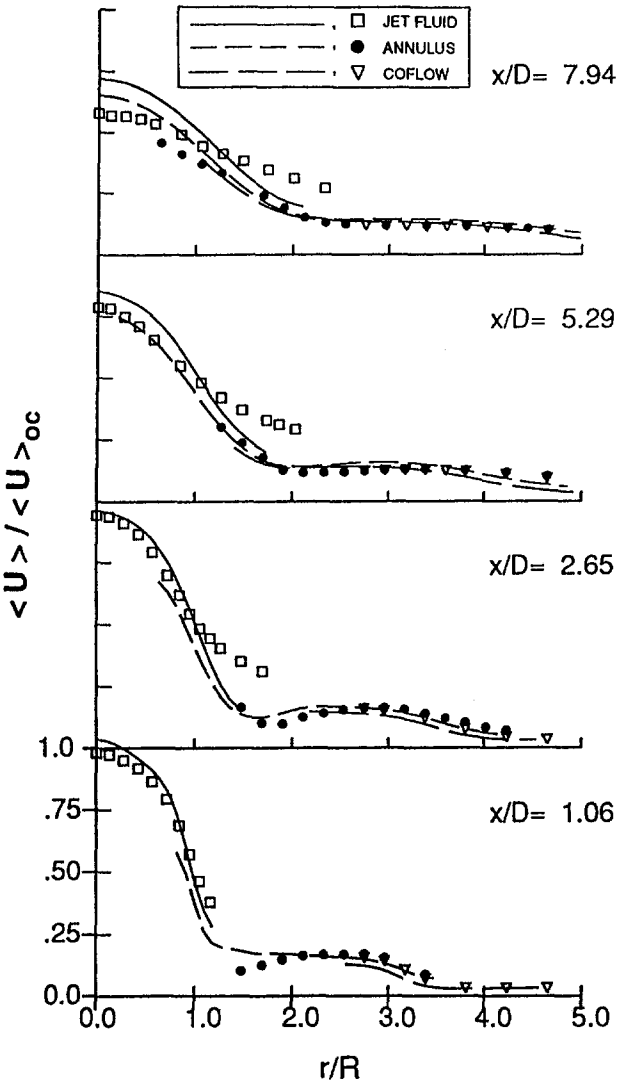


Fig. 5 Radial profiles of computed conditional mean axial velocity (lines) compared against data (symbols) for the 30 deg swirl case (Case 3)

Results for the 30 deg swirl case (Case 3) will now be presented. Figure 5 shows the radial profiles of mean conditional axial velocity at different downstream stations in the developing region. For clarity of the figure, the calculated unconditional velocity is omitted. The spreading of the jet is much faster than in Case 2 as a result of the enhanced mixing due to swirl in Case 3. The location of the shear layer is at a larger radial distance and the width of the shear layer is also larger than for the nonswirling case (Fig. 2), for example at $x/D = 7.94$. Differences between the conditional means from the three streams are evident.

Overall, the computations are in good agreement with the data in terms of the trends, locations, and magnitudes of the conditional velocities; however, some differences exist. The computations show a slightly slower rate of spreading of the hydrogen jet than the data. Although the spreading rate in the computations could be adjusted by adjusting the constants in the Langevin equation and the turbulent frequency equation, the differences are not significant enough to undertake such an exercise; hence, the constants used in previous studies (e.g., Anand et al., 1993) were retained. The data, especially at $x/D = 2.65$ and 5.29, indicate the outer edge of the hydrogen jet spreads especially faster than the bulk of the jet. The differences between the conditional velocities and the differences between

Downloaded 02 Jun 2010 to 171.66.16.105. Redistribution subject to ASME license or copyright; see http://www.asme.org/terms/Terms_Use.cfm

the computations and the data diminish at the downstream locations $x/D = 15.9$ and 26.5 (not shown here).

Figure 6 shows the conditional mean tangential (or swirl) velocities for Case 3. The development and decay of the swirl in the three streams are well predicted, although the computations show larger differences between the swirl velocities of the different streams than indicated by the data. The computations show that the swirl velocities for the initially nonswirling hydrogen jet and coflowing stream lag behind those for the annular swirling jet as one may expect.

The calculated Reynolds-averaged mean temperatures $\bar{T}$ are compared against data in Fig. 7. The agreement between that computation and the data is better than in Case 2 in terms of the magnitude and shape of the temperature peaks. For the swirling case (Case 3), the measured temperature peaks are lower at corresponding axial stations than in Case 2 (see Fig. 3) and the profiles show more spreading indicative of enhanced turbulent mixing due to swirl. Also, at the corresponding axial stations the peaks are located at a slightly larger radial distance for Case 3 than for Case 2 due to the centrifugal action of the swirl. These observations are consistent with the observations made for the mean axial velocity profiles shown in Fig. 5.

Figure 7 also includes the calculated profiles of $\bar{T}$ without the explicit inclusion of molecular diffusion in the computations.

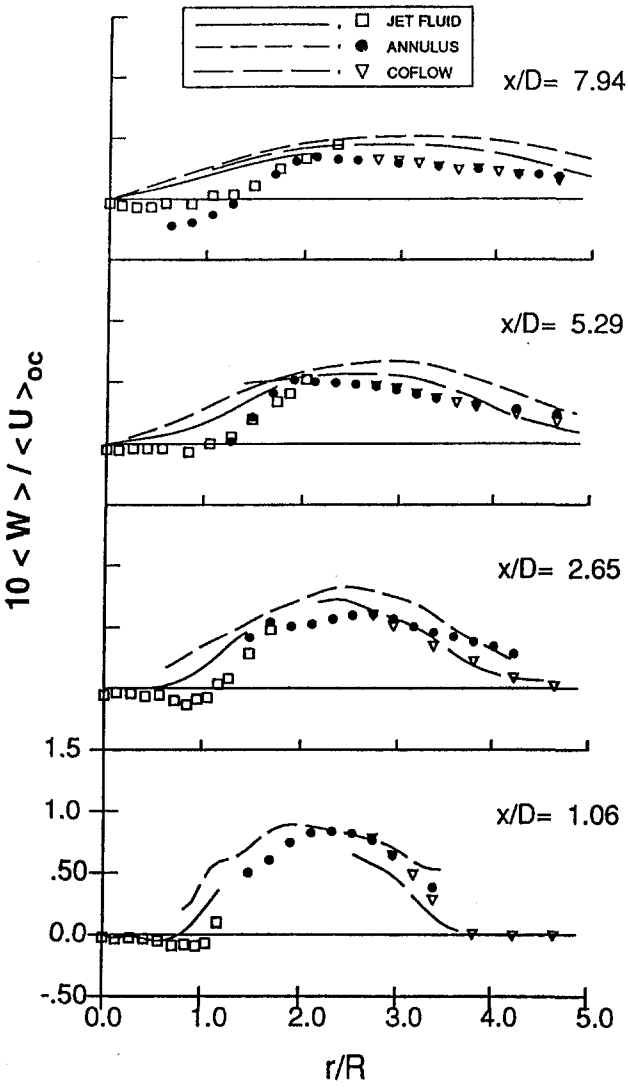


Fig. 6 Radial profiles of computed conditional mean tangential velocity (lines) compared against data (symbols) for the 30 deg swirl case (Case 3)

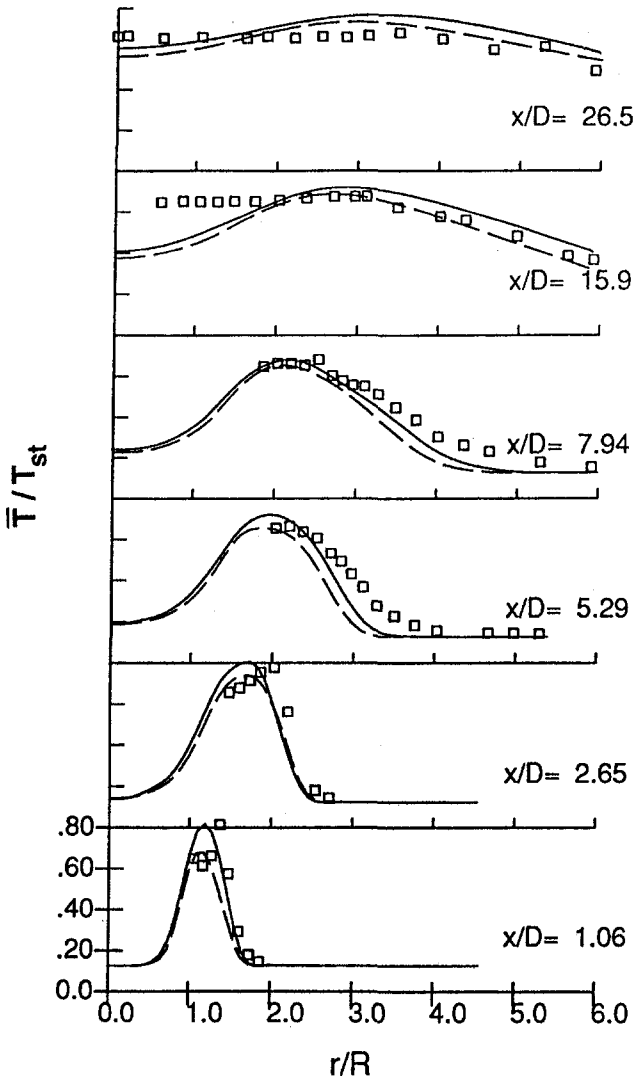


Fig. 7 Computed profiles of Reynolds-averaged mean temperature with (solid lines) and without (dotted lines) the inclusion of molecular diffusion compared against data (symbols) for the 30 deg swirl case (Case 3)

Overall, the inclusion of molecular diffusion improves the agreement of the computations with the data. It is interesting to note that the computed mean and other velocity statistics were nearly the same with or without the inclusion of molecular diffusion although the mean temperature profiles (and other scalar statistics) changed. This indicates that small changes in the local heat release rate do not have a very strong influence on the hydrodynamics of the flames studied.

The measured and calculated temperature variances are shown in Fig. 8. The comments regarding the inner peak in the computations made in conjunction with Fig. 4 are more clearly illustrated in this figure. The magnitudes and shapes of the outer peaks are well predicted, although the predictions are slightly higher for the downstream locations $x/D \geq 7.94$.

Figures 5–8 show that the peak temperature (i.e., the flame) still lies at the outer edge of the shear layer between the jet and the annulus flows, but the broadening of the temperature peaks show that the flame is spreading into the shear layer more than in the nonswirling case. Overall, the computations and data (Figs. 5–8) show enhanced mixing and spreading of the flame due to swirl compared to Case 2. The computed velocity and temperature statistics are in good agreement with the data, and

Downloaded 02 Jun 2010 to 171.66.16.105. Redistribution subject to ASME license or copyright; see http://www.asme.org/terms/Terms_Use.cfm

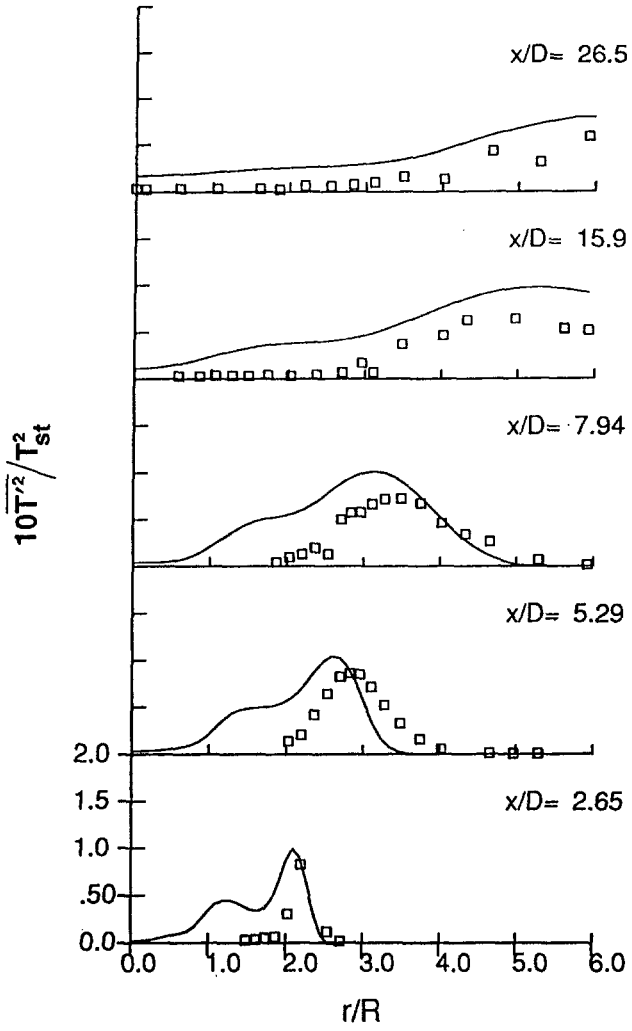


Fig. 8 Computed profiles of Reynolds-averaged temperature variance (lines) compared against data (symbols) for the 30 deg swirl case (Case 3)

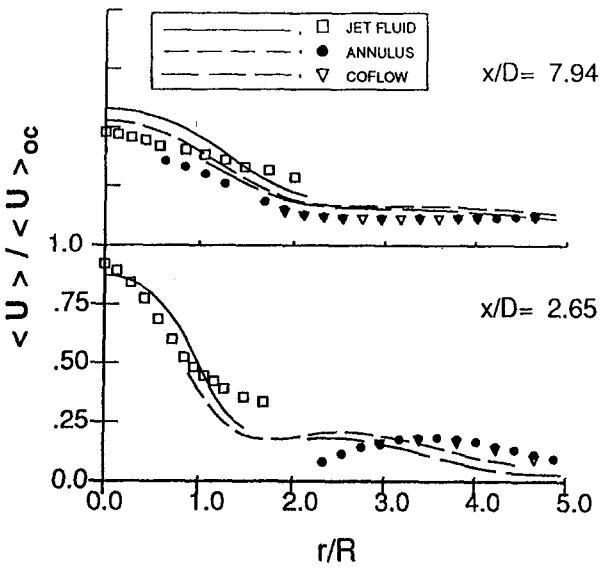


Fig. 9 Radial profiles of computed conditional mean axial velocity (lines) compared against data (symbols) for the 45 deg swirl case (Case 4)

the spreading and decay of the mean and swirl velocities are well predicted.

Figures 9, 10, and 11 show the conditional mean axial and swirl velocities and the unconditional Reynolds-averaged temperature, respectively, at two axial stations for the 45 deg swirl case (Case 4). The axial and swirl velocity data indicate much higher mixing and spreading than the 30 deg swirl case (Case 3) as expected. The location of the peak temperature (see data in Fig. 11) at $x/D = 2.65$ is at a significantly larger distance for Case 4 ($r/R \sim 2.5$) than for Case 3 ($r/R \sim 2.0$), while at $x/D = 7.94$ the peak temperature is located at nearly the same location ($r/R \sim 2.15$) for both cases. This indicates that the peak flame location expands to a larger radius in the near nozzle region for the 45 deg swirl case, but moves back (indeed contracts) to about the same location as for the 30 deg swirl case, at the downstream locations. This expansion near the nozzle is due to the larger centrifugal force in the higher swirl case forcing both the annular swirling air and the hydrogen jet to a larger radius (the volume expansion of the annulus air due to combustion induces a radial velocity in the annular jet for all the cases). Indeed, the data for mean radial velocities at the initial plane (presented in Takahashi et al., 1994c, d) show that the outer edge of the hydrogen jet and the bulk of the annulus air have outward mean radial velocities of approximately 5 m/s for Case 4 and about 2 m/s for Case 3. Evidence of this movement can be seen in the apparent radial shift in the corresponding radial profiles of the mean axial and tangential velocities at $x/D = 2.65$ in Figs. 9 and 10.

The centrifugal motion, coupled with the volume expansion of the annular air in the flame zone, causes the data rate for the annulus air seed to be low enough that data cannot be collected in a region between the hydrogen jet and the annulus air near the nozzle exit. These voids in the data can be noticed in Figs. 9 and 10 (up to $x/D = 2.65$ for Case 4) and in Figs. 5 and 6 (up to $x/D = 1.06$ for Case 3). The radial velocities in the bulk of the annular swirling jet in the nonreacting cases were less than 2 m/s and directed inward (Takahashi et al., 1992, 1993b) and hence did not cause such a problem for LDV measurements.

Another interesting observation is that although the initial swirl velocity is higher for Case 4 than Case 3, the peak swirl velocity of the annular air is approximately the same for the two cases at $x/D = 2.65$ as dictated by the conservation of

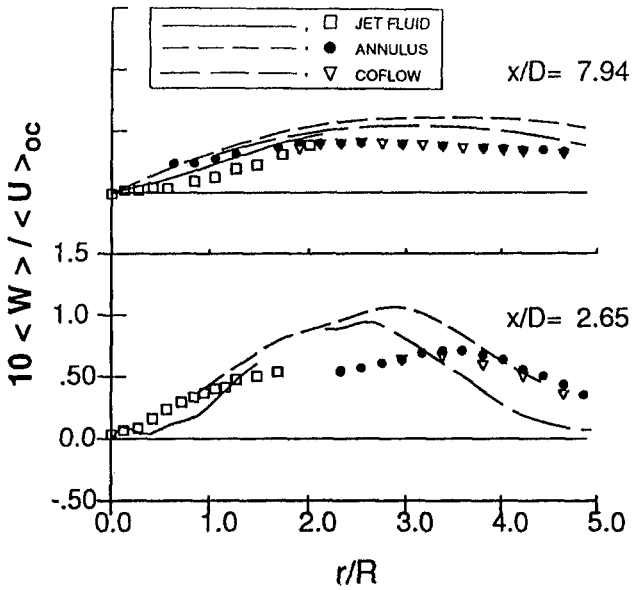


Fig. 10 Radial profiles of computed conditional mean tangential velocity (lines) compared against data (symbols) for the 45 deg swirl case (Case 4)

Downloaded 02 Jun 2010 to 171.66.16.105. Redistribution subject to ASME license or copyright; see http://www.asme.org/terms/Terms_Use.cfm

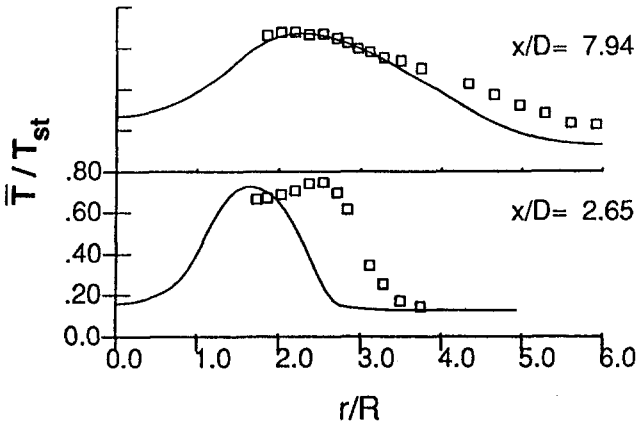


Fig. 11 Computed profiles of Reynolds-averaged mean temperature (lines) compared against data (symbols) for the 45 deg swirl case (Case 3)

angular momentum, due to the larger radial movement of the annular air in the former case.

The computations for Case 4 (Figs. 9, 10, and 11) are in good agreement with data and predict the jet spreading, the decay of the swirl, and the temperature profile well for $x/D = 7.94$ and beyond. There are some significant discrepancies between the data and the computations, especially in the mean temperature profile for $x/D \leq 2.65$. The preceding discussion of the strong swirl and radial velocity and the suggestion by the data in Fig. 9 that the flow is tending toward recirculation indicate that the boundary layer assumptions are seriously violated in the near-nozzle region and, hence, the calculated radial and mean pressure gradients are in error. Therefore, it is not reasonable to expect that the boundary layer algorithm will accurately calculate the flow in this region. Some evidence of this is also seen in Figs. 5 and 6 at $x/D = 1.06$, but the problem is more severe for the 45 deg swirl case. The large density ratio between the fuel/burned gas and the cold air also compounds the problem. It is emphasized that the shortcoming is not that of the pdf method, but rather it is due to the fact that the boundary layer assumptions are not valid under the conditions encountered in this region. Elliptic flow calculations with the pdf method, such as in Anand et al. (1990), planned for the future are expected to give a better agreement in the near-nozzle region.

The temperature and velocity profiles for Case 4 again indicate that the peak temperature location falls at the outer edge of the shear layer between the jet and the annulus; however, it is more into the shear layer and spreads faster into the shear layer than in the two cases presented previously (compare velocity and temperature profiles at $x/D = 7.94$ for example).

Higher order turbulence correlations are now presented to compare the details of the structure of turbulence computed by the pdf method against the data. Correlations of any order, including velocity-scalar correlations (not presented here), can be extracted from the pdf solution just as velocity correlations of any order can be extracted from the LDV data. Figures 12–15 present sample higher order correlations in the developing region of the flame for the 30 deg swirl case (Case 2). The correlations presented are the turbulent kinetic energy (k), the turbulent shear stress ($\langle uv \rangle$), the triple correlation ($\langle u^2 v \rangle$), and the fourth-order correlation ($\langle v^4 \rangle$), respectively. The correlations are in very good agreement with the data in terms of magnitudes and trends, and, as in the nonreacting case (Anand et al., 1993), show significant differences between the statistics of the fluids originating from different streams, especially between the jet and the annulus fluids. These differences diminish as the flow proceeds downstream and the streams mix. It should be noted that the conventional second-order closure models

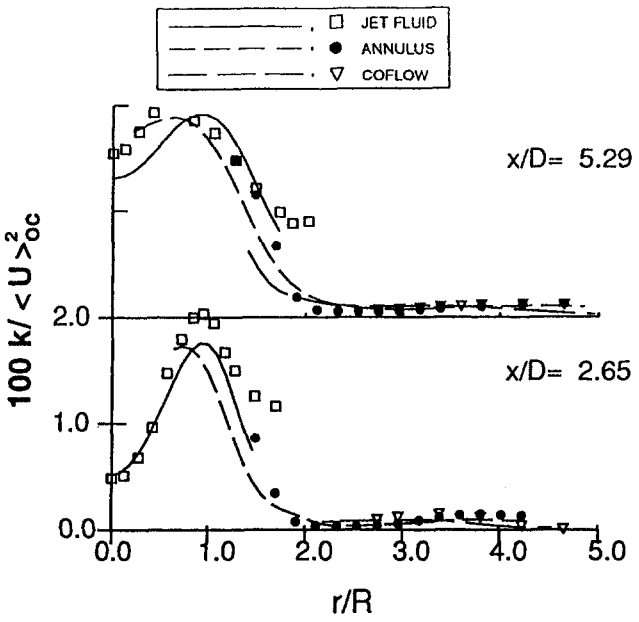


Fig. 12 Radial profiles of computed conditional turbulent kinetic energy (lines) compared against data (symbols) for the 30 deg swirl case (Case 3)

compute only up to the second-order correlations and the third-order correlations are modeled. Given that the higher order correlations are both difficult to measure and compute to a high level of accuracy, the good agreement between the data and computations observed for all quantities validates the computations and the data.

The cases took from approximately 15 minutes (for Case 2) to 23 minutes (for Case 4) of CPU time on an IBM RS6000/370 workstation. The nominal number of particles used in the simulations was 110,000 and the number of spatial bins used (for averaging) was 110. Calculations with 300,000 particles yielded nearly identical results. The number of basis functions used for the spline fits was 20.

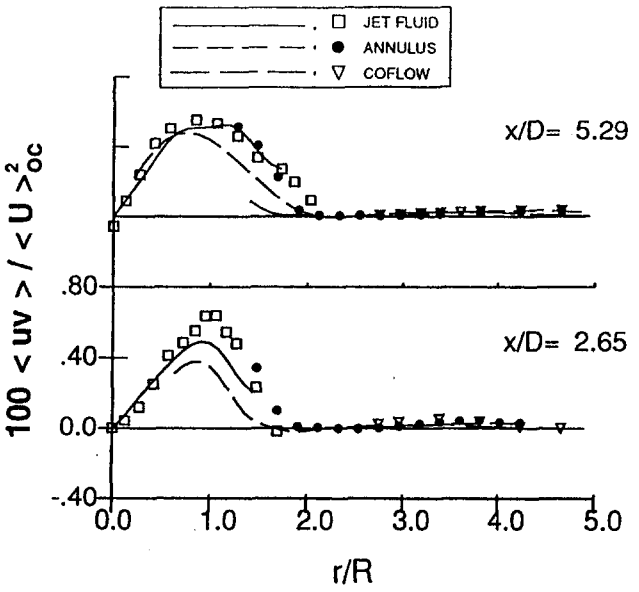


Fig. 13 Radial profiles of computed conditional turbulent shear stress (lines) compared against data (symbols) for the 30 deg swirl case (Case 3)

Downloaded 02 Jun 2010 to 171.66.16.105. Redistribution subject to ASME license or copyright; see http://www.asme.org/terms/Terms_Use.cfm

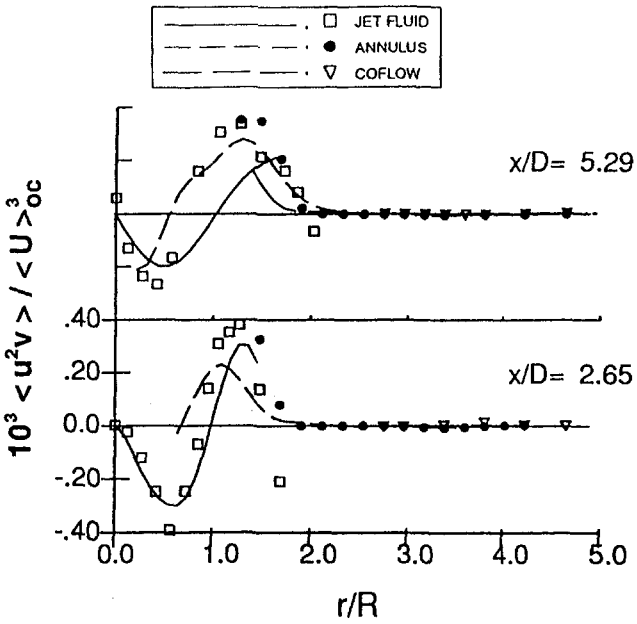


Fig. 14 Radial profiles of computed conditional triple correlation $\langle u^2v \rangle$ (lines) compared against data (symbols) for the 30 deg swirl case (Case 3)

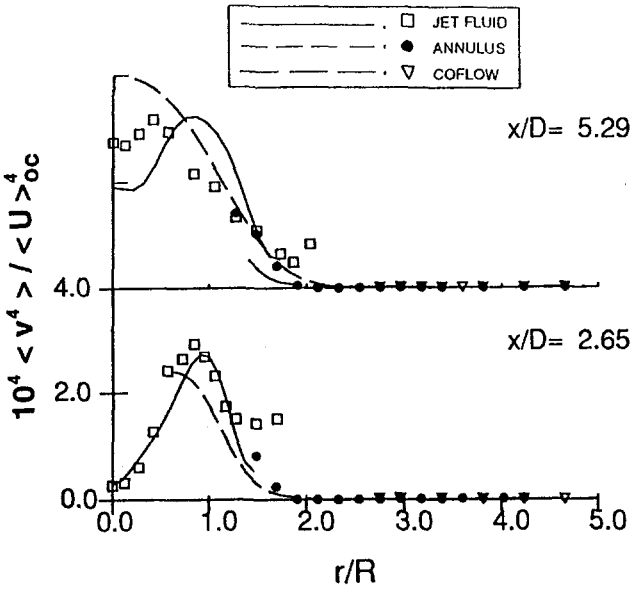


Fig. 15 Radial profiles of computed conditional fourth moment $\langle v^4 \rangle$ (lines) compared against data (symbols) for the 30 deg swirl case (Case 3)

Conclusions

Computations using the joint velocity-scalar pdf method as well as detailed benchmark quality measurements have been presented for nonswirling and, for the first time, swirling hydrogen jet diffusion flames. The measurements and computations reported include velocities (mean and higher moments up to fourth order) conditional upon the jet of origin of the fluid and temperature (mean and variance) near the burner exit and downstream locations up to 26.5 jet diameters. The velocities were measured with a three-component LDV and the temperature was measured using CARS.

The hydrogen flame, due to the low value of the stoichiometric mixture fraction for hydrogen/air combustion, is stabilized at the outer edge of the shear layer between the hydrogen and the surrounding air jet as expected. As the swirl in the air jet increases, the location of the peak temperature moves radially outward along with the shear layer while still remaining at the outer edge of the shear layer. The flame broadens and spreads more into the shear layer due to enhanced mixing due to swirl. Other relative features of the flames have been studied and discussed in detail.

The computations are in good agreement with data including those for fourth-order turbulent correlations, demonstrating and further validating the ability of the pdf method to accurately compute the details of the flow and the local turbulence structure. An important finding is that although Favre (density-weighted) averages are recommended and typically used in the computation of reacting flows, the conventional Reynolds average is the appropriate average to compare against temperature data from CARS.

A relatively simple boundary-layer algorithm with a relatively simple model for thermochemistry used for the computations provided a remarkably good agreement with velocity and temperature data, except very close to the nozzle for the high swirl case where the boundary-layer assumptions are not likely to be valid. Given the current agreement with the data, further complexities in the modeling of the thermochemistry such as multistep chemistry, differential diffusion of species, and nonunity Lewis number effects may not be warranted for the flames studied. The computations took a maximum of 23 minutes on an IBM RS6000/370 workstation.

Acknowledgments

This work was supported by the Air Force Wright Laboratory, Aero Propulsion and Power Directorate, Fuels and Lubrication Division, Wright-Patterson Air Force Base, Ohio, under Contract Nos. F33615-87-C-2821 to Allison (Technical Monitor, J. S. Stutrud) and F33615-92-C-2207 to UDRI (Technical Monitor, C. W. Frayne). The authors would like to thank Dr. Mel Roquemore (Wright Laboratory), Dr. Mohan Razdan (Allison), and Dr. Dilip Ballal (UDRI) for their support of this activity. The first author would like to thank Professor S. B. Pope (Cornell University) for useful discussions, and Dr. Mohammad Nikjoo (Allison) for his help in setting up the equilibrium tables. The use of the computer resources of the National Aerodynamic Simulation (NAS) program through a grant from NASA Lewis Research Center is gratefully acknowledged.

References

Anand, M. S., and Pope, S. B., 1987, *Combustion and Flame,* Vol. 67, p. 127.

Anand, M. S., Pope, S. B., and Mongia, H. C., 1990, *CFD Symposium on Aeropropulsion,* NASA Lewis, Cleveland, OH, NASA CP-3078, 347.

Anand, M. S., Pope, S. B., and Mongia, H. C., 1993, AIAA Paper No. 93-0106 (to be published in *AIAA Journal*).

Barlow, R. S., and Carter, C. D., 1994, *Combustion and Flame,* Vol. 97, p. 261.

Bilger, R. W., 1982, *AIAA Journal,* Vol. 20, No. 7.

Bilger, R. W., 1989, *Annual Review of Fluid Mechanics,* Vol. 21, p. 101.

Chen, J. Y., and Kollmann, W., 1992, *Combustion and Flame,* Vol. 88, p. 397.

Drake, M. C., 1988, *Twenty-First Symposium (International) on Combustion,* The Combustion Institute, Pittsburgh, 1579.

Haworth, D. C., and El Tahry, S. H., 1991, *AIAA Journal,* 29, 208.

Magre, P., and Dibble, R. W., 1988, *Combustion and Flame,* Vol. 73, p. 195.

Masri, A. R., Bilger, R. W., and Dibble, R. W., 1988, *Combustion and Flame,* Vol. 74, p. 267.

Nandula, S. P., Brown, T. M., and Pitz, R. W., 1994, *Twenty-Fifth Symposium (International) on Combustion,* Irvine, CA.

Norris, T., and Pope, S. B., 1994, *Twenty-Fifth Symposium (International) on Combustion,* Irvine, CA.

Pope, S. B., 1982, *Combustion Science and Technology,* Vol. 28, p. 131.

Pope, S. B., 1985, *Progress in Energy and Combustion Science,* Vol. 11, p. 119.

Pope, S. B., 1990, *Twenty-Third Symposium (International) on Combustion,* The Combustion Institute, Pittsburgh, p. 591.

Pope, S. B., 1991, *Physics of Fluids A,* Vol. 3, No. 8 (see also Erratum, Pope, S. B., 1992, *Physics of Fluids* A, Vol. 4, No. 5).

Downloaded 02 Jun 2010 to 171.66.16.105. Redistribution subject to ASME license or copyright; see http://www.asme.org/terms/Terms_Use.cfm

Takahashi, F., Vangsness, M. D., and Belovich, V. M., 1992, Paper No. AIAA-92-0580.

Takahashi, F., Durbin, M. D., and Vangsness, M. D., 1993a, Report UDR-TR-93-88, University of Dayton, Dayton, OH.

Takahashi, F., Vangsness, M. D., and Durbin, M. D., 1993b, Report UDR-TR-93-22, University of Dayton, Dayton, OH.

Takahashi, F., Durbin, M. D., Schmoll, W. J., and Vangsness, M. D., 1994a, Report UDR-TR-94-115, University of Dayton, Dayton, OH.

Takahashi, F., Vangsness, M. D., Schmoll, W. J., and Durbin, M. D., 1994b, Report UDR-TR-94-89, University of Dayton, Dayton, OH.

Takahashi, F., Durbin, M. D., Schmoll, W. J., and Vangsness, M. D., 1994c, Report UDR-TR-94-116, University of Dayton, Dayton, OH.

Takahashi, F., Durbin, M. D., Schmoll, W. J., and Vangsness, M. D., 1994d, Report UDR-TR-94-117, University of Dayton, Dayton, OH.

Tiang, S., Masri, A. R., and Pope, S. B., 1993, *Combustion and Flame*, Vol. 95, p. 133.

Downloaded 02 Jun 2010 to 171.66.16.105. Redistribution subject to ASME license or copyright; see http://www.asme.org/terms/Terms_Use.cfm

Optimization of Multiple Jets Mixing With a Confined Crossflow

Th. Doerr[1]

M. Blomeyer

D. K. Hennecke

Department of Flight Propulsion,
Technical University Darmstadt,
Darmstadt, Federal Republic of Germany

An experimental investigation of a nonreacting multiple jet mixing with a confined crossflow has been conducted. Flow and geometric conditions were varied in order to examine favorable parameters for mixing. The requirement for a rapid and intense mixing process originates from combustion applications, especially the RQL-combustion concept. Thus, the jets were perpendicularly injected out of one opposed row of circular orifices into a heated crossflow in a rectangular duct. Spacing and hole size were varied within the ranges referring to combustor applications. The results presented are restricted to an in-line orientation of opposed jet axis. Temperature distribution, mixing rate, and standard deviation were determined at discrete downstream locations. Best, i.e., uniform mixing can be observed strongly depending on momentum flux ratio. For all geometries investigated, an optimum momentum flux ratio yields to a homogeneous temperature distribution in the flow field downstream of the injection plane. Overly high ratios deteriorate the mixing process due to the mutual impact of the opposed entraining jets along with a thermal stratification of the flowfield. Correlations are introduced describing the dependency of optimum momentum flux ratio on mixing hole geometry. They allow the optimization of jet-in-crossflow mixing processes in respect to uniform mixing.

Introduction

Multiple jets injected into a confined crossflow are relevant to a wide variety of applications. They are of particular importance for combustion research. New combustor approaches to reduce NO_x emissions require the knowledge of jet mixing with crossflow, especially for the Rich Burn–Quick Quench–Lean Burn-combustion concept (RQL). The RQL-combustion initially takes place under fuel-rich conditions in the primary zone. In a succeeding quenching stage air is added to achieve a lean combustion condition in the secondary zone. This air addition must be rapid and intense to avoid stoichiometric operation with the formation of thermal NO_x (Simon, 1990). Therefore, an experimental investigation of a nonreacting mixing process of jets with a heated crossflow was carried out. The jets were perpendicularly injected out of one opposed row of circular orifices into a rectangular duct (Fig. 1). In contrast to previous jet mixing studies (Kamotani and Greber, 1974; Holdeman, 1990; Holdeman and Walker, 1977; Holdeman et al., 1987) this investigation concentrates on fast and homogeneous jet mixing due to the RQL application. Jet trajectories and temperature profile development were of minor importance. Geometries were tested with respect to a uniform and rapid equalization of the mixing streams. Recent studies (Doerr and Hennecke, 1993; Liscinsky et al., 1992, 1993, 1994) placed emphasis on this specific mixing problem, but only few investigations worked on the optimization of multiple jets mixing even at high momentum flux ratios up to $J = 200$ (Doerr and Hennecke, 1993). The results and correlations presented are restricted to one row of opposed jets with in-line hole axis, varying hole size, spacing, and momentum flux ratio. Staggered arrangements of the opposed jets were investigated within this research program (Doerr, 1994), but not shown in this place.

[1] Present address: BMW Rolls-Royce GmbH, Eschenweg, 15827 Dahlewitz, Germany.

Contributed by the International Gas Turbine Institute and presented at the 40th International Gas Turbine and Aeroengine Congress and Exhibition, Houston, Texas, June 5–8, 1995. Manuscript received by the International Gas Turbine Institute March 15, 1995. Paper No. 95-GT-313. Associate Technical Editor: C. J. Russo.

Test Procedure

A parametric variation of flow and geometric conditions has been carried out, keeping the mainstream conditions constant. The main flow is heated up (Fig. 2) using temperature as an indicator of mixing. It enters the mixing chamber with a temperature of $T_\infty = 325$ K at a velocity $v_\infty = 19$ m/s ($Re_\infty = 10^5$). The upper and lower jet flows are led parallel to the mainstream to the mixing ports. They are ejected at a temperature of $T_j = 300$ K. Mixing quality is measured by traversing a thermocouple probe in y–z planes downstream of the injection port. In contrast to real combustors the density ratio is about 1. As long as momentum flux ratio is kept constant, the influence of the density ratio on the mixing process and on jet penetration is of second order (Holdeman, 1990; Holdeman and Walker, 1977).

Definition of Mixing Quality

The degree of mixing can be determined measuring the distribution of the time-averaged temperature downstream of the injection ports. The local dimensionless temperature Θ_i is defined by:

$$\Theta_i = \frac{T_i - T_j}{T_\infty - T_j} \tag{1}$$

The local mixing rate ϵ_i is introduced to quantify the jet mixing process:

$$\epsilon_i = \begin{cases} \dfrac{T_i - T_j}{T_{adb} - T_j} & \text{for} \quad T_j < T_i < T_{adb} \\ \dfrac{T_i - T_\infty}{T_{adb} - T_\infty} & \text{for} \quad T_{adb} < T_i < T_\infty \end{cases} \tag{2}$$

The adiabatic, ideal mixing temperature is expressed in terms of:

$$T_{adb} = \frac{\dot{m}_\infty \cdot T_\infty + \dot{m}_j \cdot T_j}{\dot{m}_\infty + \dot{m}_j} \tag{3}$$

Copyright © 1997 by ASME

Downloaded 02 Jun 2010 to 171.66.16.105. Redistribution subject to ASME license or copyright; see http://www.asme.org/terms/Terms_Use.cfm

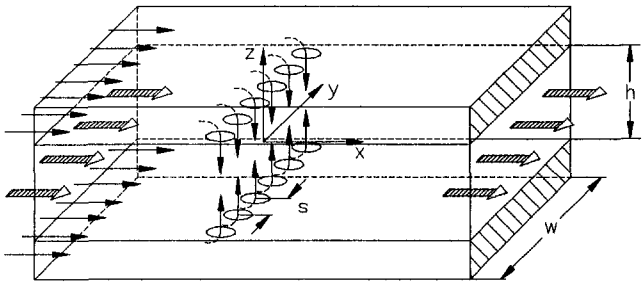


Fig. 1 Schematic of multiple jet mixing

or dimensionless:

$$\Theta_{adb} = \frac{\dot{m}_\infty}{\dot{m}_\infty + \dot{m}_j} \tag{4}$$

The local quantities Θ_i and ϵ_i are measured in the $y-z$ plane at discrete downstream locations x/h. The overall mixing rate ϵ in the $y-z$ plane is defined by:

$$\epsilon = \frac{1}{n} \cdot \sum_{i=1}^{n} \epsilon_i \tag{5}$$

($\epsilon = 0$ corresponds to an unmixed system, $\epsilon = 1$ characterizes a fully mixed flow field).

Comparing different geometries by varying momentum flux ratio, the mass addition can be calculated by:

$$\frac{\dot{m}_j}{\dot{m}_\infty} = \frac{\pi}{2} c_D \sqrt{\frac{\rho_j}{\rho_\infty}} \sqrt{J} \left(\frac{s}{d}\right)^{-1} \left(\frac{h}{d}\right)^{-1} \tag{6}$$

Since a fixed massflow ratio has to be achieved according to the applications, the total effective discharge area of the jets ($c_D \cdot A_j$) must be constant. Looking for different mixing configurations, i.e., hole geometries, at a fixed momentum flux ratio can imply a varying number of jet rows to provide the same massflow addition.

Experimental Facility

The experiments were carried out in the institute's mixing chamber test facility (Fig. 2). The airflow is supplied by a radial compressor (maximum 2.6 kg/s at 4 bars). By means of throttles, the flow is divided into the jetstream and the mainstream, which is subsequently heated. Upper and lower jetstream and the mainstream pass settling chambers and flow straighteners with nozzles and enter the mixing section (Fig. 1). The atmospheric mixing chamber consists of three parallel ducts of constant rectangular cross sections. The test section itself is 300 mm in width and 100 mm in height. The blockage effect of the probe is 5 percent related to the duct height. The mixing configurations are 2-mm-thick plates, which can be exchanged. A three axis traversing mechanism reaches $y-z$ planes over 600 mm in the streamwise direction. Traversing of the probe, data acquisition, and operation of the test rig are controlled by a PC 386.

For temperature measurements, iron–constantan thermocouples were used with a bent design (90 deg) to reduce the impact on the flowfield. The mass flow of each stream was measured by orifice flow meters. Conventional pressure transducers in combination with scanivalve devices provide the pressure acquisition.

Mixing Configurations

Based on the different mixing configurations investigated by Doerr and Hennecke (1993), the variation of geometries extends over the ranges:

$$\text{relative spacing } 1.5 \leq \frac{s}{d} \leq 6$$

$$\text{relative hole size } 5 \leq \frac{h}{d} \leq 20$$

These ranges cover common combustor mixing port arrangements. Figure 3 shows some mixing configurations out of the full test series. Originally several tests were carried out with constant massflow addition ($\Sigma A_j = \text{const}$). Due to a simultaneous variation of spacing and hole size the observed effects can not be separated and attributed.

Results and Discussion

The geometry defined by the ranges of parameters mentioned above are tested varying the momentum flux ratio. Mixing quality depends strongly on momentum flux ratio J, hole size h/d, and spacing s/d. For each geometry, an optimum momentum flux ratio J_{opt} has been determined using the mixing rate ϵ as a distinctive feature for mixing. Moreover, a conventionally defined standard deviation σ has been derived to get an additional criterion for the degree of mixing. Both mixing rate ϵ and standard deviation σ provide similar results in respect of tendency and optimum values of J.

Effect of Momentum Flux Ratio—Definition of Mixing Optimum. Figure 4 shows the influence of momentum flux ratio on jet mixing process. Mixing rate is increasing up to $J = 20$ for a particular geometry of $h/d = 6.67$ with $s/d = 2$. Exceeding this momentum flux ratio lowers mixing rate and deteriorates the mixing process as Fig. 13 illustrates by means of Θ distributions. The dimensionless temperature Θ is shown

Nomenclature

A_j = jet orifice area
A_∞ = mainstream area
c_D = discharge coefficient
d = jet diameter
h = height of duct
J = momentum flux ratio = $(\rho_j \cdot v_j^2)/(\rho_\infty \cdot v_\infty^2)$
s = spacing of jet centerlines
$\dot{m}_j$ = jet massflow
$\dot{m}_\infty$ = mainstream massflow, before mixing
n = number of data points in $y-z$ plane
Re_∞ = Reynolds number based on duct height
T_{adb} = adiabatic, ideal mixing temperature
T_i = local temperature
T_j = jet temperature
T_∞ = mainstream temperature, before mixing
v_j = jet velocity
v_∞ = mainstream velocity, before mixing
w = width of duct
x = downstream location from jet centerline
y = lateral distance from middle of channel
z = vertical distance from middle of channel
ϵ_i = local mixing rate
ϵ = overall mixing rate
Θ_{adb} = adiabatic, ideal mixing temperature
Θ_i = local temperature
ρ_j = jet flow density
ρ_∞ = mainstream density
σ = standard deviation from ideal mixing temperature

Downloaded 02 Jun 2010 to 171.66.16.105. Redistribution subject to ASME license or copyright; see http://www.asme.org/terms/Terms_Use.cfm

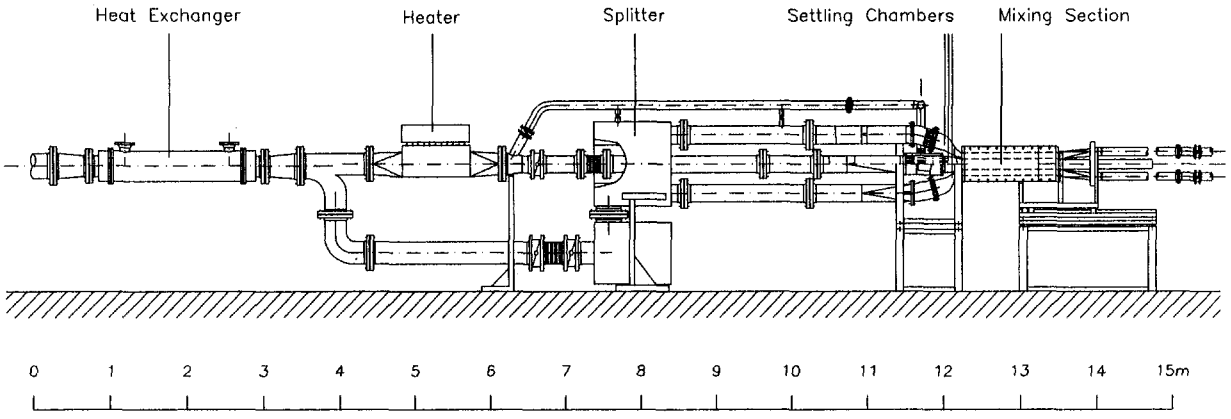


Fig. 2 Mixing chamber test facility

for three different momentum flux ratios: $J = 10$, 20, and 40. For the momentum flux ratio of $J = 20$ an optimum jet penetration depth can be observed. The jet cores are maintained offering maximum transfer surface between jets and mainstream for thermal equalization. Underpenetration ($J = 10$) keeps the crossflow in the middle of the channel unaffected by the entraining jets. For $J = 40$ an overpenetration merges the jets in the centerplane of the duct. Over- and underpenetration decrease the thermal transfer surface between the jets and the crossflow. The initial three-dimensional flow field becomes a two-dimensional mixing layer problem with worse heat transfer. A further increase of momentum flux ratio ($J > 40$) yields to an impact of opposed jets in the vicinity of the injection plane. Jet backflow can be observed, which enlarges the mixing region upstream of the mixing ports. Despite this effect, mixing efficiency diminishes due to a stratification of the flow field. In cases of large spacing ($s/d > 4$) jet backflow can enhance mixing (see Figs. 7 and 8).

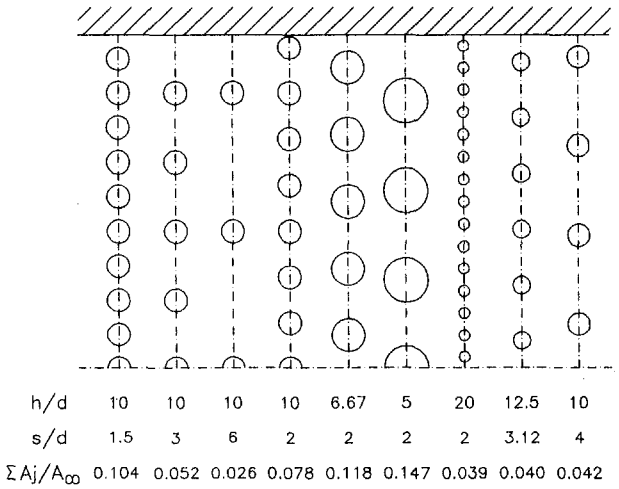


Fig. 3 Mixing configurations

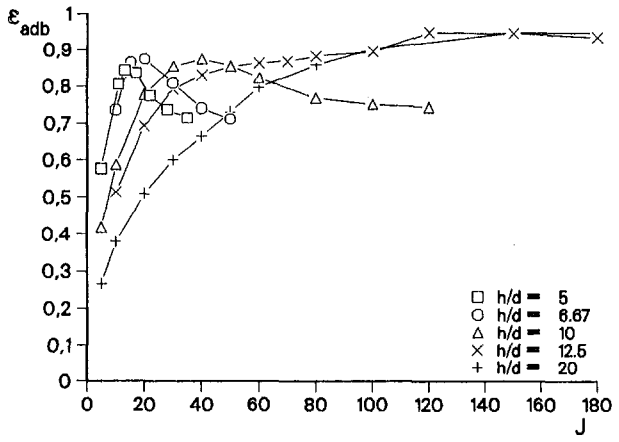


Fig. 5 Mixing rate ϵ versus J, h/d variation at constant spacing $s/d = 2$

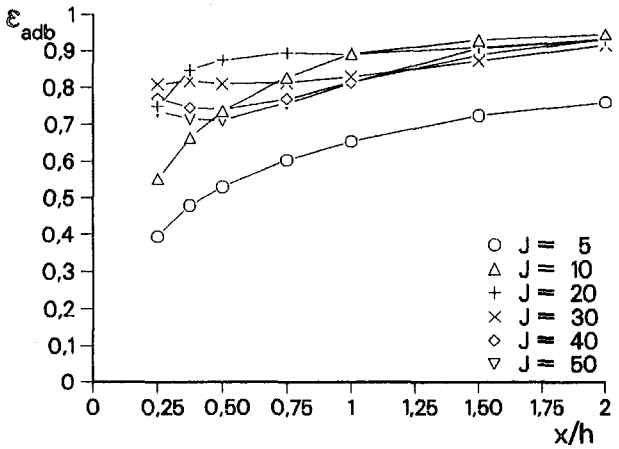


Fig. 4 Mixing rate for $h/d = 6.67$, $s/d = 2$, ϵ versus x/h

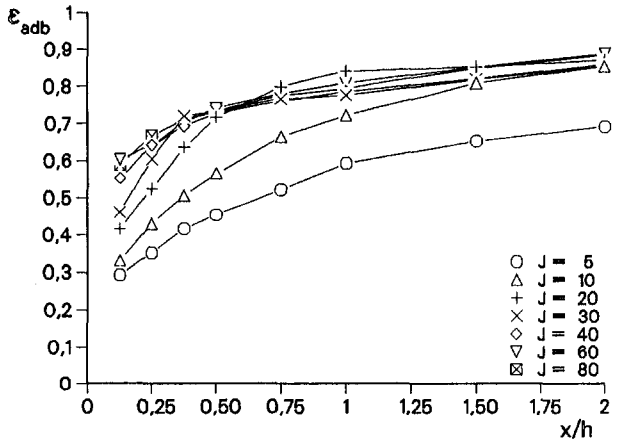


Fig. 6 Mixing rate ϵ versus x/h, $h/d = 10$, $s/d = 4$

Downloaded 02 Jun 2010 to 171.66.16.105. Redistribution subject to ASME license or copyright; see http://www.asme.org/terms/Terms_Use.cfm

Effect of Hole Size h/d. Keeping the relative spacing between the jets constant ($s/d = 2$), Fig. 5 can be derived. Because of the decrease of penetration depth for smaller hole diameters, the optimum momentum flux ratio is shifted to higher values by an increase of h/d ratios. A characteristic downstream location of $x/h = 0.5$ has been chosen. How far the location of the $y-z$ plane influences the determination of the mixing optimum is shown later. Beyond momentum flux ratios of $J = 80$ a satisfactory mixing quality can only be achieved for $h/d > 12.5$.

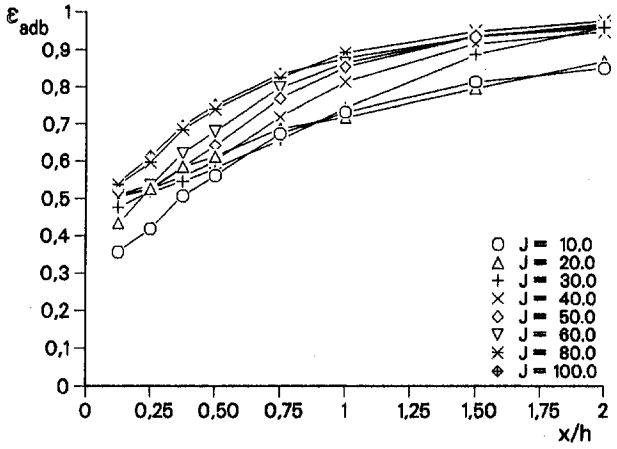


Fig. 7 Mixing rate ϵ versus x/h, $h/d = 10$, $s/d = 6$

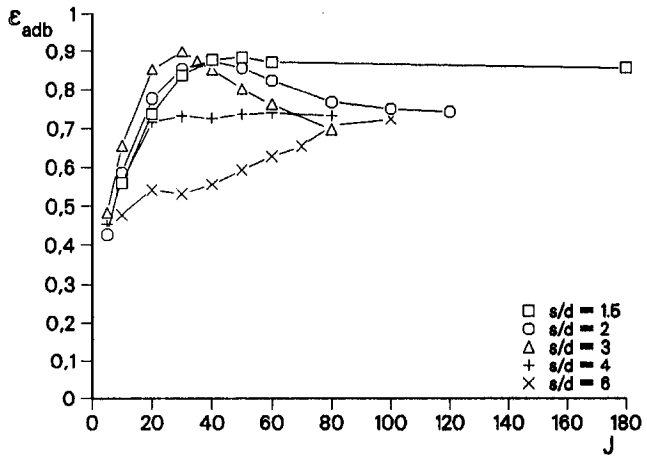


Fig. 8 Mixing rate ϵ versus J, s/d-variation, $h/d = 10$

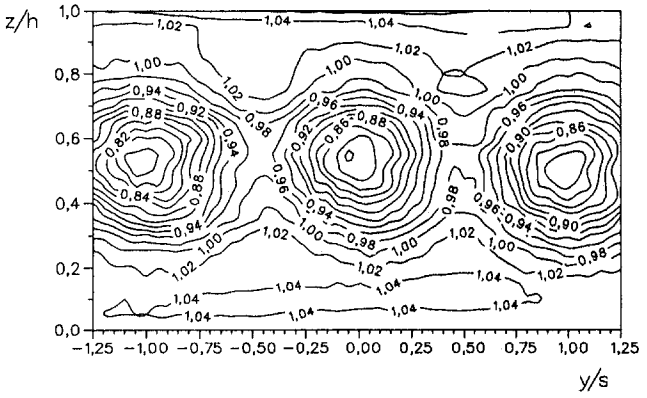


Fig. 9 Dimensionless temperature distributions for $h/d = 10$, $s/d = 6$, upstream of injection plane

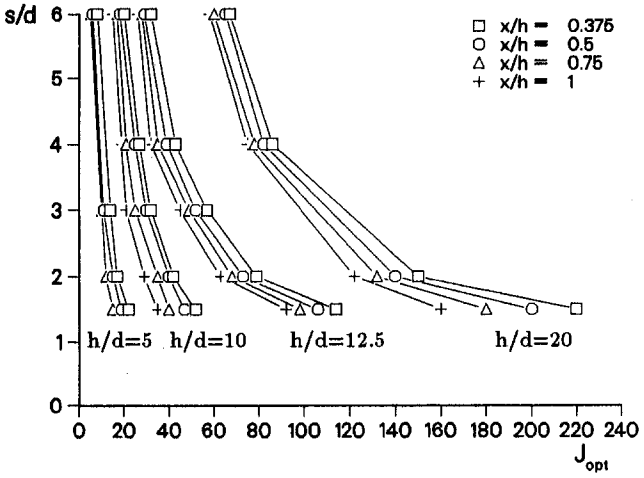


Fig. 10 Optimum momentum flux ratio, data base

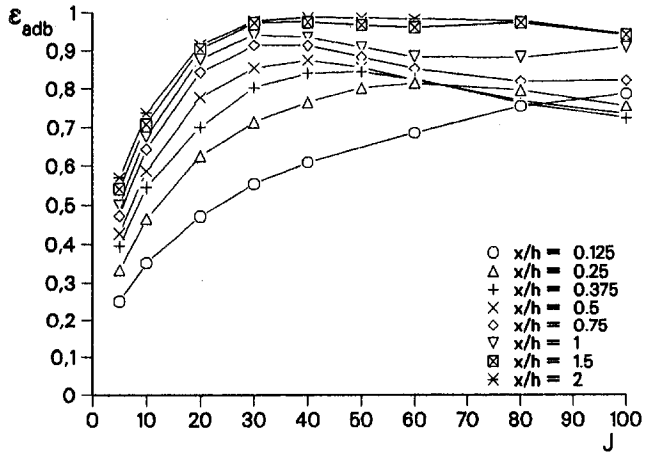


Fig. 11 Mixing rate ϵ versus J for $h/d = 10$, $s/d = 2$

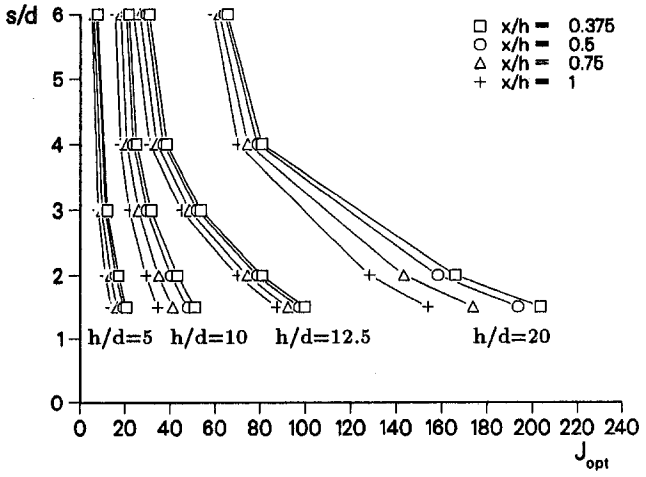


Fig. 12 Optimum momentum flux ratio, correlation

Effect of Spacing s/d. Varying the spacing s/d affects the blockage of the jets toward the mainstream and therefore the penetration depth of the jet cores. The three-dimensional mixing flow field is enhanced by enlarging the spacing. Figures 6 and 7 show the mixing rate versus the downstream measurement plane x/h for $h/d = 10$ with $s/d = 4$ and $s/d = 6$. For $s/d =$

Downloaded 02 Jun 2010 to 171.66.16.105. Redistribution subject to ASME license or copyright; see http://www.asme.org/terms/Terms_Use.cfm

4, ϵ reaches a maximum at $J = 20-30$, depending on x/h. Exceeding this limit mixing rate does not decrease in contrast to geometries with close spacing. In Fig. 8 the mixing rate is plotted versus momentum flux ratio for different spacings, keeping the downstream position constant $x/h = 0.5$. In the case of $s/d = 6$, the mixing rate increases continuously up to momentum flux ratio of $J = 100$ as Figs. 7 and 8 show. At $J = 20$ an effect similar to that at $J = 30$ for $s/d = 4$ in Fig. 8 can be observed. This point corresponds to a homogeneous distribution of the jet cores in the $y-z$ plane and thus to the mixing optimum defined above. Figure 14 clarifies the events in the flow field by means of temperature distributions. The enhancement of mixing rate, which can be noticed when exceeding $J = 20$ (Fig. 7), is facilitated by a highly three-dimensional mixing process. The opposed jets impinge on each other and evade in the gaps between the mixing port axes. An enlarging of contact surface increases mixing rate. A major drawback of this effect is jet backflow. It can be locally observed in the jet centerplanes as Fig. 9 shows for the $y-z$ plane $x/h = -0.07$ upstream of the injection plane.

In accordance with the application to a RQL-combustor jet, backflow is an unwanted flow field configuration because of the shift of primary zone equivalence ratio and with the increase of NO_x emissions. Therefore, the definition of the mixing optimum for large spacings is based on even and homogeneous distribution of the jet cores in the measurement plane. The improvement of mixing quality due to an increase of three-dimensional mixing effects in the flowfield is not taken into account.

Optimum Momentum Flux Ratio. With the definition of an optimum momentum flux ratio, the thermal transfer surface of the streams is maximized. Figure 10 can be derived by summarizing the range of geometries investigated. High h/d ratios along with a close spacing must be chosen to meet good mixing efficiencies at high momentum flux ratios. As indicated in Fig. 10 there is an influence of the downstream location of J_{opt}. Emphasis is placed on the downstream locations between the range $0.375 \leq x/h \leq 1$, which is the most interesting range to evaluate mixing quality. The range $x/h \geq 1$ does not allow a

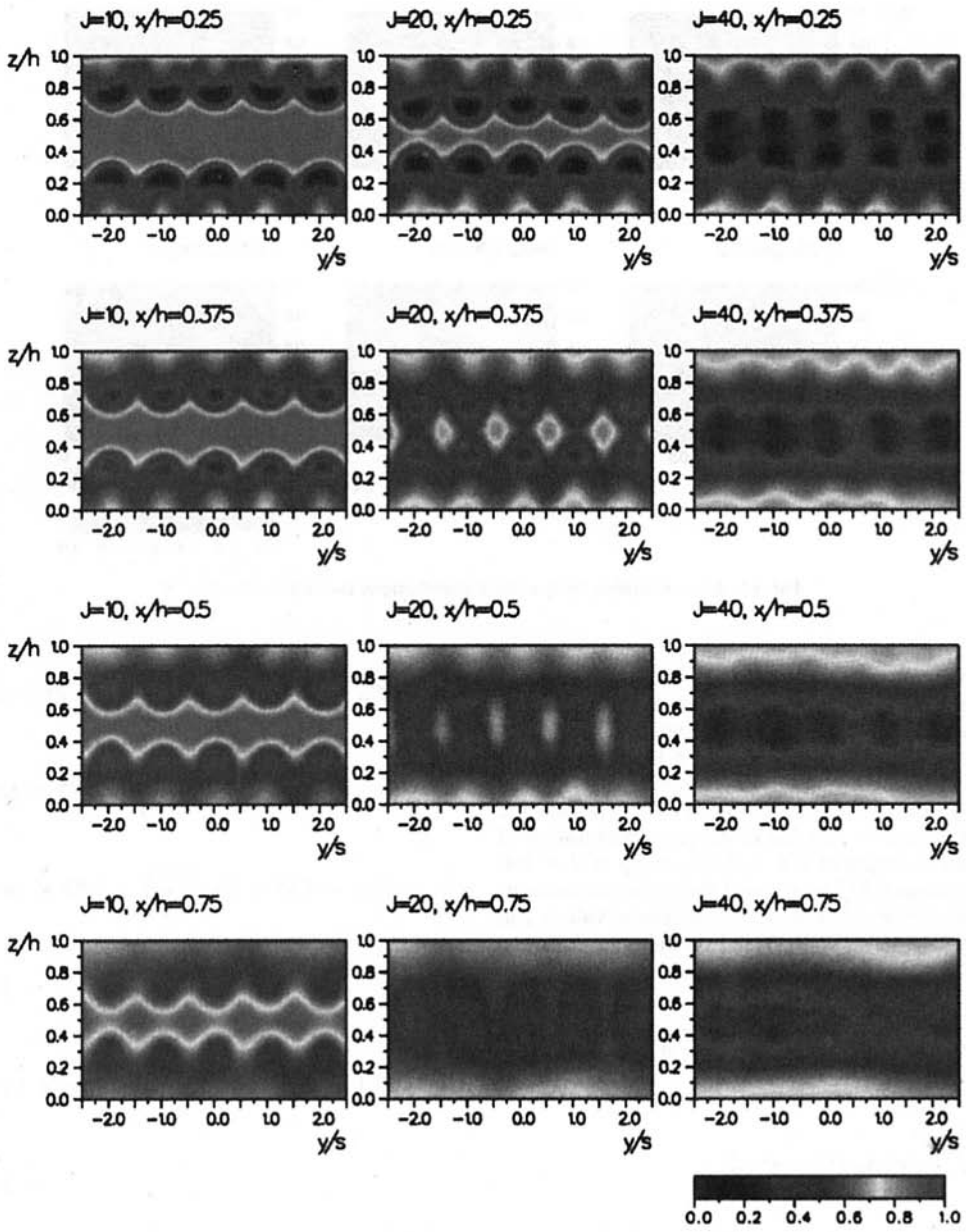


Fig. 13 Dimensionless temperature distributions for $h/d = 6.67$, $s/d = 2$

Downloaded 02 Jun 2010 to 171.66.16.105. Redistribution subject to ASME license or copyright; see http://www.asme.org/terms/Terms_Use.cfm

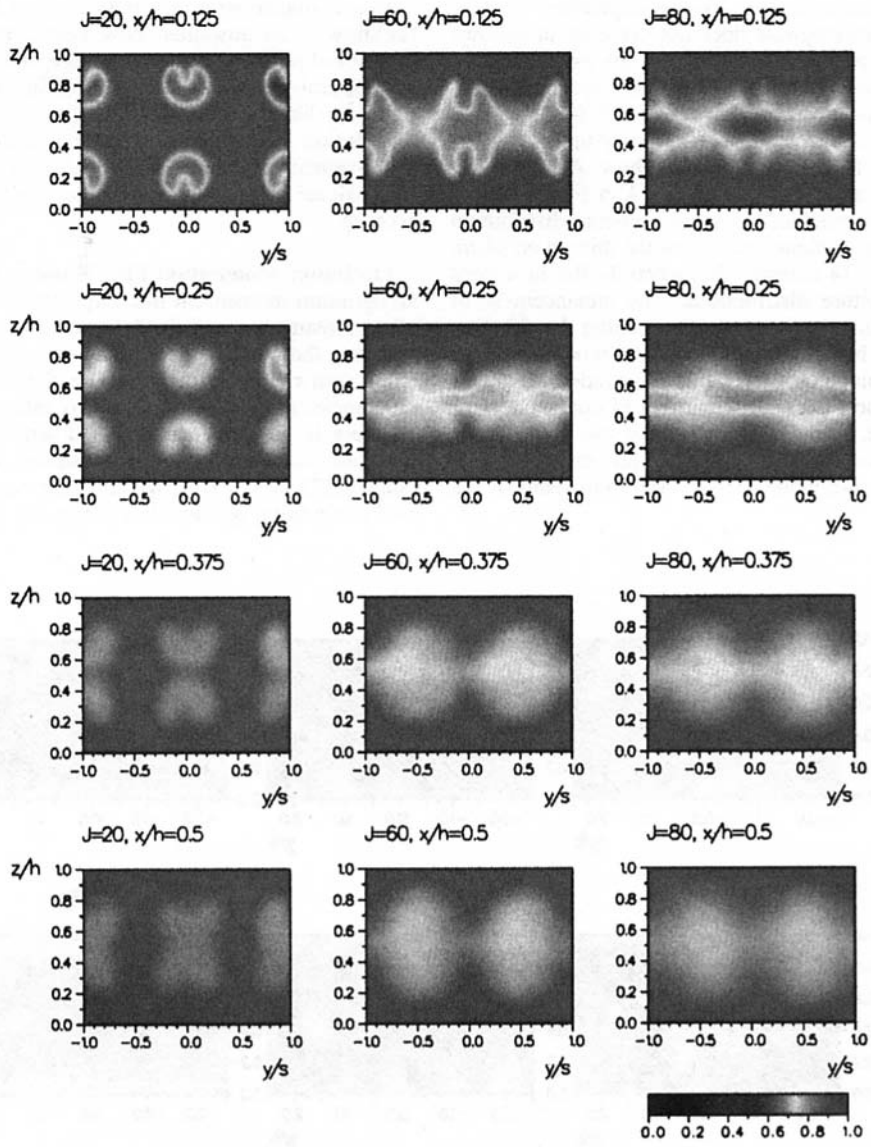


Fig. 14 Dimensionless temperature distributions for $h/d = 10$, $s/d = 6$

distinction of mixing processes. For $x/h \leq 0.375$ an originally good mixing process can deteriorate farther downstream, because of a mutual impact of opposed jets, which is not fully developed yet in far upstream region. Figure 11 illustrates the shift on J_{opt} for the different planes x/h. A geometry $h/d = 10$ with $s/d = 2$ has been chosen. Looking at $x/h = 0.125$, the best mixing is found at $J = 100$ due to the good penetration of the jets. Farther downstream at $x/h = 0.25$ mixing at $J = 100$ gets worse. In the range $0.375 \leq x/h \leq 1$ the optimum momentum flux ratios are observed at $J = 30-50$. These values can be obtained using Fig. 10 as well. Based on the data shown in Fig. 10, a correlation is described by:

$$J_{opt}\left(\frac{s}{d}, \frac{h}{d}, \frac{x}{h}\right) = C_1 + C_2\left(6 - \frac{s}{d}\right)^{2.7} \tag{7}$$

with:

$$C_1 = C_{11} + C_{12}\frac{x}{h}$$

$$C_2 = C_{21} + C_{22}\frac{x}{h}$$

$$C_{11} = -2.77 + 2.04\left(\frac{h}{d}\right) + 7.79 \times 10^{-2}\left(\frac{h}{d}\right)^2$$

$$C_{12} = 4.64 - 2.15\left(\frac{h}{d}\right) + 7.17 \times 10^{-2}\left(\frac{h}{d}\right)^2$$

$$C_{21} = 2.29 - 7.37 \times 10^{-1}\left(\frac{h}{d}\right) + 7.57 \times 10^{-2}\left(\frac{h}{d}\right)^2 - 1.88 \times 10^{-3}\left(\frac{h}{d}\right)^3$$

$$C_{22} = 2.01 - 7.25 \times 10^{-1}\left(\frac{h}{d}\right) + 7.08 \times 10^{-2}\left(\frac{h}{d}\right)^2 - 2.13 \times 10^{-3}\left(\frac{h}{d}\right)^3$$

The mathematical frame of the correlation is a parabola in

Downloaded 02 Jun 2010 to 171.66.16.105. Redistribution subject to ASME license or copyright; see http://www.asme.org/terms/Terms_Use.cfm

$s/d = 6$ with an exponent of 2.7. Figure 12 presents the optimum momentum flux ratios, which are obtained by the correlation. The deviation to the data set is less than 6 percent on average. Maximum discrepancy occurs at $h/d = 5$ with approximately 20 percent.

Application to Combustors

The use of the correlation provides a rapid and intense mixing of the jets emanating into the crossflow. The momentum flux ratio J_{opt} corresponds to the optimum penetration depth. The correlation can be applied to combustor design as far as homogeneous mixing is required like the quenching in the RQL combustor. Since the massflow ratio of jet to mainstream changes with s/d, h/d, and J, highest massflow addition is achieved with low h/d ratios along with a close spacing.

Considering that momentum flux ratio is fixed by density ratio and pressure drop across the liner, mixing geometry and thus massflow addition results from the correlation. As a consequence the mixing port configuration can consist of several stages of opposed in-line rows to meet the massflow ratio according to the stoichiometric requirement of the specific mixing process. The RQL combustion demands a massflow addition of $\dot{m}_j/\dot{m}_\infty \approx 2$ at an initial momentum flux ratio of $J \approx 180$. Choosing an in-line hole axis configuration yields to a geometry $h/d > 12.5$ for the first row of jets. At least three rows have to be combined to ensure the massflow ratio. Since jet backflow has to be avoided, in-line mixing port arrangements offer only half of the duct height for jet penetration. Staggered arrangements can enlarge the possible penetration depth to the full duct height. Since the spacing is appropriate, the opposed jets can pass each other at high momentum flux ratios. Hence, staggered arrangements of the opposed rows may increase the massflow ratio and thus reduce the number of mixing rows. The aim is to minimize the axial extent of the RQL quenching zone.

Conclusions

The investigation of nonreacting multiple jet-in-crossflow mixing shows that mixing efficiency strongly depends on momentum flux ratio of the streams:

- For all configurations investigated an optimum momentum flux ratio can be determined.
- Over- and underpenetration deteriorates the mixing process and yields to a thermal stratification of the flow field downstream of the injection plane.
- Jet backflow abates mixing quality for $s/d \leq 4$.
- The correlation presented is a good representation of the data base. It provides the optimum mixing port arrangement in dependency of momentum flux ratio or vice versa.
- High h/d and low s/d ratios are preferred to increase the mixing efficiency at high momentum flux ratios (for an in-line mixing port arrangement). This lowers the massflow addition per mixing stage.

Acknowledgments

The authors are indebted to the Deutsche Forschungsgemeinschaft DFG and the Fritz und Margot Faudi-Stiftung for the financial support, which made this research project possible.

References

Doerr, Th., and Hennecke, D. K., 1993, "The Mixing Process in the Quenching Zone of the Rich-Lean-Combustion Concept," *Proc. 81st Symposium on "Fuels and Combustion Technology for Advanced Aircraft Engines,"* AGARD-PEP Fiuggi.

Doerr, Th., 1995, "Ein Beitrag zur Reduzierung des Stickoxydausstoßes von Gasturbinenbrennkammern—Die Optimierung des Mischungsprozesses der Fett-Mager-Stufenverbrennung," Ph.D. Thesis, Darmstadt, Germany.

Holdeman, J. D., and Walker, R. E., 1977, "Mixing of a Row of Jets With a Confined Crossflow," *AIAA Journal,* Vol. 15, No. 2, pp. 243–249.

Holdeman, J. D., Srinivasan, R., Coleman, E. B., Meyers, G. D., and White, C. D., 1987, "Effects of Multiple Rows and Noncircular Orifices on Dilution Jet Mixing," AIAA *Journal of Propulsion and Power,* Vol. 3, No. 3, pp. 219–226.

Holdeman, J. D., 1990, "Mixing of Multiple Jets With a Confined Subsonic Crossflow," *Prog. Energy Combustion Science,* Vol. 19, pp. 31–70.

Kamotani, Y., and Greber, I., 1974, "Experiments on Confined Turbulent Jets in Crossflow," NASA CR-2392.

Liscinsky, D. S., True, B., Vranos, A., and Holdeman, J. D., 1992, "Experimental Study of Cross-Stream Mixing in a Rectangular Duct," Paper No. AIAA-92-3090.

Liscinsky, D. S., True, B., and Holdeman, J. D., 1993, "Experimental Investigation of Cross Flow Jet Mixing in a Rectangular Duct," Paper No. AIAA-93-3037.

Liscinsky, D. S., True, B., and Holdeman, J. D., 1994, "Mixing Characteristics of Directly Opposed Rows of Jets Injected Normal to a Crossflow in a Rectangular Duct," Paper No. AIAA-94-0217.

Simon, B., 1990, "Entwicklung neuer Brennkammerkonzepte für schadstoffarme Flugzeugantriebe," *MTU Focus,* Vol. 2, pp. 10–17.

Downloaded 02 Jun 2010 to 171.66.16.105. Redistribution subject to ASME license or copyright; see http://www.asme.org/terms/Terms_Use.cfm

The Effects of Different Sulfur Compounds on Jet Fuel Oxidation and Deposition

R. E. Kauffman
University of Dayton Research Institute,
Dayton, OH 45469-0161

This paper presents research that supports a proposed fuel oxidation/deposition mechanism involving acid:base reactions between "oxidizable" sulfur compounds, "basic" nitrogen compounds, and oxygen-containing polymers. The reported research presents experiments that study the effects of different sulfur compounds on the high-temperature (160–220°C) oxidation products and deposition tendencies of jet fuel. Surface analyses incorporating elemental analyses and depth profiles of deposits formed on steel surfaces were performed to identify the species involved in the initial stages of deposition by jet fuels. Experiments to study the effects of acid neutralizing compounds on the deposition tendencies of jet fuels are also presented.

Introduction

Future engine designs will utilize fuel recirculation due to higher operating temperatures and improved fuel efficiency. Fuel recirculation and higher operating temperatures will require fuels (1) to operate at higher temperatures, (2) to operate for longer periods of time at elevated temperatures in the presence of dissolved oxygen, and (3) to undergo numerous heating and cooling cycles prior to combustion. These increased fuel requirements will result in increased fuel deposition at heated surfaces and increased bulk particles causing valves to stick and filters to clog. Although hydrotreating and other fuel treatments can be employed to reduce deposition at higher temperatures, hydrotreating is expensive and may result in reduced stability toward dissolved oxygen, allowing fuel to oxidize during recirculation, leading to gum formation on valves and filters.

Therefore, a multidirectional research program is being sponsored by the U.S. Air Force to develop additive packages capable of increasing the upper temperature limits of straight-run jet engine fuels by 100°F and capable of stabilizing the fuel against oxidation and bulk particle formation during recirculation. One of the goals of the research program is to gain a better understanding of the fuel reaction mechanisms, which produce the compounds responsible for the surface deposits and bulk particles. Additive packages can then be designed to inhibit or alter the specific reactions that produce the surface deposits and bulk particle precursors.

It is well known that dissolved oxygen must be present for deposition to occur and that fuel deposits contain concentrated levels of sulfur and nitrogen in comparison to the heated fuel. It has also been reported that phenol-containing compounds present in jet fuel inhibit fuel oxidation at elevated temperatures (Kauffman, 1994) and increase the deposition tendencies of jet fuels (Hazlett et al., 1986). Further research in our laboratory (Heneghan and Harris, 1992; Heneghan et al., 1992; Kauffman, 1992) has shown that straight-run (>500 ppm S) and hydrotreated (<10 ppm S) fuels oxidize at different rates (hydrotreated fuels oxidize faster) at elevated temperatures to produce different type soluble and insoluble compounds. The straight-run fuels produce phenols and bulk particles containing concentrated (~2–4 percent) levels of sulfur and nitrogen. The hydrotreated fuels produce soluble hydroperoxides, organic acids, and bulk particles with minimal levels (<0.2 percent) of sulfur and nitrogen. The bulk particles contain single carbon-to-oxygen bonds (ether type) for the straight-run fuels and contain both single and double carbon-to-oxygen bonds (carbonyl type) for the hydrotreated fuels.

Therefore, the reaction mechanism shown in Fig. 1 was proposed to explain the oxidation and deposition processes of hydrotreated and straight-run jet fuels.

Hydrotreated fuels that contain minimal levels of sulfur oxidize as detailed in reactions O1 through O4. Straight-run fuels that contain significant levels of sulfur oxidize as detailed in reactions O1 through O4, then deposit as detailed in reactions D1 through D5.

The proposed oxidation/deposition mechanism explains the need for oxygen to form deposits and explains the sulfur, nitrogen, and oxygen contents of deposits. The mechanism also explains the reported results (Hazlett et al., 1986) that phenols increase the tendency of fuels to form deposits. The proposed mechanism also predicts that the addition of sulfur compounds to hydrotreated fuels will decrease the hydroperoxide content and increase the phenol content of oxidized sulfur containing hydrotreated fuels. The sulfur-contaminated hydrotreated fuel should produce sulfur–nitrogen-containing bulk particles and deposits in which the sulfur compound is oxidized and should produce metal surface deposits that contain concentrated levels of the oxidized sulfur compounds. Also, the addition of sulfonic acids would be expected to increase deposits with minimal oxidation, as recently reported (Hazlett et al., 1991).

To evaluate the accuracy of the proposed oxidation/deposition mechanism, various sulfur compounds were dissolved in a hydrotreated jet fuel (Jet A-1). The neat Jet A-1 fuel, sulfur-contaminated Jet A-1 fuels, and a commercial straight-run fuel (Jet A) were heated in two different oxidation tests to determine the effects of the different sulfur compounds on fuel chemistry: soluble oxidation products (hydroperoxides versus phenols), bulk particles (S, N content of particulates), and initial deposits formed on steel wire surfaces (sulfur oxide content near metal surface). In an attempt to inhibit the deposition process of Jet A, various compounds with acid neutralizing capabilities were added to the Jet A fuel prior to oxidation to inhibit deposition reactions D3 and D5, which require acid/base reactions and acidic attack on metal surfaces, respectively. The results are reported herein.

Experimental

Sulfur Compounds. The sulfur compounds used in this study were 92–98 percent pure and were obtained from Aldrich

Contributed by the International Gas Turbine Institute and presented at the 40th International Gas Turbine and Aeroengine Congress and Exhibition, Houston, Texas, June 5–8, 1995. Manuscript received by the International Gas Turbine Institute February 27, 1995. Paper No. 95-GT-222. Associate Technical Editor: C. J. Russo.

Copyright © 1997 by ASME

Downloaded 02 Jun 2010 to 171.66.16.105. Redistribution subject to ASME license or copyright; see http://www.asme.org/terms/Terms_Use.cfm

Oxidation Process

Fuel + O_2 → Fuel Radical + • O_2H	(O1)
Fuel Radical + O_2 → Hydroperoxide Radical	(O2)
Hydroperoxide Radical + Fuel → Hydroperoxide + Fuel Radical	(O3)
Hydroperoxide → Aldehydes, Organic Acids, → Polymers	(O4)

Deposition Process

Hydroperoxide + Sulfur Compound → Phenol + Acidic Sulfur Oxide + Ketone	(D1)
Phenol + Hydroperoxide Radical → Phenol Radicals + Hydroperoxide	(D2)
Acidic Sulfur Oxide + Basic Nitrogen Compounds →S•N Compound	(D3)
S•N Compound + Phenol Radicals → Bulk Particles	(D4)
Acidic Sulfur Oxide + Metal Surface → Initial Deposition	(D5)
Initial Deposition + Bulk Particles → Surface Deposition	(D6)

Fig. 1 Proposed reaction mechanism for jet fuel oxidation and deposition processes

Chemical Company, Milwaukee, WI. The dodecylbenzene sulfonic acid (90+ percent purity) was obtained from Conoco Petroleum, Conostan Standards Div., Hammond, IN.

Fuels. The jet fuels used in this study were a straight-run, commercial fuel (Jet A) and a hydrotreated, commercial fuel (Jet A-1) provided by U.S. Air Force Wright Laboratory, Aero Propulsion and Power Directorate. The fuels' chemical and performance characteristics are listed in Table 1. The sulfur-contaminated hydrotreated fuels were produced by dissolving (room temperature, shaken by hand) the selected sulfur compounds into different portions of the Jet A-1 fuel. The weight of each sulfur compound added to the Jet A-1 fuel was determined based on producing a Jet A-1 fuel with a sulfur concentration of 1000 ppm (sulfur level of Jet A fuel, Table 1).

Oxidation Tests

Flask Test. The flask test was used to evaluate the tendencies of the jet fuels and sulfur compounds to produce bulk particles. The flask test was performed by heating 20 mL of fuel in a 50 ml erlenmeyer flask placed on a hot plate (200°C surface temperature) with stirring capability. The fuel was added to the flask and was heated with stirring (magnetic stir bar). When the fuel temperature reached 100°C, the test time was initiated and an air flow (0.5 liter per hour) was initiated through a disposable glass pipette situated on the bottom of the flask. The test was stopped at 30 minutes (bulk temperature: 160°C), the flask was removed from the hot plate, and the heated fuel was allowed to cool to room temperature. The oxidized fuel was stored in a glass vial for subsequent hydroperoxide and phenol analyses. All of the fuels had reached their maximum hydroperoxide values by 30 minutes. The phenol concentrations increased with time for the entire test period.

The phenol and hydroperoxide contents of the cooled fuels were determined by cyclic voltammetry and the remaining fuel was filtered through a 0.4 μm filter to isolate the bulk particles for elemental analysis by X-ray Photoelectron Spectroscopy (XPS). The isolated particles were washed with acetone/hexane (to remove residual fuel and soluble polymers) prior to XPS analysis. The filtered fuels were then heated under a stream of nitrogen to reduce the fuel volume causing the least soluble oxidation polymers to precipitate. The precipitated polymers were isolated by filtration and analyzed for elemental content by XPS.

Table 1 Chemical properties of studied fuels

	Jet A Fuel	Jet A-1 Fuel
Hydrotreated	No	Yes
Aromatics, Vol %. (D1319)	19	19
Mercaptan Sulfur, Wt %	0.001	0.000
Sulfur, Total Wt % (D4294)	0.10	0.00
JFTOT Breakpoint, °C	282	332
Hydroperoxides, mmole/L[a]	0.03	0.01
Phenols, mmole/L[a]	2.6	0.4

[a] by cyclic voltammetry

Sealed Ampoule Test. The sealed ampoule test was used to evaluate the tendencies of the fuels and sulfur compounds to produce deposits on metal surfaces. The sealed ampoule test was performed by pippetting 3 mL of fuel into a 4 mL glass ampoule. A low-carbon steel wire was then placed inside each ampoule ($\frac{3}{4}$ of wire covered by fuel). The prepared ampoules were sealed under an air atmosphere. The sealed vials were $\frac{3}{4}$ fuel and $\frac{1}{4}$ air (allow for fuel expansion during heating). The ampoules were heated for 10 minutes in an oven set to 210°C (fuel at 210°C after 5 minutes). The ampoules were removed and allowed to cool for 10 minutes to room temperature or for 24 hours to enhance deposit formation. The ampoules were then broken open, the wires removed and cleaned with acetone/hexane (to remove fuel and soluble polymers), and the cleaned wires were analyzed by Auger spectroscopy to determine deposit thickness and to determine elemental depth profiles.

Bulk Particle and Deposit Elemental Analyses. Auger electron spectroscopy (AES) was used to perform depth profiles of the deposits formed on metal surfaces. AES depth profiles were obtained from a Varian scanning Auger spectrometer using an electron beam energy of 5 keV to obtain spectra and a 1 keV argon ion beam to sputter the samples. The sputter rate for the deposits that formed on the steel wires was estimated to be 2 nm min^{-1} based on measurements of a thin silicon nitride film whose thickness had been measured with ellipsometry.

Nomenclature

C = carbon
L = liter
mmole = millimole
ml = milliliter
N = nitrogen
nm = nanometers
O = oxygen
ppm = parts per million
S = sulfur
V = volt
Vol = volume
wt = weight

Abbreviations

AES = Auger Emission Spectroscopy
ASTM = American Society of Testing Materials
Jet A = commercial, straight-run jet fuel
Jet A-1 = commercial, hydrotreated jet fuel
JFTOT = Jet Fuel Thermal Oxidation Tester
XPS = X-ray Photoelectron Spectroscopy

Downloaded 02 Jun 2010 to 171.66.16.105. Redistribution subject to ASME license or copyright; see http://www.asme.org/terms/Terms_Use.cfm

X-ray photoelectron spectroscopy (XPS) was used to perform elemental surface analyses (top 3 nanometers of compound) of the bulk particles and deposits. XPS spectra were obtained with an extensively modified AEI ES-100 photoelectron spectrometer. Modifications to this instrument have included the addition of a 2001 s^{-1} turbomolecular pump and a 1101 s^{-1} ion pump for evacuation of the sample chamber. This instrument is equipped with a magnesium X-ray source.

Cyclic Voltammetric Fuel Tests

Introduction. The theory of cyclic voltammetry has been described in detail (see Kauffman, 1992). The cyclic voltammetric tests were performed with a commercially available voltammograph equipped with a glassy carbon disk (3 mm diameter) working electrode, a platinum wire (0.5 mm diameter) reference electrode, and a platinum wire (0.5 mm diameter) auxiliary electrode. The cyclic voltammetric procedure applies a small voltage ramp (0–1 V) to a platinum wire electrode and measures the produced current (μamp) at the active surface of a glassy carbon electrode. If a species in the diluted fuel sample undergoes oxidation in the applied voltage range, the oxidation of the species causes an increase in the current measured by the cyclic voltammograph. The quantity of current increase is directly proportional to the concentration of the species in the fuel. The voltage at which the current increase occurs is indicative of the type of species present in the fuel, e.g., dihydroxyaromatics (0.5–0.6 V), primary and secondary aromatic amines (0.7–0.8 V), substituted phenols (0.8–1.0 V), and so on.

Two cyclic voltammetric-based tests, the new hydroperoxide method and the phenol test, were studied.

Hydroperoxide Method. The hydroperoxide method (Kauffman, 1994) uses the same aqueous potassium iodide and acetic/hydrochloric acid solutions as prepared in the current standard hydroperoxide test, ASTM D3703-85. Hydroperoxide analyses performed using the new hydroperoxide and ASTM D3703-85 test methods have been shown to be in good agreement (Kauffman, 1994). The hydroperoxides in the fuel sample react with the acidic potassium iodide solution to produce iodine. Consequently, the concentration of iodine produced is directly proportional to the concentration of hydroperoxides in the reacted fuel sample. The hand-held voltammetric instrument used to measure the produced iodine was calibrated using blank (0 mmole) and standard (1 mmole) iodine solutions.

The fuels were analyzed for hydroperoxide concentrations by dispensing 1 to 5 ml of fuel, 0.25 ml of aqueous potassium iodide solution, and 1 ml of acetic acid solution into a 10 ml vial. The vial was capped and shaken vigorously by hand for 30 seconds. The vial was opened, 1 ml of water added, the vial was recapped, and gently shaken for 2 seconds. The vial was allowed to sit undisturbed for approximately 10 seconds. The lower layer that formed was pipetted into a new vial. The iodine produced was determined by inserting the voltammograph electrode into the pipetted layer and scanning the voltage of the auxiliary electrode from 0.0 to −1.0 V (referenced to platinum reference electrode) at a rate of 0.1 V/s. The current produced by the glassy carbon electrode was compared against the blank and standard (1 mmole) to measure the produced iodine, and consequently, the concentration of hydroperoxide in the reacted fuel sample. The calculated concentrations of the hydroperoxides in the studied fuels are listed in Table 1.

Phenol Test. To determine the concentration of phenols present in the jet fuels, samples of the fuels (0.1 ml) were diluted with 3 ml of ethanol (fuel soluble) containing an inorganic base (potassium hydroxide: 0.25 percent) (Kauffman, 1994). The electrode was inserted into the diluted fuel and the voltage of the auxiliary electrode was increased from 0.0 to 1.0 V (referenced to the platinum reference electrode) at a rate of 0.05 V/s. The current produced by the glassy carbon electrode was plotted versus scan voltage by a strip chart recorder interfaced to the voltammograph. The height(s) of the peak(s) produced by the fuels were measured and compared to solutions containing known concentrations of ethyl phenol and 1-naphthol. The calculated concentrations of phenols in the studied fuels are listed in Table 1.

Results and Discussion

Introduction. Research was performed to evaluate five predictions of the proposed oxidation/deposition mechanism:

1 Addition of oxidizable sulfur compounds will reduce hydroperoxide content and increase phenol content of oxidized Jet A-1 (hydrotreated) fuel
2 Jet A-1 fuel (in the absence of oxidizable sulfur compounds) will produce bulk particles and soluble polymers, which contain minimal amounts of sulfur and nitrogen and contain double carbon-to-oxygen bonds (aldehyde-acid polymers)
3 Addition of oxidizable sulfur compounds will produce bulk particles from Jet A-1 fuel, which contain sulfur oxides, nitrogen, and single carbon-to-oxygen bonds (phenol polymers)
4 Addition of oxidizable sulfur compounds will produce initial deposits on metal surface that have concentrated levels of sulfur oxides.
5 Addition of acid neutralizing compounds to Jet A (straight run) fuel will inhibit metal surface deposits and bulk particle formation.

The chemical and performance characteristics of the Jet A and Jet A-1 fuels used in this study are listed in Table 1. The sulfur compounds used in this study included hexadecyl mercaptan, diphenyl disulfide, benzyl phenyl sulfide, diphenyl sulfoxide, diphenyl sulfone, and dodecyl benzene sulfonic acid. The acid-neutralizing compounds used in this study were laboratory grade and included ferric oxide powder (less than 0.1 μm particle size) and calcium oxide powder (less than 20 μm particle size).

Effects of Sulfur Compounds on Jet A-1 Oxidation Products. To test the effects of sulfur-containing compounds on the oxidation products of Jet A-1 fuel, Jet A-1 fuels containing the various sulfur compounds listed in Table 2 were oxidized for 30 minutes at a maximum temperature of 160°C using the flask oxidation test. Since the flask oxidation test is open to the air and a glass pipette is used to bubble air continuously through the heated fuel, oxygen is available for fuel oxidation during the entire test period. The hydroperoxide (reaction O3) and phenol (reaction D1) concentrations of the heated Jet A-1 fuels contaminated with the various sulfur compounds are listed in Table 2.

The results shown in Table 2 indicate that the presence of certain type sulfur compounds affects the hydroperoxide/phenol ratios of oxidized Jet A-1 fuel. The neat (uncontaminated) Jet A-1 fuel oxidized to produce hydroperoxides and very little phenols (reaction O3 dominant) (Table 2). The addition of a mercaptan compound to the Jet A-1 fuel inhibited oxidation (reaction O2 and O3 inhibited) and produced low levels of phenols (reaction D1 activated) and undetectable (below 0.01 mmole/L of fuel) levels of hydroperoxide. The disulfide and sulfide compounds inhibited oxidation to varying degrees and produced high levels of phenols (reaction D1 activated) and low levels of hydroperoxides (Table 2). In contrast to the other sulfur compounds, the sulfoxide and sulfone compounds did not affect the oxidation products (reaction D1 inactive) and produced primarily hydroperoxides. In agreement with the sulfide and disulfide compounds, the Jet A fuel oxidized to produce primarily phenol type compounds (reaction D1 activated).

Downloaded 02 Jun 2010 to 171.66.16.105. Redistribution subject to ASME license or copyright; see http://www.asme.org/terms/Terms_Use.cfm

Table 2 Effects of different sulfur compounds on the oxidation products of Jet A-1 and Jet A fuels obtained from the flask oxidation test

Fuel	Sulfur Compound [a]	Initial Oxidation Products mmoles/L of Fuel		Bulk Particle XPS Analyses (% Atomic Wt)		
		Peroxides	Phenols	% O	% N	% S
A-1	---	5.5	0.75	11[b]	< 0.2[b]	< 0.2[b]
	Hexadecyl Mercaptan	< 0.01	3.3	25	1.8	4.4 (>98%)[c]
	Diphenyl Disulfide	1.5	7.5	22	1.0	1.7 (>98%)[c]
	Benzyl Phenyl Sulfide	2.0	6.0	18	0.4	0.8 (57%)[c]
	Diphenyl Sulfoxide	6.0	0.75	13[b]	< 0.2[b]	< 0.2[b]
	Diphenyl Sulfone	8.0	0.75	12[b]	< 0.2[b]	< 0.2[b]
A	---	0.4	4.6	20	1.9	2.8 (>98%)[c]

a Concentration 1000 ppm by sulfur. b Polymer obtained by evaporating fuel. c % oxidized sulfur

Effects of Sulfur Compounds on Jet A-1 Bulk Particles. To test the effects of sulfur-containing compounds on the bulk particles produced by oxidized Jet A-1, the stressed fuels obtained from the flask oxidation tests (Table 2) were filtered to isolate the bulk particles produced during the oxidation of sulfur contaminated Jet A-1 fuels. The oxidized Jet A-1 fuel had to be evaporated to isolate soluble material formed by oxidation. The XPS elemental analyses of the bulk particles and soluble material isolated from the oxidized Jet A-1 fuels are also listed in Table 2.

The results given in Table 2 show that the soluble material isolated from the oxidized Jet A-1 fuel contains minimal amounts of sulfur and nitrogen. Infrared spectroscopy determined the soluble material contained a large number of carbonyl (C = O) type carbon-to-oxygen bonds (polymer resulting from reaction O4). The oxidized Jet A-1 fuels contaminated with mercaptan, disulfide, and sulfide compounds produced bulk particles (Table 2) containing significant levels of sulfur oxide (reactions D1 and D3) and significant levels of nitrogen (reaction D3). Infrared spectroscopy determined the bulk particles mainly contained ether (C-O) type carbon-to-oxygen bonds (polymers resulting from reactions D2 and D4). The oxidized Jet A-1 fuel contaminated with sulfoxide and sulfone compounds produced soluble material similar to the material produced by the neat oxidized Jet A-1 fuel, i.e., minimal amounts of sulfur and nitrogen and high levels of carbonyl type carbon-to-oxygen bonds.

In agreement with the mercaptan, sulfide, and disulfide compounds, the Jet A fuel oxidized to produce bulk particles that contain sulfur oxides, nitrogen, and primarily ether type carbon-to-oxygen bonds. The addition of dodecyl benzene sulfonic acid to Jet A fuel produced visible bulk particles within 24 hours at room temperature. The isolated particles had a significant nitrogen content (reaction D3), ether type carbon-to-oxygen bonds (reaction D4) and produced elemental analyses similar to the particles produced by the oxidized Jet A fuel (Table 2).

Effects of Sulfur Compounds on Initial Metal Surface Deposits. To test the effects of different sulfur compounds on the thickness and composition of the initial deposits formed on metal surfaces, Jet A-1 fuels containing the various sulfur compounds listed in Table 2, Jet A-1 fuel and Jet A fuel were heated at 210°C for 10 minutes in sealed glass ampoules containing low-carbon steel wires. After cooling to room temperature (about 10 minutes), the heated glass ampoules were opened so that the exposed wires could be removed and rinsed with hexane and acetone prior to analysis by Auger emission spectroscopy. The removed wires appeared to be clean or slightly tarnished and the Auger depth analyses (performed by ion sputtering) determined the produced deposits to be less than 6 nm in thickness (Fig. 2). Consequently, the thin deposits present on the metal surfaces represent the initial deposits formed by the heated fuels.

The Auger elemental analysis and depth profiles of the wires heated in the presence of neat Jet A-1 fuel (Fig. 2) indicate that the metal surface is covered by a thin oxide layer with minimal amounts of nitrogen and sulfur present. The Jet A-1 fuels containing mercaptan, sulfide, and disulfide compounds produced deposits 2–4 nm in thickness, which contain from 9 to 16 percent sulfur and less than 1 percent nitrogen (Fig. 2). The Jet A-1 fuels containing sulfoxide and sulfur compounds produced wires with metal oxide layers containing less than 1 percent nitrogen and sulfur (similar to Jet A-1 in Fig. 2). In agreement with the Jet A-1 fuels containing mercaptan, sulfide, and disulfide compounds, Jet A fuel produced a deposit 2 to 4 nm in thickness, which contained a maximum of 9 percent sulfur and 1 percent of nitrogen (Fig. 2).

For the fuels producing deposits in Fig. 2, the sulfur content of the deposit is at its maximum at the metal oxide surface of the steel coupon as predicted by reaction D5. XPS analyses determined the fuel deposits produced by the sulfur-contaminated Jet A-1 fuels and the Jet A fuel contained sulfur, which was >90 percent sulfur oxides as predicted by reaction D5.

Effects of Acid Neutralizing Compounds on Fuel Deposition. To study the effects of acid-neutralizing compounds on fuel deposition, Jet A fuels containing varying amounts of superfine iron oxide and calcium oxide powders were heated at 210°C for 10 minutes in sealed glass ampoules containing low-carbon steel wires. To increase the thickness of the deposits, the heated ampoules were allowed to cool for 24 hours prior to opening. The wires were removed from the opened ampoules, rinsed with hexane then acetone to remove residual fuel, and analyzed by Auger emission spectroscopy. The measured thicknesses of the produced deposits are listed in Table 3.

The results in Table 3 indicate that the iron oxide powder (<1 μm particle size) at 50 ppm and the calcium oxide powder (<20 μm particle size) at 100 ppm are capable of inhibiting the formation of deposits on the steel surface. The results in Table 3 also indicate that the deposition-inhibiting capabilities of the oxide powders decrease as the concentrations of the oxides decrease. Additional tests with other metal and oxide powders demonstrated that only powders with acid neutralizing capabilities were able to inhibit the deposition process. For instance, superfine alumina and silicon dioxide powders (unreactive toward sulfur containing acids) had no effect on the deposition process of Jet A even at concentrations of 1000 ppm powder. The addition of cyclohexane amine (a strong organic base) inhibited the deposition process in agreement with reported research (Hazlett et al., 1986).

Downloaded 02 Jun 2010 to 171.66.16.105. Redistribution subject to ASME license or copyright; see http://www.asme.org/terms/Terms_Use.cfm

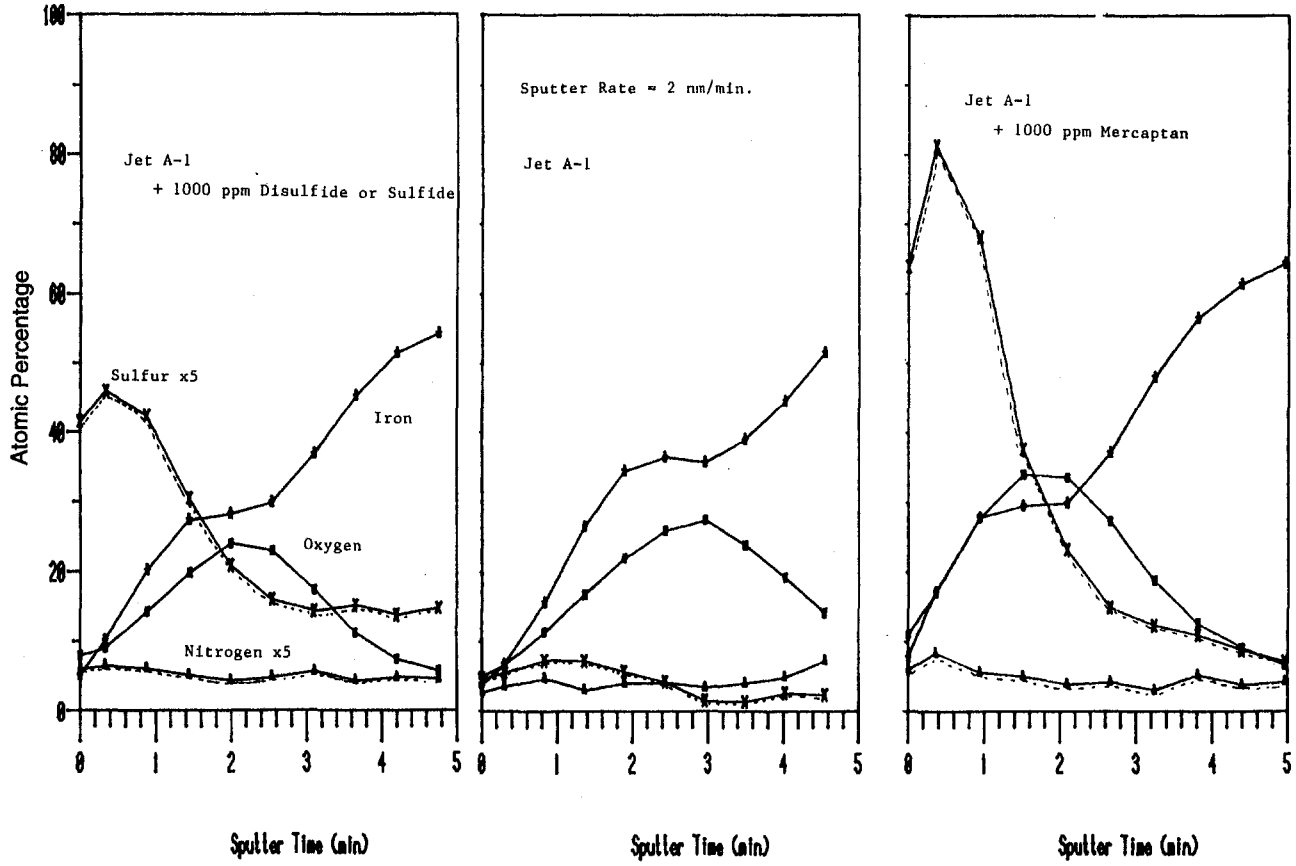


Fig. 2 Auger emission spectroscopic depth profiles of deposits formed on steel wires during sealed ampoule testing (ten minute cool down) at 210°C by Jet A-1 fuels containing different sulfur compounds (1000 pm sulfur)

The fact that the deposits are much thicker for the 24 hour cooled steel wire than the 10 minute cooled wires, indicate that bulk particles are responsible for the thickness of the deposition (reactions D5 and D6). The fact that acid neutralizing powders are able to inhibit deposition thickness indicates that acid–base reactions are important in the formation of bulk particles (reaction D4). The acid-neutralizing powders heated in the Jet A fuel were isolated by filtration and analyzed for sulfur and nitrogen. All of the isolated powders contained significant levels of sulfur oxides and nitrogen, further indicating the powders had reacted with acidic sulfur compounds.

Table 3 Thickness measurements by AES depth profiling for deposits formed on steel surfaces by Jet A fuels with and without acid neutralizing powders

POWDER	Concentration (ppm)	Deposit Thickness [a] (nm)
Ferric Oxide	12	900
	25	300
	50	80
Calcium Oxide	50	400
	100	80
Aluminum Oxide	1000	1700
Silicon Dioxide	1000	1600
None	-	1800

a Sealed Ampoule Test (cooled 24 hours), Jet A-1 deposit thickness 70 nm

Summary

The results presented herein strongly support the oxidation (reactions O1–O5)/deposition (reactions D1–D6) reaction scheme proposed for jet fuels. The results show that the "oxidizable" sulfur compounds (mercaptan, sulfide, and disulfide) inhibit hydroperoxide production, increase phenol production, increase bulk particle formation, and increase surface deposition for sulfur contaminated Jet A-1 fuel. The "nonoxidizable" sulfur compounds, sulfoxide and sulfone, have very little effect on the oxidation/deposition processes of sulfur contaminated Jet A-1 fuel (in agreement with Mushrush et al., 1994). The results also show that the addition of "oxidizable" sulfur compounds to Jet A-1 fuel cause the contaminated Jet A-1 fuel to undergo oxidation/deposition processes similar to those of Jet A fuel. Consequently, the results herein demonstrate that "oxidizable" sulfur compounds have a very strong effect on the oxidation/deposition processes of jet fuels.

The exact identity of the oxidizable sulfur compounds responsible for the deposition processes cannot be assigned from this initial study due to the low purity levels (92–95 percent) of the mercaptan, disulfide, and sulfide compounds. However, XPS analyses were used to confirm that the sulfur contents of the "oxidizable" compounds were below 0.3 percent oxidized sul-

Downloaded 02 Jun 2010 to 171.66.16.105. Redistribution subject to ASME license or copyright; see http://www.asme.org/terms/Terms_Use.cfm

fur prior to use. Since the oxidized sulfur contents of the produced bulk particles were 57–98 percent (Table 2), the "oxidized" sulfur content was produced during the fuel oxidation reaction (reaction D1).

The fact that acid-neutralizing powders such as iron oxide and calcium oxide effectively inhibit surface deposition and the addition of sulfonic acid promotes bulk particles supports the acid (sulfur)/base (nitrogen) reaction proposed herein and previously (Hazlett et al., 1986) as an initial step of the deposition process. Dispersants or soluble compounds with acid-neutralizing capabilities will be studied in future work for inhibiting bulk particle formation as well as surface deposition.

Further research is also planned for identifying the "basic" nitrogen compounds, e.g., alkyl amines, aromatic amines, indoles, pyrroles, substituted pyridines, etc., which combine with the oxidized sulfur compounds to produce bulk particles and surface deposits. It is interesting to note that all of the "oxidizable" sulfur compounds produced bulk particles with significant nitrogen contents. An initial assessment of the XPS bulk particle analyses (Buckley, 1994) indicate that pyrrole and pyridine type nitrogen compounds are present. The XPS analyses also indicate that ionic type nitrogen compounds (salt from acidic sulfur: basic nitrogen reaction) are also present in the bulk particles, especially the particles from the Jet A fuel oxidation tests. The XPS analyses are in agreement with deposit-causing nitrogen compounds identified by other researchers (Hazlett et al., 1991).

The role of phenols in the bulk particle and deposition processes is more complicated than the roles of the "oxidizable" sulfur and "basic" nitrogen compounds. The phenols can act as both oxidation inhibitors (reaction D2) and deposition promoters (reaction D4). The high oxygen contents (12–17 percent) of the bulk particles and the ether type (C–O) carbon-to-oxygen bonds strongly indicate phenols or other type oxygenated compounds are involved in the deposition processes. Other researchers (Hazlett et al., 1986) have also proposed a role for phenols in the deposition process.

Acknowledgments

This research was supported by the U.S. Air Force Wright Laboratory, Aero Propulsion and Power Directorate, Wright-Patterson Air Force Base, Ohio under Contract No. F33615-92-C-2207 with W. M. Roquemore serving as Technical Monitor and D. R. Ballal serving as Principal Investigator. Tom Wittberg of the University of Dayton Research Institute performed the XPS and Auger analyses reported in this paper.

References

Buckley, A. N., 1994, "Nitrogen Functionality in Coals and Coal-Tar Pitch Determined by X-Ray Photoelectron Spectroscopy," *Fuel Processing Technology,* Vol. 37, pp. 165–179.

Hazlett, R. N., et al., 1986, "The Chemistry of Deposit Formation in Distillate Fuels," Report No. MRL-R-986, Materials Research Laboratories, Victoria, Australia.

Hazlett, R. N., et al., 1991, "Distillate Fuel Insolubles: Formation Conditions and Characterization," *Energy and Fuels,* Vol. 5, pp. 269–273.

Heneghan, S. P., and Harrison, W. E., 1992, "Antioxidants in Jet Fuels: A New Look," *Proc. 203rd National Meeting of the American Chemical Society, Division of Petroleum Chemistry, Symposium: Structure of Jet Fuels III,* pp. 404–411, San Francisco, CA.

Heneghan, S. P., Martel, C. R., Williams, T. F., and Ballal, D. R., 1992, "Studies of Jet Fuel Thermal Stability in a Flowing System," ASME Paper No. 92-GT-106; ASME JOURNAL OF ENGINEERING FOR GAS TURBINES AND POWER, Vol. 115, 1993, pp. 480–485.

Kauffman, R. E., 1992, "New Techniques to Predict and Evaluate the Effectiveness of Antioxidants in Jet Fuels," *Proc. 203rd National Meeting of the American Chemical Society, Division of Petroleum Chemistry, Symposium: Structure of Jet Fuels III,* San Francisco, CA, pp. 412–419.

Kauffman, R. E., 1994, "New, Rapid Techniques for Determining the Hydroperoxide Content, Oxidation Stability, and Thermal Stability of Jet Fuels," ASME Paper No. 94-GT-346.

Mushrush, G. W., et al., 1994, "Liquid Phase Oxidation of Organo-Sulfur Compounds by Tert-butyl Hydroperoxide and Fuel Instability Reactions," *Fuel,* Vol. 73, No. 9, pp. 1481–1485.

Downloaded 02 Jun 2010 to 171.66.16.105. Redistribution subject to ASME license or copyright; see http://www.asme.org/terms/Terms_Use.cfm

An Experimental and Numerical Study of the Isothermal Flowfield Behind a Bluff Body Flameholder

C. N. Raffoul

A. S. Nejad

Aero Propulsion and Power Directorate,
Wright-Patterson AFB, OH 45433

R. D. Gould

Mechanical & Aerospace Engineering Dept.,
North Carolina State University,
Raleigh, NC 27695

S. A. Spring

CFD Research Corp.,
Huntsville, AL 35085

An experimental and numerical investigation was conducted to study the turbulent velocities and stresses behind a two-dimensional bluff body. Simultaneous three-component laser-Doppler velocimeter (LDV) measurements were made in the isothermal incompressible turbulent flowfield downstream of a bluff body placed at midstream in a rectangular test section. Mean velocities and Reynolds stresses were measured at various axial positions. Spanwise velocity measurements indicated that the flow is three dimensional in the recirculation zone of the bluff body. Confidence in the accuracy of the data was gained by calculating the mass fluxes at each axial station. These were found to agree with each other to within ±3 percent. A parallel Computational Fluid Dynamics (CFD) study was initiated to gage the predictive accuracy of currently available CFD techniques. Three solutions were computed: a two-dimensional steady-state solution using the standard $k-\epsilon$ model, a two-dimensional time-accurate solution using the standard $k-\epsilon$ model, and a two-dimensional time-accurate solution using a Renormalized-Group (RNG) $k-\epsilon$ turbulence model. The steady-state solution matched poorly with the data, severely underpredicting the Reynolds stresses in the recirculation zone. The time-accurate solutions captured the unsteady vortex shedding from the base of the bluff body, providing a source for the higher Reynolds stresses. The RNG $k-\epsilon$ solution provided the best match to the data.

Introduction

Simple two-dimensional and three-dimensional bluff bodies have been the subject of experimental investigations for a number of years. Bluff-body flows exist in many places, such as the flows around flameholders in gas turbine and ramjet engines, and flows around buildings, bridges, and support structures. Some examples of recent bluff-body studies include hot-wire measurements in the flowfield behind a normal flat plate by Perry and Steiner (1987) and the work by Mansingh and Oosthuizen (1990) in the flow behind a square cylinder. Hosokawa et al. (1993), and Geropp and Leder (1985) used single-component laser-Doppler velocimeters (LDV) to document the flowfield behind a two-dimensional bluff body. Some researchers have found that the flowfield consists of a pair of symmetric vortices behind the bluff body with elevated turbulence levels. However, other researchers have noticed that the turbulence is created by a regular pattern of vortices shed from the trailing edge, and that the symmetric flow only exists as a time-average (Perry and Steiner, 1987; Mansingh and Oosthuizen, 1990; Raffoul et al., 1994).

In recent years, LDV has become increasingly effective as a tool for nonintrusively measuring the instantaneous velocities at points in complex turbulent flows. Sjunnesson et al. (1991) have used two-component LDV to study two-dimensional bluff bodies of various shapes, while Larousse et al. (1991) employed two-component LDV for their study of surface mounted three-dimensional bodies. Few simultaneous three-component measurements have been reported to date, due mainly to the increase in instrumentation and signal processing equipment required to make the measurements. In addition, optical access is required for all three components. All of these difficulties have been overcome in the present study. Simultaneous three-component velocity measurements were made in the highly turbulent and recirculating flow past a two-dimensional bluff body. The three-orthogonal mean velocities ($\bar{U}$, $\bar{V}$, $\bar{W}$) were obtained producing profiles in the transverse and spanwise directions at 8 axial stations in the nearfield and at 11 axial stations in the farfield. All six Reynolds stresses ($\overline{uu}$, $\overline{vv}$, $\overline{ww}$, $\overline{uv}$, $\overline{uw}$, $\overline{vw}$) were also measured, as well as all triple products.

Like the experimental studies, many CFD researchers have conducted numerical studies on simple bluff-body geometries. These studies have produced solutions using techniques varying in sophistication from steady-state algebraic stress models (Sjunnesson et al., 1991) to the dynamic subgrid-scale Large-Eddy Simulations (LES) of Yang and Ferziger (1993). Some early solutions modeled only half of the symmetric geometry, thus imposing symmetry on the flow. However, more detailed studies have shown that the instantaneous flowfield consists of a structured pattern of alternating large-scale vortices. A symmetry plane enforced by the numerical model precludes the formation of the shed vortices, relying on the turbulence model to predict any turbulent fluctuations in the wake. Comparisons to data have shown such predictions to be inadequate for bluff-body flowfields. Recently, researchers have improved the numerical modeling by including the entire flowfield. When solved with time-accurate algorithms, the flow is free to oscillate about the geometric symmetry plane. Such oscillations add significantly to both the turbulent normal and shear stresses in the wake of the bluff body. Of particular interest is the Renormalization Group (RNG) theory first applied to the $k-\epsilon$ turbulence model by Yakhot and Orszag (1986), and later improved by Yakhot et al. (1992). The goal of the RNG theory is systematically to remove the smallest turbulent scales to a point where the remaining scales are resolvable. The constants used in the

Contributed by the International Gas Turbine Institute and presented at the 40th International Gas Turbine and Aeroengine Congress and Exhibition, Houston, Texas, June 5–8, 1995. Manuscript received by the International Gas Turbine Institute February 10, 1995. Paper No. 95-GT-102. Associate Technical Editor: C. J. Russo.

Copyright © 1997 by ASME

Downloaded 02 Jun 2010 to 171.66.16.105. Redistribution subject to ASME license or copyright; see http://www.asme.org/terms/Terms_Use.cfm

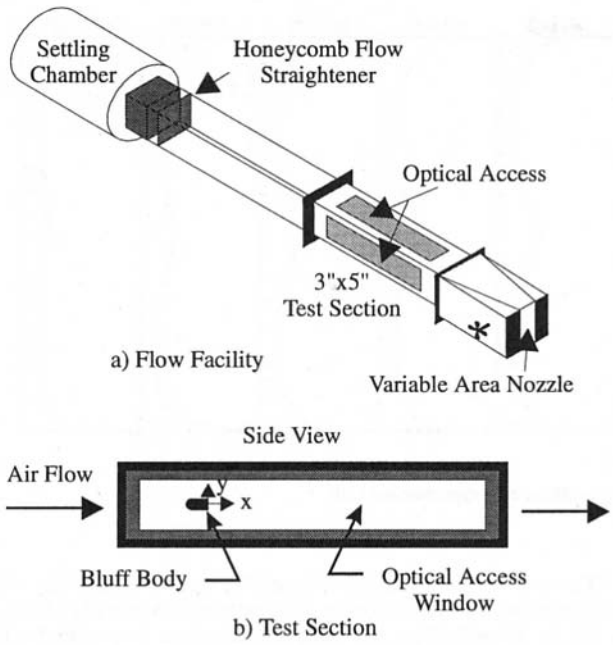


Fig. 1 Experimental test facility

RNG $k-\epsilon$ model are derived from theory, removing much of the ad-hoc nature of the standard $k-\epsilon$ model, and represents the major functional difference between the models. The current study presents results from three solutions: (1) a symmetric, steady-state $k-\epsilon$ solution; (2) a standard $k-\epsilon$, time-accurate solution; and (3) an RNG $k-\epsilon$, time-accurate solution. All solutions are two dimensional, and the mean velocities and Reynolds stresses are compared to the data.

Experimental Setup

Facility. A schematic of the tunnel and the two-dimensional test section is shown in Fig. 1. The test facility is located in Test Cell 18 at the Aero Propulsion and Power Directorate of Wright Laboratory, and was specifically designed and constructed to accommodate flow visualization and laser based diagnostics. Full-view fused quartz windows on the top, bottom, and the two side walls provide optical access to the 76.2 mm × 127 mm × 762 mm (3 in. × 5 in. × 30 in.) test section. The air flow was supplied by a radial fan blower followed by a 152.4 mm (6 in.) diameter honeycomb flow straightening section and settling chamber. The flow straightener was placed close to the fan outlet to minimize the large-scale turbulence produced by the fan. The air was further conditioned by passing through another honeycomb flow straightener placed 304.8 mm (12 in) upstream of the test section. For the current study, the inlet centerline reference velocity (U_{ref}) was constantly monitored upstream of the bluff body at $x/H = -24$, using a pitot/static tube connected to a high resolution manometer. The inlet reference velocity was 23.78 m/s (78 ft/sec), corresponding to a tunnel Reynolds number of 2.0×10^4 based on inlet flow conditions and the bluff-body base height.

Bluff Body. A schematic of the bluff-body model and its orientation to the coordinate system is shown in Fig. 2. The 25.4-mm (1-in.) long model consisted of: (1) a 6.35-mm (0.25-in.) radius hemispherical nose, (2) a 15.875-mm (0.625-in.) long rectangular center section, and (3) a 3.175-mm (0.125-in.) base/dump plate. The bluff-body height (H) was 12.7 mm (0.5 in.), and spanned the entire test section, giving a tunnel blockage of 16 percent. In order to measure the inlet flow conditions, the model was mounted four inches into the test section

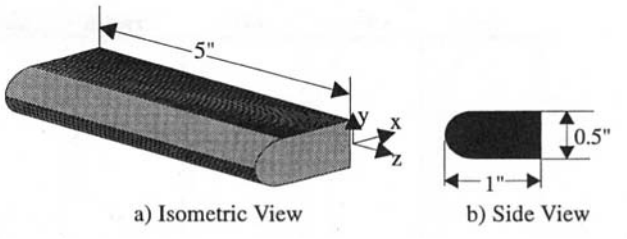


Fig. 2 Bluff-body model schematic

(downstream of the side window leading edge), directly to the side wall windows. This arrangement provided the best optical access for probing the entire flowfield surrounding the bluff body. Care was taken to align the bluff body with respect to the LDV probe volume by running the laser beam along the edge of the bluff body.

Laser Velocimeter. A three-component LDV system operating in the forward scatter mode was mounted around the rectangular test section to make simultaneous measurements of the $\bar{U}$, $\bar{V}$, and $\bar{W}$-velocity components. The optical system used in these experiments involved two separate TSI Inc. laser-Doppler systems. The first system used the blue (488 nm) and green (514.5 nm) wavelengths from an argon-ion laser. These beams were conditioned and steered directly into the test section with a focal length of 300 mm. The beams passed through the side windows of the test section, allowing for the measurement of the axial and transverse (U, V) velocity components. The beams were oriented at ±45 deg relative to the mean flow direction, providing measurement capability very close to the base of the bluff body. For the third component, the violet laser line (476.5 nm) from another argon-ion laser was directed via fiber-optic cable to a TSI model 9274 one-component fiber-optic probe, with a focal length of 350 mm. The violet beams were oriented orthogonal to the others, entering through the top and exiting through the bottom test section windows. Both argon-ion lasers were operated at 1.0 W. To allow measurement of negative velocities, all three components were Bragg-shifted 40 MHz. The approximate probe volume dimensions were 600 μm long and 80 μm diameter for the blue and green beams and 1.5 mm long and 100 mm diameter for the violet beam. The entire system was mounted on a three-axis traversing table allowing the probe volume to be positioned to within 0.03 mm (0.001 in.).

For seeding, titanium tetrachloride was introduced just downstream of the fan outlet duct, producing particles of TiO_2 less than one micron in diameter. Data rate counts of 15,000/s/channel were routinely achieved with the TiO_2 seed. However, the coincident data rate ranged from 1000/s in the recirculation zone to 5000/s in the free stream and the far wake. The smooth data profiles indicated that the data rate and the applied sample size of 5120 were quite sufficient to obtain steady estimates, even for the higher moments.

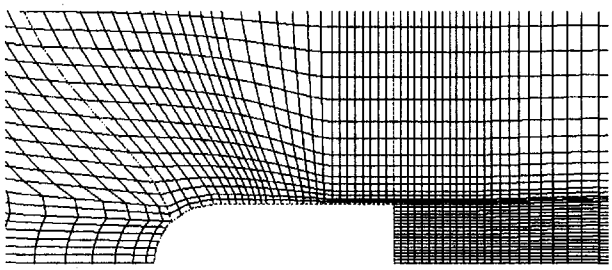


Fig. 3 Grid near bluff body used for CFD analyses

Downloaded 02 Jun 2010 to 171.66.16.105. Redistribution subject to ASME license or copyright; see http://www.asme.org/terms/Terms_Use.cfm

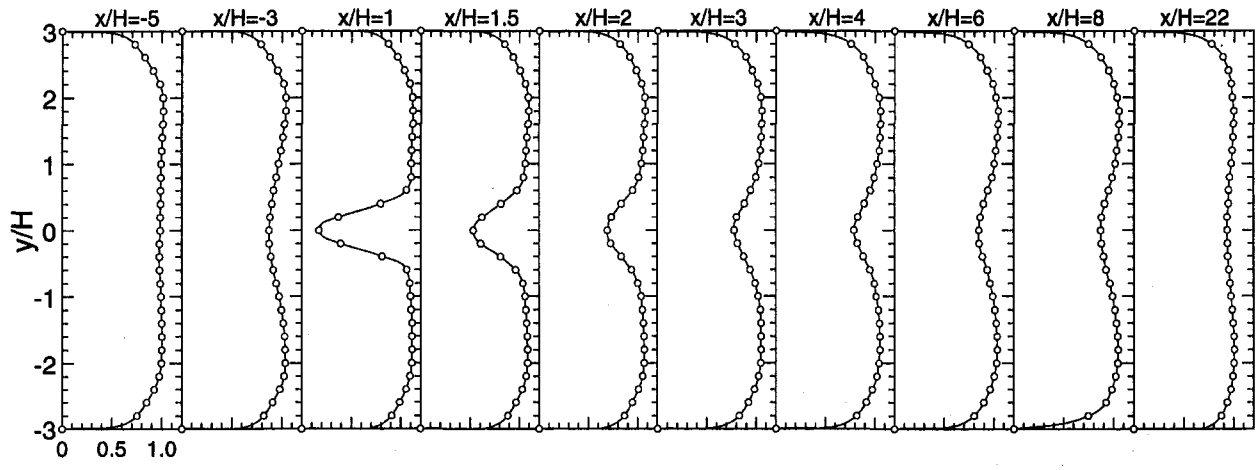


Fig. 4 Normalized mean axial velocity profiles; one-dimensional LDV

Data Acquisition and Analysis. The data collection and processing system consisted of a three-channel IFA-750 Digital Burst Correlator and Analyzer by TSI, Inc. The IFA-750 allows for measurement of the Doppler frequencies of all three velocity components and has electronics to ensure that the measurements are coincident to within 20 μs. In addition to the frequency data, the time between data (TBD) and the particle residence time are recorded. All sample sets included 5120 individual velocity measurements for each velocity component. The data were filtered using a $\pm 3\,\sigma$ cut-off limit before statistical parameters were calculated. In most cases, the signal-to-noise ratio was high and very few samples were discarded. No velocity bias corrections were used in this study.

Numerical Technique

The numerical analysis for the current study was accomplished using a commercially available CFD code, CFD-ACE (Avva, 1993). CFD-ACE is a pressure-based finite-volume code designed for the analysis of incompressible through hypersonic flowfields, using a modified SIMPLEC algorithm. All solutions used second-order accurate central differencing, stabilized with upwind biasing to solve the two-dimensional incompressible Navier–Stokes equations. The computational domain extended 63.5 mm (2.5 in.) upstream of the bluff body ($x/H = -5$) and 508 mm (20 in.) downstream ($x/H = 40$). All solutions used a constant inflow profile matched to the experimental data, and a fixed pressure exit condition.

The first solution enforced symmetry by modeling only half of the geometry. The solution was converged to steady state on a 102 × 38 grid (Fig. 3), using the standard $k-\epsilon$ model with wall functions.

The Reynolds stresses for the steady-state solution were calculated from the Boussinesq equation:

$$\overline{u_i u_j} = \frac{\mu_t}{\rho}\left(\frac{\partial \bar{U}_i}{\partial x_j} + \frac{\partial \bar{U}_j}{\partial x_i}\right) - \frac{2}{3}k\delta_{ij} \tag{1}$$

where

$$\mu_t = 0.09\rho\frac{k^2}{\epsilon} \tag{2}$$

The second solution modeled the entire flowfield on a 102 × 77 grid (mirror of symmetric grid) and required a time-accurate solver. Again, the standard $k-\epsilon$ model was used with wall functions. The solution was first advanced 200 iterations in a steady-state mode to establish the flowfield, and to allow an asymmetry to develop. The solution was then restarted in a time-accurate mode and advanced 4500 time steps at 5.0×10^{-6} s per time step. Finally the solution was advanced ~2500 time steps to collect the turbulence statistics. Care was taken to ensure that the statistics were collected over a whole period of the vortex shedding cycle. Turbulence statistics were calculated in a fashion similar to the experimental procedure, with each time step producing one sample.

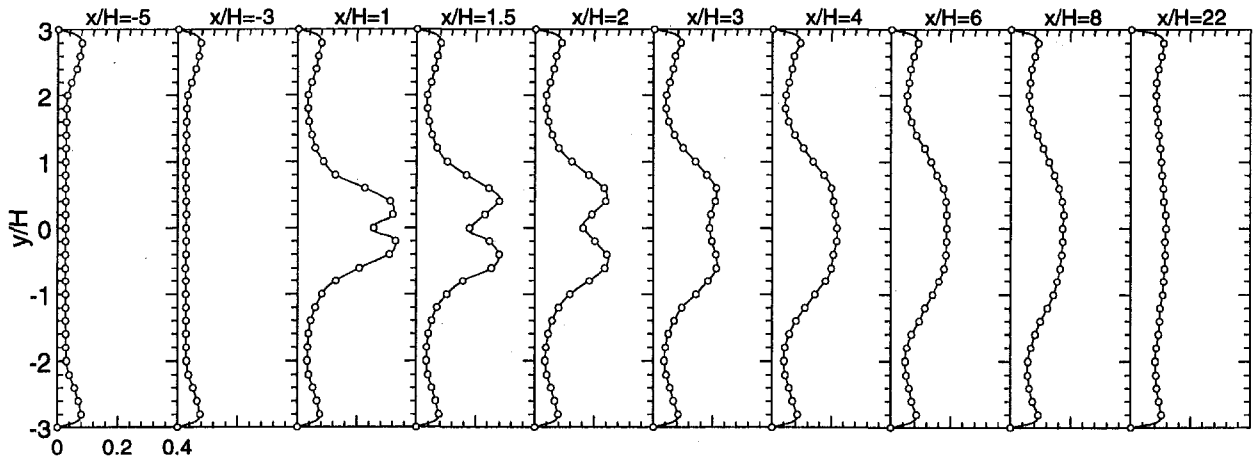


Fig. 5 Normalized rms axial turbulent velocity profiles; one-dimensional LDV

Downloaded 02 Jun 2010 to 171.66.16.105. Redistribution subject to ASME license or copyright; see http://www.asme.org/terms/Terms_Use.cfm

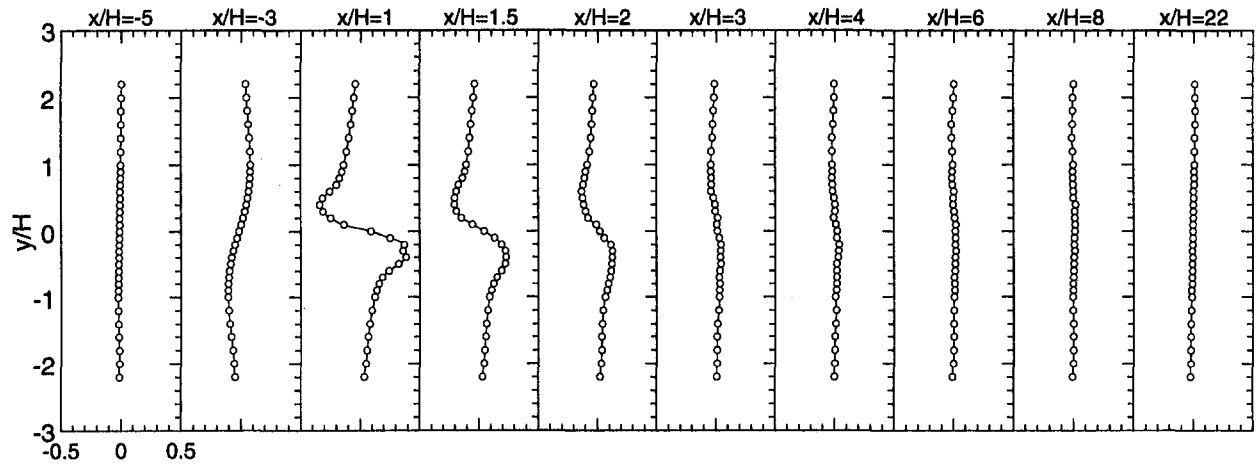


Fig. 6 Normalized mean transverse velocity profiles; three-dimensional LDV

Some researchers have found that the $k-\epsilon$ model damped the unsteady flow behind bluff bodies (Franke and Rodi, 1991). However, other researchers have found the damped behavior to be a function of the differencing scheme and not the turbulence model (Przulj and Younis, 1993). In the current study, the $k-\epsilon$ model converged to a steady state with first order differencing, but properly predicted the vortex shedding with central differencing.

The third solution was completed in a similar manner except the RNG $k-\epsilon$ model was employed. One of the major differences between the standard $k-\epsilon$ model and the RNG $k-\epsilon$ model is that many of the constants are derived from the RNG theory, removing much of the ad-hoc nature of the standard $k-\epsilon$ model. For comparison, the standard $k-\epsilon$ constants used in the current study are as follows: $C_\mu = 0.09$, $C_{\epsilon 1} = 1.44$, $C_{\epsilon 2} = 1.92$, $\sigma_\kappa = 1.0$, and $\sigma_\epsilon = 1.3$.

In contrast, the RNG theory derives the following constants; $C_\mu = 0.085$, $C_{\epsilon 2} = 1.68$, $\sigma_\kappa = 0.7179$, and $\sigma_\epsilon = 0.7179$.

$$C_{\epsilon 1} = 1.42 - \frac{\eta\left(1 - \frac{\eta}{\eta_o}\right)}{1 + \beta\eta^3} \tag{3}$$

where $\eta = Sk/\epsilon$, $S = \sqrt{2S_{ij}S_{ij}}$, $\eta_o = 4.38$, and $\beta = 0.015$.

Note that $C_{\epsilon 1}$ is no longer a constant. Using the new constants, the RNG $k-\epsilon$ model was found by Speziale and Thangam (1992) to give excellent results for the backward-facing step flow of Kim et al. (1978). The reader is referred to Yakhot et al. (1992) for more information on the RNG theory.

Experimental Results and Discussion

Mean Velocity Data. Measurements of the normalized mean axial velocity and the normalized fluctuating axial velocity are shown in Figs. 4 and 5, respectively. All measurements are normalized with respect to the reference velocity, $U_{\text{ref}} = 23.78$ m/s (78 ft/sec), and the bluff-body height, $H = 12.7$ mm (0.5 in.). At first, single-component velocity measurements were made using the green laser beam, which allowed measurements to be made from top to bottom walls. Such detailed measurements of the mean axial velocity allowed for the calculation of the mass flow rates at each axial station. These were found to be within ±3 percent of each other throughout the flowfield. Three-component measurements gave virtually identical results (Raffoul et al., 1994). The bluff-body dump plane (i.e., the trailing edge) is assigned the axial position $x = 0$, with negative x values referring to measurement stations upstream of the bluff body. Figure 4 shows that the inlet flow is very symmetric and uniform. At the downstream stations, the presence of the wake from the bluff body can be clearly seen in the center of the flow, as well as the presence of two shear layers. The recirculation zone behind the bluff body is roughly one bluff-body thickness in length, significantly smaller than the recirculation region behind a backward-facing step, which is

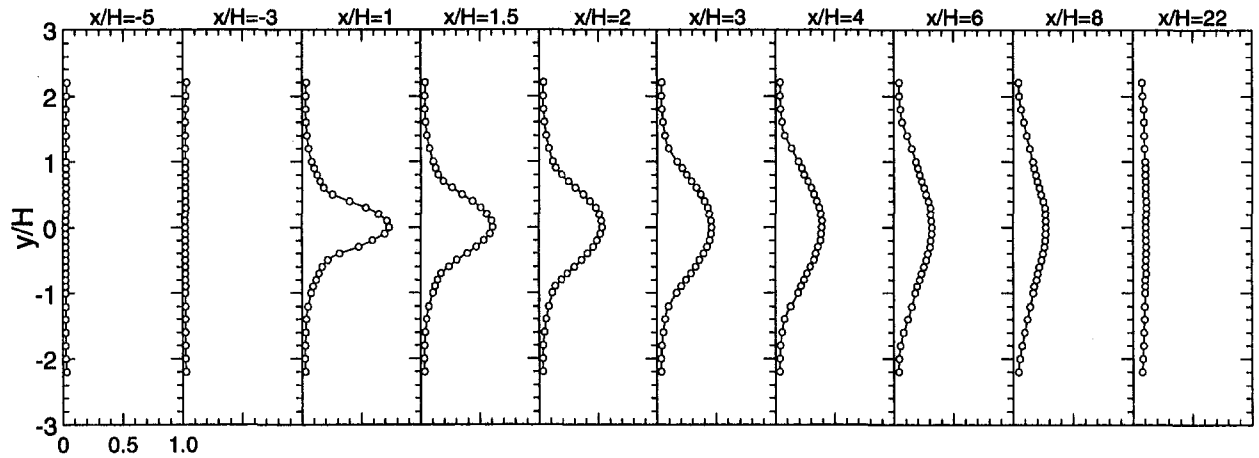


Fig. 7 Normalized rms transverse turbulent velocity profiles; three-dimensional LDV

Downloaded 02 Jun 2010 to 171.66.16.105. Redistribution subject to ASME license or copyright; see http://www.asme.org/terms/Terms_Use.cfm

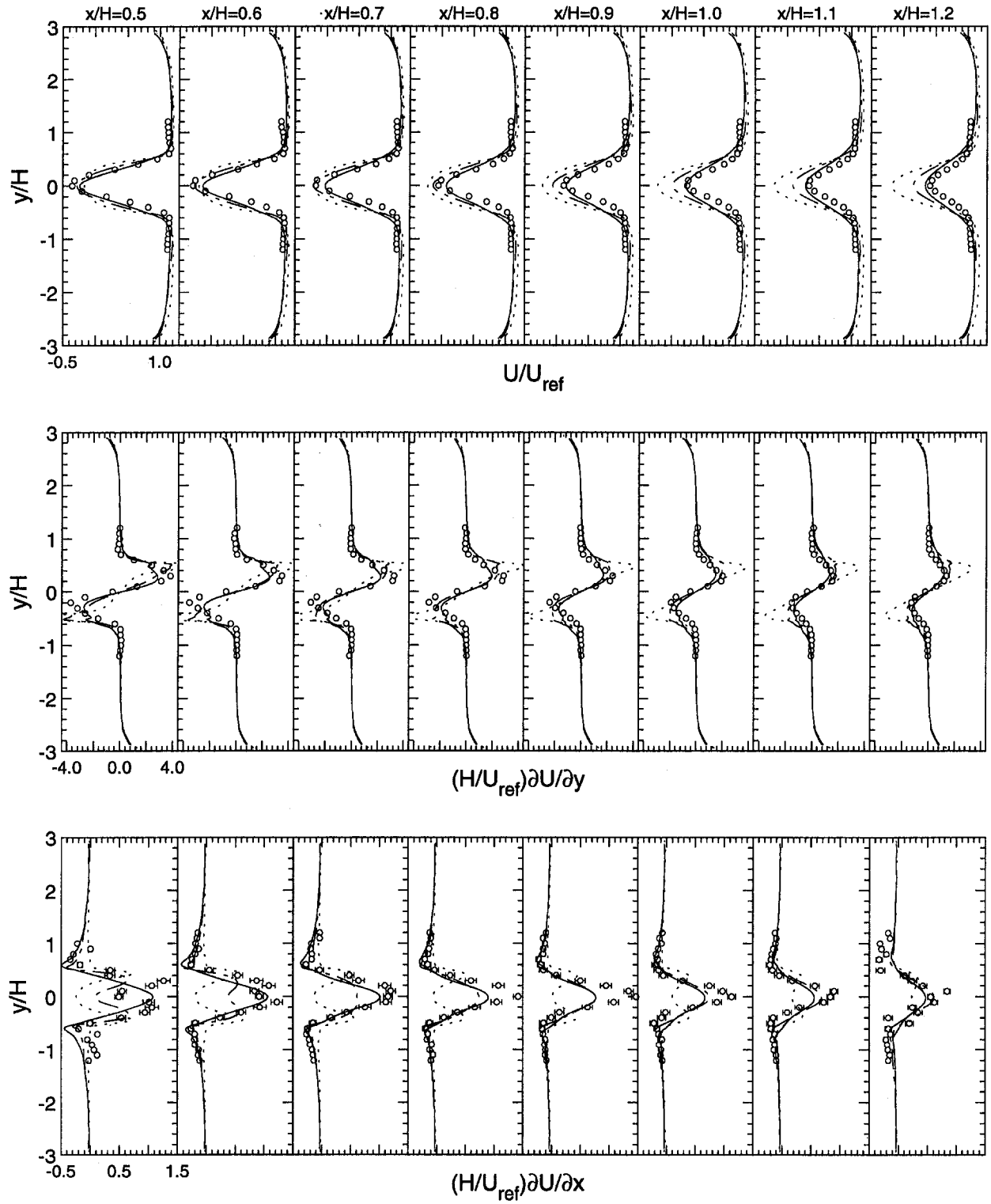


Fig. 8 Normalized mean axial velocity and velocity gradient distributions (○ data, ----- steady state $k-\epsilon$, -- unsteady $k-\epsilon$, — unsteady RNG)

known to be 7 to 8 step-heights. Negative axial velocities were found for $x/H < 1$, as shown in Fig. 8. The magnitude of the reverse flow is high, which results in a rather intense vortex roll-up. Figure 5 shows the double hump behavior expected due to the presence of the shear layers near the top and bottom of the bluff body.

Figures 6 and 7 show the normalized transverse mean and fluctuating velocities. Due to optical access restrictions, these measurements do not extend to the top and bottom walls. Figure 6 shows that the mean transverse velocity profile at $x/H = 1$ is antisymmetric as expected, since the transverse velocity is directed toward the centerline at this location. Comparison of the peak axial and transverse fluctuating velocities show that the transverse values are more than double the axial values. The velocity data were time-averaged over a 2–3 second interval for the statistics calculations. Raffoul et al. (1994) showed that the present configuration produces unsteady flow as periodic vortex pairs are shed from the back face. Transformation of the

Downloaded 02 Jun 2010 to 171.66.16.105. Redistribution subject to ASME license or copyright; see http://www.asme.org/terms/Terms_Use.cfm

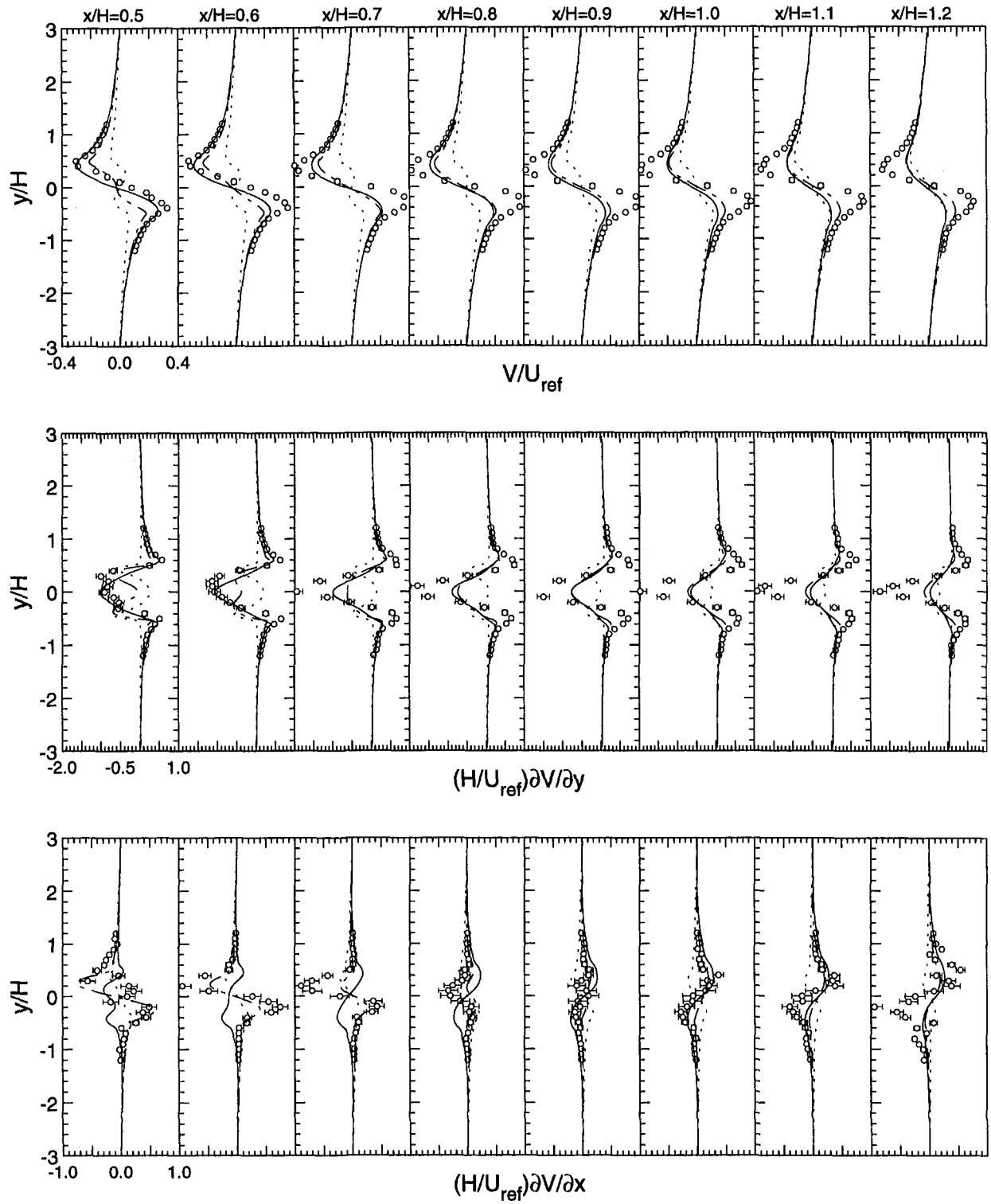


Fig. 9 Normalized mean transverse velocity and velocity gradient distributions (○ data, ---- steady state $k-\epsilon$, -- unsteady $k-\epsilon$, — unsteady RNG)

velocity-time data for a point on the centerline of the wake at $(x/H = 1)$ revealed a dominant frequency of $f = 454$ Hz, with a corresponding Strouhal number, St = 0.243, where:

$$\mathrm{St} = fH/U_{\mathrm{ref}} \tag{4}$$

Figures 8, 9, and 10 show the evolution of the normalized mean axial, transverse, and spanwise velocities and velocity gradient distributions in the near wake, at eight axial stations. The experimental data are represented by circular symbols. The continuous lines in Figs. 8, 9, and 11–13 represent the numerical predictions and will be discussed later. Figure 8 depicts negative velocities in the recirculation zone up to $x/H = 0.9$. The velocity gradients in the x and y directions are computed using a central difference smoothing algorithm developed by Gould (1994). The first station, located one-half bluff-body height downstream, shows a maximum velocity deficit of −0.5. The normalized y derivative shows a maximum and a minimum at an absolute value of 4.0 while the normalized x derivative shows a maximum of −1.0. Figure 9 shows approximately equal maxi-

Downloaded 02 Jun 2010 to 171.66.16.105. Redistribution subject to ASME license or copyright; see http://www.asme.org/terms/Terms_Use.cfm

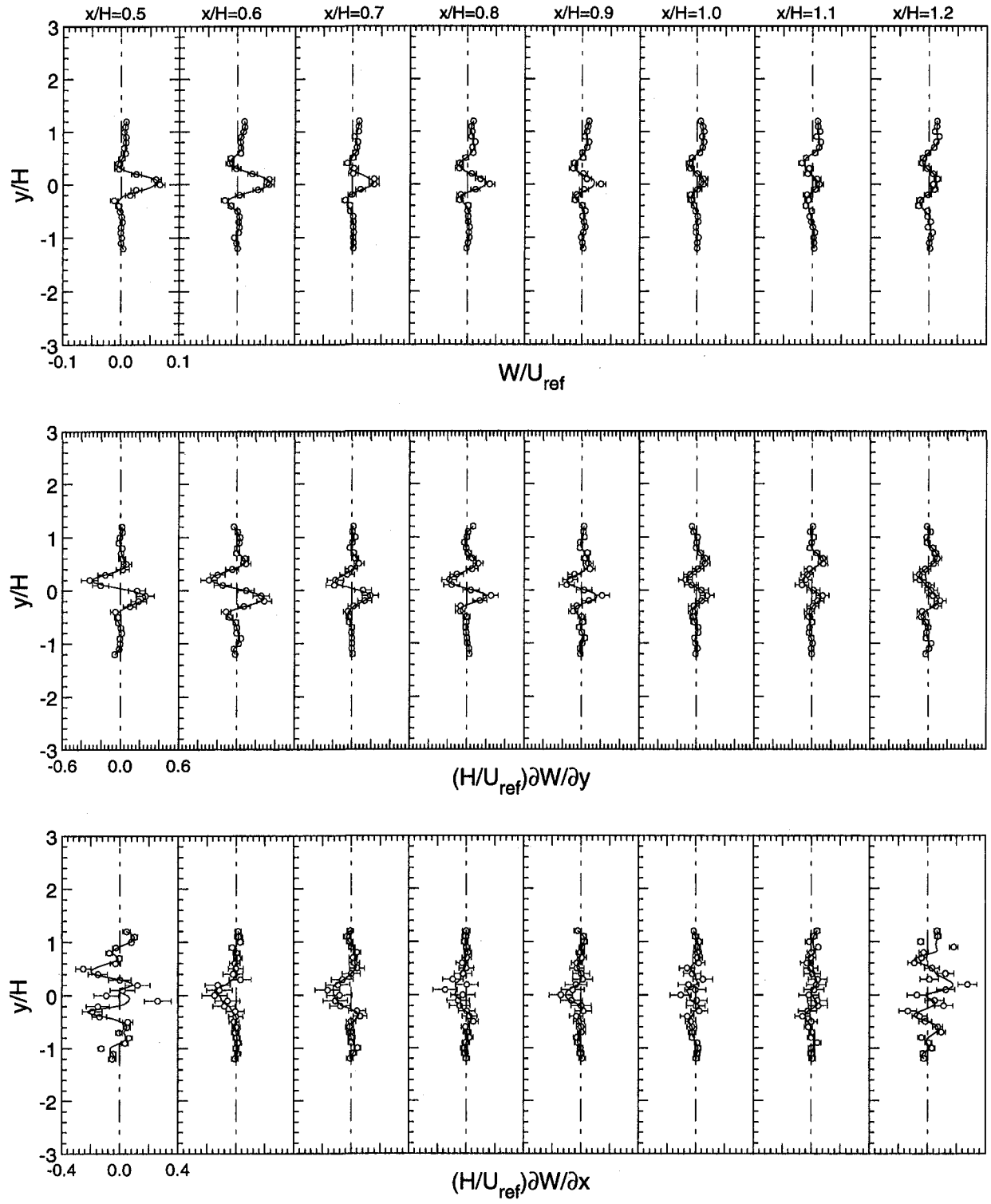


Fig. 10 Normalized mean spanwise velocity and velocity gradient distributions (○ data, — smoothed curve-fit)

mum and minimum transverse velocities (V) for all the stations. The normalized y derivatives of the V velocity have a minimum of -2.0 except for $x/H = 0.5$ and 0.6. The normalized x derivatives of the V-velocity are relatively small, but exhibit a unique feature in that they change slope at the recirculation bubble location, where the gradient is nearly nonexistent. Figure 10 shows the three dimensionality of the flow in the wake. The continuous lines in Figs. 10 and 14 represent the smoothed curve-fitted data. The spanwise component (W) peaks at nearly 10 percent of the free-stream velocity at the first station and decreases in magnitude with downstream locations. The normalized y derivative of the W velocity has a maximum absolute value of about 0.4, while the normalized x derivative of the W velocity has a small deficit that was roughly comparable to the error band.

Turbulent Normal and Shear Stresses. Figures 12, 13, and 14 show profiles of the three measured normalized turbulent normal stresses ($\overline{uu}$, $\overline{vv}$, $\overline{ww}$). Peak values of the axial normalized turbulent intensity (i.e., the square root of the turbulent normal

Downloaded 02 Jun 2010 to 171.66.16.105. Redistribution subject to ASME license or copyright; see http://www.asme.org/terms/Terms_Use.cfm

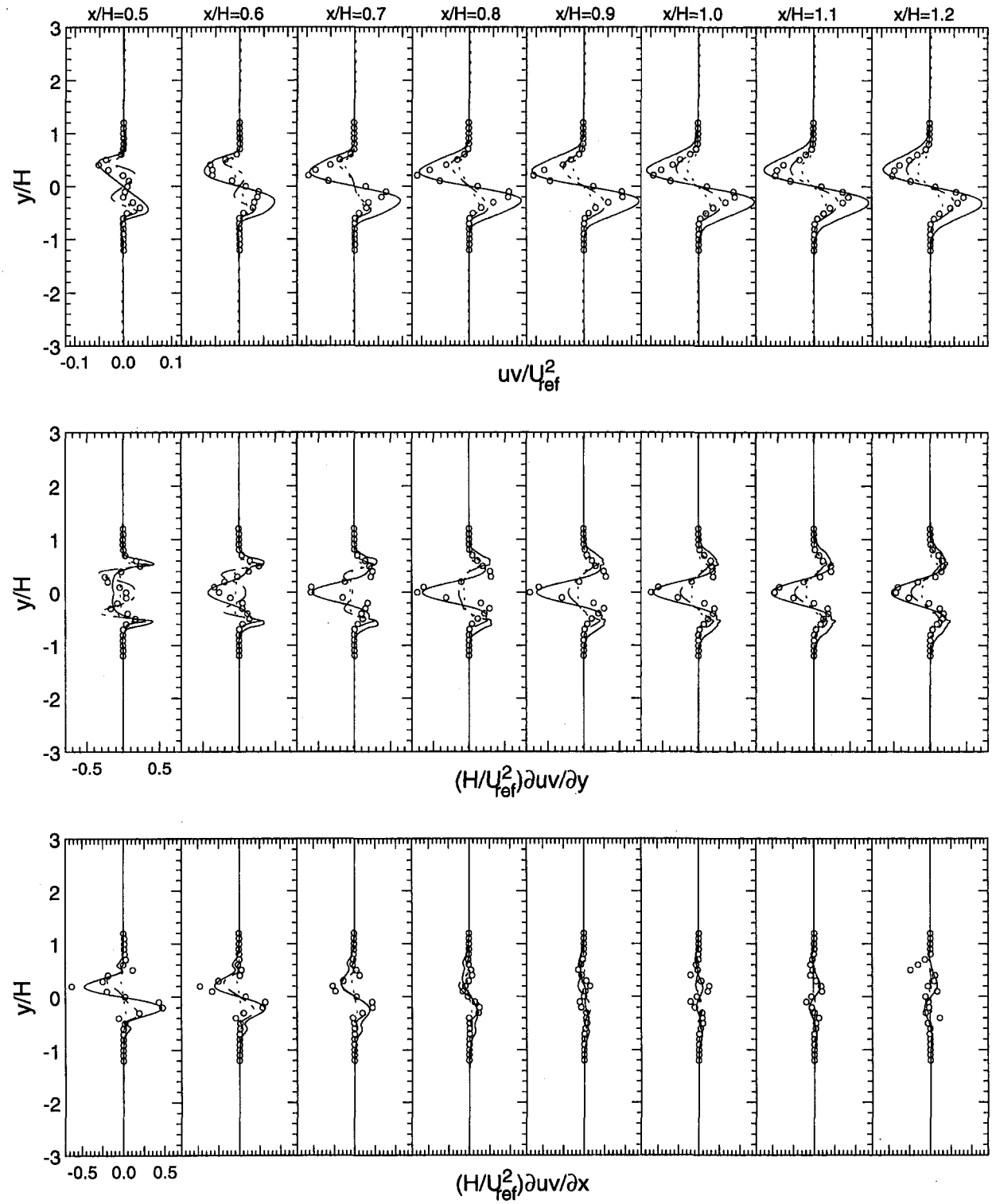


Fig. 11 Normalized uv turbulent stress and stress gradient distributions (○ data, ---- steady state $k-\epsilon$, -- unsteady $k-\epsilon$, — unsteady RNG)

stress) occur at $x/H = 1$, in the shear layer, and reach a value of 31 percent of the free-stream velocity. This value is slightly above that obtained behind of a backward-facing step (25 percent), as reported by Gould et al. (1988). It is noteworthy that the peak transverse normalized turbulence intensity is 77 percent, approximately 2.5 times the value of the peak axial normalized turbulence intensity. The axial, transverse, and spanwise turbulent normal stresses are clearly different in value and profile shapes. The different shapes indicate that the structure of turbulence in and near the recirculation zone is quite anisotropic, and remains so until $x/H \cong 8$. The anisotropy implies the existence of multiple length scales in the turbulence structure. The y derivatives of the transverse normal stress are the only significant derivatives of the normal stresses. The derivatives reach a maximum normalized absolute value of 1.5 at the first station and diminish to a value of 1.0 at $x/H = 1.2$. The normalized turbulent shear stresses ($\overline{uv}$, $\overline{uw}$, $\overline{vw}$) have also been obtained. These measurements indicate that the $\overline{uv}$ shear stress (Fig. 10) is the only significant one of the three, thus the only one presented. The values of $\overline{uv}$ were found to be small at $x/H = 0.5$, growing to a peak value of 0.1 at x/H

Downloaded 02 Jun 2010 to 171.66.16.105. Redistribution subject to ASME license or copyright; see http://www.asme.org/terms/Terms_Use.cfm

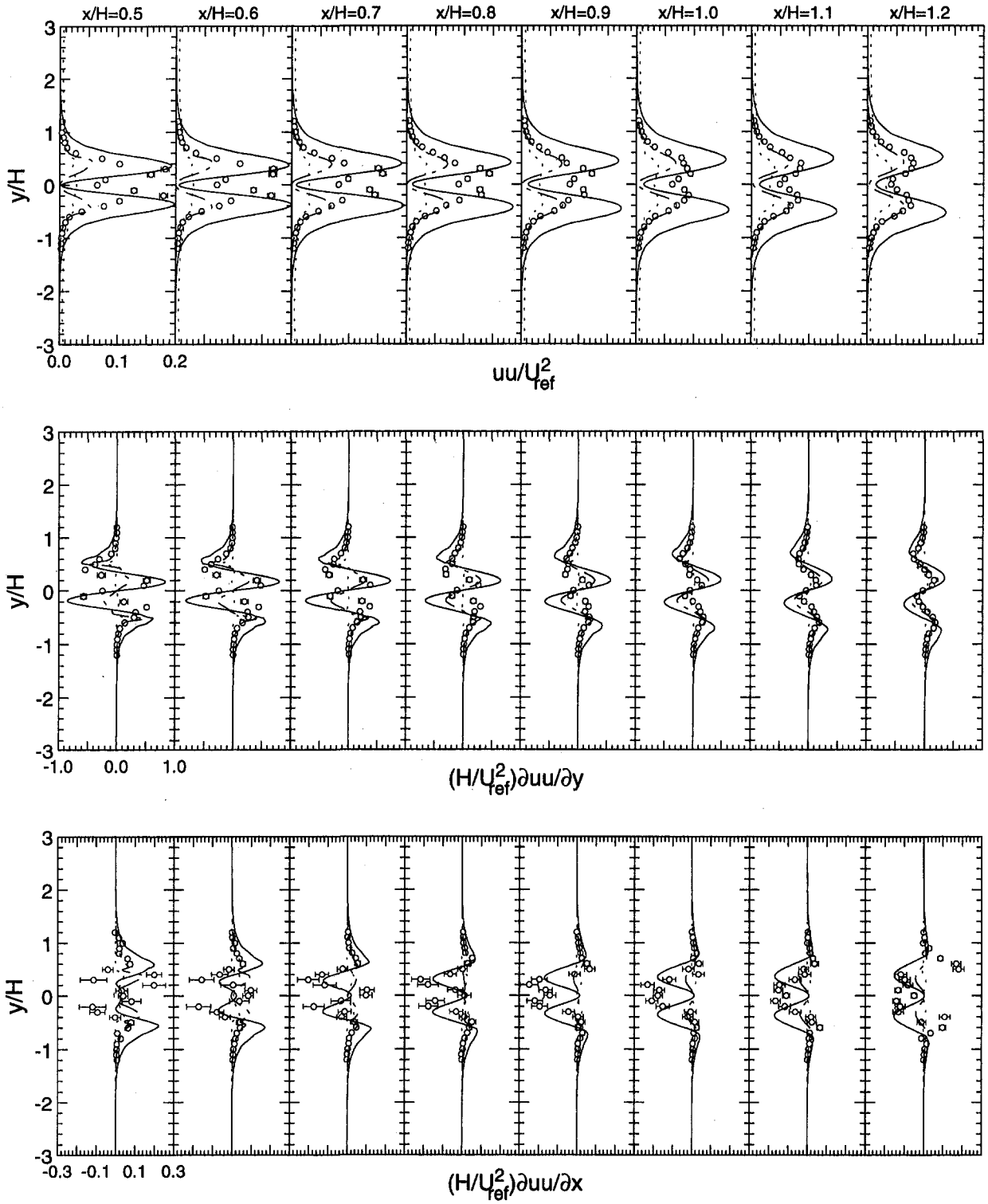


Fig. 12 Normalized *uu* turbulent stress and stress gradient distributions (○ data, ---- steady state $k-\epsilon$, -- unsteady $k-\epsilon$, — unsteady RNG)

$= 0.9$, the free stagnation point. The normalized y derivatives of $\overline{uv}$ had a minimum of -1.0 at $x/H = 0.9$, while the x derivatives did not show any appreciable value.

Numerical Results and Discussion

Three solutions were computed as part of the current study. First, a steady-state solution utilizing a symmetry plane was obtained. A time-accurate solution was then completed using the standard $k-\epsilon$ turbulence model. Finally, another time-accurate solution was completed using an RNG $k-\epsilon$ turbulence model to capture the subgrid turbulence.

The velocities and Reynolds stresses for the steady-state solution are shown with the experimental measurements in Figs. 8, 9, and 11–13. The velocities indicate that the numerical recirculation bubble extends to $x/H = 2$, much farther downstream than the experimental bubble. The numerical prediction has a bubble length of four step heights, similar to a backward-facing step. This is to be expected since the model resembles a backward-facing step with a slip wall at the centerline. The

Downloaded 02 Jun 2010 to 171.66.16.105. Redistribution subject to ASME license or copyright; see http://www.asme.org/terms/Terms_Use.cfm

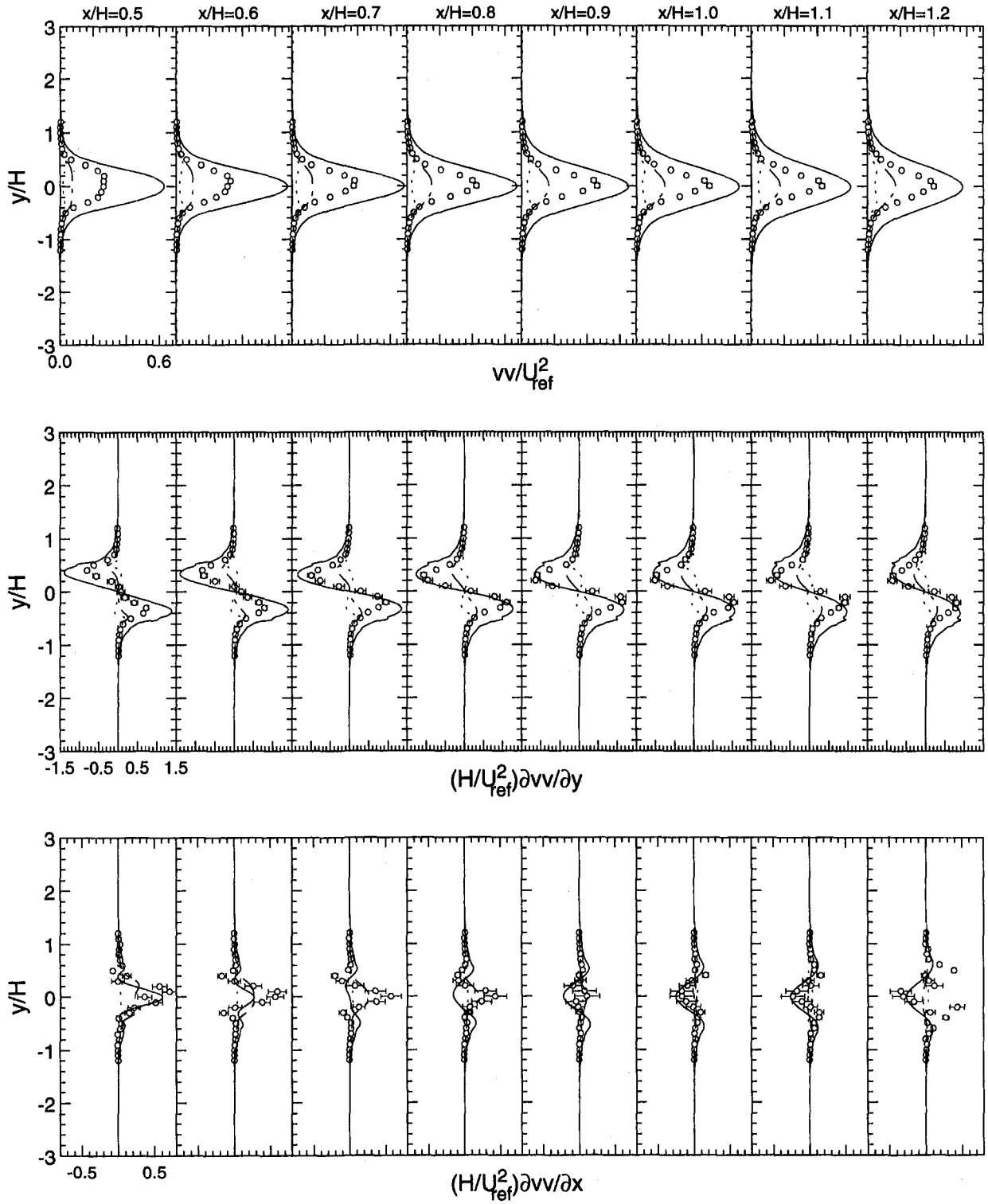


Fig. 13 Normalized *vv* turbulent stress and stress gradient distributions (○ data, ---- steady state $k-\epsilon$, -- unsteady $k-\epsilon$, — unsteady RNG)

Reynolds stresses are also comparable to those of a backward-facing step. However, the experimentally measured Reynolds stresses for the bluff-body flow are typically five times higher than those found in a backward-facing step flow. The underprediction of the Reynolds stresses by the steady-state solution leads to the incorrect bubble length in the recirculation zone. For the purpose of fuel injection and mixing studies, such an analysis is not sufficient.

The time-accurate solutions were able to predict the vortex shedding behind the bluff body. The standard $k-\epsilon$ solution predicted a Strouhal number, St = 0.240, which compared well to the experimental value of 0.243. The time-averaged velocities and Reynolds stresses are also shown in Figs. 8, 9, and 11–13. The separation bubble calculated with this method is considerably shorter than that predicted using the steady-state solution method, extending to $x/H = 1.0$. However, the bubble is still longer than what the measurements indicate, and the predicted wake spreads slightly faster than the experimental wake. While the magnitudes of the Reynolds stresses are higher than those predicted using the steady-state method, they are still lower than the experimental results.

Downloaded 02 Jun 2010 to 171.66.16.105. Redistribution subject to ASME license or copyright; see http://www.asme.org/terms/Terms_Use.cfm

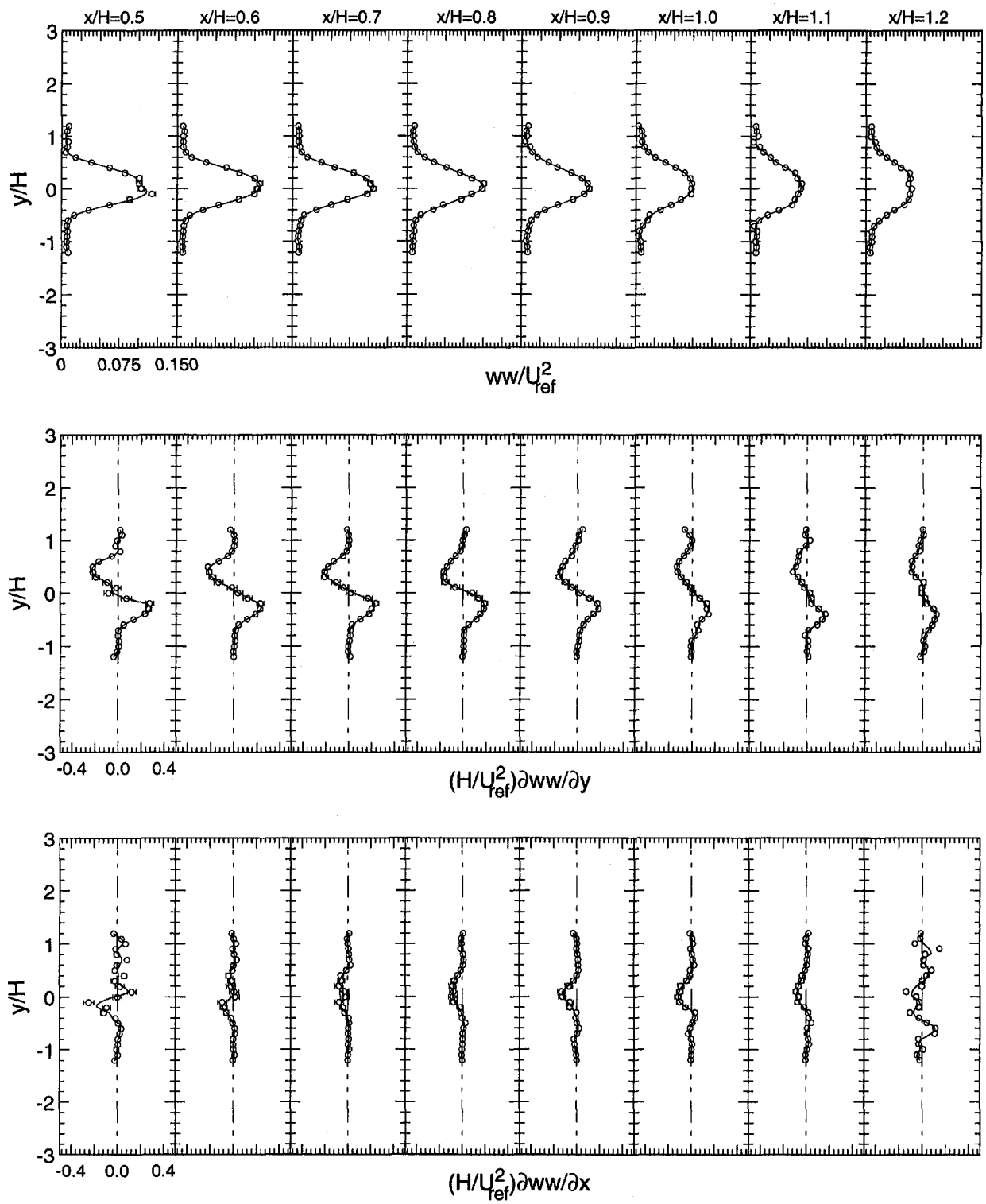


Fig. 14 Normalized *ww* turbulent stress and stress gradient distributions (○ data, — smoothed curve fit)

To improve the time-accurate results, the RNG $k-\epsilon$ turbulence model developed by Yakhot et al. (1992) was tested. The Strouhal number predicted by the RNG model was 0.253, slightly higher than that obtained from the experimental data. However, the mean velocity predictions were significantly improved, as shown in Figs. 8 and 9. The separation bubble has shortened and now ends slightly ahead of the experimental measurements ($x/H = 0.7$). The overall mean velocity field is predicted fairly well, except for the transverse velocity just downstream of the reattachment point. The discrepancy of the transverse velocities may be a result of the three-dimensional effects near the bluff body. The spanwise velocities observed in the experiments are most likely due to the interaction of the tunnel wall boundary layers with the bluff-body flowfield; they are also probably symmetric about the spanwise centerline. If so, the vortices shed from the bluff body will experience some degree of vortex stretching in the near-field wake. Such vortex stretching could amplify the transverse velocities.

The comparisons of the Reynolds stresses to the measurements are improved. However, the normal stresses are overpre-

Downloaded 02 Jun 2010 to 171.66.16.105. Redistribution subject to ASME license or copyright; see http://www.asme.org/terms/Terms_Use.cfm

dicted, leading to the shorter separation bubble. The largest discrepancy occurs with the transverse normal stress, the values of which are overpredicted by a factor of three. Martensson et al. (1991) obtained similar results using LES, and found that the transverse normal stress was reduced significantly when simulated with a three-dimensional analysis. A three-dimensional solution can be expected to produce lower Reynolds stresses due to the three-dimensional filament distortion of the shed vortices. The two-dimensional vortex filament makes no contribution to the spanwise stresses. However, if the filament is allowed to distort in the spanwise direction, the vortex will make a contribution to the spanwise stresses, dependent upon the magnitude of the local distortion. Any contribution to the spanwise stresses will result in a similar decrease in the transverse and axial stresses, dependent upon the direction of the local distortion. The proper prediction of the vortex filament distortion may be sensitive to the spanwise extent of the computational domain and may require the entire spanwise domain to be included. A three-dimensional analysis was attempted in the present study, using a spanwise domain of one base-height and periodic boundary conditions. However, the results degraded significantly. Arnal and Friedrich (1991) report that three-dimensional solutions of a backward-facing step with a spanwise extent less than four step heights can give erroneous results. A three-dimensional solution with a larger spanwise extent for the current geometry is under investigation.

Conclusions

Simultaneous three-component LDV measurements have been completed on a two-dimensional bluff body. The measurements revealed that the flowfield was dominated by strong, periodic vortex shedding in the wake, yielding a symmetric vortex pair in the mean flow. The mean spanwise velocity component was measured in the wake. Significant spanwise flow was found at axial stations less than $x/H = 1.2$; however, the source for this spanwise component has not been clearly identified. The mean flow recirculation bubble behind the bluff body ended at $x/H = 0.9$, significantly shorter than the recirculation zone found in a backward-facing step flow. The dominant vortex-shedding frequency was found to be 454 Hz. The Reynolds stress terms involving the axial (U), and transverse (V) velocity components were of the same order of magnitude directly behind the bluff body, while those involving the spanwise (W) velocity component were negligible. Beyond the recirculation zone only the contributions involving the transverse velocity were significant.

The numerical simulations showed that the bluff-body flowfield cannot be accurately predicted using a steady-state calculation, because no mechanism exists to predict the amplified time-averaged Reynolds stresses that result due to vortex shedding. The time-accurate standard $k-\epsilon$ model predicts the vortex-shedding frequency accurately, but underpredicts the Reynolds stresses and overpredicts the length of the recirculation bubble by 20 percent. The RNG $k-\epsilon$ model predicts a higher vortex-shedding frequency, but obtains the closest match to the mean velocities. However, the Reynolds stresses tended to be overpredicted. A three-dimensional calculation covering the entire spanwise domain should improve the results.

Acknowledgments

This work was performed at Wright Laboratory, Aero Propulsion and Power Directorate, Wright-Patterson Air Force Base, Ohio. Special thanks goes to the Air Force Office of Scientific Research and to Dr. Julian Tishkoff for providing sponsorship. The authors would also like to thank Mr. Cliff Smith and Dr. Andy Leonard of CFD Research Corporation for their assistance with the numerical effort.

References

Arnal, M., and Friedrich, R., 1991, "Large-Eddy Simulation of a Turbulent Flow With Separation," *Turbulent Shear Flows 8,* Springer-Verlag.

Avva, R., 1993, "CFD-ACE: Theory Manual," CFDRC Report GR-93-1.

Choudhury, D., and Kim, S., 1993, "Calculation of Turbulent Separated Flows Using a Renormalization Group Based $k-\epsilon$ Turbulence Model," *Separated Flows,* ASME FED-Vol. 149.

Franke, R., and Rodi, W., 1991, "Calculation of Vortex Shedding Past a Square Cylinder With Various Turbulence Models," *Turbulent Shear Flows 8,* Springer-Verlag.

Geropp, D., and Leder, A., 1985, "Turbulent Separated Flow Structures Behind Bodies With Various Shapes," presented at the International Conference on Laser Anemometry—Advances and Application, Manchester, United Kingdom.

Gould, R., Stevenson W., and Thompson, D., 1988, "Turbulence Characteristics of an Axisymmetric Reacting Flow," NASA Contractor Report 4110.

Gould, R., 1994, "Analysis of Laser Doppler Velocimetry Data," Final Report for Summer Research Program, WL, AFOSR.

Hosokawa, S., Ikeda, Y., Minato, M., and Nakajima, T., 1993, "Flow Measurements Behind V-Gutter Under Non-combusting Condition," Paper No. AIAA-93-0020.

Kim, J., Kline, S., and Johnston, J., 1978, "Investigation of Separation and Reattachment of a Turbulent Shear Layer: Flow Over a Backward-Facing Step," Report MD-37, Thermo Sciences Division, Dept. of Mechanical Engineering, Stanford University.

Kodali, V., and Amano, R., 1986, "Prediction of Turbulent Flows Behind Bluff Bodies by Using an Algebraic-Stress Model," Paper No. AIAA-86-1061.

Larousse, A., Martinuzzi, R., and Tropea, C., 1991, "Flow Around Surface-Mounted, Three-Dimensional Obstacles," *Turbulent Shear Flows 8,* Springer-Verlag, pp. 127–139.

Mansingh, V., and Oosthuizen, P., 1990, "Effects of Splitter Plates on the Wake Flow Behind a Bluff Body," AIAA *Journal,* pp. 778–783.

Martensson, H., Eriksson, L., and Albraten, P., 1991, "Numerical Simulations of Unsteady Wakeflow," 10th International Symposium on Air-Breathing Engines (ISABE), Vol. 2, Nottingham, England.

Pearce, J., Qasim, A., Maxwell, T., and Paramesawaran, S., 1992, "A Computational Study of Coherent Wake Structures Behind 2-D Bluff Bodies," *J. of Wind Engineering and Industrial Aerodynamics,* Vol. 41–44, pp. 2853–2861.

Perry, A., and Steiner, T., 1987, "Large-Scale Vortex Structures in Turbulent Wakes Behind Bluff Bodies: Part 1. Vortex Formation Processes," *J. Fluid Mech.,* Vol. 174, pp. 233–270.

Przulj, V., and Younis, B., 1993, "Some Aspects of the Prediction of Turbulent Vortex Shedding," *Separated Flows,* ASME FED-Vol. 149.

Raffoul, C., Nejad, A., Spring, S., Kirkendall, C., and Smith, C., 1994, "Entrainment and Mixing Characteristics of Bluff Body Flameholders: an Experimental and Numerical Study," Paper No. AIAA 94-0710.

Ryden, R., Eriksson, L., and Olovsson, S., 1993, "Large-Eddy Simulation of Bluff Body Stabilised Turbulent Premixed Flames," ASME Paper No. 93-GT-157.

Sjunnesson, A., Olovsson, S., and Sjoblom, B., 1991, "Validation Rig—A Tool for Flame Studies," presented at the 10th International Symposium on Air Breathing Engines (ISABE), Nottingham, England.

Speziale, C., and Thangam, S. 1992, "Analysis of an RNG Based Turbulence Model for Separated Flows," NASA CR 189600.

Werner, H., and Wengle, H., 1991, "Large-Eddy Simulation of Turbulent Flow Over and Around a Cube in a Plate Channel," *Turbulent Shear Flows 8,* Springer-Verlag.

Yakhot, V., and Orszag, S., 1986, "Renormalization Group Analysis of Turbulence. I. Basic Theory," *J. Sci. Comput.,* Vol. 1, p. 3.

Yakhot, V., Orszag, S., Thangan, S., Gatski, T., and Speziale, C., 1992, "Development of Turbulence Models for Shear Flows by a Double Expansion Technique," *Phys. Fluids,* Vol. A.4(7).

Yang, K., and Ferziger, J., 1993, "Large-Eddy Simulation of Turbulent Obstacle Flow Using a Dynamic Subgrid-Scale Model," AIAA *Journal,* Vol. 31, No. 8.

Downloaded 02 Jun 2010 to 171.66.16.105. Redistribution subject to ASME license or copyright; see http://www.asme.org/terms/Terms_Use.cfm

G. A. Richards

M. J. Yip

U.S. Department of Energy.

E. Robey

EG&G Technical Services of West Virginia.

Morgantown Energy Technology Center,
Morgantown, WV 26505

L. Cowell

D. Rawlins

Solar Turbines, Inc.,
San Diego, CA

Combustion Oscillation Control by Cyclic Fuel Injection

A number of recent articles have demonstrated the use of active control to mitigate the effects of combustion instability in afterburner and dump combustor applications. In these applications, cyclic injection of small quantities of control fuel has been proposed to counteract the periodic heat release that contributes to undesired pressure oscillations. This same technique may also be useful to mitigate oscillations in gas turbine combustors, especially in test rig combustors characterized by acoustic modes that do not exist in the final engine configuration. To address this issue, the present paper reports on active control of a subscale, atmospheric pressure nozzle/combustor arrangement. The fuel is natural gas. Cyclic injection of 14 percent control fuel in a premix fuel nozzle is shown to reduce oscillating pressure amplitude by a factor of 0.30 (i.e., −10 dB) at 300 Hz. Measurement of the oscillating heat release is also reported.

Background

Reduction of combustion oscillations often presents a difficult challenge during turbine combustor development. Combustion oscillations are undesirable because the resulting pressure oscillations can shorten component lifetime. Although a significant body of literature on combustion instability exists, practical solutions to instability problems are often clouded by uncertainties over the specific mechanisms driving a given oscillation. Prevention of instabilities during the design and development phase is further complicated because acoustic modes and operating conditions may be different between test rigs and final engine designs. Likewise, operation of a given combustor at new conditions, or with different fuel, may be accompanied by oscillating combustion.

Solution of combustion instability has typically required hardware modifications (i.e., passive control), or limiting the range of engine operation. Both of these solutions are costly, or unacceptable for certain cases. As an alternative, active control has been proposed as a different approach to eliminate combustion oscillations. Active control uses an external control device to mitigate the combustion instability. Active control attempts to limit the combustion oscillation by disrupting (in real time) the processes that create periodic heat release. Combustion that would otherwise oscillate is then stabilized by repeated adjustment of parameters affecting the combustion process. Many different control devices and strategies have been proposed in the last five years. Review articles by Candel (1992) and McManus et al. (1993) describe tests using sound input, periodic boundary layer disruption, spark discharge, and variable air flow as possible control techniques.

Among the various possible control techniques, periodic fuel injection seems to be a practical option for engine applications. The process is shown schematically in Fig. 1. A turbine combustor is outfitted with an auxiliary fuel injector capable of adding a portion of the fuel in an unsteady manner. In principle, combustion oscillations could be negated by simply adding fuel out of phase with the established oscillation. Langhorne et al. (1990) were the first to attempt this type of control. Tests on a 0.25 MW afterburner rig showed that closed-loop control, using the pressure signal to modulate just 3 percent of the total fuel input, could reduce the dominant pressure oscillation by 12 dB. Sivasegaram and Whitelaw (1992) tested a similar concept, again using periodic fuel injection to control the oscillation in a laboratory test rig. In their tests, the injected fuel flow was controlled in both open and closed-loop configurations. Depending on the particular control approach, oscillating pressure amplitude was reduced by as much as 15 dB. A recent article by Schadow et al. (1992) reports on a number of control strategies, including fuel input modulation. Various levels of control were reported, depending on the specific situation. Finally, Schadow et al. (1993) compared fuel modulation to a slightly different strategy, using a spark discharge to burn a portion of the combustion fuel before entering the main combustion region of a dump combustor. Again, depending on the control conditions, a reduction in the peak pressure amplitude by as much 14 dB was achieved at one condition. Schadow et al. (1993) also reported the first test results at elevated pressure (1.9 atm).

These citations provide encouraging evidence that active control using pulsed fuel injection is a viable control technique for turbine combustor oscillations. Contemporary gas turbines have popularized the lean premixing fuel nozzle for pollutant control. Thus, this paper reports application of active control to a premixing fuel nozzle, using natural gas fuel. The approach is similar to the references mentioned above for afterburners and dump combustors. Fuel pulses are periodically injected into the fuel nozzle, and are shown to produce a significant reduction in oscillating amplitude.

Experiment Description

The experimental rig is shown in Fig. 2. This atmospheric pressure rig consists of a 76-mm-dia refractory lined duct, with provision to mount premix fuel nozzles at the top of the duct. The duct geometry includes an extension leg, which can be shortened (or lengthened) to support different acoustic modes. These modes can be readily calculated be treating the duct geometry as a classic acoustic branch (Kinsler et al., 1982). Calculating the impedance at the exhaust duct and setting the reactance to zero determines the resonant modes. At gas temperatures of 1475 K, this procedure predicts the following resonant

Contributed by the International Gas Turbine Institute and presented at the 40th International Gas Turbine and Aeroengine Congress and Exhibition, Houston, Texas, June 5–8, 1995. Manuscript received by the International Gas Turbine Institute February 27, 1995. Paper No. 95-GT-224. Associate Technical Editor: C. J. Russo.

Copyright © 1997 by ASME

Downloaded 02 Jun 2010 to 171.66.16.105. Redistribution subject to ASME license or copyright; see http://www.asme.org/terms/Terms_Use.cfm

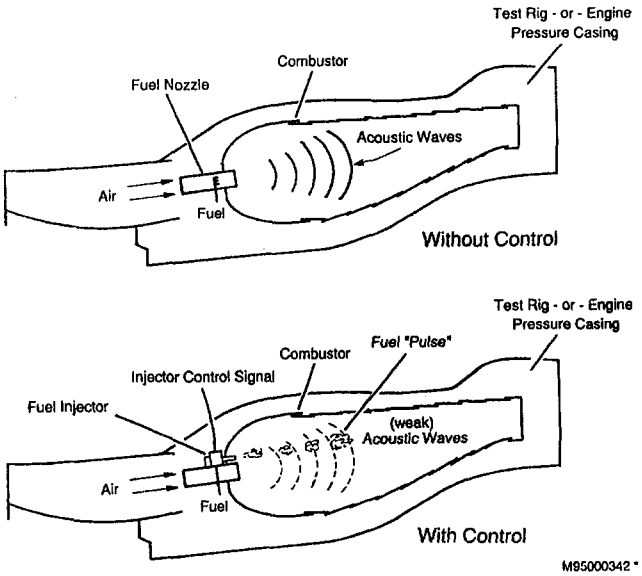


Fig. 1 Schematic of active control process using periodic fuel injection

frequencies: 87, 190, 300, 460, 600 Hz, and higher. As will be seen, the fuel nozzle preferentially excites the 300 Hz mode.

Unsteady pressure was measured using a piezoelectric pressure transducer mounted at the bottom of the extension leg of the combustor duct. Time-varying heat release was recorded with a fiber-optic OH emission probe mounted near the exit of the nozzle. The probe is a 1.6-mm-dia sapphire rod, connected with a fiber optic cable to an optical filter and photomultiplier tube. The filter is centered at 310 nm (10 nm bandwidth), and will detect emission from excited OH radicals, which exist momentarily during the combustion reaction. As described by Keller and Saito (1987), the excited state OH emission is approximately proportional to the rate of combustion in the region viewed by the probe. The sapphire rod accepts radiant emissions from a conic region with a 15 deg viewing angle, extending from the probe tip. The probe was mounted at a slight angle from the duct axis, viewing through the combustion zone. Thus, the OH measurement is a line of sight measure of the heat release through the portion the flame within the probe viewing angle.

Also shown in Fig. 2, thermocouples designated "A" and "B" record the gas temperature (approximately) at the duct centerline, 6.3 cm and 47 cm downstream of the fuel nozzle.

A detailed sketch of the fuel nozzle used in these experiments is shown in Fig. 3. A central 12.7 mm stainless steel tube is used to supply premixed fuel and air to the pilot flame on the nozzle axis. The pilot air flow rate was 0.56 g/s with the pilot fuel set to establish the peak flame temperature on thermocouple "A" (i.e., stoichiometric). It is mentioned that subsequent testing has shown that both the oscillating behavior and control effects are sensitive to the quantity of pilot fuel flow; this is discussed later. The pilot flame is lit with an internal spark electrode approximately 75 mm upstream of the nozzle exit. The pilot tube is surrounded by the premixing annulus. Natural gas and air are mixed in the annulus upstream of a wire mesh flow straightener. The premixed fuel and air pass through straight-finned swirl vanes, angled 45 deg from the nozzle axis. For the results described here, premix fuel and air flow rates are 0.4 g/s and 9.9 g/s, respectively, corresponding to a heat input of approximately 20 kW.

A bypass route for the premix fuel is provided as shown on Fig. 2. The bypass valve was adjusted to send a small portion of the premix fuel to the bypass port, to induce oscillating combustion; see the discussion below. The total flow rate of premix fuel is unchanged by opening this bypass. The natural gas fuel injector, used for control, is connected through the control port, located across the diameter of the nozzle from the bypass port. The fuel injector is a commercial automotive fuel injector, used for natural gas powered automobiles. The length of tubing between the bypass valve and the fuel nozzle was 37.5 cm. Likewise, the tubing length between the fuel injector solenoid and the nozzle was also 37.5 cm. These lengths are critical, because acoustic resonance in the tubes contributes to the combustion oscillation, described later.

Results

The nozzle shown in Fig. 3 was initially tested with the control fuel injector turned off, and the bypass valve closed. In this configuration, the nozzle produced essentially steady

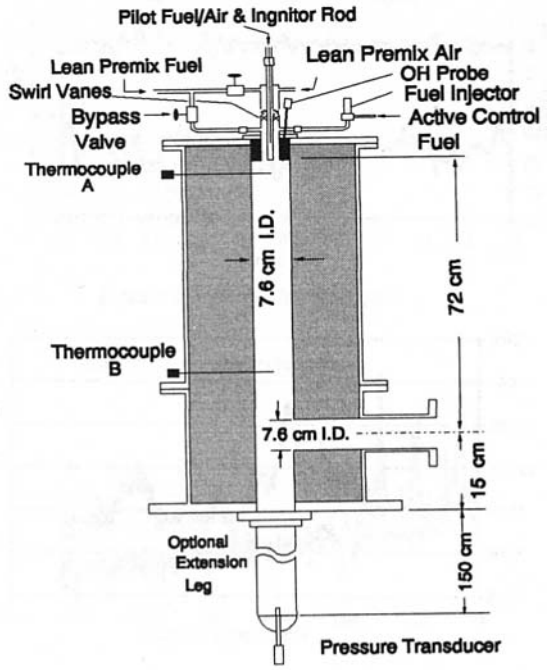


Fig. 2 Experimental configuration

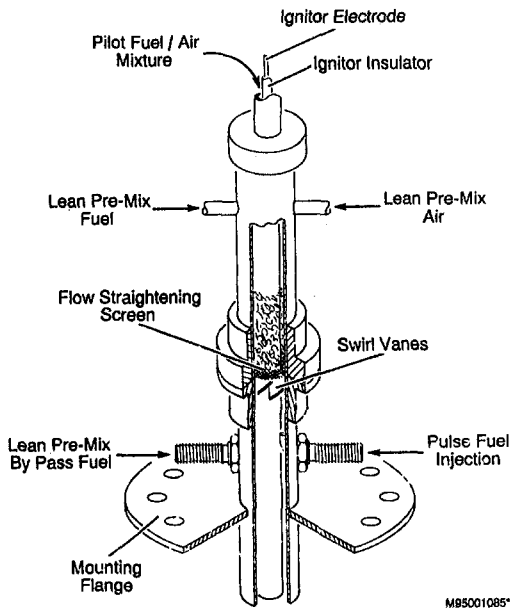


Fig. 3 Detailed view of the premix fuel nozzle

Downloaded 02 Jun 2010 to 171.66.16.105. Redistribution subject to ASME license or copyright; see http://www.asme.org/terms/Terms_Use.cfm

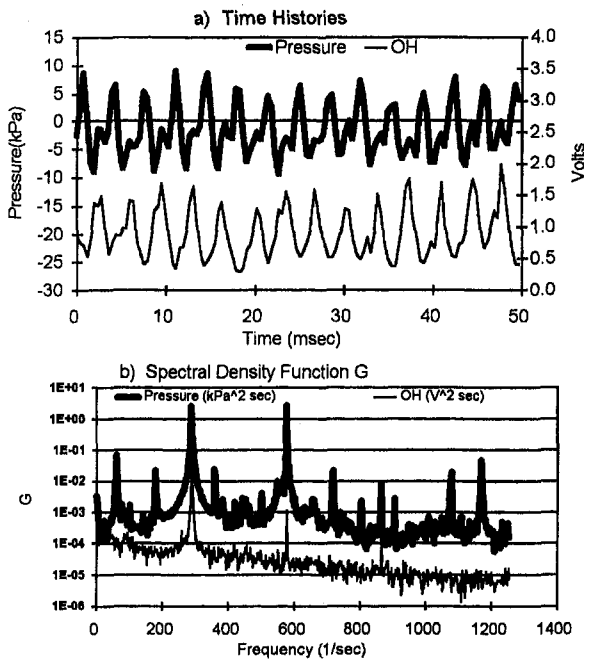


Fig. 4 Time histories and spectra of pressure and OH (heat release) signals with no control fuel

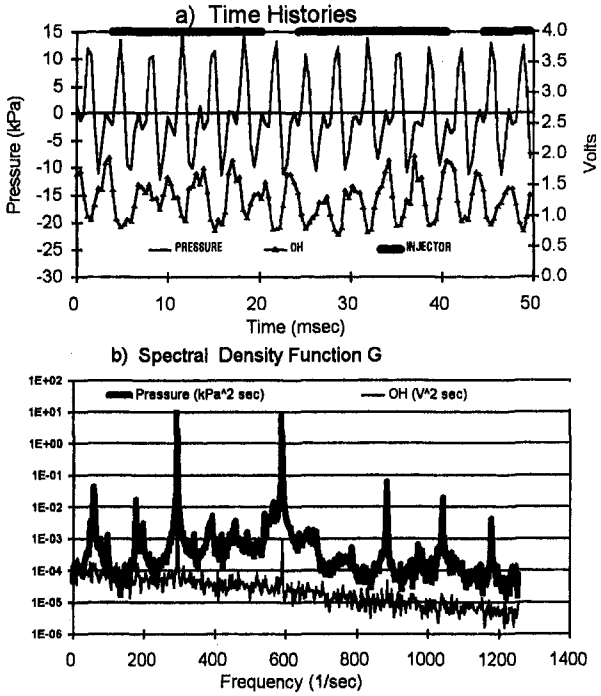


Fig. 6 Time histories and spectra of the pressure and OH signals with 0.067 g/s control fuel, 50 Hz (thick lines in (*a*) indicate pulse width)

combustion. In contrast to this stable operation, a significant instability was readily established when approximately 15 percent of the premix fuel was sent to the bypass port. Figure 4 shows the pressure and OH signal corresponding to this bypass condition. A 4.5 kPa rms pressure signal is established at 300 Hz. Figure 5 shows an ensemble average of one cycle of the pressure and heat release oscillation. Notice that the pressure has an initial inflection point followed by a further increase in amplitude, while the OH curve has no corresponding inflection point. The "double peaks" appearing in the pressure curve are believed to result from the phase difference between the heat release and acoustics. Because the pressure transducer was not located at the point where combustion occurs, the exact phase relation between pressure and heat release cannot be inferred from Fig. 5.

The exact mechanism driving this oscillation is only briefly discussed here. Given the magnitude of the pressure fluctuations inside the combustor, significant pressure and velocity variations are expected inside the premixing annulus. The acoustic response of the gas in the bypass tube produces a periodic variation in the

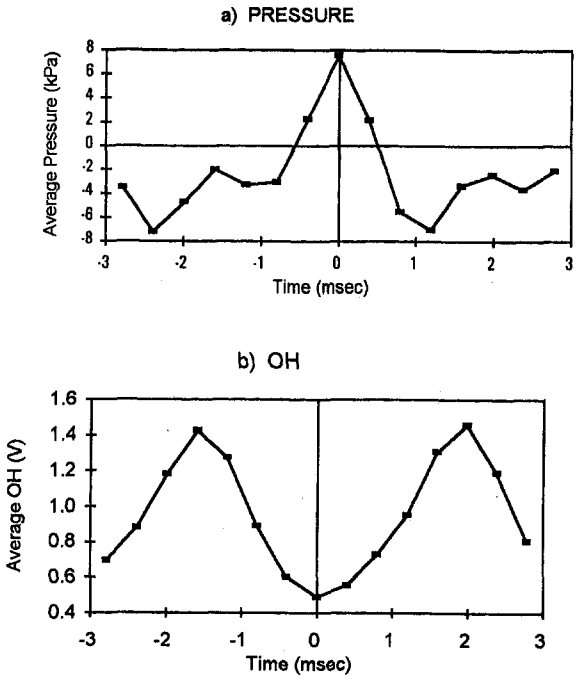


Fig. 5 Ensemble average of a single cycle of the signal shown in Fig. 4

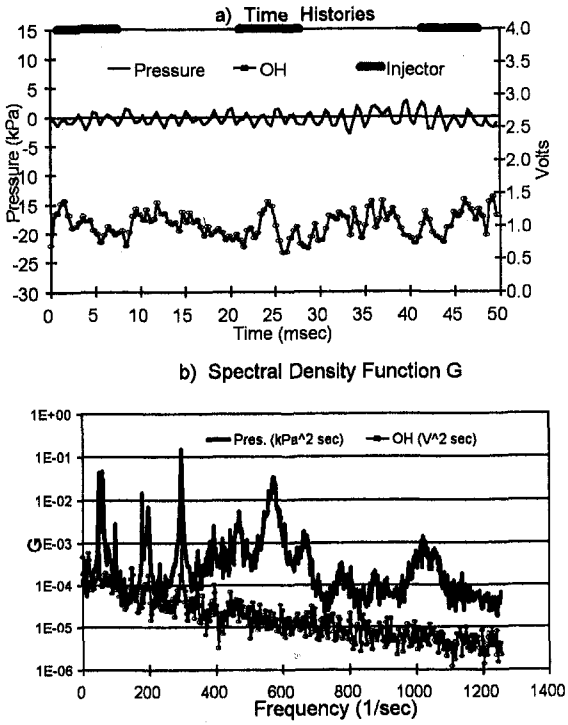


Fig. 7 Time histories and spectra with narrow pulse width at conditions comparable to Fig. 6

Downloaded 02 Jun 2010 to 171.66.16.105. Redistribution subject to ASME license or copyright; see http://www.asme.org/terms/Terms_Use.cfm

bypass fuel flow. The resulting oscillation in the premix fuel/air ratio causes a variation in heat release that drives the pressure oscillation. This fuel/air variation has been well documented in rocket oscillations (Harrje and Reardon, 1972), and in some gas turbine combustors (Kenworthy et al., 1989). Experimental and theoretical work in progress is aimed at developing a detailed description of the oscillation mechanism in this nozzle.

Active control of the oscillation was attempted by adding 0.067 g/s of natural gas control fuel through the pulse injector. This represents 14 percent of the total flow rate of fuel, and produces an overall equivalence ratio of 0.85. The control fuel injector was operated with a frequency of 50 Hz, and a pulse width of 16 ms. The resulting pressure oscillation in the combustor duct is shown in Fig. 6. Notice the injector open duration is shown on this plot by thick lines above the pressure signal. The duration was relatively long compared to the pressure cycle. The added control fuel contributes to the oscillation in the same manner as the bypass fuel. Comparing Figs. 4 and 6, the added control fuel produced an even larger oscillation. Again, the only difference between these two figures was the addition of control fuel at 50 Hz, with a long pulse duration. Notice in Fig. 6 that the heat release (OH) spectra do not show any appreciable signal at the fuel injector driving frequency (50 Hz). This confirms that the long pulse width is essentially equivalent to steady fuel input.

Without changing any other operating conditions, the effect of shorter pulse width (7.2 ms) is shown in Fig. 7. Comparing to the previous figure, and Fig. 4, the oscillation has been noticeably reduced. Statistical analysis of the waveforms shows that the rms pressure amplitude was reduced by a factor of 0.30 from the uncontrolled case (Fig. 4). An enlarged view of the OH spectra shows the control frequency of 50 Hz is evident, indicating the control fuel injection is indeed causing a variation in heat release at the control frequency.

Tests were conducted over a range of pulse widths. Figure 8 shows the rms pressure level as a function of the pulse width, at the driving frequency of 50 Hz. The pulse width is expressed as a percent of the fuel injector period at 50 Hz. The oscillation is seen to drop off dramatically at a pulse width of less than 35 percent; this is comparable to three periods of the 300 Hz oscillation. Variation in the pulse width was tested several times to determine the pulse width required for effective control. In practice, a precise value could not be determined; there is some latitude in where the control takes effect. Further tests were conducted at a fixed pulse width, but with a driving frequency between 50 and 80 Hz. The driving frequency had little effect on control until reaching 80 Hz, where the large amplitude pressure oscillations resumed. Tests in progress will map out the required combination of pulse width and frequency needed for control.

Before concluding, it is mentioned that ongoing tests have shown that both the baseline oscillation and the control behavior are remarkably sensitive to a number of geometric and operating parameters. For example, lowering the pilot tube into the combustion region by as little as 3 mm could negate the baseline oscillation. Changing the pilot fuel flow by just a few percent or changes in the temperature of the refractory combustor duct could likewise negate (or promote) either the oscillation or the control effect. While the control behavior described here could be qualitatively established by carefully setting flow rates, the quantitative level of the control achieved was affected by apparently minor changes in nozzle geometry (i.e., orientation of the swirl vanes, precise location of the pilot tube, etc.). This sensitivity may be an inherent feature of swirl stabilized flames. In a nozzle similar to the one studied here, Starner and Bilger (1986) report that even a 0.2 deg misalignment of the central fuel tube can produce significant asymmetries in observed (diffusion) flame structure. Milosavljevic et al. (1990) showed that a swirl nozzle with a central fuel tube can produce both symmetric and asymmetric flame structures, depending on the flow rates. For the present investigation, it is suggested that the (delicate) orientation of flame asymmetries with respect to the bypass or control ports may play a role determining the magnitude of the oscillating or controlled response; this issue is under investigation.

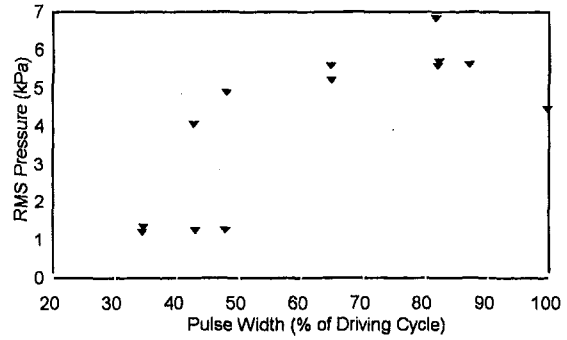


Fig. 8 Effect of pulse width on combustor dynamic pressure

Summary and Conclusions

A 20 kW atmospheric pressure natural gas combustor has been used to study the active control of combustion oscillations. Combustion oscillations arising from fuel/air variations in a premixing fuel nozzle are controlled by periodic injection of fuel in the premixing zone of the fuel nozzle. Specifically, a 300 Hz oscillation with 4.5 kPa rms pressure amplitude was reduced by a factor of 0.30 (−10 dB). Control was accomplished using 50 Hz open-loop injection of 14 percent of the total fuel. In addition to recording the transient pressure signal, transient heat release was measured using a fiber-optic flame emission probe. Heat release measurements show that short-duration fuel pulses produce a corresponding variation in the heat release, at the control frequency. Work in progress is aimed at identifying the specific parameters required for successful control, and understanding the observed sensitivity to various operating and geometric parameters.

References

Candel, S. M., 1992, "Combustion Instabilities Coupled by Pressure Waves and Their Active Control," *The Twenty-Fourth (International) Symposium on Combustion,* pp. 1277–1296.

Harrje, D. T., and Reardon, F. H., 1972, *Liquid Propellant Rocket Combustion Instability,* NASA SP-194.

Kenworthy, M. J., Bahr, D. W., Mungur, P., Burrus, D. L., Mehta, J. M., and Cifone, A. J., 1989, "Dynamic Instability Characteristics of Aircraft Turbine Engine Combustors," AGARD CP-450, ISBN 92-835-0503-4.

Keller, J. O., and Saito, K., 1987, "Measurements of the Combusting Flow in a Pulse Combustor," *Combust. Sci. Tech.,* Vol. 53, pp. 137–163.

Kinsler, L. E., Frey, A. R., Coppens, A. B., and Sanders, J. V., 1982, *Fundamentals of Acoustics,* 3rd ed., Wiley, New York, p. 235.

Langhorne, P. J., Dowling, A. P., and Hooper, N., 1990, "Practical Active Control System for Combustion Oscillations," *J. Propulsion,* Vol. 6, No. 3, pp. 324–333.

McManus, K. R., Poinsott, T., and Candel, S. M., 1993, "A Review of Active Control of Combustion Instabilities," *Prog. Energy Comb. Sci.,* Vol. 19, pp. 1–29.

Milosavljevic, V. D., Taylor, A. M., and Whitelaw, J. H., 1990, "The Influence of Burner Geometry and Flow Rates on the Stability of Swirl-Stabilized Nonpremixed Flames," *Comb. Flame,* Vol. 80, pp. 196–208.

Schadow, K. C., Hendricks, E. W., and Hansen, R. J., 1992, "Recent Progress in the Implementation of Active Combustion Control," *Proc. 18th ICAS Congress,* Bejing, China, Sept 20–25, Vol. 1, Paper No. ICAS-92-2.5.3, pp. 942–952.

Schadow, K. C., Wilson, K. J., Gutmark, E., Yu, K., and Smith, R. A., 1993, "Periodic Chemical Energy Release for Active Control," *11th ISABE—International Symposium on Air Breathing Engines,* Tokyo, Japan, Sept. 20–24, Vol. 1, pp. 479–485.

Sivasegaram, S., and Whitelaw, J. H., 1992, "Active Control of Combustors With Several Frequency Modes," ASME DSC-Vol. 38, pp. 69–74.

Starner, S. H., and Bilger, R. W., 1986, "Joint Measurements of Velocity and Scalars in a Turbulent Diffusion Flame With Moderate Swirl," *The Twenty-First Symposium (International) on Combustion,* pp. 1569–1577.

Downloaded 02 Jun 2010 to 171.66.16.105. Redistribution subject to ASME license or copyright; see http://www.asme.org/terms/Terms_Use.cfm

Hydrocarbon Fuel Cooling Technologies for Advanced Propulsion

D. R. Sobel

L. J. Spadaccini

United Technologies Research Center,
East Hartford, CT 06108

Storable hydrocarbon fuels that undergo endothermic reaction provide an attractive heat sink for future high-speed aircraft. An investigation was conducted to explore the endothermic potential of practical fuels, with inexpensive and readily available catalysts, under operating conditions simulative of high-speed flight applications. High heat sink capacities and desirable reaction products have been demonstrated for n*-heptane and Norpar 12 fuels using zeolite catalysts in coated-tube reactor configurations. The effects of fuel composition and operating condition on extent of fuel conversion, product composition, and the corresponding endotherm have been examined. The results obtained in this study provide a basis for catalytic-reactor/heat-exchanger design and analysis.*

Introduction

As aeropropulsion technologies advance into the twenty-first century, increasingly severe demands are being placed on structural and thermal capabilities of the engine, fuel economy, and pollutant-emissions control. At high supersonic and hypersonic flight speeds, the temperature of the ram air taken on board the vehicle is too high to cool the structure, and it is necessary to utilize the fuel as the primary coolant.

The heat sink afforded by conventional liquid hydrocarbon fuels is limited by operation at moderate temperatures to preclude deposit formation and avoid fouling the cooling or fuel injection systems. Cryogenic fuels, such as liquid methane and liquid hydrogen, can provide sufficient cooling but require large vehicles (because of their low densities) and present cost, logistics, operational, and safety problems. By contrast, endothermic liquid hydrocarbon fuels offer potential for increased cooling by undergoing chemical decomposition (cracking) on a catalyst prior to injection into the combustor (Lander and Nixon, 1971). The products of the endothermic reaction are gaseous fuels with high heating values, short ignition delay times, and rapid burning rates. In addition, waste heat absorbed by the fuel can be returned to the cycle, enhancing performance. Endothermic fuels have handling characteristics that are very similar to current fuels and have deposit formation rates sufficiently low for potential application in high-speed tactical aircraft and missiles.

The total heat sink available from an endothermic fuel comes both from the physical heating of the fuel (raising its temperature) and from a heat-absorbing (endothermic reforming) chemical reaction. The transfer of heat into the fuel is accomplished in a catalytic heat-exchanger reactor. Within a reactor flow passage, the rate at which fuel is reformed depends on the balance among the heat transfer through the wall, the mass transfer of fresh reactant to the catalyst, and the chemical kinetics associated with the reaction. Therefore, the reactor design should provide rapid transfer of heat into the reactor, such as can be obtained with plate-fin heat exchangers; highly turbulent fuel flows for maximum heat and mass transfer; and minimum thermal resistance through the use of high-conductivity materials and very thin (micron thickness) catalyst coatings bonded to the reactor walls. A good catalyst should provide nearly complete conversion of the fuel and high selectivity to the desired products at temperatures of interest.

Fuels and Catalysts

Types of Reactions. Many types of catalytic endothermic reactions of hydrocarbon fuels are possible. *Dehydrogenation* of saturated ring compounds (e.g., MCH and decalin) to form aromatics has been successfully demonstrated at reasonable temperatures and pressures with relatively large endothermic heats of reaction (Nixon et al., 1964, 1967; Lipinski et al., 1989). Dehydrogenation of normal alkanes, and ring fracture of aromatics and cycloalkenes generally require very high temperatures. *Dehydrocyclization* of normal alkanes to form saturated ring compounds is not highly endothermic and proceeds slowly on known catalysts; otherwise the saturated rings could be further dehydrogenated to form aromatics. *Dedimerization* reactions can proceed at low temperatures, but absorb little heat. *Isomerizations* do not involve molar changes, therefore entropy changes are low, and these reactions are not thermodynamically favored. *Catalytic cracking* of normal and iso-alkanes to form olefins and hydrogen is strongly endothermic and can be performed at temperatures and pressures that are compatible with existing materials. Unlike the saturated ring (naphthenic) endothermic fuels, which react to form aromatics, catalytic cracking results in the formation of olefinic and low-molecular-weight paraffinic species, which are less likely to pose problems related to soot formation and increased radiative heating of the combustor liner. In addition, normal- and iso-alkanes can be blended to meet handling, safety, and other system concerns. Consequently, the aim of this investigation was to exploit the cracking reactions.

In general, thermal and catalytic cracking of normal and iso-alkanes may follow several different reaction paths and produce hydrogen and a spectrum of saturated and unsaturated hydrocarbon products. The product compositions may be affected by the reaction pressure and temperature, and correspond to different amounts of heat being absorbed. Depending on the temperature at which the reaction begins and the products formed, the endothermicity of the decomposition can vary substantially. As shown for n-heptane in Fig. 1, increased unsaturation of the products results in increased heat absorption, but requires higher reaction temperatures for comparable conversions. Based on these and similar calculations, it can be concluded that formation of saturated products (such as methane, Fig. 1(d)) and aromatics (such as toluene, Fig. 1(c)) tends to decrease the

Contributed by the International Gas Turbine Institute and presented at the 40th International Gas Turbine and Aeroengine Congress and Exhibition, Houston, Texas, June 5–8, 1995. Manuscript received by the International Gas Turbine Institute February 15, 1995. Paper No. 95-GT-226. Associate Technical Editor: C. J. Russo.

Copyright © 1997 by ASME

Downloaded 02 Jun 2010 to 171.66.16.105. Redistribution subject to ASME license or copyright; see http://www.asme.org/terms/Terms_Use.cfm

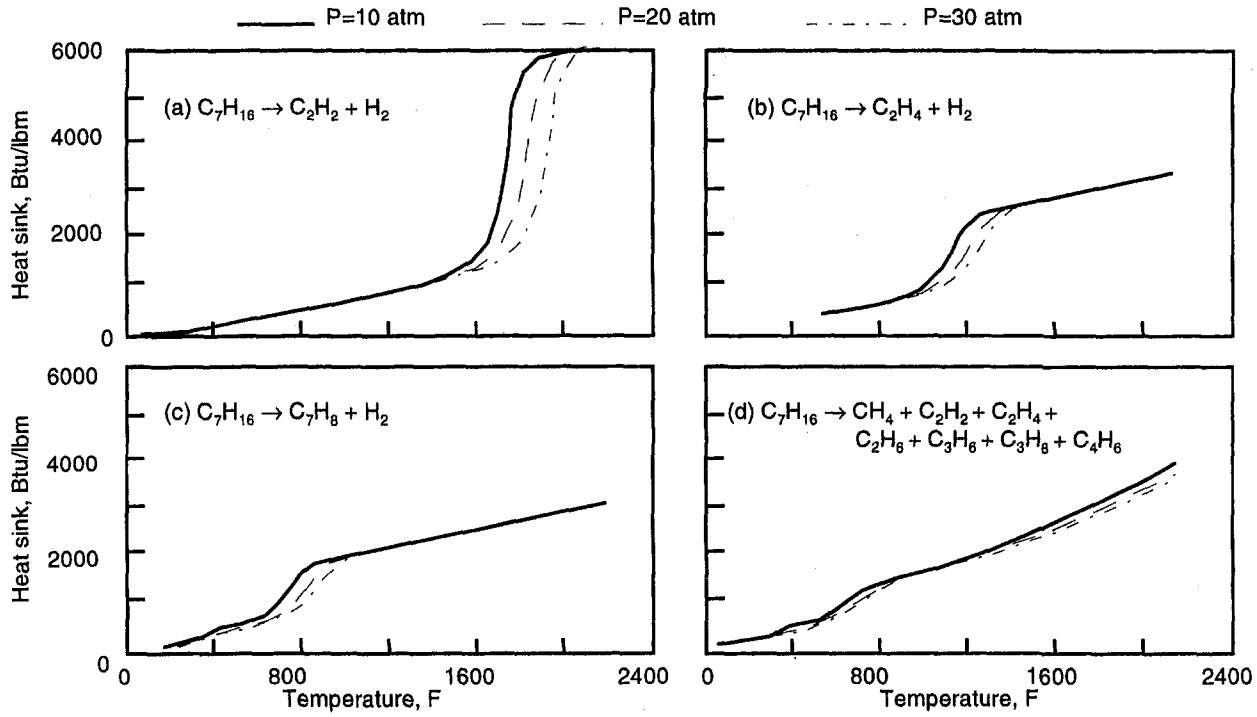


Fig. 1 Endothermic cracking of *n*-heptane

endotherm, but increase the equilibrium fractional conversion at a given temperature. Production of alkenes (such as ethylene and propylene, Fig. 1(*b*)) leads to a substantial heat absorption, and formation of alkynes (such as acetylene, Fig. 1(*a*)) leads to even greater heat absorption but requires reaction temperatures above 1300°F. In addition, a multiplicity of low-molecular-weight products is desirable. The formation of large numbers of products increases the entropy change during the reaction, which in turn makes the reaction more favorable thermodynamically.

Thus, the most desirable products of the endothermic fuel reaction are hydrogen and low-molecular-weight olefins, such as ethylene. In addition to providing high heat absorption, these products would result in a fuel with excellent combustion characteristics. Small amounts of alkanes (methane) and aromatics are acceptable to enhance the thermodynamic driving force for high-conversion levels at a given temperature.

Fuel Types and Properties. A goal of this investigation has been to identify practical endothermic fuels with a high cooling capability and performance and handling characteristics very similar to current aircraft fuels. The physical and chemical properties of two candidate endothermic fuel blends, namely *n*-heptane and Exxon Norpar 12, are listed in Table 1 along with those for methylcyclohexane (MCH), and current jet fuels JP-7 and JP-8 for comparison. Norpar 12 is an inexpensive mixture of normal alkanes, principally C_{10} to C_{13} (i.e., decane, undecane, dodecane, and tridecane).

Characteristics that would limit the usefulness of a fuel include high freezing point, low flash point, and high vapor pressure. MCH has a low flash point and high vapor pressure, which may restrict its application in many aircraft systems. Norpar 12 has physical properties that are very similar to JP-7, and could be readily modified to satisfy the property requirements for current fuels. (For example, its freezing point could be lowered considerably by broadening the blend to include lighter paraffinic components, such as octane.) Previous experience with JP-7 has indicated that the presence of a low concentration of aromatic species is desirable to maintain the elasticity of seals. Addition of aromatic species (e.g., toluene) to Norpar 12 would also result in a lowering of the freezing point.

Because the efficient catalytic conversion of endothermic fuels requires high temperatures, high thermal oxidative stability is a prerequisite for such fuels to be applicable as coolants. Coke formation at elevated reaction temperatures can reduce the effectiveness of heat exchanger surfaces and cause rapid degradation of the catalyst. Fuel thermal decomposition and deposit formation can take place in fuel preheaters and reactors by both autoxidation and pyrolysis mechanisms. Deposits may also form in transfer lines and valves downstream of the heat exchanger/reactor as a result of the condensation of high-molecular-weight products of the cracking reactions. Decomposition and surface deposition are governed by several factors, including the temperature and composition of the surfaces in contact with the fuel, the bulk temperature of the fuel, the levels of oxygen or sulfur in the fuel, and the residence time at the high temperature conditions. Oxygen is known to promote the formation of coke deposits at temperatures below 700°F, and removal of oxygen dissolved in the fuel and oxides from contact surfaces prior to heating has been found to decrease deposit formation.

It is possible that a low rate of fuel deposit formation can be achieved by very rapid heating of the liquid at supercritical pressure, through the autoxidation region, followed by additional heating of the fuel beyond its critical temperature. In addition, supercritical heating in the presence of the catalyst results in a reformation reaction that upgrades the structure of the fuel by breaking the weaker chemical bonds and improves the thermal stability. Moreover, the hydrogen product can combine with free radical species (coke precursors) that are formed, providing alternative paths for reaction.

Catalysts and Catalyst Support Techniques. The cracking of normal alkanes is similar to reforming reactions carried out in the petroleum industry, wherein molecules are stripped of hydrogen, unsaturated carbon bonds are formed, and rearrangement of molecules to both lighter and heavier species takes place. However, aircraft applications are volume and

Downloaded 02 Jun 2010 to 171.66.16.105. Redistribution subject to ASME license or copyright; see http://www.asme.org/terms/Terms_Use.cfm

Table 1 Fuel properties

	MCH	*n*-Heptane	Norpar 12	JP-7	JP-8
Boiling point, F	213	209	370-426	360-484	284-572
Freezing point, F	-196	-131	‡	-47	-53
Net heating value					
Gravimetric, Btu/lb	18,649	19,171	18,980*	18,875	18,400
Volumetric, Btu/gal	119,746	109,396	118,793*	123,500	124,378
Viscosity @ 20 C, cSt	0.86	0.55	1.68	2.0	1.65
Flash point, F	25	30	156	145	100
Specific gravity @ 60 F	0.77	0.68	0.75	0.79	0.81
Vapor press. @ 100 F, psia	1.6	1.6	0.8	0.02	0.15
Critical pressure, psia	504	397	290*	306	340
Critical Temp., F	570	513	682*	746	772
Composition					
Aromatics, percent vol				3	20
Naphthenes, percent vol	100			32	20
Paraffins, percent vol		100	99	65	58
Olefins, percent vol					2
Sulfur, ppmw	<5	<1	<1	60	500

* estimated property
‡ varies with blend

weight limited, and require specific flow rates that are more than 100 times those used in petroleum reforming. Reforming reactions are typically carried out on zeolite catalysts. These are skeletal aluminosilicate compounds that are processed from natural clays and have a narrow distribution of pore sizes that provide access to a cagelike inner structure in which the bulk of reaction occurs. The catalytic activity and selectivity of each zeolite depend upon how readily a fuel molecule can enter its internal cages, and whether products of a certain molecular geometry can pass through the pores.

Beyond the requisite high activity and selectivity characteristics of the catalyst itself, the implementation of the reactor design must provide several other characteristics if high endothermic performance is to be achieved. Primary among these are the ability to provide high rates of heat transfer to the reacting surface (i.e., the fuel/catalyst interface) and high rates of mass transfer in order to provide a continual supply of fresh fuel to the catalytic surfaces. If either requirement is not satisfied, the performance capability of the reactor will be reduced. If heat transfer rates are lower than the mass transfer or the kinetics rates, the temperature of the fuel in contact with the catalyst will fall, reducing the reforming rate until the processes are again in balance. If local mass transfer rates are too low, reaction products will accumulate around the catalytically active sites, blocking the supply of fresh fuel and retarding the reaction process. The balance between the heat and mass transfer rates depends on the reactor implementation and the catalyst support configuration. In addition, incorporation of a reactor into a practical aircraft thermal management system requires that the unit impose as small a fuel flow resistance as possible (low pressure drop) and that the size and the weight of the unit be minimized.

The reactor concept can be implemented in two different ways with regard to use in the thermal management of a flight system, namely for either direct or indirect cooling (see Fig. 2). Direct cooling refers to the incorporation of the reactor into the structure of a hot component, such as an augmentor or an exhaust nozzle. With indirect cooling, a secondary fluid, such as air or a recirculating nonreacting coolant, is cooled by the fuel in a remote reactor, then used to cool the hot component structures. There are important differences between these configurations, both in the levels of local heat flux occurring and in the mechanical arrangement of the reactor. Indirect cooling implies a "conventional" heat exchanger, with relatively modest levels of heat flux. In the direct cooling configuration, the heat exchanger is part of the hot structure, and may be exposed to very hot, high-velocity flow, resulting in correspondingly high heat flux levels.

Packed-Bed and Coated-Wall Catalyst Supports. In catalyst systems considered for aircraft applications, the catalyst is affixed to some stationary support in a manner allowing ready contact with the flowing fuel and good thermal contact with the heat source. Two methods for supporting the catalyst have been examined. The first is a packed bed in which the catalyst is formed into pellets or coated onto existing pellets, and the pellets are placed in the fuel passage. The second technique involves coating of the catalyst directly on the wall of the fuel passage.

In a packed bed, the heat must flow from the hot source, through the passage wall, and into the bulk of the fuel flow. Because the pellets form a noncontinuous structure, heat must reach the interior catalytic surface by means of convection due to fluid motion. While this heating mechanism may be adequate for certain low heat load applications, it is very inefficient and

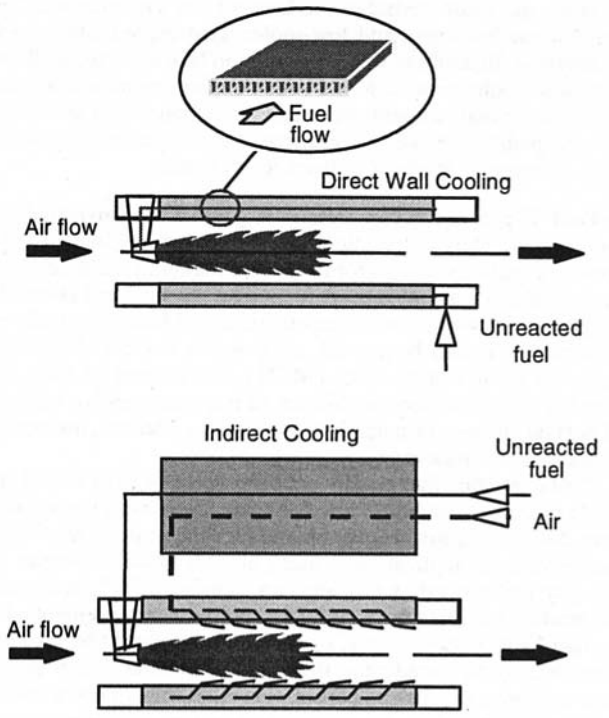


Fig. 2 Catalytic reactor configurations

Downloaded 02 Jun 2010 to 171.66.16.105. Redistribution subject to ASME license or copyright; see http://www.asme.org/terms/Terms_Use.cfm

leads to heavy, high-volume heat exchangers. Furthermore, in a packed bed, the temperature difference between the wall and the bulk fuel may be substantial. The fuel is the hottest at the wall where there is no catalyst, possibly leading to undesirable pyrolytic reactions with potential for coke deposit formation. Moreover, the endothermic reaction occurs at the coolest point in the fuel, i.e., the fuel/catalyst-pellet interface.

The alternative approach for supporting the catalyst is applicable for either direct or indirect cooling systems and entails coating the catalyst onto the walls of the fuel passages. Since the flow of heat is from the wall through the catalyst to the fuel, the reaction occurs where the fuel is the hottest, i.e., at the catalyst/fuel interface, and undesirable thermally driven, noncatalytic reactions can be avoided. Furthermore, although the zeolite catalysts used for thermal cracking of paraffinic hydrocarbons have relatively low thermal conductivities, similar to ceramics, the typical thickness of the coating is very small (i.e., less than 10 μm) and thus presents negligible additional thermal resistance. Another advantage associated with the coated-wall catalyst support technique is that the coating poses very little added resistance to fluid flow and therefore, minimal additional pressure loss. Packed-bed reactors, on the other hand, depending on particle size and void fraction, may impose substantial pressure loss for the required conversion efficiency.

It should be noted that additional heat transfer enhancement can be achieved if the fuel passages are of a fin-plate construction, and subsequently coated after fabrication. In this arrangement, heat flows from the hot absorption surface to the larger heat rejection surface by conduction within the metallic fins, which are coated with catalyst. With a tight packing of fins, and use of staggered or interrupted fins to increase turbulence and enhance heat transfer, the effective thermal resistance from the hot source into the fuel may be significantly reduced.

Coating Application. The effective implementation of a coated-wall configuration requires a method for providing a very thin catalyst coating directly on the wall of the surface to be cooled. The binding agents within the coating must form a strong bond with the surface, tolerating high heat flux and thermal cycling, and must expose the catalyst to the flow without reducing its effectiveness.

For this application, zeolite catalysts were applied to the inside surface of small-diameter tubes (<0.10 in.) simulating the internal passages of a plate-fin heat exchanger. This was accomplished using a ceramic binding medium because of its compatibility with the zeolite materials and because it formed a strong bond with the surface that tolerated high heat flux and thermal cycling and left the catalyst particles exposed to the flow. The coatings have been successfully applied to several metals (Inconel 625, Haynes 214, and stainless steel), indicating that substrate material is not a critical issue in the bonding process. The thickness of the coating was 3 to 5 μm and the catalyst, when applied in this manner on the inside of small-diameter tubes, was found to be effective in endothermic fuel/reactor tests discussed below.

Bench-Scale Testing

Tests were designed to allow screening of fuel/catalyst combinations through measurement of endotherm of reaction, extent of conversion, and identification of reaction products. Parametric studies of reactor geometry configurations were conducted to provide a design data base and the basis for validation and upgrading of analytical models. This section comprises descriptions of the bench-scale apparatus flow path and analysis procedures, and representative test results.

Bench-Scale Test Apparatus. The high-pressure bench-scale endothermic fuel test apparatus is shown schematically in Fig. 3. Fuel is first sparged with nitrogen to reduce the amount of dissolved oxygen, then metered into the system at supercritical

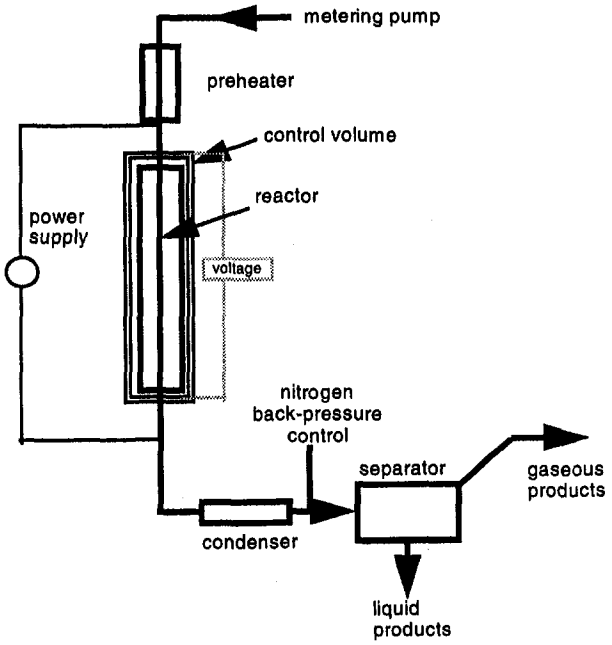


Fig. 3 Bench-scale reactor

pressure through a positive-displacement pump. The fuel is then heated above its critical temperature to 700–750°F in a preheater to reduce reactor length while minimizing thermal cracking reactions. (Alumina spheres, used in the preheater to promote heat transfer, were examined periodically and did not show signs of significant coke deposit.)

Several reactor configurations have been tested in this apparatus, differing in both methods of catalyst support, i.e., packed-bed and coated-wall, and heat input. Coated-wall reactors are prepared with the coating process described earlier. Since the coated-wall reactor tubes are generally small diameter (<0.10 in.) to simulate practical heat exchanger reactor passages, only tube outer wall temperature measurements are made along the reactor; fuel temperatures are measured at the reactor inlet and exit.

Two different methods of heat input to the reactor have been used, viz., resistive heating (shown in Fig. 3) and constant surface temperature. Resistive heating, that is, heating by an electric current, has the characteristic that the heat transfer rate is nearly uniform for a given tube cross-sectional area along the length of the reactor and the fuel and wall temperatures vary from inlet to exit. Furthermore, this mode of heating allows a direct measurement of the endotherm through a calculated energy balance. (The technique for endotherm calculation is described below.) However, aircraft-application heat exchangers are more nearly constant temperature and have substantial lengths at elevated temperatures.

A technique for providing a more uniform temperature distribution is to clasp the reactor tube between isothermal copper blocks, which are maintained at a desired temperature by heating strips. This mode of heating provides greatest surface temperature uniformity; however, since heat transfer rate from the block to the tube is not readily measurable, the endotherm cannot be directly calculated. In a constant-temperature reactor, a measure of the endotherm can be determined only through thermochemical calculations based on product analysis and measurement of the extent of conversion. During the course of this investigation, tests were conducted with both resistively heated and constant-temperature reactors. The actual temperature distributions characteristic of individual reactor configurations are shown in Fig. 4.

Downloaded 02 Jun 2010 to 171.66.16.105. Redistribution subject to ASME license or copyright; see http://www.asme.org/terms/Terms_Use.cfm

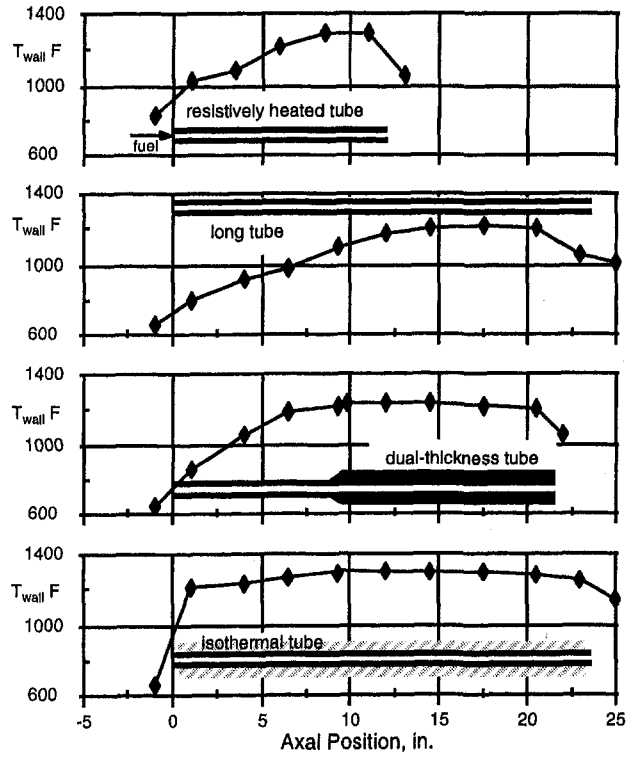


Fig. 4 Axial temperature distributions for coated-tube reactor configurations

During a reactor test, in addition to the fuel and reactor-wall temperature measurements, the fuel pressure is measured upstream and downstream of the reactor to correlate reactor performance as well as to measure and track in time the reactor pressure drop, which is indicative of coke deposition. Downstream of the reactor, the products are quenched in a water-fed heat exchanger and the liquid and gaseous components are separately metered and analyzed. The extent of conversion of the fuel to gaseous products is determined by collecting and measuring the liquid product for a specified period of time and comparing this with the known flow rate of the unreacted fuel.

Analysis Procedures. For resistively heated reactor tubes, the endotherm can be computed by analyzing an energy balance on the control volume depicted in Fig. 3. The power input, Q_{in}, is converted to heat and transferred to the fuel on the inside of the reactor and, by natural convection, to the environment on the outside. The portion of heat lost to the environment through natural convection, Q_{env}, is accounted for through calibration without fuel flow prior to a given test (the reactor is well insulated to minimize this loss). The remaining energy input, i.e., that supplied to the fuel, can be further divided into that which results in raising the temperature of the fuel/products (sensible heating, Q_{sens}) and that which is absorbed in the reaction (endotherm, Q_{endo}). The sensible heating is determined by temperature measurements at the reactor inlet and exit, the fuel mass flow rate, and output from the NIST computer program SUPERTRAPP (Ely and Huber, 1990), which provides the physical and thermodynamic properties of hydrocarbon mixtures as a function of composition, pressure, and temperature. The net endotherm can then be computed as

$$Q_{endo} = Q_{in} - Q_{sens} - Q_{env}$$

Endotherm can also be computed from the extent of conversion and the product composition. (In the case of the constant-temperature reactor, this is the only available measure of endotherm.) Product chemical analyses were performed using a cryocooled Hewlett Packard Gas Chromatograph/Mass Spectrometer (GC/MS) system with a DB-1 megabore column. To enhance the ability to quantify low-molecular-weight species, gaseous product analysis was also performed with a thermal conductivity detector coupled with a packed column. The product chemical composition analysis allows assessment of the catalyst selectivity to be made and is used to compute the heat of reaction and thereby provide an independent measure of the endotherm.

Test Results. A broad range of fuels and catalysts has been tested, including simple, single-component fuels (e.g., MCH, *n*-heptane), and fuel blends (e.g., Norpar 12) (Spadaccini et al., 1993a, b). Tests have been conducted primarily with zeolite catalysts; however, a limited number of tests have been performed without catalysts (to explore pure thermal decomposition), and with precious metal catalysts. Testing has been conducted with both packed-bed and coated-tube reactors at operating conditions that simulate those of a single passage in a practical plate-fin catalytic heat exchanger/reactor.

Early tests were conducted with *n*-heptane using zeolite catalysts in packed-bed reactors. These tests were conducted at Liquid Hourly Space Velocities (LHSV) of up to 700 h^{-1} and pressures up to 50 atm. (LHSV is defined as the volumetric flow rate of the fuel in its liquid state divided by the volume of the reactor, and has units of h^{-1}.) The results indicated very high conversion, approaching 100 percent at 1300°F (see Fig. 5), with a corresponding maximum endotherm of approximately 850 Btu/lb. The products of reaction were primarily light unsaturated hydrocarbons and no significant aromatic compounds were detected.

To explore the potential for more compact and efficient reactors, tests were also conducted with coated-foil reactors. In these tests, the catalyst pellets were replaced with a corrugated foil having a thin catalytic coating. The results of these tests compared favorably with those of the packed bed and provided the basis for coated-wall testing.

The positive results achieved with *n*-heptane led to more extensive testing with Norpar 12, a fuel blend simulative of current jet fuels. The total heat sink determined for Norpar 12 is shown in Fig. 6, corresponding to a series of bench-scale tests covering a broad range of operating conditions for both packed-bed and coated-tube reactors. It comprises the sensible heating, manifested in an increase in temperature, and the energy that can be absorbed in reforming the fuel, i.e., the endotherm. As a point of reference, the heat sink associated with

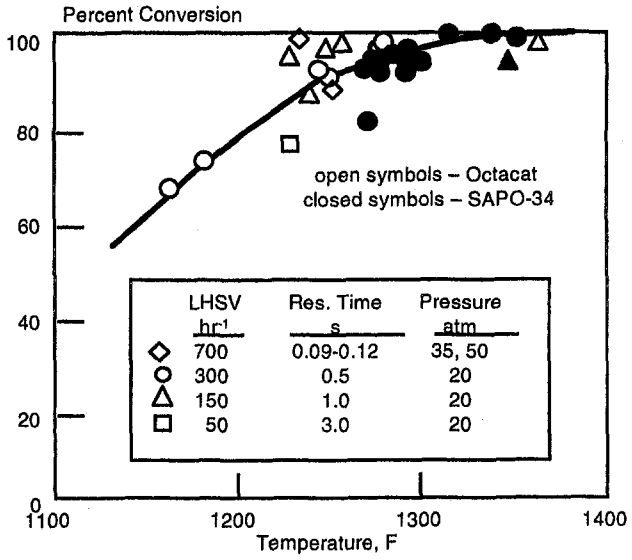


Fig. 5 Decomposition of *n*-heptane on zeolite catalysts

Downloaded 02 Jun 2010 to 171.66.16.105. Redistribution subject to ASME license or copyright; see http://www.asme.org/terms/Terms_Use.cfm

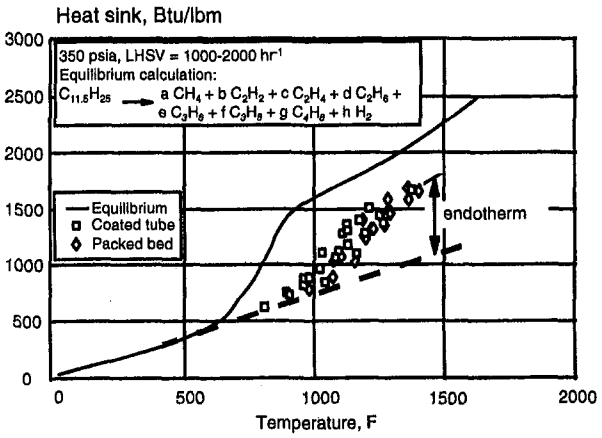


Fig. 6 Norpar 12 heat sink

conversion of the Norpar 12 to an equilibrium composition of the products indicated is also shown. The variance between the equilibrium calculation and data can be attributed to kinetics and differences in reaction products. The correspondence between the results achievable between the packed-bed and coated-tube tests indicates that, in light of the advantages of the coated tube support structure described earlier, the coated passage is clearly a preferable catalyst support technique for applications where size and weight are important.

In the following discussion, salient features of the endothermic fuels decomposition process are described using the results of Norpar 12 on zeolite catalysts in coated-tube reactors. The cooling capability is presented in terms of the endotherm (i.e., the heat absorbed in the cracking reaction) rather than the total heat sink to isolate the chemical reforming aspect of the process.

Thermal and Catalytic Cracking. Cracking of hydrocarbon fuels is known to occur at high temperatures even in the absence of catalyst. The effectiveness of the catalyst in the conversion of the fuel to desirable products, however, is evident in the product analysis shown in Fig. 7. This figure represents the mass spectrometer results showing the product distribution for Norpar 12 conversion with SAPO-5 zeolite catalyst compared

Table 2 Product composition

Species	Mole Fraction
Methane (CH_4)	0.043
Ethylene (C_2H_4)	0.353
Ethane (C_2H_6)	0.197
Propene (C_3H_6)	0.201
Propane (C_3H_8)	0.057
Higher Carbon Number Species (C_{4+})	0.149

to that without catalyst. Both of these tests were performed at approximately 325 psia, a space velocity of 1130/h and a fuel exit temperature of approximately 1200°F. In the absence of the catalyst, the products represent the result of thermal cracking yielding high-molecular-weight species that are primarily saturated, corresponding to a low endotherm. With the zeolite catalyst, the products are substantially lower in molecular weight and are primarily unsaturated, making them more desirable from the point of view of both high endotherm and favorable combustion characteristics. It was also found that the maximum temperature at which the reactor could be operated was substantially lower in the absence of catalyst due to the propensity for coking. It is concluded that any practical system will benefit from a catalytic surface to achieve adequate endotherm and produce desirable reaction products.

Catalytic Cracking of Norpar 12. Representative results in terms of extent of conversion and measured endotherms are presented in Fig. 8 for the catalytic cracking of Norpar 12. In this figure, results are presented for the conversion of Norpar 12 on zeolite catalysts for two of the different coated-tube reactor configurations shown in Fig. 4. The difference in the extent of conversion and endotherm between the two configurations is attributable to the increased length of the dual-thickness tube that is at high temperature.

The product distribution for the operating condition indicated in Fig. 8 is presented in Table 2. Based on this product distribution, the measured extent of conversion, and the known composition of unreacted Norpar 12, a thermodynamic calculation was

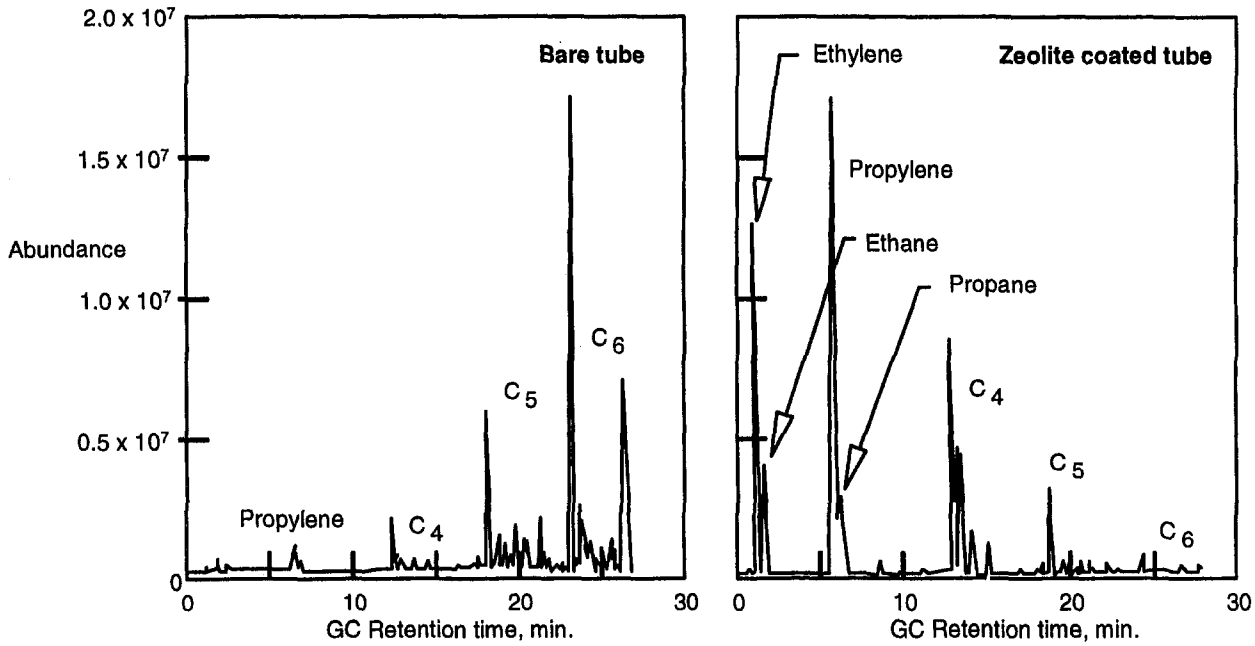


Fig. 7 Norpar 12 gaseous product distribution

Downloaded 02 Jun 2010 to 171.66.16.105. Redistribution subject to ASME license or copyright; see http://www.asme.org/terms/Terms_Use.cfm

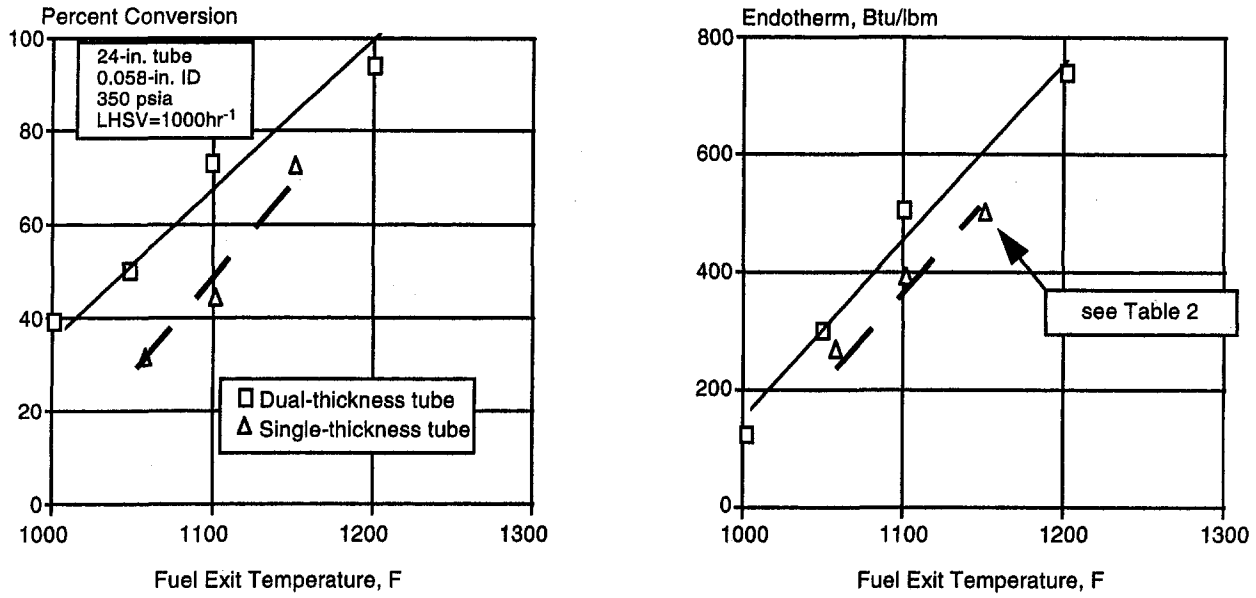


Fig. 8 Catalytic cracking of Norpar 12

performed to compute the endotherm for comparison to the measured value. The calculated value is 465 Btu/lbm, comparing favorably with the measured value of 489 Btu/lbm. Also, the hydrogen-to-carbon atom ratio for the products (H/C = 2.23) compares favorably with that of the unreacted Norpar 12 (H/C = 2.18), confirming the product analysis.

Space Velocity Effects. During the course of this investigation, tests were run at flow rates ranging from 500 to 1200 ml/h. A commonly used measure of throughput is the liquid hourly space velocity. (For example, a 1-gal reactor operating at a LHSV of 1000 h^{-1} would process a fuel flow rate of 1000 gal/h.) It is used for scaling reactor size for a well-characterized configuration, but does not represent the reactor physics (as would, for example, the Reynolds number) and should therefore not be used for performance estimation. For example, a coated-tube reactor element 12 in. long with an inner diameter of 0.050 in. would have the same LHSV at a given flow rate as a $\frac{3}{4}$ in. ID tube that is 1 in. long. Clearly, the performance of the two reactors would be substantially different. For a given reactor, however, the LHSV is a measure of flow rate, or conversely, residence time. Figure 9 shows the effect of LHSV, or flow rate, on measured endotherm. For both of the tests shown, the fuel pressure was 350 psi; therefore, the residence time of the fuel vapor varies inversely with LHSV. As expected, the measured endotherm decreased with increasing LHSV (increasing flow rate, decreasing residence time). The magnitude of the space velocity that is required is application dependent and must be based on a detailed thermal management analysis, which has not been performed in this investigation. The values shown, however, are of the order believed to be required for high-speed aircraft applications.

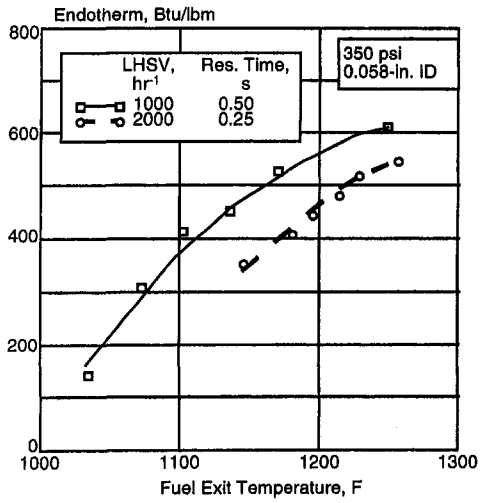


Fig. 9 Effect of space velocity on reactor performance

Long-Duration Tests. A typical operating condition (viz., T_{wall} = 1300°F, LHSV = 1000 h^{-1}, 0.058-in. zeolite-coated tube), was selected and maintained to permit examination of the performance of the reactor over an extended period of time. For the first 15 hours of operation, there was relatively little change in endotherm; however, the pressure began to rise slowly. The fuel flow was stopped and it was determined that deposits were building downstream of the reactor where temperature decreases below 700°F at the entrance to the water-cooled condenser. Apparently, heavy-molecular-weight species were condensing and forming carbon deposits in the liquid phase. This would not occur in an actual reactor since the reforming products would not be cooled before they were injected into the combustion chamber. After removing the carbon buildup downstream of the reactor, the fuel flow was restarted and the test continued. This process was repeated several times and was terminated after a cumulative run time of 60 hours had been achieved. In that time, no significant change in reactor performance or degradation of the catalyst was observed.

Conclusions

High endotherms and attractive reaction products have been achieved through the endothermic cracking of storable liquid hydrocarbon fuels using inexpensive zeolite catalysts. These results provide the basis for the continued development of high-heat-sink thermal-management systems, which enable high-speed flight with practical fuels. The following specific conclusions can be drawn from the results of this study:

- High heat sinks can be realized by catalytic cracking of paraffins, including fuel blends simulative of current jet fuels.

Downloaded 02 Jun 2010 to 171.66.16.105. Redistribution subject to ASME license or copyright; see http://www.asme.org/terms/Terms_Use.cfm

- Efficient endothermic reactions can be achieved at high throughputs and elevated pressures using inexpensive zeolite catalysts. Substantial catalyst lifetime has been demonstrated.
- Catalyst-coated surfaces, which are essential to the practical implementation of endothermic fuels in flight-weight heat exchangers, are effective in reforming fuels at operating conditions consistent with aircraft applications.
- Catalytic cracking can be carried out with good product selectivity, providing a fuel that should have excellent combustion characteristics.

Acknowledgments

This paper is based on work performed for the Air Force Wright Laboratory and NASA-Lewis Research Center. The authors gratefully acknowledge the technical contributions of Mr. John Hawkins (UTRC) for reactor testing, Dr. Marvin Glickstein (Pratt & Whitney) for reactor modeling and consultation, and Dr. Abdus S. Khan (Pratt & Whitney) for coatings.

References

Ely, J. F., and Huber, M. L., 1990, "NIST Standard Reference Database 4—NIST Thermophysical Properties of Hydrocarbon Mixtures."

Lander, H., and Nixon, A. C., 1971, "Endothermic Fuels for Hypersonic Vehicles," *Journal of Aircraft,* Vol. 8, No. 4, pp. 200–207.

Lipinski, J., Armstrong, J., Johnson, R., White, C., and Kretzinger, K., 1989, "Design, Fabrication, and Testing of a Boilerplate Endothermic Methylcyclohexane Fuel Heat Exchanger Reactor System," AFWRDC-TR-89-2045.

Nixon, A. C., Ackerman, G. H., Hawthorne, R. D., Ritchie, A. W., Henderson, H. T., and Bjorklund, I. S., 1964, "Vaporizing and Endothermic Fuels for Advanced Engine Application," AFAPL TDR 64-100, Parts I, II, and III.

Nixon, A. C., Ackerman, G. H., Faith, L. E., Hawthorne, R. D., Henderson, H. T., Ritchie, A. W., Ryland, L. B., and Shryne, T. M., 1967, "Vaporizing and Endothermic Fuels for Advanced Engine Application," AFAPL TDR 67-114, Parts I, II, and III.

Spadaccini, L. J., Colket, M. B., Marteney, P. J., Roback, R., Glickstein, M. R., and Stiles, A. B., 1993a, "Endothermic Fuel/Catalyst Development and Evaluation—Phase I," AFWRDC-TR-89-2141.

Spadaccini, L. J., Sobel, D. R., Colket, M. B., Marteney, P. J., and Glickstein, M. R., 1993b, "Endothermic Fuel/Catalyst Development and Evaluation—Phases II, III and IV," AFWL-TR-91-2126.

Downloaded 02 Jun 2010 to 171.66.16.105. Redistribution subject to ASME license or copyright; see http://www.asme.org/terms/Terms_Use.cfm

Differential Mass and Energy Balances in the Flame Zone From a Practical Fuel Injector in a Technology Combustor

D. L. Warren
Mechanical Engineering Department.

P. O. Hedman
Chemical Engineering Department.

Advanced Combustion Engineering Research Center,
Brigham Young University,
Provo, UT 80642

This paper presents further analysis of experimental results from an Air Force program conducted by researchers at Brigham Young University (BYU), Wright-Patterson Air Force Base (WPAFB), and Pratt and Whitney Aircraft Co. (P&W) (Hedman et al., 1994a, 1995). These earlier investigations of the combustion of propane in a practical burner installed in a technology combustor used: (1) digitized images from video and still film photographs to document observed flame behavior as fuel equivalence ratio was varied, (2) sets of LDA data to quantify the velocity flow fields existing in the burner, (3) CARS measurements of gas temperature to determine the temperature field in the combustion zone, and to evaluate the magnitude of peak temperature, and (4) two-dimensional PLIF images of OH radical concentrations to document the instantaneous location of the flame reaction zones. This study has used the in situ velocity and temperature measurements from the earlier study, suitably interpolated, to determine local mass and energy balances on differential volume elements throughout the flame zone. The differential mass balance was generally within about ±10 percent with some notable exceptions near regions of very high shear and mixing. The local differential energy balance has qualitatively identified the regions of the flame where the major heat release is occurring, and has provided quantitative values on the rate of energy release (up to -400 kJ/m^3 s). The velocity field data have also been used to determine Lagrangian pathlines through the flame zone. The local velocity and temperature along selected pathlines have allowed temperature timelines to be determined. The temperature generally achieves its peak value, often near the adiabatic flame temperature, within about 10 ms. These temperature timelines, along with the quantitative heat release data, may provide a basis for evaluating kinetic combustion models.

Introduction

As part of an earlier study, a practical fuel injector was used in a technology combustor to investigate flame behavior in a jet engine combustor (Hedman et al., 1994, 1995). This earlier study investigated the combustion of gaseous propane with a practical injector installed in a technology combustor that simulates the flow and geometric characteristics of a real jet engine (Sturgess et al., 1992). The technology combustor with the practical high swirl injector is referred to in this paper as the Task 150-HS combustor. These previously reported experimental results were obtained from identical technology combustors located at both BYU and WPAFB. This earlier study was conducted as part of an ongoing investigation into the combustion characteristics of jet engine combustors that has been conducted by the Aero Propulsion and Power Laboratory at Wright Patterson Air Force Base, Pratt and Whitney Aircraft, Inc., and Brigham Young University.

The earlier study used: (1) digitized film and video images to document flame behavior as fuel equivalence ratio was varied, (2) sets of LDA data to quantify the velocity flow fields existing in the burner, (3) CARS measurements of gas temperature to determine the temperature field in the combustion zone, and to evaluate the magnitude of peak temperature, and (4) two-dimensional PLIF images of OH radical concentrations to document the instantaneous location of the flame reaction zones.

The LDA measurements presented previously (Hedman et al., 1994, 1995) have quantified the axial, radial, and tangential velocity components in the combustor for two operating conditions (ϕ = 0.72 and ϕ = 1.49) at an air flow rate of 500 slpm. This information has yielded local mean axial and radial velocity data in the flame zone. CARS gas temperature data were also collected for the Task 150-HS technology at an air flow rate of 500 slpm and at fuel equivalence ratios (ϕ) of 0.75, 1.00, 1.25, and 1.50.

The appropriately interpolated mean gas temperatures for ϕ = 0.75 and 1.50, along with the companion set of gas velocity data, have been used to determine the local mass balance on differential volumes through the flame zone, to determine a local differential energy balance (local energy release rate), Lagrangian pathlines, and temperature time lines through selected regions of the flame. This additional analysis of the measured mean flow and temperature properties was conducted in an attempt to gain additional insights about the combustion processes, and to provide some rate data that might be useful in the evaluation of kinetic models of the combustion processes.

Combustor Test Facility

The Task 150-HS combustor utilized in this study was a modification of a burner designed to investigate lean blowout in the combustors of aircraft gas turbine engines (Sturgess et al., 1992). The Task 150-HS burner, shown schematically in Fig. 1, uses a practical liquid fuel injector with air blast atomi-

Contributed by the International Gas Turbine Institute and presented at the 40th International Gas Turbine and Aeroengine Congress and Exhibition, Houston, Texas, June 5–8, 1995. Manuscript received by the International Gas Turbine Institute February 10, 1995. Paper No. 95-GT-112. Associate Technical Editor: C. J. Russo.

Copyright © 1997 by ASME

Downloaded 02 Jun 2010 to 171.66.16.105. Redistribution subject to ASME license or copyright; see http://www.asme.org/terms/Terms_Use.cfm

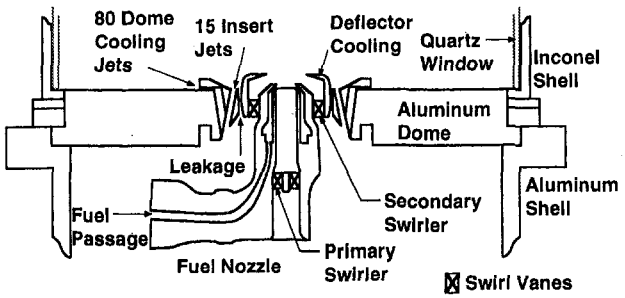


Fig. 1 Schematic of the T150-HS injector

zation, involving coswirling airsheets on either side of a coswirling annular (normally liquid) fuel sheet. The outer air passage and the fuel passage both converge on the central air passage. For this study, the burner was fueled by gaseous propane. Only data from a high-swirl configuration are reported in this paper.

The geometry of the technology combustor is shown schematically in Fig. 2. The cross section of the combustion chamber is square with filleted corners to minimize secondary flow development. The hydraulic diameter is 150 mm. This box-section combustor with corner fillets allows reasonable optical access while providing a cross section that approximates a two-dimensional axisymmetric cross section. The bluff body provides a recirculation region, which can stabilize the flame. Optical windows of fused quartz, about 60 mm in width and 490 mm in length, are provided on the four flat sides to allow laser-based optical diagnostic instruments to be used. Exit blockage of 45 percent is achieved by means of an orifice plate. The only air addition in this configuration is through the dome. This configuration allows measurements to be made in a geometry that embodies features of an actual jet engine combustor, but in a near axisymmetric configuration that is easier to model mathematically.

The combustor is mounted on a 240-mm-long spool piece containing a mounting pad for the fuel injector flange. The combustor and spool piece are situated on an inlet air conditioning section, also shown in Fig. 2. Reactants are supplied at ambient temperature and pressure. Ignition is by means of a removable torch-ignitor.

In an actual engine combustor, additional combustion and cooling air is added to the combustor downstream of the actual fuel injector. This adds an additional complexity to the flow and combustion characteristics, which has not been a part of this investigation. Only the analyses of the flame zone near the injector are presented in this paper.

The work reported herein was accomplished in identical combustors available in the Combustion Laboratories at BYU and WPAFB, respectively. The combustors were designed by researchers at P&W (Sturgess et al., 1992) and fabricated at WPAFB. The high-swirl (HS) injector has a nominal swirl number (based on vane angle) of 1.41, a total air passage effective area of 0.176 in.^{2}, and outer to inner flow splits of 2.8. The outer swirler vane angle was 55 deg. The inner swirler vane angle was 70 deg. The injector was mounted in a plain bulkhead dome containing insert jets angled at 12.5 deg into the flame, and radially outward flowing film cooling jets. This arrangement closely simulates that of an engine combustor. The total effective air flow area of the dome, excluding the fuel injector, was 0.160 in^2.

In order to separate the effects of liquid fuel atomization and spray droplet evaporation from the effects associated with fuel/air mixing and aerodynamic flow pattern, the results reported in this paper were for experiments using only a gaseous propane fuel.

Photographic Flame Characterization

The structure of the flame zone with the Task 150-HS burner was found to be strongly dependent on the fuel equivalence ratio (Hedman et al., 1994). The flame attaches to the burner or lifts from the burner as the fuel equivalence ratio (ϕ) is changed. Each flame shape indicates a different mode of operation, which differ from one another in the location of the flame fronts, or by some structure such as thickness or intensity. The different structures observed arise from changes in the flow fields, mixing patterns, or fuel equivalence ratio as operating conditions are varied.

Isochromatic contours from digitized and filtered video images have been used to record the flame shapes observed visually. Example images at ϕ = 0.75, 1.00, 1.25, and 1.50 are presented in Fig. 3 to provide the reader an indication of the variation in flame structure as ϕ is changed from fuel-lean to fuel-rich operation. The fuel equivalence ratios where the flame transitions from one flame structure to another were determined as a function of fuel flow rate. The flames for both Task 150 injectors were attached to the outside of the insert air jets when the burner was operated very fuel-rich. The flame would then lift, reattach, and lift again as the fuel equivalence ratio was progressively reduced depending on the injector (high swirl versus low swirl) and the air flow rate. During the reattachment phase, the flame would take on many of the characteristics of a strong vortex.

The observed characteristics of the flame as the fuel equivalence ratio was varied were discussed previously (Hedman et al., 1994). However, there are two structures that are of particular interest to this study, those at ϕ = 0.75 and ϕ = 1.50. At ϕ = 0.75, the flame was strongly attached to the center of the burner. At ϕ = 1.50, the flame was lifted, and seemed to be attached to the supplemental air entering the burner through the insert jets. Evaluation of the local stoichiometry from an air flow partitioning analysis showed that in this fuel-rich case, the local fuel equivalence ratio directly over the injector was in excess of the rich flammability limit (Hedman et al., 1994).

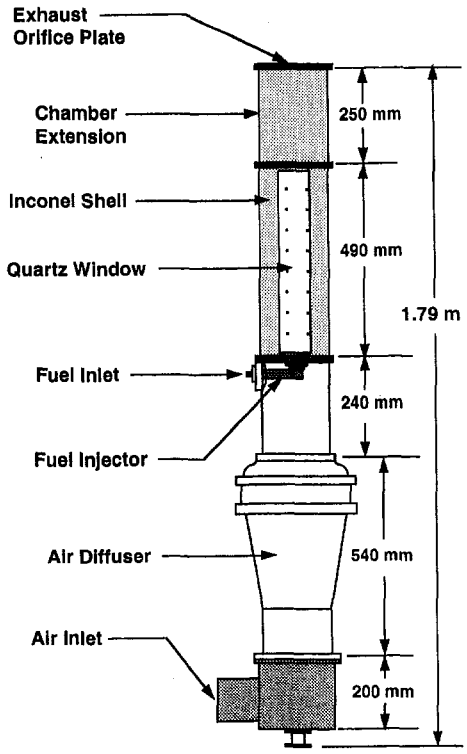


Fig. 2 Laboratory-scale gas turbine combustor (LSGTC)

Downloaded 02 Jun 2010 to 171.66.16.105. Redistribution subject to ASME license or copyright; see http://www.asme.org/terms/Terms_Use.cfm

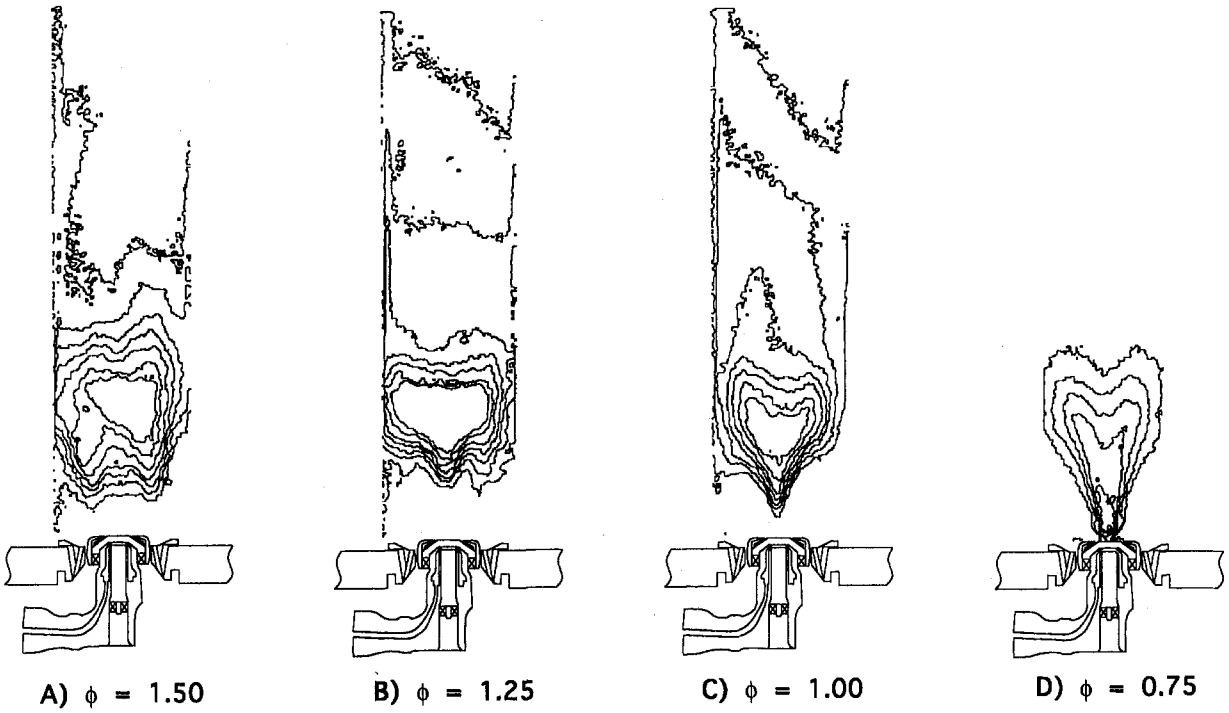


Fig. 3 Flame characteristics of the task 150-HS injector

Both mean gas velocity and mean gas temperature data were available for these two cases (ϕ = 0.75 and 1.50) from the earlier investigation (Hedman et al., 1994). Consequently, the differential mass balance, differential energy balance, pathline, and temperature timeline analyses were performed for these two specific cases and are discussed below.

Gas Velocity Measurements

LDA is a well-accepted diagnostic method for determining instantaneous gas velocity (e.g., Yeh and Cummins, 1964; Durst et al., 1976). Sample studies (Driscoll and Pelaccio, 1979; Zimmerman, 1985) are representative of the many investigations where velocity in combustion systems was determined using a LDA system.

A laser-Doppler anemometer (LDA) was used to make extensive measurements of mean and rms axial, radial, and tangential velocity data throughout the central part of the flame zone at two experimental conditions (500 slpm air flow rate, and ϕ = 0.72 and 1.49). These experimental data were reported in detail in the previous studies (Hedman et al., 1995; Hedman and Warren, 1994).

To obtain the local in situ data, the burner was translated along coordinate centerlines with respect to the laser diagnostic volume in X, Y, and Z coordinate directions. Translation in the X direction along the Y coordinate centerline allowed axial and radial velocity data to be obtained. The edge of the windows limited translation in this direction to about ±30 mm. Translation in the Y direction along the X coordinate centerline allowed axial and tangential velocity data to be obtained. As the diagnostic volume was brought near the quartz windows, significant optical noise was added to the Doppler signals. The quartz windows were approximately ±75 mm from the center of the reactor. The optical noise from the windows generally limited data collection to ±60 mm from the burner centerline.

Typically, data were collected at 0.5 or 1.0 mm radial increments where the velocity gradients were large. Data were collected at up to 10 mm increments where velocity profiles were relatively flat. A typical set of data was taken at axial locations of 10, 15, 20, 25, 50, 75, 100, 125, 150, 200, and 240 mm above the dome of the reactor. Occasionally, other intermediate locations were examined where large velocity gradients or other interesting behavior were found.

The radial and axial velocity data out to about ±30 mm from the centerline have been used in the differential mass and energy balance analysis, and in the pathline analysis. The mean radial and axial velocity data from the previous study (Hedman et al., 1995) for the two cases of interest (ϕ = 0.72 and 1.49) are summarized in Figs. 4 and 5. A more detailed discussion of the velocity results was made in the earlier paper. Figures 4 and 5 have been included in this paper to provide the reader with examples of the velocity results, and to provide an indication of the major flow features as evidenced by the isocontours of axial and radial velocity.

The LDA measurements shown in Figs. 4 and 5 are for the Task 150-HS burner. Mean radial and axial velocities are shown in Fig. 4 for lean conditions (ϕ = 0.72) where the flame was well attached to the central part of the injector, and in Fig. 5 for fuel-rich conditions (ϕ = 1.49) where the flame was attached to the dome and insert jets. Tangential velocity data do not affect either the differential mass or energy balances, and have not been shown herein. For the fuel lean case (ϕ = 0.72), the flame was fully attached to the center of the injector, and was relatively stable. The sharp peak in axial velocity component shown in Fig. 4 near the injector is clearly evident. The rapid decay of the high-velocity region near the injector as one moves downstream is also apparent. The recirculation zone directly over the injector is dramatic, and clearly shows a significant region of flow reversal. Recirculation patterns caused by the dome jets are not seen, but visual observations confirmed that recirculation in the corner between the dome and wall exists.

The radial velocity data are also presented in Fig. 4. These data are limited to a radial location of about 30 mm. The radial flow velocities are all very low in magnitude, but do show some interesting structures. The low magnitudes of these velocities are close to the resolution of the LDA instrument. A similar set of gas velocity data for the Task 150-HS combustor operating at a fuel equivalence ratio of 1.49 is presented in Fig. 5 for the mean axial and radial velocity measurements. The flame at this

Downloaded 02 Jun 2010 to 171.66.16.105. Redistribution subject to ASME license or copyright; see http://www.asme.org/terms/Terms_Use.cfm

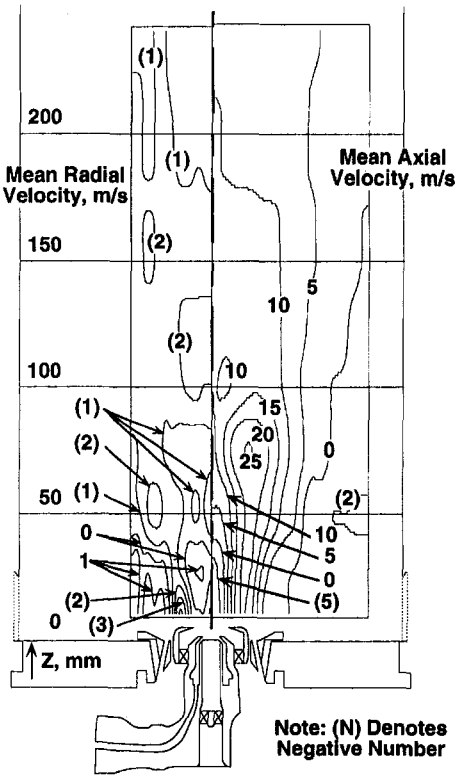


Fig. 4 Isovelocity contours at ϕ = 0.72 (T150-HS burner, 500 slpm air flow)

operating condition was attached to the insert and dome jets. As in Fig. 4, the radial data in Fig. 5 are limited to a radial location of about 30 mm, but the axial data in Fig. 5 were a composite of those collected along with both the radial (ca ± 30 mm) and the tangential (ca ± 60 mm) sets of data.

As for the ϕ = 0.72 case, the sharp peaks in mean axial velocity component associated with the injector are still clearly evident, but seem to decay more rapidly in the ϕ = 1.49 case. The recirculation zone directly over the injector is still dramatic, and shows little difference in the magnitude of the reversed velocity or in the size and shape of the recirculation pattern when compared to the ϕ = 0.72 case. The other major recirculation pattern in the combustor is of a similar shape to that observed with the ϕ = 0.72 case, but seems to be much stronger (i.e., has much larger reversed flow velocity components). The recirculation patterns caused by the dome jets are still absent. As with the ϕ = 0.72 case, visual observations confirmed that the corner recirculation still existed in this combustion flow case, but it was not possible to collect LDA close to the window near the bottom of the reactor because of optical noise near the quartz windows.

The radial velocity data for the ϕ = 1.49 case are also presented in Fig. 5. Again, the radial flow velocities are all very low in magnitude, but do show interesting structures that are quite different than seen with the lean flame. The low magnitudes of these velocities are also close to the resolution of the LDA instrument.

The differences in velocities between the lean flame and the rich flame show that there is a strong influence of the location of the flame zone on the flow fields as characterized by the measured velocity fields.

Lagrangian Pathline Analysis

Lagrangian pathlines were generated from the mean radial and axial velocity data by tracking fluid particles in the axial-radial flow field. The particles were introduced into the properly interpolated velocity data set at equally spaced positions along the sides and bottom of the flow field. Each particle's position was monitored as a function of time. Selected pathlines are presented in Figs. 6 and 7 for the ϕ = 0.72 and 1.49 cases of interest. The pathline analysis was only done for one-half of the combustor, doubled and reversed on the computer, and superimposed on the other side of the chamber.

These pathlines show two vortex centers and a stagnation point. The stagnation point occurs on centerline about 30 mm downstream of the injector. The vortex centers are associated with the recirculation zone just above the injector and the zone just outside the funnel shaped vortex. These pathlines give detailed information on the boundaries and intersections of the flow regions of the burner.

Comparing the pathlines for the two cases yields even subtler observations about the flow structure. The near injector region, in particular, shows significant differences. The stagnation point has moved slightly and the recirculation zones have changed accordingly in the fuel rich case (ϕ = 1.49, Fig. 7). Along the bottom, the flow between 15 and 30 mm is no longer axially positive, indicating a change in the outer recirculation zone. The small recirculation zone directly over the injector observed at ϕ = 0.75 (Fig. 6) is much smaller when ϕ = 1.50 (Fig. 7).

These Lagrangian pathlines mark representative reaction paths through the flame zone. As such, they have been used in a subsequent section to determine temperature time lines along representative paths in the base recirculation zone, in the mid or central recirculation zone just above the injector, and along a path leaving the injector and flowing directly out of the combustor for both the ϕ = 0.72 and 1.49 cases.

Gas Temperature Measurements

Eckbreth (1988) provides an excellent summary of CARS, a proven technique for determining gas temperature and limited

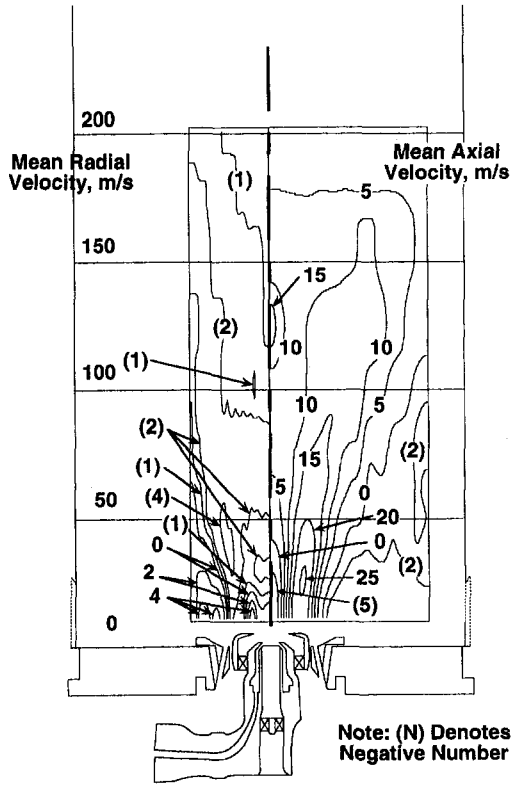


Fig. 5 Isovelocity contours at ϕ = 1.49 (T150-HS burner, 500 slpm air flow)

Downloaded 02 Jun 2010 to 171.66.16.105. Redistribution subject to ASME license or copyright; see http://www.asme.org/terms/Terms_Use.cfm

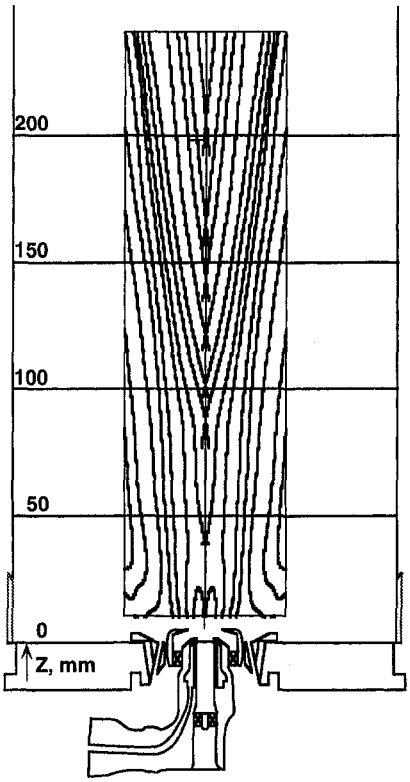


Fig. 6 Mean flow pathlines at ϕ = 0.72 (T150-HS burner, 500 slpm air flow)

species concentrations in turbulent combustion environments. Representative studies (Eckbreth et al., 1984, Greenhalg, 1987; Goss et al., 1988; Boyack and Hedman, 1990; Hancock et al., 1991; Zhu et al., 1993) provide examples of the broad application of CARS to obtain temperature and/or species concentration in combustion environments. The BYU CARS instrument has been described in detail elsewhere (Boyack and Hedman, 1990; Hancock et al., 1991).

Coherent anti-Stokes Raman spectroscopy (CARS) was used to obtain a set of gas temperature measurements in the Task 150-HS combustor at ϕ = 0.75, 1.00, 1.25, and 1.50; and at an air flow rate of 500 slpm (Hedman et al., 1994). Like the gas velocity measurements, the CARS temperature measurements were taken at closely spaced radial increments where large gradients in temperature were found and in a courser grid where the temperature gradients were relatively shallow. Temperature data were taken at similar axial locations as well. The temperature data were taken along the X coordinate, and consequently are available only out to a radius of about 30 mm, but were taken to an axial location of about 300 mm.

Figure 8 and 9 present isocontour plots of mean temperature data for the Task 150-HS combustor operating with an air flow rate of 500 slpm and at fuel equivalence ratios of 0.75 and 1.50, the two cases of interest in this paper. The isocontour plots were duplicated, flipped, and added to the opposite side of the combustor to give a better representation of the temperature field in the vicinity of the injector.

The relatively cold region (600 K to 1000 K) directly above the injector in both cases generally corresponds the central recirculation zone seen in the gas velocity plots (Figs. 4 and 5). Surrounding the cold central zone is an intermediate temperature region that seems to be associated with the penetration of the very high axial velocity into the combustor. Higher temperatures exist on either side of this penetration zone. It is unfortunate that temperature data could not be obtained in the lower corners of the combustor where the recirculation zones near the dome are located. The data do suggest that this region is relatively cool for the ϕ = 0.75 case, but seem to indicate a relatively hot region in this corner recirculation zone for the ϕ = 1.5 case. This observation seems to be consistent with the observed relocation of the flame zone from the central core of the vortex when operating fuel-lean to the outer recirculation zone when operating fuel-rich.

For the ϕ = 0.75 case, the peak temperature measured was 2085 K, which is about 178 K below the theoretical stoichiometric (ϕ = 1.00) adiabatic flame temperature of 2263 K. The peak temperature (1875 K) in the fuel-rich case is about 99 K below the predicted adiabatic flame temperature of 1974 K for ϕ = 1.50.

Differential Control Volume Analysis

With both mean temperature and mean velocity data sets available at identical flow conditions, it became possible to combine the information to extract information unmeasurable by other means, which gives further insights into the combustion processes. To accomplish this analysis, it was necessary to adapt numerical methods normally employed for theoretical modeling to extract these additional observations (differential mass and energy balances, and temperature timelines through the flame from the Lagrangian pathline analysis) from the experimental results.

This study made use of differential control volumes, commonly used in thermal and fluid sciences, to determine the local mass and energy balance throughout the flame zone. The shape of a control volume is arbitrary but is always bounded by a closed control surface. For this analysis, the cylindrical steady-state finite difference control volumes illustrated in Fig. 10 were used. Each cylindrical control volume has four distinct sides across which mass and energy transfer. The region over which data were collected was divided into control volumes 1 mm wide and 2 mm high rotated about the centerline. Since a region

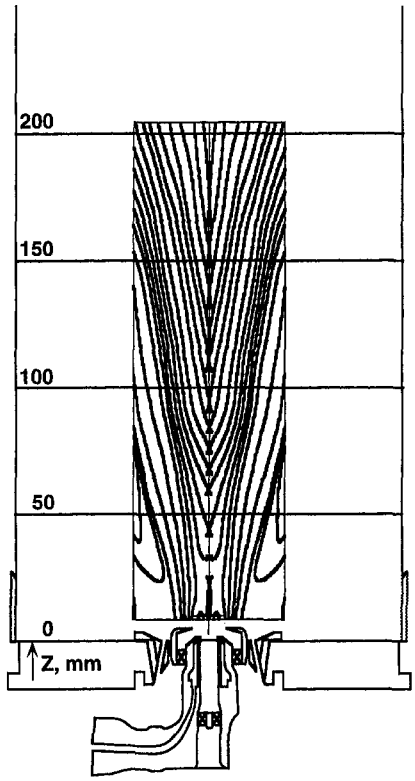


Fig. 7 Mean flow pathlines at ϕ = 1.49 (T150-HS burner, 500 slpm air flow)

Downloaded 02 Jun 2010 to 171.66.16.105. Redistribution subject to ASME license or copyright; see http://www.asme.org/terms/Terms_Use.cfm

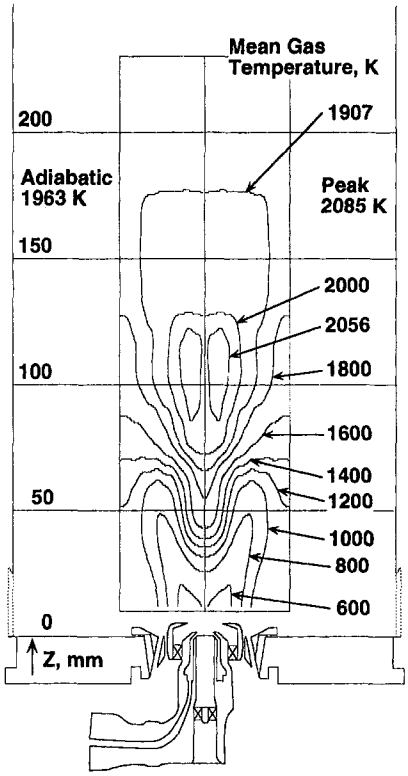


Fig. 8 Isotemperature contours at ϕ = 0.75 (T150-HS burner, 500 slpm air flow)

of about 30 mm from the centerline and from 10 mm to 200–240 mm in axial coordinate was analyzed, about 2850 to 3450 separate cylindrical control volumes were considered in the

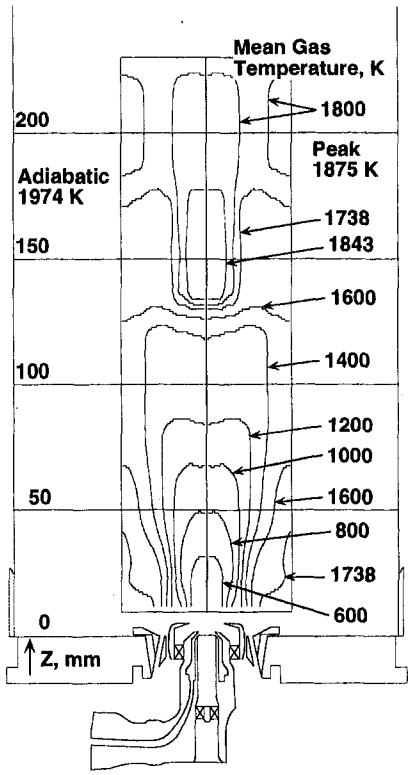


Fig. 9 Isotemperature contours at ϕ = 1.50 (T150-HS burner, 500 slpm air flow)

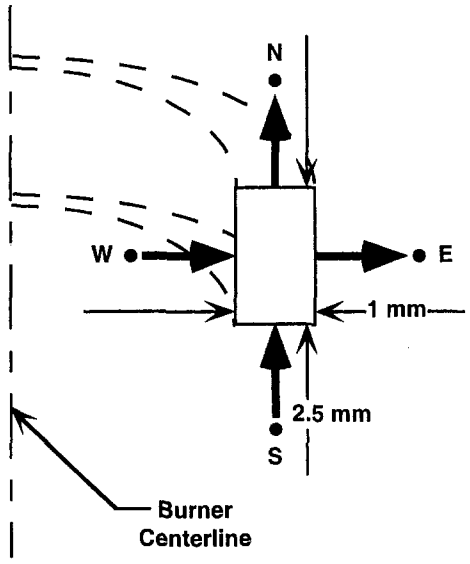


Fig. 10 Differential two-dimensional axisymmetric control volume

flame zone. Suitable interpolation of the velocity and temperature data provided the velocities and temperatures at the boundaries of each of the control volumes to be determined.

The first check done on the control volumes was to check the mass storage term. Being at steady state, the mass entering the control volume should be balanced by the mass leaving the control volume. The mass crossing any given side of the control surface was calculated from

$$\dot{m} = \rho V A \tag{1}$$

where

$\dot{m}$ is the mass flux,
ρ is the gas density,
V is the velocity perpendicular to the control surface,
and A is the area of the side.

Some estimate of the density must be made to use this equation. Density is a function of temperature, pressure, and gas composition. Pressure and composition were not measured in this study and therefore were approximated. The pressure was assumed to be constant at 1 atm. All properties that depended upon composition were calculated assuming the physical properties of air. Although temperature data were interpolated to obtain control volume temperatures, the temperature used in the density calculation was based on an upwind scheme. In this scheme, if the vertical velocity carried mass from the control volume labeled S (south) into the P control volume, the mass flux is considered to have the properties associated with the characteristics of the S control volume. By applying these assumptions to each side of the control volumes, estimates for the mass fluxes were obtained. These results were used to calculate an estimated conservation of mass error for each control volume in the combustor using Eq. (2). This local error provides an estimate on the quality of data, and indicates regions where high quality data are difficult to obtain.

$$\text{percent error} = \frac{\text{mass}_{\text{in}} - \text{mass}_{\text{out}}}{\text{mass}_{\text{in}}} \times 100 \text{ percent} \tag{2}$$

Images of the local "conservation of mass" error are presented in Figs. 11 and 12 for ϕ = 0.75 and 1.50, respectively. In general, the error in local mass balance was less than ±10 percent. There were exceptions in regions of the burner where the local error exceeded ±20 percent for the ϕ = 0.75 case, and ±50 percent for the ϕ = 1.50 case. These areas were in

Downloaded 02 Jun 2010 to 171.66.16.105. Redistribution subject to ASME license or copyright; see http://www.asme.org/terms/Terms_Use.cfm

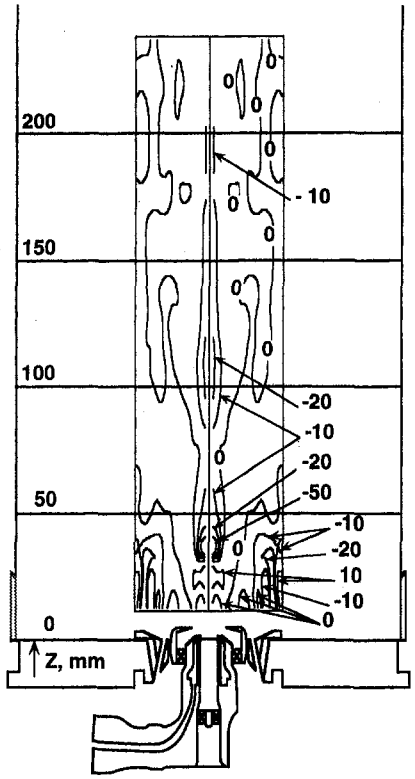


Fig. 11 Differential mass balance (percent) at $\phi = 0.75$ (T150-HS burner, 500 slpm air flow)

the high shear areas associated with the insert jets, or the strong recirculation zone on the centerline just above the injector.

Calculation of the enthalpies and kinetic energies associated with each mass flow was a relatively simple process. Initial efforts for the energy balance, however, were met with failure. The amount of energy being transported through each control volume is much greater than the amount being released. Thus, even small errors in mass balance cause severe numerical noise. A simpler, more robust scheme was developed that forced the mass balance before doing the energy calculations.

The simplified scheme calculated the heat release in a given control volume using:

$$H_r = \dot{m} \times (h_{in} - h_{out}) \tag{3}$$

where:

H_r is the energy release
$\dot{m}$ is the net mass flux into the volume.
h_{in} is the net enthalpy of the gas entering the volume
h_{out} is the net enthalpy of the gas leaving the volume

The incoming thermal energy is associated with the incoming mass and its enthalpy; the outgoing energy calculation was done with the mass entering the control volume and the characteristics of the control volume (as per the upwind scheme). This scheme has the significant advantage of not losing mass and its associated energy while lacking only the capability of calculating the kinetic energy (due to the unknown outgoing velocities). In the relatively low velocity flows in this study, kinetic energy (~0.2 kJ/kg) was negligible in comparison to the thermal energy (150 kJ/kg) being released by the combustion processes, and was neglected in the energy balances performed.

The calculated heat release has been reported as the total heat release in the differential control volume per unit time normalized by the differential volume. Images mapping the heat release per unit volume are presented in Figs. 13 and 14 (ϕ = 0.75 and ϕ = 1.50, respectively) and can be compared to the isochromatic video images (Fig. 3(*D*) and 3(*A*)) for the same test conditions. Figure 13 is remarkable in its similarity to the visible flame. The fuel-rich case (ϕ = 1.5) reveals a band of energy release about 125 mm downstream. This extra energy release is likely the result of the hot, fuel-laden combustion products encountering more oxygen, most likely from the dome jets. This region of higher energy release generally corresponds to the visual flame structure (Fig. 3(*A*)). In general, the flame structure at the fuel-rich condition (ϕ = 1.5) is not as coherent as the structure observed for the lean condition. This is evident in both the energy release contour plots and in the digitized video images.

An integration of the energy released was also done over the entire computational domain. The computational domain was limited by the optical access into the burner and did not include the entire combustion zone. The result of the integrations, along with the chemical energy being introduced into the burner, is summarized in Table 1. There are some factors that are not considered. Radiation heat losses and heat release, which take place outside the computational field of view, were not considered. Also, the chemical energy that left the combustor as unburned fuel was not included.

Table 1 reports the amount of thermal energy being released and the chemical energy being released. The thermal energy being released does not include any corrections for radiation losses nor does it include any energy released outside the computational range.

At ϕ = 0.75, almost 79 percent of the energy introduced into the burner is released in the computational flame zone analyzed. However, at ϕ = 1.50, only about 21.5 percent of the energy introduced into the burner as fuel is released in this zone. The large discrepancy in the fuel-rich case is thought to be primarily due to heat release outside the computational field (e.g., in the corner recirculation zone) and chemical energy leaving the system as unreacted fuel.

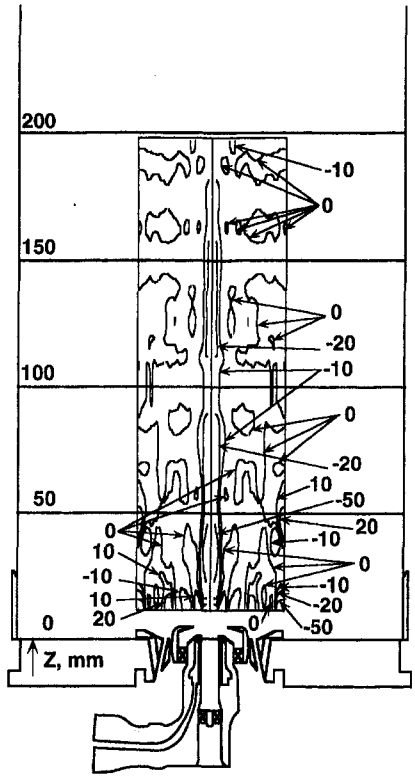


Fig. 12 Differential mass balance (percent) at $\phi = 1.50$ (T150-HS burner, 500 slpm air flow)

Downloaded 02 Jun 2010 to 171.66.16.105. Redistribution subject to ASME license or copyright; see http://www.asme.org/terms/Terms_Use.cfm

Temperature Timelines

The local velocity and temperature data were combined with the Lagrangian pathline analysis in an attempt to gain some additional insights about the reactions rates associated with the combustion of the propane fuel. In this analysis, the combination of velocity data along a pathline allowed the time as a function of position to be easily determined. The convolution of this time and position with the known local temperature allowed temperature timelines along the Lagrangian pathline to be determined. As the fluid particle traces out the pathline, both the elapsed time and the particle's position are known.

By referencing the particle's position to the temperature field, a temperature versus time plot was obtained for that fluid particle. Examples of the temperature timelines for selected pathlines are presented in Figs. 15 and 16 for the ϕ = 0.75 and 1.50 cases, respectively. Temperature timelines on pathlines leaving the injector, in the base recirculation zone, and in the midrecirculation region are shown.

The timeline plots give considerable insight about the combustion rate of the propane fuel. The timeline data presented include the effects associated with the turbulent mixing of the fuel and air in the diffusion burner, and the chemical kinetics of the complex reaction mechanisms associated with the oxidization of propane. In the fuel lean case, Fig. 15, the three curves (injector, midrecirculation, and base recirculation) are very similar. Each curve has an almost identical slope. The similar slopes indicate that each fluid particle experienced similar combustion rates. The particles in the midrecirculation zone also lost energy (i.e., lower temperature) before entering a reaction zone. These decreases were likely due to the mixing of more fuel and air mixture from the injector. This conclusion is supported in the base recirculation zone, which lost even more temperature in the mixing prior to reaction, but also gained more temperature during combustion. This figure implies the primary combustion zone lies on the boundary of the injector flow and the outside recirculation zone.

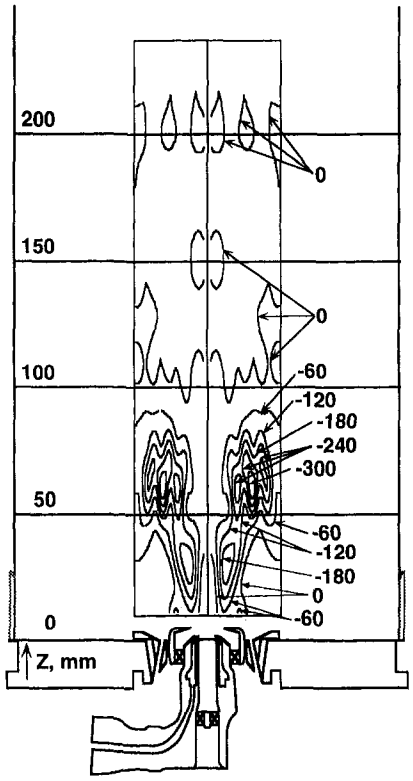


Fig. 13 Energy release (kJ/m^3·s) at ϕ = 0.75 (T150-HS burner, 500 slpm air flow)

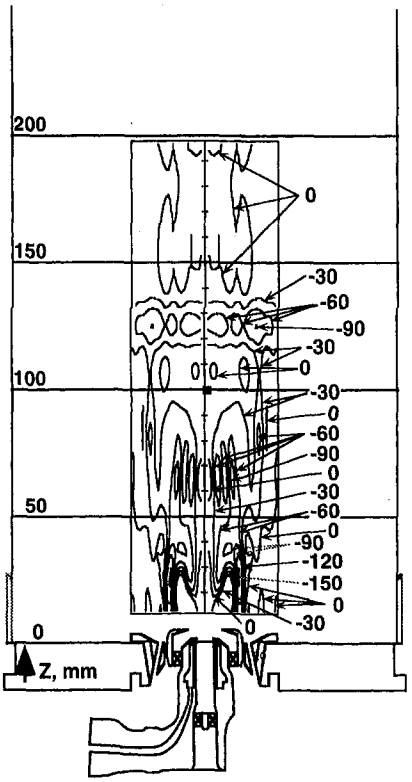


Fig. 14 Energy release (kJ/m^3·s) at ϕ = 1.50 (T150-HS burner, 500 slpm air flow)

In the fuel-rich case, Fig. 16, only the particle that started near the injector underwent a large temperature change. These particles began with a temperature higher than the temperature of the reactants being introduced into the chamber through the injector. This high temperature was slightly cooled before entering the combustion zone, indicating the injected gases mixed with the hot recirculation products prior to mixing with the injector combustor air stream.

Comparing Figs. 15 and 16 with the corresponding CARS temperature figures (Figs. 8 and 9) confirms the same trends observed in the CARS data, namely, the recirculation zone when ϕ = 1.50 was much hotter than when ϕ = 0.75. The rate of temperature rise was nearly double (300,000–400,000 K/s) for the lean case than for the fuel-rich (ca 150,000 K/s) suggesting either a slower diffusion process or again, a slower combustion process for the richer case.

Observations and Conclusions

This study has contributed to an improved understanding of the operational characteristics of a practical injector. However, much more needs to be done before a full understanding of the combustion characteristics of a practical gas turbine combustor is achieved.

The location of the flame fronts, the flame shape, and the stability of the flame were found to be a strong function of the fuel equivalence ratio. The different flame structures arose from changes in the flow fields and mixing patterns as fuel equivalence ratio was varied. The flames were attached to the insert air jets when the burner was operated very fuel-rich, but would lift, reattach, and lift again as the fuel equivalence ratio was progressively reduced. When attached to the burner, the flame took on the characteristics of a strong vortex flow. Two different flame structures were the subject of this analysis, one where the flame was well attached to the injector (ϕ = 0.72), and one at fuel-rich conditions (ϕ = 1.49) where the flame was attached to the dome and insert jets.

Downloaded 02 Jun 2010 to 171.66.16.105. Redistribution subject to ASME license or copyright; see http://www.asme.org/terms/Terms_Use.cfm

Table 1 Energies associated with the task 150-HS burner

Phi	Thermal Energy Released (kW)	Chemical Energy Introduced (kW)
0.75	16.3	20.7
1.50	8.9	41.4

Gas velocity measurements were made with an LDA at both the fuel-lean ($\phi = 0.72$) and fuel-rich conditions ($\phi = 1.49$). Gas velocity data near the injector have shown sharp peaks in mean axial velocity near the outlet of the injector, and a corresponding strong tangential component in this same location. The insert jets had a marked influence on the axial and radial components. The sharp gradients in axial and tangential velocity components decayed rapidly, becoming nearly uniform across the duct by the 150 mm axial location.

CARS gas temperature measurements were also made in the Task 150-HS combustor. The variation in temperature field as the fuel equivalence ratio changes from fuel-lean to fuel-rich was consistent with the observations made from the digitized video images. In general, the temperature measurements were consistent with visual flame observations, PLIF images of the OH radical, and velocity measurements.

A differential control volume analysis was used to compute mass and energy balances on 1 mm by 2 mm cylindrical control volumes throughout the computational flame zone. The mass balance showed modest errors through most of the flame (ca ± 10 percent) except near regions of high shear and mixing (insert jets and central recirculation zone) where differential mass balance errors of about ±20 percent were seen for the fuel lean case, and ±50 percent for the fuel rich case.

The differential energy balance analysis showed the regions of high energy release very well, and provided quantitative values for the rate of energy release in the flame zone (up to ca 400 kJ/m^3·s at $\phi = 0.75$ and ca 200 kJ/m^3·s at $\phi = 0.75$). This technique worked best when the flame consumed nearly all chemical energy available within the computational field of view.

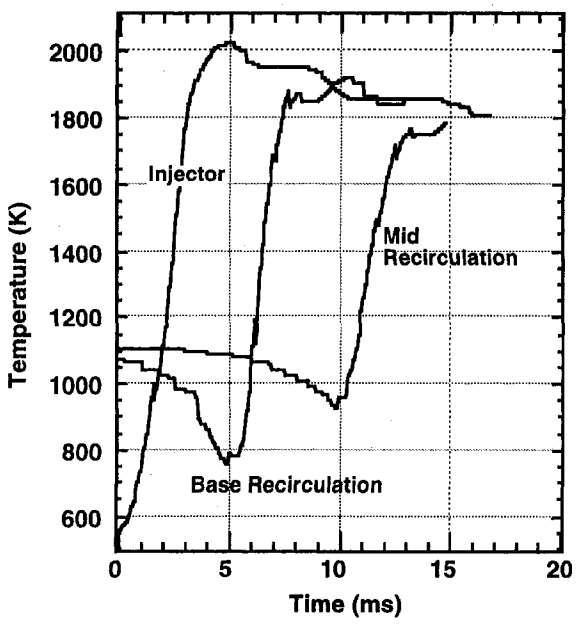


Fig. 15 Temperature–time histories along selected pathlines through the flame zone (500 slpm air flow, $\phi = 0.75$)

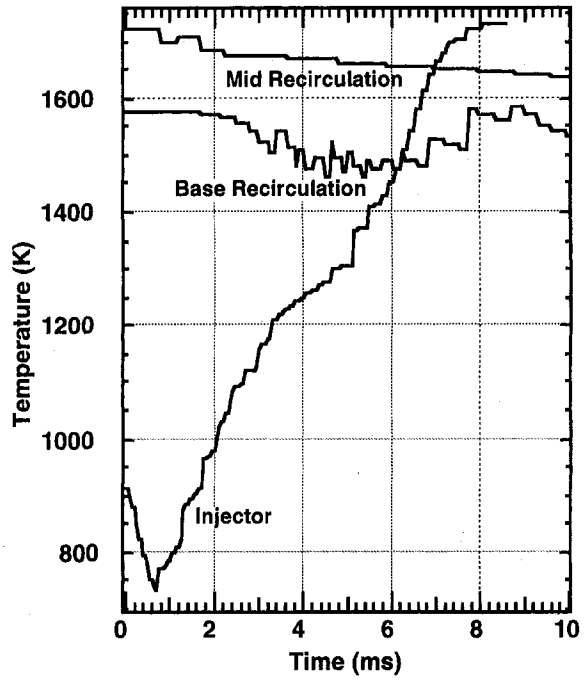


Fig. 16 Temperature–time histories along selected pathlines through the flame zone (500 slpm air flow, $\phi = 1.5$)

The local mean axial and radial velocity data were appropriately interpolated, and used to determine Lagrangian pathlines throughout the computational flame zone. These pathlines indicate regions of recirculation and stagnation points. They also provide a convenient locus of gas particles through the flame zone, which can be used to track path dependent combustion phenomena. These pathlines along with the local velocity and temperature were used to deduce temperature timelines throughout the computational flame zone. These temperature timelines show that complete combustion of propane, including mixing and chemical reaction rate effects, takes from 5 to 10 ms to occur depending on path and overall stoichiometry. The analysis also shows temperature rise rates of about 150,000 K/s for the fuel-rich ($\phi = 1.50$) case, and about 300,000–400,000 K/s for the fuel-lean ($\phi = 1.50$) case.

Acknowledgments

This paper presents results from an Air Force Office of Scientific Research (AFOSR) program being conducted at Brigham Young University (BYU), Provo, Utah, and at Wright-Patterson Air Force Base (WPAFB). This study is part of an extensive research effort being carried out by the Fuels Combustion Group of the Aero Propulsion and Power Laboratory at Wright-Patterson Air Force Base (APPL, WPAFB), Dayton, Ohio, in which simple and complex diffusion flames are being studied to better understand the fundamentals of gas turbine combustion. The program's long-term goal is to improve the design methodology of gas turbine combustors.

References

Boyack, K. W., and Hedman, P. O., 1990, "Dual-Stokes CARS System for Simultaneous Measurement of Temperature and Multiple Species in Turbulent Flames," *Twenty-Third Symposium (International) on Combustion,* The Combustion Institute, Pittsburgh, PA, pp. 1893–1899.

Driscoll, J. F., and Pelaccio, D. G., 1979, "Laser Velocimetry Measurements in a Gas Turbine Research Combustor," *Laser Velocimetry and Particle Sizing,* Proc. Third International Workshop on Laser Velocimetry, D. H. Thompson and W. H. Stevenson, eds., Hemisphere publishing Co., Washington, DC.

Durst, F. A., Melling, A., and Whitelaw, J. H., 1976, *Principles and Practice of Laser Anemometry,* 1st ed., Academic Press, London.

Downloaded 02 Jun 2010 to 171.66.16.105. Redistribution subject to ASME license or copyright; see http://www.asme.org/terms/Terms_Use.cfm

Eckbreth, A. C., 1988, *Laser Diagnostics for Combustion Temperature and Species,* Abacus Press, Cambridge, MA.

Eckbreth, A. C., Dobbs, G. M., Stufflebeam, J. H., and Tellex, P. A., 1984, "CARS Temperature and Species Measurements in Augmented Jet Engine Exhausts," *Applied Optics,* Vol. 23, pp. 1328–1339.

Goss, L. P., Trump, D. D., and Roquemore, W. M., 1988, "Combined CARS/LDA Instrument for Simultaneous Temperature and Velocity Measurements," *Experiments in Fluids,* Vol. 6, Springer-Verlag, pp. 189–198.

Greenhalg, D. A., 1987, "Quantitative CARS Spectroscopy," *Advances in Non-linear Spectroscopy,* Chap. V, R. J. H. Clark and R. E. Hester, eds., Wiley, New York.

Hancock, R. D., Hedman, P. O., and Kramer, S. K., 1991, "Coherent Anti-Stokes Raman Spectroscopy (CARS) Temperature and Species Concentration Measurements in Coal-Seeded Flames," *Combustion and Flame,* Vol. 71, pp. 593–604.

Hedman, P. O., and Warren, D. L., 1994, "Turbulent Velocity and Temperature Measurements From a Gas-Fueled Technology Combustor with a Practical Fuel Injector," Paper No. 25-705, The Twenty-Fifth International Symposium on Combustion, The University of California at Irvine, Irvine, CA.

Hedman, P. O., Sturgess, G. J., Warren, D. L., Goss, L. P., and Shouse, D. T., 1995, "Observations of Flame Behavior From a Practical Fuel Injector Using Gaseous Fuel in a Technology Combustor," ASME JOURNAL OF ENGINEERING FOR GAS TURBINES AND POWER, Vol. 117, pp. 441–452.

Sturgess, G. J., Sloan, D. G., Lesmerises, A. L., Heneghan, S. P., and Ballal, D. R., 1992, "Design and Development of a Research Combustor for Lean Blowout Studies," ASME JOURNAL OF ENGINEERING FOR GAS TURBINES AND POWER, Vol. 114, pp. 13–19.

Yeh, Y., and Cummins, H. Z., 1964, "Localized Fluid Flow Measurements With an He–Ne Laser Spectrometer," *Applied Physics Letters* Vol. 4, pp. 176–178.

Zhu, J. Y., Tsuruda, T., Sowa, W. A., and Samuelsen, G. S., 1993, "Coherent Anti-Stokes Raman Scattering (CARS) Thermonetry in a Model Gas Turbine Can Combustor," ASME JOURNAL OF ENGINEERING FOR GAS TURBINES AND POWER, Vol. 115, pp. 515–521.

Zimmerman, D. R., 1985, "Laser Anemometer Measurements of the Flow From a Simulated Fuel Nozzle," *International Symposium on Laser Anemometry,* A. Dybbs and P. A. Pfund, eds., Winter Annual Meeting of ASME, FL.

Downloaded 02 Jun 2010 to 171.66.16.105. Redistribution subject to ASME license or copyright; see http://www.asme.org/terms/Terms_Use.cfm

Numerical Simulation of Blade Fault Signatures From Unsteady Wall Pressure Signals

V. Dedoussis[1]

K. Mathioudakis

K. D. Papailiou

Laboratory of Thermal Turbomachines,
National Technical University of Athens,
P.O. Box 64069
Athens, 15710 Greece

A method for establishing signatures of faults in the rotating blades of a gas turbine compressor is presented. The method employs a panel technique for the calculation of the flow field around blade cascades, with disrupted periodicity, a situation encountered when a blade fault has occurred. From this calculation, time signals of the pressure at a location on the casing wall, facing the rotating blades, are constituted. Processing these signals, in combination with "healthy" pressure signals, allows the constitution of fault signatures. The proposed method employs geometric data, as well as data about the operating point of the engine. It gives the possibility of establishing the fault signatures without the need of performing experiments with implanted faults. The successful application of the method is demonstrated by comparison of signatures obtained by simulation to signatures derived from experiments with implanted blade faults, in an industrial gas turbine.

Introduction

A fundamental requirement for any diagnostic procedure is the existence of experience on the symptoms caused by the presence of a fault. These symptoms usually take the form of a "signature," which can be used for identifying the particular fault. The existence of a data base of fault signatures is an essential part of an automated diagnostic system, as it has been established today and has been discussed by many authors (e.g., Hewitt and Bosmans, 1991; Loukis et al., 1993). Building up such a data base, however, is a difficult task. The main alternative approaches that can be used are:

(*a*) A posteriori observations of failures occurring in operating engines.
(*b*) Observations from experimental investigations with implanted faults on the engines of interest.
(*c*) Computational modeling and simulation of faults.

Approach (*a*) may prove too costly, since occurrence of some of the failures can be catastrophic and engine users would have preferred it not to have happened anyway. On the other hand, if failures occur in an uncontrolled manner, it is not certain that all the necessary information can be collected for constituting the signatures. Finally, it is possible that long time intervals may be needed before a reliable knowledge base, with a reasonable coverage of fault cases, is assembled. These drawbacks can be overcome by setting up experiments, i.e., approach (*b*). Here, faults representative of realistic cases expected in field operation are implanted in engines and their influence on engine operation is studied. Such experiments are still very costly, while they provide information that is useful for particular engines and faults with specific characteristics and sevirities.

An efficient alternative way of producing fault signatures is via the application of approach (*c*), namely by computation. For this approach, the quantities employed for diagnosis are obtained by modeling both "healthy" and "faulty" operation, which are combined for the derivation of the signatures. The computed quantities and corresponding signatures should be obtained in direct correspondence to the actual measured quantities on an engine and the subsequent processing applied to the experimental data. Application of this approach requires a knowledge of the physics of the processes taking place in an engine, as well as a capability for describing them with models that are as accurate as possible.

Modeling overall engine behavior is a task that can be achieved without the need of application of complex numerical techniques. The simulation of faults related to aerothermodynamic performance is therefore a relatively straightforward task and has been undertaken by many authors. When fast response measurements are used, however, modeling may be very complex and limitations are imposed by the current computational capabilities for the relevant local phenomena such as vibration. For this reason, fault signatures for gas turbine faults have been mainly derived by experimentation. Only a few authors have attempted simulations of this kind. For example, Barschdorf and Korthauer (1986) have derived approximate fault signatures for turbomachinery blade faults, by using a semi-empirical approach on the form of the power spectra of unsteady pressure signals. Rihak and Schmidt (1992) applied a simplified model for shaft vibration, in order to predict shaft vibration features of turbomachines, for the purpose of optimal choice of a monitoring system.

The interest of the present work is focused on the case of blade faults of industrial gas turbines, which are to be identified by employing fast response instrumentation. In particular, fault signatures are derived for the case where wall casing unsteady pressure measurement is used for fault identification (see Fig. 1). The approach followed consists of first calculating the flow field both in healthy and faulty bladings. Unsteady pressure signals are then synthesized from the computed pressure fields. These signals are subsequently processed in the same way as the experimental data would have been processed (Mathioudakis et al., 1991).

Calculation of the Pressure Field in Non-periodic Cascades

Choice of Numerical Method. Over the years many numerical procedures, mainly field methods, have been developed that calculate the inviscid or viscous (laminar or turbulent) flow through two-dimensional (linear) or three-dimensional blade cascades (e.g., Lakshminarayana, 1991). In all these procedures

[1] Present address: Univ. of Piraeus, Dept. of Industrial Management.

Contributed by the International Gas Turbine Institute and presented at the 39th International Gas Turbine and Aeroengine Congress and Exposition, The Hague, The Netherlands, June 13–16, 1994. Manuscript received by the International Gas Turbine Institute February 25, 1994. Paper No. 94-GT-289. Associate Technical Editor: E. M. Greitzer.

Copyright © 1997 by ASME

Downloaded 02 Jun 2010 to 171.66.16.105. Redistribution subject to ASME license or copyright; see http://www.asme.org/terms/Terms_Use.cfm

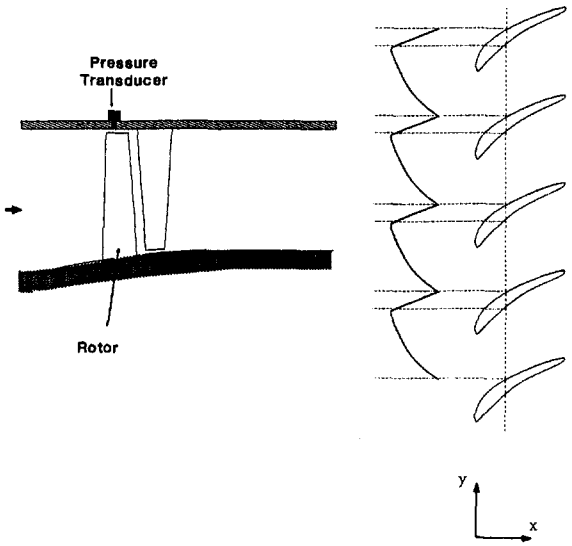


Fig. 1 Placement of fast response pressure transducer and corresponding points on the rotor cascade plane

advantage has been taken of the fact that the flow through a cascade of blades is periodic. The calculation, therefore, is carried out for a *single* passage only, with periodic boundary conditions on the lateral computational boundaries. This approach, however, cannot be applied directly to the case of cascades that contain blades locally different from the rest of the cascade. This is, for example, the case of a cascade containing blades unequally spaced or "faulty" blades, namely blades deformed from their original shape and position in the cascade. This is because the passages immediately before and after the faulty blade are not only different from one another, but also different from the "representative" passage of the cascade, the passage between intact blades of the cascade. It should be mentioned, however, that regardless of the kind of fault in an actual annular turbomachine blade row, periodicity is established for computational domains spanning the entire rotor circumference (locations spaced one full circumference apart, having identical local conditions).

Experimental observations (Mathioudakis et al., 1991) as well as a posteriori observations of the computational results, indicate that periodic conditions (to within engineering practice accuracy) are established after a few blade passages before and after a faulty blade of an ordinary blade row. Thus, the computational domain could extend over these passages, so that the periodic boundary conditions at the outermost lateral boundaries could be applied, without impairing the quality of the solution. It is apparent, therefore, that in order to compute this "multi"-passage flow using an ordinary (cascade flow) field solver, a multidomain strategy should be employed. Apart from the numerical and programming difficulties associated with the multidomain approach itself, extra effort is required for the construction of the computational grid, discretizing the passages immediately above and below the faulty blade.

In order to circumvent the aforementioned difficulties of field methods, a panel method (e.g., Hess and Smith, 1966), in conjunction with the so-called "multiple cascade approach" (to be explained in the following section) has been adopted in the present work. Panel methods reduce the dimensionality of the problem by one (instead of satisfying the flow equations in the two-dimensional domain around the body concerned, equations are satisfied on the surface—contour line—of the body). This feature results to computational algorithms that are very fast in comparison to field solvers, while they are numerically robust and quite accurate. The main drawbacks of panel methods are that they are limited to inviscid and mainly incompressible flow conditions. An interesting review on the role of panel methods in modern computational fluid mechanics has been published by Hess (1990).

Multiple Cascade Approach. The flow configuration of interest in this work consists of a *linear* cascade, which contains a "faulty" blade. The particular fault examined here consists of a single blade section, which is twisted with respect to the rest of the blades of the cascade, as presented schematically in Fig. 2(*a*). As is pointed out in the previous section, the effect of the faulty blade on the flow field dies out at a distance "far away" from it. This implicitly indicates that the effect of the geometric details of the cascade configuration "far away" from the considered point in the flow field is only marginal.

For the sake of argument, it is assumed that the effect of the faulty blade radiates up to two cascade spacings distance away from the blade. In accordance with these arguments, the actual geometry configuration of the faulty cascade is simulated by the one shown in Fig. 2(*b*). This configuration is constructed by conceptually isolating and infinitely repeating the group, which consists of the faulty blade supplemented by two intact, i.e., healthy, blades above and below it. Obviously, the number of healthy blades involved in the representative group is associated with the assumed effective radiation distance (here taken as two spacings). The periodic pattern of Fig. 2(*b*), therefore, is equivalent to the configuration of multiple, here an array of five, aligned simple cascades, offset in the y direction by the spacing of the original cascade. The different cascades involved in the periodic pattern are indicated with different shading pattern in Fig. 2(*b*). It is evident that these simple cascades have a spacing five times the spacing of the original one.

Surface Source Panel Method. Quite a few panel methods have been developed for calculating the flow through two-dimensional multiple blade cascades, which employ either source,

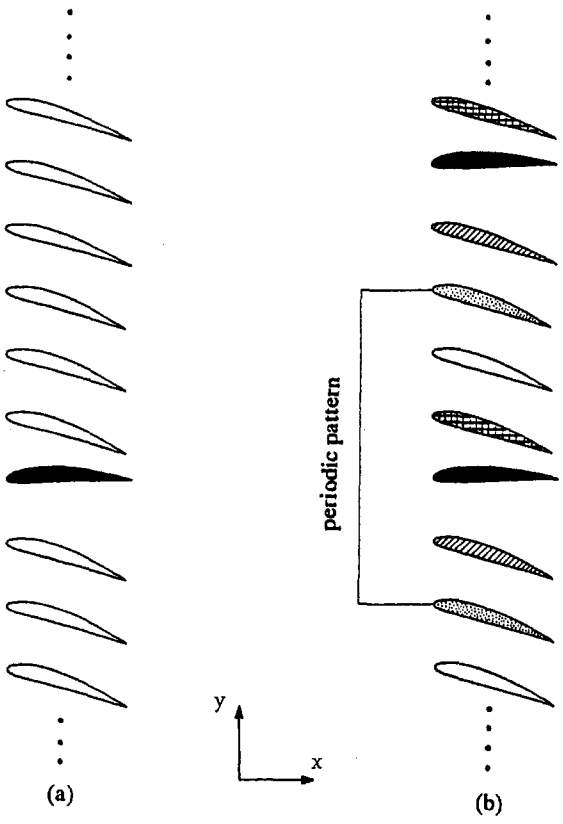


Fig. 2 Configuration of blade cascade that contains a single "faulty" (twisted) blade: (*a*) actual geometry; (*b*) multiple cascades simulating the actual geometry in the computations (five cascades, four "healthy" and one "faulty" are shown in the figure)

Downloaded 02 Jun 2010 to 171.66.16.105. Redistribution subject to ASME license or copyright; see http://www.asme.org/terms/Terms_Use.cfm

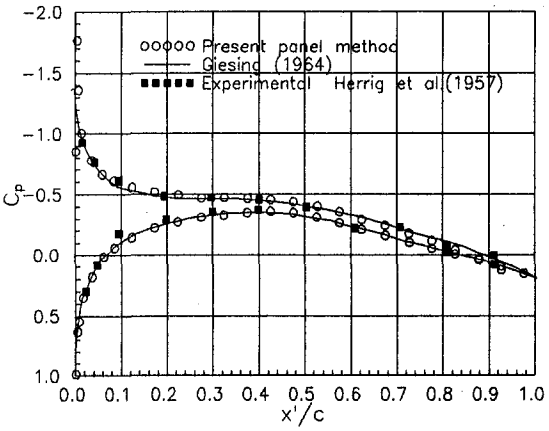


Fig. 3 Pressure coefficient distribution for NACA 65010 fully periodic, healthy, cascade with γ = 21 deg, β_{avg} = 26.276 deg and h/c = 0.66

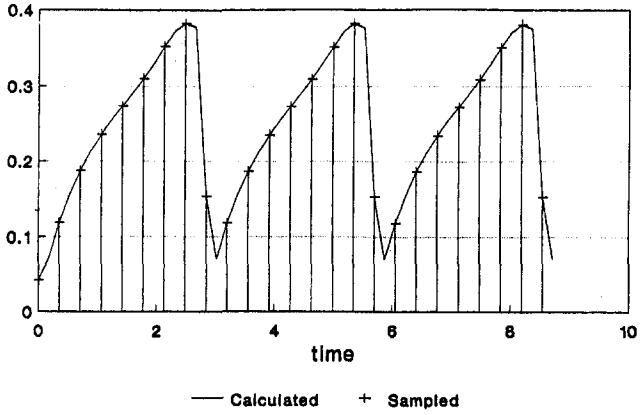


Fig. 4 Obtaining a sampled data signal from computed values

e.g., Giesing (1964) and Dedoussis (1983), or vortex singularities, e.g., Minassian (1976). In the present work the efficient and accurate surface-source singularity method of Hess and Smith (1966) as it has been adapted by one of the present authors (Dedoussis, 1983) is employed to calculate the two-dimensional incompressible potential flow through the multiple cascades of blades, shown in Fig. 2(*b*). The method assumes that each blade of any one of the different cascades considered is approximated by a large number of small line segments or panels. On each panel, a constant surface-source distribution is assumed. Their strength is determined by requiring the net velocity normal to the surface at each panel to be zero (since blade surfaces are streamlines). The blade lift is accounted for by considering an extra uniform surface vortex sheet distribution, whose strength is adjusted by the Kutta condition at the trailing edges. Detailed presentation of the panel method adopted is beyond the scope of the present paper. For the sake of completeness, a concise description of the implementation of the method is included in the appendix.

In order to demonstrate the reliability of the present panel method, periodic, i.e., healthy, cascade test cases were calculated for which computational or analytical or experimental results exist. An indicative result is shown in Fig. 3, where the (nondimensional) pressure distribution for a NACA 65010 linear cascade is plotted against the nondimensional chord length. The agreement of our results with experimental ones (Herrig et al., 1957) and those of another method (Giesing, 1964) is very good.

Constitution of Simulated Time Signals and Spectral Patterns (Signatures)

Having determined the strength of the source and vortex sheet distributions on the blade surfaces, it is possible to calculate the static pressure at any location of the flow field, and therefore to simulate the signals measured by a sensor placed on the casing of the compressor, facing the rotor blades. In this section we present the way of producing these signals from the computational results, as well as the method of producing the corresponding spectral patterns.

We are interested in the pressure sensed by a transducer positioned as shown in Fig. 1. As the rotor blades move in front of the transducer, the pressure that it senses corresponds to successive points on the cascade plane, indicated in Fig. 1. In order to reconstitute the pressure signal, we need to define the values of the pressure for different time instants. We define a coordinate system x–y (Fig. 1) and the zero time instant is chosen as the time that the origin is positioned in front of the transducer. For any subsequent time instant t, the point of the cascade facing the transducer will be the one with coordinate y, which is:

$$y = U \cdot t \tag{1}$$

where U is the linear velocity of the blades (= peripheral velocity at the tip of the cascade). The pressure can be computed for any time instant in this way, and therefore the pressure signal can be reconstituted.

This procedure gives the possibility of producing continuous time signals, since it can be applied for any desired time instant. When measuring, however, it is not the continuous signal that is recorded, but its values at the time instants specified by a particular sampling frequency. In order to reproduce sampled time signals, the pressure values should be calculated only for the corresponding time instants (see Fig. 4).

It should be mentioned that the results of the computation are available for a segment of the cascade that does not cover a full circumference of the rotor. Of course, in order to reconstitute a long time signal, it is necessary to have the data for a full circumference, which are then repeated with the period of one rotor revolution. It has been discussed above that it is not necessary to carry out computations for an assembly of blades covering the full circumference, since after a certain number of blades on both sides of the twisted one, there is no significant variation of the obtained results. If the domain of calculation contains less blades than the rotor circumference, then the procedure depicted in Fig. 5 is applied: the pressure variation for one "healthy" blade passage is padded to the signal for the

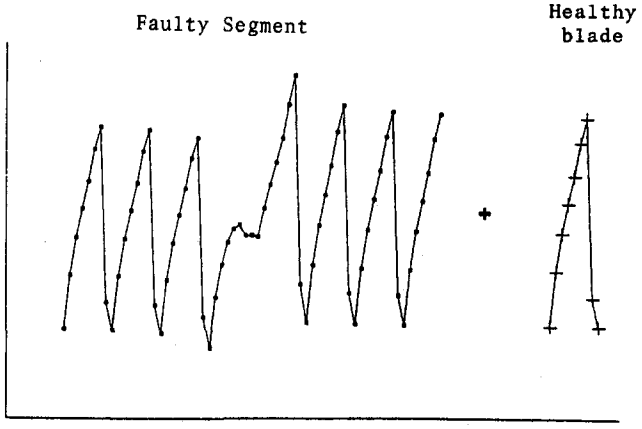


Fig. 5 Padding "healthy" blade-to-blade pressure variations to a restricted blade range, in order to reconstitute the signal for one rotor revolution

Downloaded 02 Jun 2010 to 171.66.16.105. Redistribution subject to ASME license or copyright; see http://www.asme.org/terms/Terms_Use.cfm

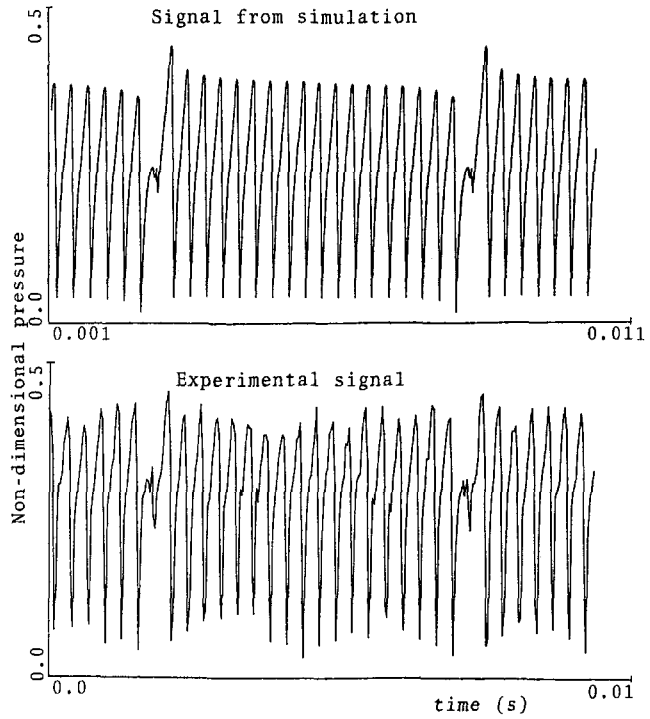


Fig. 6 Pressure time signal from experiment and from simulation

calculated segment of the circumference, until a length of one full circumference is reached.

Having obtained sampled time signals, in order to calculate fault signatures, the same procedure as the one for the experimental data is applied. This consists of the following steps:

(*a*) Reconstitute the time signal for a healthy cascade.
(*b*) Reconstitute the time signal for the cascade with the twisted blade.
(*c*) Compute power spectra for both signals.
(*d*) Compute the desired fault index from these power spectra (here we examine only spectral differences).

Application to the Case of an Industrial Gas Turbine

Fault Signatures. The procedure described above has been applied to the reproduction of signatures from measurements with a pressure transducer facing the first rotor of the compressor of an industrial gas turbine. The corresponding experimental investigation has been discussed by Mathioudakis et al. (1990) and Loukis et al. (1991).

The pressure time signals resulting from the flow field calculation are shown in Fig. 6. In the same figure the corresponding measured pressure signal is also included. The two signals show remarkable similarity. It should be noticed that the experimental signal contains random noise, which is not present in the simulated one. This accounts for local differences between blades as well as random flow fluctuations. The main feature, however, is that the presence of the twisted blade is correctly represented, as it can be seen from the form of the signal at corresponding locations.

The power spectra of simulated and experimental signals are shown in Fig. 7. It is noticed that the simulated data produce spectra characterized by the absence of the random noise. This feature is not so important for the spectra themselves, since the interest lies in the spectral differences which serve as fault signatures.

The fault signatures corresponding to the spectra of Fig. 7 are shown in Fig. 8. It is seen that the simulated signature has the same form as the experimental one. However, the presence

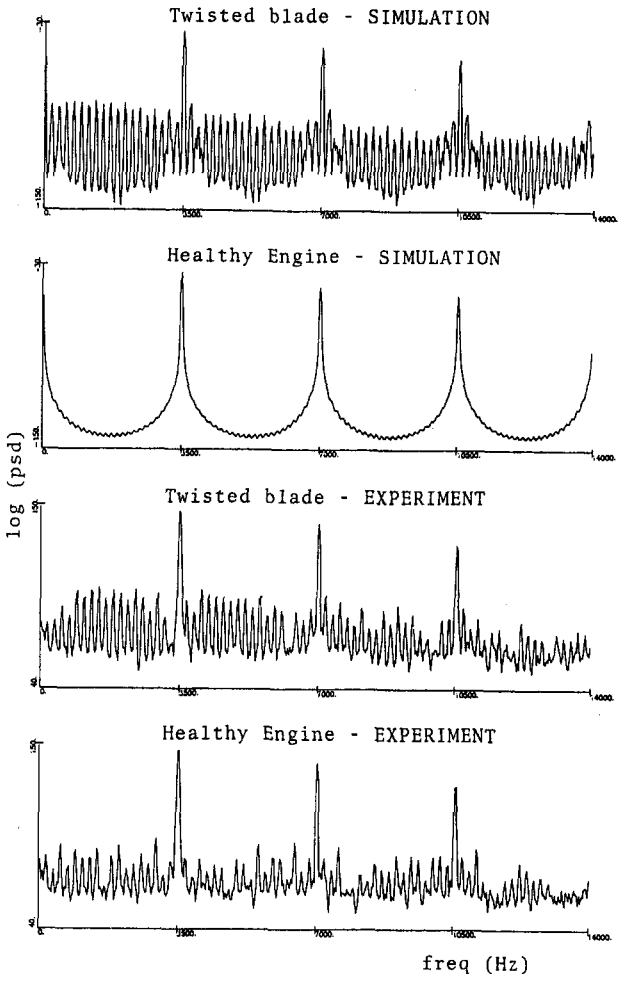


Fig. 7 Power spectra for unsteady pressure from simulated and experimental data

of noise in the experimental data gives local differences, which result in the observed differentiation. As has been concluded from the experimental study, the differentiation between the first two blade passing frequency harmonics is the important one for identifying the faults. The similarity of the signatures in this region is remarkable.

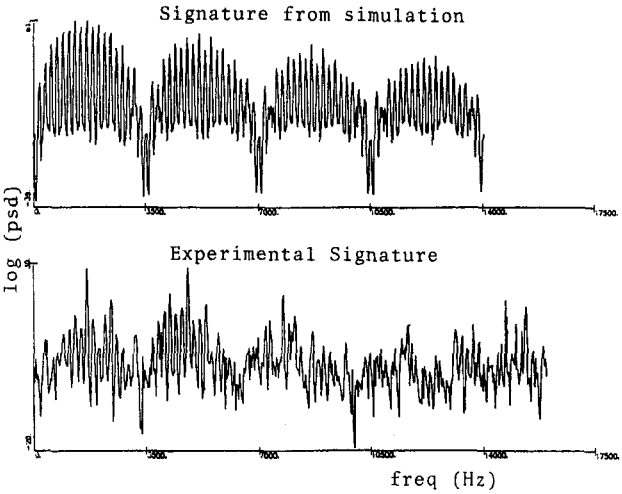


Fig. 8 Fault signatures from unsteady pressure for simulated and experimental data

Downloaded 02 Jun 2010 to 171.66.16.105. Redistribution subject to ASME license or copyright; see http://www.asme.org/terms/Terms_Use.cfm

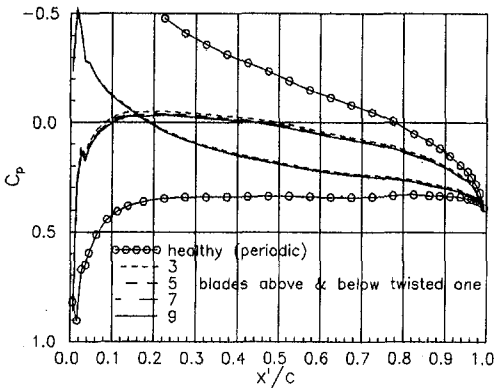


Fig. 9 Comparison between the pressure distributions of healthy and twisted blades, calculated with various cascade configurations

Features of the Calculation Procedure. A first point to be examined is how many healthy passages on each side of the faulty blade have to be considered in the configuration of the periodic pattern (refer to Fig. 2(*b*)). In Fig. 9 the pressure distributions around a healthy blade (corresponding to a rotor without twisted blades) are compared to the corresponding ones around a twisted blade, by 7 deg, for various configurations. The numbers for the different calculations indicate the number of passages on each side of the twisted blade, which have been considered in the calculation. It is observed that except for the case of three passages the results are almost identical.

Another interesting point is to examine at what distance from the faulty blade conditions close to periodic are established, as well as how the disruption of the pressure field is reduced with the distance from the faulty blade. In Fig. 10 the pressure distributions at the end blades, for a domain with three blades on both sides of the twisted one, are shown. It is observed that the two blades at the two ends of the domain considered have practically the same pressure distribution, which is very close to the healthy one. In Fig. 11, the evolution of the pressure distributions as we move away from the twisted blade is shown. It can be seen that as the end blades are approached, the pressure distributions become closer to those of the healthy blade.

Finally, it is useful to show some features of the flow field when the twisted blade is present. The velocity vector fields for the healthy and the faulty cascades are compared in Fig. 12. The corresponding spanwise (i.e., in the peripheral sense) variation of the inlet to the cascade flow angle (angle formed between local velocity vectors and the axis of the machine in the region upstream and close to the cascade) is presented in Fig. 13. As is expected, the twisted blade perturbs the flow significantly

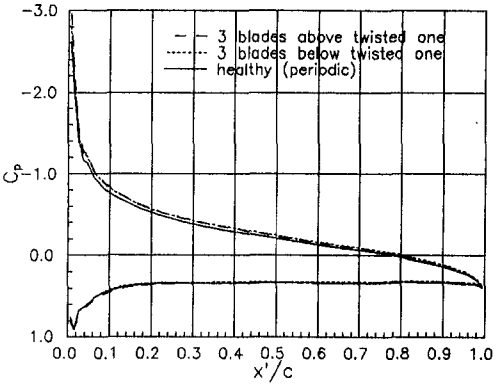


Fig. 10 Pressure distributions for the healthy blade and the end blades of the calculation domain, for three blades above and below the twisted one

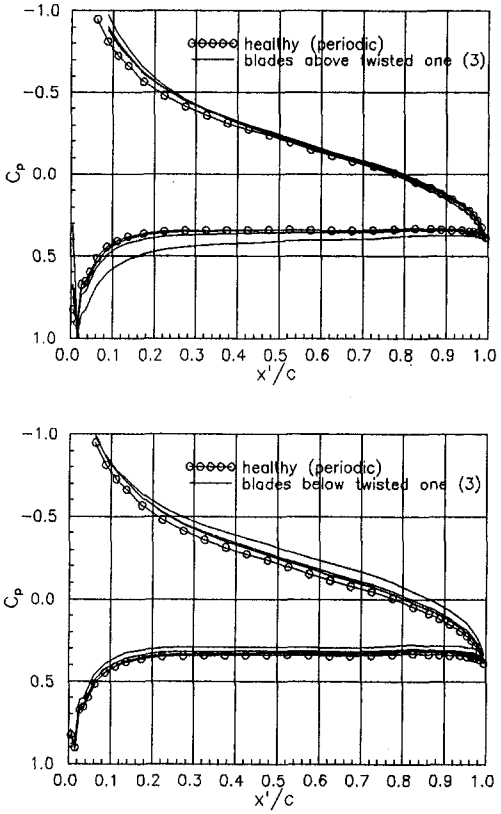


Fig. 11 Evolution of pressure distributions for the blades adjacent to the twisted one (flow calculation with three healthy blades above and below)

(with respect to its "healthy" behavior) only in the region very close to it. "Far away" from the fault the flow seems not to "understand" its presence.

Discussion

A question that may arise about the method is how a two-dimensional cascade inviscid solution gives rather satisfactory

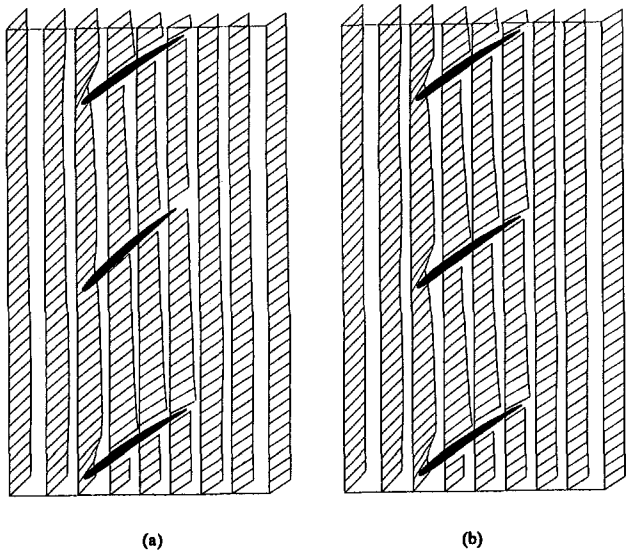


Fig. 12 Comparison of calculated velocity vector fields at the adjacent to the faulty blade passages: (*a*) faulty cascade; (*b*) healthy (periodic) cascade

Downloaded 02 Jun 2010 to 171.66.16.105. Redistribution subject to ASME license or copyright; see http://www.asme.org/terms/Terms_Use.cfm

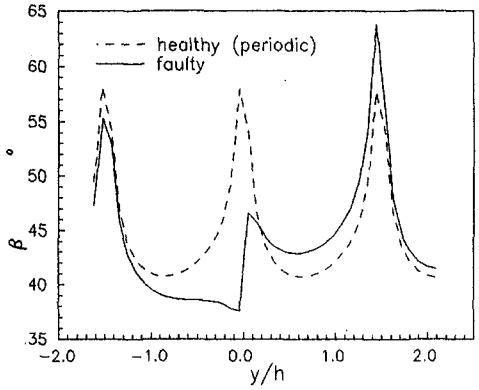


Fig. 13 Spanwise variation of flow angle across the adjacent to the faulty blade passages at a distance 5 percent of the chord upstream of the leading edge is compared to the corresponding healthy one

reproduction of the signatures which come from measurements of a complicated real flow field. The reasoning presented by Mathioudakis et al. (1990) will also be adopted here: "Since the driving mechanism of all flow phenomena in the tip region of the rotor is of mainly two-dimensional inviscid nature, changes in this driving mechanism will directly be reflected on the final real quantity measurements."

The application of the proposed method to the case of a blade fault consisting of a single twisted blade has demonstrated its capabilities. This particular test case has been chosen because experimental data for the validation of the predictions were available. It should be pointed out that the proposed method is general enough to handle other blading faults as well. This is achieved by choosing the periodic blade pattern of Fig. 2(*b*) appropriately. Cases of a bent blade or cases with more than one blade deformed can be tackled quite easily. The present method can be used, therefore, during the design of a diagnostic system, for fault simulations, in the frame discussed by Loukis et al. (1993).

The proposed method uses geometric data for the computation of the signatures and the inlet flow direction to the cascade. It is easy, therefore, to examine how signatures will change if characteristics of the fault change. One can study, for instance, signatures for different degrees of twisting a blade. The result of such a calculation is shown in Fig. 14. It is observed that the amplitude of the difference pattern is reduced for smaller twist angles, while the form remains the same. It is interesting to note that this observation is in agreement with experimental observations shown in Fig. 15. Strict quantitative comparisons are hindered by the presence of random noise in the experimental data. Another result that can be obtained is the dependence of the signature on the flow incidence angle. Such calculations were performed and showed that small variations in incidence do not influence the form of the signature. This is in agreement with experimental observations of Mathioudakis et al. (1991).

The significant feature of the present method is that it can facilitate as well as improve the effectiveness of expert systems for fault diagnosis (e.g., Doel, 1990). The data base with fault signatures can be derived without the need of extensive experimentation for fault kind and magnitude. It can even eliminate the need of a data base for particular signatures. The computational codes can form a part of the expert system itself and can be used for the derivation of the signature of the fault desired to be examined.

Finally, it should be mentioned that the calculation method for nonperiodic cascades can be also applied to other areas of interest. Such a case is for example that of mistuned blade rows, namely blade rows made deliberately nonperiodic in order to reduce noise emission or flutter. In this context, Funazaki

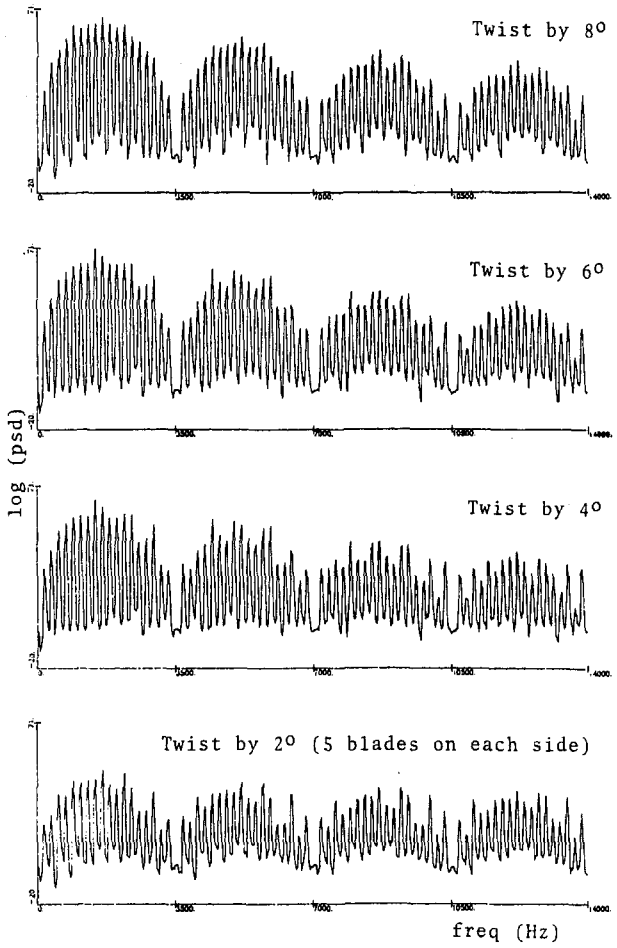


Fig. 14 Simulated fault signatures for various degrees of twist

(1993) employed a method that uses principles similar to the ones of our method.

Conclusions

A method for producing rotating blade fault signatures of a gas turbine using only theoretical computations has been presented.

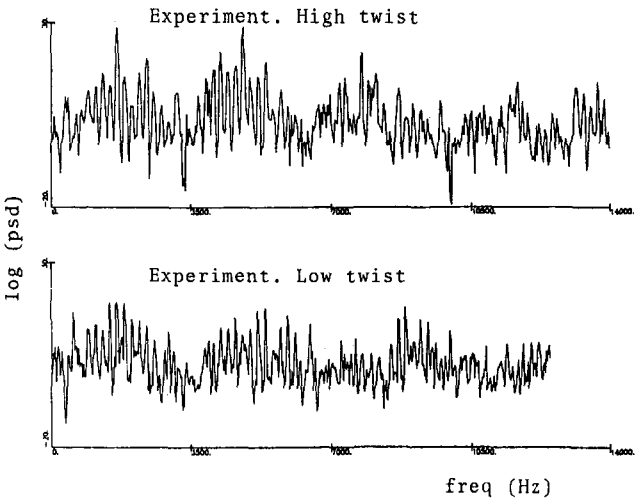


Fig. 15 Experimental fault signatures for high and low twist

Downloaded 02 Jun 2010 to 171.66.16.105. Redistribution subject to ASME license or copyright; see http://www.asme.org/terms/Terms_Use.cfm

The method is based on an original calculation procedure of the flow field in nonperiodic blade cascades. The calculated blade-to-blade pressure field is used for constitution of casing wall unsteady pressure signals. These signals are then processed and the signatures are derived in the form of spectral differences.

The capabilities of the method are demonstrated by comparison to experimental data obtained from a gas turbine with an implanted rotating blade fault. Features of the method that give the possibility to improve the understanding of the influence of faults on local pressure disturbances are discussed. The capability of performing parametric studies for fault characteristics is also demonstrated.

Acknowledgments

The work described in this paper has been performed within the frame of research contract BREU-506-Project BE-4192. The authors express their thanks to the European Communities for their financial support. Thanks are expressed to Metravib RDS and European Gas Turbines for allowing inclusion of experimental data in the paper as well as their support during the execution of the project.

References

Barschdorf, D., and Korthauer, R., 1986, "Aspects of Failure Diagnosis on Rotating Parts of Turbomachines Using Computer Simulation and Pattern Recognition Methods," presented at the International Conference on Condition Monitoring, Brighton, England, 21–23 May.

Dedoussis, V., 1983, "Calculation of Inviscid Flow Through Aerofoil Cascade and Between Wind Tunnel Walls," M. Sc. Thesis, Dept. Aeronautics, Imperial College, London.

Doel, D., 1990, "The Role of Expert Systems in Commercial Gas Turbine Engine Monitoring," ASME Paper No. 90-GT-374.

Funazaki, K., 1993, "Unsteady Aerodynamic Responses of Mistuned Cascades to Incoming Wakes," *JSME International Journal*, Series B, Vol. 36, No. 1, pp. 66–73.

Giesing, J. P., 1964, "Extension of the Douglas Neumann Program to Problems of Lifting, Infinite Cascades," Douglas Aircraft Company Report No. LB 31653.

Herrig, J., Emery, J. C., and Erwin, J. R., 1957, "Systematic Two-Dimensional Cascade Tests of NACA 65—Series Compressor Blades at Low Speeds," NACA TN 3916.

Hess, J. L., and Smith, A. M. O., 1966, "Calculation of Potential Flow About Arbitrary Bodies," *Prog. Aero. Sci.*, Vol. 8, pp. 1–138.

Hess, J. L., 1990, "Panel Methods in Computational Fluid Dynamics," *Ann. Rev. Fluid Mech.*, Vol. 22, pp. 255–274.

Hewitt, J., and Bosmans, R., 1991, "Vibration Diagnostics by Expert Systems that Link to Machinery Databases," ASME Paper No. 91-GT-298.

Lakshminarayana, B., 1991, "An Assessment of Computational Fluid Dynamic Techniques in the Analysis and Design of Turbomachinery," ASME *Journal of Fluids Engineering*, Vol. 113, pp. 315–352.

Lamb, H., 1932, *Hydrodynamics*, Cambridge Univ. Press, New York, pp. 71–72.

Loukis, E., Wetta, P., Mathioudakis, K., Papathanasiou, A., and Papailiou, K. D., 1991, "Combination of Different Unsteady Quantity Measurements for Gas Turbine Blade Fault Diagnosis," ASME Paper No. 91-GT-201.

Loukis, E., Mathioudakis, K., and Papailiou, K. D., 1993, "A Methodology for the Design of Automated Gas Turbine Diagnostic Systems," ASME Paper No. 93-GT-47.

Mathioudakis, K., Loukis, E., and Papailiou, K. D., 1990, "Casing Vibration and Gas Turbine Operating Conditions," ASME JOURNAL OF ENGINEERING FOR GAS TURBINES AND POWER, Vol. 112, pp. 478–485.

Mathioudakis, K., Papathanasiou, A., Loukis, E., and Papailiou, K. D., 1991, "Fast Response Wall Pressure Measurement as a Means of Gas Turbine Blade Fault Identification," ASME JOURNAL OF ENGINEERING FOR GAS TURBINES AND POWER, Vol. 113, No. 2, pp. 269–275.

Minassian, L. M., 1976, "A Study of Multielement Cascades and Airfoils," ASME *Journal of Fluids Engineering*, Vol. 98, No. 2, pp. 208–215.

Rihak, P., and Schmidt, R., 1992, "Optimum Selection of the Vibration Monitoring System for Turbomachines," ASME Paper No. 92-GT-421.

APPENDIX

Implementation of the Surface-Source Panel Method for Multiple Cascades

The method assumes that each blade of any one of the different cascades considered is approximated by a large number, say N, of small line segments, panels. On each panel, a constant surface-source distribution is assumed. The elementary singularity, therefore, is an infinite grid of equally spaced parallel line sources of uniform strength.

Consider an infinite series of (point) sources of strength M located on corresponding points of the surface of the blades of one of the multiple cascades, which are denoted by the complex numbers $\ldots, Z - i2h, Z - ih, Z, Z + ih, Z + i2h, \ldots$ on the complex plane of Fig. A1 (note that h is the cascade spacing and $i = \sqrt{-1}$). Then the complex potential f at a point z due to this infinite series of sources is (see Lamb, 1932):

$$f(z) = \frac{M}{2\pi} \ln \left\{ \sinh \left(\frac{\pi(z - Z)}{h} \right) \right\} \qquad \text{(A1)}$$

Relation (A1) implicitly "reduces" the problem of calculating the flow over a cascade of infinite number of blades to that over a *single* blade, herein referred to as the "representative" blade of the cascade.

Denoting the strength of the uniform source distribution on a, say the nth, panel by m_n, and integrating df/dz along the panel, we get the following expression for the complex velocity $W_n(z)$, at any point z, induced by this panel:

$$W_n(z) = e^{-i\theta_n} \frac{m_n}{2\pi} \ln \left(\frac{\sinh[\pi(z - Z_{1n})/h]}{\sinh[\pi(z - Z_{2n})/h]} \right) \qquad \text{(A2)}$$

where θ_n is the angle between the nth panel and the (real) x axis and Z_{1n}, and Z_{2n} are the points defining the nth panel on the complex plane (see Fig. A1). The x- and y-velocity components, induced by the nth source panel of the representative blade of the cascade, are provided by the real and imaginary parts, respectively, of the conjugate of the complex velocity W_n. Equation (A2) is used to calculate the velocity field induced by any panel on the surface of any other panel, i.e., to determine the effect of the panels on one another.

The actual blade cascade is simulated by a number of NC different cascades, one of which has as representative blade section the faulty one, while the rest of the cascades are represented by the $(NC - 1)/2$ healthy blade sections above and below it. For the sake of symmetry NC is considered to be an

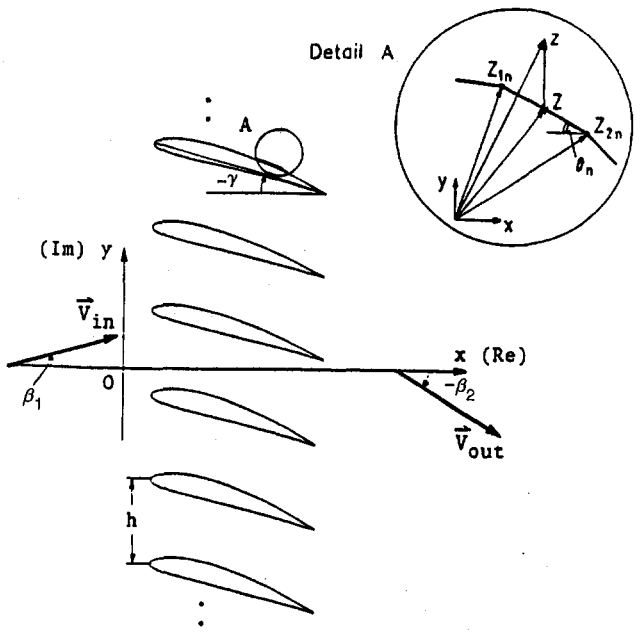


Fig. A1 Infinite linear cascade of blades. Schematic representation of panel and cascade parameters.

Downloaded 02 Jun 2010 to 171.66.16.105. Redistribution subject to ASME license or copyright; see http://www.asme.org/terms/Terms_Use.cfm

odd integer. It is also assumed that all the representative blades are approximated by the same number of N panels. In order to discriminate between different cascades, an index j is introduced indicating each one of the different cascades. Obviously, $j = 1, \ldots, NC$. Thus, the total number of panels on *all* the representative blades of the cascades is: $\bar{N} = N \times NC$. As far as the numbering of the panels is concerned, the panels of the representative blade of, say the jth cascade, are denoted by the index p with $p = (j-1)N + 1, \ldots, jN$.

The net velocity normal to the panels, approximating the blades, due to both the surface source distributions on *all* the "representative" blades and the uniform oncoming (onset) flow is zero (since blade surfaces are streamlines). The control points, i.e., the points on the surface of the blades on which this boundary condition is satisfied, are the panel midpoints. This condition reads:

$$\sum_{n=1}^{\bar{N}} \tilde{A}_{pn}\tilde{m}_n + V_{av}\tilde{b}_p = 0 \quad \text{with} \quad p = 1, \ldots, \bar{N} \qquad \text{(A3)}$$

$\tilde{}$ denotes a matrix or a column vector if a quantity with two or one index respectively is involved. Matrix $\tilde{A}_{pn}$ represents the normal to the pth blade panel velocity component induced by a *unit* surface source distribution on the nth panel. It is evaluated using equation (A2). $\tilde{A}_{pn}$ is referred to as the *influence-coefficient matrix* (associated with normal surface velocity). Column vector $\tilde{b}_p$, on the other hand represents the normal velocity on the pth panel due to *unit* onset, average, velocity field $\vec{V}_{av}$ ($\vec{V}_{avg} = \frac{1}{2}(\vec{V}_{in} + \vec{V}_{out})$; see Fig. A1).

The unknown surface source distribution vector $\tilde{m}_n$ is provided via the solution of the system of linear equations (A3) as:

$$\tilde{m}_n = -V_{avg} \sum_{p=1}^{\bar{N}} \tilde{A}_{np}^{-1}\tilde{b}_p \quad \text{with} \quad n = 1, \ldots, \bar{N} \qquad \text{(A4)}$$

Having evaluated $\tilde{m}_n$, the net tangential velocity component on the pth panel is

$$\tilde{q}_p = \sum_{n=1}^{\bar{N}} \tilde{B}_{pn}\tilde{m}_n + V_{av}\tilde{f}_p \quad \text{with} \quad p = 1, \ldots, \bar{N} \qquad \text{(A5)}$$

Similar to Eq. (A3), matrix $\tilde{B}_{pn}$ is the influence-coefficient matrix associated with the tangential velocity component and vector $\tilde{f}_p$ represents the tangential surface velocity due to the onset field. The clockwise sense is considered to be positive.

The blade circulation is taken into account by assuming uniform surface vortex sheets on the different representative blades. The strength of the vortex sheets is adjusted by the simultaneous satisfaction of the Kutta condition at their trailing edge (T.E.) points. The Kutta condition is implemented by requiring the tangential surface velocities at the panels adjacent to the T.E. of all representative blades to be equal. Denoting by Δq_j the tangential surface velocity differences between the panels of the representative blade of the jth cascade adjacent to the T.E., the Kutta condition reads:

$$\Delta q_j = 0 \quad \text{with} \quad j = 1, \ldots, NC \qquad \text{(A6)}$$

Tangential surface velocities are due to the surface source distribution (and the onset velocity field) as well as to the vortex sheets. Taking into account that the governing equations are linear, condition (A6) becomes:

$$\Delta q_j = V_{avg}\Delta q_j^{(b)} + \sum_{k=1}^{NC} (\Gamma/s)_k \Delta q_k^{(c)} = 0 \quad \text{with}$$

$$j = 1, \ldots, NC \qquad \text{(A7)}$$

Γ_k is the circulation of the kth representative blade (positive in the clockwise sense), and s_k is the perimeter of the corresponding blade (thus $(\Gamma/s)_k$ represents the uniform relevant vortex sheet strength). $\Delta q_j^{(b)}$, $\Delta q_j^{(c)}$ are the difference of the tangential surface velocities between the adjacent to the T.E. panels of the blade of the jth cascade, due to the source distribution $\tilde{m}_n$ for *unit* onset velocity and to *unit* vortex sheet distributions (blockage and circulation effects denoted by the superscripts (b) and (c) respectively).

The vortex sheet distributions induce a nonzero normal surface velocity, violating the requirement that blade surfaces be streamlines. To counteract this (vortex-induced) surface velocity, extra surface source distributions on the panels of *all* (representative) blades $\tilde{m}'_{nj}$ (source on nth panel due to the vortex sheet, circulation, of the representative blade of the jth cascade) are assumed. The extra source distributions are:

$$\tilde{m}'_{nj} = \sum_{p=1}^{\bar{N}} \tilde{A}_{np}^{-1} \sum_{r=(j-1)N+1}^{jN} \tilde{B}_{pr}\tilde{\gamma}_{rj} \quad \text{with} \quad j = 1, \ldots, NC \qquad \text{(A8)}$$

where $\tilde{\gamma}_{rj}$ represents the (uniform) vortex sheet distribution on the rth panel belonging to the representative blade of the jth cascade.

The net tangential surface velocities, on the pth panel induced by the vortex sheet distributions on the representative blade of the jth cascade and the associated extra source distributions are:

$$\tilde{q}_{pj}^{(c)} = \sum_{n=1}^{\bar{N}} \{\tilde{A}_{pn}\tilde{\gamma}_{nj} + \tilde{B}_{pn} \sum_{l=1}^{\bar{N}} \tilde{A}_{nl}^{-1} \sum_{r=(j-1)N+1}^{jN} \tilde{B}_{lr}\tilde{\gamma}_{rj}\} \quad \text{with}$$

$$p = 1, \ldots, \bar{N}$$
$$j = 1, \ldots, NC \qquad \text{(A9)}$$

$\Delta q_j^{(b)}$ and $\Delta q_k^{(c)}$ of condition (A7) are evaluated by applying respectively Eqs. (A5) and (A9) (the latter for *unit* vortex sheet strength, i.e., $\tilde{\gamma}_{rj} = 1$) at the adjacent to the TE panels. Thus, Eqs. (A7) represent a system of linear equations for the unknown blade circulations Γ_k.

Once the primary surface source distribution $\tilde{m}_n$ and the uniform circulation $(\Gamma/s)_j$ distributed around each one of the different cascades, have been determined, the incompressible flow field through the multiple cascades is effectively solved for a specified onset velocity $\vec{V}_{avg}$ (actually the resultant flow field is calculated as the superposition of the flow fields induced by the source and vortex panels). Standard incompressible inviscid flow relations are employed for evaluating important flow parameters. Note that in determining cascade related quantities, the *total* circulation (i.e., the sum of the circulations on each one of the different cascades considered) should be used.

In this work (as well as in most engineering applications), the velocity far upstream of the multiple cascades $\vec{V}_{in}$, rather than $\vec{V}_{avg}$, is prescribed. In this case, an iterative scheme that takes advantage of the well-known fact that large variations in the direction of $\vec{V}_{avg}$, i.e., in β_{avg}, lead to almost no change in the direction of $\vec{V}_{out}$ (or in β_2) is used. The overall efficiency of the method is retained since the expensive matrix inversion $\tilde{A}_{np}^{-1}$ is performed only once within the iterative procedure (since $\tilde{A}_{pn}$ depends on the geometry only).

Downloaded 02 Jun 2010 to 171.66.16.105. Redistribution subject to ASME license or copyright; see http://www.asme.org/terms/Terms_Use.cfm

The Negative Information Problem in Mechanical Diagnostics

D. L. Hall

R. J. Hansen

D. C. Lang

The Pennsylvania State University,
Applied Research Laboratory,
Post Office Box 30,
State College, PA 16804-0030

Condition-based maintenance (CBM) is an emerging technology, which seeks to develop sensors and processing systems aimed at monitoring the operation of complex machinery such as turbine engines, rotor craft drivetrains, and industrial equipment. The goal of CBM systems is to determine the state of the equipment (i.e., the mechanical health and status), and to predict the remaining useful life for the system being monitored. The success of such systems depends upon a number of factors, including: (1) the ability to design or use robust sensors for measuring relevant phenomena such as vibration, acoustic spectra, infrared emissions, oil debris, etc.; (2) real-time processing of the sensor data to extract useful information (such as features or data characteristics) in a noisy environment and to detect parametric changes that might be indicative of impending failure conditions; (3) fusion of multi-sensor data to obtain improved information beyond that available to a single sensor; (4) micro and macro level models, which predict the temporal evolution of failure phenomena; and finally, (5) the capability to perform automated approximate reasoning to interpret the results of the sensor measurements, processed data, and model predictions in the context of an operational environment. The latter capability is the focus of this paper. Although numerous techniques have emerged from the discipline of artificial intelligence for automated reasoning (e.g., rule-based expert systems, blackboard systems, case-based reasoning, neural networks, etc.), none of these techniques are able to satisfy all of the requirements for reasoning about condition-based maintenance. This paper provides an assessment of automated reasoning techniques for CBM and identifies a particular problem for CBM, namely, the ability to reason with negative information (viz., data which by their absence are indicative of mechanical status and health). A general architecture is introduced for CBM automated reasoning, which hierarchically combines implicit and explicit reasoning techniques. Initial experiments with fuzzy logic are also described.

Introduction

The emerging technology of condition-based maintenance (CBM) of mechanical equipment is aimed at developing systems that are capable of monitoring the operation of a complex piece of machinery and providing an accurate characterization of the current system state, and ideally, an accurate prediction of the remaining safe or useful life span. This approach to maintenance represents a departure from traditional maintenance approaches. Historically, maintenance philosophies involved one of two approaches: (1) run until mechanical failure occurs, then repair, or (2) schedule maintenance and inspection based on conservative probabilistic failure models (i.e., using mortality statistics). Either of these approaches can be disruptive to the operation of a factory, commercial operation, or a military mission, which depends upon critical equipment. Moreover, the first approach (run until failure) may threaten the safety of humans by waiting until a failure actually occurs, while the second philosophy (scheduled maintenance) may be expensive, and may actually increase failure rates by the implementation of unnecessary maintenance. This latter effect is analogous to the problem of *iatropic* illness in medicine, in which treatment for one condition inadvertently induces another illness or problem. Thus, even if properly performed, preventive maintenance may induce subsequent failures in equipment because of the disruption of structural integrity, or other factors.

Contributed by the International Gas Turbine Institute and presented at the 41st International Gas Turbine and Aeroengine Congress and Exhibition, Birmingham, United Kingdom, June 10–13, 1996. Manuscript received at ASME Headquarters February 1996. Paper No. 96-GT-35. Associate Technical Editor: J. N. Shinn.

The advent of sophisticated sensors, rapid evolution of microprocessors, and new algorithms permits a third philosophy, *condition-based maintenance*, to be implemented for real systems. Condition-based maintenance (CBM) offers a significant cost savings and system availability increases for some applications, e.g., Rao (1996) and Pandian and Rao (1989). This philosophy and approach, described by Hansen et al. (1995), involves monitoring a system with robust sensors, and processing the sensor data to ultimately achieve intelligent inferences regarding the current mechanical state of a system, recommendations regarding the need for maintenance actions, and predictions of remaining useful life (assuming current operating loads and conditions or a profile of expected system utilization). The general concept of a CBM monitoring system is shown conceptually in Fig. 1.

Functional elements of a CBM monitoring system include: (1) a suite of active or passive sensors to observe phenomena such as temperature, pressure, existence of oil debris, vibrations, acoustic spectra, etc.; (2) signal processing techniques to characterize the signal data and to extract significant features from the data; (3) multi-sensor data fusion techniques to combine the sensor data to obtain a more accurate characterization of the system being monitored than is available from a single sensor; (4) predictive models at the micro and macro levels to predict the onset and temporal evolution of failure phenomena; and finally (5) automated reasoning techniques to interpret the results of the sensor data, signal processing, fused multi-sensor data, and predictive models. Ancillary functions include supporting models and databases and a human computer interface. Examples of the techniques associated with these functional

Copyright © 1997 by ASME

Downloaded 02 Jun 2010 to 171.66.16.105. Redistribution subject to ASME license or copyright; see http://www.asme.org/terms/Terms_Use.cfm

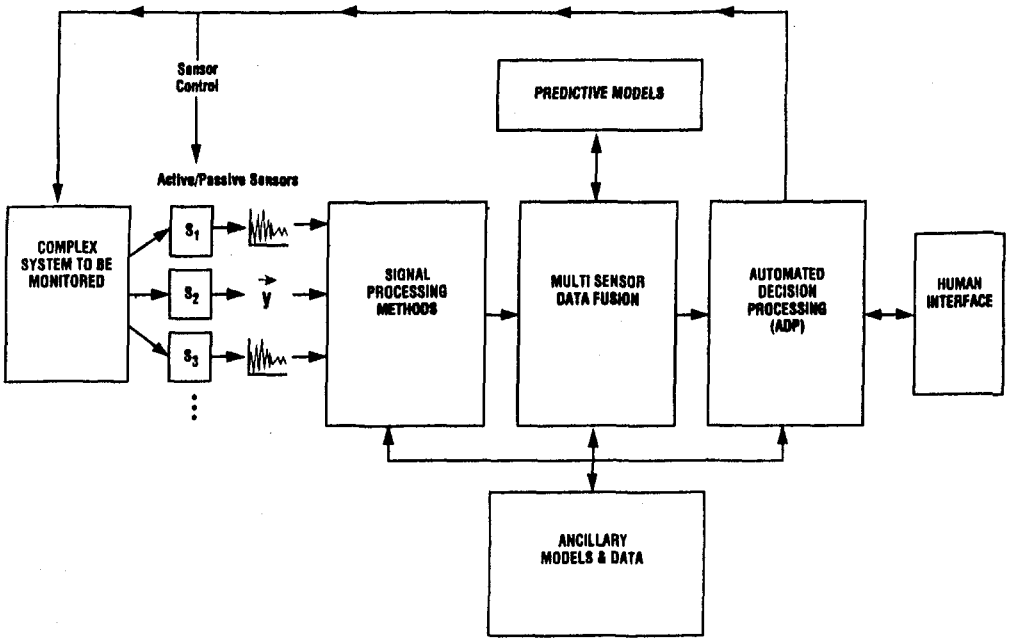


Fig. 1 Functional components for a condition-based maintenance system

components are shown in Fig. 1. Depending upon the specific CBM application, these functions may be implemented on a single *smart* sensor processing chip to monitor a single mechanical component, or in a distributed environment that uses multiple sensors and a centralized computing resource for platform level CBM, e.g., for a rotor craft, multi-engine commercial aircraft, etc.

Currently, implementation of CBM systems is limited to monitoring systems (or mechanical components or subsystems), with a primary ability to characterize the current state of a system accurately, but with limited ability to predict remaining life (not withstanding the claims of monitoring system manufacturers whose *predictive* results are based on simple trending techniques). Recent CBM systems have been reported for a variety of mechanical systems such as the space shuttle main engine (Guo and Merrill, 1991; Lin and Wu, 1991), diesel engines (Hansen et al., 1994), helicopter gearboxes and drivetrains (Jammu et al., 1995; Douses, 1994), and gas turbine engines (Loukis et al., 1994; Merrington, 1994). Techniques applied to CBM span a broad range including (but not limited to): rule-based expert systems (Hansen et al., 1994), adaptive neural networks (Ganesan et al., 1995), classic pattern recognition techniques (Upadhyaya, 1988), nonlinear difference equations (Jeon and Li, 1995), fuzzy logic reasoning systems (Isermann and Ulieru, 1993), and stochastic modeling techniques (Ray and Wu, 1994). There is much ongoing research in this area, and new techniques are appearing, including application of new signal processing techniques (Young and Gordon, 1996), new macromechanical prediction models (Harris, 1996), nonlinear dynamic models (Cusumano and Harris, 1995), and application of multi-sensor data fusion techniques (Hall, 1994).

At this time, there are many remaining issues that prevent the implementation of effective intelligent CBM monitoring systems. Figure 2 provides a brief summary of these issues and limitations for each of the CBM functional components shown in Fig. 1. The primary focus of this paper is on the challenges for automated reasoning for CBM.

Concept of Approximate Reasoning for Condition-Based Maintenance

The concept of automated approximate reasoning systems has an extensive history. The development of so-called expert systems has been a leading goal of artificial intelligence (AI) systems. These systems attempt to emulate the type of reasoning about *real-world* problems normally performed by human specialists or experts. At this time, several thousand expert (or knowledge-based) systems have been reported in the literature, and there are numerous books (Charniak et al., 1980; Hopgood, 1992) and commercially available tools to assist in their development. A guide to the extensive AI literature is provided by Gelfaud (1992). Approximate reasoning systems have been implemented for a wide variety of applications including medical diagnosis, chemical analysis, computer architecture design, planning systems, tactical threat assessment and situation assessment for military applications, and many others. It is natural then that these types of systems should be built to address condition-based maintenance.

The structure of expert systems explicitly separates a knowledge base (which represents facts, algorithms, heuristic logical relationships, etc.), about the domain of application (i.e., about the condition-based maintenance system), and the control structure or inference engine. The knowledge about the domain of interest may be represented via rules, frames, scripts, networks or direct (analogical) structures. The most popular form of representation techniques is the use of production rules of the form: *If* (there is evidence of condition [X]) *then do* (action [Y]).

An example of a rule associated with CBM is the following: *If there is evidence of increasing debris in the lubricant, then update the dynamic database to indicate that there may be excessive mechanical wear in the monitored mechanical subsystem.* Rules can be used to represent a collection of facts or procedures associated with a domain of interest. Regardless of the form of the representation technique (viz., rules, frames, etc.), uncertainty can be incorporated both in the antecedent (or left-hand side of the rule) and also in the consequence (or right-hand side of the rule). In this CBM example, uncertainty could be allocated to the evidence of debris (uncertainty about the existence of debris observed by a chip detector), as well as uncertainty in the conclusion (i.e., even if there are observed chips in the lubricant, this may not be conclusive evidence for excessive wear). The specification of a knowledge representation scheme also entails the specification of the representation technique for uncertainty, and the associated calculus of uncer-

Downloaded 02 Jun 2010 to 171.66.16.105. Redistribution subject to ASME license or copyright; see http://www.asme.org/terms/Terms_Use.cfm

CBM System Components	Description	Challenges
Sensors	Active and passive sensors to monitor mechanical systems and detect precursors to failure (e.g., accelerometers, temperature, pressure, etc.)	- Lack of robust sensors. - Non-optimal placement of sensors for existing mechanical systems - High false alarms rates - Sensor suite selection
Signal Processing	Digital Signal Processing (DSP) techniques for real-time analysis and characterization of the signal data.	- Detection and characterization of rare events - Poor signal-to-noise ratios - Real time processing
Multi-Sensor Data Fusion	Combination of multi-sensor data to improve the estimate of equipment state and detection of failure precursors.	- Lack of fusion models for CBM - Need to fuse non-commensurate sensor data
Automated Decision Processing	Automated approximate reasoning to interpret the results of sensor measurements, DSP, and predictive models for context-based interpretation of results.	- Need to combine implicit/explicit reasoning - Hierarchical reasoning - Need to address negative information
Predictive Techniques	Micro and macro level models to predict the temporal evolution of mechanical failure phenomena.	- Fundamental lack of predictive models - Need to link statistical prediction with nonlinear dynamic system evolution

Fig. 2 Challenges for automated CBM systems

tainty (i.e., the rules by which uncertainty measures are combined and propagated in an inference process).

Popular uncertainty representation schemes include probability, Dempster–Shafer evidential intervals, fuzzy membership functions, certainty factors and/or ad hoc data ambiguity indicators relating to either the collection integrity or (semantic) meaning of received data/features within a given context. An excellent review of these representation techniques is provided by Post and Sage (1990) and by Krause and Clark (1993). All of these techniques, however, are challenged by the problem of combining both positive information (e.g., symptoms of a problem) with negative information (i.e., information which by its absence or lack of symptoms is indicative of meaningful inferences).

The Challenge of Negative Reasoning

An example of negative reasoning is readily provided by the medical community. Physicians must be able to interpret and evaluate the relevancy and accuracy of information a patient gives them concerning their apparent illness in order to either make a diagnosis, or to specify additional testing if the patient-supplied data are incomplete. In many cases, both serious and not serious, patient-related symptoms are not sufficient for diagnosis and additional tests are needed.

From a physician's point of view, the doctor cannot allow himself to miss a potentially serious disease in his patient. Unless the diagnosis is trivial or readily treatable by a general antibiotic, the doctor is likely to specify a series of tests that seem relevant to the case at hand and would quickly bring to the surface the possible presence of a life-threatening condition such as a carcinoma, aneurism, arterial blockage, etc. By a careful selection of blood and body tissue tests and scans, the doctor will be able either to positively diagnose the condition or, at least, selectively eliminate candidates on the list (of hypotheses) of potential disorders. In particular, a negative test result indicates to the physician what is not the problem. This, in principle, is *negative reasoning* and appears to be an integral part of the medical community's standard approach to the treatment and diagnosis of disease. So, even though the doctor doesn't yet know exactly what is wrong with us, it may be assuring to know that whatever it is, it's probably not life threatening.

Consider the following example of the use of negative reasoning related to condition-based maintenance. Suppose that one observes excessive wear occurring on one's relatively new automobile tires. Possible mechanical rule-based faults leading to rapid tire wear are: (*a*) improper tire pressure, (*b*) front end misalignment, (*c*) damaged suspension arms, (*d*) worn shock absorbers, or (*e*) wheels out of balance. If your mechanic (the mythical Mr. Holmes), discovers nothing wrong (i.e., a negative result), he may then question you on your own driving habits. These questions could eventually lead to the information that there are several eligible drivers with access to this vehicle. His suspicions (hypothesis) of premature tire wear due to hard driving are reinforced by a quick look at the front brake pads and disks, and their installation date/mileage records. He finds both excessively worn pads, and heat glaze damage on the surface of the disks (positive result) for the age of the parts. Thus, by using a combination of positive and negative reasoning in conjunction with the vehicle maintenance history database records, machinery malfunction is ruled out.

These examples suggest that negative reasoning seems to be a natural part of the human reasoning process, although Evans et al. (1993) point out that there are numerous cognitive problems exhibited by humans that can cause erroneous reasoning. It appears, however, that negative reasoning can be invoked by humans when a situation presents itself that does not necessarily fit a given template and/or admits multiple hypotheses. The paradigm then shifts at some point from identifying what is wrong, to enumerating problems that cannot exist based on the observed data. In this way, one can at least possibly eliminate machine life critical problems that might lead to expensive operations shutdown or mission abort. In addition, within the negative reasoning context, fuzzy set theory can be used to measure degrees of set membership, e.g., machine oil may only be partially contaminated by the small addition of the wrong oil or the presence of debris versus a more concentrated degree of contamination, etc. Thus, even the degrees of negativeness in-

Downloaded 02 Jun 2010 to 171.66.16.105. Redistribution subject to ASME license or copyright; see http://www.asme.org/terms/Terms_Use.cfm

Causes/Symptoms	Symptom 01	02	03	04	05
Cause C1	✔		✔		
Cause C2		✔	✔	✔	
Cause C3	✔				✔
Cause C4			✔	✔	
Cause C5		✔			

Fig. 3 Example of use of symptomatic evidence to identify possible causes

stead of {0, 1} binary states can be incorporated into the overall analysis scheme of a diagnosis.

A Health Usage Monitoring System (HUMS) Example

In the case of an on-board helicopter Health Usage Monitoring System (HUMS), suppose that the low-oil transmission system pressure-sensor trips several hours into a flight mission. Any problems in the transmission, of course, get the pilot's attention quickly, and may necessitate a mission abort. Possible fault conditions leading to low transmission oil pressure are: (*a*) loss of fluid/seal leakage, (*b*) broken shaft in pump, (*c*) other oil pump failure, (*d*) clogged screens, or (*e*) faulty transducer/indicator system. The HUMS controller now has to decide what to do, i.e., what does it relate to the flight crew. Negative reasoning could be used effectively to identify and eliminate possible causal mechanisms.

The HUMS system should be able to cross-correlate the low oil condition with: (1) transmission oil temperature: normal temperature may suggest a false alarm/faulty sensor/electrical fault; (2) tripped oil bypass valves: if not tripped then the screens are probably fine; (3) engine oil level: if not overfull, then the dividing labyrinth seal between transmission and engine is probably not leaking; (4) check last time oil was added to the transmission; (5) check vibration signatures/levels of accelerometers in the area; and (6) check conditions of the transmission chip detectors and, when technology permits, perform an on-board oil spectroscopy analysis for ppm metal counts and rates. If no supporting evidence is found for the low oil pressure alarm, then the HUMS should: (*a*) record the event and relevant sensor information; (*b*) alert the pilot that a probable oil pressure sensor false alarm has occurred in the transmission, and that he should, if possible, perform an acceleration or change of speed maneuver carefully so HUMS can double check; (*c*) inform the pilot that the system has increased vigilance on the transmission, but to continue mission normally until further notice.

Figure 3 shows a positive matrix mapping of observations (O1, O2, . . .) across the top to causes (C1, C2, . . .) down the left side. Similarly, Fig. 4 shows the negative matrix mapping of non-observations (~O1, ~O2, . . .) to eliminated causes (hypotheses) marked by an X. Thus, for example, if the set of positive observations from Fig. 3 are {O1} ⇒ problems {C1 or C3} and the set of negative observations from Fig. 4 are {~O5} ⇒ ~{C1 or C2 or C4 or C5}, then fusion of the two positive and negative observation sets leaves C3 as the diagnosis. On the other hand, if the positive observation set is {O1 and O2} and the negative observation set is {~O3 and ~O4 and ~O5}, then there is (are) either a faulty sensor(s), or the knowledge base has a logical inconsistency.

Logically speaking, negative reasoning is closely akin to what is sometimes called the contrapositive, i.e., $P \Rightarrow Q \Leftrightarrow (\sim Q) \Rightarrow (\sim P)$, where $\sim P$ means *not* P. The statement $(\sim Q) \Rightarrow (\sim P)$ is the contrapositive of $P \Rightarrow Q$. The proof of equivalence is simple. $P \Rightarrow Q$ has the same truth table as $\{(\sim P)$ or $Q\}$. Likewise, $(\sim Q) \Rightarrow (\sim P)$ has the same truth table as $\{\sim(\sim Q)$ or $\sim P = \{Q$ *or* $\sim P\} = \{\sim P$ or $Q\}$, which is that of the original $P \Rightarrow Q$ truth table. Consequently, negative reasoning approaches are naturally built in to first-order logic (FOL) system theorem provers in which P is shown to follow from a set of propositions S by first assuming $\sim P$ and then deriving a contradiction (*resolution refutation*). Thus, negative reasoning could be utilized with first order and fuzzy logics or other inference schemes to help resolve cases of both uncertain and incomplete knowledge.

In practice, the combined positive/negative reasoning, illustrated above by Figs. 3 and 4, can be implemented using a technique called *logical templating,* originally developed for automated reasoning about tactical military situation and threat assessment. This technique combines logical relationships with the ability to identify information that must be present (or absent) in order to establish the existence of an activity, event, or condition. Logical templating may be implemented in a number of ways (e.g., Hall and Linn, 1989; Noble, 1987). More recently, these methods have begun to be implemented using knowledge-based system tools providing frame-based or case-based reasoning capabilities. Logical templating can be implemented very efficiently. Hall and Linn (1989) provide a description of the knowledge representation techniques and inference mechanisms.

A General Approximate Reasoning Architecture for CBM

Of course, the caveat of negative reasoning in diagnosis is that one needs a finite list of symptoms or hypotheses to work

Causes/Negative Evidence	Negative -01 Observation	N-02	N-03	N-04	N-05
Cause C1		✖		✖	✖
Cause C2	✖				✖
Cause C3		✖	✖	✖	
Cause C4	✖	✖			✖
Cause C5	✖		✖	✖	✖

Fig. 4 Example of use of negative information to eliminate possible causes

Downloaded 02 Jun 2010 to 171.66.16.105. Redistribution subject to ASME license or copyright; see http://www.asme.org/terms/Terms_Use.cfm

on, i.e., the doctor cannot specify an unlimited number of tests for his patients, but selects from a set of both general and system specific tests based on the reported symptoms. Unfortunately, combinatorial explosion of hypotheses is a general problem for logic systems since the more knowledge you have, the more hypotheses you are able to generate.

Due to the intricacies of real-world problems, a combination or hybridization of reasoning techniques is required to achieve some basic acceptable level of performance. These systems may be structured heuristically as a hierarchical blackboard/whiteboard architecture with intelligent numerical, parametric, and/or symbolic reasoning subsystem experts. However, in a context where either missing or uncertain knowledge is the rule rather than the exception, so-called monotonic reasoning methods appear inadequate. Due to the addition or change of input information over time, conclusions previously arrived at along the way within a diagnosis procedure may need to be revised or extended in order to accommodate the new information. For this reason, non-monotonic methodologies are often considered, i.e., those methodologies for which a conclusion can be retracted.

For example, first-order logic is monotonic since a new axiom may not invalidate any of the previous conclusions. Monotonicity, however, is generally viewed as a deficiency both in representation and reasoning for actual system applications (because it causes the inference process to become computationally intractable). On the other hand, Dempster–Shafer's method of evidential reasoning (Dempster, 1968; Buede and Martin, 1968) does permit non-monotonicity. Post and Sage (1990) provide an extensive discussion of knowledge-based methods and the issue of monotonic versus non-monotonic reasoning.

In a basic sense, automated decision making may be reduced to a (directed) search. The search may begin at the meta-level whereby the intelligent controller plans its attack against the problem, and then proceeds afterward into various top-down/bottom-up run-time control strategies generating and examining various hypotheses concerning the meaning of the data from its storehouse of knowledge. Unfortunately, searches consume time, which for many real-time processors is a constraining factor that must be carefully monitored. Any method that can effectively and validly reduce search time is then by definition good.

Consequently, negative reasoning is one tool that may be of help in reducing the overall number of hypotheses at various levels of abstraction for a given intelligent controller (I.C.) application. We believe that no one single knowledge representation scheme and inference technique is suitable for condition-based maintenance to span the inference hierarchy from a materials through platform level. Figure 5 shows a general knowledge-based system (KBS) architecture for CBM. The architecture uses a hierarchical set of reasoning approaches with an overall blackboard type of structure (see Englemore and Morgan, 1988, for a discussion of blackboard systems). In particular, at the platform level, three separate blackboards represent the *current* equipment status, predictions of *near-term* conditions, and a long-range (*far-term*) prediction. Various different knowledge representation techniques are used at the materials, element, component, subsystem, system, and platform levels to represent knowledge about mechanical faults, conditions, and predictions about the future evolution of failure mechanisms. A summary of these techniques at each level of the hierarchy is shown in Fig. 6. A particular challenge is to develop effective predictive models to predict the progression of a system state in time (e.g., the prediction of the progression of an identified failure mechanism).

Combined rule-based and negative reasoning strategies can be encoded and implemented in object-oriented languages such

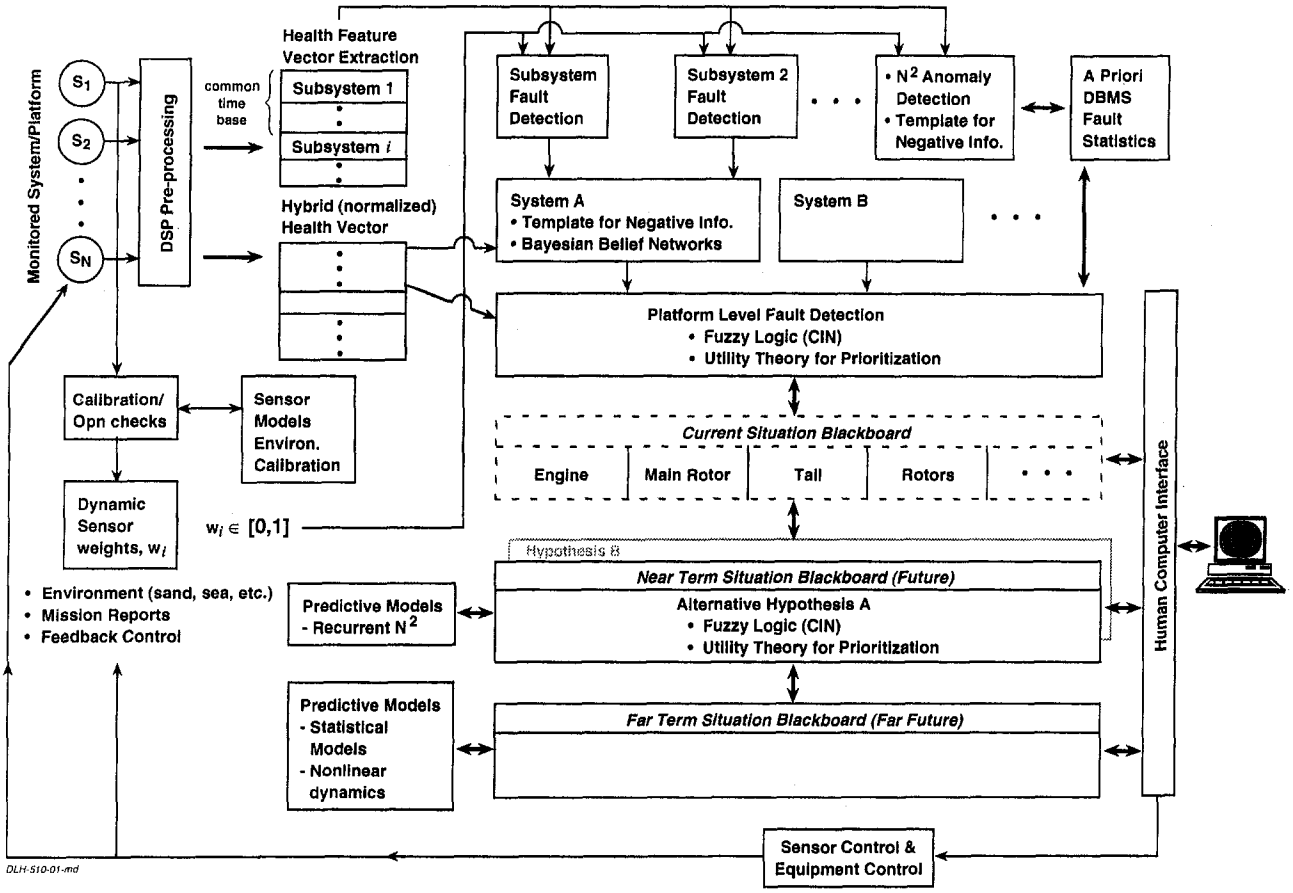


Fig. 5 A hierarchical approximate reasoning architecture for CBM

Downloaded 02 Jun 2010 to 171.66.16.105. Redistribution subject to ASME license or copyright; see http://www.asme.org/terms/Terms_Use.cfm

Hierarchical Layer	Example	Knowledge Representation and Diagnostic Models	Predictive Model
Material	Metal	- Finite Element Models - Continuous Models	- Coupled Field Damage Models
Element	Bearing Ball	- Finite Element Models - Oil Analysis	- Ioannides-Harris Model - Crack Growth Models - Probabalistic Neural Nets (PNN)
Component	Bearing	- Mechanical Dynamic Models - Wignerville/Stewart Figure of Merit [Stewart (1977)] - Time Synch, Averaging - PNN - Probability Models [Pomfret (1995)]	- Neural Networks [Lin and Ing-Chyuan (1991) and Haas, Milano and Flitter (1995)] - NaRX Models [Jean and Li (1995)] - Mortality Statistics [Harris] - Kalman Filters [Kalman (1963)] - Nonlinear Dynamics [Cusumano and Harris (1995)]
Subsystem	Hub/Swashplate/ *Lubrication*	- Logical Templates (Case-Based) - Bayesian Belief Nets [Shachter (1986)] - Dempster-Shafer's Method [Dempster (1968)] - Continous Inference Nets [Gibson, Hall and Stover (1994)] - PNN - Petri Nets [David and Hassane (1994)]	- Mortality Statistics - Nonlinear Dynamics - Stochastic Models [Ray and Tangirala] - Dynamic State Models [Frank (1990)]
System	Main Rotor System	- Continuous Inference Nets [Gibson, Hall and Stover (1994)] - Bayesian Belief Nets [Shachter (1986)] - Undirected Graph Models [Pelc (1991)] - Dempster-Shafer's Method [Lowrance and Garvey (1982)] - Logical Templates - Petri Nets [David and Hassane (1994)] - Blackboard KBS [Hall and Linn (1989)] - Expert Systems [Hansen, Autar and Pickles (1993)] - Interacting Autonoma [Peluso et al. (1994) and Phoha et al. (1993)] - Syntatic Models [Eshera and Fu (1986)]	- UMARC [Haas et al. (1995)] - Markov Modeling - Floquet Theory
Plant/Platform	Helicopter	- Continuous Inference Nets [Gibson, Hall and Stover (1994)] - Expert Systems [Hansen, Autar and Pickes (1993)] - Utility Theory - Blackboard Models [Englemore and Morgan (1988)] - Syntatic Models [Eshera and Fu (1986)] - Process Models [Dvorak (1991)]	- Scenario Models

Fig. 6 Examples of knowledge representation techniques for CBM

as $C++$ for a variety of applications. Such languages with their symbolic object structures and associated procedures seem, in particular, to enjoy success in the areas of signal and image processing. (However, some specialized languages, such as Prolog, may experience some difficulty with exploiting negative reasoning to full advantage if they operate entirely in closed-world mode, i.e., if a relation cannot be proved with the existing knowledge, it is considered false.)

We are currently experimenting with different techniques for condition-based maintenance. One component of this automated reasoning involves the use of fuzzy logic at the platform level. In particular, we have adapted a fuzzy logic controller system, originally developed for real-time control of the sensors, propulsion, and guidance of an autonomous underwater vehicle (see Gibson et al., 1994). This architecture uses a new formulation of fuzzy logic calculus, and a continuous, differentiable fuzzy membership function to map observables into fuzzy membership values for use in the explicit fuzzy reasoning. Such a control system allows integration of the evolving information on mechanical components, subsystems, systems, and at the platform level for a contextual interpretation and recommendations to platform users or crew.

Comments on Implementation

The architecture (Fig. 5) introduced in the previous section is intended to be a general structure, which is applicable to condition-based maintenance systems across the complete spectrum from mechanical components and subsystems to systems and platform level of automated inferencing. The selection of particular knowledge representation techniques and prediction algorithms (e.g., from those listed in Fig. 6), must be tailored to specific applications having specific requirements, sensor suites, mission requirements, etc. Until many systems have been implemented using this structure, it is difficult to evaluate the utility of this architecture compared. However, we are currently implementing two condition-based maintenance (CBM) systems using this approach: (1) an intelligent oil monitoring system as part of Allied Signal Engine's Full Authority Digital Electronic Controller (FADEC) system for an upgrade for turbine engines; and (2) an experimental system to monitor the health of the rotor drivetrain for a helicopter. Some general comments are provided in this section concerning our initial experiences with this architecture.

The intelligent oil monitoring system for Allied Signal Engine's FADEC system is intended to provide automated monitoring and prediction of the condition of the oil subsystem for turbine engines. This is part of an anticipated evolution of the TF 40 FADEC. Types of sensor measurements will include: engine speed, oil pump flow, oil sump pressure, gearbox oil pressure, main oil pressure, filter outlet temperature, filter inlet pressure, etc. For each of these sensors, separate signal processing will be performed with extraction of representative features to represent the current state of the system, based on single sensor data alone. Experiments are currently ongoing to establish the specific digital signal processing (DSP) to be applied to each sensor data stream. Several promising techniques appear to be the use of higher order (cycto-stationary) spectral techniques, and use of non-stationary recursive filters (Lopatinskaia et al., 1995) and wavelet techniques (Weiss, 1994). A parametric template technique monitors whether observed fea-

Downloaded 02 Jun 2010 to 171.66.16.105. Redistribution subject to ASME license or copyright; see http://www.asme.org/terms/Terms_Use.cfm

tures (e.g., measured temperature, oil debris metrics, etc.) exceed acceptable thresholds. In turn, these individual sensor data are fused using feature-based, and decision level, data fusion techniques. These latter include classic pattern recognition techniques, weighted decision techniques (i.e., voting techniques), and Bayesian inference methods. The data fusion processing is implemented using a special visual programming data fusion toolkit developed at ARL (Hall and Kasmala, 1996). This toolkit was implemented in Visual $C++$ and allows researchers to select signal processing and data fusion algorithms from an evolving library of algorithms. The techniques can be linked together and applied to either simulated or real sensor data. Graphics utilities allow ready visualization of the processing results. The tool is analogous to the toolkit *Khoros* used for image processing.

A fuzzy logic inference system, based on Stover and Gibson's continuous inference network (Gibson et al., 1994), provides an interpretation of the results. While the fuzzy logic representation is convenient to represent explicit information about interpretation of sensor observations (e.g., based on the operation of the turbine engine), there are still challenges with combining uncertainty information about sensor reliability (in a dynamic sense), a priori information about the relative likelihood of fault conditions, and the confidence of logical relationships. This problem has not yet been solved. However, we expect that appropriate combination of probability measures, fuzzy membership functions, and utility measures will be useful to address the uncertainty representation. Currently, experiments are being conducted using simulated sensor data and hypothesized profiles of system operation (viz. the operation characteristics of the system as a function of a startup, typical operation, and system shut down). In the near future, actual sensor data will be processed. The resulting signal processing, data fusion, and automated inference system will be implemented in the FADEC processing architecture. An advantage of the continuous inference network formulation for fuzzy logic is that it admits of a real-time implementation using common microprocessors. The negative information templating process, described in the previous section of this paper, is used to reduce the number of potential causes for maintenance problems.

The second system currently under development is an automated inference system to monitor and diagnose problems with the rotor drivetrain for a Huey-type helicopter. The concept involves use of accelerometers and related sensors to monitor the condition of the rotor system including the rotor assembly, mechanical drive linkages, and transmissions (see Hall and Smith, 1996). The focus on this research involves the higher level inferences for prediction and data interpretation (rather than the details of the processing of individual sensor data). Current developments use a rule-based fuzzy logic reasoning structure. Experiments are ongoing to compare standard fuzzy reasoning systems (e.g., such as those available from the commercial package, MATLAB), to the Stover and Gibson Continuous Inference Network (CIN)) structure (Gibson et al., 1994). It appears straightforward to develop fuzzy logic rules for diagnosis and prediction based on observed conditions. For example, only 50 rules are required to analyze vibration, temperature, and pressure data to diagnose bearing seizure and pump failures in a helicopter drivetrain. The negative reasoning template structure described in the previous section is again used to reduce the number of potential causes based on observed symptoms.

A general comment involves the adoption of predictive models. Currently, truly predictive models do not exist. Other research at Penn State is focusing on this area (Cusumano and Harris, 1995). In the meantime, we are utilizing trending models based on several types of neural networks to process sensor time series data. In addition, the evolution of feature-based data are tracked to provide predictions of failure trends. As more physically realistic models become available, we will incorporate them into our automated CBM model.

Summary

In this paper, we have discussed the challenges of approximate reasoning for condition-based maintenance systems. At this time, there does not appear to be a single knowledge representation and reasoning approach that will perform automated context-based reasoning for CBM, meeting the unique requirements, which include the ability to reason with negative information, the need to reason about a hierarchy of components, and the need for non-monoticity. The architecture described here utilizes a wide set of techniques to link microscopic failure phenomena, macroscale observations, and human decision factors such as mission constraints. The structure introduced here is very general, but can be readily adapted to individual CBM problems. In particular, the use of a blackboard structure and a hierarchical set of inference methods is well suited to mechanical systems because these systems can be partitioned based on physical interconnections and hierarchy. Experience with two sample CBM systems appears promising. Much research still remains, especially in the area of predictive models. Nevertheless, progress is being achieved to attain true predictive intelligent CBM systems.

References

Bernieri, A., D'Apuzzo, M., Sansone, L., and Savastano, M., 1994, "A Neural Network Approach for Identification and Fault Diagnosis on Dynamic Systems," IEEE *Transactions on Instrumentation and Measurement,* Vol. 43, No. 6, pp. 867–873.

Buede, D. H., and J. W. Martin, 1968 "Comparison of Bayesian and Dempster-Shafer Fusion," *Proc. 1987 Tri-Service Data Fusion Symposium,* Vol. 1, pp. 82–91.

Charniak, E., Riesbeck, C. K., and McDermott, D. V., 1980, *Artificial Intelligence Programming,* Lawrence Erlbaum Associates Publishers, Hillsdale, NJ.

Cusumano, J. P., and Harris, T. A., 1995, "Micro-Mechanical Modeling and Nonlinear Dynamics," presented at the 7th Annual Predictive Maintenance Technology National Conference, Indianapolis, IN.

David, R., and Hassane, A., 1994, "Petri Nets for Modeling of Dynamic Systems—A Survey," *Automatica,* Vol. 30, No. 2, pp. 175–202.

Dempster, A. P., 1968, "A Generalization of Bayesian Inference," *Journal of Raoy Statistical Society,* Vol. 30, pp. 205–247.

Douses, D. A., 1994, "Development and Integration of Onboard Drive Train Vibration Monitoring Systems," *Proc. American Helicopter 50th Annual Forum,* Washington, DC, pp. 441–457.

Dvorak, D., and Kuipers, B., 1991, "Process Monitoring and Diagnosis: A Model-Based Approach," *IEEE Expert,* pp. 67–74.

Englemore, R. S., and Morgan, A. J., eds., 1988, *Blackboard Systems,* Addison Wesley.

Eshera, M. A., and Fu, K.-S., 1986, "An Image Understanding System Using Attributed Symbolic Representation and In-Exact Graph-Matching," IEEE *Transactions on Pattern Analysis and Machine Intelligence,* Vol. PAM 1-8, pp. 604–618.

Evans, J. S. B. T., Newstead, S. E., and Byrne, R. M. J., 1993, *Human Reasoning: The Psychology of Deduction,* Lawrence Erlbaum Associates, Ltd., Hillsdale, NJ.

Frank, P. M., 1990, "Fault Diagnosis in Dynamic Systems Using Analytical and Knowledge-Based Redundancy—A Survey and Some New Results," *Automatica,* Vol. 26, No. 3, pp. 459–474.

Ganesan, R., Jionghua, H., and Sankar, T. S., 1995, "A Classification Neural Network for Rotordynamics Systems," *Mechanical Systems and Signal Processing,* Vol. 9, No. 4, pp. 397–414.

Gelb, A., 1974, *Applied Optimal Estimation,* The MIT Press, Cambridge, MA.

Gelfaud, J., 1992, *Selective Guide to Literature on Artificial Intelligence,* American Society for Engineering Education.

Gibson, R. E., Hall, D. L., and Stover, J. A., 1994, "An Autonomous Fuzzy Logic Architecture for Multi-Sensor Data Fusion," *Proc. 1994 IEEE International Conference on Multi-Sensor Fusion and Integration for Intelligent Systems,* Las Vegas, NV, pp. 443–446.

Guo, T. H., and Merrill, W., 1991, "A Diminished Fault Detection and Diagnosis System using On-Line Parameter Estimation," NASA Technical Memorandum, No. 104433.

Haas, D. J., Milano, J., and Flitter, L., 1995, "Prediction of Helicopter Component Loads using Neural Networks," *Journal of the American Helicopter Society,* Vol. XX, pp. YY–ZZ.

Hall, D. L., and Linn, R., 1989, "Comments on the Use of Templating Techniques for Multi-Sensor Data Fusion," *Proc. Third Tri-Service Data Fusion Symposium,* Vol. 1, pp. 345–354.

Hall, D. L., 1994, "Application of the JDL Data Fusion Model to Condition-Based Maintenance Systems," *Proc. 1994 Data Fusion Systems Conference,* Johns Hopkins University, Laurel, MD.

Hall, D. L., and G. Kasmala, 1996, "A Visual Programming Environment for Multi-Sensor Data Fusion," *Proc. SPIE Symposium on Aerospace/Defense Sensing and Controls,* Orlando, FL.

Downloaded 02 Jun 2010 to 171.66.16.105. Redistribution subject to ASME license or copyright; see http://www.asme.org/terms/Terms_Use.cfm

Hall, D. L., and Smith, E., 1996, "Usage and Structural Life Monitoring With HUMS," *Proc. of the 52nd American Helicopter Society AHS Annual Forum.*

Hansen, C. H., Autar, R. K., and Pickles, J. M., 1993, "Expert Systems for Machine Fault Diagnosis," *Acoustics Australia,* Vol. 22, No. 3, pp. 85–90.

Hansen, C. H., Autar, R. K., and Pickles, J. M., 1994, "Expert Systems for Machine Fault Diagnosis," *Acoustics Australia,* Vol. 22, No. 3.

Hansen, R. J., Hall, D. L., and Kurtz, S. K., 1995, "A New Approach to the Challenge of Machinery Prognostics," ASME JOURNAL OF ENGINEERING FOR GAS TURBINES AND POWER, Vol. 117, pp. 320–325.

Harris, T. A., 1996, "Prediction of Ball Fatigue Life in a Ball/V-Ring Test Rig," ASME *Journal of Tribology,* in press.

Hopgood, A. A., 1992, *Knowledge-Based Systems for Engineers and Scientists,* CRC Press, London, United Kingdom.

Isermann, R., and Ulieru, M., 1993, "Integrated Fault Detection and Diagnosis," *Proc. IEEE International Conference on Systems, Man and Cybernetics,* Vol. 1.

Jammu, V. B., Danai, K., and Lewicki, D. G., 1995, "Diagnosis of Helicopter Gearboxes Using Structure-Based Networks," *Proc. 1995 American Control Conference,* Seattle, WA.

Jeon, Y. C., and Li, J. C., 1995, "Non-linear ARX Model-Based Kullback Index for Fault Detection of a Screw Compressor," *Mechanical Systems and Signal Processing,* Vol. 9, No. 4, pp. 344–358.

Kalman, R. E., 1963, "New Methods in Wiener Filtering Theory," *Proc. First Symposium of Engineering Applications of Random Function Theory and Probability,* Wiley, New York, pp. 270–388.

Krause, P., and Clark, D., 1993, *Representing Uncertain Knowledge: An Artificial Intelligence Approach,* Kluwer Academic Publishers, Norwell, MA.

Lin, C.-S., and Wu, I.-C., 1991, "Neural Networks for Sensor Failure Detection and Data Recovery," *Proc. Artificial Neural Networks in Engineering Conference.*

Lopatinskaia, E., Zku, J., and Mathew, J., 1995, "Monitoring Varying Speed Machinery Vibrations: The Use of Non-stationary Recursive Filters," *Mechanical Systems and Signal Processing,* Vol. 9, pp. 635–645.

Loukis, E., Mathioudakis, K., and Papailiou, K., 1994, "Optimizing Automated Gas Turbine Fault Detection using Statistical Pattern Recognitions," ASME JOURNAL OF ENGINEERING FOR GAS TURBINES AND POWER, Vol. 116, pp. 165–171.

Lowrance, J. D., and Garvey, T. D., 1982, "Evidential Reasoning: A Developing Concept," *Proc. International Conference on Cybernetics and Society,* pp. 6–9.

Merrington, G. L., 1994, "Fault Diagnosis in Gas Turbines Using a Model-Based Technique," ASME JOURNAL OF ENGINEERING FOR GAS TURBINES AND POWER, Vol. 116, pp. 374–380.

Neopolitan, R. E., 1990, *Probabilistic Reasoning in Expert Systems: Theory and Algorithms,* Wiley, New York.

Noble, D. F., 1987, "Template Based Data Fusion for Situation Assessment," *Proc. Tri-Service Data Fusion Symposium,* Vol. 1, pp. 152–162.

Pandian, R., and Rao, B. M. N., 1989, "Condition-Based Maintenance for Drilling," *Proc. First International Machinery Monitoring and Diagnostics Conference,* Las Vegas, NV, pp. 291–298.

Pelc, A., 1991, "Undirected Graph Models for System-Level Fault Diagnosis," *IEEE Transactions on Computers,* Vol. 40, No. 11, pp. 1271–1276.

Peluso, E., Goldstine, J., Phoha, S., Sircar, S., Yukish, M., Licari, J., and Mayk, I., 1994, "Hierarchical Supervision for the Command and Control of Interacting Automata," *Proc. Symposium on Command and Control Research.*

Phoha, S., Sircar, S., Ray, A., and Mayk, I., 1993, "Computational Grammars for Hierarchical Command and Control Automata," *Technical Proc. 1993 Symposium on Command and Control Research.*

Pomfret, C. J., 1995, "Probabilistic Concepts for Gas-Turbine Engine Management," *Aerospace Engineering,* pp. 9–12.

Post, S., and Sage, A., 1990, "An Overview of Automated Reasoning," IEEE *Transactions of Systems, Man and Cybernetics,* Vol. 20, No. 1, pp. 202–204.

Rao, B. V. A., 1996, "Condition Monitoring-Condition-Based Maintenance," *Journal of the Institution of Engineers (India), Part ME: Mechanical Engineering Division,* Vol. 66, No. 5, pp. 123–129.

Ray, A., and Tangirala, S., 1997, "Stochastic Modeling of Fatigue Crack Dynamics for On-Line Prediction of Remaining Service Life," submitted for publication.

Ray, A., and Wu, M.-K., 1994, "Fatigue Damage Control of Mechanical Systems," *SMART Materials and Structures,* Vol. 3, No. 1, pp. 47–58.

Shachter, R. D., 1986, "Evaluating Influence Diagrams," *Operations Research,* Vol. 14, No. 6, pp. 871–822.

Stewart, R. M., 1977, "Some Useful Data Analysis Techniques for Gearbox Diagnostics," Stewart-Hughes Limited Report, University of Southampton, United Kingdom.

Upadhyaya, B. R., 1988, "Data Clustering and Prediction for Fault Detection and Diagnostics," *Proc. American Control Conference,* Vol. 88, pp. 1–3.

Weiss, L. G., 1994, "Wavelets and Wideband Correlation Processing," IEEE *Signal Processing Magazine,* pp. 13–32.

Young, R. K., and Gordon, G. A., 1996, "Wavelet Domain Characterization of Modal Acoustic Emissions From Gear Teeth During Fatigue Failure," presented at the MFPT 50 Conference, Mobile, AL.

Downloaded 02 Jun 2010 to 171.66.16.105. Redistribution subject to ASME license or copyright; see http://www.asme.org/terms/Terms_Use.cfm

Multivariable Trend Analysis Using Neural Networks for Intelligent Diagnostics of Rotating Machinery

S. Zhang

R. Ganesan

Department of Mechanical Engineering,
Concordia University,
Montreal, Quebec, Canada, H3G 1M8

The objective of this paper is the development of an efficient intelligent diagnostic procedure that considers several diagnostic indices for the quantification of developing faults and for monitoring machine condition. In this procedure, the condition monitoring is performed based on the on-line vibration measurements, and further, the fault quantification is formulated into a multivariate trend analysis. Self-organizing neural networks are then deployed to perform the multivariable trending of the fault development. The attributes for the disordering of "knots" in the trend analysis are determined. The disordering of neural network units is then eliminated by suitably altering the self-organizing neural network algorithm. Applications of this diagnostic procedure to the condition monitoring and life estimation of a bearing system are fully developed and demonstrated. The efficiency and advantages of the intelligent diagnostic procedure in precisely monitoring and quantifying the fault development are systematically brought out considering this bearing system.

1 Introduction

On-line monitoring of rotating machinery systems leads to modifications in the mechanisms and machine systems so as to minimize both the noise and the transmission of vibrations, and to increase the life of the machine. The on-line vibration signals provide useful and reliable diagnostic information since they are sensitive to most of the faults or malfunctions (Cempel, 1988). A number of quantitative indices such as the peak-to-peak value (PP), arithmetic mean value (AM), and crest factor (CR) can be extracted from the on-line vibration signal. These indices are sensitive to changes in machine condition, which are in turn caused by machine faults or malfunctions (Collacott, 1977, 1979). It has been clearly shown in past investigations (Tranter, 1989; Lipovszky et al, 1990) that the machine condition and fault development in the rotating machinery are more precisely indicated by the corresponding changes in several diagnostic indices. Moreover, the use of several diagnostic indices has been shown in these works to be essential for reliable monitoring and diagnostics. This is primarily due to the fact that there is no single index that can completely and adequately represent the development of any fault or malfunction. For the prediction of residual life of the machine system, the faults or malfunctions developing in the machine must be quantified and used as a basis, since the residual life is a function of accumulated damage or fault in the machine components. For precise quantification, it is essential to consider several diagnostic indices.

Existing diagnostic systems consider each diagnostic index separately. An automated diagnostic procedure that simultaneously considers several diagnostic indices has not so far been developed. The development of such a procedure is the prime objective of the present paper. This diagnostic procedure is developed such that it can readily be deployed in modern intelligent diagnostic systems such as the knowledge-based diagnostic systems. Recognizing the nature of the mathematical problem associated with the intelligent diagnostic procedure developed in the present work, the Self-Organizing Mapping (SOM) neural networks are considered to be highly suitable and are deployed to quantify the fault development and to determine the machine condition.

2 Trending the Fault Development

In the diagnostic procedure developed in the present work, the faults or malfunctions are detected and quantified using a trend analysis. To this end, the following multidimensional trend analysis problem is considered:

$$y = f(\mathbf{x}) + e \tag{1}$$

where $\mathbf{x} \in R^N$ is a vector consisting of N independent variables, and e is an unknown arbitrary disturbance. The task of trend analysis is to find the multivariate function $f(\cdot)$ defined in the $(N + 1)$-dimensional sample space, from a given set of data pairs $(\mathbf{x}_i, y_i)$, $i = 1, 2, \ldots, n$. In the diagnostic procedure, the set of N diagnostic indices representing the operative states or health conditions of a machine system is considered to constitute the vector $\mathbf{x}$ of Eq. (1) and further, the dependent variable y is taken to be the performance indicator for the purpose of monitoring the operation of the machine system or the performance of its components, and for predicting the degree of damage or the residual life of the machine. Correspondingly, the multivariate function $f(\cdot)$ is interpreted as representing a curve in high-dimensional (i.e., $N > 1$) space displaying continuous changes in the condition of the machine system. The function $f(\cdot)$ is determined and then used for monitoring the machine condition and to predict the future behavior of the machine system. Further, based on the current values of the components of (diagnostic) vector $\mathbf{x}$, the residual life of the machine is approximated using Eq. (1).

Considering the difficulties associated with the estimation of nonlinear high-dimensional functions from data samples, the multivariate diagnostic function $f(\cdot)$ is determined using the nonparametric regression analysis methodology that seeks neural network solutions (Cherkassky and Lari-Najafi, 1991). In particular, the piecewise linear regression method that uses linear functions, i.e., straight-line segments that are interconnected

Contributed by International Gas Turbine Institute for publication in the JOURNAL OF ENGINEERING FOR GAS TURBINES AND POWER. Manuscript received at ASME Headquarters September 1996. Associate Technical Editor: H. L. Julien.

Copyright © 1997 by ASME

Downloaded 02 Jun 2010 to 171.66.16.105. Redistribution subject to ASME license or copyright; see http://www.asme.org/terms/Terms_Use.cfm

at points known as knots (Friedman and Silverman, 1989), is deployed. More accurate results are achieved by dynamically changing the positions of knots based on some preselected criterion, as the regression analysis is performed.

3 Neural Network Solution

Quite recently, several new computational techniques that make use of neural networks have been proposed for nonparametric regression problems, including back-propagation algorithm (Baum, 1990), self-organizing mapping (Cherkassky and Lari-Najafi, 1992), probabilistic neural networks (Specht, 1991) etc. Among them, the self-organizing topological mapping has been shown to be capable of achieving adaptive placement of neurons (that are dynamically changing the positions of knots as the regression analysis is performed) on the regression surface and further, the placement of neurons has been confirmed with the distribution of the given sample data in multidimensional sample space.

In the self-organizing mapping algorithm (Kohonen, 1989), the distribution of data in a high-dimensional sample space is topologically mapped onto a lower dimensional (usually one- or two-dimensional) feature space that is represented by self-organized neurons as a discrete lattice of units. For one-dimensional maps, this neural network is a segment of ordered units represented as $\{\mathbf{w}_1, \mathbf{w}_2, \ldots, \mathbf{w}_k\}$. Each unit $\mathbf{w}_i$ is a weight vector having the same dimensionality as that of the sample vectors used for training and denotes the spacial location of the ith unit (knot) in the regression space. The self-organization procedure consists of two steps. The first step is to find the best matching unit (winning unit) to the current input vector $\mathbf{z} = (\mathbf{x}, y)$ based on the measurement of Euclidean distance in the training sample space $\mathbf{z}$. The second step is to modify the weight vectors of both the winning unit and its neighboring units, so as to reduce the distances between these units and the input vector. When the SOM algorithm is applied to trend analysis, the estimation of a multivariate function is performed through a process of constructing a topological map from a given data set $\mathbf{z}_i = \{\mathbf{x}_i, y_i\}^T$, $i = 1, \ldots, n$, in an $(N + 1)$-dimensional sample space.

Considering the fact that the direct use of SOM for nonparametric regression analysis may make the knots disordered, Cherkassky and Lari-Najafi (1991) proposed the Constrained Topological Mapping (CTM) algorithm. In this algorithm, the winning unit corresponding to an input sample data is obtained in the $\mathbf{x}$ subspace of independent variables rather than in the $\mathbf{z}$ space. However, the adjustment of the positions of knots still takes place in the $\mathbf{z}$ space.

4 Disordering of Neural Network Units

A self-organizing map for trend analysis must satisfy some conditions. In self-organizing processes for function regression, in addition to responding to the distribution of the training data, the topological ordering of the neurons in a network should reflect the ordered neighborhood relations of input signals drawn from the input sample space. As a simple condition, it can be said that, if the values of the projection of given data points on an axis is monotonically increasing (or decreasing), the projection of the units onto the same axis should be increasing (or decreasing) in an orderly fashion. Self-organizing maps that are not such ordered maps have been called disordered maps (Cherkassky and Lari-Najafi, 1991). The attributes of the disordering of knots are found out using the following two examples:

Experiment 1. A single-variable function that represents a curve on the x–y plane in the following form is now considered.

$$y = f(x) = ax^2 + bx + c \quad 0 < x < l \tag{2}$$

where a, b, and c are constants, and l is the maximum value of x. With due consideration of disturbance and noise, this model becomes

$$y = f_d(x) = (a + e_1(x))x^2 + (b + e_2(x))x + c + e_3(x) + e_4 \tag{3}$$

where

$$e_1(x) = 0.2a \sin(2\pi x/20.0)$$
$$e_2(x) = 0.08b \sin(2\pi x/7.0)$$
$$e_3(x) = v \sin(2\pi x/4.0 + 0.3)$$
$$v = 0.1 f(x)_{\max} = 0.1 f(l)$$

and e_4 is a Gaussian white noise, denoted by $\mathbf{N}(0, v)$, with zero mean and a standard deviation of v. In Eq. (3), $e_1(x)$, $e_2(x)$, and $e_3(x)$ are assumed forms of disturbance. The constants in Eqs. (2) and (3) are chosen as $a = 0.01$, $b = 0.2$, and $c = 80$. The training data are uniformly sampled from the function $f_d(x)$ in the domain [0, 140] with a minimal sampling interval of 0.25. A total of 4480 samples are obtained, i.e., $n = 4480$. Both the idealistic curve $f(x)$ without disturbance and the scatterplot of the sample data points obtained from $f_d(x)$ are presented in Fig. 1. Since the data are uniformly sampled from $f_d(x)$, the projections of data points onto the x axis are monotonically increasing and further, they are uniformly distributed.

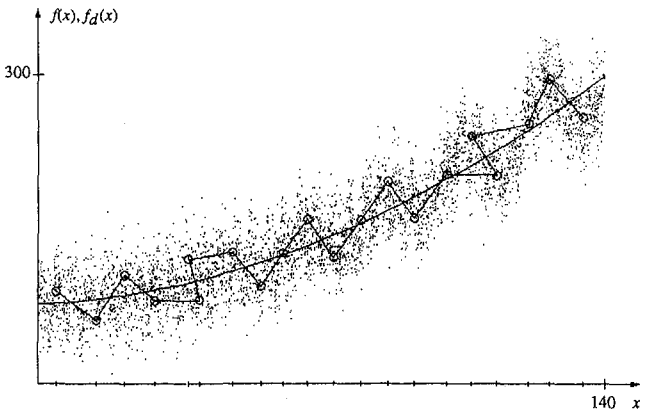


Fig. 1 A 20-unit network obtained using the SOM algorithm

A network of units $\{\mathbf{w}_1, \mathbf{w}_2, \ldots, \mathbf{w}_k\}$, $k = 20$, is established through the original SOM algorithm for estimating the underlying function from the data samples. The topological mapping is demonstrated in Fig. 1, which shows that the order of the 20 units (shown by small circles linked by straight lines) measured along the x axis has been violated. The units are not in increasing order, and are not distributed uniformly along the x axis as the distribution of the data samples on the x axis should do. The CTM algorithm provides a better result when it is deployed for obtaining a self-organizing map from the same set of data samples. Figure 2 shows one such result. A self-organizing map consisting of 20 units has been obtained using the CTM algorithm. The curve thus obtained can be considered as a proper map for the purposes of regression. However, when fitting a curve in a higher dimensional space, the CTM algorithm may also produce disordered maps. This can be seen from the following experiment.

Experiment 2. Another simulation experiment is performed to fit a high-dimensional "**S**" curve using self-organizing neural networks. Basically, in this simulation, an **S** curve is given by a sigmoid function:

$$y = f_s(x) = \frac{1}{1 + e^{-\lambda x}} \tag{4}$$

where x is an independent variable and, the constant λ controls

Downloaded 02 Jun 2010 to 171.66.16.105. Redistribution subject to ASME license or copyright; see http://www.asme.org/terms/Terms_Use.cfm

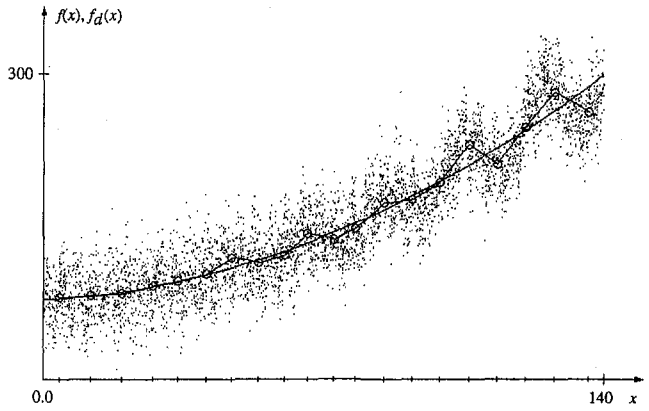


Fig. 2 Regression curve obtained using the CTM algorithm based on a 20-unit network

the shape of the **S** curve. Such an **S** curve has been very useful in describing many important engineering phenomena such as the cumulative fatigue damage process of many engineering materials.

A three-dimensional **S** curve in the sample space of $y = f(x_1, x_2)$ is given by

$$x_2 = \frac{0.6}{1.0 + e^{-0.03(x_1 - 0.5l)}} + 0.2 + e_1 \quad 0 < x_1 < l \tag{5}$$

$$f(x_1, x_2) = \frac{0.75}{1.0 + e^{-0.03(x_1 - 0.5l)}} + 0.125 + e_2 \tag{6}$$

where $x_1 = 1, 2, \ldots, l$ and l is the length of data samples. The e_1 and e_2 are Gaussian white noise defined as $\mathbf{N}(0, v)$. Standard deviation v is expressed as a percentage of the function range. The training data has been generated by Eqs. (5) and (6) with $l = 400$, $e_1 = \mathbf{N}(0, 25$ percent) and $e_2 = \mathbf{N}(0, 15$ percent). The CTM algorithm has been tested in establishing a neural network with 20 neurons to fit the three-dimensional curve. The initial locations of the 20 neurons have been set to be at equal distance (uniform distribution) in the sample space. The data points and regression results are shown in Fig. 3, where the two plots show the projections of data points onto x_1–y and x_1–x_2 planes. The projections of the final locations of the knots are shown with small circles linked by straight lines. From Fig. 3 it can be seen that the order of some knots of the neural network has been violated and that some of the knots are too close to each other. Hence, the CTM algorithm has failed in solving this function regression problem.

Both the SOM the CTM algorithms produce disordered maps when deployed for fitting high-dimensional curves. The attributes for the disordering of knots have been investigated in detail by the present authors (Zhang, 1995). It has been observed that in the regression process, the distribution of sample data is mapped onto the units of the neural network through the self-organizing process. The key reason for the disordered maps is that the nonuniform distribution of the variables (i.e., y in Eq. (3), or y and x_2 in Eqs. (5)–(6)) has exerted improper and too much influence on the selection of the best matching unit. This way it has been deduced that when the variable that has a uniform distribution is forced to exert enough influence on the selection of the winning unit, the disordering of network units can be avoided. This deduction served as a basis for developing a new efficient network algorithm.

5 An Efficient Algorithm for Machine Fault Diagnosis

Generally, the on-line diagnostic data obtained from machine systems have varied distribution, disturbance, and noise, especially wherever the sample data are collected from industrial machine systems. It is quite possible that the distribution of at least one variable in the sample space is uniform. In fact, the most widely used discrete sampling method records sample values through increasing (or decreasing, or continuously changing) one or more variables in equal intervals. One or more variables will thus have a uniform distribution and the values of other variables will be in series relative to this sampling order. A uniformly distributed variable will force the mapping algorithm to have the projection of units on the dimension corresponding to this variable, which in turn will help the learning algorithm in avoiding nonfunctional maps.

A greater weight is given in this new algorithm to the variable that has a uniform distribution. The weight factor is called the "scaling factor" and it is denoted by the symbol s, since it actually changes the scales of one or more dimensions in the Euclidean space. In selecting the winning unit, the distance between the sample data $\mathbf{z} = \{x_{1z}, x_{2z}, \ldots\}^T$ and a unit $\mathbf{w} = \{x_{1w}, x_{2w}, \ldots\}^T$ will be calculated by

$$\begin{aligned}\|\mathbf{z} - \mathbf{w}\| &= \sqrt{(x_{1z} - x_{1w})^2 + \ldots + (sx_{iz} - sx_{iw})^2 + \ldots} \\ &= \sqrt{(x_{1z} - x_{1w})^2 + \ldots + s^2(x_{iz} - x_{iw})^2 + \ldots}\end{aligned} \tag{7}$$

where it is supposed that x_i has a uniform distribution and so it has been greatly weighted by $s > 1$. Therefore, variables other than x_i can effect the winning unit selection only when the value of $s^2(x_{iz} - x_{iw})^2$ is relatively small. This strategy helps the self-organization process in producing functional maps not only along the dimension of the variable that has a uniform distribution but also in other dimensions. The algorithm is now given in terms of computational steps.

Step 1. Locate all the k units, $\mathbf{w}_i = \{\mathbf{x}_i, y_i\}^T = \{x_{i1}, \ldots, x_{iN}, y_i\}^T$, $i = 1, 2, \ldots, k$, randomly or at equal distances in the sample space $\mathbf{z}$ as their initial positions, and set the value of the scaling factor to be $s > 1.0$ (there could also be more than one scaling factor).

Step 2. Given a randomly chosen input training data vector $\mathbf{z}(t) = \{\mathbf{x}(t), y(t)\}^T = \{x_1(t), \ldots, x_N(t), y(t)\}^T$ in the sample space, find the unit j which is closest to $\mathbf{z}(t)$ according to

$$\|\mathbf{z}(t) - \mathbf{w}_j(t)\| = \min_i \{\|\mathbf{z}(t) - \mathbf{w}_i(t)\|\} \tag{8}$$

where t is the discrete iteration step. In the expression, the distance between $\mathbf{z}(t)$ and $\mathbf{w}(t)$ is determined by

$$\begin{aligned}&\|\mathbf{z}(t) - \mathbf{w}(t)\| \\ &= \sqrt{(x_{1z}(t) - x_{1w}(t))^2 + \ldots + (sx_{iz}(t) - sx_{iw}(t))^2 + \ldots} \\ &= \sqrt{(x_{1z}(t) - x_{1w}(t))^2 + \ldots + s^2(x_{iz}(t) - x_{iw}(t))^2 + \ldots}\end{aligned} \tag{9}$$

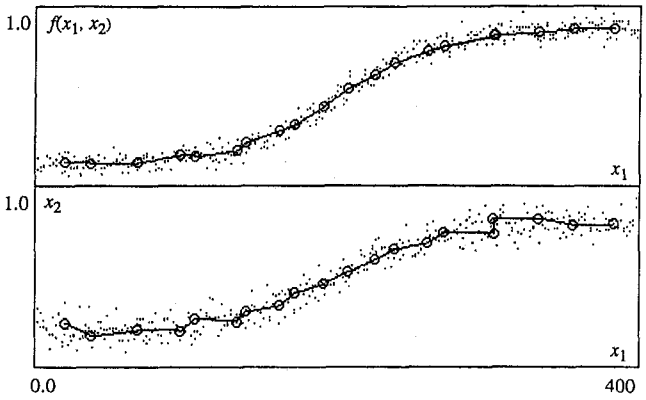


Fig. 3 Regression analysis involving an S curve using the CTM algorithm based on a 20-unit network

Downloaded 02 Jun 2010 to 171.66.16.105. Redistribution subject to ASME license or copyright; see http://www.asme.org/terms/Terms_Use.cfm

Step 3. Define a symmetric neighborhood of units i surrounding the winning unit j, $H_{ij}(t)$, and adjust the weights of the winner and all its neighboring units according to

$$\mathbf{w}_i(t+1) = \mathbf{w}_i(t) + \alpha(H_{ij}, t)[\mathbf{z}(t) - \mathbf{w}_i(t)], \quad i \in H_{ij}(t)$$
$$\mathbf{w}_i(t+1) = \mathbf{w}_i(t), \quad i \notin H_{ij}(t) \tag{10}$$

where $\alpha(H_{ij}, t)$ is the scalar learning rate monotonically decreasing with t.

Step 4. Reduce the neighbourhood and the learning rate, increase iteration number t and return to step 1, until certain number of iterations are performed.

Step 5. The accuracy of regression results is measured by the Average Residual (AR) (Cherkassky and Lari-Najafi, 1991).

For practical applications of this new algorithm, the learning rate for unit i in the neighborhood of unit j at time t is given below, which is the same as being used in the SOM and CTM algorithms (Cherkassky and Lari-Najafi, 1991).

$$\alpha(H_{ij}, t) = b(t) \exp\left[\frac{-|i-j|}{(b(t)s_0)^2}\right] \tag{11}$$

where $b(t)$ is named learning factor, the exponential term is the neighborhood function, and s_0 is the number of knots. The learning factor for the winning unit is given by the empirical relationship (Cherkassky and Lari-Najafi, 1991)

$$b(t) = b_0(b_e/b_0)^{t/t_m} \tag{12}$$

where b_0 and b_e are the initial and final values of the learning factor, t is the discrete step of iteration, $t = 1, 2, \ldots, t_m$, t_m is the maximum number of iterations, which is usually defined as the product of the training set size and the number of times this set is recycled or repeatedly presented to the network during training. These relationships are also employed in the new algorithm developed herein.

The simulation experiments performed in the previous section have again been performed using the new algorithm. When the scaling factor has been taken to be 2.0, the result of fitting the data generated by Eq. (3) to a 20-unit neural network is shown in Fig. 4. The locations of the 20 units can be seen to fit the data very well. The three-dimensional **S** curve is now considered and fitting a 20-unit network using the new algorithm with the scaling factor equal to 2.0 is performed. The result is shown in Fig. 5 in the same manner as in Fig. 3. This regression analysis is successful and does not exhibit a disordering problem. Further, the distance between any two neighboring units along the x_1-axis can be seen to be almost the same.

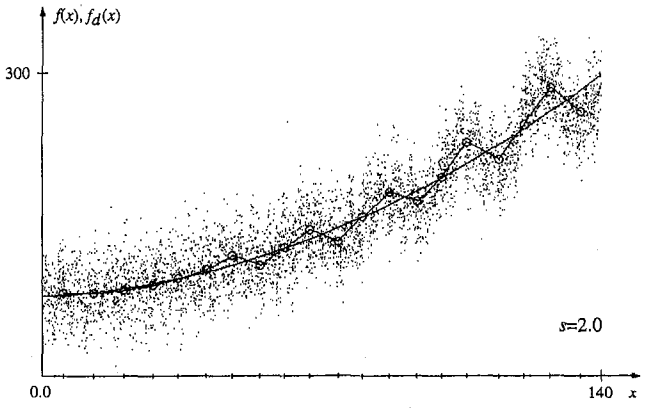


Fig. 4 Regression analysis of quadratic functions using the newly developed algorithm based on a 20-unit network

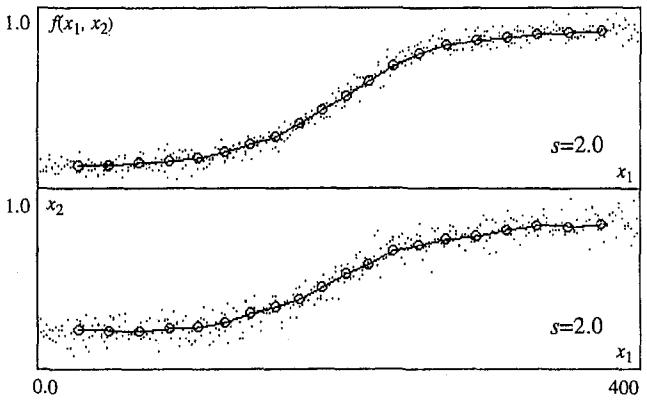


Fig. 5 Regression analysis involving an S curve using the newly developed algorithm based on a 20-unit network

6 Fault Development in Bearings

The conditions of a bearing system are now identified based on the on-line vibration measurements and using the diagnostic procedure developed in the foregoing. To this end, a bearing test rig in a bearing manufacturing plant is considered. The bearings had defects in their balls and they also had inner raceway defects. The type of bearing was a 308E with eight balls. The rotational speed of the shaft was 1470 rpm and a radial force of 2122 kgf was applied on the bearing system as the test load. An accelerometer was mounted on the house of the bearing test rig. The vibration data were collected after each time period of 4.5 minutes, until the complete failure of the bearing. The sampling frequency was 4000 Hz and the digital data was stored in 105 files. Each file has been further divided into two time series thus yielding 210 records.

The following four indices are extracted from the on-line vibration signal: the peak-to-peak value, absolute mean value, crest factor of the time domain signal, and the arithmetic mean of the power spectrum. The peak-to-peak value (PP) is the difference between the maximum and minimum amplitudes of the vibration signal. It is a time domain index and is markedly sensitive to the unusual impulses generated by bearing faults. The absolute mean value (AX) is the average value of absolute amplitudes of the on-line vibration signal in time domain, and is given by

$$AX = |\bar{x}| = \frac{1}{m}\sum_{i=1}^{m} |x_i| \tag{13}$$

where m is the number of data points in a signal record. This index is small when most of the vibration amplitudes are small and is large when the bearing defects generate large amplitude vibrations. The crest factor (CR) is defined as

$$CR = \frac{|x|_{\max}}{rms} \tag{14}$$

where rms is the root mean square value of the on-line vibration signal, which is a measure of the average vibrational energy. Typical CR values are first increasing and then decreasing during the development of bearing faults. The arithmetic mean of the power spectrum (AM) is defined as (Mathew and Alfredson, 1984)

$$AM = 20 \log\left[\left(\frac{1}{q}\sum_{i=1}^{q} A_i\right) \Big/ 10^{-5}\right] \tag{15}$$

where A_i is the ith magnitude in the discrete power spectrum of vibration signal and q is the number of points in the spectrum. It has been observed during the past investigations that the

Downloaded 02 Jun 2010 to 171.66.16.105. Redistribution subject to ASME license or copyright; see http://www.asme.org/terms/Terms_Use.cfm

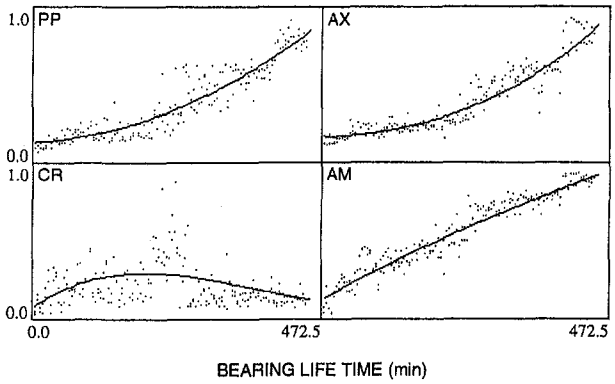


Fig. 6 The four univariate functions of bearing life obtained from the on-line vibration signal

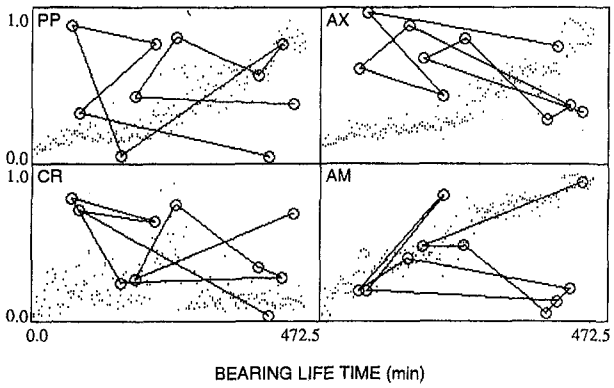


Fig. 7 Random initial positions of 10 knots of a neural network used in the present algorithm

values of AM increase monotonically until the complete failure of the bearing.

The service life of the bearing, denoted by T, is related to each and all of four indices defined above. A third-order polynomial in T is employed to represent the functional relationship between T and each of the diagnostic indices PP, AX, CR, and AM. Using the least-squares method, the coefficients of the polynomial are determined from the data. The resulting equations are given below:

$$PP = 19.013 + 0.143T + 8.603 \times 10^{-3}T^2 - 1.947 \times 10^{-6}T^3 \quad (16)$$

$$AX = 2.095 + 8.564 \times 10^{-3}T + 5.001 \times 10^{-4}T^2 + 2.676 \times 10^{-6}T^3 \quad (17)$$

$$CR = 3.4001 + 0.147T - 2.336 \times 10^{-3}T^2 + 9.468 \times 10^{-6}T^3 \quad (18)$$

$$AM = 104.307 + 0.178T - 3.696 \times 10^{-4}T^2 + 6.589 \times 10^{-7}T^3 \quad (19)$$

These four equations can be rewritten such that the bearing life T is expressed in terms of PP, AX, CR, and AM. Hence, when the values of these diagnostic indices are obtained from the bearing vibration signal, the residual life of the bearing can be estimated from any one of the four equations. The data samples and corresponding curves are shown in Fig. 6, wherein the horizontal axes of the four subplots denote time T and vertical axes denote PP (upper-left), AX (upper-right), CR (lower-left), and AM (lower-right).

The four diagnostic indices are arranged in the form $\mathbf{x} = \{PP, AX, CR, AM\}^T$ and the bearing life time T is taken to be the variable y in Eq. (1). Then, the determination of bearing life time T from the four diagnostic indices PP, AX, CR, and AM can be treated as the problem of multivariable trend analysis. Since the four indices have been extracted from the same set of time series, and further they can always be represented as four explicit functions of T (as in Eqs. (16)–(19)), the function $f(\cdot)$ represents a curve in a five-dimensional space, and this way the multivariable trend analysis essentially involves fitting a high-dimensional curve. Each data point $\mathbf{x}_i$ is extracted from the vibration data as corresponding to time T_i, which is in turn the lifetime of the bearing corresponding to the ith data pair $\{\mathbf{x}_i, T_i\}$. The data sets $\mathbf{z}_i = \{\mathbf{x}_i, T_i\}^T = \{PP_i, AX_i, CR_i, AM_i, T_i\}^T$, $i = 1, 2, \ldots, n$ with $n = 210$, constitute the training data for the neural network. Before training is initiated, the five variables are scaled so as to lie approximately in the same range. The parameters of the equation for learning factor, i.e., Eq. (12), are taken to be $b_0 = 0.6$, $b_e = 0.04$, $t_m = 50n = 10{,}500$. Considering the possible influence of the order of data presentation on the results of training, records of $\mathbf{z}$ have been rearranged into a new series every time before reusing them. From the data it has been observed that the variable T has a uniform distribution over its range but the four indices do not have such a uniform distribution.

Now, the algorithm developed in the previous section is deployed and accordingly, a scaling factor has been used to multiply the uniformly distributed variable T. Different values of scaling factor have been tested for estimating functions corresponding to the number of knots ranging from 5 to 15. When the scaling factor is greater than 1.8, violation of the order of units has not been observed. A network with 10 units and a scaling factor of 2.0 is presented in Figs. 7 and 8. Figure 7 shows the initial positions of the 10 units that have random coordinates in the sample space. After training, each unit is moved to its final position in $\mathbf{z}$ space as shown in Fig. 8. These ten units constitute the knots that connect the locally linear line segments, and the estimation of the unknown function can now be obtained by the piecewise linear regression method. However, an easier approach can also be used. That is, for any given index set $\mathbf{x}$ obtained from the same machine system, the corresponding bearing life T is simply approximated by the value T_j of the closest knot $\mathbf{w}_j$, which in turn is determined from the following equation:

$$\|\mathbf{x} - \mathbf{w}_j'\| = \min_i \{\|\mathbf{x} - \mathbf{w}_i'\|\};$$
$$1 \le j \le k, \quad i = 1, 2, \ldots, k \quad (20)$$

In order to quantify the accuracy of the network developed, two error indicators are used. The first one is known as the average residual, e_{AR}, which is the ratio between the average residual

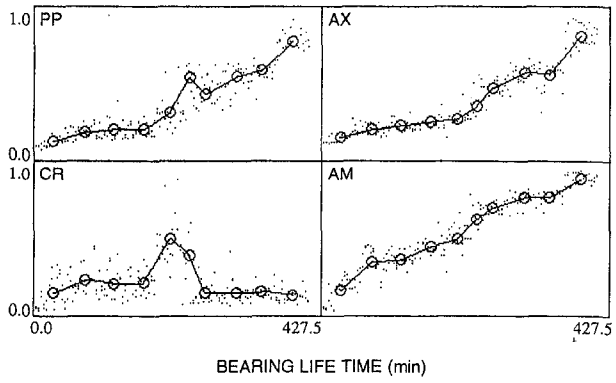


Fig. 8 Performance of the new algorithm in training a network of 10 knots with a scaling factor s = 2.0

Downloaded 02 Jun 2010 to 171.66.16.105. Redistribution subject to ASME license or copyright; see http://www.asme.org/terms/Terms_Use.cfm

and the range of T. It is expressed as a percentage value and is given by

$$e_{AR} = \frac{1}{T_a}\sqrt{\frac{1}{n}\sum_{i=1}^{n}[T_i - T_j]^2} \qquad (21)$$

In this equation, T_a represents the product of the number of data point and the time interval used for data sampling, i.e., T_a = 472.5 (minutes), which thus represents the entire time of monitoring. Further, T_i is the lifetime corresponding to each data sample $\mathbf{x}_i$, $i = 1, 2, \ldots n$, and T_j is the lifetime of the matched unit $\mathbf{w}_j$. This measure of error is in terms of standard deviation of the estimation error expressed as a percentage value. Another measure of error, e_{AE}, is now defined as the average estimation error expressed as a percentage value:

$$e_{AE} = \frac{1}{T_a n}\sum_{i=1}^{n}|T_i - T_j| \qquad (22)$$

where T_a, T_i, and T_j are the same as those defined in Eq. (21).

In order to validate the regression function determined by the neural network that has been developed in the foregoing, another set of 105 data samples was collected from the same bearing testing rig and values of e_{AR} and e_{AE} are calculated. It may be noted that these data have not been used for training the neural network. The value of e_{AR} in the present case is 7.34 percent and that of e_{AE} is 5.23 percent for the 10-knot network established using a scaling factor of 2.0. They can now be compared with that obtained from single-variable functions, i.e., Eq. (16)–(19): The values of e_{AR} and e_{AE} obtained from given values of *PP* are 20.41 and 17.82 percent, respectively. Corresponding values obtained from *AX* are 14.18 and 11.92 percent, respectively, and from *CR* are 39.17 and 34.89 percent, respectively. The best results obtained from *AM* have the values 9.92 and 7.57 percent respectively. For practical applications, the neural network established here consisting of 10 units is thus seen to be good enough for the purpose of estimating the bearing life.

The number of knots is now increased and the performance of trained neural networks obtained using the present algorithm is compared with those obtained using both SOM and CTM algorithms, in Table 1. Two different values of scaling factor have been used. It can be seen from the accuracy of results obtained using the present algorithm that even though the trend analysis is a high-dimensional regression problem, wherein the variation of data is in large ranges, and the number of data points available for learning is small, the method developed in this paper achieves reasonably good results.

Table 1 Accuracy of bearing life estimation using different algorithms

Number of knots	SOM algorithm (e_{AR}%, e_{AE}%)	CTM algorithm (e_{AR}%, e_{AE}%)	New algorithm with s=3.0 (e_{AR}%, e_{AE}%)	New algorithm with s=2.0 (e_{AR}%, e_{AE}%)
5	8.01, 6.26	8.23, 6.43	8.39, 6.55	8.08, 6.33
6	7.52, 5.75	7.51, 5.74	7.60, 5.42	7.59, 5.54
7	7.43, 5.55	7.47, 5.68	7.70, 5.44	7.58, 5.51
8	*	*	7.60, 5.38	7.35, 5.38
9	7.49, 5.49	7.46, 5.68	7.59, 5.28	7.49, 5.36
10	7.36, 5.37	7.31, 5.52	7.60, 5.21	7.34, 5.23
11	7.30, 5.42	*	7.53, 5.12	7.38, 5.12
12	*	*	7.44, 5.06	7.30, 5.15
13	*	*	7.48, 5.09	7.24, 5.11
14	*	*	7.33, 4.98	7.11, 5.09
15	*	*	7.24, 5.08	7.21, 5.10

* The network knots were disordered.

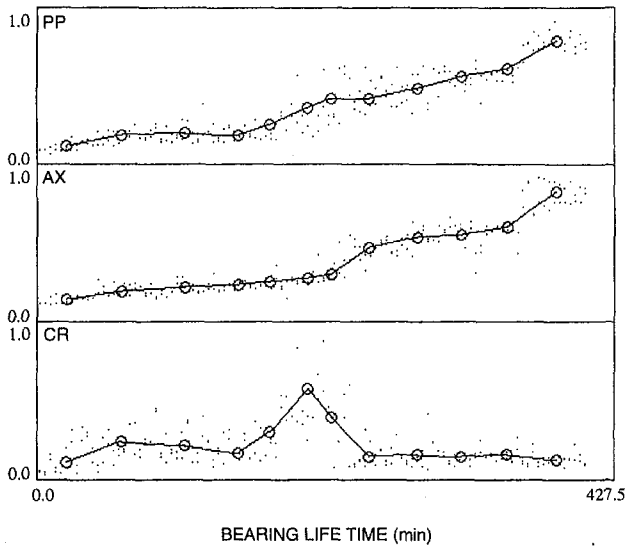


Fig. 9 Performance of the new algorithm in training a network of 12 units with a scaling factor s = 2.0

Now, the number of diagnostic indices is reduced to three. The following three diagnostic indices are considered for trend analysis: peak-to-peak value, absolute mean value, and crest factor of the time domain signal. Equations (16)–(18) involving third-order polynomials in T are now used.

The parameters of the learning factor, Eq. (12), have been taken to be $b_0 = 0.6$, $b_e = 0.04$, $t_m = 50n = 10{,}500$. A network with 12 units and a scaling factor of 2.0 has been trained. After training, each unit is moved to its final position in the $\mathbf{z}$ space as shown in Fig. 9. These twelve units constitute the knots that connect the locally linear line segments, and the estimation of the unknown function can now be obtained by piecewise linear methods. The value of e_{AR} in the present case is 7.4 percent and that of e_{AE} is 5.64 percent for the 12-knot network established using a scaling factor of 2.0. They can now be compared to that obtained from single-variable functions, i.e., Eqs. (16)–(18): The values of e_{AR} and e_{AE} obtained from given values of *PP* are 20.41 and 17.82 percent, respectively. Corresponding values obtained from *AX* are 14.18 and 11.92 percent, respectively, and from *CR* are 39.17 and 34.89 percent, respectively. For practical applications, the established neural network consisting of 12 units is thus seen to be good enough for the purpose of estimating bearing life.

7 Efficiency of the New Intelligent Diagnostic Procedure

The unequal scaling of variables is central to the new neural algorithm and further, this algorithm was originally proposed for improving the performance of Kohonen's self-organizing mapping algorithm for regression problems. This improvement has been oriented so as to avoid the nonfunctional maps obtained by both the CTM and SOM algorithms. The proposed new approach using multiple variables in trend analysis has the following important advantages:

1 No prior knowledge about the model of the unknown multivariate function is required.
2 More than one characteristic of the on-line vibration signal can be simultaneously considered.
3 Both large or small size of training data set can be handled adequately.
4 Structuring a self-organizing neural network for desired application is quite easy and further, the training process is fast in that it takes about only 10 seconds on a personal computer.

Downloaded 02 Jun 2010 to 171.66.16.105. Redistribution subject to ASME license or copyright; see http://www.asme.org/terms/Terms_Use.cfm

The new neural network algorithm: (*i*) does not violate the topological order of units, (*ii*) does not produce nonfunctional maps when real-life data from practical machine systems are considered, (*iii*) has the ability to locate all the units optimally even when the number of units is significantly large, (*iv*) can estimate the multivariate curve from finite data points in addition to estimating the multidimensional surfaces, (*v*) consumes almost the same computational time as the SOM and CTM algorithms, but yields highly accurate estimation of multivariate functions such as the service life of practical machine systems. That the proposed method produces more accurate results than the widely used single-index based trend analysis is also demonstrated considering the case of a bearing system.

8 Conclusions

In system monitoring and diagnosis, the usage of a set of diagnostic indices that are extracted from on-line vibration signals is essential (Lipovszky et al., 1990; Tranter, 1989). This is due to the fact that there is no single index that can completely represent the conditions of a machine and further, different types or stages of fault or malfunction are distinctly reflected in various different diagnostic indices. Hence, the widely used (single-index based) trend analysis cannot take into account the complete information about a system and provide accurate results about the machine conditions. It is also observed from existing works that multidimensional trend analysis has not so far been used for system monitoring and diagnosis due to the inherent complexity and difficulty involved in the modeling of function $f(\cdot)$.

Use of multivariable trend analysis in the condition monitoring and diagnosis of machine systems is proposed in the present paper. The multiple-index based trend analysis is proposed to be used as a basis to both: (*i*) obtain information on the current state of the machine; and (*ii*) estimate with prescribed accuracy the service life of the machine system being monitored. On-line vibration measurements are used as the diagnostic signal and the variables for trend analysis are obtained from the signal, i.e., the indices are extracted from the time series of the signal. The diagnostic indices are selected in such a way that each index is distinctly sensitive to a particular type of fault or malfunction in the machine system. Alternately, each and all of the commonly observed faults or malfunctions in the machine component being monitored, are adequately reflected in the variables used in the trend analysis. A new neural network algorithm, developed by the present authors, is adapted to perform this trend analysis. It is shown that the strength of the new algorithm is in preventing the knots from being disordered. The accuracy of the new algorithm's predictions is the same as that of SOM and CTM algorithms. The efficiency and practical applications of the new diagnostic procedure are fully demonstrated.

Acknowledgments

The research work reported in this paper is a part of a major project on system diagnostics and reliability under the IRIS Network of Centres of Excellence funded by the Government of Canada.

References

Baum, E. B., 1990, "When Are *K*-Nearest Neighbour and Back Propagation Accurate for Feasible Sized Sets of Examples?" in: *Proc. of Eurasia Workshop on Neural Networks,* L. B. Almedia & C. J. Wellekens, eds., Springer-Verlag, New York, pp. 2–25.

Cempel, C., 1988, "Vibroacoustical Diagnostics of Machinery: An Outline," *Mechanical Systems and Signal Processing,* Vol. 2(2), pp. 135–151.

Cherkassky, V., and Lari-Najafi, H., 1991, "Constrained Topological Mapping for Nonparametric Regression Analysis," *Neural Networks,* Pergamon, Vol. 4, pp. 27–40.

Cherkassky, V., and Lari-Najafi, H., 1992, "Nonparametric Regression Using Self-Organizing Topological Maps," *Neural Networks for Human and Machine Perception,* H. Wechsler, ed., Academic Press, Vol. 2, pp. 40–64.

Collacott, R. A., 1977, *Mechanical Fault Diagnosis and Condition Monitoring,* Chapman and Hall, London.

Collacott, R. A., 1979, *Vibration Monitoring and Diagnosis,* George Goodwin Ltd., London.

Friedman, J. H., and Silverman, B. W., 1989, "Flexible Parsimonious Smoothing and Additive Modelling," *Technometrics,* Vol. 31, No. 1, pp. 3–21.

Kohonen, T., 1989, "The Self-Organizing Map," *Proc. IEEE,* Vol. 78, No. 9, pp. 1464–1480.

Lipovszky, G., Sólyomvári, K., and Varga, G., 1990, *Vibration Testing of Machines and Their Maintenance,* Elsevier Science Publishing Co., Amsterdam.

Mathew, J., and Alfredson, R. J., 1984, "The Condition Monitoring of Rolling Element Bearing Using Vibration Analysis," ASME *Journal of Vibration, Acoustics, Stress, and Reliability in Design,* Vol. 106, pp. 447–453.

Specht, D. F., 1991, "A General Regression Neural Network," *IEEE Trans., Neural Networks,* Vol. 2, No. 6, pp. 568–576.

Tranter, J., 1989, "The Fundamentals of, and the Application of Computers to, Condition Monitoring and Predictive Maintenance," in: *Proc. of 1st Inter. Machinery Monitoring and Diagnosis Conf.,* Las Vegas, NV, Sept., pp. 394–401.

Zhang, S., 1995, "Development of a Knowledge-Base System for Rotating Machinery Diagnostics," Ph.D. Thesis, Concordia University, Montreal, Canada.

Downloaded 02 Jun 2010 to 171.66.16.105. Redistribution subject to ASME license or copyright; see http://www.asme.org/terms/Terms_Use.cfm

Split Stream Boilers for High-Temperature/High-Pressure Topping Steam Turbine Combined Cycles

I. G. Rice
Consulting Engineer,
Spring, TX 77373

Research and development work on high-temperature and high-pressure (up to 1500°F TIT and 4500 psia)[1] topping steam turbines and associated steam generators for steam power plants as well as combined cycle plants is being carried forward by DOE, EPRI, and independent companies. Aeroderivative gas turbines and heavy-duty gas turbines both will require exhaust gas supplementary firing to achieve high throttle temperatures. This paper presents an analysis and examples of a split stream boiler arrangement for high-temperature and high-pressure topping steam turbine combined cycles. A portion of the gas turbine exhaust flow is run in parallel with a conventional heat recovery steam generator (HRSG). This side stream is supplementary fired opposed to the current practice of full exhaust flow firing. Chemical fuel gas recuperation can be incorporated in the side stream as an option. A significant combined cycle efficiency gain of 2 to 4 percentage points can be realized using this split stream approach. Calculations and graphs show how the DOE goal of 60 percent combined cycle efficiency burning natural gas fuel can be exceeded. The boiler concept is equally applicable to the integrated coal gas fuel combined cycle (IGCC).

Introduction

Aeroderivative gas turbines with their low exhaust temperatures of 750 to 900°F make it impossible to achieve steam throttle temperatures high enough for the next generation of high-temperature topping steam turbines. Supplementary exhaust gas firing will be required to top the combined cycle (CC) bottom end. Similarly, the latest "*F*" and future "*G*" technology heavy-duty units have exhaust temperatures of 1100 to 1160°F—too low for throttle temperatures of 1200 to 1500°F. Potential CC efficiency gains become elusive. Currently used full gas stream supplementary firing tends to lower CC efficiency and thus will nullify potential efficiency gains.

Research and Development (R & D) work is being conducted in Europe on higher throttle temperatures and supercritical pressures (boilers and steam turbines) for more efficient conventional steam power plants. In the United States DOE and EPRI through Innovative Steam Technologies/Solar Turbine Inc. (IST/Solar) are pursuing the development of high-temperature and high-pressure (HT/HP) topping steam turbine (TST) for existing and future conventional all-steam power plants. Parallel work is also being done on the once-through boiler (OTB) by this company. Reference is made to Progress Report to DOE, Nov. 1994a, High Performance Steam Turbine and Boiler Developments (DOE contract DE-A002-87 CD 40812), by Thomas F. Duffy, Director of R & D, IST/Solar, for detailed information. Also refer to Duffy (1994b).

An overview photograph of a 4.1 MW 1500°F and 1500 psig test topping steam turbine as taken from the above-mentioned report is shown in Fig. 1. The associated OTB with a gas inlet temperature of 2500°F is presented in Fig. 2. The boiler is internally insulated to accommodate the 2500°F inlet gas temperature. The superheater tubes are made of Inconel 617 and the steam flow is 56,000 pounds per hour at 1500°F and 1500 psig. The turbine exhausts at 150 psig and 950°F. When a condensing turbine is used to expand the exhaust of the topping turbine, an additional 6 MW of electric power is produced yielding a total of 10 MW output.

The "*F*" technology gas turbine introduced a few years ago has made the reheat (RH) HRSG a reality today. Higher CC efficiency is now here, higher than ever imagined possible two decades ago. The promise of the more advanced "*G*" turbine offers even higher CC efficiency. Figure 3 shows a Henry Vogt Machine Co. RH HRSG installed at the Lauderdale Station for Florida Power and Light Company's repowering project. Four Westinghouse 501 F 160 MW gas turbines exhaust into separate Vogt HRSGs, each having natural circulation and the following capability:

1. to generate 425,000 lb/hr of 1510 psig steam at 1005°F without supplementary firing and 497,500 lb/hr with the addition of future duct firing;
2. to superheat intermediate pressure (IP) extraction steam to 1005°F in the reheater section;
3. to generate approximately 90,000 lb/hr of IP steam at 350 psig and 475°F for use in NO_x control in the gas turbine;
4. to supply low-pressure steam for deaeration of the IP makeup water.

The CC efficiency of the Lauderdale plant is reported to be about 52 percent LHV ISO burning natural gas fuel. Yet there is a distinct probability that future CC efficiency can exceed 60 percent as will be discussed in this paper.

Supplementary firing the entire exhaust gas stream increases steam turbine power output, which is an advantage, but in the process greatly increases the power output of the lower end of the steam cycle. The bottom condensing end has a low heat to power efficiency conversion level and at most is only 30 percent. Studies have shown that the higher throttle temperature does not yield a higher overall combined cycle efficiency for reasons that will be explained later in this paper. Therefore,

[1] Refer to end of paper for all Standard International conversion factors.

Contributed by the International Gas Turbine Institute and presented at the 40th International Gas Turbine and Aeroengine Congress and Exhibition, Houston, Texas, June 5–8, 1995. Manuscript received by the International Gas Turbine Institute February 8, 1995. Paper No. 95-GT-29. Associate Technical Editor: C. J. Russo.

Copyright © 1997 by ASME

Downloaded 02 Jun 2010 to 171.66.16.105. Redistribution subject to ASME license or copyright; see http://www.asme.org/terms/Terms_Use.cfm

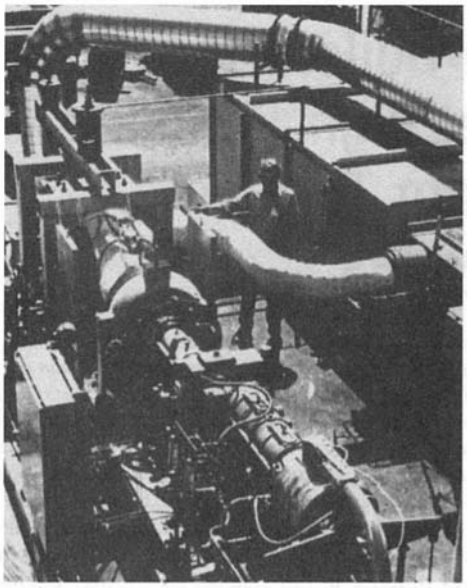


Fig. 1 An overview of Innovative Steam Technologies/Solar's High Performance steam system with the steam generator on the right and the 4.1 MW topping steam turbine and water brake dynamometer on the left. Turbine inlet is 1500 psig at 1500°F and exit is 150 psig at 950°F.

the HT/HP topping steam turbine has not been given serious consideration for combined cycles for either the aero or heavy-duty gas turbines. Conventional CCs as a rule do not incorporate supplementary firing. However, the conventional all-steam power plants do show a cycle efficiency gain when the HT/HP topping unit is utilized.

Aero-engines with high cycle pressure ratios have by cycle inheritance low exhaust temperatures. Even the new proposed GEX intercooled engine with a TIT of 2600°F and 40 pressure ratio is projected to have an exhaust temperature level of only 850°F as reported by Tittle and Van Laar at the EPRI Coal Gasification Power Plant Conference in 1993. Full exhaust flow

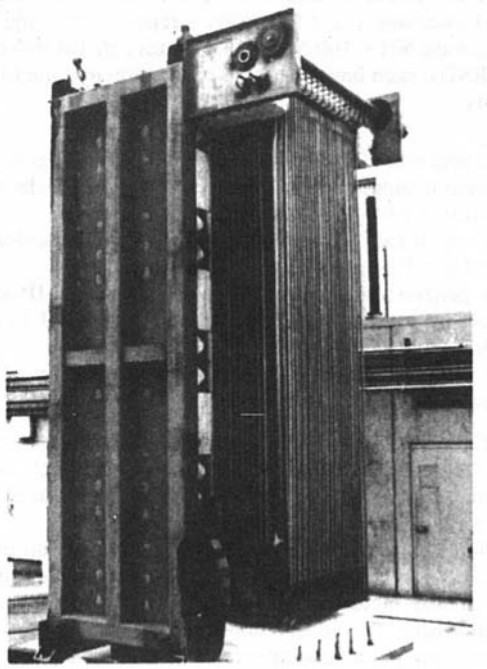


Fig. 2 Photograph of the Innovative Steam Turbine/Solar Turbine Inc. 1500°F/1500 psig once-through boiler being erected in the HPSS development test facility. Gas inlet to superheater tubes is 2500°F.

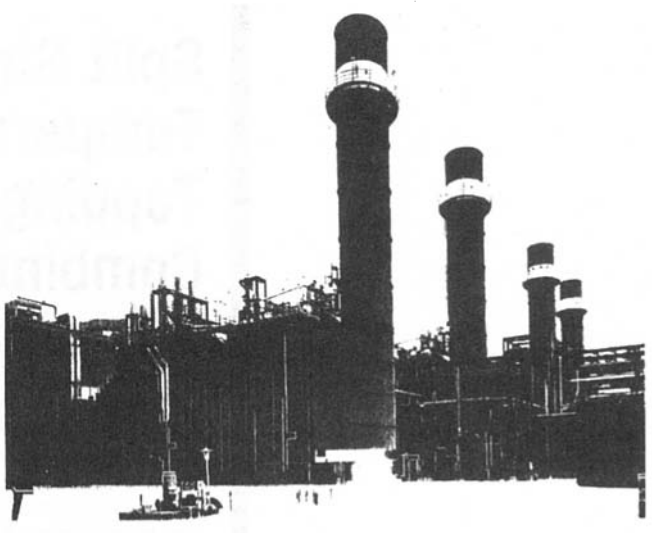


Fig. 3 Photograph of four Henry Vogt Machine Co. RH HRSGs, each recovering heat from a Westinghouse 501 F 160 MW gas turbine installed at the Florida Power and Light Co. Lauderdale Plant

supplementary firing does not render increased combined cycle efficiency when applying a high-temperature topping steam turbine. The steam injected (STIG) gas turbines have lower exhaust temperatures of about 750°F and the regenerative cycle gas turbines have even lower exit temperatures (650°F level). The addition of a HT/HP TST becomes impossible without supplementary firing in front of the HRSG but even so is not a viable solution for higher CC efficiency.

This paper presents a new concept of a split stream boiler applicable to all of the above-mentioned gas turbines whereby a small portion of the gas turbine exhaust flow is separated from the main stream and is supplementary fired to provide a suitable temperature to superheat the steam to a high level. This bypass gas stream in parallel with the main stream is subsequently used to generate a portion of the total steam flow before final superheat. A topping superheater for the total steam flow is thus formed. The side gas stream can be supplementary fired to 1600°F without special internal wall insulation and up to 2500°F with internal insulation as reported by Duffy to the DOE in the previously mentioned report wherein a once-through boiler was applied. The differential pressure drops across the two distinct heat transfer paths are optimally controlled, as will be explained. The HT/HP TST split stream boiler system is a viable way to increase CC output and efficiency. The system is workable and practical. The SSB can be readily fabricated.

The added cost of the HT/HP TST and the split stream boiler as evaluated against increased power and CC efficiency is beyond the scope of this paper. However, various aspects of incremental costs, power output, and efficiency will be mentioned.

Supplementary Firing and CC Efficiency

Supplementary firing the exhaust gas of gas turbines in front of HRSGs has been done for many years to increase HRSG output. However, such firing tends to lower CC efficiency. More power is generated but at a lower overall CC efficiency due to the increasing dominance of the lower efficiency of the bottoming part of the cycle. Foster-Pegg (1982) reported that extensive Westinghouse Electric Corp. (W) studies conclusively showed that maximum CC efficiency takes place at a point where an optimum number of drum pressure levels are used, i.e., three stages, to obtain a minimum stack temperature and where no supplementary firing is introduced. General Electric Co. (GE) studies revealed the same peaking phenomena as reported by Tomlinson and Lee (1985). Therefore, because of

Downloaded 02 Jun 2010 to 171.66.16.105. Redistribution subject to ASME license or copyright; see http://www.asme.org/terms/Terms_Use.cfm

this optimization point, CC power plants that do not export any steam for industrial use do not apply supplementary firing.

This conclusion will now be explained by referring to Fig. 4. This graph presents a plot of CC efficiency versus sensible heat transferred to steam in the HRSG for both the latest "*F*" technology heavy-duty gas turbines and the latest aero engines. Heat is absorbed by the water/steam from points *A* or *H*, as the case may be (simple cycle gas turbine efficiency), to points *B* and *I* for a minimum stack temperature (CC). Both the latest aero engines, such as the LM 6000 and the heavy duty "*F*" machines, have about the same optimum CC efficiency as shown in Fig. 4. Supplementary firing the full exhaust stream takes place from points *B* and *I* to points *C* and *J* where most of the oxygen is consumed down to about 2 percent (10 percent excess air) as is the case for a conventional power boiler. The CC efficiency falls off to a noticeable extent as shown.

If a HT/HP TST is applied to the supplementary fired boiler, the CC efficiency will rise from points *D* and *K* to points *E* and *L*. However, very little if any gain in CC efficiency takes place over the optimum points of *B* and *I* for no supplementary firing. Therefore, the HT/HP TST does not increase CC efficiency and such firing only increases bottoming power output.

A different scenario takes place when only a portion of the gas turbine exhaust stream is supplementary fired to superheat the total stream flow and where the superheater exit gas temperature is about the same as that of the gas turbine exhaust. A noticeable CC efficiency gain takes place. Heat is added as shown by double-ended arrows *O* and *P*. All of this heat is transferred to the steam to perform the topping superheating function. The CC efficiency will rise to points *F* and *M* for each type of machine, respectively. The bottoming portion downstream of the superheater remains the same. The heat input is thus converted to pure incremental topping power at about 90 percent efficiency (3800 BTU/kWh) when considering radiation heat loss and mechanical (bearings, generator, etc.) losses. The exact end points, *F* and *M*, and the heat input as represented by arrows *O* and *P* will depend upon the TST, TIT, and pressure conditions. The throttle steam, if superheated to 1500°F instead of 1200°F for instance, will add more topping power to the cycle and thus increase CC efficiency. Figure 4 assumes a 1400°F superheat temperature.

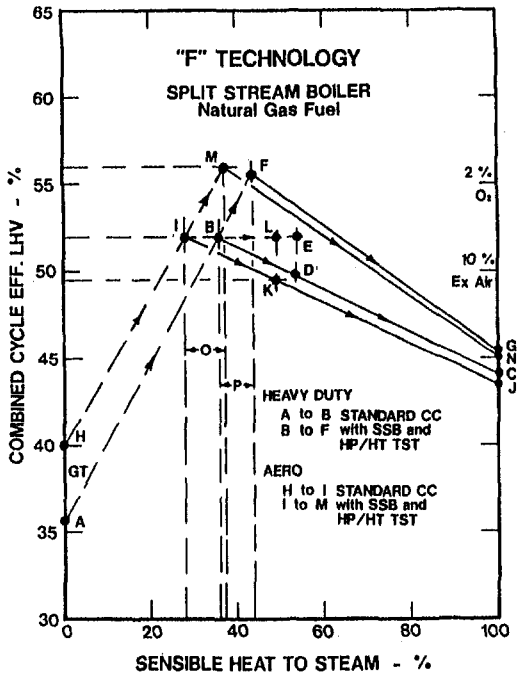


Fig. 4 Graph of combined cycle efficiency versus sensible heat to steam for "*F*" technology gas turbine exhaust down to 2 percent oxygen

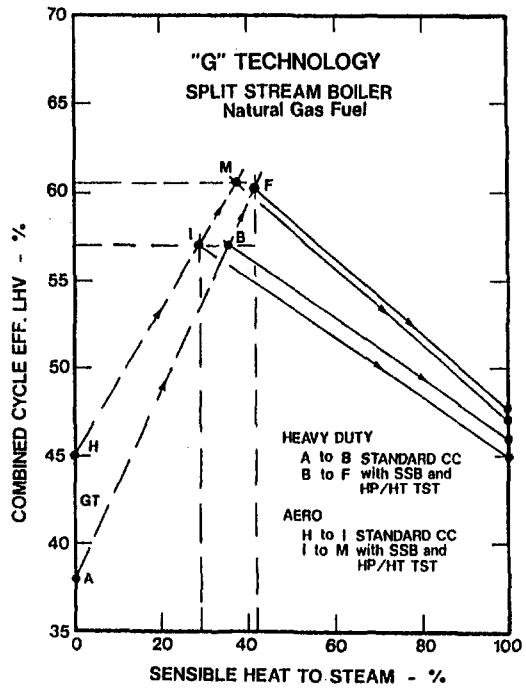


Fig. 5 Graph of combined cycle efficiency versus sensible heat to steam for "*G*" technology gas turbine exhaust down to 2 percent oxygen

Figure 5 illustrates what can be expected by applying the SSB supplementary firing (1400°F and HT/HP TST) to the future "*G*" technology heavy duty and the proposed intercooled aero turbines, both having TITs of about 2600°F or the equivalent thereof such as the reheat Asea Brown Boveri (ABB) GT-24 and 26 models. When supercritical pressure conditions are applied to the HT/HP TST, a CC efficiency of over 60 percent LHV for natural gas fuel is calculated.

Split Stream Boiler *T-H* Model

The SSB can be applied to a number of different HT/HP TSTs and different gas turbine exhaust temperatures. A generalized approach can be set forth to analyze the thermodynamics of the system. Reference is made to Fig. 6, which is a plot of temperature versus steam enthalpy. In this case, saturated steam is generated at 2450 psia and is then superheated to 1400°F by the proposed side stream superheater. The gas turbine exhaust temperature is assumed to be 750°F for the STIG LM 5000. This diagram will serve as a model to show how the SSB operates, how the boiler calculations are made, and why a CC efficiency gain takes place. In a three-part ASME paper on steam injection by the present author (Rice, 1993a, b, and c), a topping steam turbine is positioned before steam is injected, and this example presents a solution for increased cycle efficiency.

The SSB is broken down into three distinct sections: the superheater, the evaporator, and the economizer. Heat output from the gas (streams *X* and *Y*) and heat input to the steam (streams *A* and *B*) can be calculated separately, section by section. The bypass gas, stream *X*, is heated from the gas turbine exhaust temperature of 750°F, point 8, to 1500°F, point 1, by supplementary firing. Bypass gas is cooled from point 1 to point 9, 800°F in the example. However, this value can be higher or lower and is the designer's choice. It can be 750°F, the gas turbine exhaust temperature, or even as low as 700°F, point 2 (saturation temperature plus the delta pinch point preselected

Downloaded 02 Jun 2010 to 171.66.16.105. Redistribution subject to ASME license or copyright; see http://www.asme.org/terms/Terms_Use.cfm

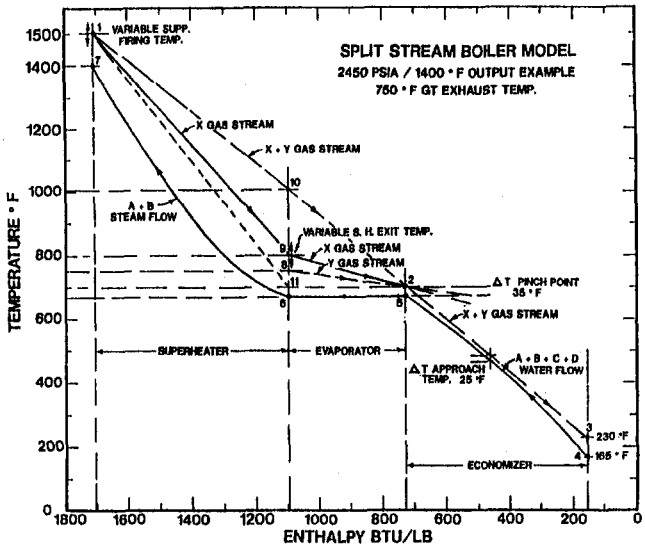


Fig. 6 Split steam boiler model of temperature versus enthalpy

to be 35°F). The superheater heat transfer surface is sized to accommodate the selections made.

The bypass gas stream X superheats the total steam (stream A plus stream B), A flow being produced by the evaporator section gas stream X and B flow being produced by gas stream Y. An oversized economizer is applied with extra flow capacity and heat transfer surface to cool the gas stream down to the minimum stack temperature. In the example, point 3 is selected to be 230°F. The total feed water is heated from point 4 (165°F) to point 5 (665°F). The excess heated feed water at point 5 is fed to a first flash tank at about 500 psia to produce incremental saturated steam. The flash water is cascaded to flash tanks 2 and 3 each at lower pressures to produce incremental saturated steam for injecting into the gas turbine.

A schematic flow diagram of the gas turbine, split stream boiler, TST, flash steam superheaters, and steam injection points is given in Fig. 7. In the example, steam enters the HT/HP TST at about 2400 psia and 1400°F, is expanded to produce power and is then exited at about 475 psia and 950°F. About 4.5 MW of incremental topping power at 3800 BTU/kWh is produced. The 950°F exit steam superheats the flash steam as shown before injection into the gas turbine. The overall CC efficiency calculates to be about three percentage points higher than for a present day 2150°F TIT STIG cycle (48 versus 45) when considering the added topping power at 3800 BTU/kWh and the savings in gas turbine fuel due to the hotter injection steam.

The calculation procedure requires iterations. By pass gas stream X flow is arbitrarily selected along with gas exit temperature, point 9. The two saturated steam flows (A and B) are calculated and added together. A check is made for heat input to the superheater. The bypass gas stream flow is adjusted and the saturated steam flows are recalculated. By iteration, a balance is obtained to determine the bypass gas flow. Finally, the economizer section feed water flow is calculated. The flash steam flow values can then be readily calculated.

Reference is again made to Fig. 6. If the total gas stream is supplementary fired to 1500°F to superheat the steam to 1400°F (100°F approach temperature), the gas cooling path would be almost a straight line from point 1 to point 2 and on to point 3, varying only by the change in specific heat of the gas at varying temperature. The SSB arrangement produces a broken line as shown. The saving in fuel is represented by the triangle bounded by lines drawn between points 1, 2, and 9. There is a saving in exergy and a higher heat transfer exergy efficiency accordingly. The gas stream more closely matches the steam generation, superheating, and feed water heating. This helps explain why there is an overall increase in cycle efficiency. More pure topping power is produced for the same amount of gas turbine injection steam.

An alternate arrangement for the HT/HP TST, the standard LM 5000 gas turbine and a condensing steam turbine for the SSB is shown in Fig. 8. Similar calculations as explained above will yield a similar overall CC efficiency gain where more topping steam power is produced for a given amount of total steam flow and thus this added power helps raise the overall CC efficiency.

When the gas turbine exhaust temperature is high enough, for instance above 850°F, some of the superheating can be done before the topping superheater. All the Westinghouse 501s, the GE Frame 7s and many of the aero engines fall into this category. Steam reheat can likewise be handled with the SSB arrangement.

The SSB concept can incorporate two gas turbines instead of one wherein a small gas turbine such as the LM 6000 (40 MW) is placed in parallel with a large gas turbine such as the MS 7001 F (160 MW). The small gas turbine's exhaust gas (stream X) is supplementary fired to the required temperature for highly superheating the total steam output of both gas turbines' exhaust gas streams (X plus Y). An efficiency increase will be realized and appreciably more power will be produced by the addition of the smaller gas turbine and the HT/HP topping steam turbine.

Split Stream Boiler Design Considerations

A schematic diagram, Fig. 9, illustrates the general layout of the SSB. The gas turbine exhaust is split with part of the gas flow (X) being fed to the supplementary fired superheater. The balance of the flow (Y) is directed to the evaporator section located to one side of the superheater. The gas flow (X) after leaving the superheater passes through an evaporator section

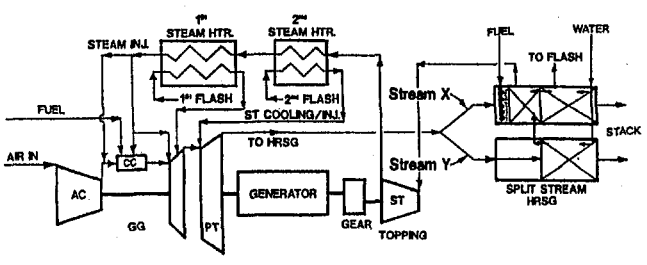


Fig. 7 SSB flow diagram of a fully steam injected gas turbine CC coupled to a topping steam turbine

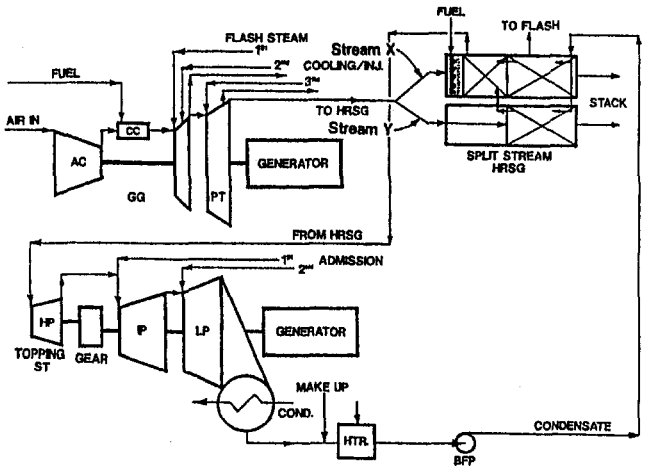


Fig. 8 SSB flow diagram of a CC incorporating a topping steam turbine

Downloaded 02 Jun 2010 to 171.66.16.105. Redistribution subject to ASME license or copyright; see http://www.asme.org/terms/Terms_Use.cfm

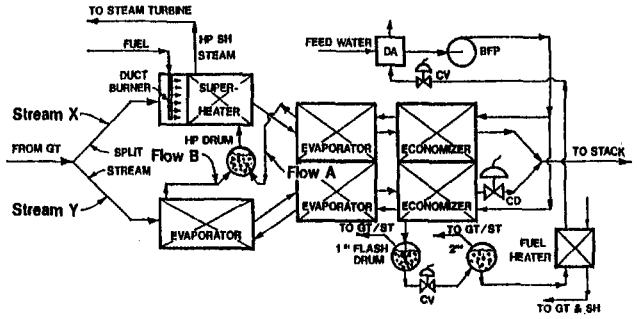


Fig. 9 Flow diagram of a SSB with two flash drums and an exit gas pressure control damper

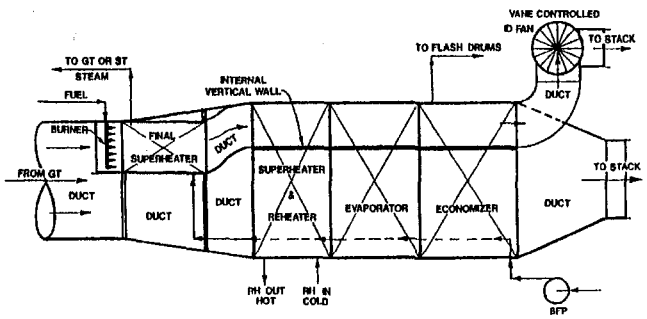


Fig. 11 Schematic diagram (plan view) of a SSB showing duct burner, final superheater, connection ducts, internal vertical wall for gas flow separation and an ID fan

and then an economizer section in parallel with stream *Y* before exiting to the stack. The nonfired gas stream (*Y*) passes through a separate double evaporator section and then an economizer section before discharging to the stack. There are two separate gas paths as shown.

The superheater gas path obviously will have a greater pressure drop because of the added superheater heat exchange surface. It might be possible to add extra heat exchange surface to the bypass stream, but this procedure could be difficult to design and would be costly. Another way to balance the flow is to place a control damper (CD) on the discharge side of the non fired gas stream as shown in Fig. 9. A similar damper could be placed at the gas turbine exit, on the hot side, but this location would increase the damper cost and lead to potentially troublesome operation. Such dampers will automatically force the right amount of gas through the burners and superheater, but will penalize the gas turbine by increasing the back pressure by about 5 in. of water. Power will be lost. Still another automatic way to control the flow of the two streams is to place an induced draft (ID) fan with variable inlet vanes and control on the bypass gas stream (*X*) after the economizer as shown in Figs. 10 and 11. Most of the power penalty will be removed and a partial inverted cycle will be formed.

Figure 9 shows two flash drums, which handle the extra hot feed water flow as discussed earlier in the paper. Also, as can be noted in Fig. 9, all the saturated steam is separated by one boiler drum. The steam from gas streams *X* and *Y* (steam flows *A* and *B*) is fed to the fired superheater.

The SSB arrangements of Figs. 9, 10, and 11 suggest rectangular box type construction, the SSB having horizontally located water and steam headers communicating with vertical arranged finned tubes with natural circulation similar to the HRSGs being manufactured in the United States. Tube bundle separation can be provided at the right location to allow a vertical wall to be installed to separate the two different gas streams. A differential pressure will be encountered between the two streams. Ducts can be installed to connect the superheater exit to the evaporator and the economizer exit to the ID fan as shown in Fig. 11.

The finned tubes can be positioned horizontally and forced circulation employed. Some European HRSG manufacturers use this approach. The topping superheater would be positioned vertically in this case. A split between tube bundles can be provided for a vertically upward gas separation wall. It might be more advantageous to apply dampers to control gas stream flow for the vertical configuration.

Still another SSB arrangement is possible using helically wound coils and a round cylinder shaped outer wall. Reference is made to the annular SSB configuration of Fig. 12. Ring headers can also be used with heat exchange tubing running parallel with the gas flow. The burners and superheater are placed on the inside of the evaporator coils as shown.

The once-through boiler (OTB) can also be applied to the SSB concept. A separate packaged unit can be placed alongside a standard drum type HRSG to provide the superheating function. Alternately, a two-stream OTB can be furnished as a single unit, as a complete package for small size units or field erected for large units.

The number of supplementary firing burners will be reduced in the SSB compared to the number in a conventionally supplementary fired HRSG. Internal wall insulation is not required for gas burner exit temperatures up to about 1600°F. If the burner exit temperature is higher, up to 2500°F, internal wall insulation will be required for the burner section and the superheater section. The higher temperature will increase the temperature differentials between the steam and the gas and thus reduce heat transfer surface and reduce back pressure. Radiant heat transfer surface can be placed next to the burners. The overall CC efficiency will be the same in either case as long as the gas temperature out the superheater is the same. The total amount of supplementary fuel burned will be the same provided the SSB superheater exit temperature is the same as that of the gas turbine exhaust.

SSB Partial Superheating and Reheating

There are two other instances where the SSB can be effectively applied. The first is where the gas turbine exhaust temper-

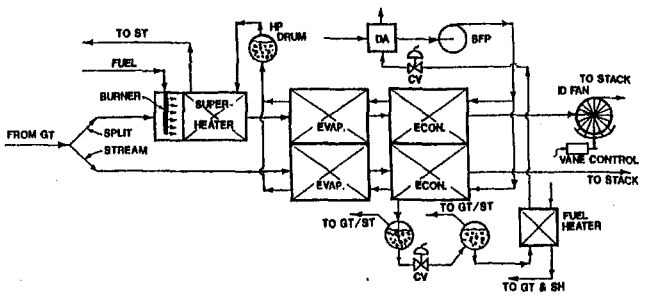


Fig. 10 Flow diagram of a SSB incorporating an induced draft fan with inlet vane control

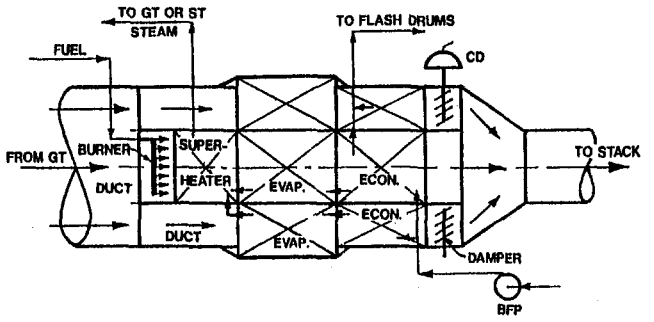


Fig. 12 Schematic diagram of a SSB having a cylinder-shaped outer wall construction and helical wound heat exchange tubes

Downloaded 02 Jun 2010 to 171.66.16.105. Redistribution subject to ASME license or copyright; see http://www.asme.org/terms/Terms_Use.cfm

ature is 900 to 1000°F and where steam is to be superheated for existing type steam turbines (1000 to 1100°F) and alternately for the HT/HP TST (1400 to 1500°F). In these cases the steam can be partially superheated by the gas turbine exhaust and then finish superheated by the topping SSB superheater. The second instance where the SSB can be effectively applied is for both superheating and reheating by a parallel/series arrangement, for both conventional reheat steam turbines and alternately for the HT/HP TST. Partial superheating and partial reheating are accomplished by the main gas turbine exhaust stream in parallel (current practice), and final superheating and reheating are done in series with the gas turbine main exhaust stream but in parallel if need be for the topping steam turbine.

Reference is made to Fig. 13. This schematic flow diagram depicts an arrangement where the steam is first partially superheated by the gas turbine main exhaust flow and is then superheated to the desired high-temperature level for the HP/HT TST by the SSB superheater. In this diagram the steam is reheated by the gas turbine main exhaust flow as can be noted. A maximum amount of high-efficiency topping steam turbine power is obtained and a minimum amount of bottoming low efficiency condensing power is produced. Cycle efficiency degradation is prevented.

Figure 14 is presented as the last arrangement in this paper. Both partial superheating (gas turbine main exhaust stream) and final superheating (SSB superheater) are performed in series. It is possible to superheat the steam to 1500°F and then reheat the steam to 1200°F in this arrangement where the gas turbine exhaust temperature level is 1100°F ("F" units). Supercritical pressure HRSGs and SSBs would be applied. Here the steam entering the condenser would be almost 100 percent quality (very little moisture). The condensing shock loss would be avoided as well as any harmful corrosion on the last two rows of rotating blades. This would appear to be an optimum arrangement but would require a higher steam volume flow directly to the condenser.

In all instances the SSB can be supplementary fired to about 1600°F (without internal insulation) or up to 2500°F (with internal insulation). The heat load will be the same and the fuel input will be the same provided the SSB superheater outlet remains constant and at the gas turbine exhaust temperature. The amount of gas turbine exhaust bypass flow X will be accordingly less for the 2500°F case.

Temperature–Enthalpy Diagrams

A temperature–enthalpy (T–H) map for steam is presented in Fig. 15. This map was generated by the steam computer program developed by Strong (1992). Steam temperature lines extend to 1500°F and a selection of pressure lines is superimposed on the map to assist in cycle analysis. Different cases for the SSB will use this diagram to illustrate thermodynamically

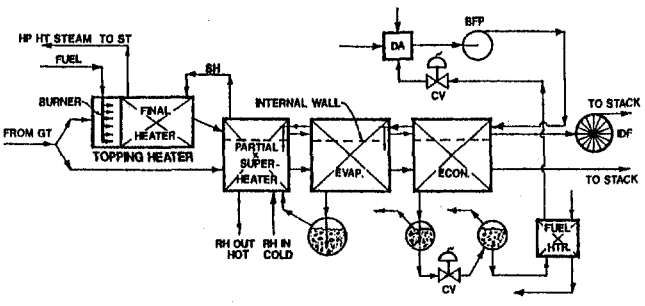


Fig. 13 Schematic diagram arrangement with partial superheating and reheating taking place in parallel with the split stream bypass flow and final superheating being accomplished by a topping supplementary fired superheater

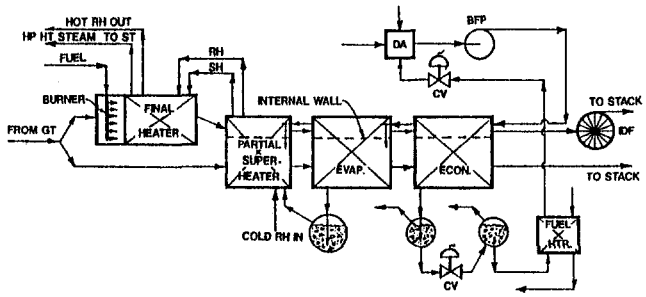


Fig. 14 Schematic diagram of the SSB with final superheating and reheating taking place in the topping superheater

what takes place (cases already reviewed by means of the schematic flow diagrams).

T–H diagrams are used opposed to the conventional boiler temperature versus heat graphs. Care must be taken to equate all steam flows to one pound of steam. Ratioing steam flows and steam enthalpies is necessary for each section: SSB superheater, the dual evaporator section, and the feed water section. The exhaust gas streams have for all practical purposes straight lines and only the beginning and end point enthalpies are required.

Simple Case-600 psia and 1000°F Steam-850°F GT Exhaust. A simple case will first be reviewed as an example of calculating procedure. Refer to Figure 15. The gas turbine is assumed to exhaust at 850°F and saturated steam is generated at 600 psia and is then superheated to 1000°F. A selection is made to exit the SSB superheater at the assumed 850°F gas turbine exhaust temperature. Appropriate lines are drawn as shown. Points A–D represent the gas side. Points E–H plot the steam side.

Saturated steam is generated by the evaporator (F to G) and then fed to the SSB superheater. The SSB gas stream is supplementary fired to raise the gas temperature from 850°F to an assumed value of 1500°F. Heat is transferred to the steam from A to B. Heat is transferred to the evaporator section from B to C. Finally, heat is transferred to the oversized economizer feed water from C to D. If the economizer flow were the same as that of the evaporator, then the stack temperature (end point J) would be about 365°F, as shown by the straight line extension of the gas line. The extra flash steam heat recovered compared to that heat required for the evaporator is: $(J_{gh} - H_{gh})/(I_{gh} - J_{gh})$ or $(365 - 240)/(515 - 365) = 0.833$, when considering

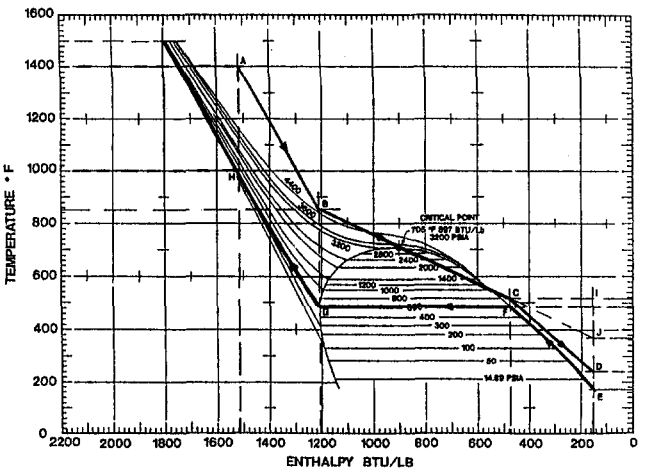


Fig. 15 Graph showing application of the SSB where 600 psia steam is being superheated to 1000°F with an 850°F gas turbine exhaust temperature

Downloaded 02 Jun 2010 to 171.66.16.105. Redistribution subject to ASME license or copyright; see http://www.asme.org/terms/Terms_Use.cfm

a constant gas specific heat value. Subscript *gh* denotes gas enthalpy and capital letters refer to Fig. 15. Therefore the total economizer flow is 1.833 times the flow required for the evaporator.

For Fig. 15, a bypass exhaust flow X is assumed. The fuel heat added in front of the SSB is represented as bypass X Gas, $Q_g(A_{gh} - B_{gh})$. This value is compared to the steam heat rise, $Q_s(H_{sh} - G_{sh})$, where Q is flow and subscripts s and sh are for steam. Iterations are made by selecting appropriate bypass flow rates to arrive at a balance for preselected 1500°F entrance and 850°F exit superheater gas temperatures. The SSB and HRSG evaporator inlet gas temperatures are the same in this example and splitting the flow for the evaporator is not necessary, although there are two separate streams, one for the SSB and one for the HRSG. The SSB heat transfer surface area and pressure drops are then calculated to meet the preselected conditions and predetermined pressure drop assumptions.

Superheating the Feed Water Flash Steam. Reference is made to Figure 16. In this example the first drum extra flash steam generated by the economizer is superheated to 950°F whereas the evaporator steam at 2450 psia is superheated to 1400°F for a HT/HP TST. An 800°F gas turbine exhaust temperature is assumed.

The ratioed amount of heat for the flash superheater is added to the superheater heat load to arrive at the total heat load. Calculations are performed as outlined in the previous example. Note that the bypass gas can exit the superheater at temperatures above the gas turbine exhaust temperature of 800°F to generate incremental steam if need be for the particular application. Also the inlet to the SSB superheater can be 1500°F as shown or other values up to 2500°F as previously explained.

Partial Superheating and Reheating—2400 psig 1000/1000°F With 900°F Gas Turbine Exhaust Temperature. This example illustrates how the SSB arrangement can be applied to a conventional 2400 psig 1000/1000°F reheat steam turbine when the gas turbine exhaust temperature is only 900°F. No HT/HP TST is used in this example. Reference is made to Fig. 17. The gas turbine exhaust temperature would have to be about 1100°F for a conventional reheat utility type steam turbine. Supplementary firing the total gas stream degrades the overall CC efficiency potential. Therefore, repowering could be difficult to justify under these gas turbine conditions.

In this example the steam is heated to about 825°F and likewise reheated to 825°F downstream of the topping superheater. Final heating and reheating to 1000°F is accomplished by the topping SSB through supplementary firing. The superheater gas exit temperature selected is 900°F in this case to match the gas turbine exhaust temperature. Figure 17 shows the partial superheating and reheating heat loads to 825°F and the final superheating and reheating heat loads to 1000°F. The supplementary firing temperature to the SSB is selected to be 1400°F as shown, but could be raised to 2500°F depending on the final cost of the SSB.

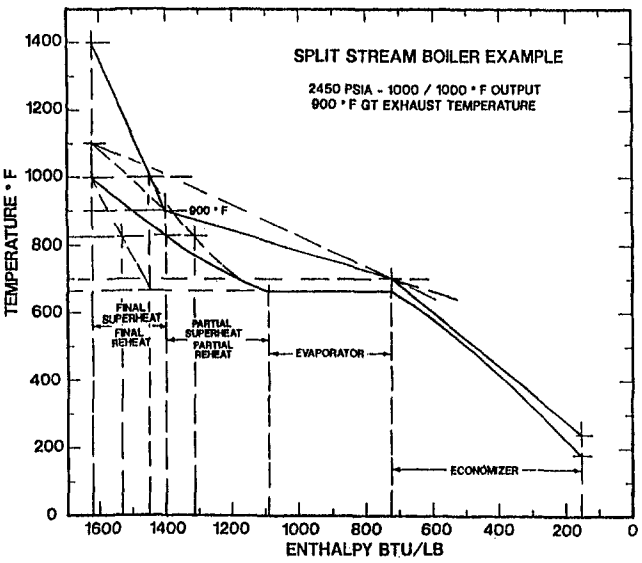


Fig. 17 SSB for a gas turbine with a 900°F exhaust temperature but superheating and reheating to 1000°F

Partial Superheating and Full Reheating—2400 psig 1400/1000°F With 1100°F Gas Turbine Exhaust Temperature. The SSB can be applied to a situation where a more or less conventional 2400 psig reheat steam turbine is topped by a HT/HP TST and where a conventional RH HRSG is placed in parallel with the SSB. See Fig. 18. The initial throttle steam at 2400 psig is superheated to 1400°F, is expanded to 190 psia, is reheated to 1000°F and is further expanded and then condensed.

The steam is partially superheated by the RH HRSG portion of the system to 1000°F and is then further heated to 1400°F by the SSB superheater. Figure 18 shows the final heat load required to heat the steam to 1400°F (incremental 1620h to 1872h). The supplemental firing temperature in front of the

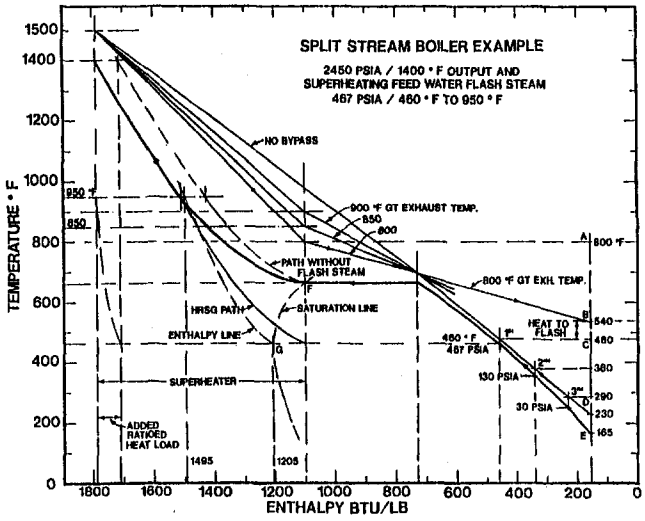


Fig. 16 SSB example where the boiler feed water flash steam is being superheated in the topping superheater

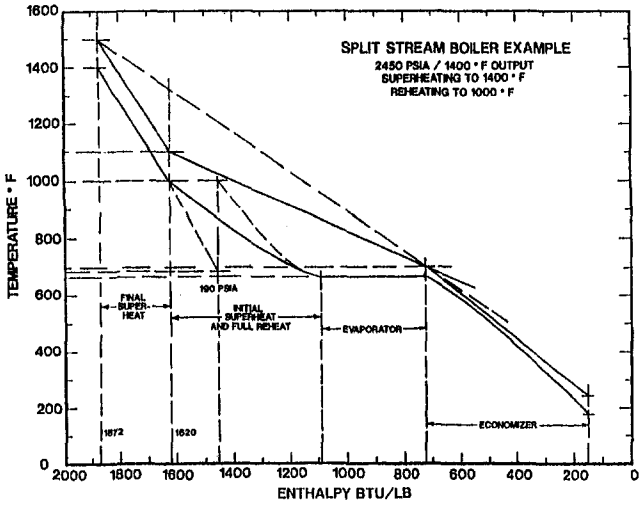


Fig. 18 SSB superheating steam to 1400°F and reheating to 1000°F when coupled to a GT having an 1100°F exhaust temperature

Downloaded 02 Jun 2010 to 171.66.16.105. Redistribution subject to ASME license or copyright; see http://www.asme.org/terms/Terms_Use.cfm

SSB superheater can be increased from the 1500°F shown to 2500°F and the bypass gas flow X to the SSB reduced without any effect on CC efficiency as previously explained. This option is a designer's choice to be based on overall SSB and RH HRSG costs.

The 190 psia exit pressure to RH is lower than normal for a RH steam turbine. This pressure can be increased by selecting a supercritical throttle pressure or by exhausting from the high-pressure section of the steam turbine at a higher than normal temperature. Here again overall cost of the different arrangements would have to be evaluated.

Partial Superheating and Full Reheating—3450 psig 1400/1000°F With 1100°F Gas Turbine Exhaust Temperature. A final case will now be presented. Reference is made to Fig. 19 where a gas turbine exhaust temperature of 1100°F is assumed. In this situation a supercritical pressure of 3450 psia is selected. The high-pressure section of the RH steam turbine exhausts at 350 psia as shown. The reheat heat load for 1000°F is added to the downstream (X and Y) heat load as shown (1343h to 1526h). Also the heat load to the SSB superheater (stream X) is indicated in Fig. 19 (incremental 1557h to 1828h).

The supercritical pressure coupled with the SSB and HT/HP TST makes it possible to obtain an incremental CC efficiency gain of 3 to 4 points over the conventional RH HRSG and RH steam turbine CC.

Conventional RH HRSG Configuration

The bottoming portion of the conventional RH HRSG where two or more drums are incorporated and where this lower pressure steam thus generated is given superheat would be the same for the preceding three examples. When a conventional RH HRSG is applied, the SSB can be physically placed in parallel. Alternately, the HRSG can be modified to incorporate the SSB function.

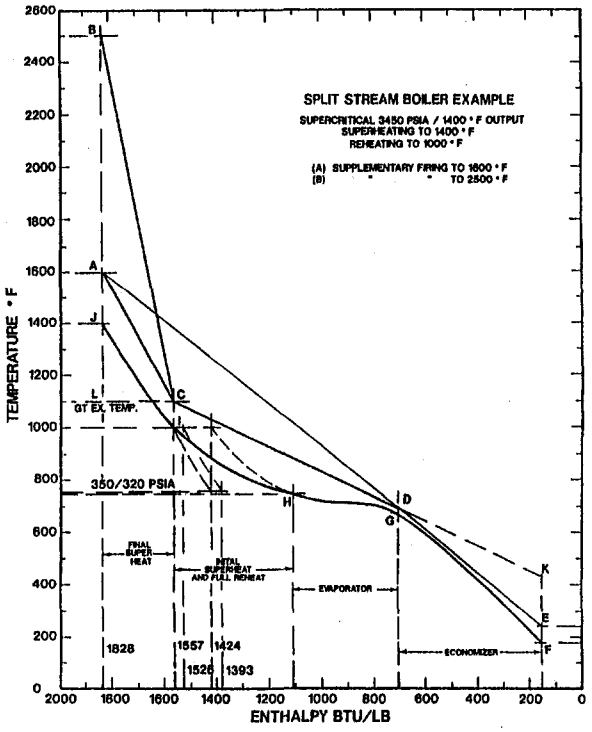


Fig. 19 SSB having a 3450 psia supercritical pressure and superheating steam to 1400°F and reheating to 1000°F where the gas turbine exhaust temperature is 1100°F

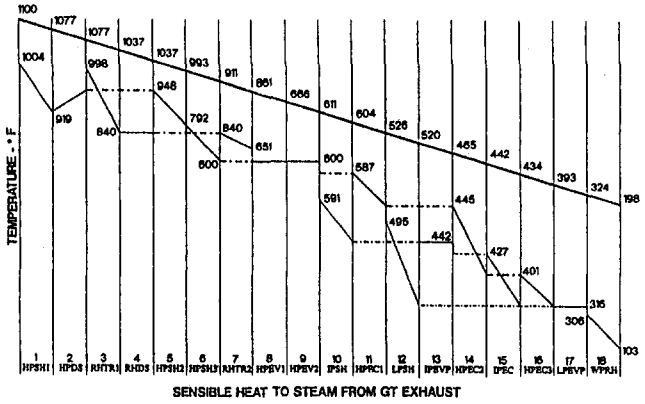


Fig. 20 Temperature profile graph for a Henry Vogt Machine Co. RH HRSG with steam conditions of 1450 psig and 1000/1000°F

A temperature profile for a typical RH HRSG (1450 psig, 1000/1000°F with RH at 369/320 psia) is presented as Fig. 20 to make this paper complete and to serve as a reference. Temperature is plotted against heat to the steam for each section of the boiler. This diagram has been furnished by Henry Vogt Machine Co. for this paper as an example of how a typical three-drum RH HRSG is arranged. Note the various superheater sections and heat loads. Table 1 provides a section identification tabulation for Fig. 20.

An overall schematic flow diagram of this typical RH HRSG is shown in Fig. 21.

Integrated Coal Gas Fuel CC (IGCC)

The SSB can be applied to the IGCC. Normally, the steam that is produced by the gasifier is superheated and reheated along with the other steam in the HRSG. When the SSB is used, all the steam can be given a final superheat and reheat by stream X. The steam can be superheated to 1100°F and reheated to this temperature level, the upper limit of presently available conventional reheat steam turbines. Incremental topping steam power is produced. Optionally, a HT/HP topping steam turbine can be applied when such a turbine becomes available for greater gains. Depending on the steam turbine and SSB configuration, a CC IGCC efficiency gain of 2 to 3 percentage points can be realized when the topping superheat is given to the total steam flow of the gasifier and that of the normal HRSG. A double effect takes place. The SSB is particularly applicable to the Shell Coal Gas Process.

Fuel Gas Chemical Recuperation

The SSB concept as taught in the preceding discussion of this paper can be effectively and advantageously applied to fuel gas chemical recuperation, generally referred to in the chemical industry as hydrocarbon reforming. This process can be applied to both the steam injected version and the condensing steam turbine arrangement of the combined cycle. Hydrocarbon fuels can be reformed into hydrogen and carbon monoxide, but natural gas (mostly methane in composition) in particular is of interest today because of the large number of combined cycles that burn natural gas fuel being installed around the world. The reformed gas when burned in gas turbines produces far less NO_x as will be explained. The SSB configuration will increase overall cycle efficiency and power output. A HT/HP TST can be utilized as an option to increase cycle efficiency and power output further.

Early conceptual work on the chemical recuperated gas turbine CC burning reformed natural gas fuel was done by Jack Janes of the California Energy Commission (CEC) (reported in 1989). General Electric Co., under contract to the CEC, made

Downloaded 02 Jun 2010 to 171.66.16.105. Redistribution subject to ASME license or copyright; see http://www.asme.org/terms/Terms_Use.cfm

Table 1 Tabulation of modular sections referenced to Fig. 20

No.	Section	Full Section Name	Rows
1	HPSH1	High Pressure Superheater #1	2
2	HPDS1	High Pressure Desuperheater #1	0
3	RHTR1	Reheater #1	5
4	RHDS1	Reheater Desuperheater #1	0
5	HPSH2	High Pressure Superheater #2	2
6	HPSH3	High Pressure Superheater #3	2
7	RHTR2	Reheater #2	5
8	HPEV1	High Pressure Evaporator #1	6
9	HPEV2	High Pressure Evaporator #2	8
10	IPSH1	Intermediate Pressure Superheater #1	1
11a	HPEC1	High Pressure Economizer #1	3
11b	HPEC1	High Pressure Economizer #1	6
12	LPSH1	Low Pressure Superheater #1	2
13a	IPEVP	Intermediate Pressure Evaporator	3
13b	IPEVP	Intermediate Pressure Evaporator	3
14	HPEC2	High Pressure Economizer #2	4
15	IPEC1	Intermediate Pressure Economizer #1	1
16a	HPEC3	High Pressure Economizer #3	2
16b	HPEC3	High Pressure Economizer #3	2
17	LPEVP	Low Pressure Evaporator	10
18	WPHR1	Water Preheater #1	12

a study of this cycle including full duct firing as previously suggested by Janes and Rice. The CEC relinquished patent rights under the contract. In turn, Horner and Hines of GE were granted a US patent on a portion of the cycle (Patent No. 5,133,180, issued July 28, 1992). In this patent the steam injected gas turbine CC is used wherein the gas turbine exhausts into a combination HRSG and hydrocarbon reformer. A full exhaust flow duct burner is positioned in front of the reformer. An excess amount of low-efficiency steam is generated in the process, which tends to degrade CC efficiency.

Some of the basic reforming theory is outlined in the patent, but more needs to be added as reported by Janes. The fuel gas as a mixture of natural gas and steam is heated in the presence of a catalyst. An endothermic reaction takes place. The extent of natural gas reforming to produce hydrogen and CO is a function of pressure, temperature, and steam/fuel ratio. The latter can be easily controlled by steam flow to and from the two boiler streams. (The steam to fuel ratio is generally considered to be 3 to 5 moles of steam to 1 mole of natural gas. Therefore, 25 to 35 percent of the HRSG output would be required for reforming.) A higher pressure tends to reduce hydrogen production but a higher temperature will appreciably increase hydrogen production. A reforming temperature of 1300 to 1500°F will produce far more hydrogen than a 1100°F temperature, as is well known in the hydrocarbon process industry and as reported by Janes. Conventional natural gas reformers generally use these higher steam/natural gas temperatures and utilize firing temperatures up to 4000°F. The key to reforming is the catalyst and the reaction temperature. New catalysts now under development could improve reforming at lower temperatures, but so far such catalysts are not commercially available for gas turbine exhaust gas reformers.

The hydrogen content is important for reducing NO_x and minimizing CO (incomplete combustion). The hydrogen component increases the flame velocity for improved combustion for low BTU/ft^3 gaseous fuels burning at low flame temperatures. NO_x formation is directly proportional to flame temperature. A low BTU/ft^3 value of a mixture of reformed natural gas and steam will burn at a low flame temperature. Very little NO_x will be formed and the CO will also be very low. Combustion tests initially sponsored by Shell Oil Co. and continued by DOE and EPRI have verified this phenomenon, as reported by Cook et al. (1995).

The SSB arrangement as suggested in this paper takes the cycle one step further than that of the Horner and Hines patent and the gas turbine and reformer arrangement suggested by Janes. Only a portion of the gas turbine exhaust flow (X) is ducted to a supplementary fired combined steam superheater and steam/natural gas heater and reformer as shown in Fig. 22. The other portion (Y) of the exhaust flow generates injection steam by means of a separate lower temperature flow path. Injection steam production is thus limited.

Natural gas and water can be introduced separately or as a mixture at the cold end of the SSB economizer as shown in Fig. 22. The gas turbine exhaust side stream (X) boils the water into steam and heats the natural gas in parallel. Gas turbine exhaust heat is recovered and this heat (excluding the steam latent heat) as well as the endothermic reforming heat is released when the reformed fuel is burned in the gas turbine. The recuperation efficiency is thus very high and this heat recovery will increase combined cycle efficiency.

The heated steam and natural gas mixture is then superheated to a high temperature up to 1500°F in the presence of a catalyst by gas stream X. Gas turbine exhaust side stream X can be supplementary fired to a temperature level of 2500°F if need be, as previously discussed to reduce the side stream X flow and to promote reforming. The steam produced from the other portion of the gas turbine exhaust flow Y is likewise superheated to any desired temperature level in parallel with the reformed natural gas and steam mixture by gas stream X. This steam can be optionally heated up to 1500°F and then fed to the HT/HP TST as shown in Fig. 22. However, the steam initially need not be superheated to this high a temperature and can be heated by cooling the 1400 to 1500°F reformed fuel and then be given final superheat. A more manageable fuel gas temperature to the gas turbine is obtained when considering the required gas stop valve and gas control valve design and material limitations.

The SSB supplementary fired fuel can be natural gas or the reformed fuel, the latter perhaps being preferred to limit possible NO_x formation.

Figure 23 is a schematic flow diagram of a CC utilizing a condensing steam turbine wherein reformed natural gas fuel is produced in the SSB reformer and then burned in the gas turbine. The steam is expanded to condenser pressure as shown.

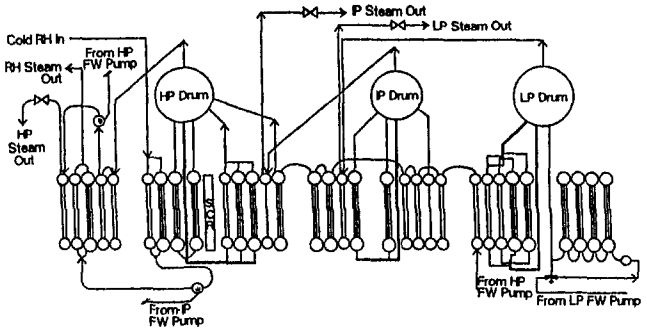


Fig. 21 Schematic arrangement of the Vogt RH HRSG for Figs. 20 and Table 1

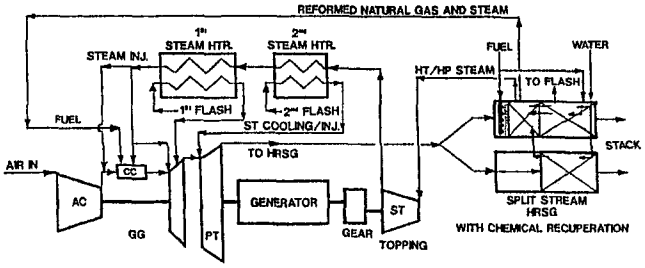


Fig. 22 Schematic flow diagram of a steam injected CC incorporating a SSB chemically recuperated arrangement

Downloaded 02 Jun 2010 to 171.66.16.105. Redistribution subject to ASME license or copyright; see http://www.asme.org/terms/Terms_Use.cfm

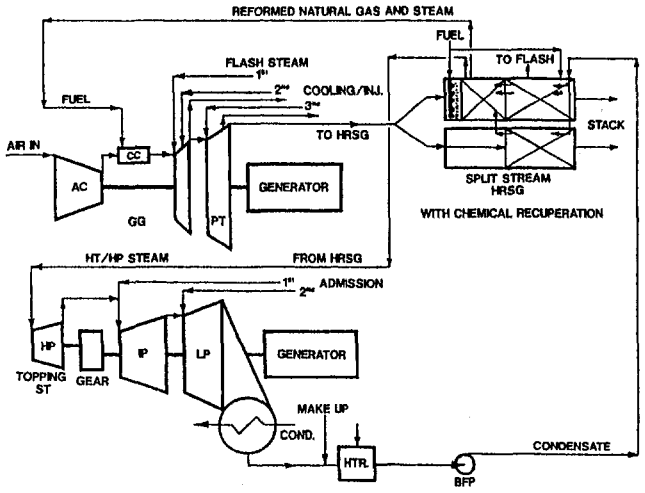


Fig. 23 Schematic flow diagram of a condensing steam turbine CC incorporating a SSB chemically recuperated arrangement.

The HT/HP TST shown is optional, but the addition of this turbine will produce more topping power and a higher CC efficiency will be realized. The preceding explanations and discussion of reforming apply equally to the CC arrangement of Fig. 23.

The Horner and Hines patent indicates that the reheat gas turbine seems to be too complicated and costly to consider, but since the US patent was granted, ABB has introduced an all new family of reheat gas turbines, the GT-24 and 26 models (165 and 230 MWs respectively). One GT-24 turbine has already been sold here in the United States. This introduction appears to neutralize the Horner and Hines concerns about complication and cost. These new reheat gas turbines will have a 30 pressure ratio and will exhaust at about 1150°F, which is still too low a temperature for extensively reforming natural gas for adequate hydrogen content for low NO_x and CO combustion. Therefore the systems suggested by Figs. 22 and 23 also can be advantageously applied to these new reheat gas turbines.

Conclusion

The split stream boiler arrangement as presented in this paper offers a way to increase combined cycle efficiency for both low and high exhaust temperature gas turbines when a high-temperature/high-pressure topping steam turbine is utilized. The projected combined cycle efficiency gain is projected to be 2 to 4 percentage points. Additional incremental power output of the cycle is also realized.

The gas turbine exhaust flow is split and a portion of the gas turbine exhaust gas is supplementary fired to raise the steam throttle temperature of the total system well above that of the gas turbine exhaust. A significant amount of pure topping power is produced without affecting the rest of the bottoming cycle. The residual heat after the fired superheater is used to generate steam in parallel with an augmented HRSG or a once-through boiler. An induced draft fan having variable inlet guide vanes is placed at the exit of the split stream boiler gas stream to control gas flow and to minimize gas turbine back pressure power loss. Chemical fuel gas recuperation can be included in the bypass gas stream portion. The SSB is well suited for the integrated coal gas fuel combined cycle (IGCC).

The paper presents a number of practical ways the split stream boiler can be applied, with and without the high-pressure and high-temperature topping steam turbine. The former produces the highest efficiency gain. Incorporating chemical fuel gas recuperation has the potential of increasing CC efficiency further.

Standard International (SI) Units Conversion Factors

°F = 9/5°C + 32	in H_2O = 2.49 Pa
BTU = 1.0555 kJ	BTU/lb = 2.3260 kJ/kg
Psia = 6.895 kPa	Psi = 14.504 bar force

Acknowledgments

The author wishes to thank his wife, Carolyn Keyes Rice, for her continued support and assistance in preparing this paper. Also appreciation is expressed to the following engineers who have been helpful in making this paper possible:

- Thomas F. Duffy, Director of R & D, Innovative Steam Technologies/Solar Turbine Inc.
- Jack Janes, Research Engineer, California Energy Commission
- Sanjeev Jolly, Senior Development Engineer, Henry Vogt Machine Co.
- Patrick H. Le, Cycle Analyst, US Department of Energy, Morgantown, WV.

References

Ali, S. A., and Webb, H. A., 1994, "Advanced Turbine Systems Program Requirements and an Approach to Implementation," ASME Paper No. 94-GT-411.

Bannister, R. L., et al., 1995, "Development Requirements for an Advanced Gas Turbine System," ASME JOURNAL OF ENGINEERING FOR GAS TURBINES AND POWER, Vol. 117, pp. 724–733.

Cook, C. S., et al., 1995, "System Evaluation and LBTU Fuel Combustion Studies for IGCC Power Generation," ASME JOURNAL OF ENGINEERING FOR GAS TURBINES AND POWER, Vol. 117, pp. 673–677.

DOE, 1994, Advanced Turbine Systems Annual Program Review, Arlington, VA, Nov. 9–11, hand-out material.

Duffy, T. E., and Knox, C. S., 1993, "High-Temperature Steam Topping Cycle Study," EPRI Final Report No. TR-102059, Feb.

Duffy, T. E., 1994a, "High Performance Steam Developments," Report to DOE, Doe Contract No. DE-A002-87 CD 40812, Nov.

Duffy, T. E., 1994b, "Once-Through Steam Generators Provide Cost and Performance Improvements for Combined Cycle and Cogeneration Projects," *Proc. Power-Gen Conf.*, Orlando, FL, Dec. 7–9, Book IV, Vol. 4.

EPRI, 1994, Collaborative Advanced Gas Turbine (CAGT) Results Workshop, Arlington, VA, Apr. 20, hand-out material.

Foster-Pegg, R. W., 1982, "Combined Cycles Have Potential for Cleaner, More Economical Use of Coal," *Power Engineering*, Apr., pp. 80–84.

Horner, M. W., and Hines, W. R., 1992, "Chemically Recuperated Gas Turbine," US Patent No. 5,133,180, issued July 28.

Janes, J., 1989, "Chemically Recuperated Gas Turbines," Preliminary Report, California Energy Commission, R&D Office, Oct.

Jury, W., and Luthi, H. K., 1994, "Advanced GT's Call for Advanced CC's (or: the 4 S's)," ASME Paper No. 94-GT-303.

Leis, D. M., et al., 1995, "Medway: A High-Efficiency Combined Cycle Power Plant Design," ASME JOURNAL OF ENGINEERING FOR GAS TURBINES AND POWER, Vol. 117, pp. 713–723.

Lugand, P., and Parietti, C., 1991, "Combined Cycle Plants With Frame 9F Gas Turbines," ASME JOURNAL OF ENGINEERING FOR GAS TURBINES AND POWER, Vol. 113, pp. 475–481.

Rice, I. G., 1993a, "Steam-Injected Gas Turbine Analysis: Steam Rates," ASME Paper No. 93-GT-132; ASME JOURNAL OF ENGINEERING FOR GAS TURBINES AND POWER, Vol. 117, 1995, pp. 347–353.

Rice, I. G., 1993b, "Steam-Injected Gas Turbine Analysis: Part II—Steam-Cycle Efficiency," ASME Paper No. 93-GT-420.

Rice, I. G., 1993c, "Steam-Injected Gas Turbine Analysis: Part III—Steam-Regenerated Heat," ASME Paper No. 93-GT-421.

Sato, M., et al., 1994, "High Temperature Demonstration Unit for a 1500°C Class Gas Turbine," ASME Paper No. 94-GT-412.

Strong, R., 1992, "Steam 92," Interactive Steam Tables Computer Program.

Tittle, L. B., and Van Laar, J. A., 1993, "Advanced Aeroderivative Gas Turbines, A Preliminary Study," presented at the EPRI 12th Conf. on Coal Gasification Power Plants, Oct.

Tomlinson, L. O., and Lee, D. T., 1985, "Combined Cycles," *Sawyer's Gas Turbine Engineering Handbook*, 3rd ed., Vol. II, pp. 7-1-7-38.

Downloaded 02 Jun 2010 to 171.66.16.105. Redistribution subject to ASME license or copyright; see http://www.asme.org/terms/Terms_Use.cfm

S. Savitsky
7212 Armistad Ave.,
El Paso, TX 79912

Preliminary Estimation of Antisurge Valve Carrying Capacity

If there is a sudden increase in the discharge volume of a pipeline entering a gas compressor, the gas turbine driving the gas compressor will surge with a sufficiently rapid reduction in the gas turbine rotational speed to cause the gas turbine to shutdown. The surge results in strong back-and-forth impacts at high frequency that could destroy the gas compressor bearings and blades. In general, surge also results in an increase in the vibration level of the gas turbine engine.

Automated systems that protect engines from surge use inputs of compressor discharge pressure and gas flow set as the difference between orifice pressures. The difference between downstream discharge pressure (P_D) and the upstream suction pressure (P_S), or their ratio (P_D/P_S), may substitute for discharge pressure. The output is a signal for the opening of a special antisurge valve for the release of the compressor outlet gas flow or for turning the outlet gas flow to the compressor inlet. The control law is usually of the relay type. Although the PID control law is sometimes used, all that is actually needed is for the antisurge valve to open as quickly as possible without producing feedback. The PID control law is used in those cases where the gas turbine can operate at a dangerously low rotational speed with a surge potential.

A more serious control problem is the need to establish the correct carrying capacity of the antisurge valve. There are no known published data on compressors under surge conditions with flow through an antisurge valve. If the carrying capacity of the antisurge valve is large enough, there is no problem; however, the practice of defining the dimensions by the size of the connected pipeline may be inadequate. The focus of this note is to establish a method for obtaining a preliminary estimate of the required carrying capacity of the antisurge valve based on the characteristics of the gas compressor and the connected pipeline volume.

Consider the point of operation shown on the compressor map in Fig. 1. It is characterized by the static equations:

$$M_{T0} - M_{C0} = 0$$

$$Q_{C0} - Q_{CV0} = 0$$

where

M_{T0} and M_{C0} = the nominal torque values of the gas turbine engine and the gas compressor, respectively
Q_{C0} and Q_{CV0} = the nominal values of gas flow through the compressor outlet and the pipeline section where the pipeline valve (PV) is installed, respectively.

For a single-shaft gas turbine engine, the nominal torque M_{T0} is difference between the engine turbine torque, M_{GT0}, and the required engine compressor torque, M_{CT0}. In a dual-shaft engine, the torque M_{T0} is equal to the torque value M_{GT0} for the power turbine driving the gas compressor.

When shutdown of the gas turbine engine occurs ($M_T \to 0$), it starts a dynamic process described by the dynamic equations:

$$J\frac{d\omega}{dt} = M_T - M_C$$

$$\frac{dW}{dt} = Q_C - Q_V$$

where

J = the moment of inertia of the rotating mechanical parts connected to the gas compressor shaft
ω = rotational speed of the gas compressor shaft
M_T and M_C = current torques of gas turbine engine and the gas compressor, respectively
W = mass of the gas in the connected pipeline volume
Q_C and Q_V = current gas flows through the compressor outlet and the antisurge valve, respectively.

In the case of shutdown, the flow of gas in the pipeline section is discontinued and the flow through the antisurge valve is rapidly increased ($Q_V > 0$).

A preliminary estimate of carrying capacity of the antisurge valve is obtained by modifying and linearizing the set of dynamic equations describing the process. The first of these equations can be written:

$$J_0\epsilon_\omega = \Delta M_T - \Delta M_C$$

where

$$J_0 = J\omega_0,$$

$$\Delta M_T = M_T - M_{T0} = 0,$$

$$\Delta M_C = M_C - M_{C0}, \quad M_{T0} - M_{C0} = 0,$$

with ω_0 being the nominal value of rotational speed and the operator ϵ_ω being defined

$$\epsilon_\omega = \frac{d\bar{\omega}}{dt}, \quad \bar{\omega} = \frac{\omega - \omega_0}{\omega_0}.$$

The third torque equation that makes this substitution work corresponds to the equilibrium condition previously established for nominal conditions. The second of the dynamic equations can be similarly transformed to:

$$W_0\epsilon_d = \Delta Q_C - \Delta Q_V$$

where according to the ideal gas law

$$W_0 = \frac{VP_{D0}}{RT_{D0}}$$

with

V = connected volume
T_D, T_{D0} = current and nominal values of the discharge temperature, assumed to be equal

Contributed by the International Gas Turbine Institute for publication in the JOURNAL OF ENGINEERING FOR GAS TURBINES AND POWER. Manuscript received at ASME Headquarters January 23, 1997. Associate Technical Editor: H. L. Julien.

Copyright © 1997 by ASME

Downloaded 02 Jun 2010 to 171.66.16.105. Redistribution subject to ASME license or copyright; see http://www.asme.org/terms/Terms_Use.cfm

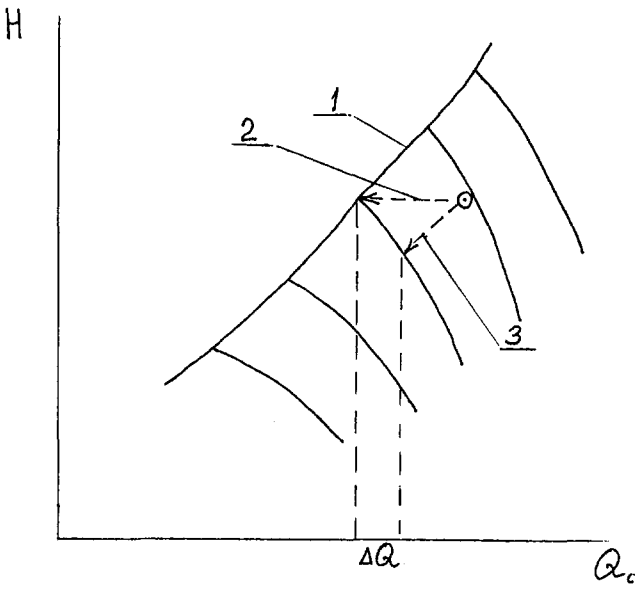


Fig. 1 Compressor map: 1—surge line; 2—α = 0; 3—α = 1

P_D, P_{D0} = current and nominal values of the discharge pressure, where P_D is taken as the characteristic value in the connected volume

and

$$\Delta Q_C = Q_C - Q_{C0}, \quad \Delta Q_V = Q_V - Q_{CV0}, \quad Q_{C0} = Q_{CV0}.$$

The last gas flow equation corresponds to equilibrium conditions established for nominal operation in a static mode. The operator ϵ_d is defined, similar to ϵ_ω, as

$$\epsilon_d = \frac{d\bar{P}_D}{dt}, \quad \bar{P} = \frac{P_D - P_{D0}}{P_{D0}}.$$

The dynamic equations are linearized using a Taylor series expansion to evaluate infinitesimal differences ΔM_C and ΔQ_C in terms of the adiabatic head H and rotational speed ω. The resulting expression for ΔM_C is:

$$\Delta M_C = H_0 \frac{\partial M_C}{\partial H} \bar{H} + Q_{C0} \frac{\partial M_C}{\partial Q_C} \bar{Q}_C + \omega_0 \frac{\partial M_C}{\partial \omega} \bar{\omega}_0$$

where

$$\bar{H} = \frac{H - H_0}{H_0}, \quad \bar{Q}_C = \frac{Q_C - Q_{C0}}{Q_{C0}}.$$

This expression reduces to:

$$\Delta M_C \simeq M_{C0}\bar{H} + M_{C0}\bar{Q}_C - M_{C0}\bar{\omega}$$

when, as a coarse approximation, it is assumed that

$$\frac{\partial M_C}{\partial H} \simeq \frac{M_{C0}}{H_0}, \quad \frac{\partial M_C}{\partial Q_C} \simeq \frac{M_{C0}}{Q_{C0}}, \quad \frac{\partial M_C}{\partial \omega} \simeq \frac{M_{C0}}{\omega_0}.$$

The expression for ΔQ_C is:

$$\Delta Q_C = \omega_0 \frac{\partial Q_C}{\partial \omega} \bar{\omega} + H_0 \frac{\partial Q_C}{\partial H} \bar{H}$$

Substituting these expressions into the modified dynamic equations,

$$J_0\epsilon_\omega = M_{C0}(1 - A_\omega)\bar{\omega} - M_{C0}(1 + A_H)\bar{H}$$

$$W_0\epsilon_d = Q_{C0}A_{\bar{\omega}}\bar{\omega} + Q_{C0}A_H\bar{H} - \Delta Q_V$$

where

$$A_H = \frac{H_0}{Q_{C0}} \frac{\partial Q_C}{\partial H}, \quad A_\omega = \frac{\bar{\omega}}{Q_{C0}} \frac{\partial Q_C}{\partial \bar{\omega}}.$$

Further manipulation of terms results in the equations:

$$\frac{J_0\epsilon_\omega}{M_{C0}} = -[(1 + A_H)\alpha + (A_\omega - 1)]\bar{\omega}$$

$$\frac{\Delta Q_V}{Q_{C0}} = (A_\omega + A_H\alpha)\bar{\omega} - \frac{W_0}{Q_{C0}} \frac{\alpha}{A_P} \epsilon$$

where

$$A_P = \frac{H_0}{P_{D0}} \frac{dP_D}{dH}, \quad \epsilon = \epsilon_\omega, \quad \alpha = \frac{\bar{H}}{\bar{\omega}}.$$

Finally, combining the dynamic equations, the equation for valve capacity is obtained:

$$\frac{\Delta Q_V}{Q_{C0}} = -T_M\left[\frac{A_\omega + A_H\alpha}{(1 + A_H)\alpha + (A_\omega - 1)} + \frac{T_V}{T_M} \frac{\alpha}{A_P}\right]\epsilon$$

where

$$T_M = \frac{J_0}{M_{C0}}, \quad T_V = \frac{W_0}{Q_{C0}}.$$

The coefficient α is introduced to emphasize that a desirable ratio between the decrease of the adiabatic head and the rotational speed may be chosen. It is reasonable to set α equal to 1, so that the percentage rates of change of H and ω are equal. This corresponds to Path 3 on the compressor map where the possible decrease in rotational speed is shown. Further assuming that the reduction in speed is a convenient exponential function of time,

$$\bar{\omega} = -\exp(-t/T_M), \quad 0 < \bar{\omega} < 1,$$

a preliminary estimate of the antisurge valve carrying capacity is:

$$\frac{\Delta Q_V}{Q_{C0}} = 1 + \frac{1}{A_P} \frac{T_V}{T_M}$$

This equation indicates that, if the PV is closed and the antisurge valve is opened ($\Delta Q_V > 0$), the antisurge valve carrying capacity must provide Q_C plus the flow (ΔQ) from the connected volume (see Fig. 1). The additional value ΔQ is:

$$\frac{\Delta Q}{Q_{C0}} = \frac{1}{A_P} \frac{T_V}{T_M}.$$

It is known that A_P depends on the ratio P_D/P_S. For example, values calculated for methane gas (k = 1.3) are:

$$A_P = \begin{cases} 10.61 & \text{for } P_D/P_S = 1.1 \\ 5.6 & \text{for } P_D/P_S = 1.2 \\ 1.56 & \text{for } P_D/P_S = 2.0 \end{cases}$$

For T_V/T_M equal to 2.0, the required antisurge valve carrying capacities for the two extreme values of P_D/P_S are calculated to be:

$$\frac{\Delta Q_V}{Q_{C0}} = \begin{cases} 1.19 & \text{for } P_D/P_S = 1.1 \\ 2.23 & \text{for } P_D/P_S = 2.0 \end{cases}$$

These preliminary estimates should be checked for each application. Further, the results are dependent on both the speed of the antisurge valve actuator and rate of the rotational speed decrease through α; if the actuator speed is significantly less than the rotational speed decrease, the value of α will be lower than the selected value of one.

Downloaded 02 Jun 2010 to 171.66.16.105. Redistribution subject to ASME license or copyright; see http://www.asme.org/terms/Terms_Use.cfm

"Snapping" Torsional Response of an Anisotropic Radially Loaded Rotor

D. E. Bently

P. Goldman

A. Muszynska

Bently Rotor Dynamics Research Corporation, Minden, NV 89423

A rotor system with two orthogonal lateral and two angular (torsional) degrees of freedom is considered. The rotor has asymmetry of the lateral stiffness and is laterally loaded with a constant radial force and a rotating unbalance. Constant driving and load torques are applied to the rotor. The important part of the research includes an analysis of "snapping" action, when, during rotation, the rotor experiences a peak of torsional acceleration. This occurs when the "strong stiffness" axis of the anisotropic rotor passes under the axis of the sideload. The numerical simulation of the analytical model exhibits a snapping (accelerated) torsional response of the rotor at twice synchronous frequency (2×), and it is especially pronounced at 1× and 2× torsional resonances. The snapping response can initiate a rotor crack in the area of stress concentration, can stimulate existing crack propagation, and can be a cause of the coupling failure. The analytical results are obtained by the Averaging Method application. They confirm the numerical results and show the possibility of combination resonance occurrences. The synchronous dynamic stiffness for the frequency range around 1× lateral resonance is analytically obtained. The specific shape of the quadrature dynamic stiffness component can serve as a shaft crack indicator and can be used for early detection of a lateral crack on the rotor.

1 Introduction

The trend to increased efficiency and higher speeds in turbomachinery results in design of more flexible shafts, which operate at rotative speeds above several of their natural frequencies. This makes rotors more prone to cracks caused by stress concentration and propagated due to high- and low-cycle fatigue. The increase in the operating temperatures leads to the shaft's vulnerability to creep and stress corrosion cracking. According to Bently and Muszynska (1986), at least 28 rotor failures due to cracks were documented during the previous ten years in the USA power industry. This explains the continuing interest in the dynamic behavior and early detection of cracks in rotors.

Many papers discussed the response of a laterally cracked rotor. Dimentberg (1945) was probably one of the first to report the effect of rotating stiffness asymmetry on the shaft vibration. Henry and Okah-Avae (1976) performed a computer study in which the weight of the rotor was reported to be responsible for 2× resonance. Mayes and Davies (1976) studied the behavior of the cracked shaft model in which opening and closing crack was modeled as a stiffness step-function. Gasch (1976) simulated the breathing crack by a spring-loaded hinge, and proved the existence of subharmonic resonances.

Grabowski (1980) used a modal approach to the problem. He developed a theoretical model of the crack mechanism, which showed a good correlation with static experiments, and used it in a dynamic model of the rotor. Inagaki et al. (1979) applied the transfer matrix method to model the breathing crack as a step-function for the bending moment, and used Fourier series expansion to find the solution. Muszynska (1982) considered both gaping and breathing cracks, and investigated the interaction between rotating and stationary stiffness asymmetries. Dimarogonas and Papadopoulos (1983) and Nelson and Nataraj (1986) analyzed lateral response spectrum changes due to the nonlinearities introduced by cracks. Bently and Muszynska (1986) emphasized the importance of the observation of 1× and 2× response amplitude and phase change in rotors for early crack detection. A significant number of papers (Chen and Wang, 1986; Dirr and Schmalhorst, 1987; Qian et al., 1991) were published on finite element modeling of cracked shafts.

It is easy to note that in comparison to the great number of papers on lateral vibration, which is considered the major effect of the cracked rotors, the number of papers on torsional vibration due to cracks is significantly smaller. Among them Dimarogonas and Massouros (1981) reported the first torsional natural frequency reduction due to a transverse crack. Christides and Barr (1986) developed partial differential equations for the torsional vibration of a cracked shaft under the assumption of uncoupled lateral and torsional modes. The finite element model was applied to the modeling of the torsional vibration of the cracked shafts in the paper by Chen and Wang (1986). Papadopoulos and Dimaragonas (1989) derived the cross-coupled local stiffness matrix, which resulted in the lateral/torsional cross-coupling effect. Another lateral/torsional coupling mechanism (due to the combination of the unbalance, shaft stiffness asymmetry, and radial sideload) was investigated analytically and experimentally in the paper by Muszynska et al. (1992).

From compilation of many early cracked shaft warnings, in our experience of vibration monitoring many rotating machines in the field, more than 70 percent of the early warnings have been at rotative speed (1×) changes. This comes from the simple rule, "If the shaft cracks, it is usually bowed." The remaining minority shows the twice rotative speed (2×) activity. Shaft-observing *XY* probes are the best transducer method and placement. For both 1× and 2× symptoms *either* phase or amplitude changes (not always increasing amplitude) are important. The concept of the "snapping" (accelerated) action when the rotor passes over top dead center, pioneered by the first author of this paper, as a major lateral action, results in significant coupling to torsional activity.

This paper is a continuation of the study of lateral/torsional cross-coupling due to the shaft asymmetry (lateral anisotropy), unbalance, and constant radial force. Special attention is paid

Contributed by the International Gas Turbine Institute and presented at the 40th International Gas Turbine and Aeroengine Congress and Exhibition, Houston, Texas, June 5–8, 1995. Manuscript received by the International Gas Turbine Institute March 7, 1995. Paper No. 95-GT-396. Associate Technical Editor: C. J. Russo.

Copyright © 1997 by ASME

Downloaded 02 Jun 2010 to 171.66.16.105. Redistribution subject to ASME license or copyright; see http://www.asme.org/terms/Terms_Use.cfm

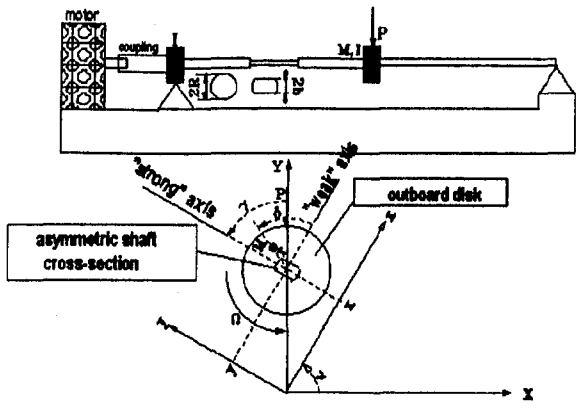


Fig. 1 The rotor with lateral anisotropy

to the 2× torsional excitation, which is responsible for the rotor-damaging snapping action, defined here not as an impulse, but smooth torsional acceleration and deceleration. The computer simulation allowed the investigation of a wide range of rotor parameters, and their influence on the rotor lateral and torsional responses. The analytical research is based on the Averaging Method of Bogolubov and Mitropolsky (1978). To the authors' knowledge, the only other attempt to utilize this technique for the solution of similar problems was made by Cohen and Porat (1985), where it was applied to a symmetric rotor with pronounced gyroscopic effect. In application to the above-described problem, the Averaging Method allows investigation of system various resonances, as well as an evaluation of the synchronous dynamic stiffness in the range of 1× lateral resonance.

2 Physical and Mathematical Models

The goal of this study is to model torsional and lateral vibrational responses of a rotor with lateral anisotropy. A simple rotor train, as shown in Fig. 1, is considered.

The system includes the motor, which is modeled as a source of the regular rotation with rotative speed Ω, connected to the main shaft through the coupling with torsional stiffness and damping K_c and D_c. The main shaft carries two disks and is supported in two relatively rigid bearings. The inboard disk has a polar moment of inertia I_0 and only one degree of freedom, described by the angular coordinate φ. The driving torque T_{dr} applied to the inboard disk from the motor through the coupling can be expressed as $T_{dr} = D_c(\Omega - \dot{\varphi}) + +K_c(\Omega t - \varphi)$. The inboard and outboard disks are connected through the shaft, which has a torsional stiffness K_t and lateral stiffnesses K_x, $K_y (K_x < K_y)$ in the rotating coordinate system Oxy (Fig. 1). The shaft stiffness anisotropy can be due to either shaft asymmetric cross section or acquired local flexibility due to a transverse crack (Mayes and Davies, 1976). The nonlinearities usually associated with cracks are neglected here. The outboard disk has a mass M and polar moment of inertia $I = I_0 + r^2M$, where r is the distance between the geometric and mass centers of the disk. The radial sideload P is applied to this disk. The outboard disk motion is described by one torsional coordinate γ and two lateral displacements: X is horizontal and Y is vertical in the stationary coordinates, or x, y in rotating coordinates (Fig. 1). Note that when $\gamma = 0$ or π, the shaft "strong stiffness" axis y passes through the direction of the radial sideload P. This creates the condition for rotor "snapping" (accelerated) action with all possible damaging consequences. The load torque T_l is applied to the outboard disk in the direction opposite to the direction of rotation. The equations of motion of the rotor are as follows:

$$\ddot{X} + \frac{D}{M}\dot{X} + \nu^2(1 - q\cos[2(\Omega t + \vartheta - \gamma_0)])X - \nu^2 q\left(Y_1 - \frac{P}{K}\right)\sin[2(\Omega t + \vartheta - \gamma_0)] = r(\Omega + \dot{\vartheta})^2\cos(\Omega t + \vartheta - \gamma_0 + \delta) + r\ddot{\vartheta}\sin(\Omega t + \vartheta - \gamma_0 + \delta);$$

$$\ddot{Y}_1 + \frac{D}{M}\dot{Y}_1 + \nu^2(1 + q\cos[2(\Omega t + \vartheta - \gamma_0)])Y_1 - \nu^2 qX\sin[2(\Omega t + \vartheta - \gamma)] = r(\Omega + \dot{\vartheta})^2\sin(\Omega t + \vartheta - \gamma_0 + \delta) - r\ddot{\vartheta}\cos(\Omega t + \vartheta - \gamma_0 + \delta) + \frac{qP}{M}\cos[2(\Omega t + \vartheta - \gamma_0)];$$

$$\ddot{\theta} + \frac{K_t + K_c}{I_0}\theta - \frac{K_t}{I_0}\vartheta = -\frac{D_t + D_c}{I_0}\dot{\theta};$$

$$\ddot{\vartheta} + \frac{K_t}{I_0}\vartheta - \frac{K_t}{I_0}\theta = -\frac{D_t}{I_0}\dot{\vartheta} + \frac{qP^2}{KI_0}\sin[2(\Omega t + \vartheta - \gamma_0)] + \frac{qPr}{I_0}\cos(\Omega t + \vartheta - \gamma_0 + \delta) + \Psi \quad (1)$$

where $Y = Y_1 - P/K$, $\gamma = \Omega t + \vartheta - \gamma_0$, $\varphi = \Omega t + \theta - \varphi_0$, $I_0 = \rho^2 M$ and $K = (K_x + K_y)/2$ is shaft average stiffness, $q = (K_y - K_x)/2K$ is stiffness asymmetry factor.

$$\gamma_0 = \frac{(K_c + K_t)}{K_c K_t}(D_t\Omega + T_l); \quad \varphi_0 = \frac{2D_t\Omega + T_l}{K_c};$$

$$\Psi = \frac{\nu^2 q}{\rho^2}\left\{\left[Y_1\left(Y_1 - \frac{P}{K}\right) - X^2\right]\sin[2(\Omega t + \vartheta - \gamma_0)] + 2XY\cos[2(\Omega t + \vartheta - \gamma_0)]\right\} + \frac{\nu^2 q}{\rho^2}r[Y_1\cos(\Omega t + \vartheta - \gamma_0 - \delta) - X\sin(\Omega t + \vartheta - \gamma_0 - \delta)] + \frac{\nu^2 q}{\rho^2}[Y_1\cos(\Omega t + \vartheta - \gamma_0 + \delta) - X\sin(\Omega t + \vartheta - \gamma_0 + \delta)] - \frac{Dr}{M\rho^2}[\dot{X}_1\sin(\Omega t + \vartheta - \gamma_0 + \delta) - \dot{Y}\cos(\Omega t + \vartheta - \gamma_0 + \delta)] \quad (2)$$

The essential behavior of the system (1) is determined by nondimensional parameters ν/Ω, ν_t/ν, $D/M\Omega$, $D_t/I_0\Omega$, rK/P, q, and I_0/Mr^2. It is important to note that if all nonlinear terms are neglected, the linear system of the last two Eqs. (1) provides two natural frequencies $\omega_{n1,2}$ and two normal coordinates $\alpha_{n1,2}$, which, in the case of stiff coupling, $K_t/K_c \ll 1$, can be approximated as follows:

$$\omega_{n1}^2 \approx \frac{K_c}{I_0}\left(1 + \frac{K_t}{K_c}\right); \quad \omega_{n2}^2 \approx \frac{K_t}{I_0}\left(1 - \frac{K_t}{K_c}\right),$$

$$\alpha_{n1} \approx \theta - \frac{K_t}{K_c}\vartheta; \quad \alpha_{n2} \approx \vartheta - \frac{K_t}{K_c}\theta \quad (3)$$

Downloaded 02 Jun 2010 to 171.66.16.105. Redistribution subject to ASME license or copyright; see http://www.asme.org/terms/Terms_Use.cfm

Table 1 The main parameters of the rotor system numerical simulation

	ν, cpm	ν_t, cpm	q	r, in	δ, rad	$\frac{P}{M}$, in / sec^2	$\frac{D}{\sqrt{KM}}$	$\frac{D_t}{\sqrt{I_0 K_t}}$
Case (a): torsional	15000	2500	0.2	0.05	0	60000	0.2	0.04
Case (b): lateral	1700	15000	0.2	0.001	0	1000	0.2	0.04
Case (c): torsional and lateral	1700	2500	0.2	0.001	0	1000	0.2	0.04

In this case, the first normal coordinate approximately represents an angular displacement of the inboard disk, and has a natural frequency close to $\sqrt{K_c/I_0}$. The second normal coordinate represents an angular displacement of the outboard disk, and has a natural frequency close to $\sqrt{K_t/I_0}$ ($\omega_{n1} > \omega_{n2}$). If the frequency region considered is significantly below ω_{n1} then θ and φ_0 can be assumed to be zero, and the angular coordinate φ of the inboard disk represents the regular rotation ($\varphi = \Omega t$). The investigation below considers this particular case.

3 Preliminary Analysis and Numerical Simulation

The computer model of the system (1) with assumed $\dot{\varphi} = \Omega$ was built using Matlab/Simulink software. Three sets of parameters used in the numerical simulation are presented in Table 1. There ν and ν_t are lateral and torsional mode natural frequencies. Since the numerical integration was performed in the range of rotative speeds from 0 to 5000 rpm, case (a) obviously does not experience any significant lateral activity, except static vertical displacement due to the radial sideload. This means that in Eqs. (1) X, Y can be assumed zero for this case, and the only important equation for the torsional activity is simplified to the following:

$$\ddot{\vartheta} + \frac{K_t}{I_0}\vartheta = -\frac{D_t}{I_0}\dot{\vartheta} + \frac{qP^2}{KI_0}\sin 2(\Omega t + \vartheta - \gamma_0) + \frac{qPr}{I_0}\cos(\Omega t + \vartheta - \gamma_0 + \delta) \quad (4)$$

Equation (4) can be considered as a linear oscillator with two forcing terms: 1 × excitation $qPr \cos(\Omega t + \vartheta - \gamma_0 + \delta)/I_0$ due to the combination of unbalance, shaft stiffness asymmetry, and radial sideload, and 2× excitation $qP^2 \sin[2(\Omega t + \vartheta - \gamma_0)]/KI_0$ due to the shaft stiffness asymmetry and radial sideload. The latter excitation describes the effect called the snapping action: The torque experiences two positive peaks when the strong stiffness axis passes the radial sideload direction with the angle 45 deg ($\gamma = \Omega t + \vartheta - \gamma_0 = \pi/4, 5\pi/4$). The results of the numerical simulation for case (a) are presented in the form of overall torsional amplitude versus rotative speed (Fig. 2). Note that the effect of the synchronous excitation is relatively small due to the low amount of unbalance. 1× and 2× filtered torsional responses are shown in Fig. 3, indicating that the two peaks in Fig. 2 are, indeed, 2× and 1× resonances.

The torsional acceleration timebase waveform (Fig. 4) at the rotative speed Ω = 1000 rpm (close to the 2× resonance at Ω = 1250 rpm) illustrates the fact that due to the snapping action, the torque experiences two positive peaks when $\gamma = \pi/4$ or $5\pi/4$. The Keyphasor® (once-per-turn marker) position here corresponds to $\gamma = 0$, when the strong axis coincides with the direction of the radial sideload. Note that since the waveform was taken below the 2× resonance, the torsional acceleration

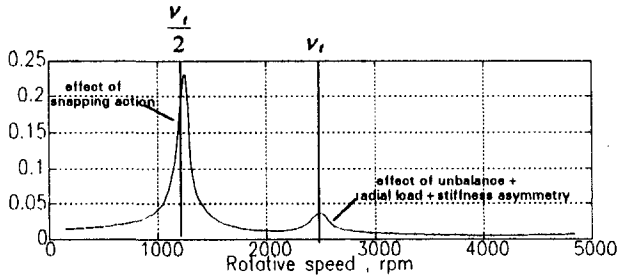


Fig. 2 Overall amplitude of the rotor torsional response obtained from the computer simulation of case (a)

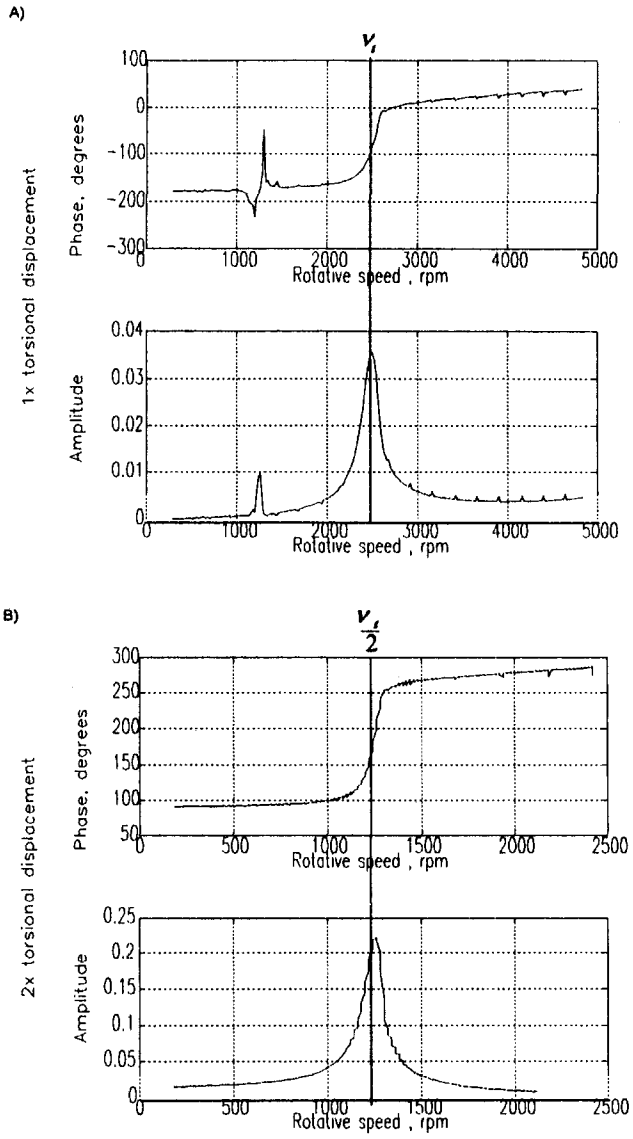


Fig. 3 Bode plot of torsional response of the rotor for case (a): (A) 1× filtered response; (B) 2× filtered response

Downloaded 02 Jun 2010 to 171.66.16.105. Redistribution subject to ASME license or copyright; see http://www.asme.org/terms/Terms_Use.cfm

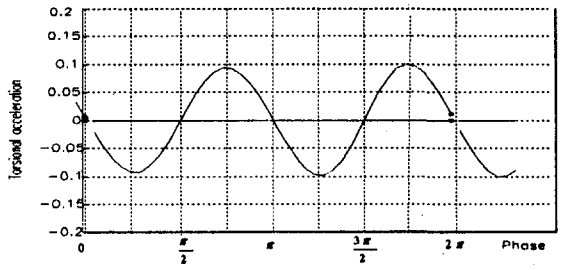


Fig. 4 Waveform of the rotor torsional acceleration at Ω = 1000 rpm, for case (*a*)

lags the excitation by π, and has negative peaks while the snapping torque has positive ones.

Case (b) (Table 1) is, in a sense, an opposite to case (a) because in the rotative speed range considered (from 0 to 5000 rpm), the rotor with case (b) parameters does not exhibit any significant torsional activity. Therefore, this case can be described by the first two Eqs. (1) in which ϑ is assumed zero. The resulting equations have been well studied (see, for example, Muszynska, 1982). The rotor lateral response for this case obtained by the computer simulation is shown in Fig. 5 in the form of overall vibration vertical and horizontal response amplitudes. They confirm that in the case of a significant difference in the lateral and torsional natural frequency values, there is no interaction between them, and the lateral response consists of mainly 1× and 2× components. The Bode plots of 1× and 2× filtered vertical and horizontal responses of the rotor are almost identical.

Case (c) overlaps the first two cases. Both lateral and torsional natural frequencies in this case are in the range of considered rotative speeds. Therefore, case (c) is expected to have both lateral and torsional vibrational activities. The results of this case simulation are presented in the form of lateral and torsional overall amplitudes versus rotative speed (Figs. 5 and 6). Note that the overall lateral amplitudes for case (c) are practically identical to those of case (b) (Fig. 5).

As shown in Fig. 6, the situation is different for the rotor torsional response: In addition to the peaks at $\Omega = \nu_t/2$, ν_t,

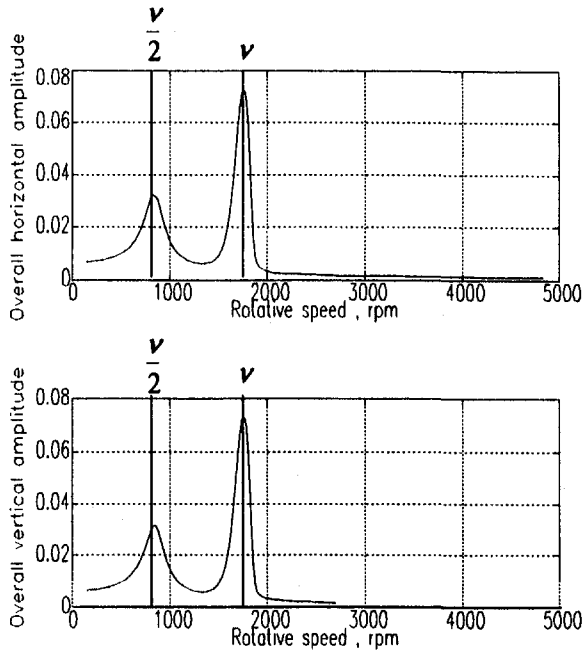


Fig. 5 Overall amplitudes of the rotor horizontal and vertical responses, cases (*b*) and (*c*)

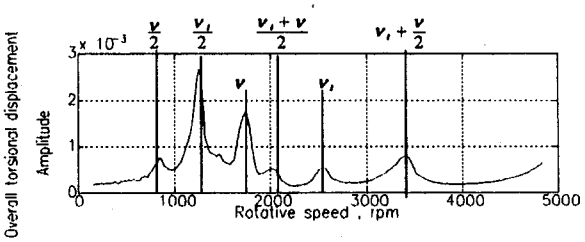


Fig. 6 Overall amplitude of the rotor torsional response, case (*c*)

which are present in Fig. 2 for case (a), the torsional response of the rotor for case (c), reflects 1× and 2× lateral resonances at $\Omega = \nu$, $\nu/2$ correspondingly, and shows the existence of combination resonances at $\Omega = (\nu_t + \nu)/2$, $\nu_t + \nu/2$. Figure 7 presents Bode plots of the 1× and filtered torsional responses for case (c), and proves that the overall peaks at $\Omega = \nu$ and ν_t are due to the 1× lateral and torsional resonances, correspondingly, and overall peaks at $\Omega = \nu/2$, $\nu_t/2$ are due to 2× lateral and torsional resonances. The analysis of the combination resonances is given in the next section of this paper.

4 Analytical Consideration

The analysis of the system (1) will be made with the assumptions that unbalance, damping, and lateral stiffness asymmetry are small values as follows:

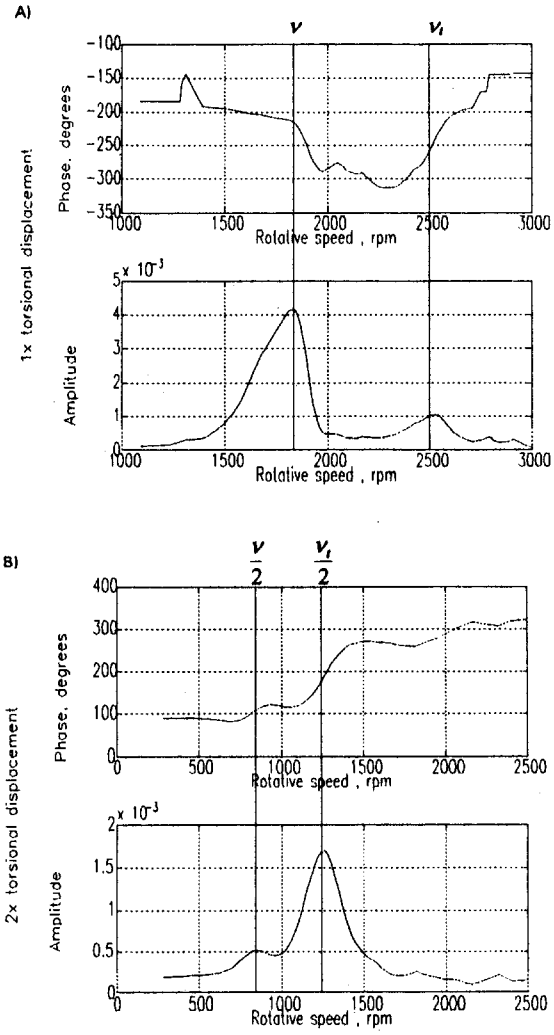


Fig. 7 Bode plots of the horizontal response of the rotor for case (*c*): (*A*) 1× filtered response, (*B*) 2× filtered response

Downloaded 02 Jun 2010 to 171.66.16.105. Redistribution subject to ASME license or copyright; see http://www.asme.org/terms/Terms_Use.cfm

$$\left[q^2, \quad \zeta = \frac{D}{2M\nu}, \quad \zeta_t = \frac{D_t}{2M\nu\rho^2}, \quad r \right] = O(\epsilon) \qquad (5)$$

where ϵ is a formal small parameter and O is a function that denotes the order of smallness.

Neglecting small terms of order higher than the first power of the parameter ϵ, Eqs. (1) for the case of stiff coupling ($\theta = 0$) can be rewritten as follows:

$$G' = \epsilon W \cos\psi + \epsilon^2 \ldots; \quad H' = -\epsilon V \sin(\psi + \phi) + \epsilon^2 \ldots$$

$$\phi' = \epsilon\left[\frac{W}{G}\sin\psi - \frac{V}{H}\cos(\psi + \phi)\right] + \epsilon^2 \ldots;$$

$$s' = -\epsilon\frac{\Xi}{n}\sin\beta + \epsilon^2 \ldots$$

$$\psi' = 1 - \epsilon\frac{W}{G}\sin\psi + \epsilon^2 \ldots;$$

$$\beta' = n - \epsilon\frac{\Xi}{ns}\cos\beta + \epsilon^2 \ldots; \quad \varphi' = m \qquad (6)$$

where $\nu_t = n\nu$, $\Omega = m\nu$, $\tau = \nu t$, $d/d\tau = '$, $Y_1 = G\sin\psi$, $X = H\cos(\psi + \phi)$, $\vartheta = s\cos\beta$, $Y_1' = G\cos\psi$, $X' = -H\sin(\psi + \phi)$, $\vartheta' = -sn\sin\beta$; V, W, Ξ are expressed through the slow variables G, H, ϕ, s and fast rotating phases ψ, β, $\Omega t = m\tau$.

The Fourier analysis of the expressions V, W, and Ξ shows the existence of several resonances in the system (6). They are summarized in Table 2 (the solution algorithm based on the Averaging Method by Bogolubov and Mitropolsky, 1978 is discussed by Goldman and Muszynska, 1994).

As it follows from Table 2, the system with isotropic stiffness ($q = 0$) allows for main lateral and integer combination resonances due to the unbalance r. The stiffness asymmetry q by itself compliments torsional resonances and fractional combination resonances of the first group. Its product with radial side-load P/K affects all resonances of the system. According to Fig. 7, the torsional response of the rotor for case (c) shows fractional combination resonances of group 2, which are due to the product qP/K. The amplitudes and phases of the rotor lateral and torsional responses, as well as conditions of existence and stability, can be obtained for all resonances in Table 2 by application of the Averaging Method to Eqs. (6). In this paper only the main lateral resonance is analyzed since it is the most important.

It is assumed that the system does not have any internal resonances (lateral and torsional natural frequencies are linearly independent). In order to consider the proximity to the main lateral resonance $m = 1$ ($\Omega = \nu$) the following variables are introduced:

$$\xi = m - 1 = O(\epsilon) - \text{detuning}$$

$$\Delta = \psi - \Omega t - \text{resonance slow variable} \qquad (7)$$

The averaging of Eqs. (6) under the resonance conditions (7) yields the torsional amplitude zero-th stationary solution. This means that the lateral resonance leads to torsional activity with amplitude of the second order of smallness, unless the other resonance relation between lateral and torsional natural frequencies is satisfied. The system (6), after averaging, allows for the following stationary solution for the lateral variables:

$$G = H = \frac{r}{2\sqrt{\zeta^2 + \xi^2 + \frac{q^2}{4}(\zeta\sin[2(\Delta + \gamma_0)] + \xi\cos[2(\Delta + \gamma_0)])}}$$

Table 2 The list of possible lateral and torsional resonances

Resonance frequency relations	Names of the resonances	Terms responsible for the resonance are proportional to:
$m = 1\ (\Omega = \nu)$	Main lateral resonance	r, qP/K
$m = \frac{1}{2}\left(\Omega = \frac{\nu}{2}\right)$	Fractional lateral resonance	qP/K
$m = kn\ (\Omega = k\nu_t)$, $m = \left(k - \frac{1}{2}\right)n\ \left(\Omega = \left(k - \frac{1}{2}\right)\nu_t\right)$, $(k = 1,2,3\ldots)$	Torsional resonances	q, qP/K, $q(p/K)^2$
$m = kn - 1\ (\Omega = k\nu_t - \nu)$, $m = 1 \pm kn\ (\Omega = \nu \pm k\nu_t)$, $(k = 1,2,3\ldots)$	Integer combination resonances	r, q, qp/K
$m = \left(k - \frac{1}{2}\right)n \pm 1$, $\left(\Omega = \left(k - \frac{1}{2}\right)\nu_t \pm \nu\right)$, $m = 1 - \left(k - \frac{1}{2}\right)n$, $\left(\Omega = \nu - \left(k - \frac{1}{2}\right)\nu_t\right)$ $(k = 1,2,3,\ldots)$	Fractional combination resonances (group 1)	q, qp/K
$m = \frac{1}{2} \pm kn\ \left(\Omega = \frac{\nu}{2} \pm k\nu_t\right)$, $m = kn - \frac{1}{2}\ \left(\Omega = k\nu_t - \frac{\nu}{2}\right)$, $m = \frac{1}{2} \pm \left(k - \frac{1}{2}\right)n$, $\left(\Omega = \frac{\nu}{2} \pm \left(k - \frac{1}{2}\right)\nu_t\right)$	Fractional combination resonances (group 2)	qp/K
$m = \left(k - \frac{1}{2}\right)n - \frac{1}{2}$, $\left(\Omega = \left(k - \frac{1}{2}\right)\nu_t - \frac{\nu}{2}\right)$, $(k = 1,2,3\ldots)$		

Downloaded 02 Jun 2010 to 171.66.16.105. Redistribution subject to ASME license or copyright; see http://www.asme.org/terms/Terms_Use.cfm

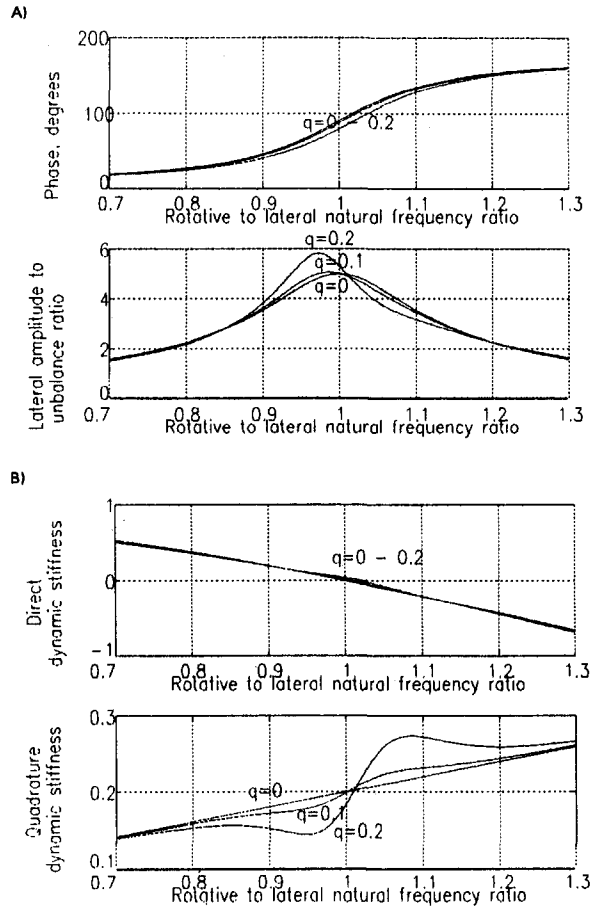


Fig. 8 (*A*) Bode plot of the rotor 1× lateral response, and (*B*) nondimensional direct and quadrature synchronous dynamic stiffnesses, in the range of rotative speeds close to the rotor lateral natural frequency

$$\Delta = \arctan \frac{\left(\xi + \frac{q}{2}\right) \tan \delta + \zeta}{\xi - \frac{q}{2} - \zeta \tan \delta} - \gamma_0, \quad \phi = 0 \qquad (8)$$

In this main lateral resonance region, the rotor lateral response can be presented in the complex vector form:

$$X + jY_1 = H[\cos(\Omega t + \Delta) + j \sin(\Omega t + \Delta)] = He^{j(\Omega t + \Delta)} \qquad (9)$$

The amplitude and phase of this vector, calculated using Eqs. (8) for damping factor $\zeta = D/(2\sqrt{MK}) = 0.1$ and several values of the stiffness asymmetry factor q, are presented in Fig. 8. Equation (9) makes it possible to calculate the system synchronous dynamic stiffness DS, as the ratio of the input force to rotor response:

$$DS = \frac{re^{j(\Omega t - \gamma_0 + \delta)}}{He^{j(\Omega t + \Delta)}} = \frac{r}{H} e^{j(\Delta - \gamma_0 + \delta)} \qquad (10)$$

where the expressions for H, Δ are given by Eqs. (8). It is obvious that the synchronous dynamic stiffness depends on the angle δ between the unbalance and the shaft weak stiffness direction. Bode plots of the rotor 1× lateral response for the case $\delta = 0$ are shown in Fig. 8(a). Note that the change of the stiffness asymmetry factor q from 0 to 0.2 has a very small effect on the phase lag, but the amplitude behavior changes noticeably. The same cases are presented in Fig. 8(b) in the format of direct (DDS) and quadrature (QDS) dynamic stiffnesses. As it follows from Fig. 8(b), the stiffness asymmetry influences mostly the quadrature dynamic stiffness in the region close to the main lateral resonance. Since the synchronous dynamic stiffness is the reciprocal of the influence vector used in the balancing, the information about its behavior is often available, and can be used for diagnostics of rotating machine health, and early detection of rotor cracks.

5 Closing Remarks

A simple rotor system with possible crack-related shaft anisotropy was considered in this paper. The lateral and torsional degrees of freedom interact with each other due to the rotor unbalance, radial sideload, and rotating asymmetry. In the absence of any torsional excitation from the driving and load torques, the rotor torsional vibrations show noticeable 1× and 2× resonances. The main source of the torsional excitation was determined to be a torsional snapping action due to the radial sideload. The snapping action is a periodic (twice per rotation) elastic energy storage occurring when the shaft strong axis passes through the radial sideload direction, followed by its release when the rotor weak stiffness axis passes through the radial sideload direction. The dramatic change of the torsional response due to the shaft anisotropy emphasizes one more time the importance of torsional vibration monitoring of machine rotors for early detection of shaft cracks.

The torsional response timebase waveform observation in the range around 2× torsional resonance (Fig. 4) allows for a good estimation of the crack angular orientation. The torsional response also reflects 1× and 2× lateral resonances. The combination resonances were numerically simulated. The lateral response of the system was not noticeably affected by the torsional vibration and consisted primarily of 1× and 2× components. The Averaging Method application to the equations provided identification of several combinational resonances in the system (Table 2). It also permitted calculation of the synchronous dynamic stiffness components in the proximity of the 1× lateral resonance. The shape of the quadrature component of the synchronous dynamic stiffness is most sensitive to the shaft stiffness asymmetry, and can be used for the shaft crack detection.

References

Bently, D. E., and Muszynska, A., 1986, "Detection of Rotor Cracks," *Proc. 15th Turbomachinery Symposium,* Corpus Christi, TX, Nov., pp. 129–139.

Bogolubov, N. N., and Mitropolsky, U. A., 1978, "Asymptotic Methods in Theory of Nonlinear Oscillations," Nauka, Moscow [in Russian].

Chen, W. H., and Wang, H. L., 1986, "Finite Element Analysis of Axisymmetric Cracked Solid Subjected to Torsional Loadings," *Eng. Frac. Mech.,* Vol. 23, No. 4, pp. 705–717.

Christides, S., and Barr, A. D. S., 1986, "Torsional Vibration of Cracked Beams of Non-circular Cross-Section," *Int. J. Mech. Sci.,* Vol. 28, No. 7, pp. 473–490.

Cohen, R., and Porat, I., 1985, "Coupled Torsional and Transverse Vibration of Unbalanced Rotor," ASME *Journal of Applied Mechanics,* Vol. 52, pp. 701–705.

Dimarogonas, A. D., and Massouros, G., 1981, "Torsional Vibration of a Shaft With Circumferential Crack," *Eng. Frac. Mech.,* Vol. 15, No. 3–4, pp. 439–444.

Dimarogonas, A. D., and Papadopoulos, C. A., 1983, "Vibration of Cracked Shafts in Bending," *J. Sound Vib.,* Vol. 91, pp. 583–593.

Dimentberg, F. M., 1945, "Flexural Vibration of Rotating Shafts" [in Russian]; English translation, Butterworths, London, 1961.

Dirr, B. O., and Schmalhorst, B. K., 1987, "Crack Depth Analysis of a Rotating Shaft by Vibration Measurement," *11th ASME Conf. Vib. Noise,* ASME DE-Vol. 2, pp. 607–614.

Gasch, R., 1976, "Dynamic Behavior of a Simple Rotor With a Cross-Sectional Crack," *Vibrations in Rotating Machinery,* Inst. of Mech. Eng., London, pp. 123–128.

Goldman, P., and Muszynska, A., 1994, "Resonances in the System of the Interacted Sources of Vibration," *International Journal of Nonlinear Mechanics,* Vol. 29, No. 1.

Grabowski, B., 1980, "The Vibrational Behavior of a Turbine Rotor Containing a Transverse Crack," ASME *Journal of Mechanical Design,* Vol. 102.

Henry, T. A., and Okah-Avae, B. E., 1976, "Vibrations in Cracked Shafts," *Vibrations in Rotating Machinery,* Inst. of Mech. Eng., London, pp. 15–19.

Inagaki, Y., Kanoki, H., and Shiraki, K., 1981, "Transverse Vibrations of a General Cracked Rotor Bearing System," ASME Paper No. 81-DET-45.

Downloaded 02 Jun 2010 to 171.66.16.105. Redistribution subject to ASME license or copyright; see http://www.asme.org/terms/Terms_Use.cfm

Mayes, I. W., and Davies, W. G. R., 1976, "The Vibrational Behavior of a Rotating Shaft System Containing a Transverse Crack," IMechE Paper No. C178/76.

Muszynska, A., 1982, "Shaft Crack Detection," presented at the Seventh Machinery Dynamics Seminar, Canada.

Muszynska, A., Goldman, P., and Bently, D. E., 1992, "Torsional/Lateral Cross-Coupled Responses Due to Shaft Anisotropy: A New Tool in Shaft Crack Detection," IMechE, C 432-090, Bath, United Kingdom.

Nelson, H. D., and Nataraj, C., 1986, "The Dynamics of a Rotor System With a Cracked Shaft," ASME *Journal of Vibration, Acoustics, Stress and Reliability in Design,* Vol. 108, pp. 189–196.

Papadopoulos, C. A., and Dimarogonas, A. P., 1989, "Coupled Vibration of Cracked Shafts," *Rotating Machinery Dynamics,* ASME DE-Vol. 18-2, pp. 7–12.

Qian, G., Gu, S., and Jiang, J., 1991, "Finite Element Model of Cracked Plates Application to Vibration Problem," *Comput. Str.,* Vol. 39, No. 5.

Downloaded 02 Jun 2010 to 171.66.16.105. Redistribution subject to ASME license or copyright; see http://www.asme.org/terms/Terms_Use.cfm

M. Berthillier

M. Dhainaut

F. Burgaud

V. Garnier

Snecma,
Moissy Cramayel, France

A Numerical Method for the Prediction of Bladed Disk Forced Response

A numerical method has been developed to predict the forced response of bladed disks due to a wake excitation from upstream blade rows. The structure is modeled by a three-dimensional finite element mesh of a bladed disk segment. Using cyclic symmetry, this model provides a modal base for the rotating structure. The aerodynamic damping of the vibratory modes and the excitation pressures on the blades due to the propagation of upstream flow defects are computed separately using the same three-dimensional unsteady Euler analysis software. A modal response solution of the aeromechanical system is then performed. This analytical methodology has been used to study the forced response of an experimental high pressure compressor blisk. The results are analyzed and compared with actual rig tests.

Introduction

It is well known that high-frequency fatigue is a major cause of failure in axial compressor components. It occurs when vibration takes place at or near resonant conditions of operation. In the design process, Campbell diagrams are used to predict the occurrence of the resonant conditions in the operating range of the compressor. Unfortunately, it is not always possible to avoid resonant conditions in some stages. Therefore, based on prior experiences, an estimation of the response and the dynamic stress is usually made to determine the acceptability of a blade design. This approach may lead to erroneous conclusions and it becomes necessary for the designer to have a tool that can predict more accurately the forced response and the dynamic stress of the components.

A large experimental effort is devoted to the subject of blade forced response. Although these experiments are very useful to assess and explain the effects of parameters such as steady blade loading, shape, and amplitude of aerodynamic forcing functions, reduced frequency (see, for example, Fleeter, 1992), they cannot provide quantitative answers in real life cases. This is why (apart from issues of design cycle time and cost) accurate predictions of blade forced response in the jet engine industrial environment can only be achieved through the use of numerical methods.

A substantial part of the numerical analyses of bladed disk forced response reported in the literature concentrate on the structural point of view. Irretier and Omprakash (1991) studied the effects of transient phenomena in the forced response but with a very simple excitation. Wildheim (1979) found all the resonant conditions for a rotating periodic structure excited by upstream flow defects. On the aerodynamic side, many methods (i.e., flow model and numerical algorithm), of varying degrees of complexity, have been proposed to compute the motion dependent and gust response aerodynamic forces. These have been recently reviewed by Verdon (1993).

A complete definition of the resonant vibratory response of the engine bladed disks includes a coupled characterization of the structural dynamics, of the aeromechanical damping and of the external excitation. An early application of a 2.5-dimensional unsteady Euler code to perform a parametric study of a stator blade row forced response was given by Joubert and Ronchetti (1989). More recently, rather precise aeromechanical studies have been conducted by Chiang and Kielb (1993) and Murthy and Stefko (1992), with simple two-dimensional aerodynamic computations. Such an approach has been used by Tatakis and Stockton (1993) to study the influence of airfoil geometric and aerodynamic parameters on forced response.

This paper presents a full three-dimensional numerical approach of the dynamic response of bladed disks. As the dominant source of excitation can be attributed to the presence of a nonuniform inlet flow, we will restrict our study to a wake excitation that can be created by a variety of sources including support struts and stator blade rows. Aerodynamic damping is computed via an Euler three-dimensional code. In addition, an equivalent viscous modal damping can be taken into account. The structure is supposed to be perfectly tuned and cyclic symmetry can be used to determine the dynamic behavior of the structure starting from a finite element model of one sector of the bladed disk. An application of this procedure has been made for an experimental high pressure compressor blisk. The computations have been fitted to actual rig tests.

Theory

Dynamic Equations of Motion. The general aeroelastic response of a bladed disk is given by the following equations:

$$[M]\{q''(t)\} + [C]\{q'(t)\} + [K]\{q(t)\} = \{f^g(t)\} + \{f^m(t)\} \quad (1)$$

where the vectors $\{q(t)\}$ and $\{f^g(t)\}$ are the displacements and forces for all the sectors of the stage. If the upstream flow defects responsible for the excitation have a cyclic symmetry of order N_w (e.g., wakes from N_w identical and equally spaced struts), the exciting forces $\{f^g(t)\}$ may be expressed as a Fourier series of N_h harmonics, all multiples of N_w. Thus, for blade j:

$$\{f_j^g(t)\} = \sum_v \mathrm{Re}[\{f_v^g\}e^{i(v\Omega t(2\pi/N)v(j-1)}] \quad (2)$$

where $v = N_w p$ with $p = 1, N_h$. In the following, the notation $\mathrm{Re}(-)$ will be omitted.

As we suppose that all the sectors of the bladed disk are identical, we can take advantage of the traveling wave representation of the displacement (see Crawley, 1988). This can be written as:

$$\{q(t)\} = [E]\{q_\beta(t)\} \quad (3)$$

Contributed by the International Gas Turbine Institute and presented at the 39th International Gas Turbine and Aeroengine Congress and Exposition, The Hague, The Netherlands, June 13–16, 1994. Manuscript received by the International Gas Turbine Institute February 25, 1994 Paper No. 94-GT-293. Associate Technical Editor: E. M. Greitzer.

Copyright © 1997 by ASME

Downloaded 02 Jun 2010 to 171.66.16.105. Redistribution subject to ASME license or copyright; see http://www.asme.org/terms/Terms_Use.cfm

where $[E]$ is the expanded Fourier matrix with:

$$[E] = \begin{bmatrix} [E_{II}] & \cdots & [E_{IN}] \\ [E_{NI}] & \cdots & [E_{NN}] \end{bmatrix} \quad \text{and}$$

$$[E_{kl}] = \text{diag}\,(e^{i(2\pi/N)(j-1)(k-1)})$$

Substituting Eq. (3) into Eq. (1) and premultiplying by $[E]^{-1}$ with $[E]^{-1} = 1/N[E]^*$ where $[E]^*$ is the complex conjugate of $[E]$:

$$[E]^{-1}[M][E]\{q''_\beta(t)\} + [E]^{-1}[C][E]\{q'_\beta(t)\} + [E]^{-1}[K][E]\{q_\beta(t)\} = [E]^{-1}\{f^g(t)\} + [E]^{-1}\{f^m(t)\} \quad (4)$$

As $[M]$, $[K]$, $[C]$ are block circulant matrices, the matrices of Eq. (4) are block diagonal (see Davis, 1979).
For example,

$$[E]^{-1}[M][E] = \text{diag}\,[M_{\beta_l}]$$

and,

$$\{q_\beta\} = \{\ldots, \{q_{\beta_l}\}, \ldots\} \quad l = -D/2, \ldots, +D/2$$

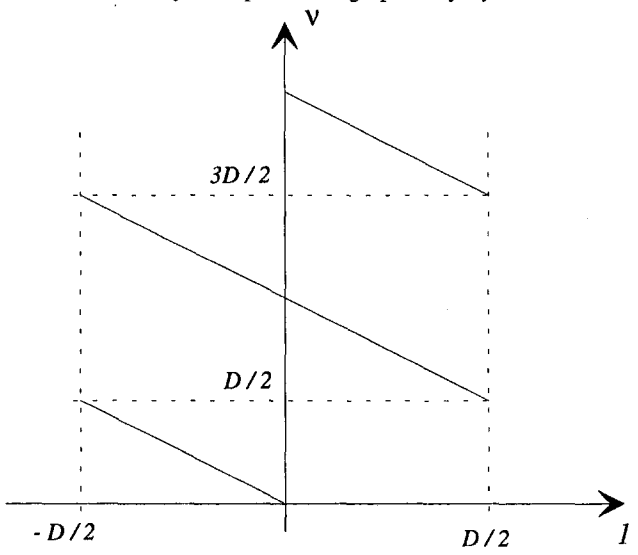
$$D = N \text{ if } N \text{ even}$$

$$D = N - 1 \text{ if } N \text{ odd}$$

The development of the right-hand term $[E]^{-1}\{f^g(t)\}$ shows that a single interblade phase angle β_l contained between $[-\pi, \pi]$ is excited by the harmonic v and is given by:

$$\beta_l = \frac{2\pi l}{N} \quad \text{with} \quad l = -v[N] \quad l \in \left[-\frac{D}{2}, +\frac{D}{2}\right] \quad (5)$$

This relation may be represented graphically by:



The system of Eqs. (4) can then be reduced to N_h separated systems of equations of smaller size, each one corresponding to an interblade phase angle β_l:

$$[M_{\beta_l}]\{q''_{\beta_l}(t)\} + [C_{\beta_l}]\{q'_{\beta_l}(t)\} + [K_{\beta_l}]\{q_{\beta_l}(t)\} = \{f^g_v\}e^{iv\Omega t} + \{f^m_{\beta_l}(t)\} \quad (6)$$

Of course if any dissymmetry was present in the structure, or if friction forces between the blades were added, some coupling between the different interblade phase angles would have to be taken into account.

We may wish to reduce the size of the different systems more, by projecting into a modal base, obtained from the undamped homogeneous form of (6). The displacement $\{q_{\beta_l}(t)\}$ can be expressed as:

$$\{q_{\beta_l}(t)\} = [Q_{\beta_l}]\{X_{\beta_l}\}e^{iv\Omega t} \quad (7)$$

where $[Q_{\beta_l}]$ is the mode shape matrix and $\{X_{\beta_l}\}$ the modal

Nomenclature

$[C]$ = structural damping matrix
$[C_{\beta_l}]$ = structural damping matrix for β_l
$[c_{\beta_l}]$ = modal damping matrix for β_l
$[A_{\beta_l}]$ = aeroelastic matrix for β_l
$[a_{\beta_l}]$ = modal aeroelastic matrix for β_l
$[K]$ = total stiffness matrix for rotation speed Ω
$[K_{\beta_l}]$ = total stiffness matrix for rotation speed Ω and β_l
$[k_{\beta_l}]$ = modal stiffness matrix for rotation speed Ω and β_l
$[K_E]_{\beta_l}$ = classical stiffness matrix for $\Omega = 0$ and β_l
$[K_G(\sigma)]_{\beta_l}$ = geometric stiffness matrix for β_l
$[K_S]_{\beta_l}$ = supplementary centrifugal stiffness matrix for β_l
$[M]$ = structural mass matrix
$[M_{\beta_l}]$ = structural mass matrix for β_l
$[m_{\beta_l}]$ = modal mass matrix for β_l
$[E]$ = expanded Fourier matrix
$[E]^*$ = complex conjugate of $[E]$
$[Q_{\beta_l}]$ = mode shape matrix for β_l
$\{f^g(t)\}$ = gust response unsteady aerodynamic forces
$\{f^g_j(t)\}$ = gust response unsteady aerodynamic forces for blade number j
$\{f^g_v\}$ = Fourier component of $\{f^g(t)\}$ for harmonic v
$\{f^m(t)\}$ = motion-dependent unsteady aerodynamic forces
$\{f^m_{\beta_l}(t)\}$ = traveling wave representation of $\{f^m(t)\}$ for β_l
$\{f_c(\Omega^2)\}$ = centrifugal forces at speed of rotation Ω
$\{f_{AS}\}$ = steady aerodynamic forces
$\{q(t)\}$ = physical displacements
$\{q_j(t)\}$ = physical displacements for sector number j
$\{q_\beta(t)\}$ = traveling wave representation of the displacements
$\{q_{\beta_l}(t)\}$ = traveling wave displacements for β_l
$\{X_{\beta_l}\}$ = modal coordinates for β_l
$\{q^j_{\beta_l}\}$ = mode shape j for β_l
N = number of blades
N_w = number of wakes
N_h = number of harmonics
β_l = interblade phase angle = $2\pi l/N$
Ω = rotation speed in rad/s
ω = eigenfrequency of the structure
σ = steady stress distribution
e_{vj} = excitability measure
m_j = modal mass for mode j
ξ = critical damping ratio

Downloaded 02 Jun 2010 to 171.66.16.105. Redistribution subject to ASME license or copyright; see http://www.asme.org/terms/Terms_Use.cfm

coordinates. Assuming linearity, we can express the motion-dependent forces as:

$$\{f^m_{\beta_l}(t)\} = [A_{\beta_l}]\{X_{\beta_l}\}e^{iv\Omega t} \quad (8)$$

Substituting Eqs. (7) and (8) into Eq. (6) and premultiplying by the transpose conjugate of $[Q_{\beta_l}]$ results in the modal equations:

$$(-(v\Omega)^2[m_{\beta_l}] + iv\Omega[c_{\beta_l}] + [k_{\beta_l}])\{X_{\beta_l}\} = [Q_{\beta_l}]^*\{f^g_v\} + [a_{\beta_l}]\{X_{\beta_l}\} \quad (9)$$

where $[m_{\beta_l}]$ and $[k_{\beta_l}]$ are the diagonal modal matrices of the structure for the selected eigenmodes.

$[c_{\beta_l}]$ is the structural modal damping matrix
$[a_{\beta_l}]$ is the modal aeroelastic matrix.

The resolution of Eq. (9) gives the amplitude of the different modes for the interblade phase angle β_l. The total response of the structure is obtained by adding the different contributions for the different interblade phase angles excited. The stresses are obtained on any point of the structure using the modal stresses distributions.

Mechanical Model. A finite element mesh is made for one blade and one sector of the disk. In order to reduce the time spent on that task, an automatic generation of mesh is possible. A static analysis can be performed for β_0 with the following general equation:

$$([K_E] + [K_G(\sigma)] + [K_S])_{\beta_0}\{q_{\beta_0}(t)\} = \{f_c(\Omega^2)\} + \{f_{AS}\}$$

where $[K_E]$, $[K_G(\sigma)]$, and $[K_S]$ are respectively the classical, geometric, and supplementary centrifugal stiffness matrices (for a more complete description, see Ferraris et al., 1983).

The stress distribution σ is initially unknown; thus an iterative procedure is used to perform the static solution. Once σ is known, the stiffness matrix $[K_{\beta_l}]$ of the structure for the rotation speed Ω and for any β_l can be constructed. For all the interblade phase angles excited by the gust-induced forces, the following dynamic system of equations can be solved:

$$(-\omega^2[M_{\beta_l}] + [K_{\beta_l}])\{q_{\beta_l}\} = \{0\}$$

Thus the mode shapes $\{q_{\beta_l}\}$ and all the terms of the matrices $[Q_{\beta_l}]^*$ and $[k_{\beta_l}]$ can be determined.

Unsteady Aerodynamic Model. This model provides an estimate of the flow forces acting on the blades. The first step is to determine the compressor operating points corresponding to the frequency crossings of interest. For each of these cases, we then have to perform a steady computation to initialize the flowfield, followed by two unsteady computations, one to determine the motion-dependent unsteady aerodynamic forces $\{f^m(t)\}$, the other to determine the gust response unsteady aerodynamic forces $\{f^g(t)\}$. All three computations are done using the same three-dimensional unsteady Euler code (Gerolymos, 1993a, b). This solver numerically integrates the three-dimensional unsteady Euler equations discretized in finite volume formulation, using Runge–Kutta schemes. A single interblade channel is considered for the computations, making use of the chorochronic periodicity of the flow field perturbed by harmonic disturbances imposed at the boundaries (i.e., blade motion and upstream vorticity). Convergence of the unsteady computation toward time and space periodicity is estimated using residuals on the first harmonic of pressure at the pitchwise boundaries. A periodicity residual of 1 percent is considered satisfactory.

To compute the motion-dependent forces $\{f^m(t)\}$, we use mode shapes determined by the mechanical model, interpolated from the structural mesh on to the aerodynamic mesh around the blade. From this is derived a distribution of movement for the aerodynamic mesh, which conforms with the blade vibration. The unsteady Euler equations are integrated in time on the moving grid, with a fixed time lag (corresponding to the interblade phase angle of the vibratory mode) imposed at the permeable pitchwise boundaries. Time integration usually covers a span of 10 vibration periods, which is sufficient to establish spatial and time periodicity, as assessed by the periodicity residuals. As the vibration amplitude is small with respect to the blade chord, only the first harmonic of the unsteady pressures on the blades are of interest. Those computations are used to build the matrix $[A_{\beta_l}]$ for each interblade phase angle β_l and thus to obtain the modal aeroelastic matrix after multiplication by $[Q_{\beta_l}]^*$.

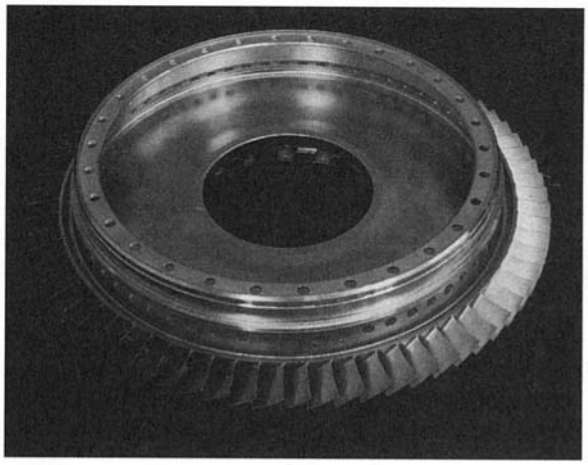


Fig. 1 Blisk geometry

To determine the gust response forces $\{f^g(t)\}$, we need an estimate of the flow defects present at the upstream boundary of the domain. In the case of wakes being shed by upstream blade rows, this is usually obtained through correlations giving a spatial total pressure distribution (depth and width) as a function of the upstream blade row loss coefficient, solidity, and distance from its trailing edge. This total pressure distribution is then Fourier transformed in the tangential direction, at each radial station of the computational grid. Usually, only the spatial harmonic corresponding to the excitation being studied is used to specify the upstream boundary condition of the computation, since in the case of small perturbation amplitude, it is the main driver of the gust response harmonic of interest. It is useful to recognize this fact, because numerically resolving the (unneeded) higher spatial harmonics present in the original wake shape would require a much finer grid than necessary, resulting in a direct computing cost penalty. In the application considered in this paper, however, the grid used could perfectly resolve all the harmonics necessary to reconstruct the original signal, so they were all kept. The Euler equations are integrated in time until convergence to periodicity is reached, which usually requires around 10 periods of wake passing. The unsteady pressures on the blades are then Fourier transformed and the first five harmonics are interpolated from the aerodynamic mesh onto the structural mesh, thus providing the gust response unsteady aerodynamic force for the forced response mechanical computation.

Application

Description of Experiment. The goal of this test series was to compare the resonant response of a blisk rotor, composed of 72 blades, shown in Fig. 1, with that found for rotors of conventional technology. Only the results obtained on the blisk

Downloaded 02 Jun 2010 to 171.66.16.105. Redistribution subject to ASME license or copyright; see http://www.asme.org/terms/Terms_Use.cfm

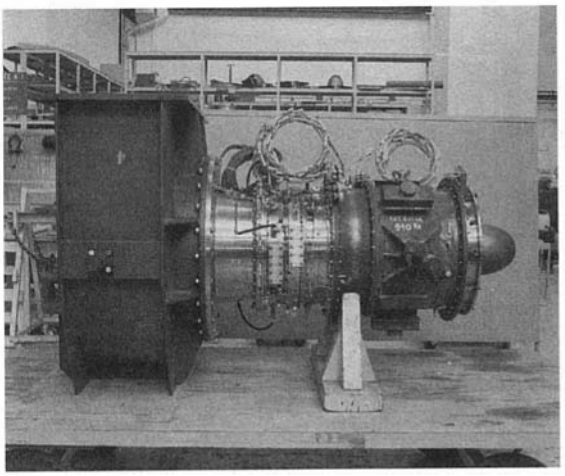


Fig. 2 Test rig

rotor will be presented here and the experimental values of blade damping and stress compared with the numerical prediction.

The compressor used (Fig. 2) is composed of three blade rows (IGVs, rotor, and stator), and is representative of the rear stages in civil HP compressors. A section of the compressor is represented on Fig. 3. The aerodynamic forcing function is provided by the wakes of cylinders inserted vertically in the flowpath and equally spaced around the circumference. The number of cylinders is variable and can be adjusted in order to excite the blisk in a resonant condition, for the first bending and first torsion modes, with several engine harmonics. Also, three different cylinder diameters were tried. Since existing correlations for wake shedding are tailored for blade profiles and are not valid for cylinders, the flow defect due to the cylinder wake was measured immediately upstream of the rotor at four heights in the annulus: 20, 40, 60, and 80 percent. The experimental data were fitted with analytical functions for Fourier transformation, subsequent discretization, and reintroduction at the upstream flow boundary. An example of a data fit is given in Fig. 4. Note that the fit was performed at the nominal operating point and with one cylinder in the annulus, and expressed as a percentage of total pressure loss. The same fit was then used for all other flow conditions and number of cylinders. For evaluation of blade forced response, strain gages were placed on seven blades; all results given subsequently (unless otherwise stated) are an average of the results of the individual blades. The Campbell diagram of the blisk is given in Fig. 5. In the following, we will concentrate on the resonant conditions $1T/22\Omega$.

The experiment itself was comparatively standard. The compressor map was first measured and is given in Fig. 6. When looking for resonant conditions, the compressor was revved without changing the throttle setting, which defines an operating line. This line and the operating point corresponding to the $1T/22\Omega$ crossing are also shown on Fig. 6. Gage data were recorded continuously, then analyzed off-line to yield blade response and damping.

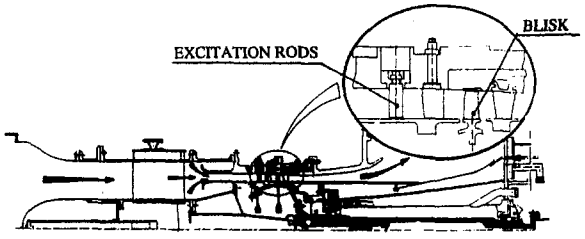


Fig. 3 Section of the test rig

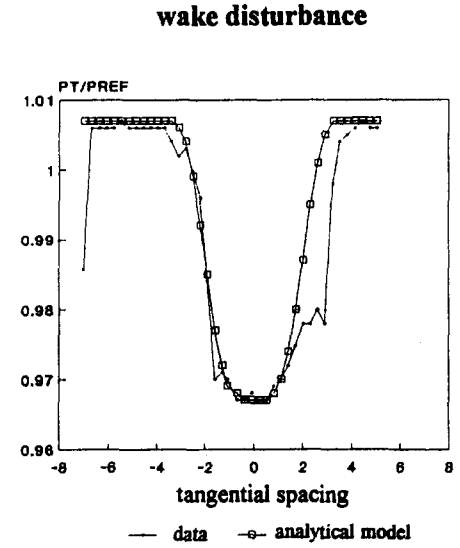


Fig. 4 Comparison of the wake modeling and data

Mechanical Model. A finite element mesh of the blisk has been performed for one sector (Fig. 7) to predict stage frequencies and blade motions using cyclic symmetry. The mesh density on the blade has been adapted for stress predictions. The interblade phase angles being taken into account in the computations are given by Eq. (5). If we consider the resonance $1T/22\Omega$, we have to study separately the Fourier order $l = -22$, $+28$, $+6$ respectively for the first three harmonics of the excitation force.

As we can see on the Campbell diagram, there is no mode excited by the frequencies 44Ω and 66Ω for the rotation speed Ω chosen here. Thus we will only consider in this case the first harmonic of the excitation force associated with the Fourier order $l = -22$. For this Fourier order, the eigenvalues and

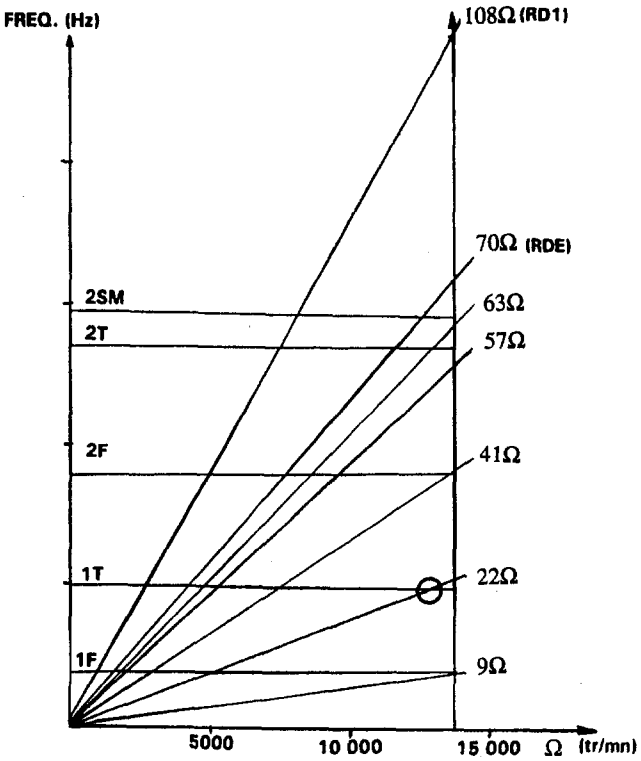


Fig. 5 Campbell diagram

Downloaded 02 Jun 2010 to 171.66.16.105. Redistribution subject to ASME license or copyright; see http://www.asme.org/terms/Terms_Use.cfm

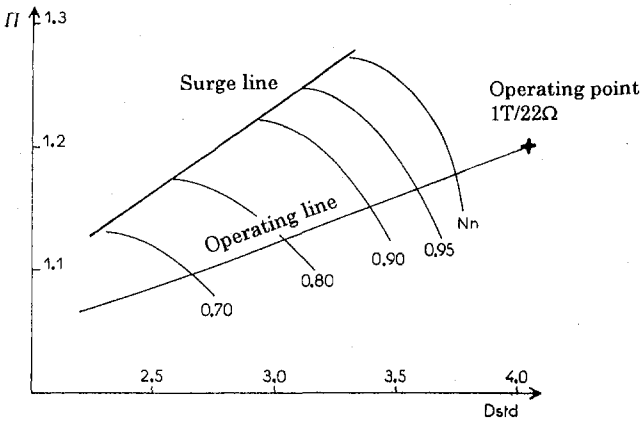


Fig. 6 Compressor map

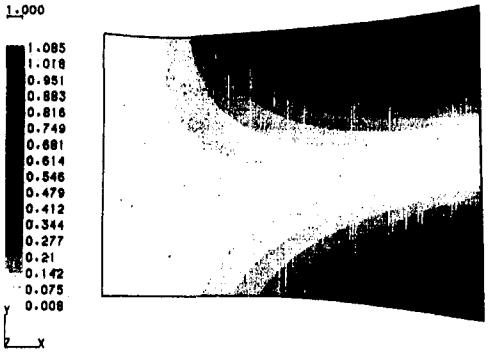


Fig. 8 Mode shape on the blade for the 1*T* mode

eigenmodes analysis show very little coupling between blade and disk motion for the first three modes. The mode shape of the mode 1*T* is represented on Fig. 8.

For the first three modes, a good correlation on the frequencies has been obtained. As the relative gap on the frequencies between the 1*T*/1*B* and 1*T*/2*B* modes is respectively 247 and 177 percent, we can neglect in the computations the dynamic coupling between the 1*T* mode and its neighboring modes. Although the program calculates general problems, the system (9) to be solved is reduced here to a single degree of freedom equation for the 1*T* mode.

Aerodynamic Model. As mentioned earlier, the unsteady three-dimensional Euler code uses H-type meshes. For this application, a mesh size of 120 (axial) × 21 (radial) × 25 (tangential) was used in order to adequately resolve the unsteady aerodynamic phenomena present in the flowfield, especially close to the leading edge. Figure 9 gives the mesh section at 90 percent blade height.

A steady computation was performed at the operating point corresponding to the crossing of interest. Since the Euler computation cannot reproduce exactly the compressor map, it was preferred to reproduce mass flow and rotational speed (for accurate upstream relative velocity) and allow a slight descrepancy on the pressure ratio.

The steady computation was used to initialize two unsteady computations: one to determine the aerodynamic damping on the modes excited by the wakes, the other to determine the gust response unsteady aerodynamic forces due to the wakes of 22 upstream cylinders. Of course, a certain amount of mistuning between blades was observed in the experiment, but the computations were performed at only one vibration frequency/rotational speed since the effect of varying this parameter over such a small range was deemed to be second order. The frequency used for the first torsion mode was 5082 Hz, which corresponds to a reduced frequency of 1.1, based on blade tip chord. The corresponding rotational speed was 13,900 rpm, for interaction of the 1*T* mode with the 22 upstream wakes.

15 periods of the unsteady phenomenon were simulated, both for flutter and gust response. Unsteady convergence was adequate after 10 periods but it was preferred to push on for another 5 periods to check that convergence was continuing to improve. CPU time for each of these computations was roughly two hours on a CRAY YMP computer. An implicit residual smoothing technique added to the four-step Runge–Kutta scheme allowed the use of large CFL numbers and thus reduced the number of iterations per period.

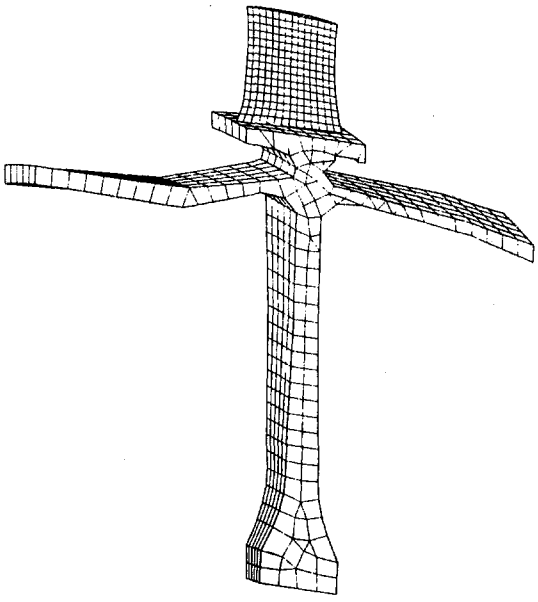


Fig. 7 Finite element mesh of a blisk sector

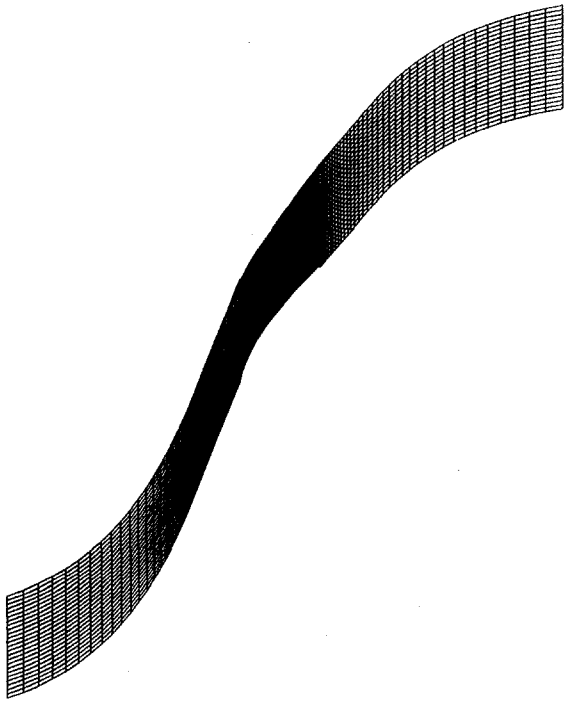


Fig. 9 Aerodynamic mesh at 90 percent span

Downloaded 02 Jun 2010 to 171.66.16.105. Redistribution subject to ASME license or copyright; see http://www.asme.org/terms/Terms_Use.cfm

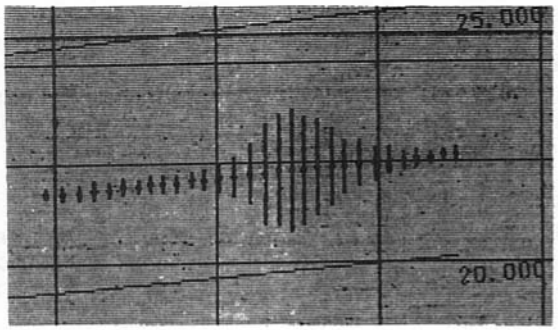


Fig. 10 Experimental Campbell analysis for the 1T/22Ω crossing

Results and Comparison. As the structure studied here is a blisk, there is no energy dissipation at the root of the blades. The only sources of damping are the internal friction in the material and the aerodynamic damping due to the aerodynamic motion dependent forces. As the former is very small for conventional steel materials, it will be neglected in the following study. We can thus compare the computed aerodynamic damping for the $1T/22\Omega$ resonant condition with the total damping measured at that point during the test and assumed here to be only aerodynamic.

The aerodynamic damping is computed by solving the eigenvalue problem associated with the homogeneous form of Eq. (9). The critical damping ratio is $\xi_{\text{zero}} = 0.54$ percent. An estimate of the experimental damping is given by the frequency bandwidth method applied to the frequency response of a strain gage obtained from the experimental Campbell analysis shown in Fig. 10. The critical damping ratio obtained is $\xi_{\text{exp}} = 0.36$ percent. The agreement between calculations and experiments, although not excellent, can be considered as satisfactory if we consider the lack of precision associated with the method we used to determine the experimental damping.

The excitation forces can be analyzed using several characteristic numbers. The first one is the force magnitude: $\|f_v^s\| = \sqrt{\{\overline{f_v^s}\}^T\{f_v^s\}}$. Here at the crossing point $1T/22\Omega$, $\|f_v^s\| = 0.011$ daN. The second one is the excitability measure for harmonic v and mode j defined as $e_{vj} = (|\{\overline{q_{\beta_l}^j}\}^T\{f_v^s\}|^2/(\{\overline{q_{\beta_l}^j}\}^T\{q_{\beta_l}^j\})(\{f_v^s\}^T\{f_v^s\}))$, where $\{q_{\beta_l}^j\}$ is the mode shape j for the phase angle β_l. e_{vj} is a real number between 0 and 1, and is independent of the mode shape normalization. It is a measure of the compatibility of the force distribution with the mode shape. For our case study, $e_{22T} = 0.004$; the excitation forces are mainly located on the lower part of the blade (see Figs. 11(*a*, *b*)).

If we want to compare the severity of different excitations for different modes, we can use the ratio $(|\{\overline{q_{\beta_l}^j}\}^T\{f_v^s\}|/m_j)$, where m_j is the modal mass for mode j.

The normalization of each mode shape is taken to induce a maximum stress equal to 1 on the blade.

After the separate analysis of aerodynamic damping and excitation forces, we performed the complete resolution of Eq. (9). The stresses obtained are compared to the measurements made with six different strain gages placed on different blades. The discrepancy between computations and measurements is of the order of the magnitude of the blade to blade variation. It is due to the mistuning, the lack of precision on the strain gage locations, and the incertainties of the measurements. An illustration is given on Fig. 12 for the strain gage location shown in Fig. 13. Only the extremum measured values are represented. The difference in frequency between the different peaks is mainly due to blade mistuning. For the computations, the frequency of the model has been updated on the mean of the experimental distribution. To draw the numerical curve, we reasonably extended, on a narrow frequency band, the unsteady aerodynamic

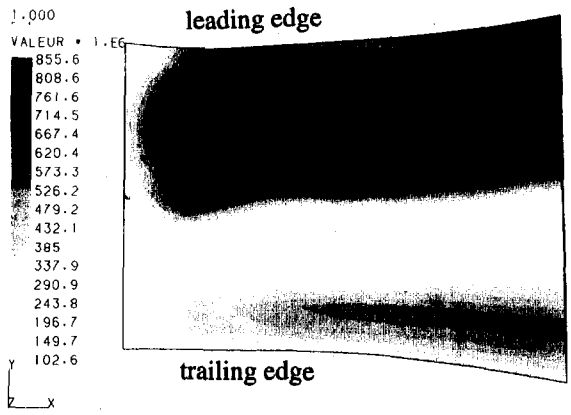


Fig. 11(*a*) Module of the excitation forces: suction surface

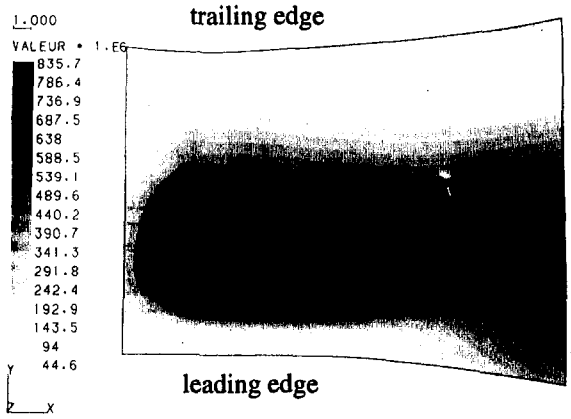


Fig. 11(*b*) Module of the excitation forces: pressure surface

pressures computed for the speed of rotation and blade frequency of the resonant condition $1T/22\Omega$. The difference between maximum and minimum experimental stresses is rather large (40 percent). As our model does not take into account the blade-to-blade mistuning, it is significant to consider the average experimental stress. The numerical result and the average experimental stress level were found to match perfectly. The good agreement between experiments and calculations on the dynamic response implies that the estimate of the gust re-

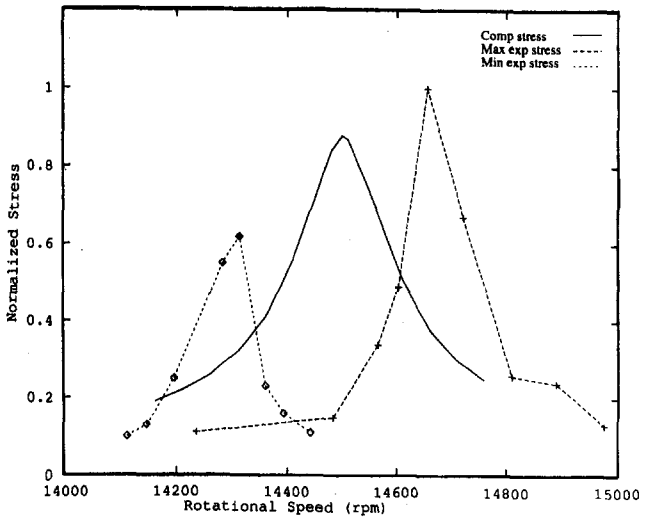


Fig. 12 Comparison between computational data stress and experimental data stress

Downloaded 02 Jun 2010 to 171.66.16.105. Redistribution subject to ASME license or copyright; see http://www.asme.org/terms/Terms_Use.cfm

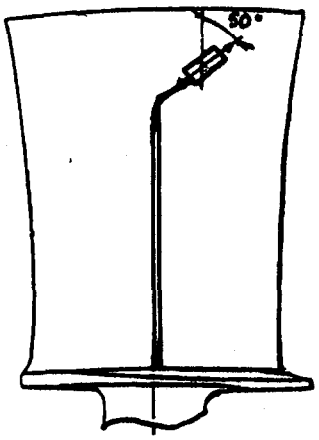


Fig. 13 Strain gage location

sponse unsteady forces is also of the right order of magnitude. Overall, the numerical method can be considered to give satisfactory agreement with the data for the case studied, at reasonable cost.

Conclusion

We have presented an aeromechanical method to predict the forced response of bladed disks to aerodynamic excitation from upstream wakes. The method is fully three dimensional, based on a finite element model of the bladed disk coupled with a time-marching nonlinear Euler solver. This degree of modeling is probably the most elaborate that can be used in an industrial environment (where reasonably fast and trouble free methods are essential) for the next couple of years. The current method has been thoroughly checked, and used in this study to predict the aerodynamic damping, gust excitation, and forced response of the $1T/22\Omega$ crossing of an HP compressor blisk. The predictions are borne out by experimental results on the configuration studied: Orders of magnitude are well predicted and are within blade-to-blade dispersion. It is therefore thought that this method is adequate for selecting or improving blade configurations with respect to aeromechanics. The method is currently being used to predict the blade response at other crossings of the configuration described here and of fans subjected to inlet or downstream distortion.

Acknowledgments

The authors would like to acknowledge the contribution of Marc Loubet for running a thorough experiment and providing high-quality data, which are essential for the correlation and validation of this analytical method.

References

Chiang, H. D., and Kielb, R. E., 1993, "An Analysis System for Blade Forced Response," ASME JOURNAL OF TURBOMACHINERY, Vol. 115, pp. 762–770.

Crawley, E. F., 1988, "Aeroelastic Formulation for Tuned and Mistuned Rotors," *AGARD Manual on Aeroelasticity in Axial-Flow Turbomachines, Vol. 2, Structural Dynamics and Aeroelasticity.*

Davis, P. J., 1979, *Circulant Matrices,* Wiley-Interscience.

Ferraris, G., Henry, R., Lalanne, M., and Trompette, P., 1983, "Frequencies and Mode Shapes of Rotating Bladed Axisymmetric Structures. Application to a Jet Engine," *Advanced Vibrations of Bladed Disc Assemblies,* ASME, 10 pp.

Fleeter, S., 1992, "Forced Response Unsteady Aerodynamic Experiments," AIAA Paper No. 92-0144.

Gerolymos, G. A., 1993a, "Advances in the Numerical Integration of the Three-Dimensional Euler Equations in Vibrating Cascades," ASME *Journal of Turbomachinery,* Vol. 115, pp. 781–790.

Gerolymos, G. A., 1993b, "Coupled Three-Dimensional Aeroelastic Stability Analysis of Bladed Disks," ASME *Journal of Turbomachinery,* Vol. 115, pp. 791–799.

Irretier, H., and Omprakash, V., 1991, "Numerical Analysis of the Transient Responses of Bladed Disks," *Machinery Dynamics and Element Vibrations,* ASME DE-Vol 36.

Joubert, H., and Ronchetti, V., 1989, "Aerodynamic Study of Forced Vibrations on Stator Rows of Axial Compressors," AGARD CP 468; *Unsteady Aerodynamic Phenomena in Turbomachines,* Aug.

Murthy, D. V., and Stefko, G. L., 1992, "FREPS: A Forced Response Prediction System for Turbomachinery Blade Rows," AIAA Paper No. 92-3072.

Tatakis, S., and Stockton, R., 1993, "Structural and Aerodynamic Influences to Airfoil Forced Response," ASME Paper No. 93-GT-243.

Verdon, J. M., 1993, "Review of Unsteady Aerodynamic Methods for Turbomachinery Aeroelastic and Aeroacoustic Applications," *AIAA Journal,* Vol. 31, No. 2, pp. 235–250.

Wildheim, S. J., 1979, "Excitation of Rotationally Periodic Structures," ASME *Journal of Applied Mechanics,* Vol 46, pp. 878–882.

Downloaded 02 Jun 2010 to 171.66.16.105. Redistribution subject to ASME license or copyright; see http://www.asme.org/terms/Terms_Use.cfm

Energy Analysis to the Design of Rotor-Bearing Systems

W. J. Chen
Centrifugal Compressor Division,
Ingersoll-Rand Company,
Mayfield, KY 42066

In the design of rotating machinery, it is often desirable and necessary to change a subset of system parameters to meet the design requirements. The success in designing rotor-bearing systems and in solving the vibration problems depends heavily upon the understanding of fundamental physical properties and insights of the systems. The modeling improvements and computational techniques have been extensively presented over the years. The design methodologies and fundamental properties have not been widely addressed to assist design engineers in solving their practical problems. The objective of this paper is to relate the various forms of energy and work and their contributions to the system dynamic characteristics. The design strategies and methodologies using the energy approach are also presented and illustrated in a turbine-driven machine.

Introduction

Over the last 20 years, there has been considerable research activity in the area of modeling and analysis of dynamic behavior of rotor-bearing-foundation systems. The dynamic characteristics of interest are critical speeds, system stability, and response to unbalance excitation. These dynamic characteristics are influenced by all the system parameters and some parameters may be more sensitive to certain dynamic behavior than others. In the design and retrofit process, it is frequently desirable and often necessary to adjust some system parameters in order to obtain a more favorable design or to meet the new operating requirements. In general, this procedure is carried out by experienced engineers with analytical tools (i.e., computer hardware and software) in an iterative process based on their experience and technical expertise. Taking advantage of rapid developments in the finite element methods and numerical optimization techniques, the design parameter changes now can be approached by systematic and automated procedures. The finite element method has been widely used in modeling and analyzing the complex rotor-bearing systems with minimal numerical problems. Recently, automated optimization techniques combined with the finite element formulation in the application of rotor bearing systems have been presented by Chen (1987) to achieve the various design goals. However, caution should always be exercised while using the "black box" as a design tool. Due to the complexity of the problems, the converged solution may not always be the global optimum. The success in designing rotor-bearing systems and in solving the vibration problems depends heavily upon the understanding of fundamental physical properties and insights of the systems.

Comprehensive coverage in computational techniques and modeling improvements has been presented in the analysis of rotor-bearing systems over the years. The design strategies and methodologies have not been well addressed to assist design engineers in solving their practical problems. The use of vibration energies in the design of rotor systems was first proposed by Simmons (1976) and the emphasis was mainly on the torsional natural frequencies using the Rayleigh quotient. The design philosophy of using energy distribution in lateral vibration was presented by Gunter and Gaston (1987) in the analysis of undamped critical speeds and was briefly discussed by Nelson and Crandall (1992). The physical insights into the rotor stability using the energy (work) calculation were presented by Adams and Padovan (1981) and then were utilized by Longxiang et al. (1993) in redesigning the bearings for a 200 MV turbine generator.

The dynamic behavior of an entire rotor-bearing-foundation system is described by the governing equations of motion, which are derived by the energy expressions. Therefore, the system dynamic characteristics are strongly influenced by the energy distribution. By knowing the energy distribution, one can predict the effects of parameter changes on the system behavior and identify the source of the vibration problem. This paper describes the various forms of energy and work and their contributions to the dynamics of the system. The design methodologies using energy and work are also presented. Using the energy approach, the definition of rigid and flexible rotors can be quantitatively identified. The computation of energy distribution can be easily incorporated into any existing rotor dynamics programs based on the finite element method. A 1500 KW turbine-driven pump is presented to illustrate the design methodology using the energy approach.

Rotor Motions

For small vibration, the motion of a discretized finite element station is usually described by two translational displacements (x, y) in the X and Y directions, respectively, and two rotational (angular) displacements (θ_x, θ_y) about the X and Y axes, respectively. The Z axis is the coordinate along the shaft centerline. The (X, Y, Z) axes describe a fixed global right-hand-ruled Cartesian coordinate system. In the rigorous definition, the rotational displacements depend upon the translational displacements and they cannot be treated as generalized coordinates in the Lagrange's equations. However, for small displacements, they lead to linearized equations of motion. For large displacements, the Eulerian angles are normally used that lead to nonlinear equations of motion for the spinning disk. The disadvantage of using Eulerian angles is that they cannot be directly expressed in the shaft element strain energy formulation without making an assumption of small displacements.

The rotor motion of most common interest is a harmonic motion with a whirl frequency of ω. At each finite element station, the rotor motion has the form:

$$x(t) = x_c \cos \omega t + x_s \sin \omega t \quad (1)$$

$$y(t) = y_c \cos \omega t + y_s \sin \omega t \quad (2)$$

Contributed by the International Gas Turbine Institute and presented at the 40th International Gas Turbine and Aeroengine Congress and Exhibition, Houston, Texas, June 5–8, 1995. Manuscript received by the International Gas Turbine Institute March 15, 1995. Paper No. 95-GT-314. Associate Technical Editor: C. J. Russo.

Copyright © 1997 by ASME

Downloaded 02 Jun 2010 to 171.66.16.105. Redistribution subject to ASME license or copyright; see http://www.asme.org/terms/Terms_Use.cfm

for translational displacements, and

$$\theta_x(t) = \theta_{xc} \cos \omega t + \theta_{xs} \sin \omega t \quad (3)$$

$$\theta_y(t) = \theta_{yc} \cos \omega t + \theta_{ys} \sin \omega t \quad (4)$$

for rotational displacements.

This simple expression can represent a steady-state synchronous unbalance response with whirl frequency ω equal to the rotor speed Ω or can be a precessional mode orbit with whirl frequency ω equal to the associated natural frequency of that mode. The whirl frequency is always a positive value, and the direction of whirling (forward or backward precession) is determined by the sign of $(x_c y_s - x_s y_c)$.

Each pair of displacements (x, y) or (θ_x, θ_y) describes an elliptical orbit with semi-major axis a and semi-minor axis b. Considering the translational orbit, the axes are:

$$a = \{\tfrac{1}{2}(x_c^2 + x_s^2 + y_c^2 + y_s^2) + \tfrac{1}{2}[(x_c^2 - x_s^2 + y_c^2 - y_s^2)^2 + 4(x_c x_s + y_c y_s)^2]^{1/2}\}^{1/2} \quad (5)$$

$$b = \frac{1}{a}\begin{vmatrix} x_c & x_s \\ y_c & y_s \end{vmatrix} = \frac{1}{a}(x_c y_s - x_s y_c) \quad (6)$$

Mathematically, a positive semi-minor axis indicates that the whirling orbit is a forward precession (progression) orbit and a negative semi-minor axis implies the motion is a backward precession (regression) orbit. In general, the rotor whirls either forward or backward. However, the rotor can also have mixed precession, i.e., the rotor can possess forward precession and backward precession simultaneously at different sections. Hence, the semi-minor axis should be evaluated at all the finite element stations to determine the direction of precession.

The elliptical orbit may also be decomposed into two circular orbits: One is a forward circular motion with an amplitude of $|\hat{u}_f|$, and the other is a backward circular motion with an amplitude of $|\hat{u}_b|$. Thus, the displacement radius vector can be expressed in the complex form:

$$\hat{r}(t) = x(t) + jy(t) = |\hat{u}_f| e^{j\phi_f} \cdot e^{j\omega t} + |\hat{u}_b| e^{j\phi_b} \cdot e^{-j\omega t} \quad (7)$$

When the forward amplitude is greater than the backward amplitude, the overall rotor motion is forward. When the backward amplitude is greater than the forward amplitude, the resulting motion is backward. The relationship between the semi-axes and the amplitudes of the circular motions are:

$$a = |\hat{u}_f| + |\hat{u}_b|, \quad \text{and} \quad b = |\hat{u}_f| - |\hat{u}_b| \quad (8)$$

These expressions are also applicable to the rotational displacements.

The motions of nonrotating components (flexible support, foundation) can be described by a total of six degrees of freedom including axial translation and rotation, although four degrees of freedom are commonly utilized.

Equations of Motion and Energy

The equations of motion that describe the dynamic behavior of the entire rotor system are obtained by assembling the equations of motion of the appropriate components. The governing equation of motion for a general rotor-bearing-foundation system is of the form:

$$\mathbf{M}\ddot{\mathbf{q}}(t) + (\mathbf{G} + \mathbf{C}^b)\dot{\mathbf{q}}(t) + (\mathbf{K} + \mathbf{K}^b)\mathbf{q}(t) = \mathbf{Q}(t) \quad (9)$$

where $\mathbf{q}$ and $\mathbf{Q}$ are the system displacement and force vectors, respectively. The mass/inertia matrix $\mathbf{M}$ is a positive definite real symmetric matrix contributed by the kinetic energy. The gyroscopic matrix $\mathbf{G}$ is a real skew-symmetric matrix, which is contributed by the part of the rotational kinetic energy caused by the gyroscopic moments. The structural stiffness matrix $\mathbf{K}$ is a real symmetric matrix contributed by the strain energy. The bearing coefficient matrices $\mathbf{C}^b$ and $\mathbf{K}^b$, in general, can be any real nonsymmetric matrices due to the fact that bearings are nonconservative in nature. Since the equations of motion are derived from the energy expressions, the system dynamic characteristics are strongly influenced by the energy distribution. A typical rotor system consists of discrete rigid disks, shaft elements with distributed mass and elasticity, general linear bearings, and flexible bearing supports. The various forms of energy for these components are presented below.

Rigid Disks. The kinetic energy of a spinning disk with translational and rotational motion may be expressed in a fixed coordinate system as the sum of the translational and rotational kinetic energies (Dimentberg, 1961):

$$T^d = \tfrac{1}{2} m_d(\dot{x}^2 + \dot{y}^2) + \tfrac{1}{2} I_d(\dot{\theta}_x^2 + \dot{\theta}_y^2) + \tfrac{1}{2}\Omega I_P(\dot{\theta}_x\theta_y - \theta_x\dot{\theta}_y) + \tfrac{1}{2}\Omega^2 I_P \quad (10)$$

The first two terms are homogeneous quadratic functions of the generalized velocities and are commonly presented in a natural system (Meirovitch, 1980). The first term is the translational kinetic energy contributed by the disk mass effect. The second term is a fraction of the rotational kinetic energy contributed by the rotatory inertia. The first two terms are always positive. The third term is linear in the generalized velocities and is referred to as the gyroscopic effect, which is contributed by the gyroscopic moments. The fourth term, caused by the pure spinning of the disk, does not depend upon the vibration coordinates and can be ignored in the vibrational analysis. Due to the gyroscopic effect, the kinetic energy given in Eq. (10) is known as nonnatural (Meirovitch, 1980) and the effect also makes the

Nomenclature

a, b = semi-major and semi-minor axes
$\mathbf{C}$ = damping matrix
EI = bending modulus
F = dissipation function
$\mathbf{G}$ = gyroscopic matrix
$\mathbf{g}$ = intermediate matrix
I_d, I_p = diametral and polar moment of inertia
$j = \sqrt{-1}$
$\mathbf{K}$ = stiffness matrix
$\mathbf{M}$ = mass/inertia matrix
m_d = mass
P = axial force
$\mathbf{Q}$ = force vector
$\mathbf{q}$ = displacement vector
$\hat{\mathbf{r}}$ = orbit radius vector
T = kinetic energy
$\mathbf{t}$ = time
$\hat{\mathbf{u}}$ = circular motion
V = potential energy
W_{cyc} = work done per cycle
(x, y, z) = translational displacements
κGA = effective shear modulus
θ = rotational displacement
ϕ = phase angle
Ψ = shape functions
Ω = rotor speed
ω = whirl frequency

Superscripts

b, d, e, s = bearing, disk, element, support

Subscripts

c, s = cosine and sine components
f, b = forward, backward
gyro = gyroscopic
T, R = translation, rotation

Downloaded 02 Jun 2010 to 171.66.16.105. Redistribution subject to ASME license or copyright; see http://www.asme.org/terms/Terms_Use.cfm

rotordynamics study unique from the general structural dynamics.

To gain insight into the gyroscopic effect, substituting the rotational displacements in Eqs. (3) and (4) and their derivatives into the rotational kinetic energy generated by the gyroscopic effect, we have

$$T_{\text{gyro}} = \tfrac{1}{2}\,\Omega I_P(\dot{\theta}_x\theta_y - \theta_x\dot{\theta}_y) = \tfrac{1}{2}\,\Omega I_P\omega(\theta_{xs}\theta_{yc} - \theta_{xc}\theta_{ys})$$

$$= \tfrac{1}{2}\,\Omega I_P\omega(-a\cdot b) = \tfrac{1}{2}\,\Omega I_P\omega(-|\hat{u}_f|^2 + |\hat{u}_b|^2) \qquad (11)$$

where a, b, and $|\hat{u}_f|$, $|\hat{u}_b|$ in Eq. (11) are parameters for the rotational displacement orbit. Since I_P, Ω, ω are all positive values, the sign of Eq. (11) is determined by the value inside the parenthesis. For the forward precessional mode ($b > 0$), the gyroscopic effect contributes negative kinetic energy (much like inertia decreased effect) and tends to raise the corresponding forward whirl frequency. For the backward precessional mode ($b < 0$), the gyroscopic effect contributes positive kinetic energy (much like inertia added effect) and tends to lower the corresponding backward whirl frequency. Thus, it is the forward vibrational modes getting the "gyroscopic stiffening" effect and the backward vibrational modes getting the "gyroscopic softening" effect. The gyroscopic effect is linearly proportional to the polar moment of inertia, spinning speed, whirl frequency, and area of rotational displacement whirl orbit. It can be significant in the study of high-speed overhung rotor system where a large wheel is mounted outside the bearing span and has large rotational displacement.

The coefficient matrices in the equations of motion can be obtained from the Lagrange equations or can be easily identified by expanding the energy expression in matrix form. The kinetic energy of a spinning disk excluding the spinning effect, $\frac{1}{2}\Omega^2 I_P$, can be conveniently written in matrix form:

$$T^d = \tfrac{1}{2}\dot{\mathbf{q}}^{d^T}(\mathbf{M}_T^d + \mathbf{M}_R^d)\dot{\mathbf{q}}^d + \mathbf{q}^{d^T}(\mathbf{g}^d)\dot{\mathbf{q}}^d \qquad (12)$$

where $\mathbf{q}^d(t) = (x, y, \theta_x, \theta_y)^T$ is the displacement vector of the finite element station at which the disk is located. The symmetric matrices $\mathbf{M}_T^d$ and $\mathbf{M}_R^d$ are the translational mass matrix and rotational inertia matrices, respectively. The only nonzero elements in these matrices are the (1, 1) and (2, 2) elements with a value of $\mathbf{m}_d$ and I_d in $\mathbf{M}_T^d$ and $\mathbf{M}_R^d$, respectively. The gyroscopic matrix $\mathbf{G}^d$ is a skew-symmetric matrix derived from the intermediate skew-symmetric matrix $\mathbf{g}^d$:

$$\mathbf{G}^d = (\mathbf{g}^d)^T - \mathbf{g}^d = -2\mathbf{g}^d = \Omega I_P\begin{bmatrix} 0 & 0 & 0 & 0 \\ 0 & 0 & 0 & 0 \\ 0 & 0 & 0 & 1 \\ 0 & 0 & -1 & 0 \end{bmatrix} \qquad (13)$$

The rigid disks possess only kinetic energy, not potential energy.

Shaft Elements. The kinetic energy of a finite element segment is obtained by integrating the differential energy for an infinitesimal rotor element over the length of the element:

$$T^e = \frac{1}{2}\left\{\int_0^l \tilde{m}(\dot{x}^2 + \dot{y}^2) + \tilde{I}_d(\dot{\theta}_x^2 + \dot{\theta}_y^2) + \Omega\tilde{I}_p(\dot{\theta}_x\theta_y - \theta_x\dot{\theta}_y)ds\right\} + \frac{1}{2}\,\Omega^2\int_0^l \tilde{I}_p ds \qquad (14)$$

Since the internal displacements $(x, y, \theta_x, \theta_y)$ are functions of spatial coordinate (s) and time (t), the finite element method is utilized to separate the variables. The internal displacements of a typical element can be approximately expressed by the following relationship:

$$\begin{Bmatrix} x(s,t) \\ y(s,t) \\ \theta_x(s,t) \\ \theta_y(s,t) \end{Bmatrix}_{4\times 1} = \begin{bmatrix} \Psi_T(s) \\ \Psi_R(s) \end{bmatrix}_{4\times 8}\mathbf{q}^e(t)_{8\times 1} \qquad (15)$$

The displacement vector $\mathbf{q}^e(t) = (q_1, q_2, q_3, \ldots, q_7, q_8)^T$ is the time-dependent end-point displacements (two translations and two rotations) of the finite rotor element. The shape function matrix, Ψ, is established by utilizing the Timoshenko Beam Theory, which includes the transverse shear deformation effect. The individual shape functions represent the static displacement modes associated with a uniform Timoshenko beam with a unit displacement of one of the end-point coordinates and the rest of the coordinates constrained to zero. The derivation of the shape function is well documented (Nelson, 1977) and will not be repeated here.

Substituting Eq. (15) into the element kinetic energy expression and neglecting the last term (spinning energy), which does not depend upon the displacements, we have:

$$T^e = \tfrac{1}{2}\dot{\mathbf{q}}^{e^T}(\mathbf{M}_T^e + \mathbf{M}_R^e)\dot{\mathbf{q}}^{e^T} + \mathbf{q}^{e^T}(\mathbf{g}^e)\dot{\mathbf{q}}^e \qquad (16)$$

where

$$\mathbf{M}_T^e = \int_0^l \tilde{m}\Psi_T^T\Psi_T ds$$

is the translational mass matrix,

$$\mathbf{M}_R^e = \int_0^l \tilde{I}_d\Psi_R^T\Psi_R ds$$

is the rotational inertia matrix, and

$$\mathbf{g}^e = \int_0^l \frac{1}{2}\,\Omega\tilde{I}_p\Psi_R^T\begin{bmatrix} 0 & -1 \\ 1 & 0 \end{bmatrix}\Psi_R ds$$

is the intermediate skew-symmetric matrix. The element gyroscopic matrix is:

$$\mathbf{G}^e = (\mathbf{g}^e)^T - \mathbf{g}^e = -2\mathbf{g}^e = \int_0^l \Omega\tilde{I}_p\Psi_R^T\begin{bmatrix} 0 & 1 \\ -1 & 0 \end{bmatrix}\Psi_R ds \qquad (17)$$

The potential (strain) energy of the rotating shaft element consists of elastic bending energy due to the bending moments, shear energy due to the shear forces, and work due to the constant axial load. The translational displacements of a typical point internal to the element consists of the deformations due to bending moment and shear force. However, the rotational displacements are only related to the bending deformation. An element under shear force alone will only possess distorsion but no rotation. The potential energy of a rotating shaft element under a constant axial load is:

$$V^e = \frac{1}{2}\int_0^l EI\left[\left(\frac{\partial\theta_x}{\partial z}\right)^2 + \left(\frac{\partial\theta_y}{\partial z}\right)^2\right]ds + \frac{1}{2}\int_0^l \kappa GA\left[\left(\frac{\partial x}{\partial z} - \theta_y\right)^2 + \left(\frac{\partial y}{\partial z} + \theta_x\right)^2\right]ds + \frac{1}{2}\int_0^l P\left[\left(\frac{\partial x}{\partial z}\right)^2 + \left(\frac{\partial y}{\partial z}\right)^2\right]ds \qquad (18)$$

where EI is the bending modulus, κGA is the effective shear modulus, and P is the axial load. The shape factor κ depends on the shape of the cross section and the Poisson ratio. Substitut-

Downloaded 02 Jun 2010 to 171.66.16.105. Redistribution subject to ASME license or copyright; see http://www.asme.org/terms/Terms_Use.cfm

ing the shape functions relationship, the potential energy can be conveniently written in matrix form:

$$V^e = \tfrac{1}{2}\mathbf{q}^{e^T}[\mathbf{K}_b + \mathbf{K}_s + \mathbf{K}_a]\mathbf{q}^e \tag{19}$$

where

$$\mathbf{K}_b = \int_0^l EI(\Psi_R')^T(\Psi_R')ds$$

is the bending stiffness matrix,

$$\mathbf{K}_s = \int_0^l \kappa GA\left(\Psi_T' + \begin{bmatrix} 0 & -1 \\ 1 & 0 \end{bmatrix}\Psi_R\right)^T\left(\Psi_T' + \begin{bmatrix} 0 & -1 \\ 1 & 0 \end{bmatrix}\Psi_R\right)ds$$

is the shear stiffness matrix, and

$$\mathbf{K}_a = \int_0^l P(\Psi_T')^T(\Psi_T')ds$$

is the geometric stiffness matrix due to axial load.

The shaft element stiffness matrices given above are all symmetric. The shear deformation effect can be important when analyzing a short stubby rotor system. Since the effect of shear deformation is included in the "shape functions" of the elements, therefore, it is taken into account not only in the potential energy calculation but also in the kinetic energy calculation. The total effect of the shear deformation is to lower the natural frequencies. The geometric stiffness matrix is positive when the element is under tensile load and negative when the element is under compressive force.

Flexible Supports. For the flexible bearing support, the kinetic energy and potential energy are of the forms:

$$T^s = \tfrac{1}{2}\dot{\mathbf{q}}^{s^T}\mathbf{M}^s\dot{\mathbf{q}}^s \tag{20}$$

and

$$V^s = \tfrac{1}{2}\mathbf{q}^{s^T}\mathbf{K}^s\mathbf{q}^s \tag{21}$$

where $\mathbf{q}^s$ is the displacement vector of the support and the mass and stiffness matrices are symmetric.

Linear Bearings. The linear bearings are generally modeled by eight bearing dynamic damping and stiffness coefficients. The associated dissipation function and potential energy are assumed to be derived from the following quadratic expressions:

$$F^b = \tfrac{1}{2}\dot{\mathbf{q}}^{b^T}\mathbf{C}^b\dot{\mathbf{q}}^b \tag{22}$$

and

$$V^b = \tfrac{1}{2}\mathbf{q}^{b^T}\mathbf{K}^b\mathbf{q}^b \tag{23}$$

where $\mathbf{q}^b$ is the displacement vector associated with the bearing coordinates. For fluid film bearings, the forces are nonconservative and the damping and stiffness matrices are nonsymmetric. The damping provides stabilizing forces to attenuate the resonant response and to overcome the disturbance. However, the cross-coupling stiffness can introduce a major destabilizing effect on the rotor system. The work done on the system (negative energy removed from the system) by a bearing per cycle of a harmonic motion is:

$$W_{\text{cyc}} = -\pi\omega[C_{xx}(x_c^2 + x_s^2) + C_{yy}(y_c^2 + y_s^2) + (C_{xy} + C_{yx})(x_c y_c + x_s y_s)] + \pi(K_{xy} - K_{yx})(a \cdot b) \tag{24}$$

With the positive $(K_{xy} - K_{yx})$, the cross-coupling stiffness can actually add energy to the system for a forward precessional motion $(b > 0)$ and destabilize the rotor system in the linear sense. Another interesting finding is that the cross-coupling damping coefficients can also either remove energy from the system or add energy to the system. This work done by the bearing can provide rich information in the determination of bearing sensitivity to the system stability.

Seal forces, aerodynamic forces, and other interaction forces acting on the rotors can be modeled as pseudo bearings.

Design Methodology

The objectives in the design of rotor systems include the placement of critical speeds, minimization of unbalance response, and maximization of the system stability. Since the system dynamic behavior is governed by the equations of motion and the system matrices are constructed by the various energies, the system dynamic characteristics depend upon the energy distribution. The analytical calculation of critical speeds, damped eigenvalues, and forced response from the equation of motion, Eq. (9), is documented by Nelson and Crandall (1992) and will not be repeated here. However, the general design methodology and criteria using energies are described below. It should be noted that the energy is also closely related to the mode shape and the amplitude of a vibration mode is a normalized eigenvector, thus the energy distribution is calculated as a percentage of the total energy of that particular mode.

Critical Speeds. The most primary consideration in the design of rotating machinery is the placement of forward synchronous critical speeds with respect to the operating speed of the machine. The other dynamic behavior (e.g., unbalance response and system stability) are all somewhat related to the position of the critical speeds. When the critical speeds are within the operating speed range, the rotor may experience large synchronous vibration. When the first critical speed is too low (e.g., lower than or around 50 percent of the design speed), the rotor may be susceptible to instability and experience high subsynchronous vibration. When the rotor is operated far below the first critical speed, it can be sensitive to the operating environment. Since damping has little effect on the position of the critical speeds, the undamped system has been widely used to predict critical speeds. Damping effects are considered in the unbalance response and system stability analyses.

Whenever possible, it is desirable to have at least 15 percent (10 percent is required in most standards) separation margin between the operating speed and the critical speeds to ensure safe and smooth operation. When the critical speeds are within the undesirable range, some parameters need to be adjusted to shift the critical speeds outside this operating range. Bearing stiffnesses, mass properties of the disks, and shaft elements of the rotating assemblies are usually the variables that can be changed to achieve this requirement. Bearing locations have a great influence in positioning the critical speeds; however, they cannot be easily changed in an existing design without major modification in the layout and general arrangement.

If the bearing stiffnesses are the only variables that can be changed, then one should look to those bearings with high potential energy density. If a particular bearing has very small potential energy density (e.g., less than 5 percent) of a particular mode, then minor modification in this bearing has little effect on that mode. In fact, increasing the bearing stiffness will have an adverse effect due to the reduction in the modal damping.

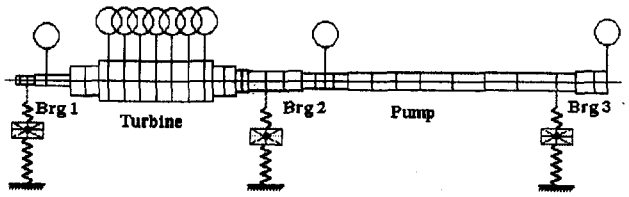


Fig. 1 System configuration

Downloaded 02 Jun 2010 to 171.66.16.105. Redistribution subject to ASME license or copyright; see http://www.asme.org/terms/Terms_Use.cfm

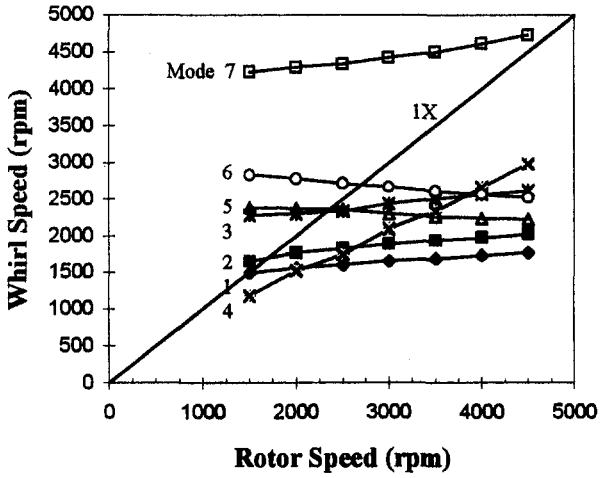


Fig. 2 Whirl speed map

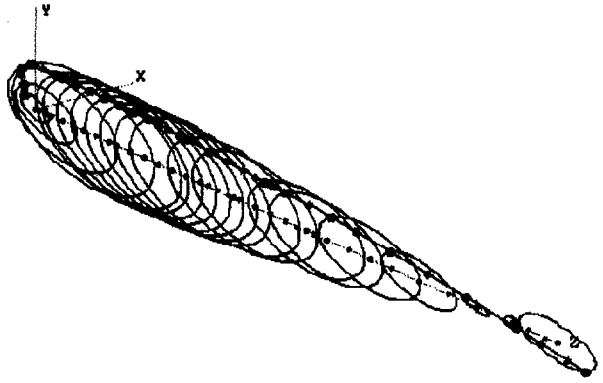


Fig. 4 First forward mode shape

An increase or decrease in diameter of the shaft elements with large potential energy density can be used effectively to raise or lower the critical speed. Decreasing or increasing the mass of a disk with high translational kinetic energy density can also significantly increase or decrease the critical speed. Caution must be taken to ensure that the center of gravity of the disk will not be moved while changing the mass properties of the disk. Also, decreasing or increasing the polar moment of inertia of a disk, which has high rotational kinetic energy density, can decrease or increase the critical speed due to the gyroscopic effects. If the kinetic and potential energies of a vibration mode are significant in the flexible bearing supports, changing the support structure can be very effective in shifting that associated frequency. For the support modes, the noncontact displacement probes measuring the shaft vibration may not be enough for a safe monitoring system and an accelerometer or velocity pickup on the bearing housing may be required.

The potential energy distribution among the rotor assembly, bearings, and flexible supports can also provide information for design purposes. If the rotor assembly (shaft elements) possesses more than 70 percent of the total potential energy of a vibration mode, then this vibration mode is characterized as a flexible rotor mode. If the rotor assembly (shaft elements) possesses less than 30 percent of the total potential energy of a vibration mode, then this vibration mode is characterized as a rigid rotor mode. Typically, the first two lowest frequency modes are the rigid rotor modes and other high-frequency modes are flexible rotor modes. In some cases, the rigid rotor modes could be overdamped or could not be excited by the synchronous excitation; thus they will not be observed in the response data. For rotors operated above the rigid bearing criticals (e.g., most high-speed compressors), it is desirable to design the bearings such that the potential energy of the critical speed can be evenly distributed among the rotor and bearings. If the critical speed falls into the rigid rotor section, the system will be more susceptible to instability (e.g., oil whirl or whip) and the vibration could be large enough in the bearing station to damage the bearing. If the critical speed falls into the flexible rotor section, the vibrations may be very large at some critical stations due to the lack of damping.

The damped critical speeds are usually determined from the whirl speed map, which is a plot of damped natural frequencies (whirl speeds) versus the rotor speed. The damped critical speeds due to the synchronous unbalance excitation are the intersections of the synchronous excitation line and the frequency curves. In the presence of gyroscopic effect and the general linearized bearing model, the frequency curves may be overlapping and complicated. The associated precessional mode shapes must be used to identify the modes and properly construct the map.

Unbalance Response and Balancing. The rotors always have some amount of residual unbalance no matter how well they are balanced. Very often some correction weights are needed to minimize the response at certain locations. Unbalance located at large modal displacements will produce a large modal unbalance force for that mode. Usually, the unbalance weights may only be placed or removed at certain disks. Therefore, one should look to the disks with large kinetic energy density to make corrections. A caution must be made since corrections for one particular mode may be quite different from that of another mode. The influence coefficient method combined with energy

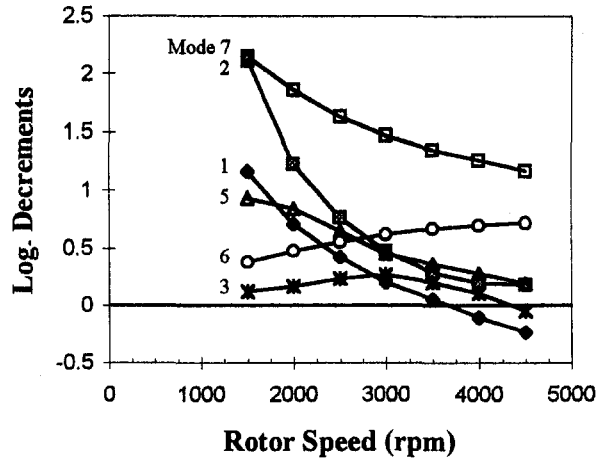


Fig. 3 Stability map

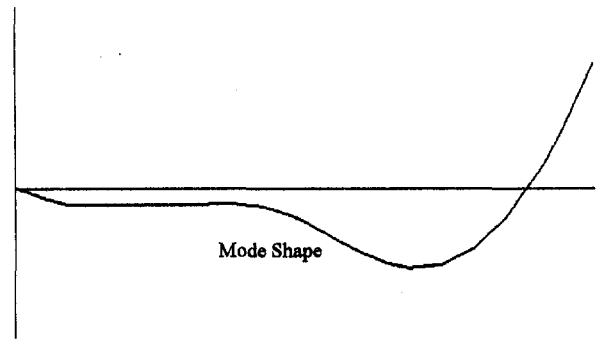


Fig. 5 The third critical speed

Downloaded 02 Jun 2010 to 171.66.16.105. Redistribution subject to ASME license or copyright; see http://www.asme.org/terms/Terms_Use.cfm

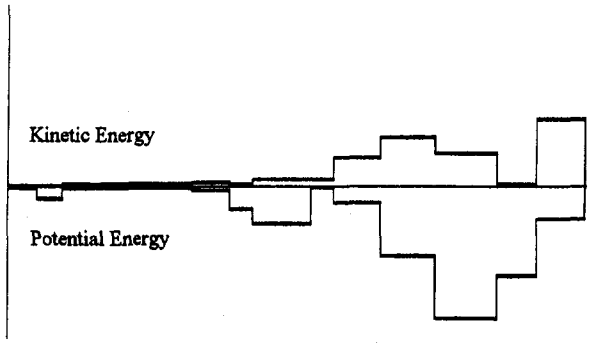


Fig. 6 Shaft energy distribution

distribution information can be very effective in balancing, which may eliminate unnecessary trial runs.

System Stability. The system stability is usually determined by the value of logarithmic decrement. The instability threshold is determined from the stability map, which is a plot of logarithmic decrements versus the rotor speed. When the logarithmic decrement is positive, the system is said to be stable. When the logarithmic decrement becomes negative, the system is said to be unstable in the linear theory. When the logarithmic decrement is zero, the system is in the state of instability threshold. Assuming that only the bearings (real or pseudo) remove/add energy from/to the system, the total energy removed/added by the bearings can also be used to determine the system stability. When the total work done on the system by the bearings is negative (i.e., energy has been removed by the bearings), the system is stable. When the total work done on the system by the bearings is positive, the system is unstable. At the threshold of instability, the total work done equals zero. By knowing the work distribution, one can not only determine the system stability but also determine the sensitivity and contribution of each bearing to the system stability. The latter information is extremely useful to the engineers in the design and retrofit process and this information does not exist by knowing the logarithmic decrement alone.

The system stability is strongly influenced by the bearings with large work done. The bearings with negative work contribute stabilizing effects and the bearings with positive work contribute destabilizing effects. If required, one should always try to maximize the energy removed by the bearings to increase the system stability. It should be noted that the bearing contribution at different vibration modes can be quite different. One question that should always be raised before any bearing modification is "what vibration mode do we want to stabilize"? Once the question is answered, work done by the bearings on the specified vibration mode is then calculated and tabulated. Bearings with large work done should be redesigned first. In this economic and efficiency-conscious age, designing bearings to maximize stability and also minimize frictional power loss can be a difficult task.

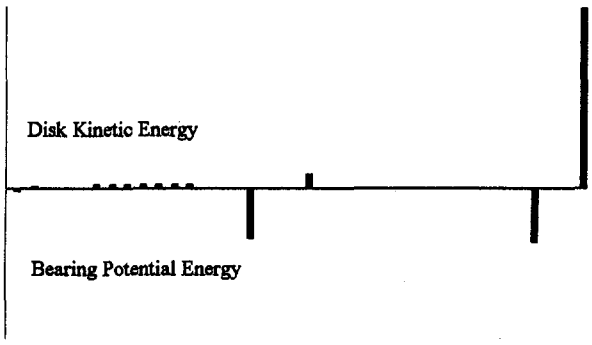


Fig. 7 Bearing and disk energies

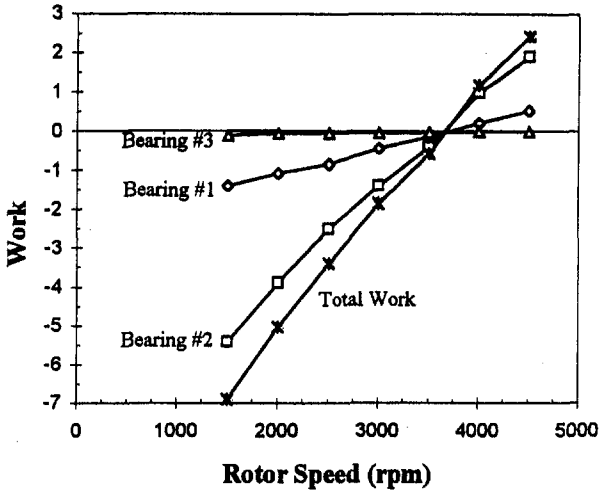


Fig. 8 Bearing work distribution

Example

A turbine-driven pump is employed as an example. The complete rotor assembly is supported by three two-axial groove bearings as shown in Fig. 1. On the left side of bearing #2 is a turbine and on the right side is a pump. The design speed is 3500 rpm. However, the actual operating speed can fluctuate from 3000 to 4000 rpm under various operating conditions.

The whirl speed map is plotted in Fig. 2. The first seven damped natural frequencies, which are below 5000 rpm, are plotted. The modes are numbered according to the values of their associated frequencies at a rotor speed of 3500 rpm. The logarithmic decrements of these modes are plotted in Fig. 3. The logarithmic decrement of the fourth mode is very high (above 10); therefore, it is not shown in Fig. 3. The first mode is a forward mode with most of the motion occurring at the turbine, as shown in Fig. 4. Shaft elements around bearing #1 possess most of the shaft potential energy and bearing #2 possesses most of the bearing potential energy. This mode becomes unstable when the rotor speed is above 3675 rpm as shown in Fig. 3. The second mode is a forward mode with most of the motion occurring at the pump side. The first two modes are

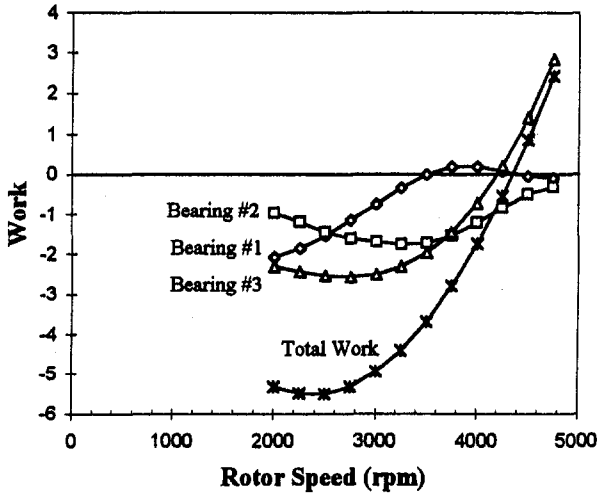


Fig. 9 Bearing work distribution (new design)

Downloaded 02 Jun 2010 to 171.66.16.105. Redistribution subject to ASME license or copyright; see http://www.asme.org/terms/Terms_Use.cfm

excited by the synchronous excitation around 1500 and 1600 rpm. Since the logarithmic decrements at these critical speeds are relatively high (above 0.5), smooth operation through these critical speeds is anticipated. The third and fifth modes are also forward modes. These two modes are excited by the synchronous excitation around 2400 rpm and some vibration is anticipated due to the relatively low logarithmic decrement (below 0.25) in the third mode. The third and fifth critical speed modes have very similar mode shapes with one associated with the $X-Z$ plane and the other associated with the $Y-Z$ plane. The undamped planar mode shape is plotted in Fig. 5. The total kinetic energy is distributed between the disks (64 percent) and shaft elements (36 percent). The supports have less than 1 percent of the total kinetic energy. The total potential energy is distributed between the bearings (32 percent) and shaft elements (68 percent). Again, the supports have an insignificant effect in the potential energy. Clearly, the mode is not sensitive to the supports. The shaft energy distributions are plotted in Fig. 6 with the kinetic energy in the upper half and potential energy in the lower half. Figure 6 shows that the shaft elements of the pump are more sensitive to this mode than those of the turbine since the pump possesses most of the kinetic and potential energies. The energy distributions for disks and bearings are plotted in Fig. 7. It shows that bearings #2 and #3 have a strong influence on this critical speed and that bearing #1 has almost no influence on this mode. Figure 7 also shows that disk #10 (impeller of the pump) has a significant effect on this mode due to its 55 percent contribution to the total kinetic energy. Changing the mass properties of disk #10 can be very effective in shifting this critical speed. The fourth mode is a bearing mode. All the motion occurs near bearing #1 and the logarithmic decrement is very high (above 10). The sixth mode is a backward precessional mode, which is not likely to be excited by the unbalance. There is a safe separation margin between the critical speeds and the operating speed in this application.

The instability (negative logarithmic decrement) occurring around 3675 rpm poses a possible problem since the rotor speed can go up to 4000 rpm. To understand the bearing contribution to the system stability, the work done by the bearings to the unstable mode is plotted in Fig. 8. It shows that the total work done is negative when the rotor speed is below 3675 rpm and becomes positive when the rotor speed is above this instability threshold. Figure 8 also shows that bearing #2 has a significant contribution to the instability and bearing #3 has little influence on the instability. To correct the instability problem, a five-pad tilting pad bearing is recommended to replace the two-axial groove bearing in bearing #2. The onset of instability threshold with this modification is raised to 4375 rpm, which is outside the operating speed range. Again, the work done by the bearings is plotted in Fig. 9. The total work done by the bearings is negative when the rotor speed is below 4375 rpm and becomes positive when the rotor speed is above 4375 rpm.

Conclusion

The calculation methods on various forms of energy and work have been presented. The energy computation can be easily incorporated into any existing rotor dynamics programs based on the finite element method. The contribution of energy and work to the dynamics of rotor systems has been described. The dynamic characteristics of rotor-bearing-foundation systems are strongly influenced by the energy distribution. Knowing the energy distribution, one can predict the effects of parameter changes on the system behavior and identify the source of the vibration problem. The design methodologies using energy and work have been presented. A 1500 kW turbine-driven pump has been analyzed to illustrate the design methodology.

References

Adams, M. L., and Padovan, J., 1981, "Insights Into Linearized Rotor Dynamics," *Journal of Sound and Vibration*, Vol. 76, pp. 129–142.

Chen, W. J., 1987, "Optimal Design and Parameter Identification of Flexible Rotor-Bearing Systems," Ph.D. Dissertation, Arizona State University, Tempe, AZ.

Dimentberg, F. M., 1961, *Flexural Vibrations of Rotating Shafts*, Butterworth, London.

Gunter, E. J., and Gaston, C. G., 1987, "CRITSPD-PC User's Manual: A Program for Undamped Critical Speed Analysis of Flexible Rotor-Bearing Systems," RODYN Vibration, Inc., Charlottesville, VA.

Longxiang, X., Jun. Z., and Lie, Y., 1993, "Contribution Factor of Bearings for Rotor-Bearing System stability," ASME *Journal of Vibration and Acoustics*, Vol. 115, pp. 81–84.

Meirovitch, L., 1980, *Computational Methods in Structural Dynamics*, Sijthoff & Noordhoff International Publishers B. V., Alphen aan den Rijn, The Netherlands.

Nelson, H. D., 1977, "A Finite Rotating Shaft Element Using Timoshenko Beam Theory," Report ERC-R-77023, Arizona State University, Tempe, AZ.

Nelson, H. D., and Crandall, S. H., 1992, "Chap. 2—Analytic Prediction of Rotordynamic Response," *Handbook of Rotordynamics*, F. F. Ehrich, ed., McGraw-Hill, Inc.

Simmons, H. R., 1976, "Vibration Energy: A Quick Approach to Rotor Dynamic Optimization," ASME Paper No. 76-Pet-60.

APPENDIX

The shape factor κ for a hollow circular cross-sectional beam is given by:

$$\kappa = \frac{6(1+\nu)(1+\Re^2)^2}{(7+6\nu)(1+\Re^2)^2 + (20+12\nu)\Re^2} \quad \text{(A1)}$$

where ν is the Poisson ratio and $\Re = r_i/r_o$ is the ratio of inner to outer diameter. The most common cases used in the rotor dynamics analysis are:

For a solid shaft,

$$\kappa = \frac{6(1+\nu)}{(7+6\nu)} \quad (\text{for } \nu = 0.3,\ \kappa = 0.886)$$

For a thin-walled tube,

$$\kappa = \frac{2(1+\nu)}{4+3\nu} \quad (\text{for } \nu = 0.3,\ \kappa = 0.531)$$

Downloaded 02 Jun 2010 to 171.66.16.105. Redistribution subject to ASME license or copyright; see http://www.asme.org/terms/Terms_Use.cfm

Nonlinear Vibrations and Stability of a Rotor-Bearing System With Nonsymmetric Clearances

R. Ganesan
Department of Mechanical Engineering,
Concordia University,
Montreal, Quebec, Canada H3G 1M8

The nonlinear vibrations of a rotordynamic system that is subjected to nonsymmetric bearing clearance effects are considered. Particular attention is paid to the nonstationary response that occurs during passage through resonance. Based on an extended Jeffcott rotor model that includes the effects of nonsymmetric bearing clearances, the steady-state oscillations and their stability are also analyzed. The "normal-loose" rotor stiffness condition that occurs due to the bearing clearance effects is modeled through a discontinuous radial stiffness model. Expressions for the amplitude and phase-modulating functions are obtained. Frequency-amplitude relationships are derived. The effects of "normal-loose" rotor stiffness condition on the modulation of both the amplitude and phase of the near-resonance vibrations, as well as the stability of the rotor system, are systematically brought out. The effects of high-speed acceleration during run-up of the rotor are both qualified and quantified. Similarly, the case of run-down is analyzed.

1 Introduction

Recent studies (Childs, 1993; Ehrich, 1992) regarding the motion characteristics of rotor-bearing systems have clearly indicated that: (*i*) A loss of the rotor's radial stiffness over a portion of its synchronous orbit is observed in rotor systems with hydrodynamic bearings. This is due to excessive bearing clearances and inadequate vertical bearing restraints. This situation leads to the so-called "normal-loose" rotor stiffness condition and this condition is a nonsymmetric bearing clearance effect; (*ii*) In the case of rotors supported on rolling element bearings, wherein a small radial clearance is normally provided to allow axial shaft motion, the continuous existence of "normal-loose" condition results. This is due to both the bearing clearances and the fixed direction side load. A key feature of the "normal-loose" condition is that it leads to the presence of major components of the response at frequencies that are not synchronous with the rotational frequency. This asynchronous response may also dominate the vibratory response of the rotor-bearing system.

The works of Bently (1979) and Ehrich (1966) clearly demonstrated the nonlinear motion characteristics due to bearing clearance effects through controlled experiments. These experimental findings have been interpreted in terms of analytical results for both linear-parametric vibratory phenomena and nonlinear subharmonic vibrations. In the works of Ehrich and O'Connor (1967) and Ehrich (1966), explanations for the asynchronous rotor motions have been provided through nonlinear analysis and simulations. Further analytical studies followed the experimental observations described above, specifically those of Childs (1982), Ehrich and Childs (1984), Muszynska (1984), Beatty (1985), Saito (1985), Choi and Noah (1987), and Kim and Noah (1991). A discontinuous radial stiffness model has been developed for the "normal-loose" condition in the work of Childs (1982). The works by Choi and Noah (1987) and Kim and Noah (1991) included the effects of a fixed-direction side load and accounted for strong nonlinearities. Numerical studies were reported by Glease and Buckley (1984) wherein the forces due to seal and nonlinear bearing forces were also included. Yamauchi (1983) presented similar numerical studies employing a harmonic balance method based on FFT. Additional works on this topic include those of Ek (1980), Shaw (1985), and Ehrich (1972, 1988, 1991, 1992).

However, the characterization of nonstationary oscillations that occur as the rotordynamic system passes through resonance, and the evaluation of modulating functions for amplitude and phase of the response, have not so far been carried out. Rotating machinery systems such as turbocompressors, feed pumps, textile machinery spindles, etc., have their operational frequencies well above the critical frequency. When the rotor system is operated beyond its critical speed, at the start-up or shut-down of the system, the rotor is passed through resonance. This resonance is manifest by the appearance of extended amplitudes of oscillations. Rotors with nonsymmetric bearing clearances, in these situations, exhibit a highly complex behavior. The information regarding the vibrational characteristics of rotors near resonance is also required as an input to parametric identification methods such as resonance testing and in diagnostic systems for rotating machinery. Such an analytical investigation regarding the vibrational and stability characteristics of a rotor system with nonsymmetric bearing clearances, is the objective of the present paper.

2 Formulation of the Problem

The equations of motion for the undamped rotor-bearing system are written, corresponding to the constant running speed condition, based on the Jeffcott model (Jeffcott, 1919) as

$$m\ddot{R}_x + kR_x = ma\omega^2 \cos\phi \tag{1}$$

$$m\ddot{R}_y + kR_y = ma\omega^2 \sin\phi - W \tag{2}$$

In these equations, R_x and R_y are the components of the rotor displacement vector $\mathbf{R}$, m is the rotor mass, k is the rotor-bearing radial stiffness representing the combined circumferentially symmetric stiffness of the rotor shaft and bearings, a is the imbalance vector magnitude, ω is the disk angular velocity

Contributed by the International Gas Turbine Institute for publication in the JOURNAL OF ENGINEERING FOR GAS TURBINES AND POWER. Manuscript received at ASME Headquarters November 28, 1996. Associate Technical Editor: H. L. Julien.

Copyright © 1997 by ASME

Downloaded 02 Jun 2010 to 171.66.16.105. Redistribution subject to ASME license or copyright; see http://www.asme.org/terms/Terms_Use.cfm

(i.e., the rotor rotational speed), W is the total weight of the rotor, and ϕ is the rotor-disk rotation with respect to the fixed inertial frame xyz so that $\phi = \phi_0 + \omega t$ with ϕ_0 being the rotation at the zero instant of time. The rotor system is shown in Fig. 1.

The "normal-loose" condition of the rotor-bearing system is represented through the discontinuous radial rotor-bearing stiffness model. The discontinuous radial stiffness model is a widely known and experimentally validated model (Childs, 1982) that represents the effects of nonsymmetric bearing clearances through a bilinear form of the combined shaft-bearing stiffness. The parameters of the discontinuous radial stiffness model such as the point of discontinuity, slope, etc., are given in Fig. 2. As can be seen from Fig. 2, the radial shaft-bearing stiffness is reduced when $R_y > 0$. From Eqs. (1) and (2), R_x and R_y can be obtained to be

$$R_x = A \cos(\phi) \tag{3}$$

$$R_y = A \sin(\phi) - (W/k) \tag{4}$$

where A is the amplitude of the synchronous motion of the rotor given by

$$A = \frac{a\omega^2}{(\lambda_0^2 - \omega^2)}; \quad \lambda_0 = \sqrt{\frac{k}{m}} \tag{5}$$

Incorporating the "normal-loose" condition, represented through the radial stiffness model mentioned above, Eqs. (1) and (2) are replaced by the following set of equations of motion:

$$\ddot{R}_x + \lambda_0^2[1 - \epsilon U(R_y)]R_x = a\omega^2 \cos\phi \tag{6}$$

$$\ddot{R}_y + \lambda_0^2[1 - \epsilon U(R_y)]R_y = a\omega^2 \sin\phi - g \tag{7}$$

where g is the gravitational acceleration and $U(R_y)$ is a singularity function defined as

$$U(R_y) = 0, \quad R_y \leq 0 \tag{8}$$

$$U(R_y) = 1, \quad R_y > 0 \tag{9}$$

Further, ϵ is a perturbation parameter representing the fractional loss in radial rotor-bearing stiffness, and it is introduced to characterize the nonlinear motion. The value of perturbation parameter is such that $0 \leq \epsilon \leq 1$. Thus, $\epsilon = 0$ represents the nominal condition and $\epsilon = 1$ represents the condition when there is a complete loss of radial stiffness.

3 Nonstationary Response Near Resonance

The rotor system is considered as being accelerated through resonance and further, the "slow" and "fast" time scales are introduced such that the method of multiple scales (Nayfeh and Mook, 1979) can be employed. The equations of motion are recast in the following form:

$$\ddot{R}_x + \lambda_0^2 R_x = \epsilon\lambda_0^2 U(R_y)R_x + \epsilon a^*\omega^2(\epsilon t)\cos(\phi_0 + \phi_1(t)) \tag{10}$$

$$\ddot{R}_y + \lambda_0^2 R_y = \epsilon\lambda_0^2 U(R_y)R_y + \epsilon a^*\omega^2(\epsilon t)\sin(\phi_0 + \phi_1(t)) - \epsilon g^* \tag{11}$$

In these equations, substitutions $a^* = \epsilon^{-1}a$, $g^* = \epsilon^{-1}g$ and $\phi = \phi_0 + \phi_1(t) = \phi_0 + \lambda_0 t + \nu(\epsilon t)$ have been made. The equation for the y-directional motion R_y is now derived. The "slow" and "fast" time scales are introduced into the equations according to

$$T_0 = t; \quad T_1 = \epsilon t \tag{12}$$

So, the time derivative of $\phi_1(t)$ with respect to time t can be written as $d\phi_1/dt = \lambda_0 + \epsilon\nu'(T_1) = \lambda_0 + \epsilon\sigma(T_1)$ where prime denotes differentiation with respect to scaled time variable T_1 and $\sigma(T_1)$ is the detuning parameter that characterizes the nearness of the system to resonance. Moreover, the derivatives in Eqs. (10) and (11) with respect to time t are written in terms of the derivatives with respect to time scales, in accordance with Eq. (12).

After employing the asymptotic expansions given below in Eqs. (10) and (11),

$$R_x = R_{xo}(T_0, T_1) + \epsilon R_{x1}(T_0, T_1) + \ldots. \tag{13}$$

$$R_y = R_{yo}(T_0, T_1) + \epsilon R_{y1}(T_0, T_1) + \ldots. \tag{14}$$

the following set of ordinary differential equations can be obtained for both the base as well as the perturbed y-directional motions of the rotor system:

$$D_0^2 R_{y0} + \lambda_0^2 R_{y0} = 0 \tag{15}$$

$$D_0^2 R_{y1} + \lambda_0^2 R_{y1} = -2D_0 D_1 R_{y0} + \lambda_0^2 U(R_{y0})R_{y0} - g^* + a^*\omega^2(T_1)\sin(\phi_0 + \phi_1(T_0, T_1)) \tag{16}$$

where

$$D_n = \frac{\partial}{\partial T_n}, \quad n = 0, 1 \tag{17}$$

The solution to Eq. (15) is employed in the form

$$R_{y0} = A_2(T_1)\exp(i\lambda_0 T_0) + \bar{A}_2(T_1)\exp(-i\lambda_0 T_0) \tag{18}$$

Nomenclature

a = imbalance vector magnitude
$f(t)$ = Fourier series
g = gravitational acceleration
k = rotor-bearing radial stiffness
m = rotor mass
r = rate of change of the rotor rotational speed
A = amplitude of the synchronous motion
A_2 = amplitude of the nonlinear steady-state motion
D = static deflection due to rotor weight
$\mathbf{R}$ = rotor displacement vector
R = magnitude of rotor displacement vector $\mathbf{R}$
R_x = rotor displacement in the x direction
R_y = rotor displacement in the y direction
R_{xo} = base solution for x-directional motion
R_{yo} = base solution for y-directional motion
t = time
T_0 = time scale of order zero
T_1 = time scale of order one
$U(\ )$ = unit step function
W = rotor weight
β = phase of the nonlinear steady-state motion
ϵ = parameter characterizing the fractional loss in radial stiffness
θ = polar coordinate
λ_0 = natural frequency
ν = slowly varying component of rotor rotation angle such that the detuning parameter is equal to its first derivative with respect to scaled time T_1
ϕ = rotor rotation angle
ϕ_0 = initial rotor rotational angle
σ = detuning parameter characterizing the nearness to resonance
σ_0 = initial value of detuning parameter used for passage through resonance
σ_f = final value of detuning parameter used for passage through resonance
ω = rotor rotational speed

Downloaded 02 Jun 2010 to 171.66.16.105. Redistribution subject to ASME license or copyright; see http://www.asme.org/terms/Terms_Use.cfm

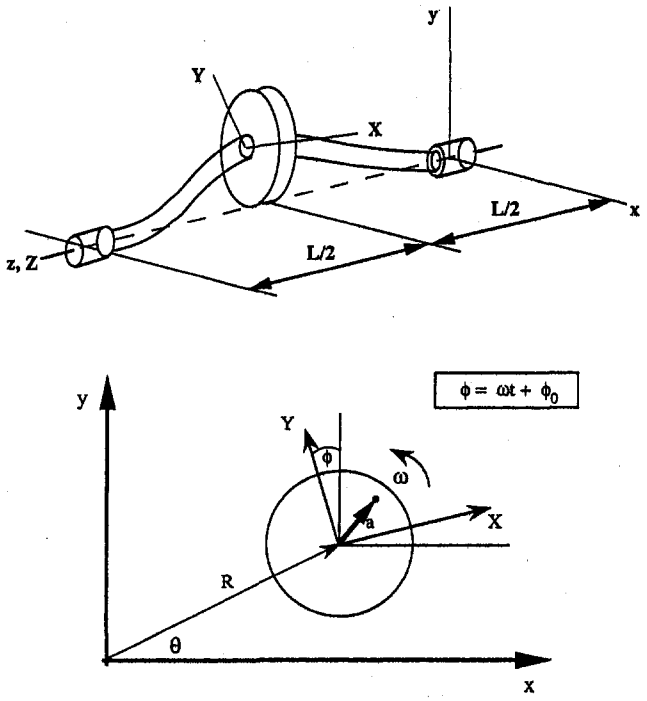


Fig. 1 The Jeffcott rotor system

where the overbar denotes the complex conjugate and $A_2(T_1)$ is an unknown arbitrary but "small" amplitude that has to be determined by the so-called "solvability condition" pertinent to Eq. (16). After substituting Eq. (18) into Eq. (16), the solvability condition is obtained to be

$$\{2i\lambda_0(A_2'(T_1)) + \tfrac{1}{2}\, ia^*\omega^2(T_1)\exp(i\nu + i\phi_0)\} = \lambda_0^2[U_1(R_y)A_2(T_1) + U_2(R_y)\bar{A}_2(T_1)] \quad (19)$$

where $U_1(R_y)$ and $U_2(R_y)$ represent the so-called "d.c. term" of $U(R_y)$ and the secular term arising from the product $U(R_y)\exp(-i\lambda_0 T_0)$, respectively. Further, the prime denotes differentiation with respect to the time variable T_1.

The function $U(R_y)$ is now set to be a function of the base synchronous motion of the rotor, in accordance with the discontinuous radial stiffness model (Childs, 1982, 1993), and this is represented by the function $U(R_{y0})$, as follows:

$$U(R_{y0}) = \frac{\xi}{\pi}[1 + f(t)] \quad (20)$$

$$f(t) = 2\sum_{j=1}^{\infty}\left(\frac{c_j}{2}\right)[\exp(ij\omega T_0) + \exp(-ij\omega T_0)] \quad (21)$$

$$c_j = -\frac{1}{2j\xi}\, i[\exp(ij\xi) - \exp(-ij\xi)] \quad (22)$$

Using Eqs. (20) – (22) together with Eq. (19), it can be shown that

$$2i\lambda_0\mathbf{A}_2'(T_1) - \lambda_0^2\mathbf{A}_2(T_1)\frac{\xi}{\pi} - \lambda_0^2\bar{\mathbf{A}}_2(T_1)\frac{1}{2\pi}\sin 2\xi\cdot\exp(2i\nu) + \frac{a^*\omega^2(T_1)}{2}\, i\exp(i\nu + i\phi_0) = 0 \quad (23)$$

The amplitude of base motion is expressed in polar form as

$$\mathbf{A}_2(T_1) = \tfrac{1}{2}\,\tilde{a}_2\exp(i\beta) \quad (24)$$

where $\tilde{a}_2$ and β are real parameters. Now, by substituting Eq. (24) in Eq. (23), the modulating functions for amplitude and phase can be obtained in the following form:

$$\tilde{a}_2' = -\frac{a^*\omega^2(T_1)}{2\lambda_0}\cos\gamma(T_1) + \frac{a_2\lambda_0}{4\pi}\sin 2\xi\cdot\sin 2(\gamma(T_1) - \phi_0) \quad (25)$$

$$\gamma' = \sigma + \frac{a^*\omega^2(T_1)}{2\lambda_0\tilde{a}_2}\sin\gamma(T_1) + \frac{\lambda_0\xi}{2\pi} + \frac{\lambda_0}{4\pi}\sin 2\xi\cos 2(\gamma(T_1) - \phi_0) \quad (26)$$

where

$$\gamma(T_1) = \nu(T_1) + \phi_0 - \beta(T_1) \quad (27)$$

4 Stationary Vibrations Near Resonance

From Eqs. (25) – (27), the frequency-amplitude equation for stationary vibrations are obtained, by letting $\tilde{a}_2' = \gamma' = 0$, as

$$\left\{\left[\sigma + \frac{\lambda_0\xi}{2\pi}\right]^2 + \left(\frac{\lambda_0}{4\pi}\right)^2\sin^2 2\xi + \frac{(2\sigma\pi + \xi\lambda_0)\lambda_0}{4\pi^2}\sin 2\xi \times\cos 2(\gamma - \phi_0)\right\}\tilde{a}_2^2 = \left[\frac{a^*\omega^2}{2\lambda_0}\right]^2 \quad (28)$$

The y-directional motion R_y is given by

$$R_y = \tilde{a}_2(T_1)\cos(\lambda_0 T_0 + \phi_0 + \beta) + O(\epsilon) \quad (29)$$

5 Instability of the Near-Resonance Response

The motion amplitude and phase $\tilde{a}_2$ and γ are decomposed into two parts as

$$\tilde{a}_2 = \tilde{a}_{20} + \tilde{a}_{21} \quad (30)$$

$$\gamma = \gamma_0 + \gamma_1 \quad (31)$$

On substituting these two equations into Eqs. (25) and (26), expanding for "small" values of $\tilde{a}_{21}$ and γ_1, noting that both

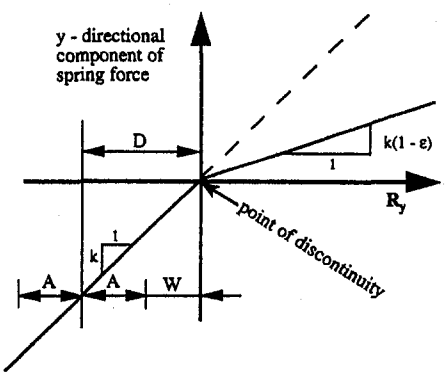


Fig. 2 The "normal-loose" rotor stiffness condition

Downloaded 02 Jun 2010 to 171.66.16.105. Redistribution subject to ASME license or copyright; see http://www.asme.org/terms/Terms_Use.cfm

$\tilde{a}_{20}$ and γ_0 satisfy Eq. (28) and then keeping linear terms in $\tilde{a}_{21}$ and γ_1, the equations for perturbed parts are obtained:

$$\tilde{a}'_{21} = \left(\frac{a^*\omega^2}{2\lambda_0}\sin\gamma_0\right)\gamma_1 + \frac{\tilde{a}_{21}\lambda_0}{4\pi}\sin 2\xi \sin 2(\gamma_0 - \phi_0) + \frac{\gamma_1\lambda_0\tilde{a}_{20}}{2\pi}\sin 2\xi \cos 2(\gamma_0 - \phi_0) \quad (32)$$

$$\gamma'_1 = -\frac{a^*\omega^2\tilde{a}_{21}}{2\lambda_0\tilde{a}_{20}^2}\sin\gamma_0 - \frac{\lambda_0\gamma_1}{2\pi}\sin 2\xi \sin 2(\gamma_0 - \phi_0) \quad (33)$$

Using the right-hand side of these two equations, the eigenvalues of the coefficient matrix are obtained, by solving the corresponding algebraic eigenvalue equation for λ. Considering the algebraic equation for λ, for unstable motions, the following condition can be obtained:

$$+\left[\frac{a^*\omega^2}{2\lambda_0\tilde{a}_{20}}\right]^2\sin^2\gamma_0 + \frac{a^*\omega^2}{4\pi\tilde{a}_{20}}\sin\gamma_0\cdot\sin 2\xi\cdot\cos 2(\gamma_0 - \phi_0) - \frac{\lambda_0^2}{8\pi^2}\sin^2 2\xi\cdot\sin^2 2(\gamma_0 - \phi_0) < 0 \quad (34)$$

If this condition is satisfied, one positive real root is obtained as the eigenvalue, and the motion becomes unstable. The left-hand side of Eq. (34) is referred to herein as the "stability indicator."

6 Numerical Results

A rotor system that was used for numerical study in the work of Lalanne and Ferraris (1990) is employed. It consists of a disk with an inner radius of 0.01 m and outer radius of 0.15 m. The thickness of the disk is 0.03 m and the material density is 7800 kg/m^3. The mass unbalance is located at a radial distance of 0.01 m, from the geometric center of the shaft. The combined circumferentially symmetric shaft-bearing stiffness is taken to be 1.195×10^6 N/m. Further, the value of ϕ_0 has been taken to be zero.

To study the vibrational characteristics of the rotor at any rotational speed, the detuning parameter σ is varied between -30 and $+5$. The amplitudes of stationary y-directional response $\tilde{a}_2$ at $t = 100$ s are calculated using the algebraic expression given as Eq. (28) and are plotted in Fig. 3, corresponding to four different values of ϵ: 0.2, 0.3, 0.4 and 0.5. The values

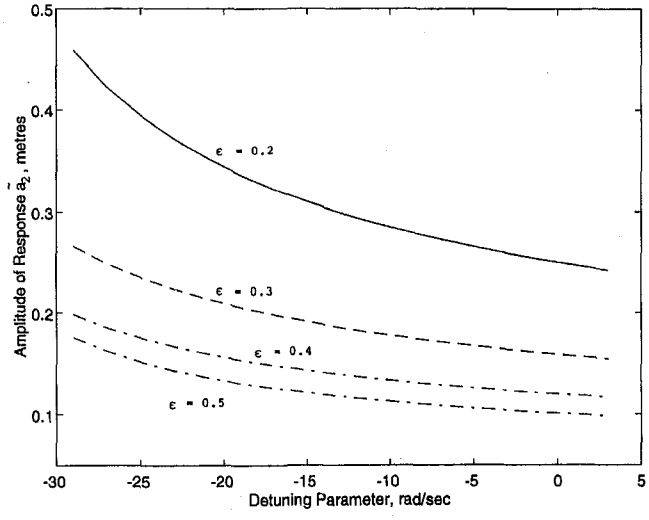


Fig. 3 Variation of the steady-state response amplitude with detuning parameter

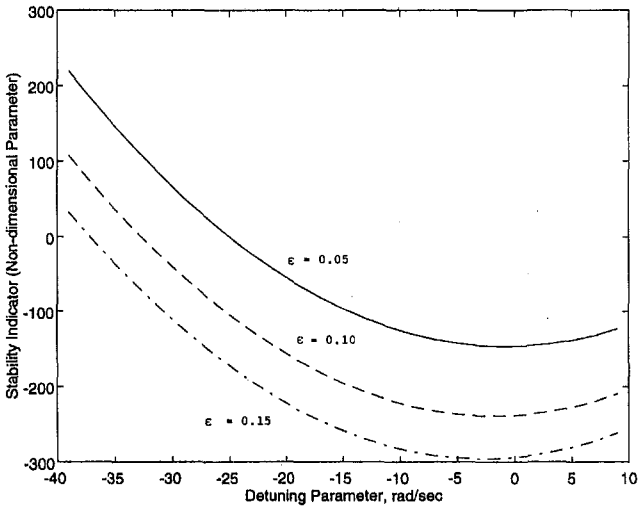


Fig. 4 Instability of the near-resonant response

of stability indicator are obtained using the algebraic expression given as Eq. (34) corresponding to three different values of the parameter ϵ: = 0.05, 0.10, and 0.15, and are plotted in Fig. 4. It can be observed from Fig. 3 that the amplitude of near-resonant response decreases when the bearing clearance effects increase. Further, the decrease in response amplitude is more pronounced near the response peaks and at rotor rotational speeds that are less than the critical speed. When the effects of bearing clearances increase, it has been observed that the response peaks are shifted to the left. Near the critical speed, when the effects of bearing clearance increase, the rotor system becomes unstable as indicated by the negative values of the stability indicator in Fig. 4. It can also be observed that beyond a certain value of ϵ, say 0.15 in the present case, most of the near-resonant vibrations are unstable. When the nonsymmetric bearing clearance effects are less, the values of the stability indicator are positive and hence unstable vibrations do not seem to occur.

Next, the shaft-bearing stiffness is increased and the amplitudes of response are calculated using Eq. (28). Corresponding to three different values of radial shaft-bearing stiffness, i.e., $k = 1.0 \times 10^6$, 2.5×10^6, and 4.0×10^6, and when $\epsilon = 0.2$ the response amplitudes are calculated and are plotted in Fig. 5. In a similar manner, using these values of radial stiffness and the parameter ϵ, the values of stability indicator are calculated using Eq. (34) and plotted in Fig. 6. It is observed from Fig. 5 that an increase in shaft-bearing stiffness leads to a corresponding decrease in response amplitudes near resonance at rotor rotational speeds that are less than the critical speed. However, increasing values of radial stiffness lead to unstable vibrations near resonance, as indicated by the negative values of the stability indicator in Fig. 6.

The effects of varying the rotor rotational speed as a function of scaled time T_1, during start-up or shut-down operations, are now considered. In order to determine these effects, the following linear variation of detuning parameter is considered:

$$\sigma(T_1) = \sigma_0 + rT_1$$

In this equation, σ_0 and r are constants. After substituting the expression into Eqs. (25) and (26), the numerical integration is performed. Here, two coupled first-order differential equations, that are Eqs. (25) and (26), have to be integrated. To this end, they are arranged in matrix state vector form, $\{\mathbf{y}'\} = [A]\{\mathbf{y}\}$, where the prime denotes the differentiation with respect to the time variable, that is T_1. The components of the state vector $\{\mathbf{y}\}$ are taken to be $\tilde{a}_2(T_1)$ and $\gamma(T_1)$, respectively. The coefficient matrix $[A]$ is formed using Eqs. (25) and (26).

Downloaded 02 Jun 2010 to 171.66.16.105. Redistribution subject to ASME license or copyright; see http://www.asme.org/terms/Terms_Use.cfm

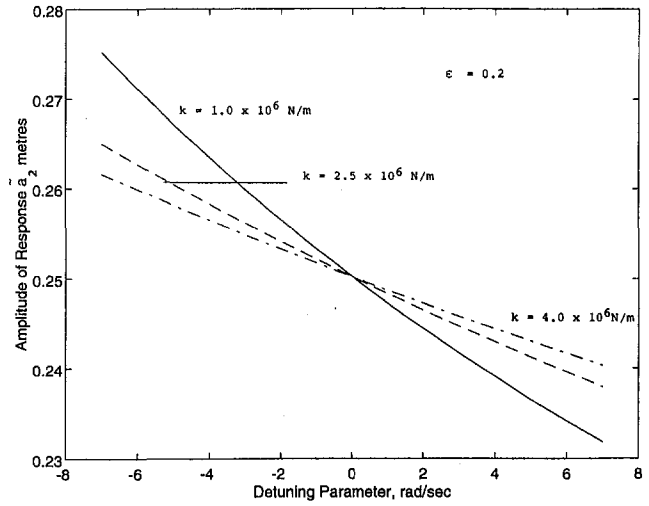


Fig. 5 Sensitivity of response amplitude to radial shaft-bearing stiffness

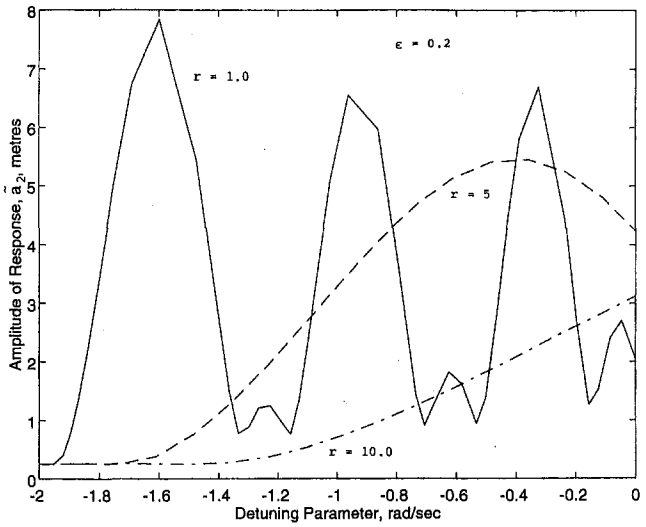


Fig. 7 Frequency-response curves corresponding to the nonstationary vibrations during run-up of the rotor; $\epsilon = 0.2$ and $r = 1.0$, 5.0, and 10.0

This matrix (first-order differential) equation in the state-vector form is integrated using the fourth-order Runge–Kutta method. The computer program entitled ODE45 that is available in the mathematical software MATLAB is employed for this purpose. The main program is written that defines the independent variable of the set of differential equations, the state vector, the components of the coefficient matrix, the tolerance value (i.e., 0.001 in the present case) and the initial and final values of the time parameter. Also, the values of response amplitude and phase that correspond to the initial value of time parameter must be calculated and should be used in the numerical integration. The main program calculates these values based on Eq. (28). The detuning parameter is varied between σ_0 and σ_f, where σ_f indicates the final value of the detuning parameter.

First, the case of increasing the detuning parameter through resonance, i.e., the case of running-up, is considered. The value of the parameter ϵ is taken to be 0.2 and the detuning parameter is varied from -2.0 to 0.0 such that $\sigma_0 = -2.0$ and $\sigma_f = 0.0$. Three different values of r, i.e., 1.0, 5.0, and 10.0, have been used and the resulting frequency-response curves are plotted in Fig. 7. The response history for the case when ϵ is taken to be 0.2 and r is taken to be 10 has been determined and plotted in Fig. 8. As can be seen from these two figures, the amplitude of the response decreases and the excitation frequency (i.e., rotor rotational speed ω) where this peak occurs increases, when the rate of increasing the excitation frequency (i.e., rotor rotational speed ω) is increased. Further, the sharpness of the frequency-response curve tend to decrease, when the rate r is increased. Now, the value of parameter ϵ is increased to 0.4 and the value of rate r is taken to be 10.0 and the resulting response history is plotted in Fig. 9. Also, the value of shaft-bearing stiffness has been increased by five times and the corresponding response history has been determined and plotted in Fig. 9. It can be observed from Figs. 7, 8, and 9 that (*i*) when the effects of nonsymmetric bearing clearances are less, the amplitudes significantly increase, and (*ii*) for the same rate of acceleration through critical speed, increasing values of shaft-bearing stiffness lead to a significant reduction in response amplitudes.

Next, the case of decreasing the detuning parameter through resonance, i.e., the case of running-down, is considered. The value of the parameter ϵ is taken to be 0.4 and the detuning parameter is varied from 6.0 to -4.0 such that $\sigma_0 = 6.0$ and $\sigma_f = -4.0$. Two different values of r, i.e., -10.0 and -15.0, have been used and the resulting frequency-response curves are plotted in Fig. 10. It is observed from this figure that the peak amplitude is increased as the rate of decreasing the excitation

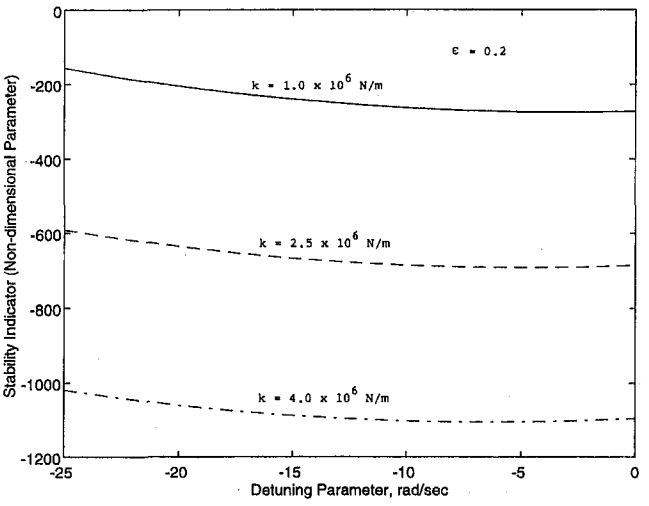


Fig. 6 Effects of radial shaft-bearing stiffness on the instability of near-resonant response

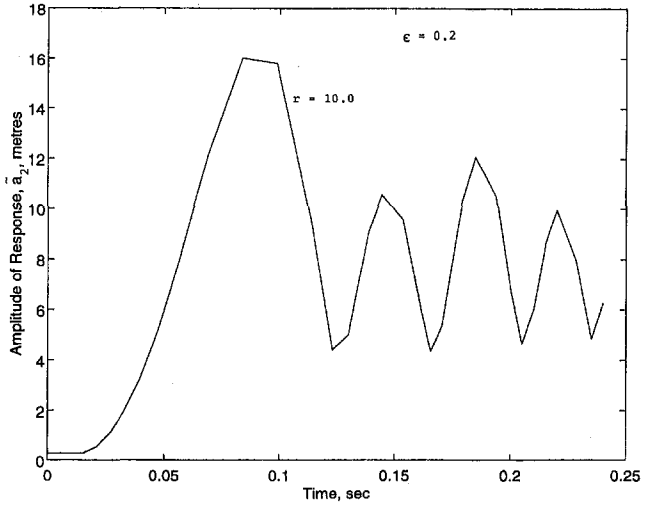


Fig. 8 Time history of the nonstationary vibrations during run-up of the rotor; $\epsilon = 0.2$ and $r = 10$

Downloaded 02 Jun 2010 to 171.66.16.105. Redistribution subject to ASME license or copyright; see http://www.asme.org/terms/Terms_Use.cfm

frequency (i.e., rotor rotational speed ω) is increased, and the rotor rotational speed ω at which the peak response occurs is lesser than the critical speed. Next, using the value $\epsilon = 0.2$, the response amplitudes have been calculated. However, the relevant plot is not shown here due to lack of space. From this, it has been observed that when the nonsymmetric bearing clearance effects are more, the amplitudes are significantly decreased.

7 Design and Diagnostics Aspects

The nonsymmetric bearing clearance effects suppress the near-resonant vibration response. During start-up or shut-down of the motor, the rotors are driven through their critical speeds by applying sufficient power, and the magnitude of this power can be significantly reduced by the "normal-loose" condition. However, the "normal-loose" rotor stiffness condition significantly affects the stability of the rotordynamic system. In the absence of the "normal-loose" condition, the rotor motions are always stable, as can be observed from the existing works. It has been shown in the present work that unstable rotor motions can occur due to nonsymmetric bearing clearance effects. An increase in the radial stiffness does not seem to stabilize the near-resonant motions. It is also observed that there exist certain threshold values of nonsymmetric bearing clearances and radial stiffness, that do not lead to unstable motions. Since the nonsymmetric bearing clearance effects help suppress the near-resonant vibrations, they can be used to advantage if these threshold values are used in design so that the unstable vibrations can also be avoided. These threshold values can be obtained from Eqs. (28) and (34).

8 Conclusions

The nonlinear response characteristics of a rotordynamic system, induced by nonsymmetric bearing clearance effects, are studied. Near-resonant motions are analyzed in particular and sensitivities to various rotor system parameters of both the amplitude and phase of the steady-state response are qualified and quantified. It has been shown that unstable vibrations may occur near the resonance condition when the effects of nonsymmetric bearing clearances are present. Moreover, the effects of bearing clearances in suppressing the large-amplitude vibrations during resonance and distorting the variation of the phase angles are noted. As can be seen from Eqs. (10) and (11), the horizontal and vertical motions of the rotor shaft are coupled. The "normal-loose" bearing condition represented by the function $U(R_y)$ affects both the horizontal and vertical rotor motions. In the present work, only the vertical rotor motions have been analyzed in detail. However, after substituting Eqs. (20)–(22) into Eqs. (10) and (11), and performing an analysis similar to the analysis presented in sections 3–5 of the present paper, the characteristics of horizontal motions can be determined. To this end, the second asymptotic series expansion given in Eq. (14) and an equation similar to Eq. (18) can be deployed. This is valid since the homogeneous part of the solution for horizontal motion R_x is similar to and is in the same form as that for vertical motion R_y, which is given by Eq. (15).

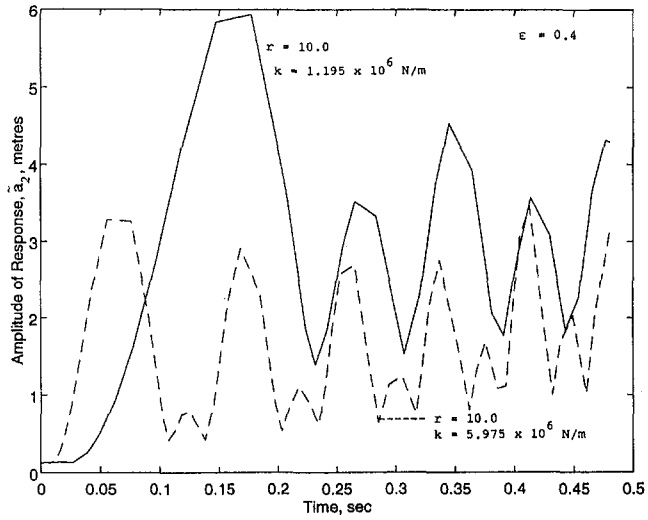


Fig. 9 Effects of shaft-bearing stiffness on the time history of response during run-up of the rotor; $\epsilon = 0.4$ and $r = 10.0$

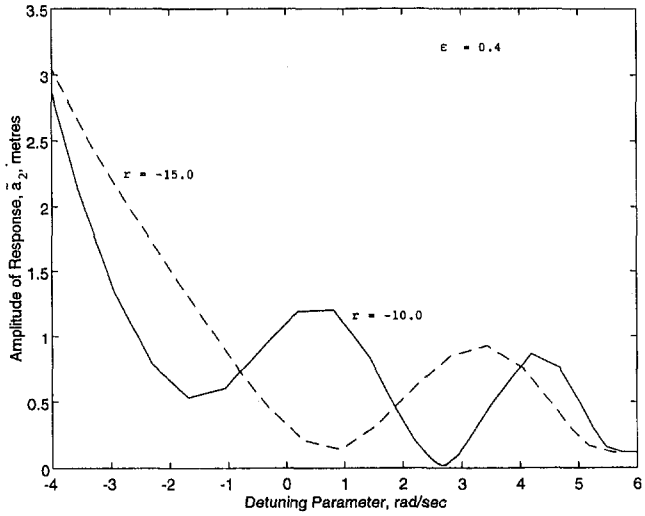


Fig. 10 Frequency-response curves corresponding to the nonstationary vibrations during run-down of the rotor; $\epsilon = 0.4$ and $r = -10.0$ and -15.0

References

Beatty, R. F., 1985, "Differentiating Rotor Response Due to Radial Rubbing," ASME *Journal of Vibration, Acoustics, Stress, and Reliability in Design,* Vol. 107, pp. 151–160.

Bently, D., 1979, "Forced Subrotative Speed Dynamic Action of Rotating Machinery," ASME Paper No. 74-PET-16.

Childs, D. W., 1982, "Fractional-Frequency Rotor Motion Due to Nonsymmetric Clearance Effects," ASME JOURNAL OF ENGINEERING FOR POWER, Vol. 104, pp. 533–541.

Childs, D. W., 1993, *Turbomachinery Rotordynamics: Phenomena, Modeling and Analysis,* Wiley, New York.

Choi, Y. S., and Noah, S. T., 1987, "Nonlinear Steady-State Response of a Rotor-Support System," ASME *Journal of Vibration, Acoustics, Stress, and Reliability in Design,* Vol. 109, pp. 255–261.

Ehrich, F. F., 1966, "Subharmonic Vibrations of Rotors in Bearing Clearance," ASME Paper No. 66-MD-1.

Ehrich, F. F., and O'Connor, J. J., 1967, "Stator Whirl With Rotors in Bearing Clearances," ASME *Journal of Engineering for Industry,* Vol. 89, pp. 381–390.

Ehrich, F. F., 1972, "Sum and Difference Frequencies in Vibration of High Speed Rotating Machinery," ASME *Journal of Engineering for Industry,* Vol. 94, pp. 181–184.

Ehrich, F. F., and Childs, D., 1984, "Self-Excited Vibrations in High-Performance Turbomachinery," *Mechanical Engineering,* Vol. 106, pp. 66–79.

Ehrich, F. F., 1988, "High Order Subharmonic Response of High Speed Rotors in Bearing Clearance," ASME *Journal of Vibration and Acoustics,* Vol. 110, pp. 9–16.

Ehrich, F. F., 1991, "Some Observations of Chaotic Vibration in High Speed Rotor Dynamics," ASME *Journal of Vibration and Acoustics,* Vol. 113, pp. 50–57.

Ehrich, F. F., 1992, "Observations of Subcritical, Superharmonic and Chaotic Response in Rotordynamics," ASME *Journal of Vibration and Acoustics,* Vol. 114, pp. 93–100.

Ek, M. C., 1980, "Solution of the Subsynchronous Whirl Problem in the High-Pressure Hydrogen Turbomachinery of the Space Shuttle Main Engine," *AIAA Journal of Spacecraft and Rockets,* Vol. 17, pp. 208–218.

Glease, J. R., and Buckley, P., 1984, "Effect of Bearing Deadbands on Bearing Loads and Rotor Stability," *MSFC Advanced High Pressure O2/H2 Technology Conference Proceedings,* G. Marshall Space Flight Center, Huntsville, AL.

Downloaded 02 Jun 2010 to 171.66.16.105. Redistribution subject to ASME license or copyright; see http://www.asme.org/terms/Terms_Use.cfm

Jeffcott, H. H., 1919, "Lateral Vibrations of Loaded Shafts in the Neighbourhood of a Whirling Speed—The Effect of Want of Balance," *Philosophical Magazine,* Vol. 37, pp. 304–314.

Kim, B., and Noah, S. T., 1991, "Response and Bifurcation Analysis of a MDOF Rotor System With a Strong Nonlinearity," *Nonlinear Dynamics,* Vol. 2, pp. 215–234.

Lalanne, M., and Ferraris, G., 1990, *Rotordynamics Prediction in Engineering,* Wiley, New York.

Muszynska, A., 1984, "Partial Lateral Rotor to Stator Rubs," IMechE Paper No. C281/84.

Nayfeh, A. H., and Mook, D. T., 1979, *Nonlinear Oscillations,* Wiley Interscience, New York.

Saito, S., 1985, "Calculation of Nonlinear Unbalance Response of Horizontal Jeffcott Rotors Supported by Ball Bearings With Radial Clearances," ASME Paper No. 85-DET-33.

Shaw, S. W., 1985, "Forced Vibration of a Beam With One Sided Amplitude Constraint: Theory and Experiment," *Journal of Sound and Vibration,* Vol. 99, pp. 199–212.

Yamauchi, S., 1983, "The Nonlinear Vibration of Flexible Rotors, 1st Report, Development of a New Analysis Technique," *Transactions of Japan Society of Mechanical Engineers,* Vol. 49, pp. 1862–1868.

Downloaded 02 Jun 2010 to 171.66.16.105. Redistribution subject to ASME license or copyright; see http://www.asme.org/terms/Terms_Use.cfm

Comparison of the Rotor Dynamic and Structure Dynamic Calculation of Compressors

M. Hohlrieder
Lödige Industries,
34144 Warburg,
Federal Republic of Germany

H. Irretier
Institute of Mechanics,
University of Kassel, 34109 Kassel,
Federal Republic of Germany

The paper presents the analysis of a compressor employing the method of cyclic symmetry incorporating gyroscopic effects and geometric nonlinearities of the whole elastic system based on the finite element method. Because of numerical difficulties, the solution of the resulting eigenvalue problem is limited to a small number of DOF's. For this reason the calculation of the impeller as an elastic model is performed including the prestress and nonlinearities due to rotation. With the knowledge of these frequencies and the mass moment of inertia of the impeller, an equivalent system of rigid disk and speed dependent spring is included in the rotor dynamic model. Further, the gyroscopic effect, speed-dependent bearing coefficients, and the elastic effects due to the rotation of the impeller are included in the rotor dynamic model. For illustration purpose, calculation is performed on a fan rotor and the results are compared with those obtained from experiment.

1 Introduction

During the development of highly loaded rotating machines like compressors and turbines, in addition to the computation of the static stresses, it is essential to know their dynamic behavior due to rotation.

The first step in the study of rotating machinery is the calculation of the natural frequencies and mode shapes, which are rotor-speed dependent. Due to the geometrically sophisticated structures, it is customary to calculate the impeller and the rotor separately by the Finite Element Method. Usually the structural dynamic model of the impeller is generated in a coordinate system fixed in the impeller to consider stiffening effects and geometric nonlinearities that arise due to rotation excluding the gyroscopic effect. For the whole system the rotor dynamic model calculation is done in a coordinate system fixed in space, modeling the impeller as a rigid disk and the shaft as an elastic beam, futher taking into account gyroscopic effects and speed dependent bearing stiffness and damping.

In classical rotor dynamics the equations of motion are usually formulated in a nonrotating coordinate system fixed in space (inertial reference system i). In this case, the stiffness and mass distribution of the shaft must be isotropic to avoid time-variant equations. The disks on the rotor must be assumed to be rigid. The stiffness and damping distribution of the bearings can be symmetric or unsymmetric (Fig. 1).

We contrast the formulation in a nonrotating coordinate system with a rotating coordinate system fixed in the rotor (bodyfixed system k). The bearing must be isotropic to result in time-invariant equations of motion. The structure can be symmetric or nonsymmetric (Fig. 2). The influence of rotation is usually taken into account only by the geometric stiffness matrix, i.e., the prestress effect due to rotation on the structural stiffness. The influence of gyroscopic forces normally is not considered in the model [1–9]. For both cases, the resulting equations of motion based on a finite element model are described in the following section.

Contributed by the International Gas Turbine Institute and presented at Cogen-Turbo Power, Vienna, Austria, August 23–25, 1995. Manuscript received by the International Gas Turbine Institute June 20, 1995. ASME Paper No. 95-CTP-51. Associate Technical Editor: C. J. Russo.

2 Numerical Model

The position of a point P of the deformed structure is described by (Fig. 3):

$$\mathbf{r} = \mathbf{r}_o + \mathbf{r}_p \tag{1}$$

where $\mathbf{r}_o$ and $\mathbf{r}_p$ are defined in the inertial reference coordinate system (index i) and in the bodyfixed coordinate system (index k), respectively. By the transformation matrix $\mathbf{T}_{ik}$, which describes a transformation from the k into the i-system equation (1) follows in the i-system as

$$\mathbf{r}_i = \mathbf{r}_{oi} + \mathbf{T}_{ik}\mathbf{r}_{pk} \tag{2}$$

The velocity follows as

$$\dot{\mathbf{r}}_i = \dot{\mathbf{r}}_{oi} + \dot{\mathbf{T}}_{ik}\mathbf{r}_{pk} + \mathbf{T}_{ik}\dot{\mathbf{r}}_{pk} \tag{3}$$

where

$$\dot{\mathbf{T}}_{ik} = \Omega_i \times \mathbf{T}_{ik} \tag{4}$$

is the cross-product between the vector Ω_i of the angular velocity and the corresponding column vector of the matrix $\mathbf{T}_{ik}$. The velocity is then described in the i and k-system by

$$\dot{\mathbf{r}}_i = \dot{\mathbf{r}}_{oi} + \mathbf{T}_{ik}\dot{\mathbf{r}}_{pk} + \Omega_i \times (\mathbf{T}_{ik}\mathbf{r}_{pk}) \tag{5}$$

and

$$\dot{\mathbf{r}}_k = \mathbf{T}_{ki}\dot{\mathbf{r}}_i = \mathbf{T}_{ki}\dot{\mathbf{r}}_{oi} + \mathbf{T}_{ki}\mathbf{T}_{ik}\dot{\mathbf{r}}_{pk} + \mathbf{T}_{ki}\Omega_i \times (\mathbf{T}_{ik}\mathbf{r}_{pk}) \tag{6}$$

respectively. From these expressions the acceleration in the i and k-system follow as

$$\ddot{\mathbf{r}}_i = \ddot{\mathbf{r}}_{oi} + \Omega_i \times (\mathbf{T}_{ik}\dot{\mathbf{r}}_{pk}) + \mathbf{T}_{ik}\ddot{\mathbf{r}}_{pk} + \dot{\Omega}_i \times (\mathbf{T}_{ik}\mathbf{r}_{pk}) + \Omega_i \times (\Omega_i \times (\mathbf{T}_{ik}\mathbf{r}_{pk})) + \Omega_i \times (\mathbf{T}_{ik}\mathbf{r}_{pk}) \tag{7}$$

and

$$\ddot{\mathbf{r}}_k = \mathbf{T}_{ki}\ddot{\mathbf{r}}_{oi} + \ddot{\mathbf{r}}_{pk} + \dot{\Omega}_k \times \mathbf{r}_{pk} + \Omega_k \times \Omega_k \times \mathbf{r}_{pk} + 2\Omega_k \times \dot{\mathbf{r}}_{pk}, \tag{8}$$

respectively. Equations (7) and (8) describe the absolute acceleration formulated in the i and k-system respectively. The vector $\mathbf{r}_{pk}$ consists in the equations given above of the resulting displacement due to the static and dynamic deformation of the system.

Copyright © 1997 by ASME

Downloaded 02 Jun 2010 to 171.66.16.105. Redistribution subject to ASME license or copyright; see http://www.asme.org/terms/Terms_Use.cfm

	Rotating Structure	
	symmetric	nonsymmetric
bearing isotropic	timeinvariant	timeinvariant
bearing anisotropic	timevariant	timevariant

Fig. 1 Equations of motion in a coordinate system fixed in space

	Rotating Structure	
	symmetric	nonsymmetric
bearing isotropic	timeinvariant	timevariant
bearing anisotropic	timeinvariant	timevariant

Fig. 2 Equations of motion in a coordinate system fixed within the structure

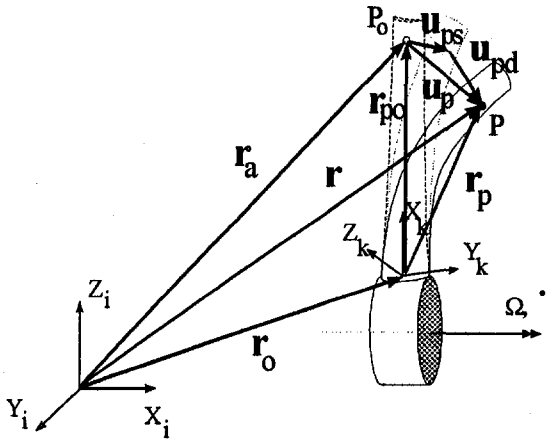


Fig. 3 Vectors and deformations

For the further considerations it is convenient to decompose this vector by [7]:

$$\mathbf{r}_{pk} = \mathbf{r}_{pok} + \mathbf{u}_{pks} + \mathbf{u}_{pkd} \tag{9}$$

where $\mathbf{r}_{pok}$ is the vector of the nonrotating and nonvibration, i.e., undeformed structure, $\mathbf{u}_{pks}$ is the displacement vector due to rotation (quasi-static part) $\mathbf{u}_{pkd}$ is the displacement vector due to vibrations (dynamic part) of the structure. From Eqs. (8) and (9) the acceleration formulated in the k-system follows as (index k is omitted)

$$\ddot{\mathbf{r}} = \ddot{\mathbf{r}}_o + \ddot{\mathbf{u}}_{pd} + \dot{\Omega} \times (\mathbf{r}_{po} + \mathbf{u}_{ps} + \mathbf{u}_{pd}) + \Omega \times \Omega \times (\mathbf{r}_{po} + \mathbf{u}_{ps} + \mathbf{u}_{pd}) + 2\Omega \times (\dot{\mathbf{u}}_{pd}) \tag{10}$$

and in a corresponding formulation in the i-system.

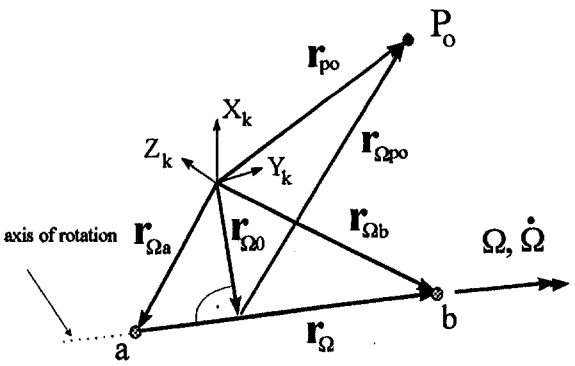


Fig. 4 Axis of rotation

In general, for a body-fixed coordinate system in a generally accelerated motion, it is not possible to take the translatory component in the acceleration $\ddot{\mathbf{r}}_o$ into account. For this reason, such a component of the acceleration is omitted in the following equations (Fig. 4):

$$\ddot{\mathbf{r}}_o = -\Omega \times \Omega \times \mathbf{r}_{\Omega o} - \dot{\Omega} \times \mathbf{r}_{\Omega o} \tag{11}$$

For the configuration of the axis of rotation and the origin of the body-fixed coordinate system as given in Fig. 4 the equations

$$\mathbf{r}_\Omega = \mathbf{r}_{\Omega b} - \mathbf{r}_{\Omega a} \tag{12}$$

$$\mathbf{r}_{\Omega o} = \mathbf{r}_{\Omega a} + \lambda \mathbf{r}_\Omega \tag{13}$$

$$\lambda = -\frac{\mathbf{r}_{\Omega a}\mathbf{r}_\Omega}{\mathbf{r}_\Omega^2} \tag{14}$$

are valid, i.e., in Eq. (10) $\mathbf{r}_{po}$ must be replaced by $\mathbf{r}_{\Omega p0}$:

$$\mathbf{r}_{\Omega po} = \mathbf{r}_{po} - \mathbf{r}_{\Omega o} \tag{15}$$

The angles of velocity and acceleration are expressed by

$$\Omega = \Omega \frac{\mathbf{r}_\Omega}{|\mathbf{r}_\Omega|} = \Omega \mathbf{e}_\Omega \tag{16}$$

$$\dot{\Omega} = \dot{\Omega} \frac{\mathbf{r}_\Omega}{|\mathbf{r}_\Omega|} = \dot{\Omega} \mathbf{e}_\Omega \tag{17}$$

which complete the set of equations to describe completely the vectors $\boldsymbol{\Omega}$, $\dot{\boldsymbol{\Omega}}$, and $\ddot{\mathbf{r}}_o$ by the indication of the vectors $\mathbf{r}_{\Omega a}$, $\mathbf{r}_{\Omega b}$, the angular velocity Ω, and the angular acceleration $\dot{\Omega}$.

The complete displacement of a point P of the structure described in the k-system is given by (the indices k and p are omitted):

Nomenclature

$\mathbf{A}$ = matrix or vector
$\mathbf{A}^T$ = transpose of a matrix/vector
$\dot{\mathbf{x}}, \ddot{\mathbf{x}}$ = derivative of time of a matrix/vector
$\mathbf{x}, \mathbf{X}$ = vector of nodel displacements, local/global
$\mathbf{r}_i, \mathbf{r}_k$ = vector in the inertia coordinate system (index i) or in the body-fixed coordinate system (index k)
$\mathbf{r}$ = vector from origin
$\mathbf{r}_o$ = vector from inertia coordinate system to body-fixed coordinate system
$\mathbf{r}_p$ = vector from body-fixed coordinate system to a point of the structure
$\mathbf{T}$ = transformation matrix
$\mathbf{u}$ = displacement vector
$\mathbf{D}$ = differential operator matrix
$\mathbf{E}$ = matrix of elasticity
$\mathbf{H}$ = matrix of shape functions
$\mathbf{F}$ = force vector
$\mathbf{M}$ = mass matrix
$\mathbf{D}$ = differential operator matrix/damping matrix
$\mathbf{C}$ = Coriolis matrix
$\mathbf{K}_E$ = elastic stiffness matrix
$\mathbf{K}_G$ = geometric stiffness matrix (initial stress)
$\mathbf{K}_N$ = nonlinear stiffness matrix (initial strain)
$\mathbf{K}_\Omega$ = centrifugal stiffness matrix
$\mathbf{K}_{\dot{\Omega}}$ = stiffness matrix due to angular acceleration

Downloaded 02 Jun 2010 to 171.66.16.105. Redistribution subject to ASME license or copyright; see http://www.asme.org/terms/Terms_Use.cfm

$$\mathbf{u} = \mathbf{u}_s + \mathbf{u}_d \tag{18}$$

corresponding to the quasi-static and the dynamic part of the displacement (Fig. 3). In the case of a nonlinear geometric and linear elastic behavior Green's strains can be calculated by

$$\epsilon = (\mathbf{D}_L + \mathbf{D}_N)^T\mathbf{u} \tag{19}$$

where $\mathbf{D}_L$ and $\mathbf{D}_N$ are the appropriate linear differential operator, which is independent from the displacement field and the nonlinear differential operator depending on the displacement field, respectively [1]. The corresponding Kirchhoff stresses are then expressed by

$$\sigma = \mathbf{E}\epsilon \tag{20}$$

where $\mathbf{E}$ is the linear elasticity matrix. Again the decomposition

$$\boldsymbol{\sigma} = \boldsymbol{\sigma}_s + \boldsymbol{\sigma}_d \tag{21}$$

corresponding to the displacement field is possible.

The equations of motion for the finite element model follow from the Lagrange–d'Alembert principle [2]

$$\int_v \rho\delta\mathbf{u}^T\ddot{\mathbf{r}}dV + \int_v \delta\epsilon^T\sigma dV = \int_v \delta\mathbf{u}^T\mathbf{p}_v dV + \int_v \delta\mathbf{u}^T\mathbf{p}_s dS \tag{22}$$

by introducing

$$\mathbf{u}(\mathbf{r}, \mathbf{t}) = \sum_{i=1}^{n} \mathbf{H}_i(\mathbf{r})\mathbf{x}_i(t) = \mathbf{H}(\mathbf{r})\mathbf{x}(\mathbf{t}) \tag{23}$$

where $\mathbf{H}(\mathbf{r})$ and $\mathbf{x}(\mathbf{t})$ are the matrices of the spatial shape functions and the time-dependent nodal displacements. Following the well-known derivation of a finite element model [1], which is also repeated in [7] according to the equations described above, the resulting equation for the static deformation of the rotating structure is

$$(\mathbf{K}_E + \mathbf{K}_G + \mathbf{K}_N + \mathbf{K}_\Omega + \mathbf{K}_{\dot\Omega})\mathbf{X}_s = \mathbf{F}_o + \mathbf{F}_\Omega + \mathbf{F}_{\dot\Omega} + \mathbf{F}_s \tag{24}$$

and the resulting equation of motion for the vibrations of this structure is [3, 7]:

$$\mathbf{M}\ddot{\mathbf{X}} + (\mathbf{D} + \mathbf{C})\dot{\mathbf{X}} + (\mathbf{K}_E + \mathbf{K}_G + \mathbf{K}_N + \mathbf{K}_\Omega + \mathbf{K}_{\dot\Omega})\mathbf{X}_d = \mathbf{F}_d \tag{25}$$

formulated in the rotating coordinate system. In these equations $\mathbf{K}_E$ is the elastic stiffness matrix, $\mathbf{K}_G$ is the geometric stiffness matrix due to rotation, $\mathbf{K}_N$ is the nonlinear stiffness matrix that may result from initial strains, $\mathbf{K}_\Omega$ is the centrifugal stiffness matrix, and $\mathbf{K}_{\dot\Omega}$ is the stiffness matrix due to angular acceleration. $\mathbf{M}$, $\mathbf{D}$, and $\mathbf{C}$ denote the mass matrix, the damping matrix, and the Coriolis matrix, respectively, and $\mathbf{F}_o$ are the forces due to the acceleration of the origin of the rotating coordinate system, $\mathbf{F}_\Omega$ and $\mathbf{F}_{\dot\Omega}$ are the inertia forces due to angular velocity and acceleration, respectively, and $\mathbf{F}_s$ and $\mathbf{F}_d$ are the static and dynamic external surface forces, respectively, where the latter, e.g., may consist of external excition forces.

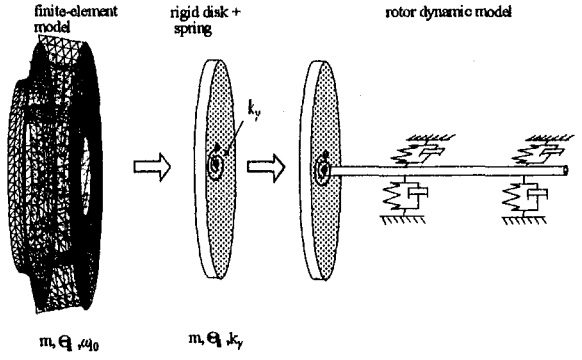
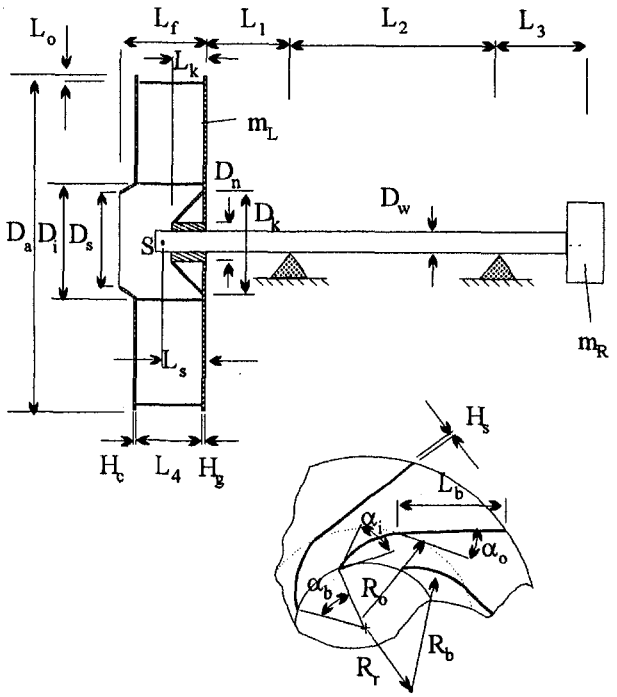


Fig. 5 Structural dynamics model and rotor dynamics model with speed-dependent rotational spring



L_o	=	10	mm	H_c	=	3.3	mm
L_1	=	80	mm	H_g	=	5	mm
L_2	=	296	mm	H_s	=	3.3	mm
L_3	=	175	mm				
L_4	=	112	mm	R_0	=	235	mm
L_b	=	206.6	mm	R_r	=	109.4	mm
L_k	=	40	mm	R_b	=	248	mm
L_f	=	137	mm	α_i	=	23	°
L_s	=	46.8	mm	α_o	=	26	°
D_w	=	50	mm	α_b	=	36	°
D_k	=	214	mm				
D_n	=	90	mm	E	=	2.1E05	N/mm^2
D_s	=	318	mm	ρ	=	7850	kg/m^3
D_i	=	355	mm	ν	=	0.3	
D_a	=	770	mm	κ	=	0.8333	

m_L	=		41.6	kg	
m_R	=		8.0	kg	
I_{zz}	=	I_p =	2.908	kg m^2	
I_{yy}	=	I_a =	1.558	kg m^2	

Fig. 6 Radial impeller and geometric and material data

3 Numerical Solution

For the numerical solution of Eqs. (24) and (25), first the static problem (24) is solved iteratively, which yields the geometric and nonlinear stiffness matrix $\mathbf{K}_N + \mathbf{K}_G$. Then the eigenvalue problem that follows from Eq. (25) is solved for the linear vibration around the state of equilibrium, which results in the natural frequencies and mode shapes of the structure. While doing this it is possible to use the advantage of the cyclic symmetry, which often is given in rotating structures as

Downloaded 02 Jun 2010 to 171.66.16.105. Redistribution subject to ASME license or copyright; see http://www.asme.org/terms/Terms_Use.cfm

compressors, impellers, etc. [7]. The numerical evaluation of the steady or transient dynamic response of the structure due to external excitations is given in detail also in [7].

The numerical calculation of the natural or forced vibrations of a rotating structure based on the equation of motion, Eq. (25), is extremely time-consuming if a complete rotor system consisting of a shaft, bearings, and more then one disk structure is completely modeled by finite elements. For this reason the classical rotor dynamic models apply finite element approximation of the shaft while the disks are modeled by rigid bodies (rotor dynamic model).

On the other hand, to calculate the frequencies and modes of rotating disk-like structures like disks, compressors, etc., only these structures are modeled by finite elements where the connection to the shaft is modeled by appropriate boundary conditions or elastic springs (structure dynamic model).

In the present study these two models are combined based on the FE-code FEARS [7] and the FE-code FEROS [5] applied for the structure dynamic calculation and rotor dynamic calculation, respectively.

It is known that in particular for the fundamental mode with one nodal diameter of the disk structure it is necessary to take into account the dynamic coupling between the structure and the rotor (Fig. 5).

Here a technique is used that combines a rotor dynamic with a structural dynamic model in the sense described above. First, the natural frequency of the one nodal diameter mode of the impeller is calculated from the structure dynamic model, including the stiffening effect due to rotation. From the known mass moment of inertia of the impeller, an equivalent rotational stiffness around the nodal diameter is determined for the different rotational speeds. Then, a rigid disk with the same mass moment of inertia as the impeller is connected to the rotor shaft by the speed-dependent rotational spring stiffness previously calculated. By this technique, the resulting rotor dynamics model takes into account both the increase of the natural frequencies of the elastic impeller and the gyroscopic effect of the impeller on the elastic shaft [7].

4 Example and Numerical Results

In Fig. 6 an impeller is shown mounted on a shaft in an overhang position. All geometric dimensions and material and other parameters are also given in Fig. 6.

First, the speed-dependent deformations and stresses were determined followed by the speed-dependent natural frequencies. The FE-code FERAS was applied where finite shell elements (FERAS/S) were used for the impeller and beam elements for the shaft. The results were compared with those from the FE-code NISA [12]. Details about the calculation and the numerical results are given in [7].

For the calculation of the natural frequencies of the one noded diameter mode of the impeller, the described technique of combination of the rotor dynamic and structure dynamics model was used. A first calculation was formed by a rigid coupling of the impeller on the shaft (FEROS $k = \infty$) followed by a second calculation where the rigid disk was connected elastically on the shaft by a speed-independent stiffness of the rotational spring (FEROS $k = 2.22\ 10^5$ N/mm) and a third one with speed-dependent stiffness (FEROS $k = 2.22 - 4.15\ 10^5$ N/mm).

The results of the natural frequency calculations of the one-nodal diameter mode are plotted in Fig. 7 referred to the rotating coordinate k-system.

For the transformation to the i-system, the speed of rotation Ω must be added to the frequency of forward mode ω_k^{gl} and subtracted from the frequencies of the backward mode ω_k^{gg}:

$$\omega_i^{gl} = \omega_k^{gl} + \Omega$$

$$\omega_i^{gg} = \omega_k^{gg} - \Omega \qquad (26)$$

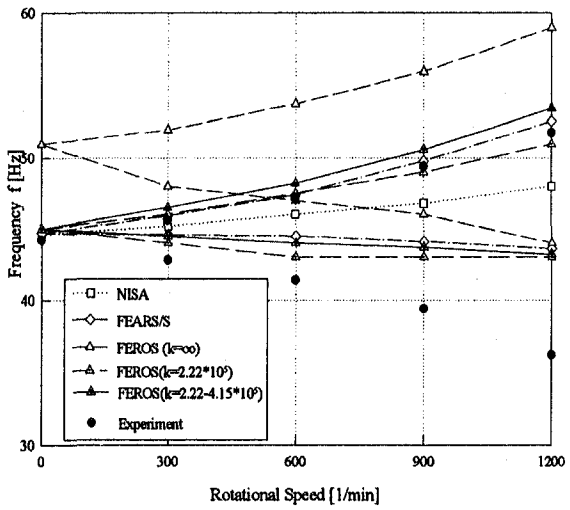


Fig. 7 Natural frequencies as function of rotational speed (K-system)

First, the increasing branches of the natural frequencies are considered, which describe the backward mode due to the description in the k-system. The lost values of these natural frequencies follow from the FE-calculation by the commercial FE-code NISA [12] because this program considers only the prestress effects due to rotation but not the gyroscopic effects. The highest values for the backward mode result from the rotor dynamic calculation by the FE-code FEROS with a rigid connection of the impeller to the shaft. The best agreement between experimental results [13] and the numerical results by the combined technique of rotor dynamic and structural dynamics calculations are described in the previous chapter in the case where speed-dependent rotational spring constants (FEROS $k = 2.22–4.15\ 10^5$N/mm) are used.

The difference between results of speed-independent and speed-dependent spring constants is approximately 5 percent. The decreasing branches of natural frequency that describe the forward mode in the case system show a good agreement between all numerical results. However, the experimental values show deviations that probably are a consequence of the elastic orthotropic real support conditions of the test rig, which was not considered in all the numerical calculations.

6 Conclusions

Numerical calculation of the natural frequencies of a rotating impeller on an elastic shaft was presented. The applied technique of the combination of a structure dynamic and a rotor dynamic model allows the simultaneous consideration of prestress effects due to rotation and gyroscopic influences. The numerically calculated results were compared with experimental values. By the presented technique it was shown how by introducing an equivalent speed-dependent rotational stiffness between the impeller and the shaft, the prestress centrifugal effect in the rotating structures can be taken into consideration in a rotor dynamic model.

References

1 Argyris, J., and Mlejnek, H.-P., "Die Methode der Finiten Elemente," Vol. I, Vieweg Verlag, 1986.

2 Argyris, J., and Mlejnek, H.-P., "Die Methode der Finiten Elemente," Vol. III, Vieweg Verlag, 1988.

3 Senker, P., "Stabilitätstheorie elastischer Rotorsysteme," Institut für Angewandte Mechanik, Universität Braunschweig, 1993.

4 Staudinger, G., "Eigenschwingungen eines schnellaufenden Rotors mit deformierbaren Scheibenläufern," Technische Universität Wien, 1992.

Downloaded 02 Jun 2010 to 171.66.16.105. Redistribution subject to ASME license or copyright; see http://www.asme.org/terms/Terms_Use.cfm

5 Brückner, G., and Mench, H., "Entwicklung des Finite Elemente Programmsystems FEROS zur dynamischen Berechnung von Rotoren," Thesis, Institut für Mechanik, Universität Gh Kassel, 1989.

6 Grimm, U., "Berechnung der freien und erzwungenen Biegeschwingungen von gleitgelagerten Rotoren mit elastisch befestigten Scheiben," Thesis, Institut für Mechanik, Universität Gh Kassel, 1993.

7 Hohlrieder, M., "Zur statischen und dynamischen Analyse rotierender elastischer Strukturen (Turbinenschaufeln, Verdichter) bei transienten Betriebsbedingungen," PhD Thesis, University of Kassel, 1994.

8 Mai, M.-M., "Zur nichtlinear statischen und dynamischen Berechnung gyroskopischer Schalen- und Balkenstrukturen mit der Finite-Elemente-Methode," PhD Thesis, Universität Stuttgart, 1985.

9 Berlioz, A., "Etude dynamique des structures a symetrie cyclique en rotation. Application a une roue de compresseur centrifuge," PhD Thesis, INSA Lyon, 1990.

10 Gasch, R., and Knothe, K., *Strukturdynamik, Vol. I, Diskrete Systeme,* Springer, 1987.

11 Gasch, R., and Knothe, K., *Strukturdynamik, Vol. II, Kontinua und ihre Diskretisierung,* Springer, 1989.

12 NISA: Engineering Mechanics Research Corporation, Troy, MI, USA, 1999.

13 Irretier, H., and Reuter, F., "Experimentelle Modalanalyse in rotierenden Maschinen," DFG-Abschlußbericht, Institut für Mechanik, Universität-Gh Kassel, 1994.

Downloaded 02 Jun 2010 to 171.66.16.105. Redistribution subject to ASME license or copyright; see http://www.asme.org/terms/Terms_Use.cfm

Synchronous Dynamics of a Coupled Shaft/Bearing/Housing System With Auxiliary Support From a Clearance Bearing: Analysis and Experiment

J. L. Lawen, Jr.

G. T. Flowers

Auburn University,
Auburn, AL 36849

This study examines the response of a flexible rotor supported by load sharing between linear bearings and an auxiliary clearance bearing. The objective of the work is to develop a better understanding of the dynamic behavior of a magnetic bearing supported rotor system interacting with auxiliary bearings during a critical operating condition. Of particular interest is the effect of coupling between the bearing/housing and shaft vibration on the rotor-dynamic responses. A simulation model is developed and a number of studies are performed for various parametric configurations. An experimental investigation is also conducted to compare and verify the rotor-dynamic behavior predicted by the simulation studies. A strategy for reducing sychronous shaft vibration through appropriate design of coupled shaft/bearing/housing vibration modes is identified. The results are presented and discussed.

Introduction

In recent years, the use of active magnetic bearings for supporting turbomachinery has been an area of interest for both academic researchers and turbomachinery users in industry. Magnetic bearings provide the potential for significant improvements over other types of rotor support, including elimination of wear and bearing friction-related energy losses as well as a means of actively suppressing rotor vibration. However, their use has been significantly limited due to a number of technical problems. A particular area of concern is the auxiliary bearing, which protects the soft iron core of the magnetic bearing and provides rotor support in case of overload or failure of the magnetic bearing.

Typically, the auxiliary bearings have relatively small clearances so that magnetic bearing rotor/stator contact does not occur during bearing failure or power loss. Due to these small clearances, contact between the rotor system and the auxiliary bearings can occur during standard operation of the magnetic bearings. When this occurs, load sharing between the magnetic bearings and the auxiliary bearings results, and the rotor system interacts with its auxiliary bearings. The dynamics of such an occurrence must be understood in order to design the auxiliary bearing system properly for a magnetic bearing supported rotor.

A number of different bearing types have been suggested as auxiliary bearings. These include bushings, rolling element bearings, and various types of journal bearings. The most commonly considered are rolling element bearings. The major disadvantage associated with using rolling element bearings (or bushings) is the requirement of a clearance between the rotor and the inner race of the bearing, without which many of the advantages associated with using magnetic bearings would be reduced or eliminated. This clearance introduces a nonlinear dynamic feature that may significantly impact the behavior of the rotor.

Contributed by the International Gas Turbine Institute and presented at the 40th International Gas Turbine and Aeroengine Congress and Exhibition; Houston, Texas, June 5–8, 1995. Manuscript received by the International Gas Turbine Institute February 22, 1995. Paper No. 95-GT-216. Associate Technical Editor: C. J. Russo.

There are quite a number of studies in the literature concerned with nonlinear rotordynamics. Ehrich (1965) and Ehrich and O'Conner (1967) studied the rotor/stator interaction with a clearance and found zones of bistable synchronous behavior. Black (1968) also found these bistable interaction zones. Ehrich extended this research by predicting subharmonic behavior (1966, 1988), superharmonic behavior (1992), and chaotic responses (1991). Bently (1974), Muszynska (1984), and Childs (1979, 1982) also observed and studied subharmonic responses due to clearance effects.

There is relatively little work available in the open literature that is specifically concerned with the dynamics between the rotor system and the auxiliary bearings. The research that has been performed to date is primarily concerned with the transient behavior of rotor drop on the auxiliary bearings due to power failure or inoperative magnetic bearings. Two papers with this focus are Gelin et al. (1990) and Ishii and Kirk (1991).

The present work is concerned with developing an understanding of the dynamic behavior of a rotor system supported by load sharing between the linear bearings and an auxiliary bearing with clearance. Of particular interest is the influence of coupled shaft/bearing/housing vibration modes on the rotor-dynamic behavior of such a system.

Simulation Model

Figure 1 shows the simulation model used for this investigation. It consists of a flexible rotor supported at both ends by magnetic bearings. A rigid disk with adjustable imbalance is placed at the midpoint of the bearing span. As a simplification, the magnetic bearings are modeled as spring and dashpot systems and interaction with a single auxiliary bearing is considered. The auxiliary bearing was modeled as an antifriction bearing with a clearance and a mass attached to a housing. The housing in turn has a mass, stiffness, and damping. Figure 2 shows the auxiliary bearing model used in the simulation.

The rotor is modeled using the free–free bending mode shapes and natural frequencies obtained through finite element analysis. The finite element code uses 19 stations and the first four modes (two rigid body and two flexible modes) are included in the simulation model.

Copyright © 1997 by ASME

Downloaded 02 Jun 2010 to 171.66.16.105. Redistribution subject to ASME license or copyright; see http://www.asme.org/terms/Terms_Use.cfm

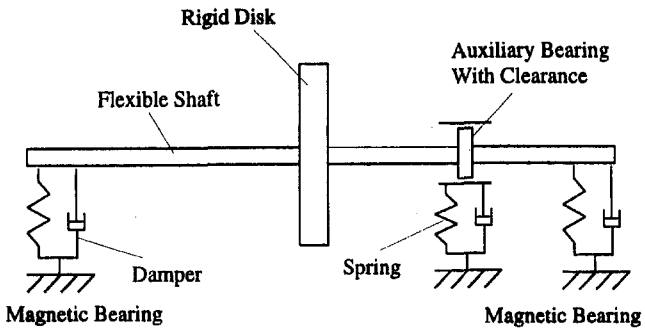


Fig. 1 Schematic diagram of simulation model

Using these simplifications, the equations of motion for the system can be written as follows:

$$\ddot{\mathbf{Q}}_x + \Omega\boldsymbol{\Gamma}\dot{\mathbf{Q}}_y + \omega_n^2\mathbf{Q}_x + \boldsymbol{\Phi}^T(F_{x,lin} + F_{x,nl}) = \boldsymbol{\Phi}^T F_{x,imb}, \quad (1a)$$

$$\ddot{\mathbf{Q}}_y - \Omega\boldsymbol{\Gamma}\dot{\mathbf{Q}}_x + \omega_n^2\mathbf{Q}_y + \boldsymbol{\Phi}^T(F_{y,lin} + F_{y,nl}) = \boldsymbol{\Phi}^T F_{y,imb}, \quad (1b)$$

$$M_b\ddot{X}_b + \frac{C_{bx}}{\Omega}(\dot{X}_b - \dot{X}_h) + K_{bx}(X_b - X_h) = F_{x,nl}, \quad (1c)$$

$$M_b\ddot{Y}_b + \frac{C_{by}}{\Omega}(\dot{Y}_b - \dot{Y}_h) + K_{by}(Y_b - Y_h) = F_{y,nl}, \quad (1d)$$

$$M_h\ddot{X}_h + \left(\frac{C_{bx}}{\Omega} + \frac{C_{hx}}{\Omega}\right)\dot{X}_h + (K_{bx} + K_{hx})X_h = \frac{C_{bx}}{\Omega}\dot{X}_b + K_{bx}X_b, \quad (1e)$$

$$M_h\ddot{Y}_h + \left(\frac{C_{by}}{\Omega} + \frac{C_{hy}}{\Omega}\right)\dot{Y}_h + (K_{by} + K_{hy})Y_h = \frac{C_{by}}{\Omega}\dot{Y}_b + K_{by}Y_b, \quad (1f)$$

where

$$\mathbf{F}_{x,lin} = \boldsymbol{\Phi}_{N_{b1}}\left(K_{xl}\mathbf{Q}_x + \frac{C_{xl}}{\Omega}\dot{\mathbf{Q}}_x\right) + \boldsymbol{\Phi}_{N_{b2}}\left(K_{xr}\mathbf{Q}_x + \frac{C_{xr}}{\Omega}\dot{\mathbf{Q}}_x\right)$$

$$\mathbf{F}_{y,lin} = \boldsymbol{\Phi}_{N_{b1}}\left(K_{yl}\mathbf{Q}_y + \frac{C_{yl}}{\Omega}\dot{\mathbf{Q}}_y\right) + \boldsymbol{\Phi}_{N_{b2}}\left(K_{yr}\mathbf{Q}_y + \frac{C_{yr}}{\Omega}\dot{\mathbf{Q}}_y\right)$$

$$\mathbf{F}_{x,imb} = \psi\Omega^2\cos\Omega t,$$

$$\mathbf{F}_{y,imb} = \psi\Omega^2\sin\Omega t,$$

$$\mathbf{F}_{x,nl} = \phi K_c(\delta - \Delta)\left(\frac{\boldsymbol{\Phi}\mathbf{Q}_x - X_b}{\delta}\right)$$

$$\mathbf{F}_{y,nl} = \phi K_c(\delta - \Delta)\left(\frac{\boldsymbol{\Phi}\mathbf{Q}_y - Y_b}{\delta}\right)$$

$$\delta = \sqrt{(\boldsymbol{\Phi}\mathbf{Q}_x - X_b)^2 + (\boldsymbol{\Phi}\mathbf{Q}_y - Y_b)^2},$$

$$\phi = 1 \text{ if } \delta > \Delta$$

$$0 \text{ otherwise}$$

$$\mathbf{Q}_x = \boldsymbol{\Phi}^{-1}\mathbf{X}_r,$$

$$\mathbf{Q}_y = \boldsymbol{\Phi}^{-1}\mathbf{Y}_r,$$

with

$$\mathbf{X}_r = \{X_{r1}, X_{r2}, \ldots, X_{rm}\}^T,$$

$$\mathbf{Y}_r = \{Y_{r1}, Y_{r2}, \ldots, Y_{rm}\}^T.$$

(m = total number of nodes)

The physical displacements of the rotor at the auxiliary bearing or magnetic bearing locations can be obtained using the following coordinate transformation:

$$X_{rk} = \sum_{i=1}^{N} \Phi_{ki}Q_{xi},$$

$$Y_{rk} = \sum_{i=1}^{N} \Phi_{ki}Q_{yi}, \quad (k = N_{b1}, N_{b2}, N_{b3})$$

Experimental Model

Experimental tests were performed in order to validate the behavior predicted by the simulation model and to gain some insight into the dynamic responses that are to be expected. A

Nomenclature

C = damping, N-s/m
K = stiffness, N/m
M_b = auxiliary bearing mass, kg
M_h = housing mass, kg
N = total number of modes considered
N_{b1} = node number at leftmost bearing
N_{b2} = node number at rightmost bearing
N_{b3} = node number at auxiliary clearance bearing
$\mathbf{Q}_x$ = rotor modal coordinate vector in X direction
$\mathbf{Q}_y$ = rotor modal coordinate vector in Y direction
t = time, s
X_r = rotor physical coordinate vector in X direction, m
Y_r = rotor physical coordinate vector in Y direction, m
X_b = auxiliary bearing physical coordinate vector in X direction, m
Y_b = auxiliary bearing physical coordinate vector in Y direction, m
X_h = housing physical coordinate vector in X direction, m
Y_h = housing physical coordinate vector in Y direction, m
Δ = radial clearance in auxiliary bearing, m
$\mathbf{I}_a$ = rotor polar mass inertia matrix, kg-m^2
$\boldsymbol{\Psi}$ = rotor free–free modal rotation matrix
Φ = rotor free–free modal displacement matrix
$\boldsymbol{\Gamma} = \boldsymbol{\Psi}^T\mathbf{I}_a\boldsymbol{\Psi}$
Ω = rotor operating speed, rad/s
ω_n = matrix of rotor free–free natural frequencies, rad/s
ψ = imbalance vector, kg-m

Subscripts

bx = auxiliary bearing, x direction
by = auxiliary bearing, y direction
c = contact
hx = housing, x direction
hx = housing, y direction
xr = rightmost bearing, x direction
xl = leftmost bearing, x direction
yr = rightmost bearing, y direction
yl = leftmost bearing, y direction

Downloaded 02 Jun 2010 to 171.66.16.105. Redistribution subject to ASME license or copyright; see http://www.asme.org/terms/Terms_Use.cfm

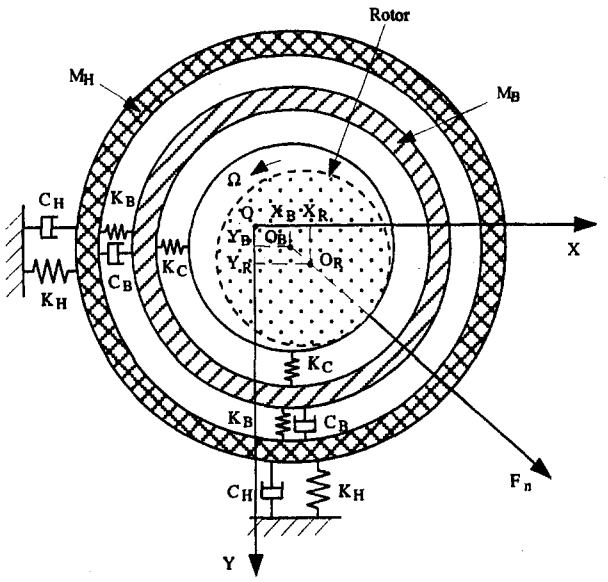


Fig. 2 Auxiliary bearing model

schematic diagram of the rotor test rig that was used in the experimental work is shown in Fig. 3.

The rotor used in this study has two basic components: a flexible shaft and an auxiliary clearance bearing. The shaft is made of steel and is 9.5 mm (0.374 in.) in diameter and 0.46 m (18.0 in.) in length. It is supported at 25.4 mm (1.0 in.) from the right end by ball bearings suspended in a frame by four springs and at 25.4 mm (1.0 in.) from the left end by a bushing with a tight clearance. These supports represent the magnetic bearings. The stiffness of the left support is 17511 N/m (101.5 lb/in.) for both the horizontal and vertical directions. It is used to isolate the rotor somewhat from the effects of the flexible coupling that attaches the rotor to the motor and to enforce low amplitude vibration at this location to protect the motor. The stiffness of the right support, for both horizontal and vertical directions, is 2539 N/m (14.5 lb/in.). This lower stiffness allows for significant vibration of the rotor in the speed range of the motor. A rigid disk with an adjustable imbalance is placed at the midpoint of the bearing span. The auxiliary clearance bearing/housing consists of a bushing suspended in a frame by four springs (Fig. 4). It is situated at the right end of the rotor. The clearance is adjustable by changing the bushing. The auxiliary bearing/housing stiffnesses are varied by interchanging the springs.

The rotor is driven by an adjustable speed motor with a feedback speed controller. Shaft vibration is measured using eddy current proximity displacement sensors fixed so as to measure displacement in the vertical and horizontal directions. The displacement signals were recorded and analyzed with a signal analyzer.

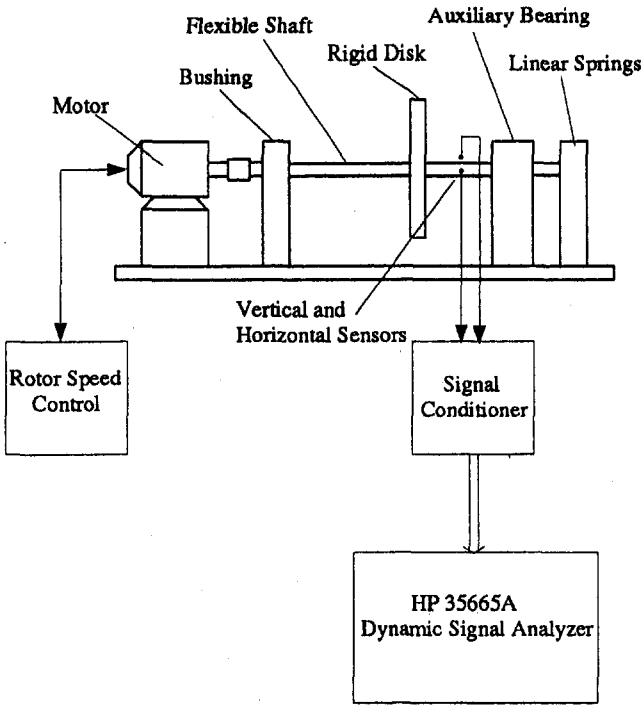


Fig. 3 Experimental model

Discussion

A series of parallel studies were conducted using the simulation and experimental models discussed in the preceding sections. The following discussion is aimed at comparing the predictions of the simulation model with experimentally observed responses, with the objective of obtaining insight into the behavior of flexible rotor system dynamics due to load sharing between the magnetic bearings and an auxiliary bearing.

Using the data from measurements and calculations, the stiffness, damping, and mass characteristics of the experimental rotor system were identified. The imbalance configuration consists of 3.0×10^{-6} kg-m located at the left end of the rotor shaft (from the flexible coupling to the electric motor) and a variable imbalance located on the rigid disk. Linear, hysteretic, and Coulomb friction damping models were considered. The support damping appears to result principally from hysteresis. If synchronous vibration is assumed, this results in a damping coefficient scaled by the rotor speed. The numerical values are given in Table 1.

The governing parameters for an auxiliary bearing are stiffness, mass, damping, clearance, and axial location. The axial location generally is fixed by other considerations, such as space requirements and the need to be close to the magnetic bearing to better protect it. This study focuses on the remaining design parameters. For the system studied, significant nonsynchronous vibration occurred only for the 2ω component and for a limited rotor speed range. Figure 5 illustrates the observed behavior for various imbalance values. The amplitudes are quite small and, interestingly, virtually independent of imbalance. The remainder of this discussion will focus on the synchronous response amplitudes.

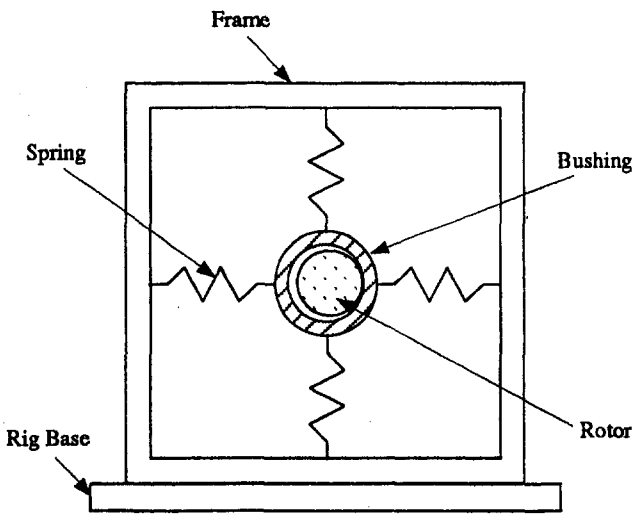


Fig. 4 Auxiliary clearance bearing

Downloaded 02 Jun 2010 to 171.66.16.105. Redistribution subject to ASME license or copyright; see http://www.asme.org/terms/Terms_Use.cfm

Table 1 Simulation model parameters

Parameter	Value	Units
K_b	471	N/m
K_h	$1.8x10^7$	N/m
K_c	87,557	N/m
K_{lx}, K_{ly}	17,510	N/m
K_{rx}, K_{ry}	2,539	N/m
C_{lx}, C_{ly}	1,000	N/m
C_{rx}, C_{ry}	500	N/m
C_{ly}, C_{ly}	1,000	N/m
C_{ry}, C_{ry}	500	N/m
C_{bx}, C_{by}	2,000	N/m
C_{hx}, C_{hy}	0	N/m
M_b	0.033	kg
M_h	0.296	kg
ψ_1	3.0×10^{-6}	kg-m
ψ_{10}	2.5×10^{-5}	kg-m
Δ	$5.0x10^{-5}$	m

The simulation responses discussed below were determined from a single-term harmonic balance analysis that was numerically implemented and verified at selected points using direct numerical integration of the governing equations of motion. The harmonic balance procedure is described by Nayfeh and Mook (1979). Figures 6(a–e) show the response amplitudes predicted from the simulation study for the parameters of Table 1. Figures 7(a–c) show some corresponding experimental results. The rotor speed range extends to above the second critical speed, with the first critical speed primarily a rotational mode and the second critical speed primarily a translational mode.

Figure 6(a) presents simulation results for varying auxiliary bearing stiffness and Fig. 7(a) shows the corresponding experimental values. There is relatively good agreement between the actual and predicted responses, except for the peak values, which are very sensitive to damping. At lower rotor speeds, the stiffness effect from the auxiliary bearing tends to dominate and serves to increase the effective lower critical speed. At higher rotor speeds, the inertial effects of the bearing tend to dominate and the added mass serves to lower the effective second critical speed. This effect is balanced somewhat for higher stiffnesses (as is expected), as can be seen for the case with K_b = 2625 N/m. The damping added to the system from the auxiliary bearing serves to attenuate the peak response amplitudes for both critical speeds. The response amplitudes between the two response peaks are affected little by the auxiliary bearing, with the rotor and bearing/housing vibrations tending

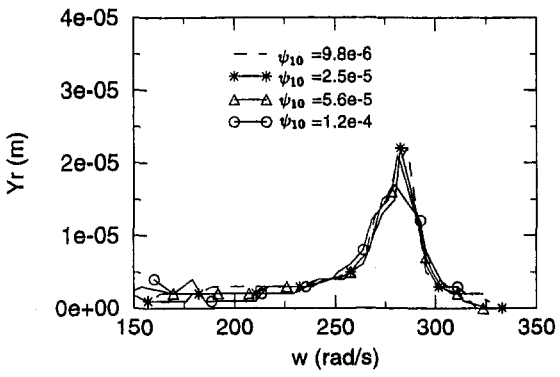


Fig. 5 Experimental results for 2ω component

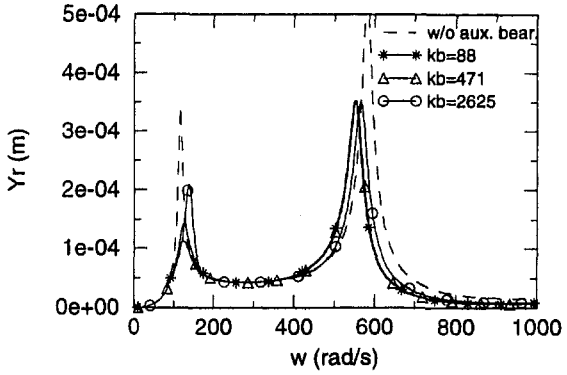


Fig. 6(a) Simulation results for varying auxiliary bearing stiffness

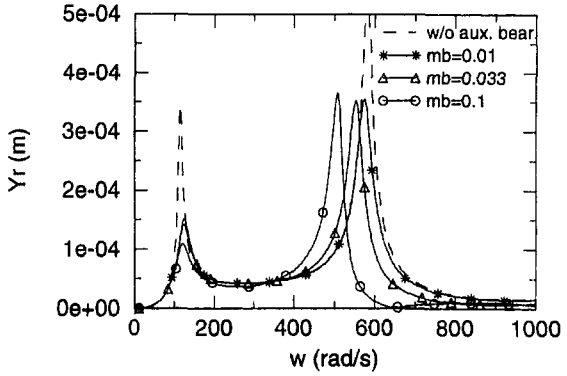


Fig. 6(b) Simulation results for varying auxiliary bearing mass

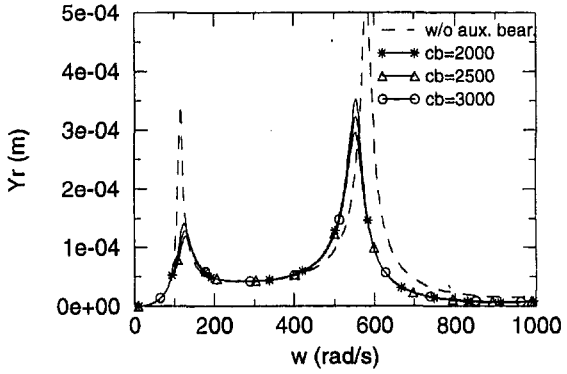


Fig. 6(c) Simulation results for varying auxiliary bearing damping

to decouple for response amplitudes below the clearance. Above the second critical speed, the presence of the auxiliary bearing serves to reduce the response amplitudes for the remainder of the plot. For this region, there is significant coupling between the rotor/bearing/housing vibration and the response amplitudes are below the clearance for speeds greater than about 550 rad/s. The rotor speed ranges for which coupling of the rotor/bearing/housing vibration will occur depend upon the phase of the combined system response, as described by Black (1968). For the purposes of this study, K_b = 471 N/m is chosen as a reasonable value and variations of other parameters are performed with this auxiliary bearing stiffness.

Figure 6(b) shows the predicted rotor response for the parameters of Table 1 with the bearing mass varied. These results show that the more massive bearing/housing configurations can result in much lower amplitude rotor responses. In fact, for sufficiently high mass values, the response amplitude is dramatically reduced for the rotor speed range from about 600 rad/s to about 780 rad/s, where it merges with other amplitude response curves. Figure 6(c) shows the effect of auxiliary bearing damping on the rotor response. While the response amplitudes remain

Downloaded 02 Jun 2010 to 171.66.16.105. Redistribution subject to ASME license or copyright; see http://www.asme.org/terms/Terms_Use.cfm

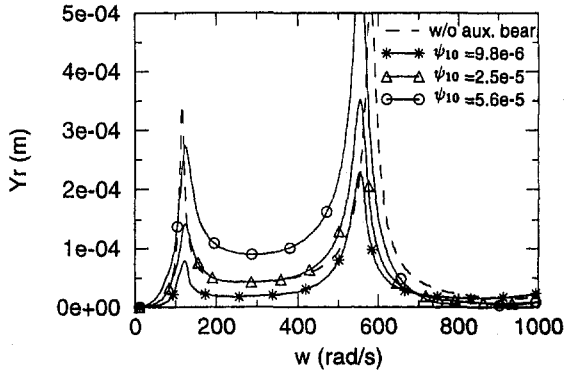


Fig. 6(*d*) Simulation results for varying imbalance

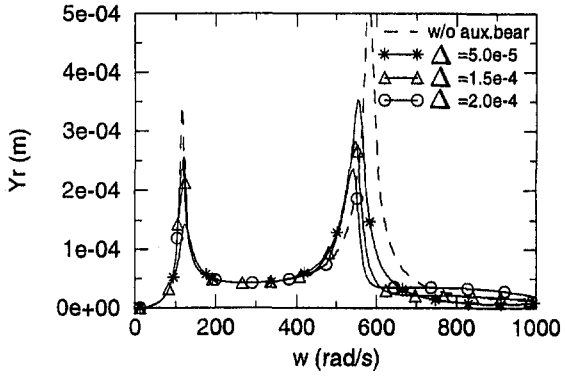


Fig. 6(*e*) Simulation results for varying auxiliary bearing clearance

relatively unchanged for the majority of rotor speeds, higher damping does serve to reduce the rotor response amplitudes significantly through the critical speeds. Damping also affects the phase characteristics of the combined rotor/bearing/housing system and changes the rotor speed ranges for which coupled responses occur. Figures 6(*d*) and 7(*b*) show the rotor response for the parameters of Table 1 with the imbalance varied. As expected, the response amplitudes increase with increasing imbalance. Figures 6(*e*) and 7(*c*) show the rotor response amplitudes with the auxiliary bearing clearance varied. As the clearance increases, the dynamics of the combined rotor/bearing/housing vibration tend to decouple over a wider speed range between the two critical speeds. Again, such behavior is expected from the analysis work for a rotor operating in an annular clearance performed by Black (1968).

Close examination of these results reveals a very interesting trend. Turbomachines are designed to operate at rotor speeds between the various system critical speeds so as to minimize synchronous response amplitudes. For the present system, the lowest amplitude responses (for operation above the second critical speed) occur for the auxiliary bearing configurations where there is the largest decrease of the second effective critical speed, which is due to a coupling of rotor/stator/housing vibration. While not really suprising, this result indicates an interesting strategy for the design of auxiliary support using clearance bearings. Selection of combined shaft/auxiliary bearing/housing vibration characteristics such that the effective critical speeds nearest the operating speed (directly above and below) shift away from it should result in lower amplitude rotor vibration and provide the best opportunity to protect the magnetic bearing. However, the phase characteristics of the combined system must be such that vibration coupling occurs and care must be taken to ensure that this is the case if the maximum benefit is to be derived from the auxiliary bearing.

Conclusions

A study of the dynamic behavior of a flexible rotor supported by linear bearings (representing a set of magnetic bearings) and an auxiliary bearing with clearance has been presented. Parallel simulation and experimental studies have been performed for a variety of parametric configurations. The influence of bearing mass, stiffness, damping, clearance, and imbalance were examined. It was observed that the dynamic behavior of a rotor interacting with an auxiliary bearing depends very strongly on the structural parameters of the auxiliary bearing and associated housing. Appropriate selection of these parameters is critical if acceptable vibration characteristics are to be obtained for such systems. In general, one must carefully consider the influence of housing/bearing dynamics and how best to take advantage of favorable coupled modes of vibration in the development of auxiliary bearing designs.

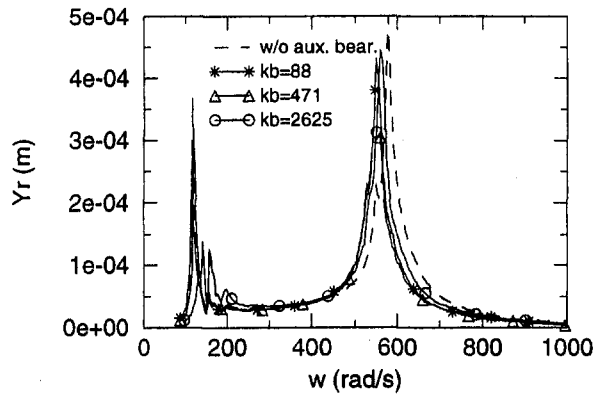


Fig. 7(*a*) Experimental results for varying auxiliary bearing stiffness

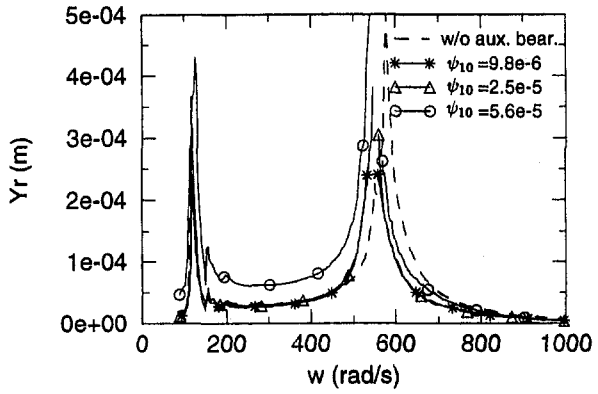


Fig. 7(*b*) Experimental results for varying imbalance

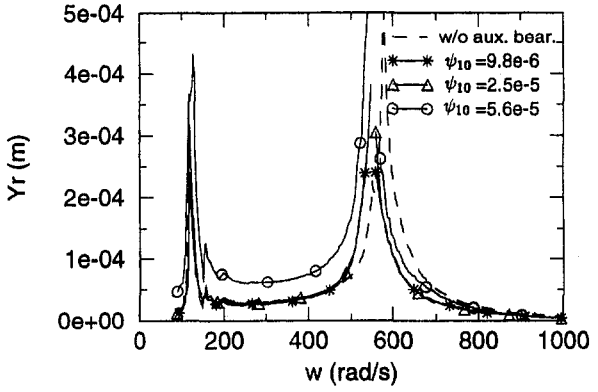


Fig. 7(*c*) Experimental results for varying auxiliary bearing clearance

Acknowledgments

This work was supported by NASA under Grant No. NGT-70312 and Grant No. NAG3-1507. The Government has certain rights in this material. Appreciation is expressed to S. C. Sinha,

Downloaded 02 Jun 2010 to 171.66.16.105. Redistribution subject to ASME license or copyright; see http://www.asme.org/terms/Terms_Use.cfm

S. G. Ryan, and A. F. Kascak for their advice and assistance in this research effort.

References

Bently, D. E., 1974, "Forced Subrotative Speed Dynamic Action of Rotating Machinery," ASME Paper No. 74-PET-16.

Black, H. F., 1968, "Interaction of a Whirling Rotor With a Vibrating Stator Across a Clearance Annulus," *Journal Mechanical Engineering Science,* Vol. 10, No. 1, pp. 1–12.

Childs, D. W., 1979, "Rub-Induced Parametric Excitation in Rotors," ASME *Journal of Mechanical Design,* Vol. 101, pp. 640–644.

Childs, D. W., 1982, "Fractional-Frequency Rotor Motion Due to Nonsymmetric Clearance Effects," ASME JOURNAL OF ENGINEERING FOR POWER, Vol. 104, pp. 533–541.

Ehrich, F. F., 1965, "Bistable Vibrations of Rotors in Bearing Clearance," ASME Paper 65-WA/MD-1.

Ehrich, F. F., 1988, "High Order Subharmonic Response of High Speed Rotors in Bearing Clearance," ASME *Journal of Vibration, Acoustics, Stress, and Reliability in Design,* Vol. 110, pp. 9–16.

Ehrich, F. F., 1992, "Observations of Subcritical Superharmonic and Chaotic Response in Rotordynamics," ASME *Journal of Vibration and Acoustics,* Vol. 114, pp. 93–100.

Ehrich, F. F., 1991, "Some Observations of Chaotic Vibration Phenomena in High-Speed Rotordynamics," ASME *Journal of Vibration, Acoustics, Stress, and Reliability in Design,* Vol. 113, pp. 50–57.

Ehrich, F. F., 1966, "Subharmonic Vibration of Rotors in a Bearing Clearance," ASME Paper No. 66-MD-1.

Ehrich, F. F., and O'Conner, J. J., 1967, "Stator Whirl With Rotors in Bearing Clearance," ASME *Journal of Engineering for Industry,* Vol. 89, pp. 381–390.

Gelin, A., Pugnet, J. M., and Hagopina, J. D., 1990, "Dynamic Behavior of Flexible Rotors With Active Magnetic Bearings of Safety Auxiliary Bearings," *Proc. 3rd International Conference on Rotordynamics,* Lyon, France, pp. 503–508.

Ishii, T., and Kirk, R. G., 1991, "Transient Response Technique Applied to Active Magnetic Bearing Machinery During Rotor Drop," *Rotating Machinery and Vehicle Dynamics,* ASME DE-Vol. 35, pp. 191–199.

Muszynska, A., 1984, "Partial Lateral Rotor to Stator Rubs," IMechE Paper No. C281/84.

Nayfeh, A. H., and Mook, D. T., 1979, *Nonlinear Oscillations,* Wiley, pp. 59–61.

Ryan, S. G., 1991, "Limit Cycle Vibrations in Turbomachinery," NASA Technical Paper 3181.

Downloaded 02 Jun 2010 to 171.66.16.105. Redistribution subject to ASME license or copyright; see http://www.asme.org/terms/Terms_Use.cfm

Modeling and Simulation Methods for MDOF Structures and Rotating Machinery With Impact Dampers

J. M. McElhaney

A. Palazzolo

Department of Mechanical Engineering,
Texas A&M University,
College Station, TX 77843

A. Kascak

US Army at NASA-Lewis,
Cleveland, OH 44135

Previously published work on applied impact damping typically relates to SDOF models or simple MDOF models such as the classical cantilever beam. Structural models often require an extremely large number of DOF with mode shapes that are generally very complex. Dynamics simulation of these typically becomes both complicated and time consuming. The nonlinear behavior of impact dampers further complicates such simulation in that standard linear solutions are not possible. The primary objective in this research extends previous work by applying impact dampers to MDOF structures that are modeled with general three-dimensional "beam" finite elements. Modal-based models of the MDOF systems and efficient impact damper tracking algorithms were also developed that significantly reduced CPU time for simulation. Significant among the objectives was obtaining an impact damper design for the MDOF casing structure of the Space Shuttle Main Engine (SSME), High-Pressure Oxygen Turbo-Pump (HPOTP), subject to pump rotor shaft unbalance. Impact damper performance is based on suppression of vibration at casing critical frequencies for rotor speed ranges, at rotor full speed, and very high unbalance to simulate a defect such as losing an impeller blade fragment or a cracked bearing [6]. Simulations show significant reductions in vibration at the casing critical frequencies and very high unbalance levels while little or no improvement was observed off resonance. Additionally, the previous work with an experimental rotor bearing system (RBS) and impact damper was modeled using the developed modal-based methods. Simulation of the resulting model response shows remarkable agreement with the experimental. Finally, both the RBS and the HPOTP were modeled and simulated as unstable systems with attached impact dampers. The simulations predict that the impact damper is an excellent stabilizing mechanism for a range of instability driver values. Simulation of the models in this research with the developed modal based algorithms were accomplished with excellent efficiency, and accurate results.

1 Introduction

Most practical structural models require MDOF representation for accurate simulation results. Thus the current work extends impact damper modeling to MDOF systems. All models for this work are developed with three-dimensional "beam" finite elements. One MDOF structure developed in this work is the space shuttle main engine, high-pressure oxygen turbopump (HPOTP) casing.

Small HPOTP rotor unbalance causes vibration of the casing, which can be significantly amplified at critical frequencies or with a small defect such as the loss of an impeller fragment. The vibration can be reduced by adapting some form of damping to the casing, which is difficult given the lack of space for attachment and the extreme temperature environment. One solution to this problem is to adapt an impact damper to the pump casing.

The impact damper consists of a housing cavity fixed to a structure with an internal impactor that moves relative to the cavity walls. Collisions between the housing and impactor attenuate vibration by dissipating the structure's kinetic energy. An advantage of the impact damper is that it is an inertial device, as opposed to conventional dampers, which require an attachment to ground. Considering temperature constraints, previous work by Nale and Klusman [1], and Moore and Palazzolo [2] confirms the effectiveness of the impact damper in high and cryogenic temperature environments, respectively. In addition, Radil and Palazzolo show only small variation in the COR as a function of temperature and impact velocity for readily available materials. Considering these advantages, the impact damper should serve as an ideal retrofit device.

The focus of this work will thus be to model and simulate MDOF structures with impact dampers to determine their benefits in vibration. Correlation studies of previous work [2] with impact dampers applied to a SDOF oscillator and an experimental RBS with flexible bearing supports are conducted. HPOTP reduction in vibration at casing critical frequencies, at steady rotor speed, and high levels of rotor unbalance with impact dampers is investigated as well.

Simulating a time response for large DOF systems often requires CPU time that is very impractical. This provided the motivation to develop an efficient modal-based method for simulating the impact damper with general MDOF systems. Since steady-state, nonlinear solutions such as the Harmonic Balance or Collocation methods require iterative searches within the clearance of the impact damper, the frequency response was then obtained by conducting transient forced responses out to a steady amplitude for a range of frequencies. The improvement in simulation efficiency of modal-based solutions would then

Contributed by the International Gas Turbine Institute and presented at the 40th International Gas Turbine and Aeroengine Congress and Exhibition, Houston, Texas, June 5–8, 1995. Manuscript received by the International Gas Turbine Institute March 2, 1995. Paper No. 95-GT-397. Associate Technical Editor: C. J. Russo.

Copyright © 1997 by ASME

Downloaded 02 Jun 2010 to 171.66.16.105. Redistribution subject to ASME license or copyright; see http://www.asme.org/terms/Terms_Use.cfm

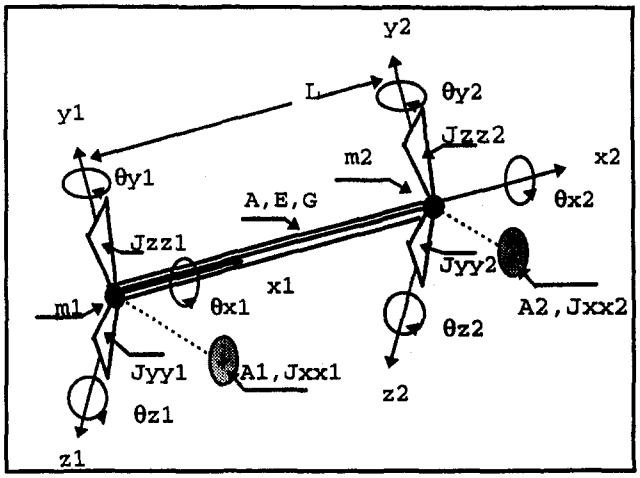


Fig. 2.1.1 Three-dimensional beam finite element configuration

be beneficial. Additionally, most of the previous work published on impact dampers relates SDOF applications or MDOF applications to more classical examples such as the cantilever beam. In previous work, an assumption was usually made as to the number of impacts that occur per cycle of vibration, which isn't done for the present work. The present work thus extends previous work to more general MDOF structures with impact dampers.

The effects of an impact between the impactor mass and a MDOF structure are accounted for by applying conservation of momentum (COM) and coefficient of restitution (COR) relationships between the impactor mass and the lumped mass at the impactor location in the MDOF model. This is justified by assuming that the impact occurs over an infinitesimal time duration. The impulse (Force × Time) product exerted on the remaining part of the MDOF system is zero since the reaction forces between the impactor housing and the structure are finite, but the impulse duration is infinitesimal. This assumption has been validated by the author in simulating the contact dynamics of an impactor applied to the HPOTP structure. Excellent agreement between the contact dynamics model using a very large surface stiffness and the COR/COM model with COR of 1.0 confirmed the COR/COM model approach.

2 Modeling

2.1 Finite Element Modeling. All finite element models for this work are constructed using three-dimensional "beam" type elements. An example of a single-beam element and its associated DOF configuration is shown in Fig. (2.1.1). where the element DOF vector in local frame coordinates is

Table 2.2.1 CPU time comparison between MDOF physical and modal subspace models

Model	Time Step (μ sec)	Real Time per Simulation Time	
Full 126 DOF	50	4.5	min.
	5	48	min.
Modal System	50	4.2	sec.
	10	21.7	sec.
	5	40	sec.

$$U_{e,L} = [x_1 y_1 z_1 \theta_{x1} \theta_{y1} \theta_{z1} x_2 y_2 z_2 \theta_{x2} \theta_{y2} \theta_{z2}]^T \quad (2.1.1)$$

Beam element inertia is modeled as a lumped parameter, while the stiffness matrix includes compensation for shear deformation. For the physical coordinate-based models, dampers are uncoupled and concentrated. Modal space models are assigned "tare" damping to individual modes. The usual element-to-global transformations are employed for system assembly, resulting in

$$[M_G]\ddot{U}_G + [C_G]\dot{U}_G + [K_G]U_G = F_G(t) \quad (2.1.2)$$

2.2 Modal Space Modeling. The uncoupled system equations result with a modal transform of Eq. (2.1.2) with use of Eq. (2.2.1).

$$U = [\Phi]q \quad (2.2.1)$$

where $[\Phi]$ is the modal matrix of (Eq. 2.1.2), and (q) is the modal coordinate vector. Substituting (U) into Eq. (2.1.2) and multiplying through by $[\Phi]^T$ results in

$$[\Phi]^T[M_G][\Phi]\ddot{q} + [\Phi]^T[C_G][\Phi]\dot{q} + [\Phi]^T[K_G][\Phi]q = [\Phi]^T F_G(t) \quad (2.2.2)$$

where the ith modal coordinate equation is described by

$$m_i\ddot{q}_i + 2\zeta_i m_i \omega_i \dot{q}_i + m_i \omega_i^2 q_i = F_i(t) \quad (2.2.3)$$

Simulation is conducted in the modal subspace with good accuracy and large reductions in CPU time due to truncation of the higher modes. Table 2.2.1 compares the CPU time to simulate the forced response between the full MDOF physical coordinate, and modal subspace HPOTP model, where the modal subspace included the first ten modes.

The ten-mode model was employed to replicate the filtering system on the HPOTP tests. Simulation results between the modal model and the full DOF physical coordinate model were almost identical.

2.3 SDOF Impact Damper Modeling. Three different structures were simulated in this study to include a MDOF cantilever beam, a rotor shaft system with asymmetric bearing supports, and the HPOTP casing. The dynamic coupling for

Nomenclature

IPS = Impacts Per Second
HGM = Hot Gas Manifold
FEM = Finite Element Model
RBS = Rotor Bearing System
HPOTP = High-Pressure Oxygen Turbo-Pump
IDC = Impact Damped Cantilever Beam
SSME = Space Shuttle Main Engine
MDOF = Multiple Degree of Freedom
SDOF = Single Degree of Freedom
FFT = Fast Fourier Transform
EOM = Equations of Motion
COM = Conservation of Momentum
COR = Coefficient of Restitution
q, U = modal and physical coordinates
M, C, K, F = Mass, Damping, Stiffness, Force
E = Linear Elastic Modulus
J, I = Mass and Area Moment of Inertia
A, L = Area, Length
F = Modal Matrix
ω = angular velocity
ζ = damping ratio
μ = mass ratio
t = time
e = coefficient of restitution
D = Impact Damper Clearance Gap
IC = Initial Conditions

Downloaded 02 Jun 2010 to 171.66.16.105. Redistribution subject to ASME license or copyright; see http://www.asme.org/terms/Terms_Use.cfm

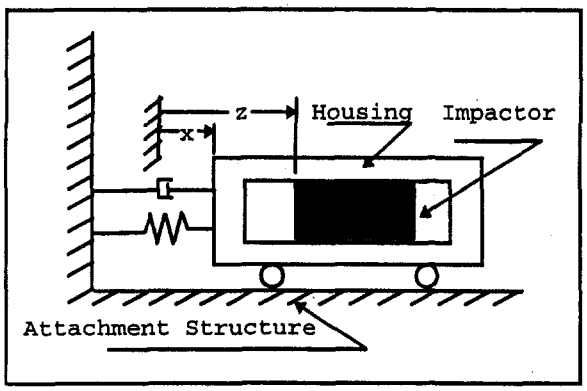


Fig. 2.3.1 Zero friction SDOF impact damper model

these structures has been verified to be negligible; thus the SDOF damper is applied independently for each coordinate.

The SDOF impact damper consists of a housing cavity fixed to a structure and an impactor moving relative to the cavity walls as shown in Fig. 2.3.1.

The impact damper is physically characterized by the mass of both the housing and impactor, and the clearance that defines the gap between them with the impactor against a cavity wall. Kinetic energy of the vibrating structure is dissipated by collisions between the housing and impactor in the form of elastic waves, heat, and sound. Damping performance depends on several factors to include amplitude range, impactor to housing mass ratio, clearance gap, and the COR of the impacting materials. Performance for a given damper is thus primarily a function of the amplitude range, where for very low and high amplitude ranges, the impact damper is generally less effective. Between these ranges, regular impacts each half cycle of vibration occur leading to more optimal performance.

A free decay response with an initial condition was simulated for the model in Fig. 2.3.1 to illustrate the behavior in these ranges. For very low amplitudes, less impactor contact is made with the housing, where the absence of regular impacts each half cycle of vibration results. This is commonly referred to as "impact failure" and is illustrated by Fig. 2.3.2 where the variables (X_{left} X_{right}) denote the boundaries of the impactor. Their difference defines the damper clearance.

For very high amplitudes with the housing moving toward the impactor, the impactor spends much time "bouncing" on one of the walls of the housing where the impactors kinetic

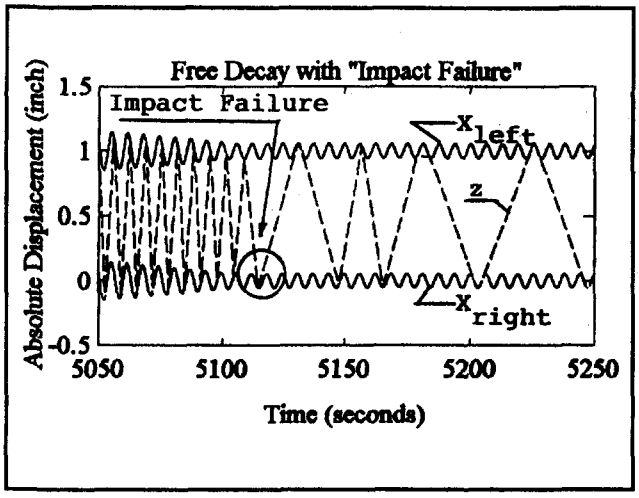


Fig. 2.3.2 SDOF model free decay response with impactor showing 'impact failure' (COR = 0.6, μ = 0.01)

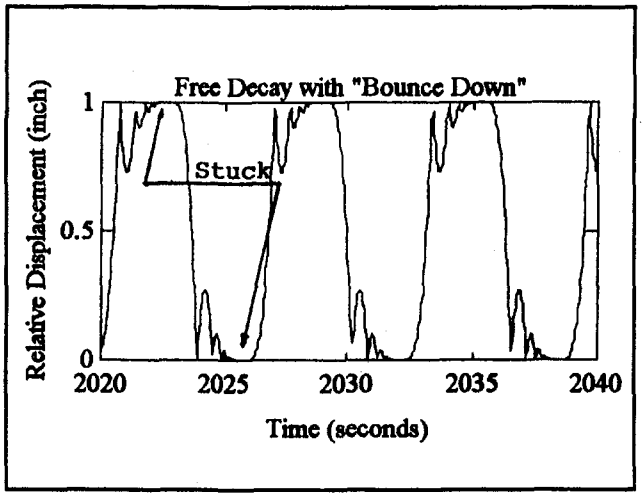


Fig. 2.3.3 SDOF model free decay response with impactor, showing "bounce down" (COR = 0.6, μ = 0.01)

energy drops through collisions. This phenomenon, commonly referred to as "bounce down," is illustrated in Fig. 2.3.3 for the same SDOF simulation.

Modeling the impact damper includes the impactor collisions with the housing, impactor motion between collisions, and the temporary condition when the impactor is "stuck" to a cavity wall. Collisions are modeled through use of COR/COM relationships where each impactor is modeled as a SDOF particle with no friction. The COR (Eq. (2.3.1)) and linear COM (Eq. (2.3.2)) result from integrating equal and opposite contact forces over the assumed infinitesimal impulse period,

$$e = (\dot{z}^+ - \dot{x}^+)/(\dot{z}^- - \dot{x}^-) \tag{2.3.1}$$

$$m_h\dot{x}^- + m_i\dot{z}^- = m_h\dot{x}^+ + m_i\dot{z}^+ \tag{2.3.2}$$

where the $(+/-)$ superscripts indicate velocities at the beginning and end of the impulse period, respectively.

Defining the impact damper mass ratio with

$$\mu = m_i/m_h \tag{2.3.3}$$

substituting into Eq. (2.3.2), and solving Eqs. (2.3.1) and (2.3.2) for the housing and impactor velocities just after impact leads to,

$$\dot{x}^+ = [(1 - \mu e)\dot{x}^- + \mu(1 + e)\dot{z}^-]/(1 + \mu) \tag{2.3.4}$$

$$\dot{z}^+ = [(1 - \mu e)\dot{x}^- + (\mu - e)\dot{z}^-]/(1 + \mu) \tag{2.3.5}$$

where with negligible friction after the collision, the impactor becomes a particle in free motion with constant velocity (z^+) as described by

$$z(t - t_i) = z(t_i) + (\dot{z}^+)(t - t_i) \tag{2.3.6}$$

where t_i is the time of the instantaneous impact.

The "stuck" impactor condition is modeled for the case that the impactor undergoes "Bounce Down" as pointed out in Fig. 2.3.3 where the impactor is "stuck" on a wall with (0 or 1) relative displacement. In theory, infinite impacts are possible during "bounce down." To reduce CPU time it is thus desirable to truncate the impacts. The impactor is at a wall surface during "bounce down" and if the relative velocity becomes small enough, it becomes reasonable to model the impactor as being "stuck." The impactor is again freed when the impactor housing acceleration changes sign due to the vanishing of the impactor to housing contact force. This is explained mathematically by realizing that the impactor has the same acceleration as the housing and has only the contact force under the zero

Downloaded 02 Jun 2010 to 171.66.16.105. Redistribution subject to ASME license or copyright; see http://www.asme.org/terms/Terms_Use.cfm

friction assumption. Since the impactor has the same acceleration as the housing, the contact force changes sign when the acceleration changes sign. The impactor then continues with the velocity that the housing had at the time the contact force vanished.

The "stuck" condition is invoked if a second impact occurs on one wall within (0.2 percent) of the period of the highest frequency considered significant in the simulation. An example of this is the simulation of a structure with impact damper where only the first ten lower modes significantly contribute to the response. If the 10th natural frequency is 1000 Hz, its period is 1 ms. On "bounce down," a "stuck" impactor would then be invoked if a second impact occurred within 0.2 percent of this period or 2 μs. This criterion has been verified as a conservative assumption.

For simulation in the physical coordinate space, the "stuck" impactor mass is simply added to the inertia matrix. For modal subspace simulation it becomes necessary to store a complete additional set of modal system parameters, that is modal mass, stiffness, damping, and force. The "free" and "stuck" impactor condition thus requires two different modal subspaces for the simulation since the added mass for the "stuck" condition produces a different modal system. This results in two respective sets of physical coordinates as stated by,

$$U_f = [\Phi_f]q_f \quad \text{(free coordinates)} \tag{2.3.7}$$

$$U_s = [\Phi_s]q_s \quad \text{(stuck coordinates)} \tag{2.3.8}$$

When transitioning from "free" to "stuck," integration of modal equations switches to the "stuck" set of equations, which require new initial conditions for the modal coordinates (q_s). Similarly, when transitioning from "stuck" to "free," integration of the "free" modal equations is initiated and new initial conditions for the modal coordinates (q_f) are required. Obtaining the transforms leading to the initial conditions begins with obtaining the transform from physical to modal coordinates. For the "free" system coordinates the procedure begins with an identity (2.3.9),

$$[M_f]U_f = [M_f][\Phi_f]q_f \tag{2.3.9}$$

where $[M_f]$ is the physical coordinate mass matrix. Equation (2.3.9) is next premultiplied by $[\Phi_f]^T$ to yield Eq. (2.3.10),

$$[\Phi_f]^T[M_f]U_f = [\Phi_f]^T[M_f][\Phi_f]q_f$$

$$\text{diag}\,(m_f) = [\Phi_f]^T[M_f][\Phi_f],$$

'free' modal mass matrix. (2.3.10)

Solving Eq. (2.3.10) for (q_f) yields the transform,

$$q_f = AU_f,$$

$$A = \text{diag}\,(1/m_f)*[\Phi_f]^T[M_f] \tag{2.3.11}$$

The same procedure results in obtaining "stuck" modal coordinates in terms of "stuck" physical coordinates and is described by

$$q_s = BU_s,$$

$$B = \text{diag}\,(1/m_s)*[\Phi_s]^T[M_s] \tag{2.3.12}$$

To obtain the transform between "stuck" and "free" modal coordinates, the two modal expansions (2.3.7) and (2.3.8) are equated at the instant the impactor is "stuck" or "freed." Substituting (Us) of Eq. (2.3.8) into Eq. (2.3.11), and (U_f) of Eq. (2.3.7) into Eq. (2.3.12), results in the transforms:

$$q_f = A[\Phi_s]q_s \tag{2.3.13}$$

$$q_s = B[\Phi_f]q_f \tag{2.3.14}$$

2.4 Planar Impact Damper Modeling. The SDOF impact damper cannot be applied to structures with destabilizing forces in more than one coordinate despite negligible dynamic coupling. The solution to this problem resulted in modeling a planar impact damper with cylindrical impactor and housing illustrated by Fig. 2.4.1. The impactor mass is concentrated at its center and moves within the circumference of the housing with zero surface friction. The "stuck" impactor condition is modeled in analogy to the SDOF impactor by applying the COR/COM relationships and the "stuck" condition in the direction of the line of centers. The "stuck" condition contact force now vanishes with a sign change in the "normal" acceleration upon which the impactor is "freed." ICs at the time of separation then become the position of the impactor and velocity of the housing. For a "stuck" condition with no friction, the impactor contacts the housing in the line of centers direction. The model accounts for arbitrary angles of impact between the impactor and its housing. Relative velocities are modeled by tracking the absolute velocities and applying the equations of section (2.3). To avoid the condition where the impactor may slide around the full circumference of its housing, an algorithm was implemented to offset its position. This was accomplished by aligning the impactor on a housing surface point defined by a line through the housing center over the course of one time step. In simulations, the algorithm only takes effect when the impactor is considered "stuck" at the housing surface where line of centers relative velocities are small. For a housing orbit type of motion, the impactors angular displacement is thus slightly greater. In practice, "flats" are machined onto the impactor surface to prevent rolling on the housing circumference.

3 Simulation

3.1 Physical Coordinate Space. Simulations for this study began with the use of finite element model assembly code, which produces symmetric mass, stiffness, and damping parameter matrices for the structure under consideration. Symmetric matrices permitted data storage in banded form requiring less RAM and much less CPU time. These data were then used as input to a simulation code for "direct" integration of the structural. Figure 3.1.1 shows the code logic.

3.2 Modal Coordinate Space. Though the banded form of the system equations has much benefit in terms of reduced RAM storage and CPU time, large DOF systems still require very much CPU time for numerical integration in a simulation. To save CPU time, a modal space simulation code was developed that makes use of modal transformations that yield the physical coordinate response. This code is especially useful in that any subspace of the defined modal space can be simulated, as for example when only a number of the lower frequency modes are required to represent the dynamics of a system. The modal space code requires data from the modes to facilitate transforms into the physical coordinate space. This requires assembling the system of equations with a finite element code

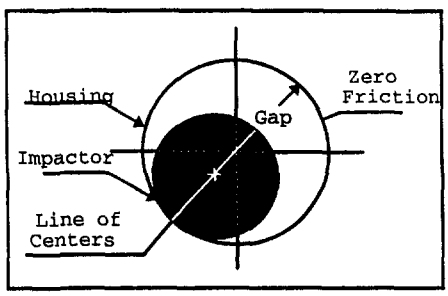


Fig. 2.4.1 Two-dimensional cylindrical impact damper

Downloaded 02 Jun 2010 to 171.66.16.105. Redistribution subject to ASME license or copyright; see http://www.asme.org/terms/Terms_Use.cfm

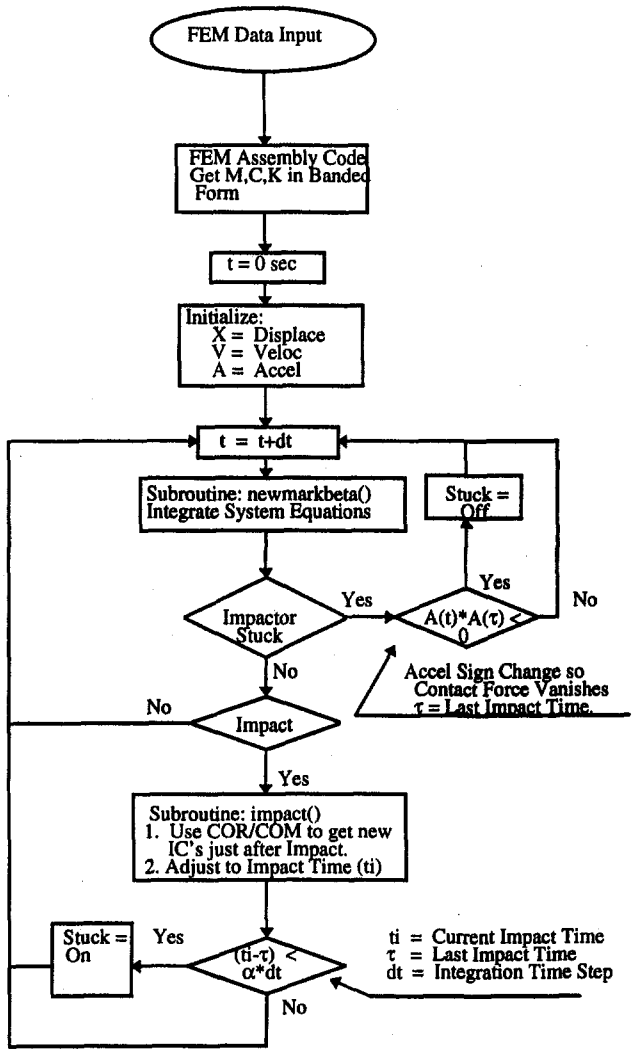


Fig. 3.1.1 "Direct" integration code logic

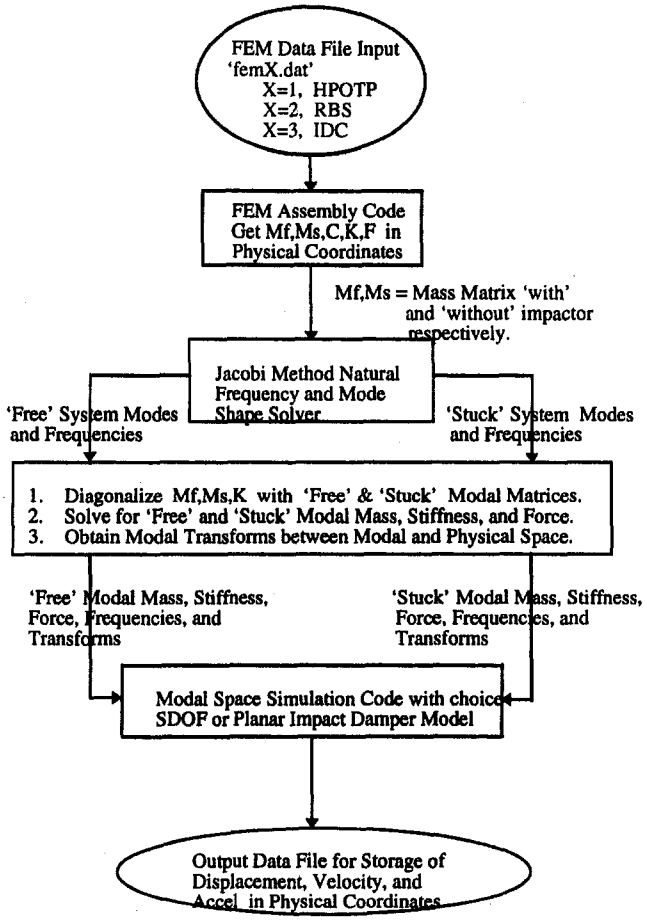


Fig. 3.2.1 Modal space code implementation

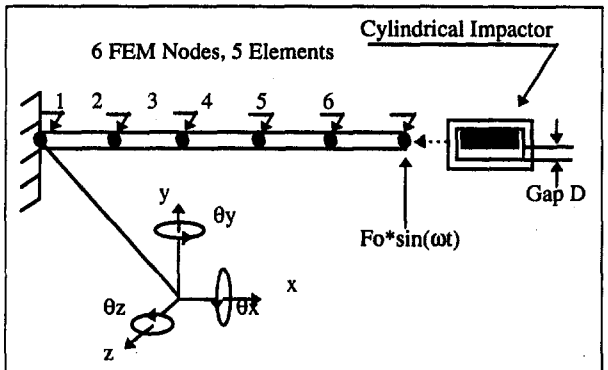
then finding the natural frequencies and mode shapes. Figure 3.2.1 illustrates the logic.

4 Results

4.1 Cantilever Beam With Impact Damper. A previously investigated SDOF oscillator with impact damper [2] is analogously modeled using a 30 DOF cantilever beam for the purpose of correlating the impact damper model and simulation algorithms for this work. This involved simulating the frequency response of the cantilever with impact damper and sinusoidal force at the tip. Figure 2.3.1 shows the SDOF model, and Fig. 4.1.1 describes the cantilever model.

The cantilever analog resulted by assuming a large section area to prevent longitudinal stretch, and negligible inertia at all nodes except the impactor node. The elastic modulus was obtained equating the natural frequency of the SDOF oscillator to the natural frequency of a massless cantilever beam with concentrated mass at the free end. The first mode corresponding to a free end lateral DOF formed the subspace used in the simulation. Frequency response for both models proceeded with an assumed forcing amplitude (F_o = 0.0172 lb), and (4 percent) mass ratio. Figures 4.1.2 and 4.1.3 show excellent agreement in the two models with and without impact damper, where Moore [2] uses a stiffness value of unity; thus (Uo) in Fig. 4.1.2 equates to (Fo) in Fig. 4.1.3.

Note that the response with impactors shows significant attenuation of the vibration close to the center frequency, and resonance to either side of center. This illustrates the impact damper's dependency on amplitude. The beat response near the center



Symb	Value	Units	Description
E	28.135	lb/in^2	Elastic Modulus
I	40.0	in^4	Transverse Area MOI
A	10^6	in^2	Section Area
L	3.0	inch	Element length
m_h	1.0	lb-sec^2/in	Impactor Node Mass
m_n	10^{-6}	lb-sec^2/in	Mass at Nodes, n =(1-5)
D	1.0	inch	Clearance Gap

Fig. 4.1.1 Cantilever FEM analog to the SDOF oscillator

Downloaded 02 Jun 2010 to 171.66.16.105. Redistribution subject to ASME license or copyright; see http://www.asme.org/terms/Terms_Use.cfm

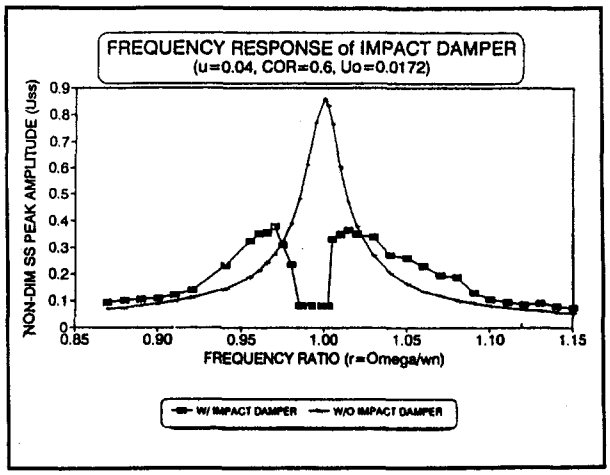


Fig. 4.1.2 SDOF model frequency response (μ = 4 percent)

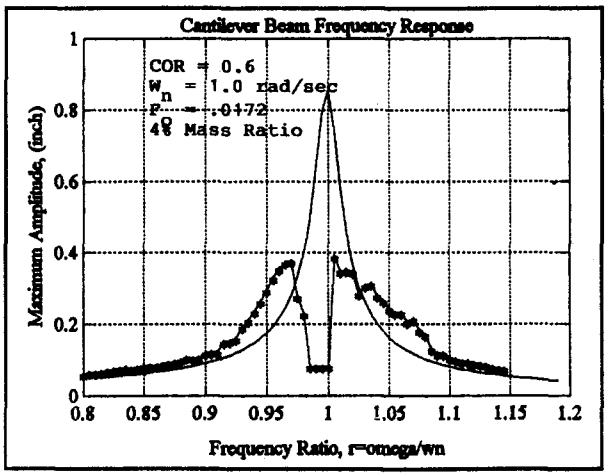


Fig. 4.1.3 Cantilever model frequency response (μ = 4 percent)

has a frequency equal to the deviation from the center. The beat periods are shorter as the input frequency moves to either side of the center and are longer as the input approaches the center. Since amplitude drops at the completion of a beat cycle, "impact failure" occurs more often as the input frequency moves away from center, resulting in amplitude gains. With the input frequency closer to the center, the beat periods are much longer, hence "impact failure" occurs less often, resulting in less amplitude gain. The phenomenon illustrated in Fig. 4.1.4 with frequency ratio (r = 1.015) shows how "impact failure" at the completion of a beat period results in amplitude gain.

4.2 Rotor Bearing System With Impact Damper. Additional correlation studies are conducted by modeling an experimental RBS [2] with impact damper and then comparing simulation results. A modal subspace using the first 10 modes of the 38 node, 6 DOF/node RBS FEM was derived and then used to simulate the frequency response. A description of the RBS model is contained in Appendix A. The impact damper comprises six equally spaced cylinder impactors housed within a squirrel cage that is mounted to the shaft bearing race and ground through asymmetric flexible supports as shown conceptually by Fig. A.3. Friction at the ends of the impactors was neglected because of highly polished surfaces. Exact values of the support stiffness weren't known; thus some "tuning" was done to match the model's natural frequencies with the experimental RBSs without impactors. "Tare" damping ratios assigned to individual modes were obtained by trial and error

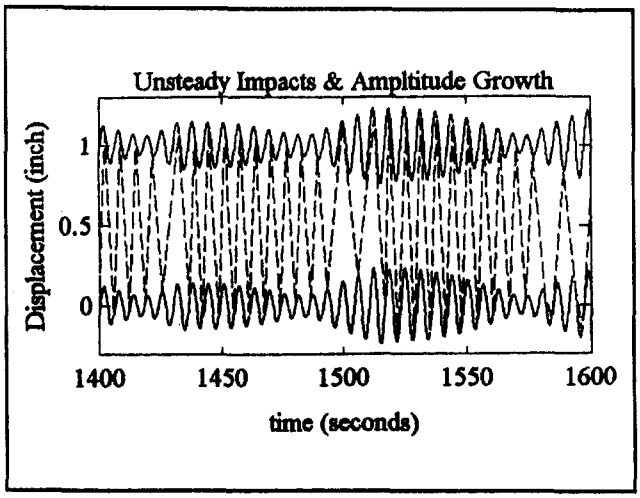


Fig. 4.1.4 Cantilever model forced response snap shot in time (1.015 frequency ratio, 4 percent mass ratio)

until amplitudes in the model response without impactors agreed with the experimental at the critical speeds. The damping ratios indicated in Fig. A.2 range from 0.5 to 2.88 percent and are consistent with typical structural damping for low to medium stress levels.

The RBS modal subspace model response was simulated for the 1-Y and 2-Y modes shown in Fig. 4.2.1 with excellent prediction of the experimental shown in Fig. 4.2.2. Note that the "with" impactor simulation proceeded without any parameter "tuning." This remarkable agreement the model has with the experimental gave much confidence in the simulation algorithms to produce accurate results.

4.3 SSME-HPOTP Casing With Impact Damper

Modeling. The HPOTP FEM assembled from data provided by NASA-Marshall is shown in Fig. 4.3.1 with its casing cantilevered from the "Hot Gas Manifold" (HGM).

HGM boundary stiffness was modeled with a super element matrix and piping connections were modeled with linear springs. Excitation was modeled with HPOTP rotor mass unbalance properties also obtained at NASA. The rotor is modeled as rigid with resultant forces transmitted through bearings located at model nodes (4, 15). Maximum acceleration in model simulations was verified to be within an average 1.5–2.0 G's near the bottom of the casing, which agrees with NASA's speci-

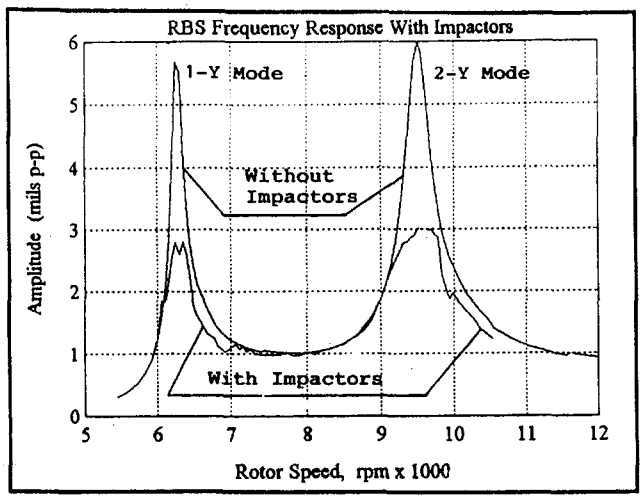


Fig. 4.2.1 RBS model response (1-Y & 2-Y modes)

Downloaded 02 Jun 2010 to 171.66.16.105. Redistribution subject to ASME license or copyright; see http://www.asme.org/terms/Terms_Use.cfm

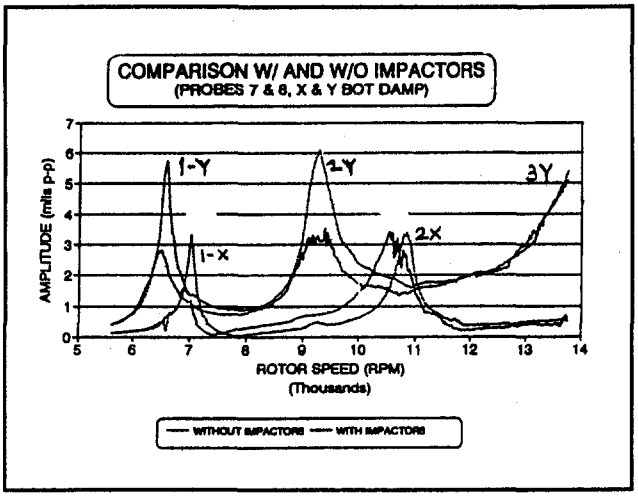


Fig. 4.2.2 Experimental RBS response

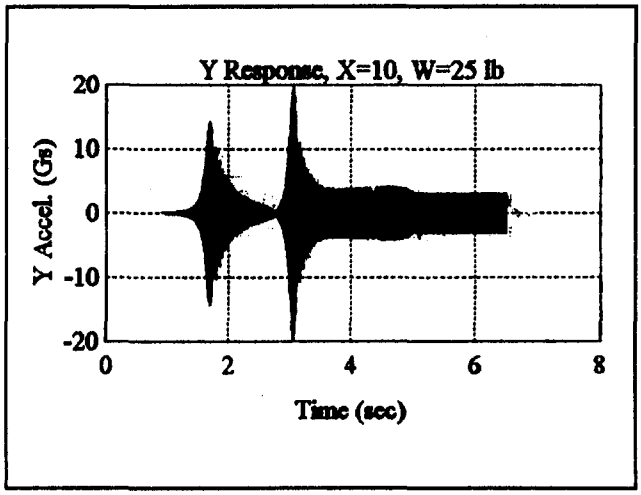


Fig. 4.3.2 Impactor node response without impactors

fication. The impact dampers comprise twelve cylindrical impactors that permit damping in the plane normal to the pump axis at node 1 in Fig. 4.3.1. The impactor weight is about equal to the damper housing weight with an allowable maximum total of about 50 lb.

Simulation. Simulation of the HPOTP was accomplished in a modal subspace of the first ten modes of the system. Accuracy of the model was verified by convergent responses of subspaces with modes greater than five, where modes higher than the 10th mode contributed to acceleration levels but were considered unimportant due to their minuscule displacements and the use of an 800 Hz low-pass filter on the test stand accelerometer data taken at NASA-Marshall.

An example of a typical transient impactor node (y) response with and without impactors is shown in Figs. 4.3.2 and 4.3.3, respectively where excellent attenuation of the vibration is seen with impactors as casing modes are excited with the pump input rotor speed ramp modeled by Eq. (4.3.1):

$$\Omega_{\text{shaft}}(t) = \begin{cases} \Omega f\,*(t/5), & (0 \leqslant t < 5)\ \text{s} \\ \Omega f, & (t \geqslant 5)\ \text{s} \\ \Omega f = 2400\ \text{rad} \end{cases} \tag{4.3.1}$$

Impact Damper Parameter Optimization. Parametric studies were conducted where the maximum (y, z) "in plane" response at the impactor node with impactors was compared to the response without impactors. Simulations were conducted with equal impactor and damper housing weights of W = 5, 15, 25 lb, clearance gap range of D = 1-4 mils, and unbalance distribution multiplier range of X = 1-10, where the displacement and acceleration response were plotted as a function of clearance gap for combinations of W, X. Figure 4.3.4 illustrates a sample optimization plot with parameters W = 25 lb, X = 10 for maximum z acceleration at casing criticals and for steady

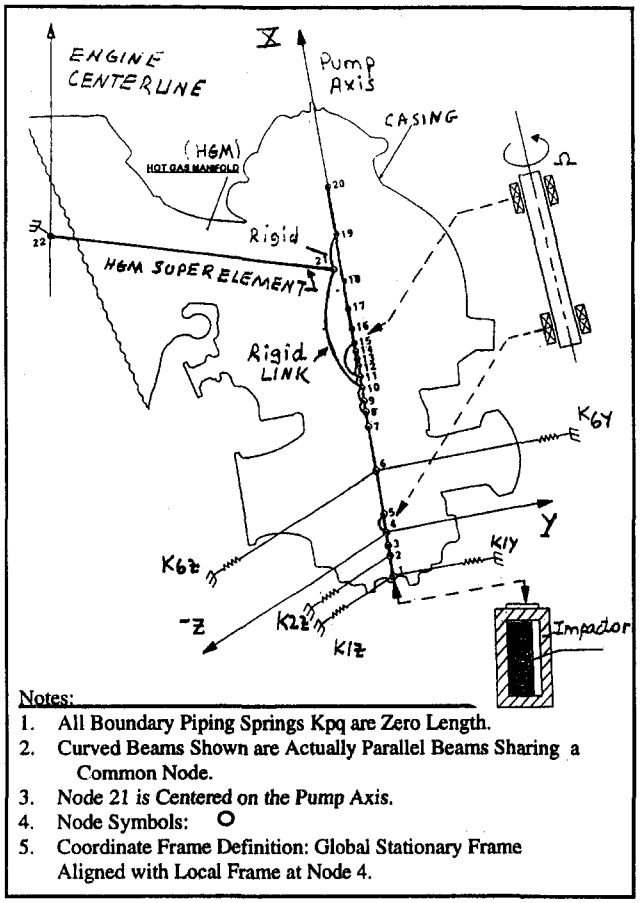


Fig. 4.3.1 HPOTP finite element model

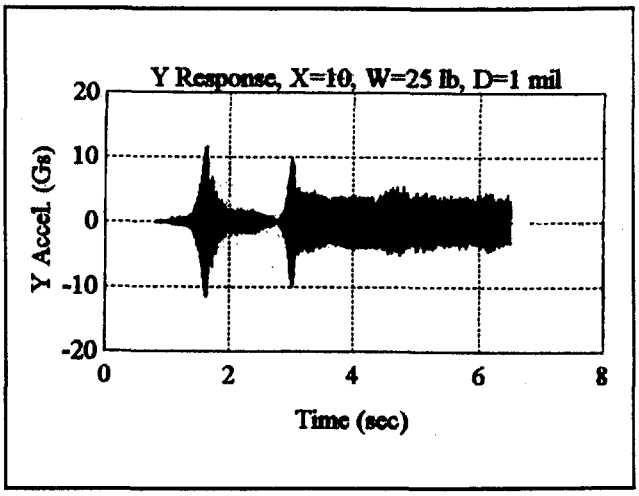


Fig. 4.3.3 Impactor node response with impactors

Downloaded 02 Jun 2010 to 171.66.16.105. Redistribution subject to ASME license or copyright; see http://www.asme.org/terms/Terms_Use.cfm

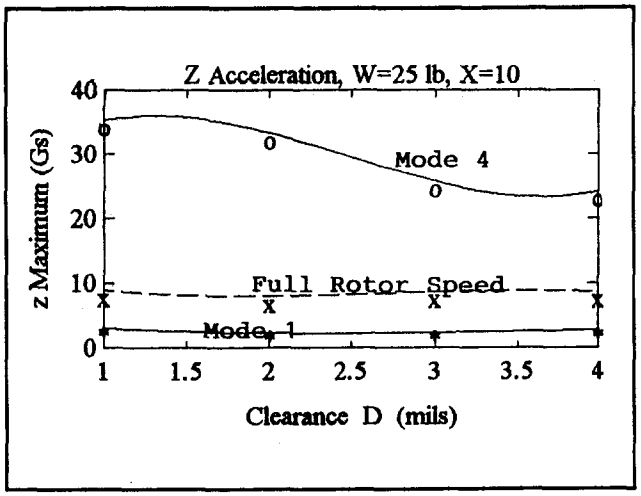


Fig. 4.3.4 *Z*-coordinate acceleration versus clearance

rotor speed modeled by Eq. (4.3.1). Figure 4.3.5 shows the corresponding acceleration ratio of the response "without" to "with" impactors.

Optimal clearance selection began by finding clearances that minimize the worst case vibration for combinations of W, X where parametric studies show that acceleration levels with W = 25 lb are roughly $\frac{1}{2}$ those with for W = 5 lb. The optimal gap is thus chosen from simulations with the 25 lb weight. Optimal gaps (D = 1, 1.7 mils) are possible up to a base unbalance multiple of X = 7 with W = 25 lb. Since acceleration and displacements are significantly lower and do not vary appreciably for this range of gaps below the unbalance multiple X = 7, the most effective gap is D = 1.7 mils. For X = 10 the improvement in using the optimal 3.3 mil gap is only about 3 gs as compared to the 1.7 mil gap. The combination W = 25 lb, D = 1.7 mil is thus selected with the predicted worst case vibration explained by Table 4.3.1 showing remarkable damper performance with the greatest reduction in acceleration from 66.5 gs to 31.2 gs at the highest unbalance level, which notably could be associated with a significant unbalance defect in the operation of the pump. Performance off resonance or at steady rotor speed results in slightly higher vibration with impactors, where the reduction factor can be less than 1.0. An example of the predicted worst case acceleration increase for this behavior is explained in Table 4.3.2 for X = 1, 10. This slight increase

Table 4.3.1 Predicted worst case vibration for impact damper parameters (W = 25 lb, D = 1.7 mil)

Unbalance	Displacement			Acceleration		
Multiple	Mode	mils	Reduct	Mode	G's	Reduct
1	4	0.7	1.4	4	4.1	1.4
3	4	1.8	1.9	4	11.0	1.8
7	2	3.3	1.8	4	18.1	2.5
10	2	6.6	1.4	4	31.2	2.1

Table 4.3.2 Worst case full-speed vibration with impactors

Unbalance Multiple	Planar Coord	Units	Without Impactors	With Impactors
1	z	g's	0.77	0.9
10	z	g's	7.2	9.1

is the cause of impactors exciting other modes as shown in Fig. 4.3.6 where the "steady state" z displacement is plotted "with" and "without" impactors. Note that the response "without" impactors is at the running speed of the pump rotor, 381 Hz and the fundamental in the response "with" impactors is the first mode (78 Hz). This is evidence that at least the first mode at 77 Hz is being excited.

4.4 Unstable Structures With Impact Dampers

Rotor Shaft Stability. The experimental RBS [2] was modeled by assuming an equal cross coupled stiffness *Kcc*, "in plane" at the rotor shaft lower bearing. At a constant rotor speed of 7878 rpm, trial simulations without the impactors show the onset of instability at about *Kcc* = 8250 lb/in. At this *Kcc* and housing weight, W = 1.5 lb, an axial view of the planar instability indicates that the vibration orbit is elliptical and oriented at about 37 deg clockwise relative to the vertical. This is simply evidence of the support structure's asymmetry. Simulation of the unstable RBS was done with impactors installed for ranges of *Kcc*, impactor weight, and clearance gaps. Table 4.4.1 explains the simulation results and explains why quantifying parameters is critical since different combinations have different effects.

For the results obtained, a combination of W = 3 lb, D = 6.9 mil stabilizes the RBS for the full range of *Kcc* considered up to a max (13500 lb/in), though this combination doesn't always result in the lowest vibration. Note that the system couldn't be stabilized for *Kcc* greater than the maximum with

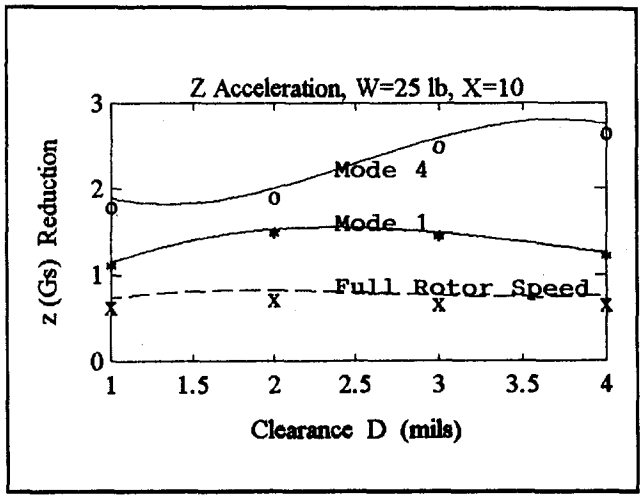


Fig. 4.3.5 *Z*-coordinate acceleration ratio of "without" to "with" impactor's response

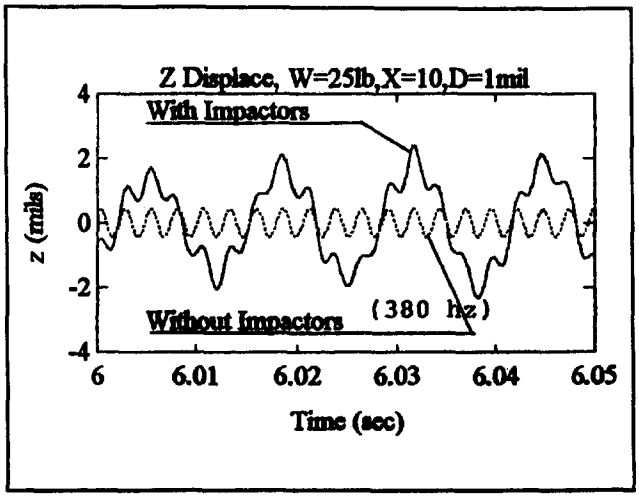


Fig. 4.3.6 Steady-state response "with" and "without" impactors showing modal excitation

Downloaded 02 Jun 2010 to 171.66.16.105. Redistribution subject to ASME license or copyright; see http://www.asme.org/terms/Terms_Use.cfm

Table 4.4.1 RBS with destabilizing cross-coupled stiffness result (housing weight = impactor weight)

Kcc lb/in	Impactor Weight lbs	Steady Radial stab/unst Gap (mils) 6.9	1.0	Steady State Amp.(rms-mils) Gap (mils) 6.9	1.0	Impacts/sec Gap (mils) 6.9	1.0
8500	1.5	stab	stab	1.14	0.41	3690	1346
	3.0	stab	stab	0.52	0.46	111	1307
	6.0	stab	stab	0.55	0.72	128	1312
11250	1.5	stab	unst	3.45	---	1759	---
	3.0	stab	stab	2.32	0.45	1594	1305
	6.0	stab	unst	1.6	---	780	---
13500	1.5	unst	unst	---	---	---	---
	3.0	stab	unst	3.82	---	1362	---
	6.0	unst	unst	---	---	---	---

the range of impact damper parameters considered. With the maximum *Kcc* (60 percent) greater than the minimum required to destabilize the RBS, the impact damper clearly shows remarkable effectiveness in controlling instability.

HPOTP Casing Stability. HPOTP casing instability was modeled by assuming a pseudo-destabilizing cross-coupled stiffness. This approach is simply a theory tool used to create instability. Simulations were also conducted for an impactor weight, clearance gap, and *Kcc* stiffness range. The minimum (*Kcc* = 222,000 lb/in.) value used was again obtained by trial simulation without impactors until instability resulted. For this *Kcc* with a housing weight $W = 25$ lb, the vibration observed along the pump axis from the bottom end indicates the weakest stiffness plane oriented at about 41 deg relative to the $+Z$ axis.

Results summarizing the stability with impactors are presented in Table 4.4.2, which indicate that the largest impactor weight ($W = 25$ lb), and smallest gap ($D = 1$ mil), produce the lowest level of vibration up to a maximum (*Kcc* = 240,000 lb/in.). Responses could not be stabilized for values above this *Kcc* with the impact dampers considered.

Discussion of Stability Simulation Results. Numerical integration in simulating the latter two systems required many time step convergence studies in that each new simulation with an increase in *Kcc* results in larger eigenvalues that drive the systems faster. This required using a smaller time step to prevent numerical instability and consequently permit distinguishing between this and physical instability of the models. Convergent responses were obtained for time steps of 10 μs or less.

The key to effective impact damper performance with instability is in maximizing the IPS, which depends on impactor weight, clearance, and amplitude range. As the unstable structure gains amplitude, the IPS must respond quickly to stabilize

Table 4.4.2 HPOTP casing with destabilizing pseudo-cross-coupled stiffness results (housing weight = impactor weight)

Kcc lb/in	Impactor Weight lbs	Steady Radial stab/unst Gap (mils) 1.0	3.0	Steady State Amp.(rms-mils) Gap (mils) 1.0	3.0	Impacts/sec Gap (mils) 1.0	3.0
222500	5.0	unst	stab	---	0.67	---	438
	15.0	stab	stab	0.47	0.72	386	358
	25.0	stab	stab	0.48	0.76	316	330
232500	5.0	unst	unst	---	---	---	---
	15.0	stab	stab	1.48	4.21	1950	1960
	25.0	stab	stab	0.54	0.85	1200	667
240000	5.0	unst	unst	---	---	---	---
	15.0	unst	unst	---	---	---	---
	25.0	stab	stab	1.32	3.76	2006	2036

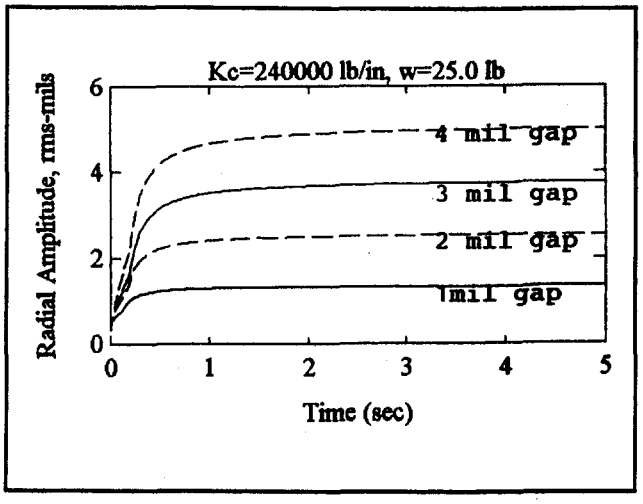


Fig. 4.4.1 HPOTP casing, radial displacement stability response with impact damper for clearances $D = 1, 4$ mils

the vibration. If the relative velocity and impactor mass are then large enough, the amplitude gains are quickly suppressed. If the relative velocity and impactor mass are too low, the structure's response becomes more unstable. Too much weight results in a slow IPS response, while not enough weight results in too little dissipation of the structures energy. Large gaps allow higher relative velocities, however, with a slower IPS response as well. Small gaps result in lower relative velocities but with increases in the IPS rate. Different combinations of weight and gap thus produce different effects. This suggests the necessity of a design tool if optimal performance is desired.

An example of different parameters affecting stability is shown for different gaps of the (y, z) radial displacement response for the HPOTP casing with impactor weight ($W = 25$ lb), gap ($D = 1, 2, 3, 4$ mils), and base level unbalance multiple ($X = 1$) in Fig. 4.4.1.

As shown in Fig. 4.4.1, the larger gaps results in greater amplitude, which is due to a slow IPS response. Increasing the gap even more would eventually lead to the structure becoming unstable.

5 Summary

Three different structures were modeled and simulated with impact dampers to include a cantilever beam, a rotor shaft system with a flexible bearing support, and finally the SSME-HPOTP casing structure.

For ranges of excitation frequency and rotating unbalance, impact damper performance was studied at critical frequencies, steady excitation frequency, large unbalance to simulate a defect, and with instability drivers.

All models studied for this work were constructed with three-dimensional "beam" finite elements and integrated either "directly" or in derived modal subspaces. Modal space methods were found to be accurate and faster than the "direct" method resulting in CPU time reductions by as much as 60 to 1.

Integration of all models in this work was done using the "newmark-beta" algorithm. For algorithmic accuracy, time step convergence studies were conducted with convergent results. To ensure accuracy often limited by round-off error in digital computing, time scaling of the EOM was used and resulted in more convergent responses.

A SDOF impact damper model was used for all simulations in this study due to negligible dynamic coupling; however, a two-dimensional version was required with planar instability drivers. Simulation of the two-dimensional model predicted the

Downloaded 02 Jun 2010 to 171.66.16.105. Redistribution subject to ASME license or copyright; see http://www.asme.org/terms/Terms_Use.cfm

individual responses in each orthogonal coordinate of the SDOF model with excellent agreement.

The cantilever beam simulation was conducted to correlate the present study algorithms and impact damper models with those developed in previous research [2]. Free and forced response simulations of the IDC show excellent agreement with former results.

The nature of two resonance peaks on either side of a natural frequency for the structure with impact damper was shown to be the related to the amount of time the impactor undergoes "impact failure" between beat envelope periods.

The experimental RBS with impact damper [2] was modeled and simulated to correlate present study methods with larger DOF systems. The RBS model with 227 DOF, flexible asymmetric bearing supports and impact damper showed remarkable agreement with the experimental frequency response.

The HPOTP casing model frequencies and modes agree well with the model developed at NASA-Marshall. Simulations of the HPOTP with impact damper were conducted with a base level rotor unbalance and multiples thereof for a rotor speed ramp up to 23,000 rpm. Effectiveness of the impact damper was studied at casing criticals, at steady rotor speed, and with high multiples of base level unbalance to simulate defects.

The impact damper was shown to attenuate vibration levels by as much as 300 percent at casing criticals and for high levels of unbalance. Only slightly higher levels resulted off resonance due to impulse excitation of other modes with impactors as compared to simulation without impactors.

Instability driver simulations show that the impact damper could possibly serve as a stabilizing mechanism. For the RBS, a destabilizing cross-coupled stiffness (Kcc) was simulated at its lower bearing. The onset of instability was determined to be Kcc = 8250 lb/in., and stable responses were observed up to a maximum (Kcc = 13,500 lb/in.) for a range of justifiable impact dampers. For the HPOTP, simulation of a pseudo-cross-coupled stiffness at the lower rotor bearing was used. With the casing's relatively stiff structure and allowable maximum impactor mass of about 25 lb, the damper showed remarkable ability in suppressing amplitude gains due to the destabilizing forces.

References

1 Nale, T. A., and Klusman, S., "Rotor Dynamic Test Results for Synchronous and Subsynchronous Vibration," *Proc. 2nd International Congress on Recent Developments in Air and Structural Borne Sound and Vibration,* 1900.

2 Moore, J., Palazzolo, A., Gadangi, R., et al., "A Forced Response Analysis and Application of Impact Dampers to Rotor Dynamic Vibration Suppression in a Cryogenic Environment," *Proc. ASME 14th Conference on Vibration,* ASME DE-Vol. 62, 1993, pp. 11–24.

Downloaded 02 Jun 2010 to 171.66.16.105. Redistribution subject to ASME license or copyright; see http://www.asme.org/terms/Terms_Use.cfm

APPENDIX A

RBS Experimental Configuration

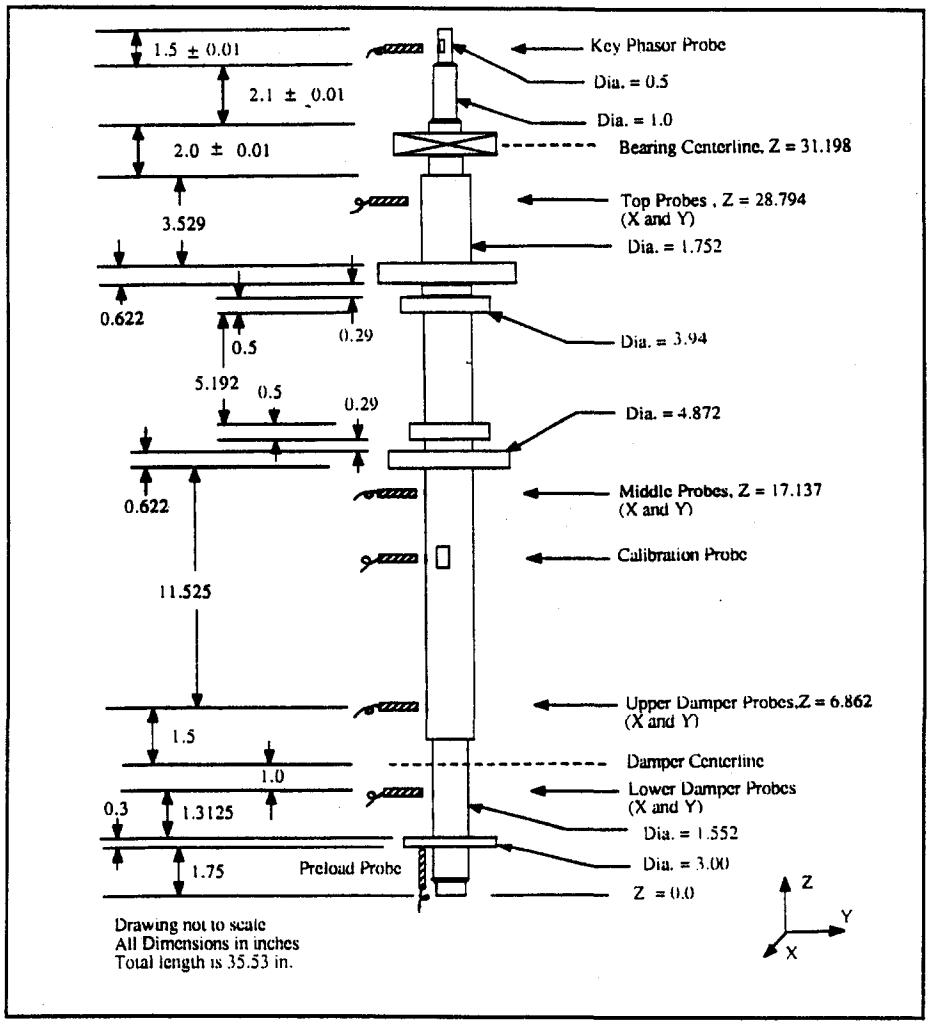


Fig. A.1 Rotor shaft layout

	Stiffness		Damping	
Coord	Lower Brg (lb/inch)	Upper Brg (lb/inch)	Mode	Percent
Y	32,000	27,500	1-Y	1.05
Z	42,000	51,000	1-Z	1.88
			2-Y	1.6
			2-Z	2.88
			All Others	0.5

Fig. A.2 Stiffness and damping properties

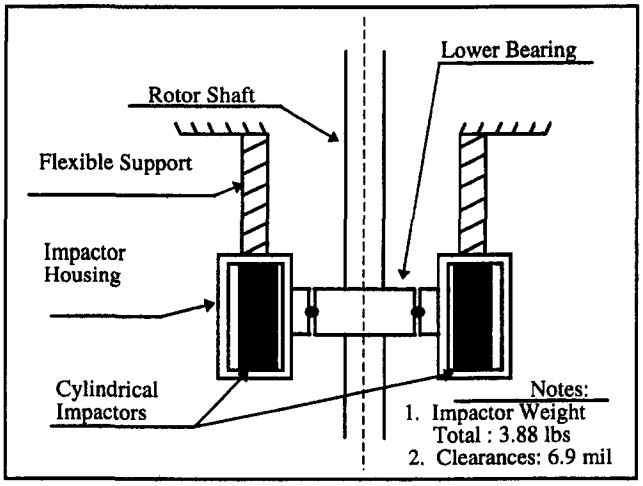


Fig. A.3 Impact damper sectional view

Downloaded 02 Jun 2010 to 171.66.16.105. Redistribution subject to ASME license or copyright; see http://www.asme.org/terms/Terms_Use.cfm

Dynamic Response of a Cracked Rotor With Some Comments on Crack Detection

G. Meng
Northwestern Polytechnical University, Xian, China

E. J. Hahn
School of Mechanical and Manufacturing Engineering, University of New South Wales, Sydney, New South Wales, Australia

By considering time-dependent terms as external excitation forces, the approximate dynamic response of a cracked horizontal rotor is analyzed theoretically and numerically. The solution is good for small cracks and small vibrations in the stable operating range. For each steady-state harmonic component, the forward and backward whirl amplitudes, the shape and orientation of the elliptic orbit, and the amplitude and phase of the response signals are analyzed, taking into account the effect of crack size, crack location, rotor speed, and unbalance. It is found that the crack causes backward whirl, the amplitude of which increases with the crack. For a cracked rotor, the response orbit for each harmonic component is an ellipse, the shape and orientation of which depend on the crack size. The influence of the crack on the synchronous response of the system can be regarded as an additional unbalance whereupon, depending on the speed and the crack location, the response amplitude differs from that of the uncracked rotor. The nonsynchronous response provides evidence of crack in the subcritical range, but is too small to be detected in the supercritical range. Possibilities for crack detection over the full-speed range include the additional average (the constant) response component, the backward whirl of the response, the ellipticity of the orbit, the angle between the major axis and the vertical axis, and the phase angle difference between vertical and horizontal vibration signals.

Introduction

Transverse cracks in rotors of rotating machinery, generally from fatigue, creep, stress corrosion, or from shock loading, may result in catastrophic damage, and huge economic loss (Jack and Patterson, 1977; Haas, 1977). A good review of the early literature may be found in Wauer (1990). Thus, Gasch (1976) and Dimarogonas and Papadopoulos (1983) explain the changes in the synchronous amplitude and phase angle; explain the occurrence of a twice synchronous component; show the existence of unstable speed ranges and show that the crack position has a large influence on the system response. Though behavior of, and crack detection in, such rotor systems have recently received increasing attention (Nelson and Nataraj, 1986; Muszynska et al., 1992), on-line crack detection methods depend mainly on rotor acceleration and deceleration in the subcritical range (Iman et al., 1989). Crack detection in the supercritical range is still a problem, especially when the rotor is running at a constant speed.

The difficulty is that because of the closing and opening of the crack during rotation, the equations of motion of a cracked rotor have time-dependent stiffness coefficients. Gasch (1992) introduced a perturbation method, which, under so-called weight dominance conditions, enabled cross-stiffness change and dynamic response terms to be omitted. This paper relaxes some of these assumptions. Thus, following the approach used by Gasch (1992), but including the influence of the cross-stiffness change and assuming only that the response without a crack is large compared to the additional response due to the crack, the dynamic response of a cracked rotor is investigated, with a view to seeking information that can be used for crack detection in both sub- and supercritical speed ranges.

Contributed by the International Gas Turbine Institute and presented at the 39th International Gas Turbine and Aeroengine Congress and Exposition, The Hague, The Netherlands, June 13–16, 1994. Manuscript received by the International Gas Turbine Institute February 4, 1994 Paper No. 94-GT-29. Associate Technical Editor: E. M. Greitzer.

Theory for Approximate Response

For a Jeffcott rotor with a crack as shown in Fig. 1, the equation of motion is:

$$m\ddot{z} + c\dot{z} + k_x x + ik_y y = mg + am\omega^2 e^{i(\omega t+\varphi)}. \quad (1)$$

The opening and closing of the crack as the rotor rotates results in a periodic change in rotor stiffness. The rotor stiffness in the crack and cross directions can be written as:

$$\begin{bmatrix} k_\xi \\ k_\eta \end{bmatrix} = \begin{bmatrix} k \\ k \end{bmatrix} - f(\Phi)\begin{bmatrix} \Delta k_\xi \\ \Delta k_\eta \end{bmatrix} \quad (2)$$

where $f(\Phi)$ is a periodic function depending on both the crack and the rotor movement. For linearly elastic crack and rotor deflections, Δk_ξ and Δk_η may be assumed constant. For all but very large cracks, the stiffness change Δk_η is small compared with the main stiffness change Δk_ξ. Hence Δk_η is often assumed to be zero, but its effect is included here. If the dynamic deflection of the rotor is much smaller than the static deflection (the case of weight dominance), and the crack is small, one can use a rectangular function model (Grabowski, 1980), e.g.:

$$f(\Phi) = \begin{cases} 1 & 0 \le \Phi \le \dfrac{\pi}{2} \quad \text{and} \quad \dfrac{3\pi}{2} \le \Phi \le 2\pi \\ 0 & \dfrac{\pi}{2} < \Phi < \dfrac{3\pi}{2} \end{cases} \quad (3)$$

Hence

$$f(\Phi) = \frac{1}{2} + \frac{2}{\pi}\cos\Phi - \frac{2}{3\pi}\cos 3\Phi + \frac{2}{5\pi}\cos 5\Phi \ldots \quad (4)$$

$$= \frac{1}{2} + \frac{1}{\pi}(e^{i\Phi} + e^{-i\Phi}) - \frac{1}{3\pi}(e^{3i\Phi} + e^{-3i\Phi}) + \frac{1}{5\pi}(e^{5i\Phi} + e^{-5i\Phi}) - \ldots. \quad (5)$$

Copyright © 1997 by ASME

Downloaded 02 Jun 2010 to 171.66.16.105. Redistribution subject to ASME license or copyright; see http://www.asme.org/terms/Terms_Use.cfm

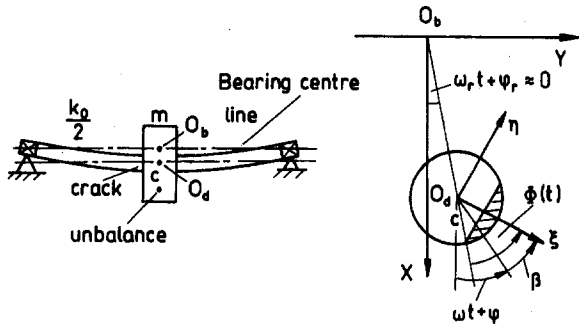


Fig. 1 Schematic diagram of a cracked rotor

Since $z = (x + iy) = (\xi + i\eta)e^{i\Phi}$, and utilizing Eq. (2), the stiffness force is given by:

$$k_x x + ik_y y = F_x + iF_y = (F_\xi + iF_\eta)e^{i\Phi} = (k_\xi \xi + ik_\eta \eta)e^{i\Phi}$$
$$= \tfrac{1}{2}(k_\xi + k_\eta)z + \tfrac{1}{2}(k_\xi - k_\eta)\bar{z}e^{2i\Phi},$$
$$= [k - \tfrac{1}{2}f(\Phi)\Delta k_1]z - \tfrac{1}{2}f(\Phi)\Delta k_2 \bar{z}e^{2i\Phi} \quad (6)$$

On substituting Eq. (6) into Eq. (1), one obtains:

$$Z'' + \frac{2D}{\Omega}Z' + \frac{1}{\Omega^2}Z - \frac{f(\Phi)}{2\Omega^2}[\Delta K_1 Z + \Delta K_2 \bar{Z}e^{2i\Phi}]$$
$$= \frac{1}{\Omega^2} + Ue^{i(\omega t+\varphi)} \quad (7)$$

Equation (7) is a set of linear equations with periodic coefficients. The stability of its response can be analysed by Floquet theory (Fridemann et al., 1977). Assuming that the cross-stiffness change ΔK_η and the damping ratio D are small enough to be omitted, Eq. (7) is unstable within the speed range (Meng and Gasch, 1993):

$$\frac{2}{N}\left(1 - \frac{1}{4}\Delta K_\xi\right) < \Omega < \frac{2}{N} \quad (N = 1, 2, 3, 4, 5, 6). \quad (8)$$

If ΔK_η or D is not equal to zero, the unstable speed range would be smaller due to the smaller stiffness asymmetry or the influence of external damping.

The solution of Eq. (7) can be written in the form

$$Z = 1 + Z_e(t) + \Delta Z(t) \quad (9)$$

where $Z_e(t)$ is the unbalance response of the uncracked rotor and $\Delta Z(t)$ is the additional response due to the crack.

If the response is stable and if the weight and unbalance response are dominant, so that $1 + Z_e(t) \gg \Delta Z(t)$, the $\Delta K \Delta Z(t)$ terms may be assumed to be small enough to be omitted in the response analysis. Substitution of Eq. (9) into Eq. (7) finally yields:

$$\Delta Z'' + \frac{2D}{\Omega}\Delta Z' + \frac{1}{\Omega^2}\Delta Z$$
$$= \frac{f(\Phi)}{2\Omega^2}[\Delta K_1[1 + Z_e(t)] + \Delta K_2[1 + \bar{Z}_e(t)]e^{2i\Phi}] \quad (10)$$

where

$$Z_e(t) = Ee^{i(\omega t+\varphi-\psi)}. \quad (11)$$

Substituting Eq. (5) into Eq. (10), and truncating all terms above the fourth harmonic, gives:

$$\Delta Z'' + \frac{2D}{\Omega}\Delta Z' + \frac{1}{\Omega^2}\Delta Z$$
$$= \frac{1}{\Omega^2}\{A_o + \sum_{n=1}^{4}(A_n e^{in\Phi} + A_{-n}e^{-in\Phi})\}, \quad (12)$$

Nomenclature

a = unbalance eccentricity
A_j, A_{-j} = coefficients given by Eq. (13)
c = external damping
D = external damping ratio = $c/(2m\omega_c)$
$E = U\Omega^2/\sqrt{(1-\Omega^2)^2 + (2D\Omega)^2}$
$E_n = 1/\sqrt{[1 - n\Omega^2]^2 + (2nD\Omega)^2}$
ΔE_n = difference between major and minor axes of n-order harmonic orbit
$f(\Phi)$ = a periodic crack function defined by Eq. (3)
k = stiffness of uncracked shaft
k_ξ = stiffness of cracked shaft in ξ direction
Δk_ξ = maximum stiffness change in ξ direction due to crack
ΔK_ξ = stiffness change ratio = $\Delta k_\xi / k$
ΔK_1, ΔK_2 = $\Delta K_\xi + \Delta K_\eta$, $\Delta K_\xi - \Delta K_\eta$
m = mass of rotor
n = order of harmonic component (n = 0, 1, 2, 3, 4)
P_n = amplitude of n-order forward whirl
Q_n = amplitude of n-order backward whirl
t, τ = time, $\tau = \omega t$
U = unbalance ratio = a/δ
x, y, X, Y = fixed Cartesian coordinates, $X = x/\delta$
$X(t)$, $Y(t)$ = dimensionless response in x and y direction = x/δ, y/δ
$X_n(t)$, $Y_n(t)$ = dimensionless n-order harmonic component of the response
X_n, Y_n = dimensionless amplitude of $X_n(t)$, $Y_n(t)$
z, Z = $x + iy$, $Z = z/\delta$
$Z_n(t)$ = dimensionless n-order harmonic component of response = $X_n(t) + iY_n(t)$
α_n = angle between the major axis of the n-order harmonic response orbit and the X axis
β = crack angle, i.e., the angle between crack centerline and unbalance
γ = defined by Eq. (14)
δ = static deflection of the uncracked rotor = mg/k
$\mu = 2\pi U\Omega^2/(2 - \pi E)$
$\nu = 2\pi U\Omega^2/(2 + \pi E)$
ξ, η = body fixed rotating coordinates; ξ is in the crack direction as shown in Fig. 1
φ = initial unbalance angle
φ_r = initial whirl angle
φ_{xn}, φ_{yn} = the phase angle change of $X_n(t)$ and $Y_n(t)$ caused by crack
$\Delta\varphi_{xyn} = \varphi_{xn} - \varphi_{yn}$
Φ = angle determining degree of opening of crack = $\omega t + \varphi + \beta$
$\Phi_n = n\Phi - \psi_n$
$\psi = \tan^{-1}(2D\Omega/(1 - \Omega^2))$
$\psi_n = \tan^{-1}(2nD\Omega/(1 - n^2\Omega^2))$
ω = angular velocity of rotor
ω_c = pin–pin critical speed = $\sqrt{(k/m)}$
ω_r = rotor whirl speed
Ω = speed ratio = ω/ω_c
$(\dot{})$, $(')$ = d/dt, $d/d\tau$

Downloaded 02 Jun 2010 to 171.66.16.105. Redistribution subject to ASME license or copyright; see http://www.asme.org/terms/Terms_Use.cfm

where:

$$A_o = \frac{1}{4}(\Delta K_\xi + \Delta K_\eta) + \frac{\gamma}{2\pi}$$

$$A_1 = \frac{1}{\pi}\Delta K_\xi + \frac{\gamma}{4}, \qquad A_{-1} = \frac{1}{3\pi}(\Delta K_\xi + 2\Delta K_\eta)$$

$$A_2 = \frac{1}{4}(\Delta K_\xi - \Delta K_\eta) + \frac{\gamma}{2\pi}, \quad A_{-2} = -\frac{\gamma}{6\pi}$$

$$A_3 = \frac{1}{3\pi}(\Delta K_\xi - 2\Delta K_\eta), \qquad A_{-3} = -\frac{1}{15\pi}(\Delta K_\xi + 4\Delta K_\eta)$$

$$A_4 = -\frac{\gamma}{6\pi}, \qquad A_{-4} = -\frac{\gamma}{10\pi} \tag{13}$$

and

$$\gamma = E[\Delta K_1 e^{-i(\psi+\beta)} + \Delta K_2 e^{i(\psi+\beta)}]. \tag{14}$$

The solution of Eq. (12) is then given by:

$$\Delta Z(t) = A_o + \sum_{n=1}^{4} E_n\{A_n e^{i\Phi_n} + A_{-n} e^{-i\Phi_n}\}. \tag{15}$$

Hence, the approximate solution of Eq. (7), is

$$Z(t) = 1 + Z_e(t) + A_o + \sum_{n=1}^{4} E_n\{A_n e^{i\Phi_n} + A_{-n} e^{-i\Phi_n}\}. \tag{16}$$

Results and Discussion

Each harmonic component of the approximate response $Z(t)$ is investigated before summing all the solution components as required by Eq. (16) to obtain the approximate response. The assumption of $\Delta k_\eta = \Delta k_\xi/6$ is used for simplicity throughout.

Average Deflection. The average deflection determines the response center (the average position) of the cracked rotor and is given by:

$$X_o(t) = 1 + \tfrac{1}{4}(\Delta K_\xi + \Delta K_\eta) + E\Delta K_\xi \cos(\psi + \beta)/\pi \tag{17}$$

$$Y_o(t) = -\Delta K_\eta E \sin(\psi + \beta)/\pi \tag{18}$$

It can be seen that in addition to the static deflection $X_0 = 1$ of the uncracked rotor, there are two additional deflection contributions caused by the rotor crack in the direction of the weight. The angle $\psi + \beta$ determines the sign of the third contribution. For small D, $\psi = 0$ in the subcritical range ($\Omega < 1$) and $\psi = \pi$ in the supercritical range ($\Omega > 1$), so that when $\Omega < 1$, the average deflection X_0 will have its largest value when the crack is in the direction of unbalance ($\beta = 0$) and its smallest value when the crack is in the opposite direction to the unbalance ($\beta = \pi$). When $\Omega > 1$, the opposite holds. The change of X_0 with crack and crack angle for different speed ratios is shown in Fig. 2. This additional average deflection could be used for crack detection, especially in the supercritical range.

Synchronous Component. The synchronous component of the system response is very important for crack detection and is given by:

$$Z_1(t) = Ee^{i(\omega t+\varphi-\psi)} + E_1(A_1 e^{i\Phi_1} + A_{-1}e^{-i\Phi_1})$$
$$= P_1 e^{i(\Phi_1+\theta_{f1})} + Q_1 e^{-i\Phi_1} \tag{19}$$

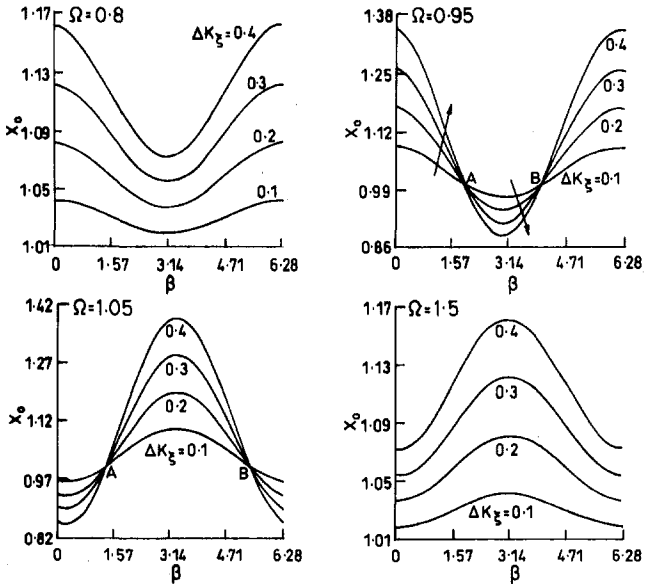


Fig. 2 Variation of X_o with crack angle β (D = 0.01, U = 0.2, $\Delta K_\eta = \Delta K_\xi/6$)

where

$$P_1 = E_1\left\{\left[\frac{1}{\pi}\Delta K_\xi + \frac{E}{2}\Delta K_\xi \cos(\psi + \beta) + U\Omega^2 \cos\beta\right]^2 + \left[\frac{E}{2}\Delta K_\eta \sin(\psi + \beta) + U\Omega^2 \sin\beta\right]^2\right\}^{1/2}, \tag{20}$$

$$Q_1 = \frac{E_1}{3\pi}(\Delta K_\xi + 2\Delta K_\eta), \tag{21}$$

and

$$\tan\theta_{f1} = -\frac{\frac{E}{2}\Delta K_\eta \sin(\psi + \beta) + U\Omega^2 \sin\beta}{\frac{1}{\pi}\Delta K_\xi + \frac{E}{2}\Delta K_\xi \cos(\psi + \beta) + U\Omega^2 \cos\beta}. \tag{22}$$

Hence, the orbit of the synchronous component is an ellipse with the major half and minor half axes given by $P_1 + Q_1$ and $P_1 - Q_1$, respectively. The difference between the major and the minor axes ΔE_1 is $4Q_1$ if $P_1 \geq Q_1$ or $4P_1$ if $P_1 < Q_1$ and the angle between the major axis and the X-axis α_1 is $\frac{1}{2}\theta_{f1}$.

The synchronous component is formed by a forward and a backward whirl. The backward whirl is caused solely by the crack and is not related to the crack angle β nor the unbalance ratio U. If $P_1 > Q_1$, the final synchronous movement is forward; if $P_1 < Q_1$ it is backward. Generally $P_1 > Q_1$, but $P_1 < Q_1$ is possible, e.g., when $\psi + \beta \approx \pi$, $\Omega < 1$, $\psi \approx 0$, $E < 4/3\pi$, and $\mu < \Delta K_\xi < (2\Delta K_\eta + 3\pi U\Omega^2)/(2 - 3\pi E/2)$. If, further, $\Delta K_\xi = \mu$ then $P_1 = 0$, and the synchronous orbit is a backward circle. An example of $P_1 < Q_1$ and $P_1 = 0$ is shown in Fig. 3(*b*). If $\beta = \pi$, then in the speed range $\Omega < 1$ (where $\psi \approx 0$), when $E > 2/\pi$, P_1 will increase with ΔK_ξ; when $E < 2/\pi$, P_1 will decrease with ΔK_ξ if $\Delta K_\xi < \mu$, will equal almost zero if $\Delta K_\xi = \mu$ and will increase with ΔK_ξ if $\Delta K_\xi > \mu$ (Fig. 3(*b*)). In the speed range $\Omega > 1$ (where $\psi \approx \pi$), P_1 will decrease with ΔK_ξ if $\Delta K_\xi < \nu$ (Fig. 4(*b*)) will equal almost zero if $\Delta K_\xi = \nu$, and will increase with ΔK_ξ if $\Delta K_\xi > \nu$.

The backward whirl is one important evidence of a crack. Another one is the difference between the major and minor axes

Downloaded 02 Jun 2010 to 171.66.16.105. Redistribution subject to ASME license or copyright; see http://www.asme.org/terms/Terms_Use.cfm

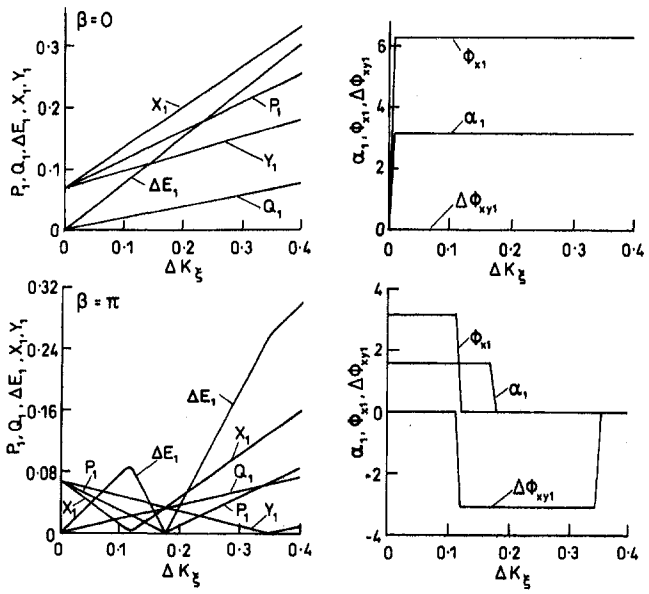


Fig. 3 Variation of synchronous (1X) characteristics with stiffness change ratio ΔK_ξ ($D = 0.01$, $U = 0.2$, $\Delta K_\eta = \Delta K_\xi/6$, $\Omega = 0.5$)

ΔE_1, which is four times the backward whirl amplitude Q_1 when $P_1 > Q_1$, and so the evidence of a crack is enlarged four times if ΔE_1 is used for crack detection instead of Q_1. Besides, it is easier to measure ΔE_1 than Q_1. Hence, by measuring the increase in ΔE_1, the development of a crack can be diagnosed and monitored. It can also be seen that the influence of the stiffness change ratio ΔK_η on Q_1 and ΔE_1 cannot be simply omitted because the influence of ΔK_η is magnified.

The angle α_1 is zero or $\pi/2$ for an uncracked rotor. α_1 depends largely on β, so it may be large even for very small cracks, even when it is very difficult to distinguish the change in response amplitude from measurement errors. Hence α_1 can also be used for small crack diagnosis.

For vibration measurement, two transducers are generally used, with one in the horizontal and the other in the vertical direction. For comparison purposes, it is useful to consider the synchronous components in the X and Y directions. Thus, from Eq. (19):

$$X_1(t) = X_1 \cos(\Phi_1 + \varphi_{x1}), \tag{23}$$

and

$$Y_1(t) = Y_1 \cos(\Phi_1 + \varphi_{y1}), \tag{24}$$

where

$$X_1 = [(P_1 \cos\theta_{f1} + Q_1)^2 + (P_1 \sin\theta_{f1})^2]^{1/2}, \tag{25}$$

$$\tan\varphi_{x1} = \frac{P_1 \sin\theta_{f1}}{Q_1 + P_1 \cos\theta_{f1}}, \tag{26}$$

and

$$Y_1 = [(P_1 \cos\theta_{f1} - Q_1)^2 + (P_1 \sin\theta_{f1})^2]^{1/2}, \tag{27}$$

$$\tan\varphi_{y1} = \frac{P_1 \sin\theta_{f1}}{P_1 \cos\theta_{f1} - Q_1}. \tag{28}$$

Substitution for P_1 and Q_1 gives:

$$X_1 = E_1\left\{\left[\frac{4}{3\pi}\Delta K_\xi + \frac{E}{2}\Delta K_\xi \cos(\psi+\beta) + \frac{2}{3\pi}\Delta K_\eta + U\Omega^2\cos\beta\right]^2 + \left[-\frac{E}{2}\Delta K_\eta \sin(\psi+\beta) - U\Omega^2\sin\beta\right]^2\right\}^{1/2}, \tag{29}$$

$$Y_1 = E_1\left\{\left[\frac{2}{3\pi}\Delta K_\xi + \frac{E}{2}\Delta K_\xi \cos(\psi+\beta) - \frac{2}{3\pi}\Delta K_\eta + U\Omega^2\cos\beta\right]^2 + \left[-\frac{E}{2}\Delta K_\eta \sin(\psi+\beta) - U\Omega^2\sin\beta\right]^2\right\}^{1/2}. \tag{30}$$

The amplitude X_1 or Y_1 may be less in some cases than the amplitude E of an uncracked rotor and may decrease with increasing crack when $\pi/2 < \beta < 3\pi/2$, especially when the crack is in the opposite direction to the unbalance. Thus, when $\beta = \pi$, $E < 8/3\pi$, and $\Omega < 1$, X_1 will decrease with increasing crack when:

$$\left(\frac{4}{3\pi} - \frac{E}{2}\right)\Delta K_\xi + \frac{2}{3\pi}\Delta K_\eta < U\Omega^2 \tag{31}$$

and X_1 or Y_1 may even equal zero when:

$$\left(\frac{4}{3\pi} - \frac{E}{2}\right)\Delta K_\xi = U\Omega^2 - \frac{2}{3\pi}\Delta K_\eta \quad \left(\Delta K_\eta < \tfrac{3}{2}\pi U\Omega^2\right). \tag{32}$$

One example of $X_1 = 0$ or $Y_1 = 0$ is shown in Fig. 3(b), where the synchronous orbit is a straight line (see Fig. 6).

The influence of crack on rotor response can be regarded as an additional unbalance. Therefore, the combined influence of the crack and the original unbalance may increase or decrease the response amplitude of the cracked rotor. Hence, crack detection by measuring the increase of response amplitude is sometimes not possible. However, decrease of response amplitude is important evidence of a crack. The response amplitude of a cracked rotor can also be reduced by adding suitable unbalance, for example in the opposite direction to the crack for $\Omega < 1$, if the cracked rotor is required to run for some time before it is replaced.

The phase difference between the responses with and without a crack in the X and Y directions is given by:

$$\psi_{x1} = \Phi_1 + \varphi_{x1} - (\omega t + \varphi - \psi) = \beta + \varphi_{x1} \tag{33}$$

and

$$\psi_{y1} = \Phi_1 + \varphi_{y1} - (\omega t + \varphi - \psi) = \beta + \varphi_{y1}. \tag{34}$$

Depending on the crack position (i.e., on β), these could be large even for a small crack and hence could be used for crack detection. However, it is difficult to determine the reference phase angle for the uncracked case. An alternative approach is to measure the phase difference between the horizontal and vertical vibration signals. For an uncracked rotor, this phase

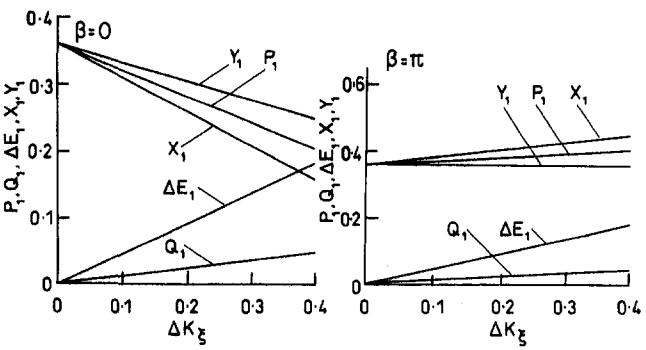


Fig. 4 Variation of synchronous (1X) characteristics with stiffness change ratio ΔK_ξ ($D = 0.01$, $U = 0.2$, $\Delta K_\eta = \Delta K_\xi/6$, $\Omega = 1.5$)

Downloaded 02 Jun 2010 to 171.66.16.105. Redistribution subject to ASME license or copyright; see http://www.asme.org/terms/Terms_Use.cfm

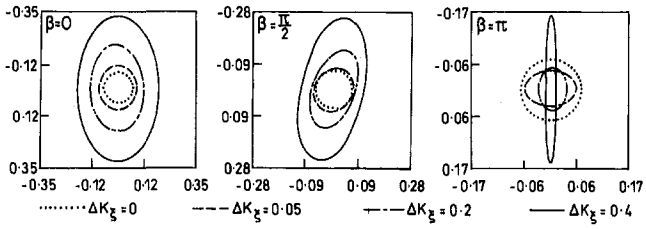


Fig. 5 Variation of synchronous (1*X*) orbit with stiffness change ratio ΔK_ξ (D = 0.001, U = 0.2, $\Delta K_\eta = \Delta K_\xi/6$, Ω = 0.5)

difference should be $\pi/2$, but for a cracked rotor there is an additional phase difference of:

$$\Delta\varphi_{xy1} = \varphi_{x1} - \varphi_{y1} = -\tan^{-1}\left(\frac{2P_1Q_1\sin\theta_{f1}}{P_1^2 - Q_1^2}\right). \quad (35)$$

Examples of the variation of the synchronous component characteristics P_1, Q_1, ΔE_1, X_1, Y_1, α_1, φ_{x_1} and $\Delta\varphi_{xy_1}$, with speed ratio Ω, stiffness change ratio ΔK_ξ, crack angle β, and unbalance ratio U together with synchronous orbits are shown in Figs. 3–9.

Figures 3 and 4 show the variation of synchronous component characteristics with ΔK_ξ for $\beta = 0$ and π. It can be seen that Q_1 increases almost linearly with ΔK_ξ. ΔE_1 increases linearly with ΔK_ξ in all speed ranges except when β is near π. When $\beta = \pi$ (Fig. 3), ΔE_1 will increase with ΔK_ξ when $P_1 > Q_1$, but experiences a dip when $P_1 < Q_1$.

When $\beta = 0$, P_1, X_1, and Y_1 increase almost linearly with ΔK_ξ except in a speed ratio range near but larger than the critical $\Omega = 1$, where P_1, X_1, and Y_1 decrease with ΔK_ξ. Also, α_1 almost equals π, φ_{x1} almost equals 2π, and $\Delta\varphi_{xy1}$ almost equals zero. When $\beta = \pi$, as already noted above, P_1, X_1 and Y_1 may decrease with increasing ΔK_ξ, and P_1 may be less than Q_1 or even equal zero. Compared with P_1, X_1 will have its minimum value for a smaller ΔK_ξ and Y_1 will have its minimum value for a larger ΔK_ξ (Fig. 3). It can be seen that in most cases, the variations in ΔE_1 and X_1 are more sensitive to crack stiffness ratio changes than the variations in P_1, Q_1 and Y_1. Hence, the variations in ΔE_1 and X_1, especially the decrease in X_1, can be used for crack detection.

Figures 5 and 6 show the variation in synchronous orbits with ΔK_ξ for $\beta = 0$, $\pi/2$, and π. It can be seen that except for the case when β is near π, the vibration amplitude and the orbit ellipticity increase as ΔK_ξ increases. When $\beta = \pi$, the vibration amplitude decreases and the orbit ellipticity increases for $\Omega > 1.2$; while for $\Omega = 0.5$, the vibration amplitude decreases at first and then increases with ΔK_ξ, and the orbit ellipticity increases at first, decreases and then increases again with ΔK_ξ (Fig. 5).

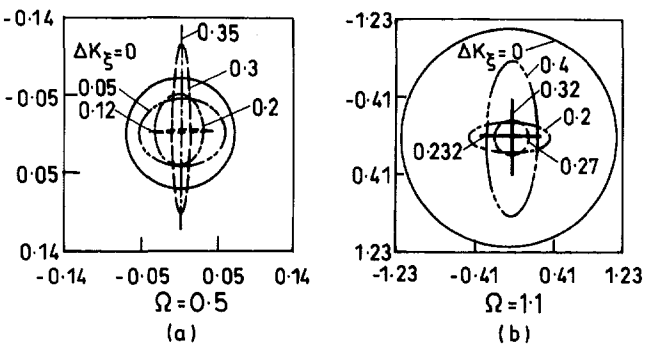


Fig. 6 Variation of synchronous (1*X*) orbit with stiffness change ratio ΔK_ξ (D = 0.001, U = 0.2, $\Delta K_\eta = \Delta K_\xi/6$, $\beta = \pi$, Ω = 1.1)

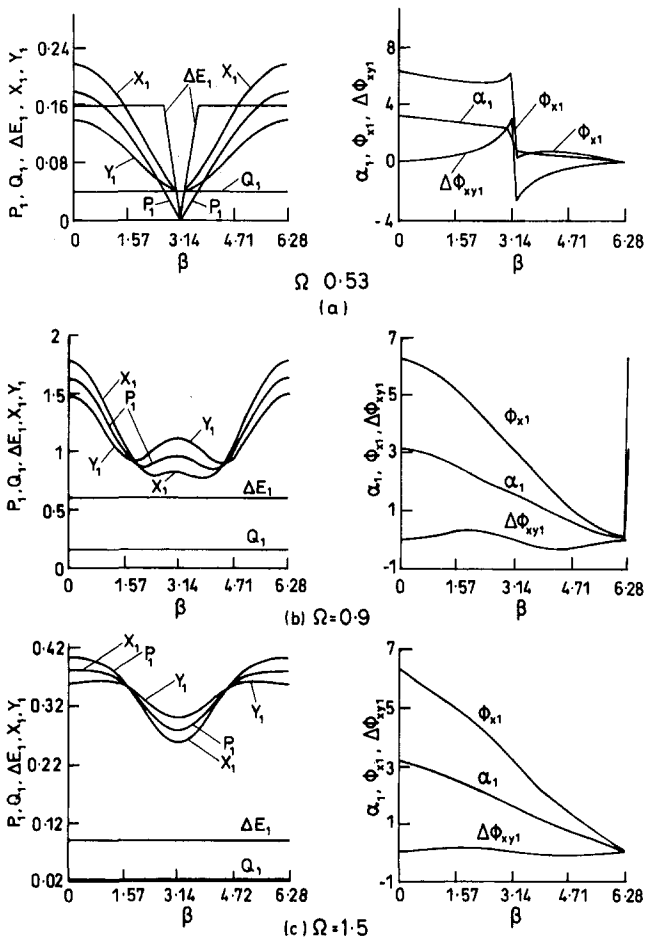


Fig. 7 Variation of synchronous (1*X*) characteristics with crack angle β (D = 0.01, U = 0.2, ΔK_ξ = 0.2, $\Delta K_\eta = \Delta K_\xi/6$)

As already noted, P_1, X_1, and Y_1 may equal zero when $\beta = \pi$. $P_1 = 0$ means that the synchronous response is a pure backward whirl and the response is a circle with a radius of Q_1. $X_1 = 0$ or $Y_1 = 0$ means that the synchronous orbit is a straight line in the Y-axis direction or in the X-axis direction, respectively (Fig. 6).

Figure 7 shows the variation of the synchronous component characteristics with β. Q_1 does not change with β. ΔE_1 does not change with β when $P_1 > Q_1$. When $P_1 < Q_1$, ΔE_1 decreases with β when $\beta < \pi$ and increases with β when $\beta > \pi$. The variations of P_1, X_1, and Y_1 with β depend largely on Ω. When Ω is far from the critical $\Omega = 1$, P_1, X_1, and Y_1 decrease with β when $\beta < \pi$ and increase with β when $\beta > \pi$. When Ω is near but less than the critical $\Omega = 1$, P_1, X_1, and Y_1 may decrease with β when $\beta < \pi/2$ and $\pi < \beta < 3\pi/2$ and may increase with β when $\pi/2 < \beta < \pi$ and $\beta > 3\pi/2$. When $P_1 > Q_1$, the angle α_1 decreases from π to zero and the angle φ_{x1} decreases from 2π to zero as β increases from zero to 2π. When $P_1 < Q_1$, the angles α_1 and φ_{x1} may increase a little just before $\beta = \pi$ but experience a sudden decrease at $\beta = \pi$.

Figure 8 shows the variation of the synchronous orbit with β. The position of the major axis of the elliptic orbit obviously changes with β. For small cracks, changes in vibration amplitude in the supercritical range may be too small to be detected, but changes in the position of the major axis may be large enough to be detected.

Figure 9 shows the variation of the synchronous component characteristics with U. Q_1 does not change with U. ΔE_1 does not change with U when $P_1 > Q_1$, but at first decreases and then increases with U when $P_1 < Q_1$. P_1, X_1, and Y_1 increase

Downloaded 02 Jun 2010 to 171.66.16.105. Redistribution subject to ASME license or copyright; see http://www.asme.org/terms/Terms_Use.cfm

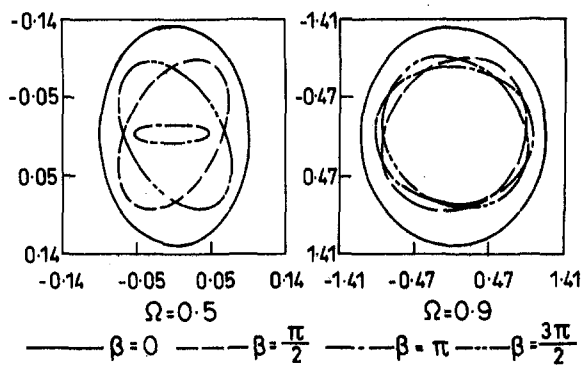


Fig. 8 Variation of synchronous (1X) characteristics with crack angle β (D = 0.001, U = 0.2, ΔK_ξ = 0.1, $\Delta K_\eta = \Delta K_\xi/6$, Ω = 0.5)

with U when the crack is primarily in the direction of the unbalance. When the crack is on the opposite side of the unbalance, especially when the crack is in the opposite direction to the unbalance ($\beta = \pi$), P_1, X_1, and Y_1 may decrease at first, have their minimum value (of zero) at a certain value of U, and then increase with U. Hence, depending on crack orientation, the vibration amplitude of a cracked rotor may actually decrease with increasing unbalance.

2X -Order Harmonic Component. The $2X$-order component is also useful for crack detection, and is given by:

$$Z_2(t) = E_2\{A_2 e^{i\Phi_2} + A_{-2} e^{-i\Phi_2}\} = P_2 e^{i(\Phi_2+\theta_{f2})} + Q_2 e^{-i(\Phi_2+\theta_{b2})}, \quad (36)$$

where

$$P_2 = E_2\left\{\left[\frac{1}{4}(\Delta K_\xi - \Delta K_\eta) + \frac{E}{\pi}\Delta K_\xi \cos(\psi+\beta)\right]^2 + \left[\frac{E}{\pi}\Delta K_\eta \sin(\psi+\beta)\right]^2\right\}^{1/2}, \quad (37)$$

$$Q_2 = \frac{E}{3\pi} E_2\{[\Delta K_\xi \cos(\psi+\beta)]^2 + [\Delta K_\eta \sin(\psi+\beta)]^2\}^{1/2}, \quad (38)$$

$$\tan\theta_{f2} = -\frac{\Delta K_\eta \sin(\psi+\beta)}{\frac{\pi}{4E}(\Delta K_\xi - \Delta K_\eta) + \Delta K_\xi \cos(\psi+\beta)}, \quad (39)$$

and

$$\tan\theta_{b2} = \frac{\Delta K_\eta}{\Delta K_\xi}\tan(\psi+\beta). \quad (40)$$

Hence, the $2X$-component also consists of a forward and a backward whirl, due to the crack. The $2X$-response is also elliptic, with its major half and minor half axes given by $P_2 + Q_2$ and $P_2 - Q_2$, respectively. The difference between the major and the minor axes ΔE_2 is $4Q_2$ if $P_2 \geq Q_2$ or $4P_2$ if $P_2 < Q_2$, and the angle between the major axis and the X axis is $\alpha_2 = \frac{1}{2}(\theta_{f2} - \theta_{b2})$. Depending on β, α_2 may be large for small cracks, suggesting a possibility for crack detection. P_2, Q_2, and ΔE_2 have two peaks near Ω = 0.5 and Ω = 1.

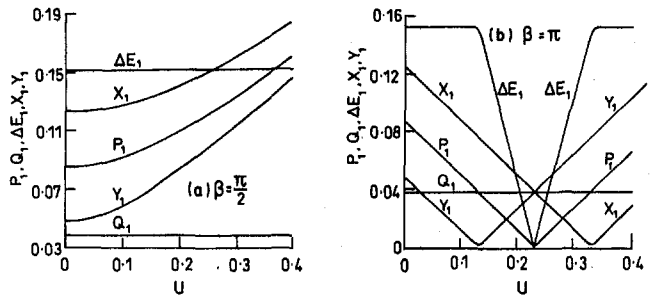


Fig. 9 Variation of synchronous (1X) characteristics with unbalance ratio U (D = 0.01, ΔK_ξ = 0.2, $\Delta K_\eta = \Delta K_\xi/6$, Ω = 0.5)

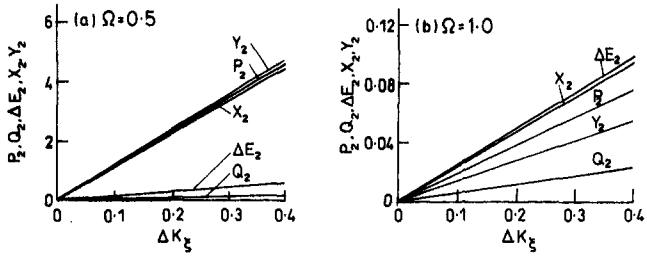


Fig. 10 Variation of nonsynchronous (2X) characteristics with stiffness change ratio ΔK_ξ (D = 0.01, U = 0.2, $\Delta K_\eta = \Delta K_\xi/6$, β = 0.0)

The $2X$-components in the X and Y directions are given by:

$$X_2(t) = X_2 \cos(\Phi_2 + \varphi_{x2}), \quad (41)$$

and

$$Y_2(t) = Y_2 \sin(\Phi_2 + \varphi_{y2}), \quad (42)$$

where

$$X_2 = E_2\left\{\left[\frac{1}{4}(\Delta K_\xi - \Delta K_\eta) + \frac{2E}{3\pi}\Delta K_\xi \cos(\psi+\beta)\right]^2 + \left[\frac{4E}{3\pi}\Delta K_\eta \sin(\psi+\beta)\right]^2\right\}^{1/2} \quad (43)$$

$$Y_2 = E_2\left\{\left[\frac{1}{4}(\Delta K_\xi - \Delta K_\eta) + \frac{4E}{3\pi}\Delta K_\xi \cos(\psi+\beta)\right]^2 + \left[\frac{2E}{3\pi}\Delta K_\eta \sin(\psi+\beta)\right]^2\right\}^{1/2} \quad (44)$$

$$\tan\varphi_{x2} = -\frac{\frac{4E}{3\pi}\Delta K_\eta \sin(\psi+\beta)}{\frac{1}{4}(\Delta K_\xi - \Delta K_\eta) + \frac{2E}{3\pi}\Delta K_\xi \cos(\psi+\beta)}, \quad (45)$$

$$\tan\varphi_{y2} = -\frac{\frac{2E}{3\pi}\Delta K_\eta \sin(\psi+\beta)}{\frac{1}{4}(\Delta K_\xi - \Delta K_\eta) + \frac{4E}{3\pi}\Delta K_\xi \cos(\psi+\beta)}. \quad (46)$$

and the additional phase difference between $X_2(t)$ and $Y_2(t)$ is:

$$\Delta\varphi_{xy2} = \varphi_{x2} - \varphi_{y2}. \quad (47)$$

X_2 and Y_2 also have two peaks near Ω = 0.5 and Ω = 1.

P_2, Q_2, ΔE_2, X_2, and Y_2 all increase with ΔK_ξ. Q_2 and ΔE_2 may have a maximum near $\psi + \beta = 0$ and π, and a minimum near $\psi + \beta = \pi/2$ and $3\pi/2$. P_2, X_2, and Y_2 may equal zero when $\psi + \beta = \pi$. From Eqs. (37), (43), and (44), it can be shown that P_2, X_2, and Y_2 will equal zero when

$$E = \frac{5\pi}{24}, \frac{5\pi}{16}, \text{ and } \frac{5\pi}{32} \text{ respectively,} \quad (48)$$

Figure 10 shows the variation of the $2X$-harmonic characteristics with ΔK_ξ. It can be seen that P_2, Q_2, ΔE_2, X_2, and Y_2,

Downloaded 02 Jun 2010 to 171.66.16.105. Redistribution subject to ASME license or copyright; see http://www.asme.org/terms/Terms_Use.cfm

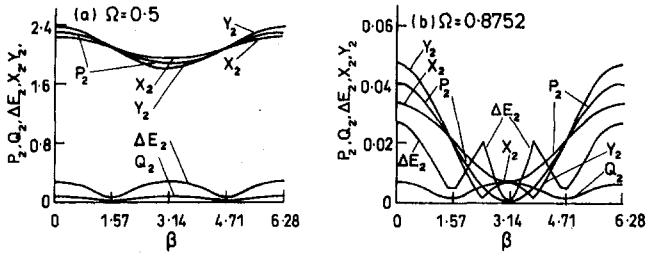


Fig. 11 Variation of nonsynchronous (2X) characteristics with crack angle β (D = 0.01, U = 0.2, ΔK_ξ = 0.2, $\Delta K_\eta = \Delta K_\xi/6$

increase linearly with ΔK_ξ since it is assumed that $\Delta K_\eta/\Delta K_\xi = \frac{1}{6}$.

Figure 11 shows the variation of the $2X$-harmonic characteristics with β. It can be seen that P_2, Q_2, ΔE_2, X_2, and Y_2 change greatly with β and when $\Omega < 0.8$, P_2, X_2, and Y_2 have their maximum value near $\beta = 0$ and their minimum value near $\beta = \pi$; whereas Q_2 and ΔE_2 have their maximum value near $\beta = 0$, π and their minimum value near $\beta = \pi/2$, $3\pi/2$. When $\Omega < 0.8$, the angle φ_{x2} and the X and Y phase difference $\Delta\varphi_{xy2}$ are virtually constant when β changes from 0 to 2π, but the angle α_2 decreases from $\pi/2$ near $\beta = 0$ to zero near $\beta = \pi$ and to $-\pi/2$ near $\beta = 2\pi$, i.e., the major axis of the elliptic orbit changes from the Y direction if $\beta = 0$ to the X direction if $\beta = \pi$. When $\Omega = 0.8752$, P_2 almost equals zero and P_2 is less than Q_2 when the crack angle is near $\beta = \pi$. $P_2 < Q_2$ means that the $2X$-response is a backward movement.

P_2, Q_2, ΔE_2, X_2, and Y_2 increase with U for $\beta = 0$ and $\Omega < 1$ or for $\beta = \pi$ and $\Omega > 1$. When $\beta = 0$ and $\Omega > 1$, or when $\beta = \pi$ and $\Omega < 1$, P_2, X_2, and Y_2 decrease at first with U, equal almost zero for values of U given by Eq. (48) and increase again as U increases further. Q_2 always increases with U and ΔE_2 increases with U whenever $P_2 > Q_2$.

3X -Order Harmonic Component. The $3X$-order component can also be used for crack detection and is given by:

$$Z_3(t) = E_3\{A_3 e^{i\Phi_3} + A_{-3} e^{-i\Phi_3}\} = P_3 e^{i\Phi_3} + Q_3 e^{-i(\Phi_3 - \pi)} \quad (49)$$

where

$$P_3 = \frac{E_3}{3\pi}(\Delta K_\xi - 2\Delta K_\eta), \quad (50)$$

and

$$Q_3 = \frac{E_3}{15\pi}(\Delta K_\xi + 4\Delta K_\eta). \quad (51)$$

Hence, the $3X$-component is also formed by a forward and a backward whirl due to the crack. The $3X$-response is also elliptic with the difference between the major and the minor axes ΔE_3 given by $4Q_3$ if $P_3 \geq Q_3$ or $4P_3$ if $P_3 < Q_3$, and the angle between the major axis and the X axis α_3 given by $\pi/2$, so that the major axis of the response orbit is the Y axis, perpendicular to the weight direction. It can again be seen that the influence of the cross-stiffness change ratio ΔK_η cannot be omitted.

The $3X$-components in the X and Y directions are given by:

$$X_3(t) = X_3 \cos(3\Phi - \psi_3), \quad (52)$$

and

$$Y_3(t) = Y_3 \sin(3\Phi - \psi_3), \quad (53)$$

where

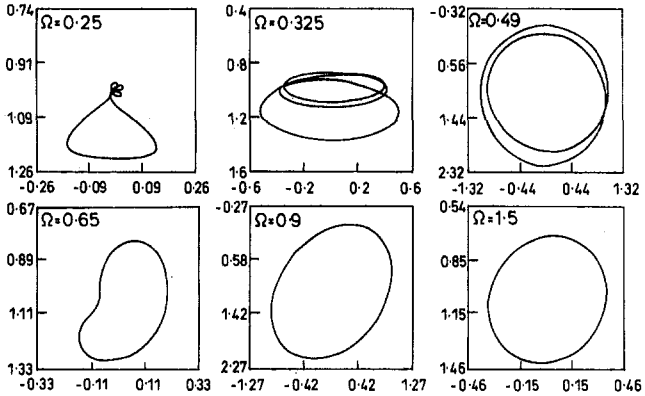


Fig. 12 Variation of approximate response with speed ratio Ω (D = 0.001, U = 0.2, ΔK_ξ = 0.2, $\Delta K_\eta = \Delta K_\xi/6$, $\beta = \pi/2$)

$$X_3 = \frac{2E_3}{15\pi}(2\Delta K_\xi - 7\Delta K_\eta), \quad (54)$$

$$Y_3 = \frac{2E_3}{5\pi}(\Delta K_\xi - \Delta K_\eta), \quad (55)$$

and the phase difference between $X_3(t)$ and $Y_3(t)$ is $\pi/2$.

P_3, Q_3, ΔE_3, X_3, and Y_3 have a peak value near $\Omega = \frac{1}{3}$, though except near $\Omega = \frac{1}{3}$, the $3X$-harmonic component is very small. It can be seen that β and U have no influence on the $3X$-harmonic component.

4X -Order Harmonic Component. The $4X$-order component may also be used for crack detection when a cracked rotor runs up or coasts down past a quarter of the critical speed ($\Omega = \frac{1}{4}$). The $4X$ component is also formed by a forward and a backward whirl and the orbit of the $4X$-response is an ellipse.

The $4X$-components in the X and Y directions are given by:

$$X_4(t) = X_4 \cos(\Phi_4 + \varphi_{x4}), \quad (56)$$

$$Y_4(t) = Y_4 \sin(\Phi_4 + \varphi_{y4}), \quad (57)$$

where

$$X_4 = \frac{2EE_4}{15\pi}\{[4\Delta K_\xi \cos(\psi + \beta)]^2 + [\Delta K_\eta \sin(\psi + \beta)]^2\}^{1/2} \quad (58)$$

$$Y_4 = \frac{2EE_4}{15\pi}\{[\Delta K_\xi \cos(\psi + \beta)]^2 + [4\Delta K_\eta \sin(\psi + \beta)]^2\}^{1/2} \quad (59)$$

$$\tan\varphi_{x4} = -\frac{1}{4}\frac{\Delta K_\eta}{\Delta K_\xi}\tan(\psi + \beta), \quad (60)$$

$$\tan\varphi_{y4} = 4\frac{\Delta K_\eta}{\Delta K_\xi}\tan(\psi + \beta) \quad (61)$$

X_4 and Y_4 have one peak at $\Omega = \frac{1}{4}$ and may have one peak at $\Omega = 1$ or two peaks near $\Omega = 1$ (one below and one above the critical) depending on the value of β. Except near $\Omega = \frac{1}{4}$, the $4X$-component is very small compared with the synchronous component and has almost no influence on system response.

Approximate Response. The overall approximate response of the cracked rotor can be obtained by summing the components as required by Eq. (19). Figures 12–15 show the overall response orbits. In all figures, the center of the figure is $X = 1$ ($x = \delta$) and $Y = 0$, corresponding to the static deflection of the uncracked rotor.

Downloaded 02 Jun 2010 to 171.66.16.105. Redistribution subject to ASME license or copyright; see http://www.asme.org/terms/Terms_Use.cfm

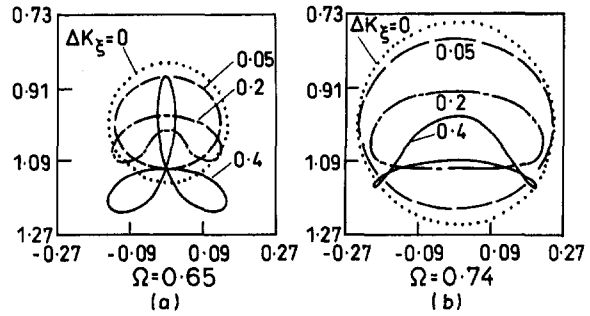


Fig. 13 Variation of approximate response with stiffness change ratio ΔK_ξ ($D = 0.001$, $U = 0.2$, $\Delta K_\eta = \Delta K_\xi/6$, $\beta = \pi$, $\Omega = 0.65$)

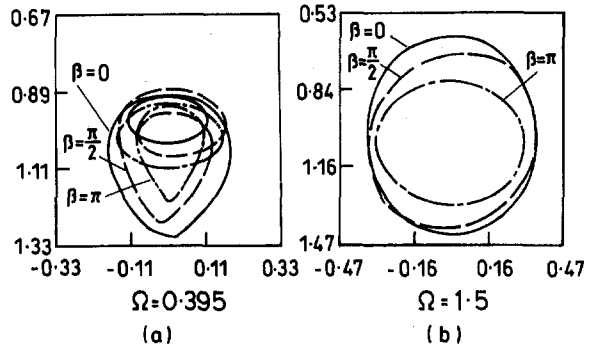


Fig. 14 Variation of approximate response with crack angle β ($D = 0.001$, $U = 0.2$, $\Delta K_\xi = 0.2$, $\Delta K_\eta = \Delta K_\xi/6$, $\Omega = 1.5$)

The response of the cracked rotor is generally nonsynchronous when $\Omega < \frac{2}{3}$, particularly when $\Omega < \frac{1}{2}$. The response will change from synchronous to nonsynchronous when $\Omega < \frac{1}{2}$ even if the crack is very small. The nonsynchronous component will increase with increasing crack, but the synchronous component may increase or decrease with increasing crack depending on the crack angle. When $\frac{2}{3} < \Omega < 1$, the response is generally synchronous, but may become nonsynchronous for large cracks. The response is generally synchronous and the orbit is elliptic when $\Omega > 1$, even for very large cracks.

A small crack can be detected by measuring the nonsynchronous components in the speed range $\Omega < \frac{1}{2}$ or when the rotor

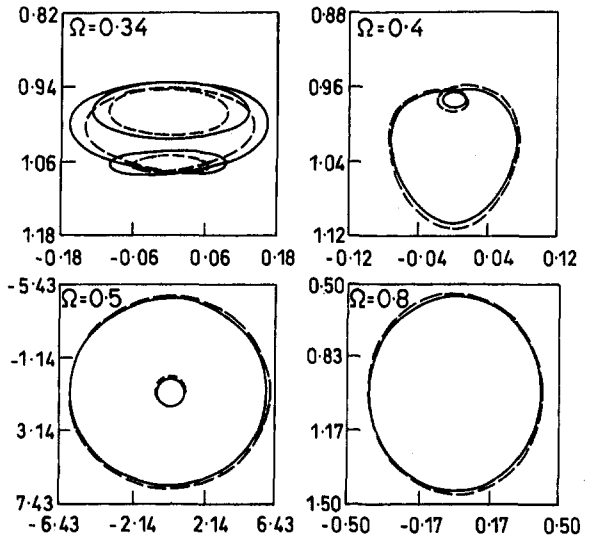


Fig. 15 Comparison of approximate and accurate response ($D = 0.001$, $U = 0.2$, $\Delta K_\xi = 0.05$, $\Delta K_\eta = \Delta K_\xi/6$, $\beta = 0.0$)

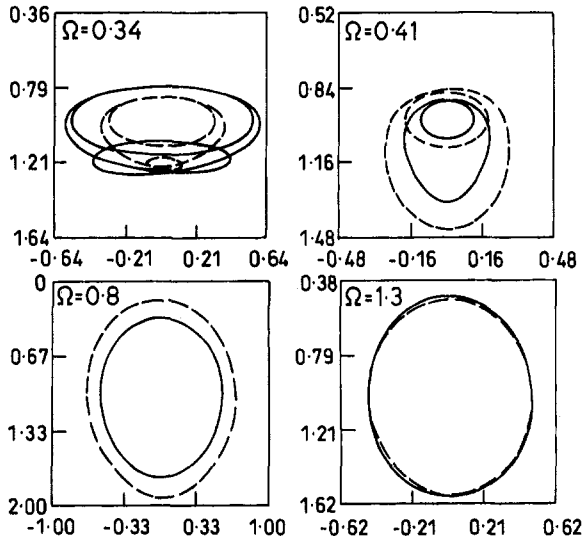


Fig. 16 Comparison of approximate and accurate response ($D = 0.001$, $U = 0.2$, $\Delta K_\xi = 0.02$, $\Delta K_\eta = \Delta K_\xi/6$, $\beta = 0.0$)

speeds up or slows down. If the rotor cannot be stopped and needs to run continuously at operating speed in the supercritical range ($\Omega > 1$), nonsynchronous components cannot be used for crack detection. Detection of a crack under such conditions still remains a difficult problem to this very day though there are a few methods, such as vector pattern recognition (Bently Nevada, 1986), that could be used. However, as discussed above, in such cases the crack could be detected by the increasing ellipticity of the response orbit, the variation of the major axis direction, or by the shifting down or up of the average position of the response from that of the uncracked rotor. Another important indication of crack in the supercritical range is a decrease in the response amplitude as may be caused by a crack on the opposite side of the unbalance.

For a nonsynchronous orbit, the inner or outer loop direction changes greatly with β while for a synchronous elliptic orbit, its major axis direction changes greatly with β. Additionally, the response amplitude may increase or decrease. Depending on β, increase in the unbalance ratio U may also increase or decrease the response amplitude. The influence of U is mainly on the synchronous component of the response.

Accuracy of Simplified Solution Approach. The accuracy of this simplified series solution approach was checked by also solving Eq. (7) directly using fourth-order Runge–Kutta.

Comparisons show that the simplified series solutions and the full numerical solutions are in very good agreement for small cracks ($\Delta K_\xi < 0.2$) when the speed ratio Ω is outside the range of Eq. (8). For large cracks ($\Delta K_\xi > 0.2$), the series solution differs to a larger extent when $\Omega < \frac{2}{3}$ or near $\Omega = 1$, but it is still a good approximation in the supercritical range ($1.1 < \Omega < 1.8$). Figures 15 and 16 are two examples of such comparisons.

Since the detection of small cracks is of major importantance, the approximate analysis technique and the resulting response given here are reasonable and useful. The simplified analysis, apart from yielding analytical results, achieves significant savings in computation time.

Conclusions

The dynamic response of a Jeffcott rotor with small cracks is analyzed both theoretically and numerically. The zero to fourth-order harmonic components of the system response are obtained approximately.

Downloaded 02 Jun 2010 to 171.66.16.105. Redistribution subject to ASME license or copyright; see http://www.asme.org/terms/Terms_Use.cfm

The rotor crack causes the average position of a cracked rotor to shift down or up from its uncracked static position.

The rotor crack causes backward whirl. Its amplitude generally increases with the crack and in some cases may be larger than the forward whirl amplitude. The backward whirl amplitude has no relation to the crack angle β or the unbalance ratio U.

The orbit of each harmonic component of the response is elliptic. The ellipticity of the orbit increases and the angle between the major axis and the X axis may change significantly as the crack increases.

The influence of a crack on rotor response can be regarded as an additional unbalance and hence, the response amplitude of a cracked rotor may be reduced by adding a suitable unbalance, provided this is accompanied by careful on-line monitoring to ensure safety.

Rotor cracks cause nonsynchronous response in the subcritical range, especially for speed ratio $\Omega < \frac{2}{3}$, but the response in the supercritical range is still synchronous even if the crack is large.

The influence of the cross-stiffness change ratio ΔK_η is significant and should not be omitted.

Possible evidences of a rotor crack include: (*i*) nonsynchronous response, especially when $\Omega = \frac{1}{2}, \frac{1}{3}$, and $\frac{1}{4}$, generally negligible in the supercritical range; (*ii*) increase or decrease in response amplitude, especially the latter, with the response amplitude in the weight direction being more sensitive to small cracks; (*iii*) increase in the ellipticity of the response orbit (or the response orbit of the synchronous and nonsynchronous harmonic components of the response); (*iv*) change in the angle between the weight direction and the major axis of the elliptic response orbit (or the elliptic orbit of the synchronous and nonsynchronous components of the response); (*v*) variation in the phase difference between the responses (or the synchronous components of the responses) with and without a crack in both the X and Y directions, especially in the X (weight) direction; (*vi*) variation in the phase difference between the X and Y vibration signals; (*vii*) the appearance of and increase in backward whirl, and the decrease or increase in forward whirl; and (*viii*) the shifting down or up of the average response position.

Outside the unstable range, and for small cracks and small dynamic vibrations, the simplified approximate response obtained in this paper is a good approximation.

Acknowledgments

The support of the Australian Research Council and Pacific Power (Northern Region) is gratefully acknowledged. The authors also wish to thank Dr. N. S. Feng and Prof. R. Gasch for their useful suggestions.

References

Bently Nevada, 1986, "Early Shaft Crack Detection on Rotating Machinery Using Vibration Monitoring and Diagnostics," Technical Bulletin No. L1036-00, No. 1.

Dimarogonas, A. D., and Papadopoulos, C. A., 1983, "Vibration of Cracked Shaft in Bending," *J. Sound and Vibration,* Vol. 91, pp. 583–593.

Fridemann, P., et al., 1977, "Efficient Numerical Treatment of Periodic Systems With Application to Stability Problems," *Intl. J. for Numerical Methods in Engineering,* Vol. 11, pp. 1117–1136.

Gasch, R., 1976, "Dynamic Behaviour of a Simple Rotor With a Cross Sectional Crack," C178/76, *Proc. I Mech E, Vibrations in Rotating Machinery*, pp. 123–128.

Gasch, R., 1993, "A Survey of the Dynamic Behaviour of a Simple Rotating Shaft With a Transverse Crack," *J. Sound and Vibration,* Vol. 157, No. 1.

Grabowski, B., 1980, "The Vibrational Behaviour of a Turbine Rotor Containing a Transverse Crack," ASME *Journal of Mechanical Design,* Vol. 102, pp. 140–146.

Haas, H., 1977, "Major Damage Caused by Turbine or Generator Rotors in the Range up to Tripping Speed," *Der Maschinenschaden,* Vol. 50, pp. 193–215.

Iman, I., et al., 1989, "Development of an On-Line Rotor Crack Detection and Monitoring System," ASME *Journal of Vibration, Acoustics, Stress, and Reliability in Design,* Vol. 111, pp. 241–250.

Jack, A. R., and Patterson, A. N., 1977, "Cracking in 500MW LP Rotor Shaft," *I Mech E Conference on The Influence of the Environment on Fatigue.*

Meng, G., and Gasch, R., 1992, "The Nonlinear Influence of Whirl Speed on the Stability and Response of a Cracked Rotor," *J. of Machine Vibration,* No. 4, pp. 216–230.

Muszynska, A., et al., 1992, "Torsional/Lateral Vibration Cross-Coupled Responses Due to Shaft Anisotropy: A New Tool in Shaft Crack Detection," C432/090, *Proc. of I Mech E, Vibrations in Rotating Machinery,* pp. 257–262.

Nelson, H. D., and Nataraj, C., 1986, "The Dynamics of a Rotor System With a Cracked Shaft," ASME *Journal of Vibration, Acoustics, Stress, and Reliability in Design,* Vol. 108, pp. 189–196.

Wauer, J., 1990, "On the Dynamics of Cracked Rotors: A Literature Survey," *Appl. Mech. Review,* Vol. 43, No. 1, pp. 13–17.

Downloaded 02 Jun 2010 to 171.66.16.105. Redistribution subject to ASME license or copyright; see http://www.asme.org/terms/Terms_Use.cfm

Balanced Model Reduction and Control of Rotor-Bearing Systems

J. T. Sawicki
Associate Professor,
Department of Mechanical Engineering,
Cleveland State University,
Cleveland, OH 44115

W. K. Gawronski
Member of Technical Staff,
Jet Propulsion Laboratory,
California Institute of Technology,
Pasadena, CA 91109

An effective technique is applied to the suppression of vibrations in flexible rotor-bearing systems with small gyroscopic effects. A balanced linear-quadratic-Gaussian (LQG) controller design procedure is implemented. The size of the controller is reduced in two stages by using (i) a balanced model reduction, and (ii) an LQG balanced reduction. The condition for a gyroscopic matrix is developed that allows one to ignore the rotor gyroscopic effects in the process of the controller design, although they are included in the rotor dynamics. The approach is illustrated on a typical rotor-bearing system represented by a 48 degree-of-freedom finite element model.

1 Introduction

Rotor vibration analysis is an important part of the design and operation of nearly every type of rotating machinery. As the power output, speed, and performance are pushed to practical limits, the level of dynamic sensitivity of this type of machinery increases considerably. Dynamic problems can be caused, for example, by unbalance, misalignment, internal friction, loose parts, support perturbations, and bearing characteristics. Many of these causes manifest themselves as dynamic instabilities, i.e., self-excited vibrations, which may severely restrict the operational range of a rotor. Therefore, the performance demanded of the rotordynamic vibration active control systems is currently increasing rapidly.

In rotor dynamics, the finite element method (FEM) is most often applied for spatial discretization of the system elements. However, the finite element based models of realistic rotordynamic systems produce too many degrees of freedom—*too many* not only from a computational point of view (e.g., developing transient solutions), but also, more importantly, from a control point of view. If one takes into account that the complexity of the controller depends on the plant order, then it is not difficult to see that a full-order controller for a high-order plant is difficult to implement. The difficulty with a high-order plant model is common to all structural dynamics problems but is exacerbated in rotordynamic systems by their inherent nonsymmetric nature, due to rotation-related factors such as gyroscopic effects and fluid dynamic forces in bearings and seals. Rotor-bearing dynamic instabilities and bifurcation of spectrum frequencies are direct consequences of these nonsymmetries.

The reduced-order model (ROM) can be achieved by adapting the modal techniques currently used in structural dynamics (e.g., Meirovitch, 1974; Childs, 1975,). More recently, with the introduction of FEM codes, several techniques have been proposed, examples of which are the dynamic reduction technique (Rouch and Kao, 1980; Genta, 1985; Kane and Torby, 1991), or the "component mode synthesis" approach (Glasgow and Nelson, 1980; Li and Gunter, 1982).

Recently, a wealth of literature on control-oriented rotor modeling techniques and rotor vibration control strategies has been published. For example, Salm and Schweitzer (1984) investigated modal space-output feedback-optimal control for the steady-state response of a rotor. A similar approach was applied by Palazzolo et al. (1989) to transient rotor vibrations due to a sudden unbalance. A seven-mass rotor system was considered and a normal mode approach was used to obtain a ROM. The influence of various configurations of sensors and actuators on the rotor response was analyzed. The spillover effect was examined by comparing results from collocated and noncollocated sensor configurations. Results were verified by experimental data.

Despite the existence many ROM related techniques, Tasaltin (1992) concluded that the dominant mode and internal balancing methods were potentially the most suitable for reducing the order of a multi-mode rotor-bearing system. The concept of the balanced realization method has been used recently by Fan et al. (1993). He applied the complex mode method and the balanced realization method to obtain ROM for a 52 degree-of-freedom rotor model. The conclusion was drawn, in this particular case, that the balanced truncation method alone is not the best choice; however, it can be still effective if applied to the complex mode ROM to obtain further order reduction. The procedure developed for vibration control was illustrated using the simulation results.

The present paper applies the balanced realization method (Moore, 1981) and LQG balanced control (Jonckheere and Silverman, 1983; Gawronski, 1994) to the modeling and control design of rotordynamic systems with small gyroscopic effects. The system model is converted into a state-space form and the degree of observability and controllability of each state is examined. In the balanced realization, the states that little affect the response and are weakly excited by the input can be removed from the model and ignored in the controller design. In this way, a model of the smallest size is found that best captures the dynamics of the system. The use of reduced-order models in feedback control schemes, however, may lead to instability due to excitation of unmodeled modes, an effect known as *spillover* (Balas, 1978). How to suppress *spillover* phenomena has been one of the important problems in active vibration control of flexible rotor systems. The presented balanced LQG controller design procedure addresses the spillover problem through numerical simulation. In this paper we

(*a*) apply the balanced LQG controller design procedure to the synchronous vibration suppression of flexible rotor-bearing systems,
(*b*) show that the independently adjusted LQG weights allow for the straightforward performance enhancement of the closed-loop system,
(*c*) reduce the controller size in two stages, namely using (*i*) the open-loop balanced reduction, and (*ii*) the LQG

Contributed by the International Gas Turbine Institute for publication in the JOURNAL OF ENGINEERING FOR GAS TURBINES AND POWER. Manuscript received by the International Gas Turbine Institute April 14, 1996. Associate Technical Editor: R. E. Kielb.

Copyright © 1997 by ASME

Downloaded 02 Jun 2010 to 171.66.16.105. Redistribution subject to ASME license or copyright; see http://www.asme.org/terms/Terms_Use.cfm

balanced reduction. The size of the LQG controller obtained is much smaller than the size of the plant model,

(*d*) derive the conditions that permit the omission of gyroscopic phenomena in the controller design procedure, although they are not ignored in the rotor dynamics, and

(*e*) illustrate the overall approach with the simulation of a three-disk rotor supported on flexible bearings.

2 Linearized Rotordynamic System and Model Reduction

2.1 Equations of Motion. In general, the rotordynamic system can be represented by the following linear second-order matrix differential equation:

$$M\ddot{q} + (D + G)\dot{q} + (K + H)q = f \qquad (1a)$$

Here, q is the displacement vector and f is the external force vector (e.g., gravity, rotating unbalance, side/maneuver loads). The system mass matrix M is the real, symmetric, and positive definite. The symmetric dissipation matrix D and skew-symmetric circulatory matrix H represent nonconservative forces. Conversely, the skew-symmetric gyroscopic matrix G and symmetric stiffness matrix K yield conservative forces (Adams and Padovan, 1981).

The equations of motion for an actively controlled rotor, with the symmetric stiffness matrix (e.g., supported by pivoted-pad bearings), can be written as follows:

$$M\ddot{q} + G\dot{q} + D\dot{q} + Kq = B_c u + B_e f, \quad y = C_q q + C_v \dot{q} \qquad (1b)$$

Here, u is the control force vector, B_c is the control force distribution matrix, B_e determines the location of external forces, C_q is the displacement output matrix, and C_v is the velocity measurement matrix. The system has n_2 degrees of freedom.

Let Φ be the modal matrix ($n_2 \times p$), where p is the number of modes, $p \leq n_2$,

$$\Phi = [\phi_1, \phi_2, \ldots, \phi_p] \qquad (2)$$

where $\phi_i = [\phi_{i1}, \phi_{i2}, \ldots, \phi_{in_2}]^T$ is the ith mode of the system.

Then, the equations of motion (Eq. (1*b*)) can be represented in a modal form as

$$M_m\ddot{q}_m + G_m\dot{q}_m + D_m\dot{q}_m + M_m\Omega^2 q_m = \Phi^T B_c u + \Phi^T B_e f \qquad (3)$$

where

$$\Phi^T M \Phi = M_m \qquad (4a)$$

$$\Phi^T K \Phi = M_m \Omega^2 = \text{diag}\,(\omega_i^2) \qquad (4b)$$

$$D_m = \Phi^T D \Phi \qquad (4c)$$

and ω_i is the ith natural frequency. The modal gyroscopic matrix $G_m(p \times p)$

$$G_m = \Phi^T G \Phi \qquad (4d)$$

is a skew-symmetric one, i.e., such that

$$g_{m_{ij}} = -g_{m_{ji}}, \quad i, j = 1, \ldots, p \qquad (4e)$$

The modal mass (M_m) and stiffness (K_m) matrices are diagonal; however, the modal damping matrix (D_m) is fully populated due to concentrated damping properties of the system stemming from the fluid-film bearings. This feature is not welcome in the analysis and design of the control system, but it is shown elsewhere (Gawronski and Sawicki, 1996) that for small damping the fully populated modal damping matrix can be replaced with its diagonal part and the system dynamics changes are negligible. Thus, in further considerations the damping matrix D_m is assumed to be a diagonal one.

Left multiplication of Eq. (3) by M_m^{-1} gives

$$\ddot{q}_m + M_m^{-1}G_m\dot{q}_m + M_m^{-1}D_m\dot{q}_m + \Omega^2 q_m = M_m^{-1}\Phi^T B_o u + M_m^{-1}\Phi^T B_e f \qquad (5)$$

and conventionally, one can normalize damping as follows:

$$M_m^{-1}D_m = 2Z\Omega, \quad Z = \text{diag}\,(\xi_1, \xi_2, \ldots, \xi_{n_2}) \qquad (6)$$

where ξ_i are the modal damping coefficients and for subcritical damping $\xi_i < 1$, $i = 1, \ldots, n_2$.

If we define the state vector $x^T = (x_1^T x_2^T)^T = (q_m^T \dot{q}_m^T)^T$, then the state-space representation of Eq. (5) can be written as

$$\dot{x} = Ax + \bar{B}_c u + \bar{B}_e f, \quad y = Cx \qquad (7)$$

where

$$A = \begin{bmatrix} 0 & I \\ -\Omega^2 & (-2Z\Omega - M_m^{-1}G_m) \end{bmatrix},$$

$$\bar{B}_c = \begin{bmatrix} 0 \\ M_m^{-1}\Phi^T B_c \end{bmatrix}, \quad \bar{B}_e = \begin{bmatrix} 0 \\ M_m^{-1}\Phi^T B_e \end{bmatrix},$$

$$C = [C_q\Phi \quad C_v\Phi]. \qquad (8)$$

2.2 Model Reduction Technique. The approach taken in this work is to reduce the order of rotor-bearing model in a more formal way as part of the reduction procedure based on the state-space balanced representation (Moore, 1981). Let (A, B, C) be the state-space representation of the rotor, where just for this section $B \equiv \bar{B}_c$. For a stable A the controllability (W_c) and observability (W_o) grammians obtained from the following Lyapunov equations:

$$AW_c + W_cA^T + BB^T = 0, \quad A^TW_o + W_oA + C^TC = 0 \qquad (9)$$

characterize the system controllability and observability properties. The system triple (A, B, C) is balanced, if its controllability and observability grammians are equal and diagonal (Moore, 1981)

$$W_c = W_o = \Gamma^2, \quad \Gamma = \text{diag}\,(\gamma_1, \ldots, \gamma_n),$$
$$\gamma_i \geq 0, \quad i = 1, \ldots, n \qquad (10)$$

and γ_i is the ith Hankel singular value of the system. For the reduction convenience, the Hankel singular values in Eq. (10) are in the decreasing order, i.e., $\gamma_i \geq \gamma_{i+1}$, $i = 1, 2, \ldots, n-1$.

A reduced-order model of a rotor is obtained by truncating the states in the balanced coordinates with the corresponding smallest Hankel singular values. Let the state vector x of the system in the balanced representation be partitioned as follows, $x^T = [x_r^T, x_t^T]$, and (A, B, C) be partitioned accordingly,

$$A = \begin{bmatrix} A_r & A_{rt} \\ A_{tr} & A_t \end{bmatrix}, \quad B = \begin{bmatrix} B_r \\ B_t \end{bmatrix}, \quad C = [C_r \quad C_t] \qquad (11)$$

where x_r is a $k \times 1$ vector and x_t is an $(n-k) \times 1$ vector. The balanced grammian is divided similarly,

$$\Gamma = \begin{bmatrix} \Gamma_r & 0 \\ 0 & \Gamma_t \end{bmatrix} \qquad (12)$$

The reduced model is obtained by deleting the last $n-k$ rows of A, B, and the last $n-k$ columns of A, C, i.e.,

$$A_r = LAL^T, \quad B_r = LB, \quad C_r = CL^T, \quad L = [I_k \quad 0] \qquad (13)$$

It was shown (Gawronski, 1996) that for a flexible system

Downloaded 02 Jun 2010 to 171.66.16.105. Redistribution subject to ASME license or copyright; see http://www.asme.org/terms/Terms_Use.cfm

this approach gives almost optimal results and that the reduced system is stable.

The model reduction can be significantly improved if the reduction in the limited frequency interval is applied. The reduction is performed by fitting the reduced system dynamics into the full-size system dynamics in the frequency interval $\Omega = [0, \omega]$, where $\omega > 0$. Denote the controllability and observability grammians in the frequency interval as $W_c(\Omega)$ and $W_o(\Omega)$, and they are obtained as follows (see Gawronski and Juang, 1990, for details):

$$W_c(\Omega) = W_c S^*(\Omega) + S(\Omega) W_c,$$
$$W_o(\Omega) = S^*(\Omega) W_o + W_o S(\Omega) \tag{14}$$

where W_c, W_o are the grammians defined previously, and $S(\Omega)$ is a matrix defined as follows:

$$S(\Omega) = \frac{j}{2\pi} \ln ((A + j\omega I)(A - j\omega I)^{-1}) \tag{15}$$

By using $W_c(\Omega)$ and $W_o(\Omega)$ rather than W_c and W_o in the model reduction procedure, the model is reduced in the frequency interval Ω.

3 Condition for Gyroscopic Matrix That Preserves the Modal and Balanced Properties of Rotors

It is known (Jonckheere, 1984) that for flexible structures with small damping and no repeated frequencies, the modal representation is almost balanced. Blelloch et al. (1987) showed that for small perturbation of the state matrix, this result can be extended to lightly damped systems with gyroscopic and circulatory forces. We investigate a mechanical system with gyroscopic effects, such as shaft with disks, and we shall show the conditions when the gyroscopic effects are "small," hence the closeness of the modal and the balanced representation is preserved.

3.1 Estimation of the Modal Displacements. First, we express the magnitude of modal displacement in terms of the norm of the mode. We rewrite Eq. (5) as follows

$$\ddot{q}_m + D_g \dot{q}_m + C_m \dot{q}_m + \Omega^2 q_m = B_t u_t \tag{16}$$

where $D_g = M_m^{-1} G_m$, $C_m = M_m^{-1} D_m$, $B_t = [M_m^{-1} \Phi^T B_o \; M_m^{-1} \Phi^T B_e]$, $u_t = [u \; f]^T$.

The displacement of the proportionally damped structure q_p without a gyroscopic effect is a solution of Eq. (16) for $D_g = 0$, i.e.,

$$\ddot{q}_p + C_m \dot{q}_p + \Omega^2 q_p = B_t u_t \tag{17}$$

Denoting by $q_{pk}(\omega_i)$ the kth modal displacement at natural frequency ω_i, and letting the 2-norm of $q(\omega)$ be defined as $\|q\|_2^2 = (1/2\pi) \int_{-\infty}^{+\infty} |q(\omega)|^2 d\omega$, it can be shown (see Gawronski and Sawicki, 1996) that for a system without gyroscopic effects, one obtains

$$|q_{pk}(\omega_i)| = \frac{\kappa_{k,i}}{\alpha_i} \|q_{pi}\|_2 \tag{18}$$

where the 2-norm of $q_{pi}(\omega)$ is proportional to its absolute value at the resonance frequency (Bendat and Piersol, 1993), i.e., $\|q_{pi}\|_2 = \alpha_i |q_{pi}(\omega_i)|$, for $\alpha_i = 0.5\sqrt{c_{mi}}$, where c_{mi} is the mth row of C_m and

$$\kappa_{k,i} = \frac{b_{k,i}}{\xi_{k,i} \sqrt{\omega_{k,i}^2 + \dfrac{(\omega_{k,i}^2 - 1)^2}{4\xi_k^2}}} \tag{19}$$

where $b_{k,i} = |b_{tk}|/|b_{ti}|$, $\xi_{k,i} = |\xi_k|/|\xi_i|$, $\omega_{k,i} = |\omega_k|/|\omega_i|$, and b_{tk} is the kth row of B_t.

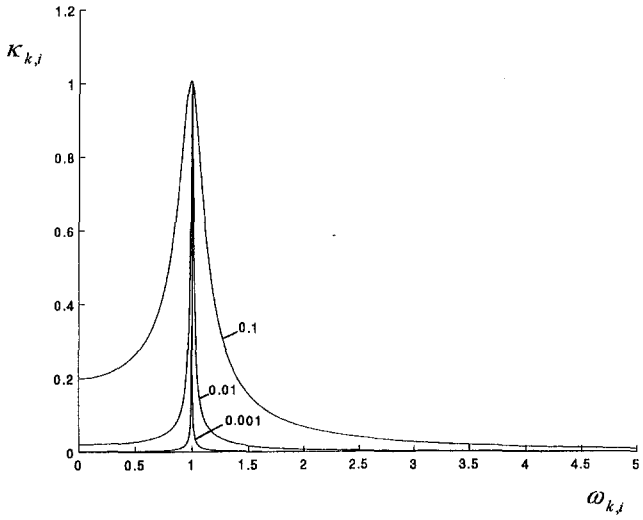


Fig. 1 Modal coupling coefficient with $\xi_{k,i} = b_{k,i} = 1$

3.2 Estimation of the Impact of the Gyroscopic Forces. Define $e = q_m - q_p$, the difference between the two solutions q_m and q_p, as given by Eqs. (16) and (17). Subtracting Eq. (17) from Eq. (16), one obtains

$$\ddot{e} + C_m \dot{e} + \Omega^2 e = -D_g \dot{q}_m \tag{20}$$

Denoting e_i the ith modal error, $e_i = q_{mi} - q_{pi}$, and d_{gi} the ith row of D_g, one obtains Eq. (20) in the frequency domain

$$e_i(\omega) = \frac{-j\omega}{\omega_i^2 - \omega^2 + jc_{mi}\omega} \sum_k d_{gik} q_{mk}(\omega) \tag{21}$$

where d_{gik} is the kth term in the ith row d_{gi}.

From the property described by Eq. (18) one obtains

$$\|e_i(\omega)\|_2 = \alpha_i |e_i(\omega_i)|$$
$$= \frac{1}{4\alpha_i} \left| \sum_k d_{gik} q_{mk}(\omega_i) \right| \le \frac{1}{4\alpha_i} \sum_k |d_{gik} q_{mk}(\omega_i)| \tag{22a}$$

By further estimation one arrives at

$$\|e_i(\omega)\|_2 \le \frac{q_{m\max}}{4\alpha_i} \sum_k |d_{gik}| = \frac{q_{m\max}\sigma_i}{4\alpha_i} \tag{22b}$$

where $\sigma_i = \Sigma_k |d_{gik}|$, and $q_{m\max} = \max_{k \neq i} |q_{mk}(\omega_i)|$ is the largest modal displacement at frequency ω_i for $k \neq i$. But, from Eq. (18) the largest displacement is expressed in terms of the ith mode amplitude

$$q_{m\max} = \frac{\kappa_i}{\alpha_i} \|q_{mi}(\omega)\|_2, \quad \kappa_i = \max_{k \neq i} (\kappa_{i,k}) \tag{23}$$

therefore, substituting Eq. (23) into Eq. (22b), one obtains $\|e_i(\omega)\|_2 \le (\kappa_i \sigma_i / 4\alpha_i^2) \|q_{mi}(\omega)\|_2$, which yields

$$\frac{\|e_i(\omega)\|_2}{\|q_{mi}(\omega)\|_2} = \frac{\|e_i(t)\|_2}{\|q_{mi}(t)\|_2} \le \frac{\sigma_i \kappa_i}{c_{mi}} \tag{24}$$

Typically, the modal coupling coefficient, $\kappa_{k,i}$, is small. Its maximal value is 1 whenever the modal frequencies ω_k and ω_i are equal (i.e., for $\omega_{k,i} = 1$). The plot of $\kappa_{k,i}$ versus $\omega_{k,i}$ and ξ_k for $\xi_{k,i} = b_{k,i} = 1$ is shown in Fig. 1. From this plot it is clear that $\kappa_{k,i}$ remains small for almost the whole domain of $\omega_{k,i}$, except for the small neighborhood of $\omega_{k,i} = 1$ (i.e., when modes are clustered). Also, the degree of modal coupling is smaller for lighter damping.

Downloaded 02 Jun 2010 to 171.66.16.105. Redistribution subject to ASME license or copyright; see http://www.asme.org/terms/Terms_Use.cfm

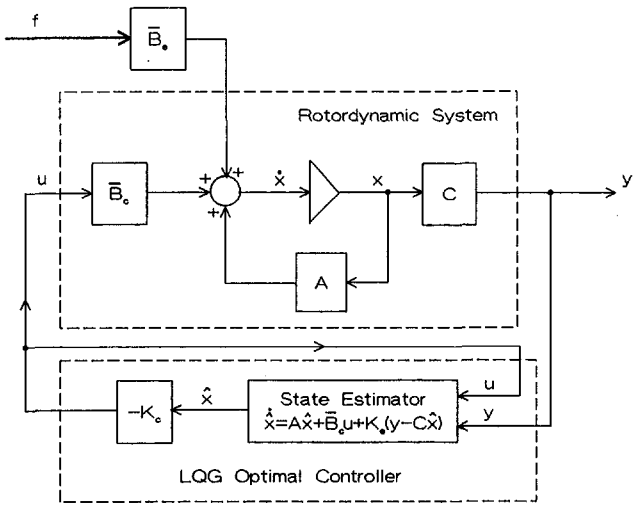


Fig. 2 Block diagram of closed-loop system with an LQG controller

From Eq. (24) it follows that the gyroscopic effects are small if the modal gyroscopic coefficients d_{gik} are of the order of modal damping coefficients. For small gyroscopic effects, the modal components are weakly coupled, thus the balanced coordinates are almost colinear with the modal ones (although rescaling is required). Therefore, the balanced procedure for the controller design is justified, although one has to keep in mind that controller application is independent of the coordinates on which it was designed, and the system dynamics does not neglect the gyroscopic effects.

4 Balanced LQG Controller

The LQG control structure for rotordynamic system is shown in Fig. 2, with the plant state-space triple $(A, \bar{B}_c, C)$, the state x, control input u, output y, and the disturbance force f with the covariance matrix V. The plant states x are approximated with estimator states $\hat{x}$.

The task is to determine the controller gain (K_c) and estimator gain (K_e) such that the performance index

$$J = E\left(\int_0^\infty (x^T Q x + u^T R u)dt\right) \tag{25}$$

is minimal, where $E(\cdot)$ denotes the mean value operator, R is a positive definite input weight matrix, and Q is a positive semidefinite state weight matrix. It is assumed $R = I$ without loss of generality. The minimum of J is obtained for the feedback $u = -K_c\hat{x}$, where the gain matrix $K_c = \bar{B}_c^T S$ is obtained from the solution S of the controller Riccati equation (CARE) (see, for example, Kwakernaak and Sivan, 1972, or Anderson and Moore, 1990)

$$A^T S + SA - S\bar{B}_c\bar{B}_c^T S + Q = 0 \tag{26}$$

The optimal estimator gain is given by $K_e = PC^T$, where P is the solution of the estimator Riccati equation (FARE)

$$AP + PA^T - PC^T CP + \bar{B}_e V \bar{B}_e^T = 0 \tag{27}$$

The LQG controller performance can be significantly modified through variations of weight Q and covariance V. Although V is formally predetermined by the disturbance f, it can be modified in a search for a more suitable solution (Anderson and Moore, 1990; Maciejowski, 1989).

4.1 Controller Design Properties. Denote a diagonal positive definite matrix $M = \text{diag}\ (\mu_i)$, $i = 1, \ldots, n$, $\mu_i > 0$. A state-space representation with the following condition satisfied:

$$S = P = \mathbf{M} \tag{28}$$

is an LQG balanced representation, and μ_i, $i = 1, \ldots, n$, are the characteristic values of $(\mathbf{A}, \bar{B}_c, \mathbf{C})$; see Jonckheere and Silverman (1983) and Opdenacker and Jonckheere (1985) for weights $Q = C^T C$, $V = B_c B_c^T$, and Gawronski (1994) for the general case of weights.

It was shown (Gawronski, 1996) that for flexible structures the open-loop balanced representation is also approximately LQG balanced, i.e., $S \cong P \cong M$. In this case, for a diagonal weight matrix $Q = \text{diag}\ (q_i I_2)$, $i = 1, \ldots, n$, the solution of Eq. (26) is $S \cong \text{diag}\ (s_i I_2)$, where

$$s_i \cong \frac{\beta_{pi} - 1}{2\gamma_i^2}, \quad \beta_{pi} = \sqrt{1 + \frac{2q_i\gamma_i^2}{\xi_i\omega_i}} \tag{29}$$

and for a diagonal $V = \text{diag}\ (v_i I_2)$, $i = 1, \ldots, n$, the solution of Eq. (27) is $P \cong \text{diag}\ (p_i I_2)$, where

$$p_i \cong \frac{\beta_{ei} - 1}{2\gamma_i^2}, \quad \beta_{ei} = \sqrt{1 + \frac{2v_i\gamma_i^2}{\xi_i\omega_i}} \tag{30}$$

For the diagonally dominant solutions of CARE and FARE, it is not difficult to find an approximately balanced solution $\mathbf{M}$ of CARE and FARE, which is also diagonally dominant, i.e.,

$$\mathbf{M} \cong \text{diag}\ (\mu_i I_2), \quad \text{where} \quad \mu_i = \sqrt{s_i p_i}, \quad i = 1, \ldots, n \tag{31}$$

Moreover, the weight $Q = \text{diag}\ (0, 0, \ldots, q_i I_2, \ldots, 0, 0)$, for $q_i \leq q_{oi}$, shifts the ith pair of complex poles of flexible structure, and leaves the remaining pairs of poles almost unchanged

$$(\lambda_{cri}, \pm j\lambda_{cii}) \cong (\beta_{pi}\lambda_{ori}, \pm j\lambda_{oii}) \tag{32a}$$

where β_{pi} as in Eq. (29), $(\lambda_{cri}, \pm j\lambda_{cii})$ is the ith pair of closed-loop poles, and $(\lambda_{ori}, \pm j\lambda_{oii})$ is the ith pair of the open-loop poles. Only the real part of the pair of poles is changed (just moving the pole apart from the imaginary axis, and thus stabilizing the system). The estimator poles are shifted in a similar manner. For $V = \text{diag}\ (0, 0, \ldots, v_i I_2, \ldots, 0, 0)$, $v_i \leq v_{oi}$, the estimator poles $(\lambda_{eri}, \pm j\lambda_{eii})$ relate to the open-loop poles $(\lambda_{ori}, \pm j\lambda_{oii})$ as follows:

$$(\lambda_{eri}, \pm j\lambda_{eii}) \cong (\beta_{ei}\lambda_{ori}, \pm j\lambda_{oii}), \quad i = 1, \ldots, n \tag{32b}$$

where β_{ei} is defined in Eq. (30).

4.2 Reduced Order Controller. Although the size of a rotordynamic model determines the size of a controller, it is crucial from an implementation point of view to obtain a controller of the smallest possible dimension that preserves the stability and performance of the full-order controller. Therefore, controller reduction is a part of the controller design. The balanced LQG design procedure provides this opportunity by introducing the reduction index σ_i as a measure of importance of closed-loop states

$$\sigma_i = \gamma_i^2 \mu_i \tag{33}$$

Thus, σ_i combines the open- and closed-loop characteristic values of a system, and serves as a controller reduction index.

The index σ_i depends on weight applied to the ith component. The more heavily weighted the component, the larger its controller reduction index. Therefore, if a particular pair of poles is easily moved (i.e., when small weight is sufficient), the respective states are easy to control and to estimate. On the other hand, if a particular pair of poles is difficult to move (i.e., a large weight is required to move the poles), the respective states are difficult to control and to estimate. In the latter case the action of the controller is irrelevant, and the states that are

Downloaded 02 Jun 2010 to 171.66.16.105. Redistribution subject to ASME license or copyright; see http://www.asme.org/terms/Terms_Use.cfm

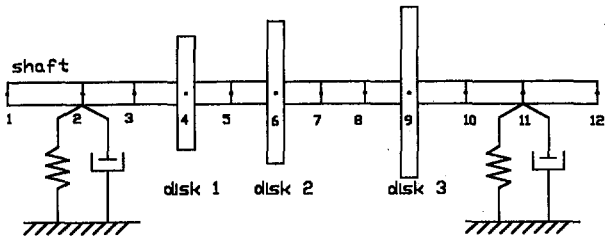


Fig. 3 Schematic diagram of rotor-bearing model

difficult to control and estimate can be reduced. Also, the index σ_i depends on the Hankel singular value of the ith component. The larger the Hankel singular value of the component, the larger the corresponding controller reduction index.

We define the matrix Σ of controller reduction indices

$$\Sigma = \Gamma^2\mathbf{M} = \text{diag}\ (\sigma_1, \sigma_1, \ldots, \sigma_n) \tag{34}$$

and assume σ_i in Eq. (34) in a descending order, i.e., $\sigma_i \geq 0$, $\sigma_{i+1} \geq \sigma_i$, $i = 1, \ldots, n$, and divide Σ as follows:

$$\Sigma = \text{diag}\ (\Sigma_r, \Sigma_t) \tag{35}$$

where Σ_r consists of the first k entries of Σ, and Σ_t the remaining ones. If the entries of Σ_t are small in comparison with the entries of Σ_r, i.e., $\|\Sigma_r\| \gg \|\Sigma_t\|$, the controller is reduced by truncating its last $n - k$ states. Note that σ_i depends on the ith weight. The increase of weight increases the value of σ_i, which can save this particular component from reduction. It is shown by Gawronski (1994) that the estimation errors of the full- and reduced-order controllers are almost the same.

5 Numerical Results and Discussion

The rotor geometry is shown in Fig. 3. The rotor is 1.042 m in length and 0.05 m in diameter. There are three heavy disks located at distances of 0.311, 0.471, and 0.711 m from the left-hand end. The rotor is supported by two oil-film journal bearings, which were represented by linearized stiffness and damping coefficients. The properties of disks and details of shaft, and coefficients of bearings, are listed in Table 1 and 2, respectively.

The mass unbalance is assumed to be localized at disk 1 only. The discretized rotor model is based on the finite element approach. The distributed properties of shafting sections are modeled by Euler–Bernoulli beam elements with the lumped mass at the stations. Each station has four degrees-of-freedom: two lateral displacements and two angular displacements. The model has 12 mass stations with added polar and transverse inertias at stations 4, 6, and 9 to account for the effects of the three disks. Thus, the discrete model has a total of 48 degrees of freedom.

The actuators are located at station 5 and apply the translational input force in two perpendicular x and y directions. The rotor vibration is measured in two perpendicular directions by displacement transducers located at station 3, 5, and 8.

The system has 96 states, two inputs, and six outputs. The rotating unbalance force is assumed as a disturbance to the system. The rigid-mass gyroscopic effects are not negligible for this system. The first four computed damped resonant frequencies corresponding to forward and backward precessional modes

Table 1 Properties of rigid disks

Station No.	Mass (Kg)	Polar Inertia (Kg-m^2)	Tranverse Inertia (Kg-m^2)	cg Eccentricity (μm)
4	11.69	6.08×10^{-2}	3.28×10^{-2}	10.0
6	18.53	14.85×10^{-2}	7.81×10^{-2}	0.0
9	26.9	30.81×10^{-2}	15.96×10^{-2}	0.0

Table 2 Shaft and bearing details

Station No.	Axial Distance (m)	Other Properties
1	0.0	shaft: diameter=0.05 m
2	0.131	Young's modulus $E=2.07\times10^{11}$ N/m^2
3	0.221	shear modulus $G=7.83\times10^{10}$ N/m^2
4	0.311	material density $\rho=7750$ kg/m^3
5	0.391	
6	0.471	bearings: direct stiffness: $K_{xx}=K_{yy}=1.0\times10^8$ N/m
7	0.551	cross stiffness: $K_{xy}=K_{yx}=5.0\times10^6$ N/m
8	0.631	direct damping: $C_{xx}=C_{yy}=2\times10^3$ Ns/m
9	0.711	cross damping: $C_{xy}=C_{yx}=0.0$ Ns/m
10	0.811	
11	0.911	
12	1.042	

are 292, 985, 2176, 2741 rad/s, and 198, 769, 1087, 2369 rad/s, respectively. Therefore, the design rotational speed is chosen as 1400 rad/s to allow the rotor be excited by passing through four resonances.

The Hankel singular values Γ (see Eq. (10)) for the rotor system (plant) are shown in Fig. 4. The order of the reduced system was chosen to be 30 based on the comparison between the values of the first and the 30th Hankel singular values. The values corresponding to the state number larger than 30 are at least a thousand times smaller than the first (largest) one; therefore, those states are deleted.

The transfer function magnitudes of the x-direction displacement at station 8 due to the x-direction force input at station 5 for the full-order model and the balanced-reduced model (30 states) are shown in Fig. 5. Both transfer functions almost coincide up to 10,000 rad/s (about 95,000 rpm).

In the process of design of LQG controller for the reduced 30 states model, the weight matrix Q and the covariance matrix V (see Eqs. (26), (27)) are chosen equal and diagonal (in this case the poles of the closed-loop system and the estimator overlap). The magnitudes of transfer function for the open- and closed-loop balanced-reduced systems are shown in Fig. 6. The nonzero entries of Q and V shift the poles to the right, so that the peaks of the open-loop transfer function (solid line) are flattened in the closed-loop transfer function (dashed line).

The unbalance responses measured at stations 3 and 8 in the x-direction for open-loop (dashed line) and closed-loop (solid line) systems are shown in Figs. 7(a) and 7(b), respectively. It can be seen that the vibrations are reduced significantly; e.g., approximately 10 times after 0.05 s at station 8 (see Fig. 7(b)),

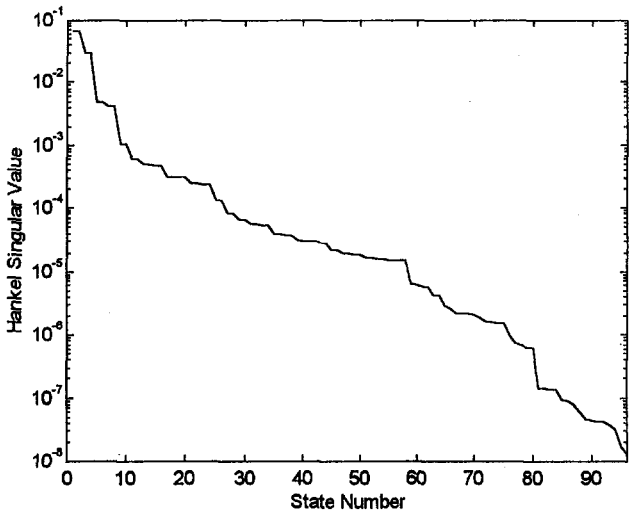


Fig. 4 Hankel singular values for the rotor system

Downloaded 02 Jun 2010 to 171.66.16.105. Redistribution subject to ASME license or copyright; see http://www.asme.org/terms/Terms_Use.cfm

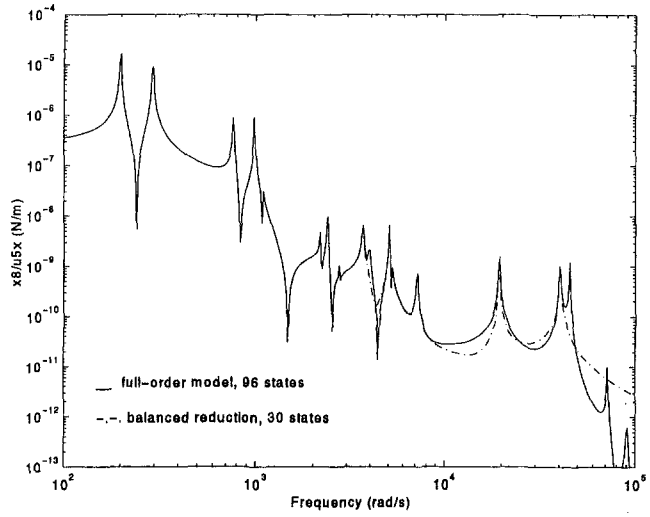


Fig. 5 Comparison of transfer function for full-order (96 states) and balanced-reduced (30 states) open-loop models

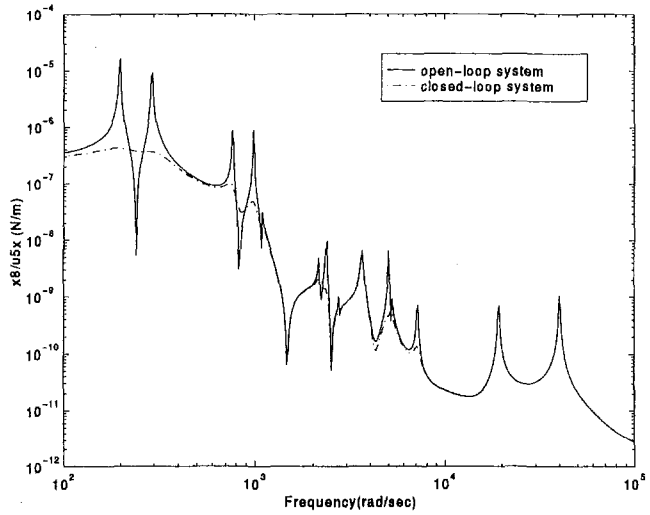


Fig. 6 Magnitudes of transfer function for open- and closed-loop rotor system

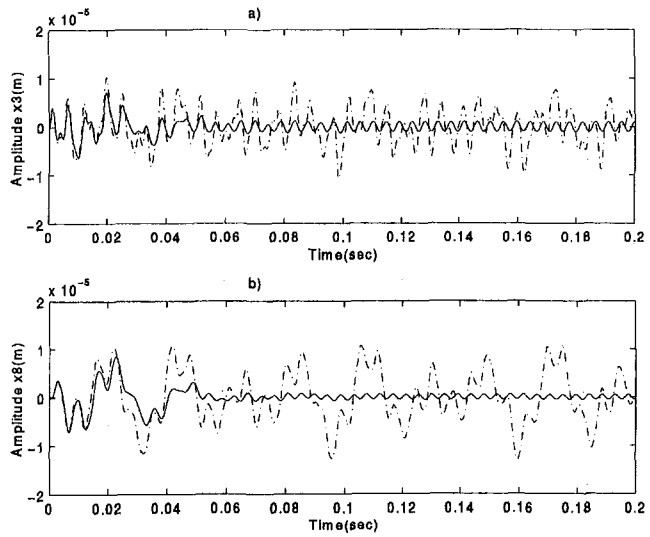


Fig. 7 Unbalance response for open- and closed-loop system measured in x-direction at (a) station 3 and (b) station 8

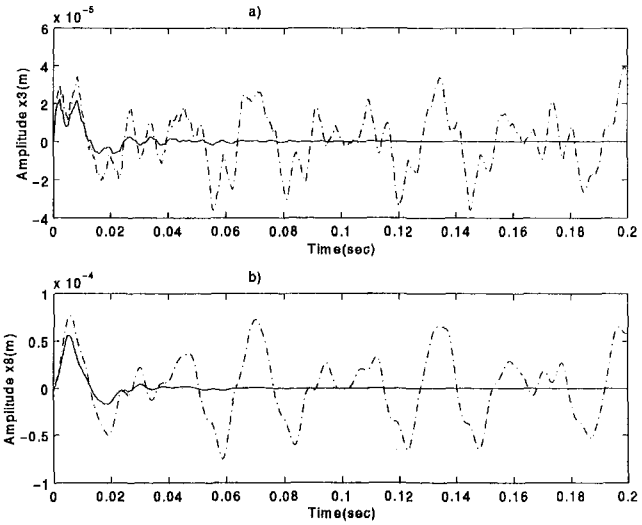


Fig. 8 Impulse response for open- and closed-loop system measured in x-direction at (a) station 3 and (b) station 8

which is also confirmed by the closed-loop transfer function (Fig. 6, dashed line). The high performance and stability of the designed controller are also demonstrated in Fig. 8, which shows the rotor impulse response measured at the same locations as described above due to impulse applied in the x-direction at station 5. Here, the rotor dynamic displacements are suppressed almost to zero in approximately 0.05 s.

The actuator forces (in the x- and y-directions) to attenuate the synchronous vibrations are demonstrated in Fig. 9. The steady-state value of the actuator forces is less than 200 N, which is lower than the magnitude of unbalance forces.

The dynamics of a rotor-bearing system are influenced by a large number of parameters; however, it is well recognized that a major source of model error arises at the interactive forces between rotating and nonrotating members, e.g., the journal bearings. Thus, in order to check the stability robustness, we allowed bearing stiffness and damping coefficients to vary ±40 percent from their nominal values. In this case the Euclidean norm of the total rotor response (measured at stations 3, 5, and 8) was calculated. The performance results in Fig. 10 indicate that the system is stable, and that ±40 percent variation of bearing damping increases the rotor amplitudes less than 20

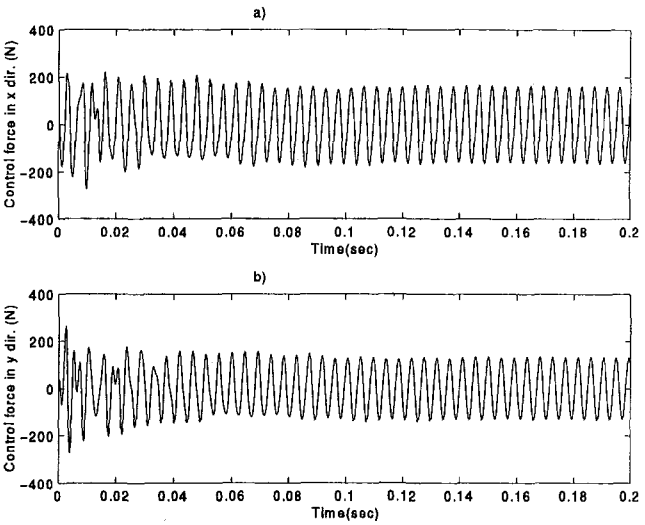


Fig. 9 Control force history in x- and y-directions

Downloaded 02 Jun 2010 to 171.66.16.105. Redistribution subject to ASME license or copyright; see http://www.asme.org/terms/Terms_Use.cfm

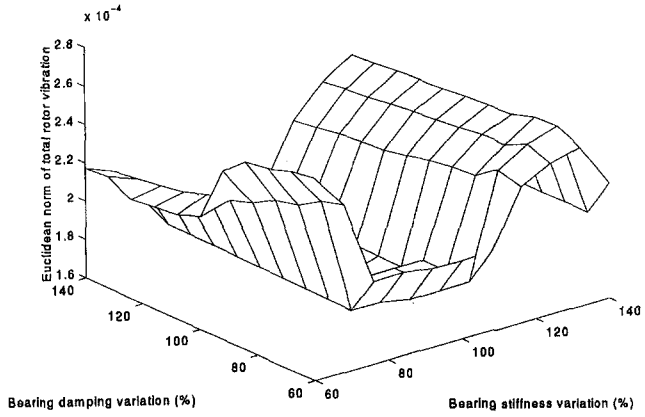


Fig. 10 Control performance versus bearing stiffness and damping variation

percent, while ±40 percent variation of bearing stiffness increases the rotor amplitudes less than 40 percent. The designed controller is the most optimal for the nominal conditions. This is clearly illustrated in Fig. 11, which presents the Euclidean norm of the rotor vibration versus the stiffness (or damping) variation only. At the nominal bearing stiffness (or damping) this norm reaches the minimum.

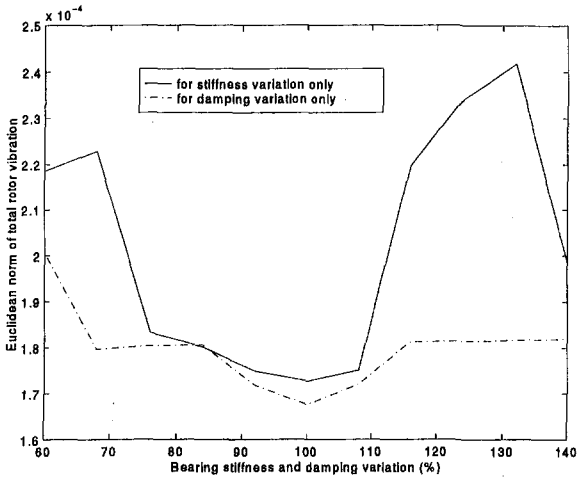


Fig. 11 Control performance versus bearing stiffness or damping variation

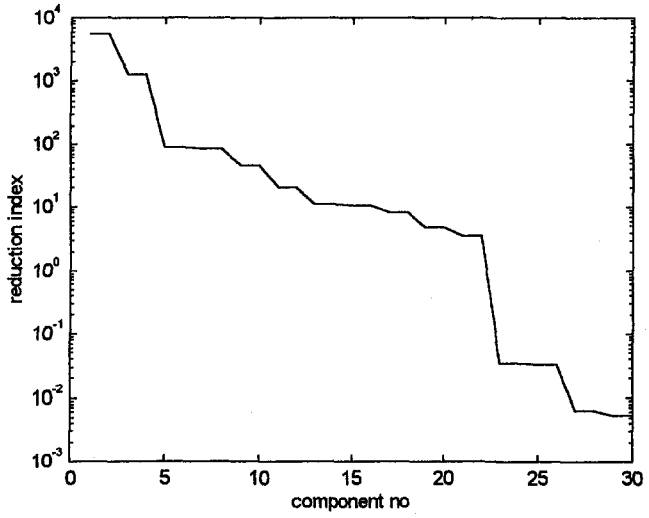


Fig. 12 Reduction indices for the controller

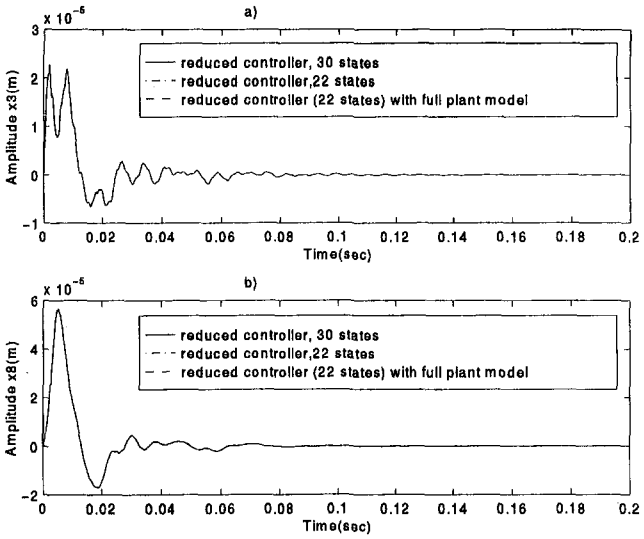


Fig. 13 Impulse responses of reduced controller with 30 states, 22 states, and full plant model measured in *x*-direction at (*a*) station 3 and (*b*) station 8

The reduced-order compensator is obtained through evaluation of the controller reduction indices σ_i, which are calculated based on Eq. (32) and plotted in Fig. 12. The already reduced (through the open-loop balanced reduction) controller of 30 states is reduced by truncating the additional 8 states (in estimator), which corresponds to the smallest reduction indices $\sigma_i < 4.0$ (see Fig. 12). The resulting reduced-order controller has 22 states.

The impulse responses of the reduced rotor model (30 states) with the reduction to 30 state (solid line) and 22 state (dashed line) controllers are compared with the impulse response of the full-order rotor model with reduction to 22 state controller. Such comparisons with the simulation in the *x*-direction at station 3 and 8 are shown in Figs. 13(*a*) and 13(*b*), respectively, with the impulse applied in the same direction but at station 5. The results show very good coincidence and lack of spillover (full order system with reduced controller is stable and moreover it demonstrates performance almost identical to the full order controller).

6 Conclusions

A balanced LQG controller design procedure has been applied to the flexible rotor-bearing system with small gyroscopic effects. A two-level reduction approach was used in the design. It was shown that under certain conditions the gyroscopic phenomena can be ignored in the controller design procedure, and that with this approach the closed-loop dynamics do not deteriorate even in the presence of gyroscopic effects. This and other properties of the LQG controller have been used to obtain a reduced-order compensator that assures the stability and performance of a full-order compensator. The approach is illustrated with numerical simulation of a flexible three-disk rotor system supported on anisotropic bearings.

References

Adams, M. L., and Padovan, J., 1981, "Insights Into Linearized Rotor Dynamics," *Journal of Sound and Vibration,* Vol. 76(1), pp. 129–142.

Anderson, B. D. O., and Moore, J. B., 1990, *Optimal Control,* Prentice Hall, Englewood Cliffs, NJ.

Balas, M. J., 1978, "Feedback Control of Flexible Structures," *IEEE Transactions on Automatic Control,* Vol. AC-23, pp. 673–679.

Bendat, J. S., and Piersol, A. G., 1993, *Engineering Applications of Correlation and Spectral Analysis,* Wiley, New York.

Downloaded 02 Jun 2010 to 171.66.16.105. Redistribution subject to ASME license or copyright; see http://www.asme.org/terms/Terms_Use.cfm

Blelloch, P. A., Mingori, D. L., and Wei, J. D., 1987, "Perturbation Analysis of Internal Balancing for Lightly Damped Mechanical Systems With Gyroscopic and Circulatory Forces," *AIAA Journal of Guidance, Control, and Dynamics*, Vol. 10, pp. 406–410.

Childs, D., 1975, "Two Jeffcott-Based Simulation Models for Flexible Rotating Equipment," ASME *Journal for Industry*, Vol. 97, pp. 1000–1014.

Fan, G. W., Nelson, H. D., Crouch, P. E., and Mignolet, M. P., 1993, "LQG-Based Least-Squares Output Feedback Control of Rotor Vibrations Using the Complex Mode and Balanced Realization Methods," ASME JOURNAL OF ENGINEERING FOR GAS TURBINES AND POWER, Vol. 115, pp. 314–323.

Gawronski, W., and Juang, J. N., 1990, "Model Reduction in Limited Time and Frequency Intervals," *International Journal of Systems Science*, Vol. 21, pp. 349–376.

Gawronski, W., 1994, "A Balanced LQG Compensator for Flexible Structures," *Automatica*, Vol. 30.

Gawronski, W., and Sawicki, J. T., 1996, "Response Errors of Non-proportionally Lightly Damped Structures," accepted for publication in *Journal of Sound and Vibration*.

Gawronski, W., 1996, *Balanced Control of Flexible Structures*, Lecture Notes in Control and Information Sciences 211, Springer-Verlag, London.

Genta, G., 1985, "Consistent Matrices in Rotor Dynamics," *Meccanica*, Vol. 20, pp. 235–248.

Glasgow, D. A., and Nelson, H. D., 1980, "Stability Analysis of Rotor Bearing Systems Using Component Mode Synthesis," ASME *Journal of Mechanical Design*, Vol. 102, pp. 352–359.

Gregory, Jr., C. Z., 1984, "Reduction of Large Flexible Spacecraft Models Using Internal Balancing Theory," *AIAA Journal of Guidance, Control, and Dynamics*, Vol. 7, pp. 725–732.

Jonckheere, A., and Silverman, L. M., 1983, "A New Set of Invariants for Linear Systems—Application to Reduced Order Controller Design," *IEEE Trans. Autom. Control*, Vol. AC-28, pp. 953–964.

Jonckheere, A., 1984, "Principal Component Analysis of Flexible Systems—Open Loop Case," *IEEE Trans. Autom. Control*, Vol. 27, pp. 1095–1097.

Kane, K., and Torby, B. J., 1991, "The Extended Modal Reduction Method Applied to Rotor Dynamic Problems," ASME *Journal of Vibration and Acoustics*, Vol. 113, pp. 79–84.

Kwakernaak, H., and Sivan, R., 1972, *Linear Optimal Control Systems*, Wiley-Interscience, New York.

Li, D. F., and Gunter, E. J., 1982, "Component Mode Synthesis of Large Rotor Systems," ASME JOURNAL OF ENGINEERING FOR POWER, Vol. 104, pp. 525–532.

Maciejowski, J. M., 1989, *Multivariable Feedback Design*, Addison-Wesley, Wokingham, England.

Meirovitch, L., 1974, "A New Method of Solution of the Eigenvalue Problem for Gyroscopic Systems," *AIAA Journal*, Vol. 12, pp. 1337–1342.

Moore, B. C., 1981, "Principal Component Analysis in Linear Systems, Controllability, Observability and Model Reduction," *IEEE Transactions on Automatic Control*, Vol. 26, pp. 17–32.

Opdenacker, P., and Jonckheere, E. A., 1985, "LQG Balancing and Reduced LQG Compensation of Symmetric Passive Systems," *Int. J. Control*, Vol. 41, No. 1, pp. 73–109, 1985.

Palazzolo, A. B., Lin, R. R., Kascak, A. F., and Alexander, R. M., 1989, "Active Control of Transient Rotordynamic Vibration by Optimal Control Methods," ASME JOURNAL OF ENGINEERING FOR GAS TURBINES AND POWER, Vol. 111, pp. 264–270.

Rouch, K. E., and Kao, J. S., 1980, "Dynamic Reduction in Rotor Dynamics by the Finite Element Method," ASME *Journal of Mechanical Design*, Vol. 102, pp. 360–368.

Salm, J., and Schweitzer, G., 1984, "Modelling and Control of a Flexible Rotor With Magnetic Bearings," *Proc. Conference on Vibrations in Rotating Machinery*, York, United Kingdom, C277.

Skelton, R. E., 1988, *Dynamic System Control: Linear System Analysis and Synthesis*, Wiley, New York.

Tasaltin, R., 1992, "Active Vibration Control Strategies for a Flexible-Rotor Bearing System," PhD Thesis, University of Bath, United Kingdom.

Williams, T., 1990, "Closed Form Grammians and Model Reduction for Flexible Space Structures," *IEEE Transactions on Automatic Control*, Vol. 35, pp. 379–382.

Downloaded 02 Jun 2010 to 171.66.16.105. Redistribution subject to ASME license or copyright; see http://www.asme.org/terms/Terms_Use.cfm

Optimization of Bearing Locations for Rotor Systems With Magnetic Bearings

S. Srinivasan
United Technologies Research Center,
East Hartford, CT 0618

E. H. Maslen

L. E. Barrett

Department of Mechanical, Aerospace, and Nuclear Engineering,
University of Virginia,
Charlottesville, VA

This paper presents a method for quickly evaluating the effect of changes in bearing location on bearing design for stability of rotating machinery. This method is intended for use by rotating machinery designers to select the "best" bearing locations prior to the bearing design process. The purpose of the method is to improve the design process by separating the problem of determining the "best" bearing locations from that of determining the actual bearing design. The method is independent of the type of bearing employed. For each candidate bearing configuration, the method provides a scalar measure of the relative ability of bearings to meet stability specifications. Within certain limits, the stability specifications are defined by the designer. The scalar measure is used to rank the candidate bearing locations and thereby select the best one. The scalar measure is compared to a practical measure of magnetic bearing design such as the infinity norm of the controller for an example design of a multistage centrifugal compressor.

Introduction

In the design of hydrodynamic or magnetic bearings for rotor systems, most of the effort has been directed toward bearing design (e.g., Barrett, 1983; Maslen, 1991a; Dhar et al., 1991; Larsonneur and Herzog 1988) while relatively little attention has been given to bearing locations. Generally the bearing designer assumes that the bearing locations are given and the design process starts from there. In many instances, poorly chosen bearing locations can result in unrealistic or unattainable bearing designs to achieve desired rotor stability or unbalance response characteristics. Thus, a proper selection of the bearing locations should be part of the overall rotor design process, preferably simultaneous with design for aero- or thermodynamic performance, in order to obtain the best system performance.

In the present work, the term *bearing configuration* means the set of selected locations for the m bearings in the system and does not directly imply anything about the bearing properties. The number of bearings, m, is typically two, but could be higher. The key system properties involved in selecting bearing configurations are controllability and observability (Kailath, 1982), which are dual properties. For collocated bearings, it turns out that the controllability and observability properties are equal and thus, in the succeeding discussion only the controllability property is discussed.

Controllability is a yes–no property that indicates whether all of the system eigenvalues can be directly affected by the bearing dynamic compliances at the given locations. Rotor systems are *controllable* by virtually all bearing configurations and therefore a *relative* measure of controllability is needed to compare potential configurations.

Measures of controllability have been defined in several ways: energy approach (Moore, 1981), size of recovery region (Vishwanathan et al., 1984), eigenvalue mobility (Maslen, 1991b), the distance between certain subspaces (Hamdan and Nayfeh, 1989) and the norm of the modal residues of the transfer matrix (Tarokh, 1990). These measures have limited practical application to free–free rotors for the following reasons:

- All of these measures emphasize the least controllable mode; for rotor systems, the lower modes are of primary interest. This subset might not include the least controllable mode.
- Moore's (1981) energy approach is undefined for undamped systems and very sensitive to uncertain structural damping for lightly damped rotors.
- The measures of Hamdan and Nayfeh (1989) and Tarokh (1990) are based upon *only* the eigenvectors while ignoring the associated eigenvalues. This can lead to the measure being decided by a higher mode.

The method of Tarokh (1990) is a formalization of the widely employed technique of comparing rotor free–free mode shape amplitudes at potential bearing locations. When such a criterion is applied only to selected mode shapes, it can provide a qualitative comparison, but provides no mechanism to decide what relative influence each of the selected modeshapes should have on the final selection. When each of the mode shapes individually indicates the same selection, then the ranking of bearing configurations is unambiguous and probably results in the same selection as would be made by the technique presented here.

Several approaches to the actuator/sensor location problem in flexible structures have been proposed (Kim and Junkins, 1991; Lim, 1992; Chiang et al., 1992; Choe and Baruh, 1992). The controllability measures obtained by these approaches are based upon the controllability Grammians of Moore (1981) or they are obtained by a nonconvex nonlinear optimization problem, which can be computationally expensive.

In this paper, a noniterative, numerically robust method is presented for selecting bearing configurations in undamped free–free rotor systems. This is important because any design method producing designs realizable in practice will probably use time consuming optimization methods. The basis for comparison is a measure of the dynamic stiffness of bearings required to produce system eigenvalues that lie in a specified region of the complex plane. As a result, the implicit objective is to achieve a certain level of damping, or logarithmic decrement, rather than directly approaching the forced response problem. Although the method can be shown to be applicable to placement of hydrodynamic bearings, the present work restricts its attention to magnetic bearings.

The proposed method is described in detail in the second section. An example is presented in the third section where three

Contributed by the International Gas Turbine Institute and presented at the 40th International Gas Turbine and Aeroengine Congress and Exhibition, Houston, Texas, June 5–8, 1995. Manuscript received by the International Gas Turbine Institute February 27, 1995. Paper No. 95-GT-217. Associate Technical Editor: C. J. Russo.

Copyright © 1997 by ASME

Downloaded 02 Jun 2010 to 171.66.16.105. Redistribution subject to ASME license or copyright; see http://www.asme.org/terms/Terms_Use.cfm

candidate bearing configurations are ranked by this technique. Magnetic bearing designs for the candidate configurations are also obtained. The infinity norm of each controller is used as a measure of "goodness." This norm is compared to the ranking predicted by the proposed method. The last section concludes the paper.

Method

The proposed method is predicated on the following assumptions:

1 The primary goal of the bearing design is to achieve a general stability objective: The rotor/bearing system eigenvalues must lie outside of a specific region in the complex plane.
2 This goal should be met with the smallest bearings possible where small is, conceptually, a combined measure of bearing stiffness and damping.

Given such a stability objective and a specification of the bearing locations along the rotor, it is possible to compute a bound for the required bearing size with a single noniterative calculation. Several candidate bearing locations can then be compared on the basis of this bearing size measure.

The dynamic character of the undamped rotor system without bearings is represented with a state space form of the model equations (see, e.g., Kim and Junkins 1991):

$$\dot{x} = A(\Omega)x + Bu + B_e f$$
$$y = Cx \tag{1}$$

where A is a $n \times n$ matrix, which contains the dynamics of the undamped free–free rotor at a given rotational speed Ω, B is a $n \times m$ matrix, which determines the bearing locations, C is a $p \times n$ matrix, which determines the sensor locations, x is an n-vector of the generalized displacements and velocities of the rotor, u is a m-vector of bearing forces, y is a p-vector of sensor outputs, and f represents other external forces acting on the rotor such as mass imbalance or aerodynamic loads.

There are no specific limitations on the dimensions n, m, and p except that the numerical conditioning and computational speed of the problem will suffer if they are too large. Numerical problems will be an issue if n gets larger than about 100, but numerical methods exist for handling the required computations even with much larger values of n. An alternative approach is to limit the rotor model size through modal truncation to contain only twenty or thirty states. This protects the numerical conditioning and preserves all of the rotor eigenvalues that are likely to have any physical significance.

A set of bearings is a dynamic feedback mechanism, which generates control forces on the rotor in response to motion of the rotor:

$$\dot{x}_c = A_c x_c + B_c y$$
$$u = C_c x_c + Ky \tag{2}$$

so that the rotor/bearing combination is described by

$$\frac{d}{dt}\begin{Bmatrix} x \\ x_c \end{Bmatrix} = \begin{bmatrix} A(\Omega) + BKC & BC_c \\ CB_c & A_c \end{bmatrix}\begin{Bmatrix} x \\ x_c \end{Bmatrix} + \begin{bmatrix} B_e \\ 0 \end{bmatrix} f$$
$$y = Cx \tag{3}$$

where the dynamic properties of the bearing ("stiffness" and "damping") are determined by A_c, B_c, C_c, and K. Clearly, the stability (closed-loop eigenvalues) of the rotor/bearing system depends upon the interaction of all of these matrices.

In this work, we take advantage of this description of bearings to permit a fairly automatic assessment of how large they must be in order to satisfy certain stability objectives for the closed-loop system. Specifically, we adopt a simpler model for the bearings, referred to as state feedback, which takes the form

$$u = Kx \tag{4}$$

to produce the closed-loop rotor/bearing combination

$$\dot{x} = [A(\Omega) + BK]x + Bu$$
$$y = Cx \tag{5}$$

The choice of state feedback rather than output feedback ($u = Ky$) is less restrictive and therefore can be expected to produce a lower bound on bearing capacity.

The system stability objectives considered (Dhar et al., 1991), are to provide acceptable log decrements for lower modes of interest while not shifting the higher modes above a cut-off frequency. In other words, the dynamic properties of the bearings must be chosen so that the eigenvalues of the rotor/bearing system lie within a certain *acceptable region* of the complex plane without much caring about the exact locations.

The acceptable region that is considered by this method is represented by the unshaded region of the complex plane shown in Fig. 1. This particular choice of acceptable region is a mathematical convenience. However, it does satisfy common rotor stability objectives: The lower modes are required to be more heavily damped than the higher modes and the highest modes are not required to be damped at all. The acceptable region is defined by the low-mode damping parameter α and the cutoff frequency β, which are to be specified by the designer. As α is made more negative, the lower modes are required to be more heavily damped; as β is made larger, the higher modes are required to be more heavily damped. As will be demonstrated, the magnitude of α must be less than that of β.

Nomenclature

s = Laplace variable in original complex plane
$\hat{s}$ = Laplace variable in transformed complex plane
$A = n \times n$ system matrix
$B = n \times m$ actuator location matrix
$C = p \times n$ sensor location matrix
$\hat{A}, \hat{B}, \hat{C}$ = system matrices in $\hat{s}$-plane
x = n-vector of system states
X = Laplace transform of x
u = m-vector of bearing forces
U = Laplace transform of u
y = p-vector of sensor outputs
α', α = low-mode damping parameters specifying acceptable region
β = cutoff frequency parameter specifying acceptable region
γ = real constant specifying bilinear transformation
δ = scale factor to select γ
a, b, c, d = real constants of bilinear transformation
J = objective function for bearing design
K = feedback matrix in s-plane
$\hat{K}$ = feedback matrix in $\hat{s}$-plane
m = scalar measure
$\|\cdot\|_F$ = Frobenius norm of matrix = $\sqrt{\sum M_{i,j}^2}$
$\|\cdot\|_\infty$ = infinity norm of transfer function: $\max_\omega |M_{i,j}(j\omega)|$
σ = real part of eigenvalue
ω = imaginary part of eigenvalue
λ_i = ith eigenvalue of system

Downloaded 02 Jun 2010 to 171.66.16.105. Redistribution subject to ASME license or copyright; see http://www.asme.org/terms/Terms_Use.cfm

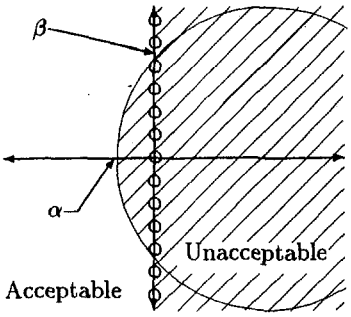


Fig. 1 Acceptable region in the S-plane: ○ symbols represent rotor free–free eigenvalues

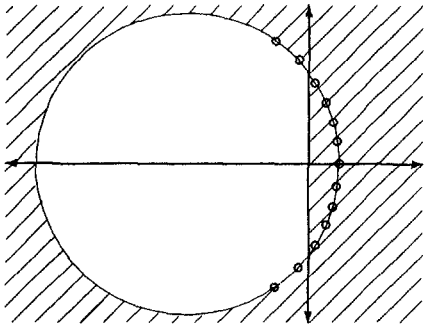


Fig. 2 Acceptable region in $\hat{S}$ plane: ○ symbols indicate free–free rotor eigenvalues

The basic idea of the proposed method is to find an unique state feedback K for which the closed-loop system eigenvalues lie in the acceptable region. This matrix is computed by solving a Linear Quadratic Regulator (LQR) problem (Molinari, 1977). Solution of the LQR is noniterative and numerically robust (Laub, 1979). In addition, the LQR approach lends itself to the stability objective described above and can be tailored to minimize K subject to this objective (treated as a constraint). The Frobenius norm of the state feedback matrix is used as the required scalar measure for the candidate actuator configuration:

$$A, B, \alpha, \beta \Rightarrow {}_{LQR}K \quad m = \|K\|_F \tag{6}$$

In some sense, the Frobenius norm measures the "effort" needed to place the system eigenvalues in the acceptable region. The choice of the Frobenius norm is somewhat arbitrary and without direct physical motivation. However, the examples in the next section demonstrate a strong correlation between this measure and some properties of bearings that are designed to place the damped eigenvalues of the system in the acceptable region.

The LQR problem is defined by two cost function matrices, Q and R, and produces the Algebraic Ricatti equation:

$$PA + A'P + Q + PBR^{-1}B'P = 0 \tag{7}$$

with the solution $K = -R^{-1}B'P$. The matrices Q and R can be freely chosen as long as they are symmetric, Q is positive semi-definite, and R is positive definite (some other restrictions also apply: see Molinari, 1977).

The specific choice of these matrices, in conjunction with the system description $\{A, B\}$, uniquely determines the location of the closed-loop eigenvalues. It is not at all apparent that the right choice of Q and R can be made that will place the closed-loop eigenvalues in the acceptable region while minimizing the Frobenius norm of K. However, if Q is made arbitrarily small, it can be shown that the resulting K matrix will stabilize the closed-loop system with a minimal control effort, which is essentially equivalent to a minimized Frobenius norm for K. Such a choice of weighting matrices forms what is called the infinite cost of control LQR (Molinari, 1977).

Using the infinite cost of control LQR (ICCLQR) eliminates the need to select Q and R and also tends to minimize $\|K\|_F$ but does not, in itself, provide a solution that satisfies the stability objective. This problem is overcome with a simple trick. It is observed that the ICCLQR problem reflects any unstable open-loop system eigenvalues across the imaginary axis into the stable half of the complex plane. If a transformation can be found that distorts the complex plane so that, in the transformed system, any eigenvalues that originally lay outside the unacceptable portion of the complex plane now lie in the right half plane, then the LQR problem applied to the transformed system will reflect the unacceptable eigenvalues into the acceptable region. This distortion is indicated in Fig. 2. The resulting state feedback can then be transformed back to the original problem space and a minimum Frobenius norm state feedback matrix K will be obtained that satisfies the stability objective.

Noting that the Laplace transform of the system differential equation is

$$sIx(s) = Ax(s) + Bu(s) \tag{8}$$

we introduce the bilinear transformation (Churchill et al., 1974)

$$s = \frac{a\hat{s} + b}{c\hat{s} + d} \tag{9}$$

where a, b, c, and d are all real numbers. After a little arithmetic (Srinivasan, 1993), the system $\{\hat{A}, \hat{B}\}$ in the $\hat{s}$ plane is

$$\hat{s}Ix(\hat{s}) = \hat{A}x(\hat{s}) + \hat{B}u(\hat{s}) \tag{10}$$

where

$$\hat{A} = (aI - cA)^{-1}(dA - bI)$$

$$\hat{B} = (c\hat{A} + dI)(aI - cA)^{-1}B \tag{11}$$

This is an invertible transformation, which does not change the dimension of the system $\{A, B\}$ when transformed into $\{\hat{A}, \hat{B}\}$. Further, the matrices $\hat{A}$ and $\hat{B}$ are real. Note that the transformation from A to $\hat{A}$ is independent of B. This coupled with the fact that ICCLQR is used implies that *the locations in the acceptable region to which the free–free eigenvalues are shifted will be the same for all the candidate actuator configurations.* However, the state feedback matrix that achieves this will be different for each configuration.

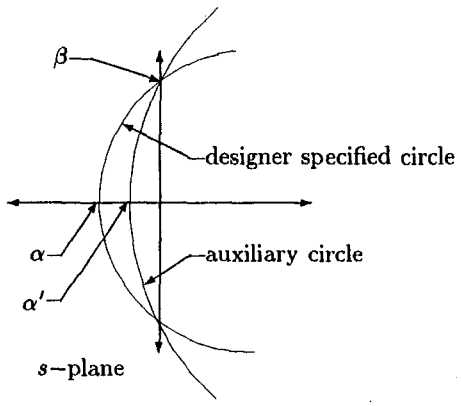


Fig. 3 Acceptable region in S plane

Downloaded 02 Jun 2010 to 171.66.16.105. Redistribution subject to ASME license or copyright; see http://www.asme.org/terms/Terms_Use.cfm

Let $\hat{K}$ be the state feedback matrix obtained by infinite cost of control LQR in the $\hat{s}$-plane:

$$\lim_{Q\to 0} P\hat{A} + \hat{A}'P + Q + P\hat{B}\hat{B}'P = 0 \quad \hat{K} = -\hat{B}'P \quad (12)$$

The equivalent state feedback matrix K in the s plane is obtained by (Srinivasan, 1993):

$$K = (I - c\hat{K}(aI - cA)^{-1}B)^{-1}\hat{K} \quad (13)$$

Equivalence means that the eigenvalues of $\hat{A} = \hat{A} - \hat{B}\hat{K}$ in the $\hat{s}$-plane are mapped to the eigenvalues of $\bar{A} = A - BK$ in the s-plane according to the bilinear transformation (9).

The constants a, b, c, and d of Eq. (9) are related to the specification of the acceptable region through

$$a = -\frac{\beta^2}{\alpha} \quad b = \gamma\alpha \quad \alpha < 0$$

$$c = 1 \quad d = \gamma \quad \beta, \gamma > 0 \quad (14)$$

The numerical conditioning of the LQR problem can be protected by selecting γ as

$$\gamma = \beta^2/|\alpha| \quad (15)$$

This choice makes the imaginary parts of the eigenvalues of $\hat{A}$ approximately the same order of magnitude as those of A. The same value should be used for all the candidate bearing locations being ranked.

From the geometry of Fig. 2, it is clear that the free–free eigenvalues on the boundary of the circle in the right half plane are reflected to locations *within* the acceptable region as long as the center of the circle, $-(\gamma/2)(1 - \alpha^2/\beta^2) < 0$. This implies that $|\alpha| < \beta$.

Another technical condition that must be satisfied arises due to the fact that $\{\hat{A}, \hat{B}\}$ must be controllable in order for LQR to work. It can be shown (Srinivasan, 1993) that if $\{A, B\}$ is controllable and A has no eigenvalue equal to $-\beta^2/\alpha$, then $\{\hat{A}, \hat{B}\}$ is controllable. This condition will always be satisfied for undamped free–free rotors.

The method, as implemented above, will place the closed-loop eigenvalues below the cutoff frequency β to *within but not on* the boundary of the acceptable region. When bearings are actually designed (Dhar et al., 1991), the system eigenvalues tend to be on or close to the boundary. In view of this, a better correlation with the bearing design method will result if the eigenvalues are placed on the boundary. A slight modification results in a state feedback, which will place all the system eigenvalues below the cutoff frequency β directly on the boundary of the acceptable region. This is achieved with the auxiliary circle shown in Fig. 3 which has the same cutoff frequency parameter β as before but a different damping parameter α':

$$\alpha' = (-\beta^2 + \beta\sqrt{\beta^2 + \alpha^2})/\alpha \quad (16)$$

The entire method described above is used with $\{\alpha', \beta\}$ instead of $\{\alpha, \beta\}$.

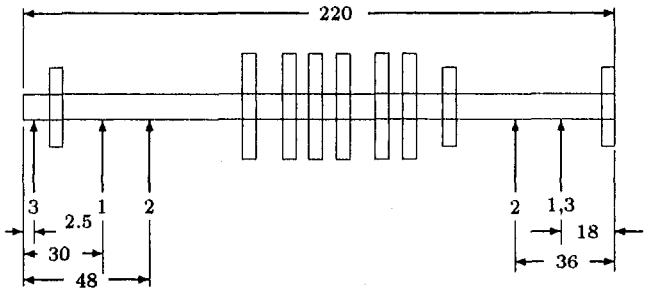


Fig. 4 Schematic of compressor with the candidate bearing configurations: all dimensions are cm

Table 1 Scalar measures M for regions A and B

Brg. Config.	Acceptable region A $\alpha = -75$, $\beta = 5500$		Acceptable region B $\alpha = -117$, $\beta = 5500$	
	m	$\frac{m}{\max(m)}$	m	$\frac{m}{\max(m)}$
1	1.391E+5	1.000	3.373E+5	1.000
2	0.935E+5	0.672	2.273E+5	0.673
3	0.549E+5	0.375	1.326E+5	0.393

A scalar measure m for the actuator configuration $\{A, B\}$ has been obtained. Assuming perfectly collocated bearings, the scalar measure of the sensor configuration will also be m by duality. The method can be summarized as follows: Given a free–free rotor system dynamic matrix A and matrices B_i each corresponding to a candidate bearing configuration:

1 Specify the acceptable region by selecting the low-mode damping parameter α and the frequency cutoff parameter β with $|\alpha| < \beta$.
2 Choose α' according to Eq. (16) and γ according to Eq. (15).
3 For the system $\{A, B\}$, obtain $\{\hat{A}, \hat{B}\}$ from Eq. (11).
4 Use ICCLQR on $\{\hat{A}, \hat{B}\}$ to compute the state feedback matrix $\hat{K}$.
5 Obtain K from Eq. (13) and $\hat{K}$.
6 Compute the scalar measure $m = \|K\|_F$.
7 Rank the candidate bearing configurations according to the magnitude of the measures m.

Example

This example compares the ranking of candidate bearing configurations to the optimized performance of actual magnetic bearing designs for the same configurations. The performance of these designs is assessed by the infinity norm of the controller transfer functions.

A multistage centrifugal compressor is depicted in Fig. 4, which shows three candidate bearing configurations, each with two bearings. The 220-cm-long rotor has an average diameter of 12.7 cm and is modeled as a beam of 41 discrete mass stations. Nine disks are modeled as lumped masses as shown. Gyroscopic effects are small for this rotor and are neglected, permitting a planar model.

The state space model $\{A, B, C\}$ was obtained by modal truncation, retaining two rigid body modes and bending modes at frequencies (in rad/s) of 733.2, 1300.2, 2917.5, 4948.7, and 6463.1. The frequency of the highest retained mode (at 6463.1 rad/s) is greater than the cutoff frequency $\beta = 5500$ and is already in the acceptable region.

Two acceptable regions are considered. Both regions have frequency cutoff parameters of $\beta = 5500$; region A has a low-mode damping parameter $\alpha = -75$ while region B has a low-mode damping parameter $\alpha = -117$. Physically, region B provides more log decrement to the lower modes than region A.

Table 2 Magnetic bearing design for acceptable region $A(\alpha = -75, \beta = 5500)$

Brg. Config.	J_{min}	brg	controller gain, zero and poles			
			k	z	p_1	p_2
1	2.27	left	1.42	−67	−16332	−3397
		right	4.46	−1685	−14464	−5536
2	1.02	left	1.99	−72	−18715	−791
		right	2.00	−57	−16057	−3585
3	0.37	left	0.73	−42	−16777	−3222
		right	0.27	−2460	−14542	−5457

Downloaded 02 Jun 2010 to 171.66.16.105. Redistribution subject to ASME license or copyright; see http://www.asme.org/terms/Terms_Use.cfm

Table 3 Magnetic bearing design for acceptable region B ($\alpha = -117$, $\beta = 5500$)

Brg. Config.	J_{min}	brg	controller gain, zero and poles			
			k	z	p_1	p_2
1	6.28	left	8.20	−150	$-6530 \pm 1031i$	
		right	0.30	−1014	$-1001 \pm 2070i$	
2	1.40	left	2.77	−252	−18811	−1159
		right	2.77	−74	−16560	−3399
3	0.51	left	1.03	−61	−16591	−3392
		right	0.15	−3874	$-7048 \pm 2337i$	

Table 1 shows the scalar measures obtained by the proposed method for the three candidate bearing configurations. Configuration 3 requires the least "effort" while configuration 1 requires the most for both regions A and B.

In designing optimized magnetic bearings for comparison, the following assumptions are made:

- A linear model of the magnetic bearing is considered.
- The magnetic bearings are collocated and the sensor at each bearing feeds back only to the same bearing.
- The sensors and actuators are infinite bandwidth.
- The open-loop stiffness of the magnetic bearings is zero.
- The controller transfer functions have the form:

$$C(s) = \frac{as + b}{s^2 + cs + d} = 10^{10}k \frac{(s - z)}{(s - p_1)(s - p_2)} \quad (17)$$

where $a, b, c, d > 0$, which ensures that the poles and zeros of $C(s)$ are always in the left half plane.

- The magnitudes of the poles are limited by requiring $c < 2.0 \times 10^4$ and $d < 1.5 \times 10^8$

The bearing design problem is to determine the parameters of the controller transfer functions such that the damped eigenvalues of the system are within the acceptable region. There may be no or multiple solutions (Johnson and Athans, 1970). If there are multiple solutions, it is desirable from a practical viewpoint to choose a solution that has the lowest infinity norm, which is the peak value of the gain of the transfer function and is denoted by $\|C\|_\infty$.

The bearing design problem can be formulated as a nonlinear constrained optimization problem. The cost function $J = 10^{-6}\|C\|_\infty$ is minimized by choice of the transfer function parameters such that the damped eigenvalues of the system are within the acceptable region. (Srinivasan, 1993)

Results are summarized in Tables 2 and 3. The ranking of the bearing configurations based on the measure $J = \|C\|_\infty$ of the controller designs is the same as was predicted by the proposed method where a large value of J_{min} is *undesirable.*

Conclusions

The locations of bearings in a rotor-bearing system determine the controllability/observability characteristics of the system, which in turn are important in bearing design for stability. A noniterative, numerically robust method for the purpose of ranking candidate bearing configurations has been presented. This method can be used by the magnetic bearing designer to determine the "best" locations before the actual bearing design. A design example on a multistage centrifugal compressor has been presented wherein magnetic bearings with minimum infinity norm controllers are designed to meet the stability specifications. The ranking of the bearing designs for the candidate bearing configurations in terms of the infinity norms are well correlated with the ranking obtained by the proposed method. This indicates the utility of the new method as a design tool.

References

Barrett, L. E., 1983, "The Optimization of Hydrodynamic Journal Bearings for Aerodynamically Excited Flexible Rotor-Bearing Systems," ASME *Journal of Mechanical Design,* Vol. 105, pp. 227–232.

Chiang, H. D., Thorp, J. S., Wang, J. C., Lu, J., and Aubert, B., 1992, "Optimal Controller Placements in Large-Scale Linear Systems," *IEEE Proceedings-D,* Vol. 139, pp. 79–87.

Choe, K., and Baruh, H., 1992, "Actuator Placement in Structural Control," AIAA *Journal of Guidance and Control,* Vol. 15, pp. 40–48.

Churchill, R. V., Brown, J. W., and Verhey, R. F., 1974, *Complex Variables and Applications,* McGraw-Hill, New York.

Dhar, D., Barrett, L. E., and Knospe, C. R., 1991, "Design of Bearings for Rotor Systems Based on Stability," *Proc. Int'l. Symp. on Magnetic Bearing Suspension Tech.,* NASA Langley Research Ctr., Hampton VA, Aug. 19–23.

Hamdan, A. M. A., and Nayfeh, A. H., 1989, "Measures of Modal Controllability and Observability," AIAA *Journal of Guidance and Control,* Vol. 12, pp. 421–428.

Johnson, T. L., and Athans, M., 1970, "On the Design of Optimal Constrained Dynamic Compensators for Linear Constant Systems," IEEE *Trans. Automat. Contr.,* Vol. AC-16, pp. 658–660.

Kailath, T., 1982, *Linear Systems,* Prentice Hall, Englewood Cliffs, NJ.

Kim, Y., and Junkins, J. L., 1991, "Measure of Controllability for Actuator Placement," AIAA *Journal of Guidance and Control,* Vol. 14, pp. 895–902.

Larsonneur, R., and Herzog, R., 1988, "Optimal Design of Structure Predefined Discrete Control for Rotors in Magnetic Bearings," *Proc., 1st Int'l. Symp. on Magnetic Bearings,* Springer-Verlag, pp. 347–356.

Laub, A. J., 1979, "A Schur Method for Solving Algebraic Ricatti Equations," IEEE *Trans. Automat. Contr.,* Vol. AC-24, pp. 913–921.

Lim, K. B., 1992, "Method for Optimal Actuator and Sensor Placement for Large Flexible Structures," AIAA *Journal of Guidance and Control,* Vol. 15, pp. 49–57.

Maslen, E. H., 1991a, "Magnetic Bearing Synthesis for Rotating Machinery," Ph.D. dissertation, University of Virginia, Charlottesville, VA.

Maslen, E. H., 1991b, "Controllability of Rotors," *Proc., ROMAG '91 Conference on Magnetic Bearings and Dry Gas Seals,* Alexandria, VA.

Molinari, B. P., 1977, "The Time Invariant Linear Quadratic Optimal Control Problem," *Automatica,* Vol. 13, pp. 347–357.

Moore, B. C., 1981, "Principal Component Analysis in Linear Systems: Controllability, Observability and Model Reduction," *IEEE Trans. Automat. Contr.,* Vol. AC-29, pp. 17–31.

Srinivasan, S., 1993, "A Stability Based Method for Selecting Bearing Locations in Rotor-Bearing Systems," Ph.D. dissertation, Univ. of Virginia, Charlottesville, VA.

Tarokh, M., 1990, "Measures for Controllability and Eigenvalue Mobility," *Proc., 29th Conference on Decision and Control,* pp. 1143–1148.

Vishwanathan, C. N., Longman, R. W., and Likins, P. W., 1984, "A Degree of Controllability Definition: Fundamental Concepts and Application to Modal Systems," AIAA *Journal of Guidance and Control,* Vol. 7, pp. 222–230.

Downloaded 02 Jun 2010 to 171.66.16.105. Redistribution subject to ASME license or copyright; see http://www.asme.org/terms/Terms_Use.cfm

Wave-Rotor-Enhanced Gas Turbine Engines

G. E. Welch
U. S. Army Research Laboratory.

S. M. Jones

D. E. Paxson

NASA Lewis Research Center,
21000 Brookpark Road, M/S 77-6,
Cleveland, OH 44135

The benefits of wave rotor topping in small (300- to 500-kW [400- to 700-hp] class) and intermediate (2000- to 3000-kW [3000- to 4000-hp] class) turboshaft engines, and large (350- to 450-kN [80,000- to 100,000-lb$_f$] class) high-bypass-ratio turbofan engines are evaluated. Wave rotor performance levels are calculated using a one-dimensional design/analysis code. Baseline and wave-rotor-enhanced engine performance levels are obtained from a cycle deck in which the wave rotor is represented as a burner with pressure gain. Wave rotor topping is shown to enhance the specific fuel consumption and specific power of small- and intermediate-sized turboshaft engines significantly. The specific fuel consumption of the wave-rotor-enhanced large turbofan engine can be reduced while it operates at a significantly reduced turbine inlet temperature. The wave-rotor-enhanced engine is shown to behave off-design like a conventional engine. Discussion concerning the impact of the wave rotor/gas turbine engine integration identifies technical challenges.

Introduction

Wave-rotor-topping units can significantly enhance the performance levels of gas turbine engines (Meyer, 1947; Goldstein et al., 1958; Mathur, 1985; Moritz, 1985; Weatherston and Hertzberg, 1967; Taussig, 1984; Zauner et al., 1993). NASA Lewis Research Center is currently characterizing the performance of wave rotors (Wilson and Fronek, 1993; Paxson, 1993, Welch, 1993; Larosiliere, 1993) with an aim toward applying wave rotor technology to increase the specific power, and decrease the specific fuel consumption, of turboshaft and turbofan engines (see Wilson and Paxson, 1993). The benefits of wave rotor topping in small (300- to 500-kW [400- to 700-hp] class) and intermediate (2000- to 3000-kW [3000- to 4000-hp] class) turboshaft engines, and large (350- to 450-kN [80,000- to 100,000-lb$_f$] class) high-bypass-ratio turbofan engines are evaluated in this paper. The wave rotor component and its performance are described. Estimates of the wave-rotor-enhanced specific power and specific fuel consumption for the three engine classes are then obtained using an engine cycle deck and computed wave rotor performance levels. Last, preliminary comments on the impact of wave rotor/engine integration are offered.

Wave Rotor Description

The wave rotor is an internal flow machine designed to exchange energy efficiently between gas streams of differing energy density. The energy exchange is accomplished within shrouded rotor passages (see Fig. 1) by shock and expansion waves, which propagate axially along the passages. The unsteady waves are initiated as the rotor passages open and close to the steady-state flows in the inlet and exhaust ports in a timed sequence dictated by the rotor speed and port azimuthal positions. In general, the wave rotor passages are alternately exposed to cold and hot gases at frequencies much higher than the reciprocal of the thermal time constant of the rotor walls (hub, shroud, and blades) and, therefore, the rotor assumes a constant temperature, which is significantly lower than the peak gas temperature in the rotor. This self-cooling feature enables topping in turbine-inlet-temperature-limited gas turbine engines; that is, the wave rotor topping increases the pressure and temperature at which heat is added in the burner without increasing the temperature of the engine turbomachinery components. Wave rotor performance is degraded by viscous, heat transfer, and shock losses within the rotor passages, leakage to and from the rotor passages and ports, mixing of nonuniform port flow fields, and mixing at gas/gas interfaces. An historical overview and detailed description of the wave rotor is presented by Azoury (1965-66).

Configuration. The number and azimuthal location of the wave rotor ports are set to effect various thermodynamic cycles. For example, three-port wave rotors have been used to divide an inlet medium total pressure stream into two output streams, one with total pressure higher than the inlet stream and one with total pressure lower than the inlet (e.g., see Kentfield, 1969, and Wilson and Fronek, 1993). No heat is added in the three-port cycle; rather, a fraction of the inlet gas is compressed by the energy of the remainder, which is expanded. In an analogous manner, two streams of high and low total pressure gas can be joined into one stream with intermediate total pressure (Kentfield, 1969). Four-port machines have been marketed as superchargers (i.e., as bottoming cycles) to enhance the specific power of internal combustion engines (Berchtold, 1985). Two-port (Goldstein et al., 1958), four-port (Mathur, 1985, Moritz, 1985), and nine-port (Taussig, 1984) wave rotors have been evaluated for gas turbine engine topping applications. Indeed, the wave rotor was first applied as a gas generator (see Azoury, 1965-66, referring to the wave-rotor-topped locomotive engine application discussed by Meyer, 1947). Various multiport configurations and heat addition schemes can be envisaged to effect the Brayton cycle of interest in the gas turbine engine topping application—some of the more simple approaches are shown schematically in Figs. 2(a–d).

Heat Addition. Some investigators (e.g., Goldstein et al., 1958) have suggested combustion internal to the wave rotor passages as shown schematically in Figs. 2(a, b). In this approach, two ports (with ductwork denoted by the arrows) are required per wave cycle, one from the compressor and one to the turbine. Conceptually, the wave rotor replaces the burner of the conventional engine; however, combustion internal to the rotor introduces potential problems related to fuel addition, ignition, flame speeds, and available combustion time, and is still in a conceptual stage (cf. Nalim, 1995). Alternatively to on-rotor combustion, heat can be added in a conventional burner, external to a four-port wave rotor, as shown in Figs. 2(c, d). In these variants, an extra component (the wave rotor) and three

Contributed by the International Gas Turbine Institute for publication in the JOURNAL OF ENGINEERING FOR GAS TURBINES AND POWER. Manuscript received at ASME Headquarters January 1997. Associate Technical Editor: L. A. Riekert.

Copyright © 1997 by ASME

Downloaded 02 Jun 2010 to 171.66.16.105. Redistribution subject to ASME license or copyright; see http://www.asme.org/terms/Terms_Use.cfm

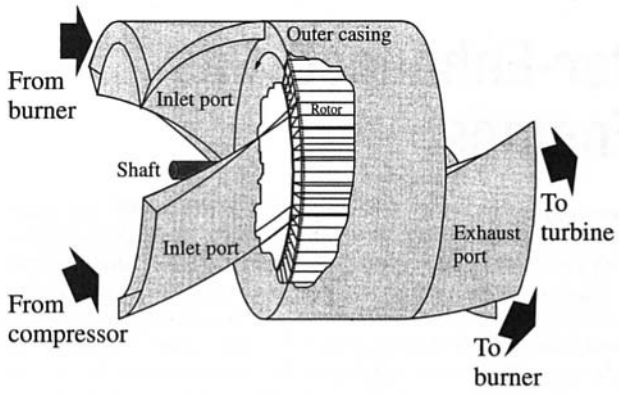


Fig. 1 Four-port wave rotor schematic diagram

ducts per cycle—from the compressor, to the turbine, and to the burner—are added to the engine. The external burner approach is attractive because heat addition is accomplished using existing burner technology; however, the addition of high-temperature ducting poses challenges to engine layout and thermal load management.

Power Extraction. In addition to the energy exchange by the gas dynamic waves, the rotor blades can be aerodynamically shaped (e.g., with stagger and camber) so as to produce shaft power efficiently (cf. Pearson, 1985). The "wave engine" approach is shown schematically in Figs. 2(b, d). The wave engine introduces essentially a new, high tip speed (albeit self-cooled) power turbine into the engine and in this way complicates the engine design. Conceptually, a wave engine can be backfitted into the baseline engine without changing the corrected flows and temperature and pressure ratios of the high-pressure turbine (HPT) and low-pressure turbine (LPT) of the untopped baseline engine. HPT first-stage cooling would come from the high-pressure compressor as in the baseline engine; therefore, an attractive feature of the wave engine approach is that the net power produced in the topping stage is extracted from the top part of the cycle so that the baseline engine is essentially unmodified. Alternatively, the pressure-gain wave rotor (Figs. 2(a, c)) has straight rotor blades and zero shaft power output by design. The net power available from the wave rotor topping is made manifest to the engine through the pressure gain across the wave rotor; that is, the HPT inlet pressure is significantly higher than the compressor discharge pressure—notably in contrast to the baseline engine, in which it is lower by the burner pressure drop. This approach is attractive in that conventional turbomachinery is used to extract the extra available net power. Because net power is not produced by the wave rotor, the rotor speed is set by the wave timing and performance optimization. The equivalent rotor tip speeds ($\sim\Omega R_T/\sqrt{T}$) are relatively low (typically 75 to 100 m/s [250 to 350 ft/s]) and give rise to relatively low mechanical stress levels. Windage and bearing friction losses can be overcome by a small drive motor or, in application, by introducing preswirl through the inflow port ducts as required to maintain rotor speed (after Zehnder et al., 1989). The corrected flow in components downstream of the wave rotor is reduced and, because the HPT inlet is at a pressure higher than the compressor discharge, film cooling in the first nozzle and first rotor of the HPT must come from the wave rotor. The present work considers only the four-port pressure-gain wave rotor with heat addition in a conventional burner, external to the wave rotor (Fig. 2(c)). The four-port pressure-gain wave rotor is a planned NASA LeRC research vehicle and is presently considered amenable to system integration within current engine design philosophy.

Four-Port Pressure-Gain Cycle. Space–time (x–t) diagrams for reverse-flow and throughflow four-port pressure-gain wave rotors are shown in Fig. 3. The x–t diagram provides a way of representing the time history of the gas dynamic waves in a single wave rotor passage as it moves through the wave rotor cycle. The compressor port and turbine port portions of the two-wave rotor cycles are identical. From a thermodynamics point of view, the two approaches therefore provide identical topping. The burner-port portions of the two cycles are different however. In the reverse-flow cycle, the fresh air enters and exits at the same end of the rotor. Only fresh air is discharged to the burner in this approach. The burned gas from the burner enters the rotor at the turbine end of the rotor. If the wave rotor is designed to have a single cycle per rotor revolution, then evidently the compressor inlet port end of the rotor will be relatively cool, while the turbine exhaust port end of the rotor will be relatively hot. Further, a buffer layer would remain in the passages. The buffer layer can be eliminated by immediately following the reverse-flow cycle by its mirror image. In this approach, a passage would experience two four-port reverse-flow cycles, one the mirror image of the other, as it rotates past eight ports in one rotor revolution. This approach introduces symmetry and assures that both ends of the rotor are washed by the relatively cold compressor discharge air; however, it also poses severe ducting challenges. Attention is therefore restricted to four-port wave rotors using the throughflow cycle in the present work. In the throughflow approach, a portion (30 to 50 percent) of once-burned air is recirculated to the burner. The recirculated gas is already burned and conceptually can bypass the burner. In reality, the recirculated gas mixes with the fresh air in the port to the burner. The fresh, relatively cold, air from the compressor traverses the full length of the rotor in the throughflow approach and, therefore, only one cycle is required to assure cooling throughout the rotor; however, an optimized wave rotor design (e.g., see Wilson and Paxson, 1995) might well have multiple wave cycles per rotor revolution.

Wave Rotor Performance. The wave rotor topping leads to the higher engine specific power (SP), that is, net shaft power (or engine thrust) per mass flow rate, and lower specific fuel consumption (SFC). This is evident from Fig. 4, which shows a total temperature–entropy diagram for the baseline and wave-rotor-enhanced engines, each operating with the same turbine inlet temperature, compressor pressure ratio, and mass flow rate. The heat addition in the wave-rotor-enhanced engine is equal to that of the baseline engine; however, because the heat addition in the wave-rotor-topped engine occurs at higher pressures and temperatures, the specific power and efficiency of the topped engine are higher.

The zero net power, pressure-gain wave rotor can be thought of as a high-pressure spool. A high-pressure spool might nomi-

Nomenclature

$\dot{m}$ = mass flow rate
p = absolute total pressure
p_T = wave rotor turbine-exhaust-port mixed-out absolute total pressure
p_C = wave rotor compressor-inlet-port absolute total pressure
R_T = wave rotor tip radius
T_T = wave rotor turbine-exhaust-port absolute total temperature (i.e., high-pressure turbine inlet temperature)
T_C = wave rotor compressor-inlet-port absolute total temperature (i.e., compressor discharge temperature)
T = absolute total temperature
Ω = shaft angular speed

Downloaded 02 Jun 2010 to 171.66.16.105. Redistribution subject to ASME license or copyright; see http://www.asme.org/terms/Terms_Use.cfm

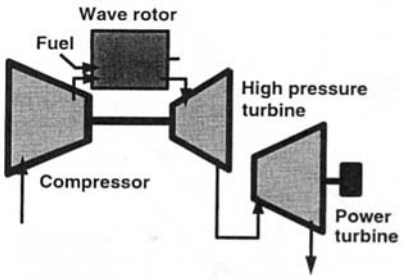


Figure 2a. Pressure–gain wave rotor with on–rotor combustion.

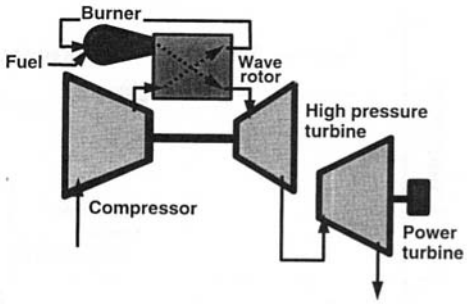


Figure 2c. Pressure–gain wave rotor with conventional burner.

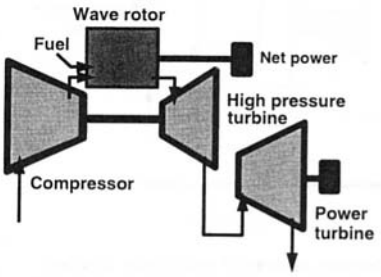


Figure 2b. Wave engine with on–rotor combustion.

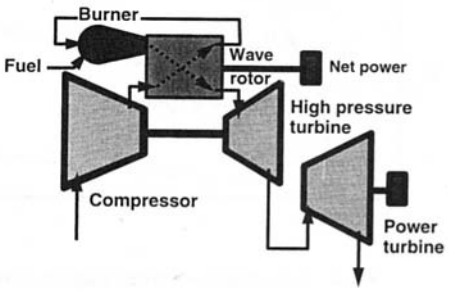
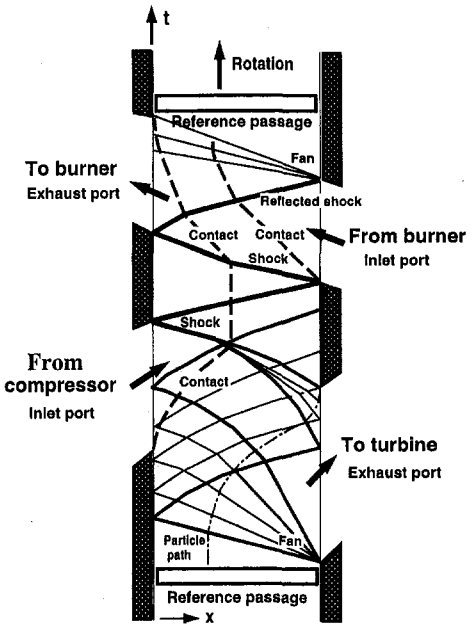


Figure 2d. Wave engine with conventional burner.

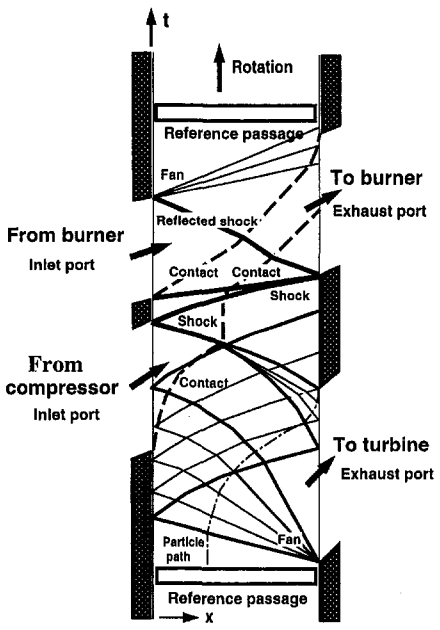
Fig. 2 Wave rotor/gas turbine engine integration variants

nally be characterized by compression ratio, the ratio of component inlet temperatures, and the component efficiencies. Alternatively (cf. Goldstein et al., 1958; Mathur, 1985; Moritz, 1985), the high-pressure spool can be characterized by the variation of pressure ratio (p_T/p_C) as a function of temperature ratio (T_T/T_C, as defined in Fig. 4). The latter approach is used here to avoid ambiguity in defining wave rotor "component" efficiencies. Figure 5 provides example performance level ranges for the small, intermediate, and large gas turbine engines calculated in the present work, along with experimentally demonstrated four-port wave rotor performance levels (reported by Mathur, 1985, and Moritz, 1985).

The solid curve in Fig. 5 illustrates the qualitative behavior of wave rotor pressure ratio as a function of temperature ratio for optimized wave rotors operating on-design. The magnitude of the solid curve varies with engine-class and depends on mass flow rate, compressor discharge conditions, rotor speed, and cooling bleed flow requirements, as indicated by the variation in the performance levels of specific small, intermediate, and large engines. Figure 5 also provides a corresponding "ideal"



(a) Reverse–flow cycle



(b) Through–flow cycle

Fig. 3 Space–time diagrams for reverse-flow and throughflow four-port wave rotors

Downloaded 02 Jun 2010 to 171.66.16.105. Redistribution subject to ASME license or copyright; see http://www.asme.org/terms/Terms_Use.cfm

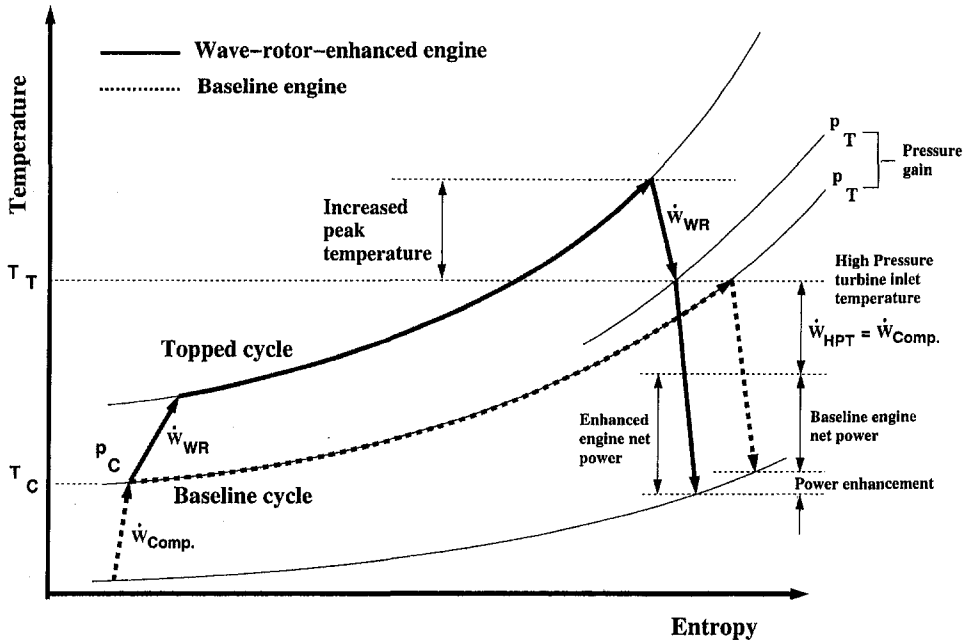


Fig. 4 Temperature–entropy diagram showing thermodynamic benefit of wave rotor topping

(dotted curve) wave rotor performance curve in which only entropy production inherent to the wave cycle itself is accounted for; that is, entropy production in the shock waves and resulting from the mixing of nonuniform port flow fields. The reduction in wave rotor performance levels indicated by the disparity between the dotted and solid curves is due primarily to viscous losses, inherent partial admission losses, and the impact of leakage flows.

According to the example solid curve of Fig. 5, an on-design wave rotor operating with a temperature ratio of 2.2 would attain an effective burner pressure gain (p_T/p_C) of 1.2. The wave-rotor-topped engine operating with this temperature ratio would, therefore, have an HPT inlet pressure 20 percent higher than its compressor discharge pressure, leading to approximately 20 percent increased specific power. An alternate way of interpreting the influence of the wave rotor performance level on engine performance is illustrated in Fig. 6 for a family of constant turbine inlet temperature engine cores. For a fixed turbine inlet temperature (1778 K [3200 R] in Fig. 6), the wave rotor temperature ratio (abscissa) is set by the particular engine compressor pressure ratio (as shown). Lines of constant SFC can be then drawn as functions of the compressor pressure ratio for the fixed turbine inlet temperature. The solid curve, similar to that in Fig. 5, indicates that for a fixed turbine inlet temperature, the wave rotor pressure ratio increases as the compressor pressure ratio decreases. The wave rotor SFC enhance-

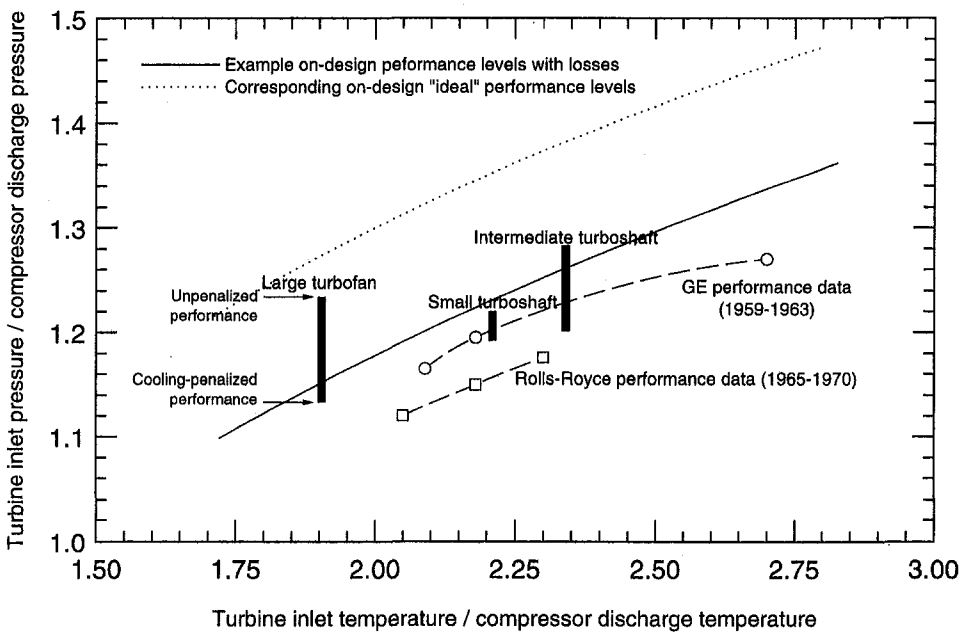


Fig. 5 Four-port pressure-gain wave rotor performance plot (p_T/p_C versus T_T/T_C) showing sample computed performance levels and GE (see Mathur, 1985) and Rolls-Royce (see Moritz, 1985) experimental performance data

Downloaded 02 Jun 2010 to 171.66.16.105. Redistribution subject to ASME license or copyright; see http://www.asme.org/terms/Terms_Use.cfm

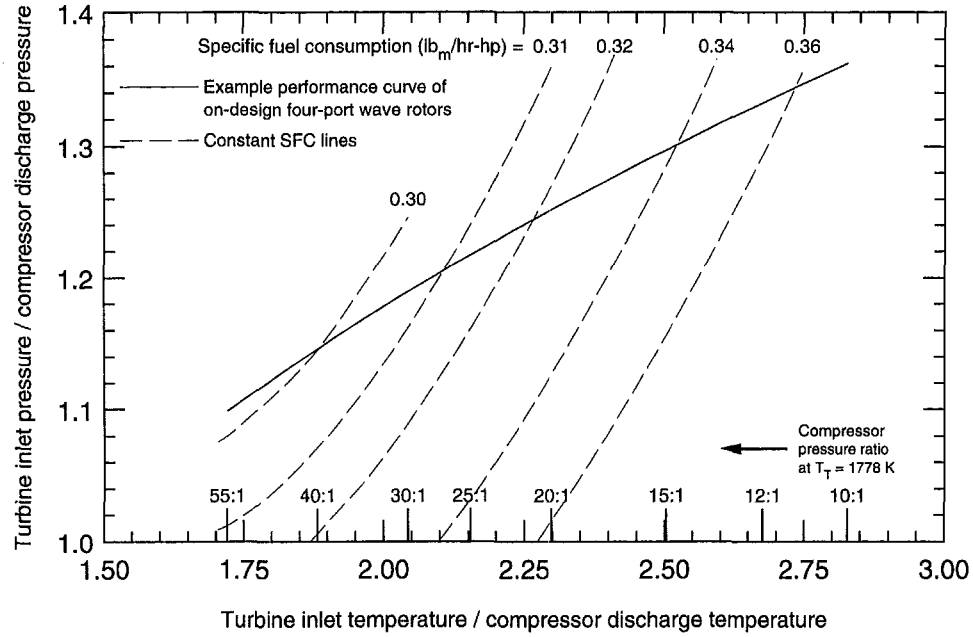


Fig. 6 Lines of constant specific fuel consumption for a family of engines with 1778 K (3200 R) turbine inlet temperature

ment is made apparent by first choosing a required engine SFC (e.g., 54.1 μg/J [0.32 lb_m/hr-hp]), and then comparing the compressor pressure ratio required for that SFC with wave rotor topping ($\simeq$21:1), and without topping ($\simeq$49:1 for a baseline engine with a 5 percent burner pressure drop [i.e., p_T/p_C = 0.95]).

Note that any high-pressure spool offers the pressure gain described for the wave rotor and can be characterized similarly; however, a high-pressure spool of conventional turbomachinery cannot withstand the higher burner exhaust temperatures (see Fig. 4) incurred in topping a baseline engine that is likely already to be turbine inlet temperature limited. The burner heat addition in the wave-rotor-topped engine occurs at pressures 2.5 to 3.5 times higher than in the untopped engine; that is, the peak pressure of the topped engine is 2.5 to 3.5 times higher than the compressor discharge pressure. The burner outlet temperature of the topped engine at these pressures is typically 280 to 450 K (500 to 800 R) above, or a factor of 1.2 to 1.25 times higher than, the turbine inlet temperature. CFD calculations (Paxson, 1993; Welch, 1993) predict that the mean wave rotor temperature will be less than, or equal to, the turbine inlet temperature as a result of the intermittent washing by the hot and cold gases. It is this self-cooling feature that suggests that the wave rotor can be operated at realistic mean rotor wall temperatures with peak gas temperatures 280 to 450 K (500 to 800 R) higher than the turbine inlet temperature.

Wave Rotor/Engine Study Results

Results of a study on the benefits of wave rotor topping in a small turboshaft engine, an intermediate turboshaft engine, and a large turbofan engine are presented in this section. The engine performance levels, with and without wave rotor enhancement, were calculated by using a one-dimensional computational model of the wave rotor and a system code to predict engine performance levels.

Wave-Rotor-Performance Calculations. The wave rotor performance is calculated using a one-dimensional design/analysis code (Paxson, 1993), which solves the unsteady viscous flow field in the rotor frame of reference. The one-dimensional code has been validated using experimental data (Wilson and Fronek, 1993). A single rotor passage is time-marched until the passage flow is periodic in time, given constant specified inlet and outlet port boundary conditions. The code can be used both to design the port timing by tracking the gas dynamic waves and to calculate the wave rotor pressure gain and burner loop pressure drop for specified turbine inlet temperature and compressor discharge conditions. The port design accounts for bleed of the highest pressure air from the port going to the burner, which is used for HPT first nozzle and first rotor cooling. The performance calculations include losses caused by gradual opening and closing of the rotor passages, viscous and heat transfer effects, and passage-to-casing and passage-to-port leakage. The wave rotor is geometrically optimized (cf. Wilson and Paxson, 1995) for the engine-specific mass flow rate, compressor discharge conditions, and wave rotor temperature ratio.

Engine Performance Calculations. The NASA Engine Performance Program (NEPP, Plencner and Snyder, 1991; Klann and Snyder, 1994) uses scalable compressor and turbine maps to calculate on- and off-design engine performance. To calculate the enhanced engine performance, the wave rotor is mimicked by replacing the pressure drop of the burner component of the baseline engine with the calculated pressure gain of the wave rotor while keeping heat addition the same. Pressure drops are added upstream and downstream of the wave rotor to simulate the losses in the ducts between the compressor and the wave rotor and between the wave rotor and the HPT. The "redesigned" wave-rotor-enhanced engine has the same airflow into the engine, heat addition (fuel flow), cooling and bleed flows, and turbine inlet temperature as the baseline engine at full power (Mach 0.0, sea level). In addition, the net thrusts of the baseline and enhanced turboshaft engines are the same, while the bypass ratios of the turbofan engines are the same (with the exception noted later). Therefore, the fan and compressor components of the baseline and enhanced engines are identical. The corrected mass flow rates ($\sim \dot{m}\sqrt{T}/p$) to the high-pressure and low-pressure turbines of the wave-rotor-enhanced engine are reduced, however. In the present calculations, the turbine maps are scaled to accommodate the lower corrected flow. In application, the change in corrected flow would require a redesign of the HPT and LPT to match the compression system of the baseline engine; alternatively, it may be possible to mix

Downloaded 02 Jun 2010 to 171.66.16.105. Redistribution subject to ASME license or copyright; see http://www.asme.org/terms/Terms_Use.cfm

and match the compressors and turbines of existing engine derivatives to accommodate the modifications in corrected flow.

Engine Performance Level Results. Table 1 provides a comparison of baseline (untopped) and wave-rotor-enhanced performance levels for 430-kW (576-hp) turboshaft, a 2500-kW (3342-hp) turboshaft, and a 385-kN (86,700-lb_f) turbofan. For a given engine type, the compressor pressure ratio, the turbine inlet temperature, and the engine (core) mass flow rate are fixed. The "unpenalized" results refer to wave-rotor-enhanced performance in which no HPT cooling bleed is extracted from the wave rotor; rather, the bleed flow is extracted from the high-pressure compressor. The "penalized" results refer to calculations in which HPT cooling is extracted from the wave rotor port leading to the burner. This cooling air extraction reduces wave rotor performance. This is simulated in the NEPP calculation by extracting bleed from the high-pressure compressor discharge to cool the HPT—even though in reality its pressure is too low—and by using a bleed-penalized wave rotor pressure ratio as the burner pressure gain. The cooling bleed percentage is that of the baseline engine. In reality, the temperature of the wave rotor discharge used for cooling is higher than the compressor discharge, commensurate with the wave rotor overall pressure ratio ($\simeq$3:1); however, the pressure is higher too so that the increased Reynolds number of the flow works to increase the heat transfer coefficient and thus offset, to some degree, the decreased cooling capability of the higher temperature wave rotor discharge. Because the specific details of the enhanced engine layout are not defined at this point, the approach outlined above is used in the present calculations and both results with and without cooling penalty are reported in Table 1. Only the penalized results are discussed below, however.

The wave rotor topping enhances the SP and SFC levels of each engine class. The most significant enhancement is found in the small and intermediate turboshaft engines that operate with relatively low compressor pressure ratios (cf. Fig. 6). If the penalized performance relative to the baseline engine performance is considered, the SP enhancement of the small and intermediate turboshaft engines is +21 and +19 percent, respectively, and the SFC levels are reduced by 17 and 16 percent, respectively. The wave rotor pressure ratio of the small turboshaft (1.192) is slightly less than that of the intermediate turboshaft (1.201) because of the lower temperature ratio (cf. Fig. 5) and higher viscous losses per mass flow rate (due to small size), in spite of lower cooling flow requirements. Even so, the small turboshaft engine benefits slightly more from the wave rotor topping than does the intermediate turboshaft engine because the higher bleed fraction of the intermediate turboshaft has reduced the fraction of working fluid experiencing the wave rotor pressure gain. The large turbofan wave rotor performance

Table 1 Baseline and wave-rotor-enhanced engine performance levels for small and intermediate turboshaft and large high bypass ratio turbofan engines. For a given engine type, shaft pressure ratio, turbine inlet temperature, and engine mass flow rate are fixed. "Penalized" denotes cases where the wave rotor supplies the HPT cooling flow.

Parameter	Small Turboshaft	Intermediate Turboshaft	Large Turbofan*
Shaft Pressure Ratio	7.77	7.89	38.1
Turbine Inlet Temperature (K [R])	1328 [2390]	1320 [2376]	1778 [3200]
Mass Flow (kg/s [lb_m/s])	2.28 [5.03]	11.9 [26.2]	1270 [2800]
Bleed Percent[1]	4.9	11.4	21.0
Baseline SFC[2]	105.1 [0.622]	90.9 [0.538]	8.87 [0.313]
Unpenalized SFC	84.8 [0.502]	72.7 [0.430]	8.50 [0.300]
Penalized SFC	86.5 [0.512]	76.4 [0.452]	8.61 [0.304]
Baseline Power[3]	429.4 [575.8]	2492 [3342]	385.8 [86,727]
Unpenalized Power	531.6 [712.9]	3116 [4178]	403.3 [90,655]
Penalized Power	521.0 [698.7]	2967 [3979]	397.6 [89,393]
Baseline SP[4]	188.2 [114.5]	209.6 [127.5]	303.8 [30.97]
Unpenalized SP	233.0 [141.7]	262.1 [159.4]	317.5 [32.38]
Penalized SP	228.4 [138.9]	249.6 [151.8]	313.1 [31.93]
Wave Rotor Temperature Ratio[5]	2.209	2.340	1.906
Baseline Burner Pressure Ratio[6]	0.96	0.96	0.95
WR Pressure Ratio[7]	1.220	1.283	1.234
Penalized WR Pressure Ratio	1.192	1.201	1.133
Burner Exhaust Temperature (K [R])	1328 [2390]	1320 [2376]	1778 [3200]
Unpenalized Exhaust Temperature	1651 [2972]	1631 [2936]	2188 [3939]
Penalized Exhaust Temperature	1657 [2983]	1649 [2969]	2221 [3998]
Baseline OPR[8]	7.77	7.89	38.1
Unpenalized OPR	25.6	26.7	123
Penalized OPR	25.1	25.5	116

*Bypass ratio = 7.00. Total flow is 1270 kg/s [2800 lb_m/s] and core flow is 159 kg/s [350 lb_m/s].
[1]Percent of compressor discharge flow used for high pressure turbine cooling.
[2]Specific fuel consumption (μg/J [lb_m/hr-hp]) for turboshafts and thrust SFC (mg/N-s [lb_m/hr-lb_f]) for turbofan.
[3]Net Power (kW [hp]) for turboshafts and thrust (kN [lb_f]) for turbofan.
[4]Power/mass flow rate (kW/kg/s [hp/lb_m/s]) for turboshafts and specific impulse (m/s [lb_f/lb_m/s]) for turbofan.
[5]Defined as ratio of total temperatures in wave rotor turbine exhaust port and the wave rotor compressor inlet port.
[6]Defined as ratio total pressure into HPT and total pressure of compressor discharge of baseline engine.
[7]Defined as ratio of total pressures in wave rotor turbine exhaust and compressor discharge (effective burner pressure gain).
[8]Defined as ratio of burner inlet pressure to compressor inlet pressure for turboshafts and ratio of burner inlet pressure to fan inlet pressure for turbofans.

Downloaded 02 Jun 2010 to 171.66.16.105. Redistribution subject to ASME license or copyright; see http://www.asme.org/terms/Terms_Use.cfm

is severely penalized by 21 percent (core flow) cooling bleed. Although the large turbofan operates at a relatively low temperature ratio of 1.905, reflective of its already high compressor pressure ratio, the unpenalized pressure ratio (1.234) is high because of very low viscous losses and low rotational speed of the large, optimized rotor. The penalized wave rotor pressure ratio of 1.133 leads to a 3 percent decrease in thrust specific fuel consumption (TSFC) and a 3 percent increase in specific impulse (I_{SP}). These modest improvements might suggest discounting wave rotor topping in the large high bypass turbofans; however, before doing so, the following variations in the approach to exploiting the wave rotor pressure gain in the large engine integration are considered.

Table 2 compares the baseline large turbofan engine with variants of wave-rotor-enhanced engines. In all cases the total engine mass flow rate is 1270 kg/s (2800 lb_m/s) and the compressor pressure ratio is 38:1. Variant A is that reported in Table 1 in which the turbine inlet temperature (T_T) and the bypass ratio are fixed at those of the baseline engine, 1778 K (3200 R) and 7.00, respectively. Variant B holds the T_T at 1778 K (3200 R) but increases the bypass ratio to 7.57. This reduces the core mass flow rate while slightly increasing the bypass mass flow rate, such that the engine thrust is that of the baseline engine (385.8 kN [86,727 lb_f]). Variant C holds the bypass ratio at 7.00 (baseline) but decreases T_T by 73 K (130 R), again, so that the engine thrust is that of the baseline engine. At this lower T_T, the required cooling bleed fraction is reduced from 21 percent in the baseline engine to 18.3 percent in Variant C. Variants B and C therefore have the same thrust (and I_{SP}) of the baseline engine, but each shows a respectable 6.6 percent reduction in TSFC. Variant B is interesting in that the reduced core mass flow rate means the engine core shrinks in size and weight; this weight reduction can be used to accommodate the weight introduced by the wave rotor and associated ducting. Variant C is interesting in that the T_T has been significantly reduced, which has an impact on engine life, maintenance, and cost of manufacturing. Considering the already high compressor pressure ratios of current large turbofan engines, the predicted 6 to 7 percent TSFC enhancement is significant. This is apparent when comparing the predicted take-off gross weight (TOGW) of a modern large subsonic transport (e.g., Boeing 777), flying a specified mission, powered by either the baseline or one of the wave-rotor-enhanced engine variants considered here. The wave rotor topping leads to TOGW reduction between 5 and 7 percent depending on the variant considered (see Table 2). An aircraft powered by a Variant B engine, for example, is 7 percent lighter at take-off than an aircraft, flying the same mission, powered by the baseline engine. Evidently, wave rotor topping of the large turbofan engines warrants further investigation.

As mentioned, the wave rotor is "self-cooling" in that the average gas path temperature on board the rotor passage is 280 to 450 K (500 to 800 R) below the burner exhaust temperature, or approximately equal to the absolute temperature into the HPT nozzle. Detailed flow calculations (see Welch, 1993) show that the time-averaged adiabatic rotor wall temperature is close to the static temperature into the HPT nozzle. The mean rotor temperatures of the small and intermediate turboshaft engines is therefore expected (see Table 1) to be $\leq$1328 K (2390 R or 1930°F). In the turbofan, however, a mean adiabatic rotor temperature near 1778 K (3200 R or 2740°F) is predicted. The low wave rotor tip speeds suggest much lower stress levels than those encountered in modern turbomachinery; however, even with robust shrouded rotor construction and low tip speeds, the 1778 K (3200 R) mean blade temperature is not tolerable. It is therefore noted that the wave rotor—with the throughflow wave cycle considered here—would require additional cooling in the large engine (T_T = 1778 K [3200 R]) application. Although cooling schemes and alternative wave cycles are readily envisaged—and although it is noted that ceramic rotors have been built and tested (Zehnder et al., 1989)—the additional cooling required for the large turbofan is not addressed in the present work.

Impact on Engine

The cycle study calculations presented above indicate that wave rotor topping significantly enhances the SFC and power (or thrust) per mass flow rate of the turboshaft and turbofan engines. Moving from cycle studies to product, however, raises questions related to the impact of wave rotor/engine integration on: (1) safety; (2) economic factors including direct operating costs, manufacturability, maintainability, and life; (3) off-design performance; (4) system dynamics (e.g., start up and other anticipated transients); and, for aeropropulsion applications, especially, (5) power (thrust) to weight. A detailed analysis of the impact (in the sense of these factors) of the wave rotor on the gas turbine engine is beyond the scope of the present work; however, preliminary comments regarding wave rotor integration, manufacturing, weight, and off-design performance are presented below.

Integration

Compatibility. The one-dimensional computations of the present study show that the component efficiencies of the throughflow wave rotor considered here are lower than those of modern turbomachinery. This is due in part to viscous losses in the shrouded passages, partial admission-related losses, and losses associated with nonuniform port flows. With expected wave rotor on-design polytropic compression efficiencies of 82 to 85 percent and polytropic expansion efficiencies of 93 to 95 percent, it is arguably desirable to use conventional turbomachinery where temperature limitations permit. A number of considerations point to the suitability of the self-cooled wave rotor to the topping application, however: The high-pressure turbine blades of modern engines approach an inveterate material temperature ceiling; the compressor of many engines is also bounded by discharge-temperature/blade-life-related constraints; further, the low corrected flow rates in small engines (and in the final compressor stages of advanced large turbofan engine cores) lead to tolerance-related inefficiencies (e.g., due to tip-leakage and blade-profile manufacturing limitations). The inherent partial admission of the wave rotor, albeit with associated losses, matches well with low corrected flow rates: The full annulus of the compressor discharge is collected into the partial inlet port sector, leading to optimum wave rotor geometry (e.g., hub-to-tip ratio) at wave rotor diameters similar to the upstream and downstream turbomachinery. Further, because the rotor is shrouded, tip-leakage-induced losses are eliminated. The leakage flows at the rotor ends can be controlled by minimizing the gap between the rotor and casing end-walls.

Packaging. Although the turbomachinery temperatures have not increased, thermodynamics dictates that the peak (burner) pressures and temperatures of the enhanced engine have increased. Indeed, the burner temperatures and pressures (see Tables 1 and 2) are significantly higher than those of untopped engines. This impacts burner size and material temperature and strength requirements. Further, using results reported by Wilson and Paxson (1995), it is inferred that optimized pressure-gain wave rotors nominally spin with low equivalent tip speeds between 75 to 100 m/s (250 to 300 ft/s) (or rotor Mach numbers based on the rotor tip speed and the compressor discharge total temperature near 0.25). The pressure-gain wave rotor spins at much lower shaft speeds than does the engine core turbomachinery; therefore, it constitutes a separate spool, whether operating on- (cf. Taussig, 1984) or off-axis. The required transitions to and from the compressor and turbine full annuli to the wave rotor ports necessitate the duct work shown schematically by arrows in Fig. 2(*c*). Packaging the wave rotor in a manner that provides tolerable mechanical and thermal

Downloaded 02 Jun 2010 to 171.66.16.105. Redistribution subject to ASME license or copyright; see http://www.asme.org/terms/Terms_Use.cfm

Table 2 Large turbofan wave-rotor-enhanced engine variants with fixed compressor pressure ratio of 38:1, total mass flow rate of 1270 kg/s [2800 lb_m/s], coolant bleed of 21 percent of core flow, and wave rotor pressure ratio of 1.13 (cooling-penalized value).

Turbofan Variant:[1]	Baseline	A	B	C
Bypass Ratio	7.00	7.00	7.57	7.00
Turbine Inlet Temperature (K [R])	1778 [3200]	1778 [3200]	1778 [3200]	1704 K[†] [3068]
TSFC (mg/N-s [lb_m/hr-lb_f])	8.87 [0.313]	8.61 [0.304]	8.27 [0.292]	8.27 [0.292]
Thrust (kN [lb_f])	385.8 [86,727]	397.6 [89,393]	385.8 [86,727]	385.8 [86,732]
I_{SP} (m/s [$lb_f/lb_m/s$])	303.8 [30.97]	313.1 [31.93]	303.8 [30.97]	303.8 [30.98]
Burner Exhaust Temperature (K [R])	1778 [3200]	2221 [3998]	2221 [3998]	≈ 2129 [3833]
Overall Pressure Ratio (OPR)[2]	38.1	116	116	≈ 116
Percent Reduction in TOGW[3]	—	6.1	7.4	5.5

[1]Variants:

A Wave-rotor-enhanced engine with baseline engine turbine inlet temperature and bypass ratio.

B Wave-rotor-enhanced engine with baseline engine turbine inlet temperature but increased bypass ratio such that thrust is same as baseline engine thrust.

C Wave-rotor-enhanced engine with baseline engine bypass ratio with reduced turbine inlet temperature such that thrust is same as baseline engine thrust.

[2]Defined as the ratio of burner inlet pressure to fan inlet pressure.

[3]Percent reduction in the take-off gross weight of aircraft with wave-rotor-enhanced engines as compared to the aircraft with baseline engines. The wave- rotor-enhanced engine weight includes the weight of wave rotor and associated ducting which is assumed to be 25% of baseline engine core weight.

[†]Reducing the turbine inlet temperature at a given compressor pressure ratio reduces the wave rotor temperature ratio, which might suggest a reduction in wave rotor pressure ratio (cf. Fig. 5); however, here, the reduction in turbine inlet temperature also leads to a reduction in bleed penalty to wave rotor, caused by a reduction in required bleed fraction from 21 to 18.3%. The reduced cooling penalty is expected to at least offset the expected pressure ratio reduction.

loads and duct pressure losses is critical to engine life, maintenance requirements, and performance. This is not addressed in the present work, which uses engine performance levels as figures of merit.

Manufacturing. The straight-bladed, zero-net-power, pressure-gain wave rotor is arguably easily designed and mass produced (Berchtold, 1985) at low cost relative to conventional turbomachinery components.

Weight. The weight of the wave rotor and its associated ducting and controls is estimated (by using numbers reported in Mathur, 1985) to be approximately 25 percent of the baseline engine weight (also, cf. Taussig, 1984, p. 13, where the wave rotor is estimated to add 23 percent of a low-bypass-ratio baseline turbofan engine weight). The power per engine weight of the small and intermediate turboshaft engines of this study would, by this preliminary 25 percent added-weight estimate, be reduced slightly. However, this estimate does not account for significant potential weight reduction won by reducing the size of the components (e.g., burner and turbines) downstream of the wave rotor to accommodate the lower corrected flows to these components. Detailed analysis of the wave-rotor-enhanced engine weight necessarily depends on the specifics of the engine layout and is to be addressed by planned work. Further, in light of the 16 to 17 percent reduction in SFC offered by wave rotor topping, the impact of adding the wave rotor weight to the engine is necessarily evaluated within the context of the specific engine application and its associated mission.

Off-Design Operation. Figure 7 illustrates the performance of the baseline, wave-rotor-enhanced, and turbomachinery "topped" small turboshaft engine operating between 43 percent (compressor pressure ratio ≃5.7, T_T = 1122 K [2020 R]) and 100 percent full power (compressor pressure ratio = 7.77, T_T = 1328 K [2390 R]). The "topped" engine is a baseline engine with a fictitious high-pressure spool comprised of a compressor and turbine unit. The burner pressure drop for the "topped" cycle is the same as that (4.0 percent) of the baseline engine. The heat addition, inlet temperature (1328 K [2390 R]) into what is now the second turbine, and the compressor discharge conditions are the same those of the baseline and the wave rotor topped engines at full power. At the full power design point, the high-spool compressor and turbine adiabatic efficiencies are set at 0.85 (0.86 polytropic) and 0.90 (0.896 polytropic), respectively, and the high spool compressor pressure ratio is 1.75. This sets the pressure gain of the high-pressure spool equal to that of the unpenalized wave rotor (1.22) at the full power design point. The turbomachinery-topped engine overall pressure ratio is 13.6 and the burner inlet and outlet temperatures are 715 K (1288 R) and 1424 K (2563 R), respectively. The turbomachinery-topped scenario increases the high-spool turbine inlet temperature to 1424 K (2563 R). These numbers can be compared with those of the baseline and wave-rotor-enhanced engines shown in Table 1.

In Fig. 7, SFC is plotted against shaft horsepower for the baseline, wave-rotor-enhanced engine, and turbomachinery-topped engines. The off-design performances of the baseline and turbomachinery-topped systems are calculated within NEPP using representative compressor and turbine maps scaled to reproduce the full-power (design) performance. The off-design wave rotor pressure ratio (also not penalized for bleed flow here) is calculated using the one-dimensional design/analysis code, and depends on wave rotor corrected speed, corrected mass flow rate, and engine corrected heat addition (cf. Paxson, 1995). In the results shown in Fig. 7, the wave rotor runs with constant 17,000 rpm throughout the 43 to 100 percent power range. Figure 7 shows that the three engines perform off-design in qualitatively the same manner, and that the performance of the "topped" engine and the wave rotor-enhanced engine is indistinguishable over the partial power range. Clearly the off-design behavior of wave-rotor-enhanced and baseline turboshaft engines is the same.

Summary

Calculated performance levels of small and intermediate wave-rotor-enhanced turboshaft engines show 19 to 21 percent increase in specific power (SP) and 16 to 17 percent decrease

Downloaded 02 Jun 2010 to 171.66.16.105. Redistribution subject to ASME license or copyright; see http://www.asme.org/terms/Terms_Use.cfm

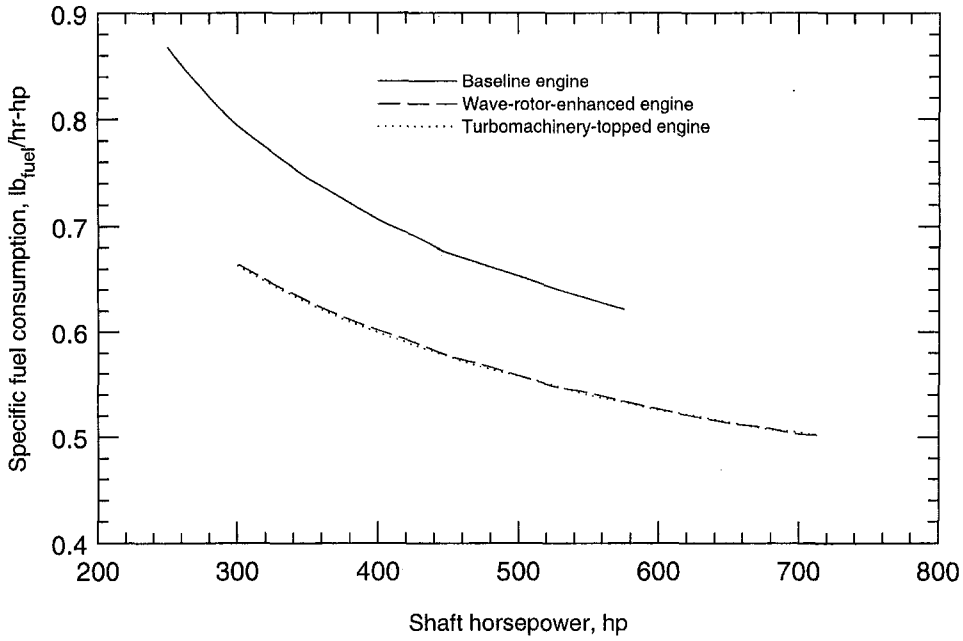


Fig. 7 Off-design performance of baseline, wave-rotor-enhanced, and turbomachinery-topped engines

in specific fuel consumption (SFC) over the baseline engines. Calculations of a wave-rotor-enhanced large turbofan engine, equal in thrust to the baseline engine, shows a 6 to 7 percent reduction in TSFC. The wave-rotor-enhanced TSFC would lead to a significant 5 to 7 percent reduction in the take-off gross weight in a large subsonic transport application. The wave-rotor-enhanced engine behaves off-design (43 to 100 percent full power) like a conventional engine. The additional weight of the wave rotor and associated ductwork is expected to be less than 25 percent of the baseline engine core weight. Discussion concerning the impact of integrating the four-port pressure-gain wave rotor has identified technical challenges regarding packaging, added ductwork with associated pressure losses, mechanical and thermal loads, and maintenance.

References

Azoury, P. H., 1965–1966, "An Introduction to the Dynamic Pressure Exchanger," *Proc. Inst. Mech. Eng.,* Vol. 180, Pt. 1, pp. 451–480.

Berchtold, M., 1985, "Supercharging With Comprex," R. P. Shreeve and A. Mathur, eds., *Proc. 1985 ONR/NAVAIR Wave Rotor Research and Technology Workshop,* Report NPS-67-85-008, Naval Postgraduate School, Monterey, CA, May, pp. 51–74.

Goldstein, A. W., Klapproth, J. F., and Hartmann, M. J., 1958, "Ideal Performance of Valved-Combustors and Applicability to Several Engine Types," *Trans. ASME,* Vol. 80, July, pp. 1027–1036.

Kentfield, J. A. C., 1969, "The Performance of Pressure-Exchanger Dividers and Equalizers," ASME *Journal of Basic Engineering,* Vol. 91, pp. 361–370.

Klann, J., and Snyder, C., 1994, "NEPP Programmer's Manual (NASA Engine Performance Program), Vols. I and II," NASA TM-106575.

Larosiliere, L. M., 1993, "Three-Dimensional Numerical Simulation of Gradual Opening in a Wave Rotor Passage," Paper No. AIAA-93-2526.

Mathur, A., 1985, "A Brief Review of G.E. Wave Engine Program (1958–1963)," R. P. Shreeve and A. Mathur, 1985, *Proc. 1985 ONR/NAVAIR Wave Rotor Research and Technology Workshop,* Report NPS-67-85-008, Naval Postgraduate School, Monterey, CA, May, pp. 171–193.

Meyer, A., 1947, "Recent Developments in Gas Turbines," *Mech. Engineering,* 69, pp. 273–277.

Moritz, R., 1995, "Rolls-Royce Study of Wave Rotors 1965–1970," R. P. Shreeve and A. Mathur, *Proc. 1985 ONR/NAVAIR Wave Rotor Research and Technology Workshop,* Report NPS-67-85-008, Naval Postgraduate School, Monterey, CA, May, pp. 116–124.

Nalim, M. R., 1995, "Preliminary Assessment of Combustion Modes for Internal Combustion Wave Rotors," Paper No. AIAA-95-2801.

Paxson, D. E., 1993, "A Comparison Between Numerically Modelled and Experimentally Measured Loss Mechanisms in Wave Rotors," Paper No. AIAA-93-2522; also NASA TM-106279.

Paxson, D. E., 1995, "A Numerical Model for Dynamic Wave Rotor Analysis," Paper No. AIAA-95-2800; also NASA TM-106997.

Pearson, R. D., 1985, "Performance Predictions for Gas Wave Turbines Including Practical Cycles With Wide Speed Range," R. P. Shreeve and A. Mathur, 1985, *Proc. 1985 ONR/NAVAIR Wave Rotor Research and Technology Workshop,* Report NPS-67-85-008, Naval Postgraduate School, Monterey, CA, May, pp. 329–378.

Plencner, R., and Snyder, C., 1991, "The Navy/NASA Engine Program (NNEP89)—A User's Manual," NASA TM-105186.

Taussig, R. T., 1984, "Wave Rotor Turbofan Engines for Aircraft," J. F. Sladky, Jr., ed., *Machinery for Direct Fluid–Fluid Energy Exchange,* AD-07, ASME, New York, Dec., pp. 9–45.

Weatherston, R. C., and Hertzberg, A., 1967, "The Energy Exchanger, a New Concept for High-Efficiency Gas-Turbine Cycles," ASME *Journal of Engineering for Power,* Vol. 89, pp. 218–228.

Welch, G. E., 1993, "Two-Dimensional Numerical Study of Wave Rotor Flow Dynamics," Paper No. AIAA-93-2525.

Wilson, J., and Fronek, D., 1993, "Initial Results From the NASA Lewis Wave Rotor Experiment," Paper No. AIAA-93-2521; also NASA TM-106148.

Wilson, J., and Paxson, D. E., 1993, "Jet Engine Performance Enhancement Through Use of a Wave-Rotor Topping Cycle," NASA TM-4486, Oct.

Wilson, J., and Paxson, D. E., 1995, "Optimization of Wave Rotors for Use as Gas Turbine Engine Topping Cycles," Paper No. SAE-951411.

Zauner, E., Chyou, Y.-P., Walraven, F., and Althaus, R., 1993, "Gas Turbine Topping Stage Based on Energy Exchangers: Process and Performance," ASME Paper No. 93-GT-58.

Zehnder, G., Mayer, A., and Matthews, L., 1989, "The Free Running Comprex," SAE Paper No. 890452.

Downloaded 02 Jun 2010 to 171.66.16.105. Redistribution subject to ASME license or copyright; see http://www.asme.org/terms/Terms_Use.cfm

An Investigation of the Effects of Flue Gas Injection on Natural Draft Cooling Tower Performance

T. V. Eldredge
Lehigh University,
Energy Research Center,
Bethlehem, PA 18015-4729

D. J. Benton
Environmental Consulting Engineers,
Knoxville, TN

J. W. Hodgson
Department of Mechanical and
Aerospace Engineering,
University of Tennessee,
Knoxville, TN 37996-2201

This paper addresses an investigation of flue gas injection on natural draft cooling tower performance through numerical simulation. The control volume finite difference method was used for discretizing the governing equations in axisymmetric form on a boundary-fitted grid. The five independent variables addressed in this study are flue gas flow rate, flue gas temperature, radial injection location, injection orientation, and liquid entrainment in the flue gas. The flue gas temperature was found to have the most significant effect on tower performance (cold water temperature), because it strongly affects the buoyancy within the tower. The total air flow through a tower is driven by buoyancy forces, and the cooling performance is a strong function of the air flow rate.

Introduction

Owing to the projected future energy needs of the United States and the world, the burning of coal will probably continue to be an essential energy source for electricity generation. Coal has several environmentally related problems, and one of these is due to flue gas emissions. The primary pollutants are sulfur dioxide and sulfur trioxide. Flue gas, as defined in this paper, constitutes the products of combustion from burning coal. According to Rittenhouse (1992), recent amendments to the Clean Air Act require utilities to cut SO_2 emissions by 10^7 tons per year by the year 2000. The scrubbing process significantly lowers the temperature of the flue gas. Traditionally, flue gas has been disposed of through tall stacks. The stacks remove the pollutants from ground level into the upper atmosphere where they are dispersed. In order to provide the buoyancy needed for adequate stack flow, the flue gas typically requires reheating through a temperature differential of 70 to 100°C based on data provided by Wark and Warner (1981).

The injection of scrubbed flue gas into natural draft cooling towers is a relatively new technology, which eliminates the process of reheating the flue gas prior to disposal. Although natural draft towers are not typically as tall as the stacks, advantage is taken of the upward momentum in the towers, along with the buoyant plume, to achieve the necessary atmospheric rise for the flue gas. Another benefit from injection into a cooling tower is that the discharged flue gas gets diluted by as much as a factor of ten before disposal to the atmosphere. The flue gas is usually injected a short distance above the fill region in the tower. Figure 1 shows a schematic of flue gas being injected into a counterflow natural draft tower. The flue gas may be forced into the tower by means of blowers, although in some applications the negative pressure in the tower is used to pull the gas from the scrubber.

The idea of injecting scrubbed flue gas into the chimney region of natural draft cooling towers emerged in Europe. Flue gas injection has been put into practice in Europe and appears to be developing into a proven technology. According to McIlvaine (1989), Rheinisch-Westfalisches Electrizitats Werke claims to have saved about 300 million German marks on its investment with 14 applications of injecting scrubbed flue gases into cooling towers.

A search of the publicly available literature indicates a need to investigate the effects of flue gas injection on natural draft cooling tower performance. This paper is based on the thesis by Eldredge (1993), and uses numerical simulation to investigate some effects of flue gas injection on counterflow natural draft cooling tower performance. The independent variables considered were flue gas flow rate, flue gas temperature, liquid entrainment rate, direction of injection, and the location of injection.

Numerical Model Development

There is significant exchange of mass, momentum, and energy between the liquid and gaseous phases within a natural draft cooling tower. Buoyancy forces drive the air flow, which necessitates an intimate coupling of the momentum, moisture transport, and energy equations. A natural draft tower represents an irregular geometry and has a number of obstructions complicating the flow field. Irregular geometries are often dealt with by either a finite element method or a finite difference method on a boundary-fitted grid. Because finite element methods are computationally less efficient, and because a natural draft tower is not highly irregular, the control volume finite difference method using a boundary-fitted grid was chosen for this analysis. The Ryskin and Leal (1983) method was used to generate orthogonal curvilinear coordinate transformations numerically for two representative cooling towers, which were subsequently modeled in this study. There is no guarantee that for an arbitrary geometry an orthogonal transformation is available. Fortunately, the geometries of natural draft towers are typically compatible with orthogonal transformations. Figure 2 shows an orthogonal grid generated using the Ryskin and Leal method.

The physical phenomena taking place within a natural draft cooling tower can be described by the conservation law equations along with a number of constitutive relations required for closure. The governing conservation law equations expressed in vector form are shown below:

Continuity equation for the gas phase mixture:

$$\vec{\nabla} \cdot (\rho \vec{V}) = M_{ev} \tag{1}$$

Contributed by the Power Division for publication in the JOURNAL OF ENGINEERING FOR GAS TURBINES AND POWER. Manuscript received at ASME Headquarters November 25, 1996. Associate Technical Editor: H. L. Julien.

Copyright © 1997 by ASME

Downloaded 02 Jun 2010 to 171.66.16.105. Redistribution subject to ASME license or copyright; see http://www.asme.org/terms/Terms_Use.cfm

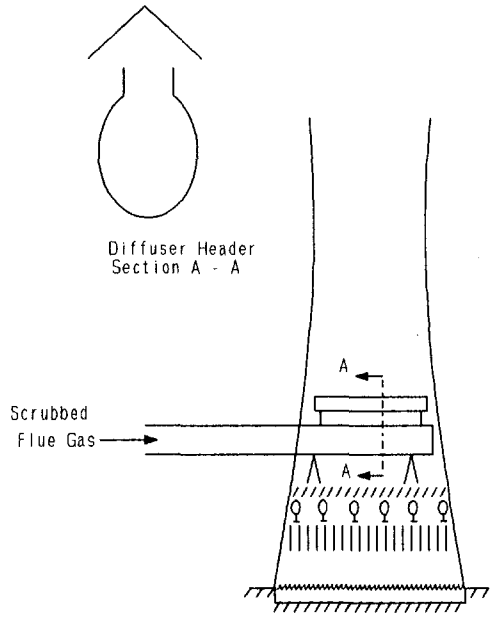


Fig. 1 Counterflow cooling tower equipped with flue gas injection

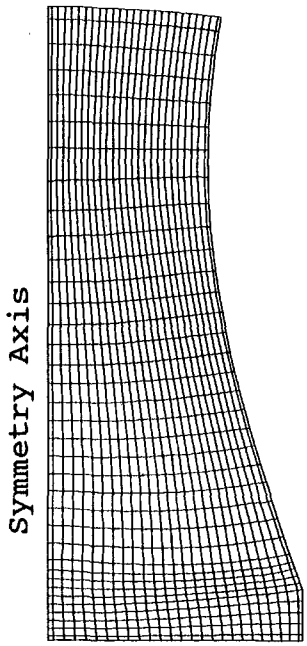


Fig. 2 Orthogonal boundary-fitted cooling tower grid

Momentum equation for the gas phase mixture:

$$\vec{\nabla} \cdot (\rho \vec{V} \vec{V}) = \vec{\nabla} \cdot \tau_{ij} + \rho \vec{g} + \vec{F} \tag{2}$$

Continuity equation for water vapor (moisture transport equation):

$$\vec{\nabla} \cdot (\rho \vec{V} C - \Gamma_{1e} \vec{\nabla} C) = M_{ev} \tag{3}$$

Energy equation for the gas phase mixture:

$$\vec{\nabla} \cdot (\rho \vec{V} \Phi - \Gamma_{2e} \vec{\nabla} \Phi) = S_p \tag{4}$$

Continuity equation for liquid water:

$$\vec{\nabla} \cdot \vec{V}_w = 0 \tag{5}$$

Energy equation for liquid water (neglecting diffusion):

$$\vec{\nabla} \cdot (\rho_w C_w T_w \vec{V}_w) = S_p \tag{6}$$

Equations (1)–(6) are expressed in vector form and do not refer to any particular coordinate system. As stated earlier, the model formulation is based on orthogonal boundary-fitted coordinates. Eldredge (1993) derived Eqs. (1)–(6) in two-dimensional axisymmetric, orthogonal, boundary-fitted coordinates. These coordinates were used for expressing and solving the governing equations, Eqs. (1)–(6), in the cooling tower model described herein.

There are a number of constitutive relations needed to provide closure for Eqs. (1)–(6). The primary relations needed are as follows:

(*a*) a relation describing the volumetric evaporation rate, M_{ev}
(*b*) a relation describing the volumetric rate of energy transfer between the two phases, S_p
(*c*) the Antoine equation of state for relating water vapor pressure to temperature
(*d*) the ideal gas equation of state for relating gaseous density to temperature and moisture content
(*e*) an appropriate turbulence model for computing effective viscosity and effective diffusivities, μ_e, Γ_{1e}, and Γ_{2e}
(*f*) relations describing the air resistance resulting from the inlet struts, rain zone, fill region, spray region, drift eliminators, and injected water drops in the chimney

The evaporation rate is usually expressed as the product of a mass transfer coefficient and a driving force term. The driving force was taken as the local difference between the saturated humidity ratio at the liquid temperature and the humidity ratio at the gas temperature. Data from the work of Lowe and Christie (1961) were used to obtain mass transfer coefficients in the fill region. The mass transfer coefficients in the rain and spray regions were computed using a Lagrangian approach and empirical relations for the droplet Sherwood number, based on the

Nomenclature

C = mass fraction of water vapor
C_w = liquid water specific heat
$\vec{F}$ = force vector acting on gas phase resulting from various flow resistances in a cooling tower
$\vec{g}$ = gravity vector
M_{ev} = volumetric evaporation rate
S_p = volumetric rate of energy exchange between the two phases
T_w = liquid water temperature
$\vec{V}$ = velocity vector for the gas phase
$\vec{V}_w$ = velocity vector for the liquid water phase
Γ_{1e} = effective moisture diffusion coefficient for water vapor
Γ_{2e} = effective thermal diffusion coefficient
ρ = gas phase density
ρ_w = liquid water density
τ_{ij} = stress tensor for the gas phase momentum equation
Φ = enthalpy of the gas phase per unit mass of mixture

Downloaded 02 Jun 2010 to 171.66.16.105. Redistribution subject to ASME license or copyright; see http://www.asme.org/terms/Terms_Use.cfm

Table 1 Inlet conditions for the TVA Paradise Tower

Inlet Dry Bulb Temperature	Inlet Relative Humidity	Hot Water Temperature	Hot Water Flow Rate	Rain Zone Drop Diameter
29.4 °C	47.5 %	43.3 °C	18105 kg/s	3.5 mm

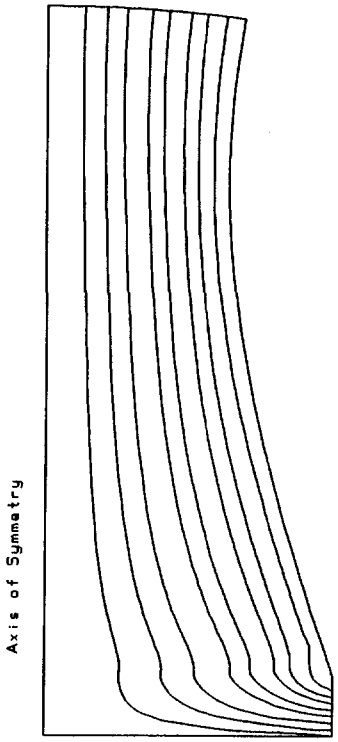


Fig. 3(*a*) Air pathlines for the base case

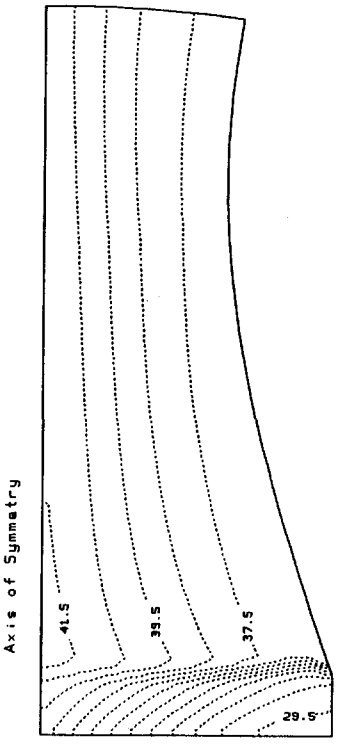


Fig. 3(*b*) Air temperature contours for the base case (29.5 to 41.5°C)

Table 2 Maximum change of each independent variable

Injection Orientation	Flue Gas Flow Rate (kg/s)	Flue Gas Temperature (°C)	Liquid Entrainment (kg/s)	Radial Injection Location (m)
Vertical & Upward	0 to 1710	32.2 to 65.6	0 to 17.1	4.5 to 33.1
Lateral & Downward	0 to 1710	32.2 to 65.6	0 to 14.3	15.2 to 33.1

work of Ranz and Marshall (1952), Whitaker (1972), and Yao and Schrock (1976).

The volumetric rate of energy exchange between the phases is given by sensible and evaporative components. The sensible rate of heat transfer is usually expressed as the product of a convective heat transfer coefficient and a driving force term. The driving force term was taken to be the local temperature difference between the liquid and gas phases. The convective heat transfer coefficients were computed from a relation between the convective Lewis number and the molecular Lewis number given by Kusuda (1965).

Turbulence is only accounted for in the gaseous phase. Because of the typical size of natural draft towers, the characteristic Reynolds and Peclet numbers are on the order of 10^7. Therefore, convection dominates and viscous effects are typically confined to relatively thin layers near bounding surfaces. For the case of flue gas injection, turbulence is generated from the interaction of the injected stream with the chimney flow.

Based on the work of Barbin and Jones (1963) and Shivaprasad and Ramaprian (1978), the superposition of the effects of entrance length and wall curvature on turbulent shear stresses tend to negate each other. Considering the effects of flue gas injection on turbulent shear stresses, a relation provided by Lee (1981) may be used to establish a reasonable upper bound on the turbulent eddy viscosity. This upper bound is approximately one order of magnitude greater than turbulent viscosities predicted by a mixing length model for fully developed pipe flow.

Based on this discussion and on numerical experiment, it was concluded that the transport phenomena in a natural draft tower are not strongly dependent on the choice of turbulence model. Cooling tower simulations were conducted for various constant values of turbulent eddy viscosity and for the fully developed mixing length model, and the results indicate that computed cold water temperatures changed less than 0.25°C. Therefore, a model based on Prandtl's mixing length theory and fully developed flow in the chimney was employed to compute turbulent viscosities. Anderson et al. (1984) reported that the turbulent Prandtl number is usually a well-behaved function. Values of turbulent diffusion coefficients for thermal and moisture transport have been computed based on assuming constant values for the turbulent Prandtl and Schmidt numbers.

Table 3 Response of tower performance to each independent variable

Injection Orientation	Flue Gas Flow Rate	Flue Gas Temperature	Liquid Entrainment	Radial Injection Location
Vertical & Upward	0.07 °C	0.70 °C	0.08 °C	0.11 °C
Lateral & Downward	0.19 °C	0.86 °C	0.08 °C	0.11 °C

Downloaded 02 Jun 2010 to 171.66.16.105. Redistribution subject to ASME license or copyright; see http://www.asme.org/terms/Terms_Use.cfm

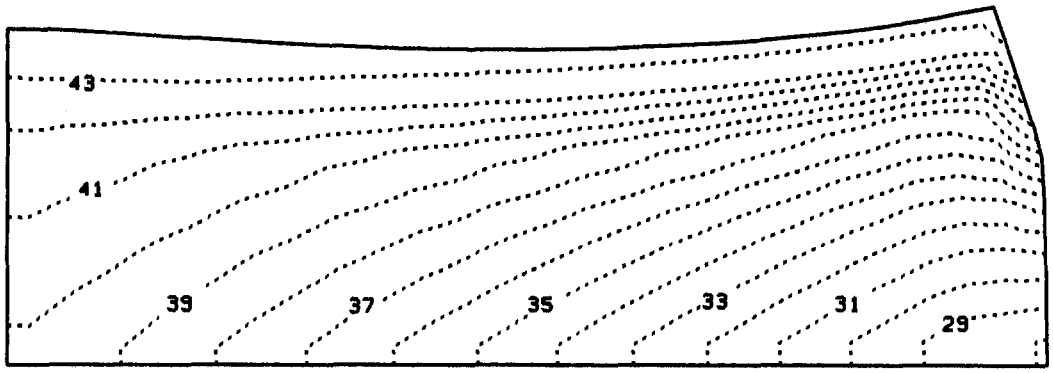


Fig. 4 Water temperature contours for the base case (28 to 43°C)

There are a number of relations needed for computing the viscous drag experienced by the gas phase. The drag forces associated with the inlet struts, fill region, and the drift eliminators were computed from empirical relations (e.g., Lowe and Christie, 1961). In the rain zone, and in the injected flue gas the drops of water impart forces on the gas phase. These net forces were computed by summing individual contributions for each drop along its trajectory. This required that the drops be tracked using a Lagrangian tracking scheme. The coupling is two-way in that droplet trajectories (and drag forces) depend on the gas flow field and the gas flow field depends on the drag forces imparted by the water drops.

There were two modeling assumptions made, regarding the injection of flue gas, which merit mentioning. The effect of neglecting condensation, resulting from injecting higher temperature flue gas, on the computed results, was shown by Eldredge (1993) to be small. Therefore condensation was neglected. Second, any heat and mass transfer from liquid drops entrained in the flue gas was considered negligible.

Results

Before applying the numerical simulation model to a tower with flue gas injection, the model was validated on two existing towers (different geometries) for different inlet conditions. The results listed below (including those with flue gas injection) are for a counterflow natural draft cooling tower located at the Tennessee Valley Authority Paradise Fossil plant. Inlet conditions are given in Table 1. This tower with these inlet conditions and with no flue gas injection is defined to be the base case.

Figures 3(*a*), 3(*b*), and 4 show air pathlines, air temperature contours, and water temperature contours, respectively, for the base case. The simulation model was found to produce results that are physically intuitive. The only available measured parameter is average cold water temperature. The simulation model computed cold water temperatures within 0.7°C of the measured values for both validation cases. In addition, the simulation model computed cold water temperatures within 1.1°C of the values computed with the model developed by Benton and Waldrop (1988), for the two validation cases.

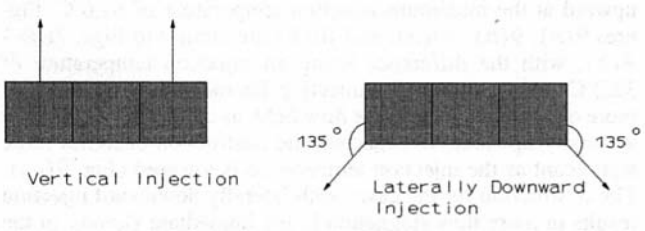


Fig. 5 Orientations of flue gas injection

The five independent variables considered were flue gas flow rate, temperature of the injected gas, the rate of liquid entrainment in the flue gas, radial location of injection, and the direction of injection. The two directions of injection addressed are shown in Fig. 5.

The most significant effect on tower performance resulted from varying the flue gas temperature. Table 2 shows the range of variation considered for each independent variable. Table 3 shows the changes in cold water temperature brought about by varying each independent variable over its entire range. The

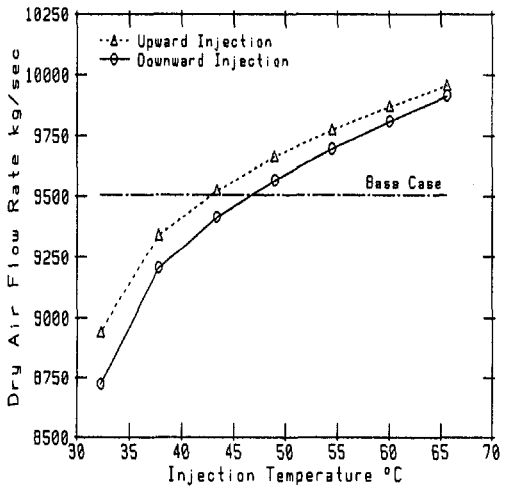


Fig. 6(*a*) Effect of injection temperature on tower air flow rate

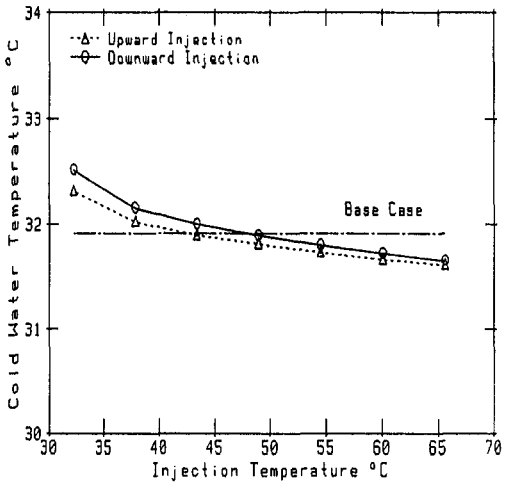


Fig. 6(*b*) Effect of injection temperature on cold water temperature

Downloaded 02 Jun 2010 to 171.66.16.105. Redistribution subject to ASME license or copyright; see http://www.asme.org/terms/Terms_Use.cfm

effect of varying each independent variable was determined by holding other independent variables constant at the operating point (Table 4). The inlet conditions (Table 1) were used for all flue gas injection scenarios so that computed cold water temperatures would be comparable to the base case. As seen in Table 3, flue gas injection temperature has the largest effect on tower performance. The reason for this is the influence of the injected flue gas on the buoyancy of the moist air in the chimney. If buoyancy is enhanced, then the tower air flow rate is increased and performance improves.

Figures 6(*a*) and 6(*b*) show the effects of injection temperature on tower air flow rate and cold water temperature for vertically upward and laterally downward injection. Agreeing with physical intuition, the results in Figs. 6(*a*) and 6(*b*) indicate that the air flow rate through the tower increases and cold water temperature decreases with increasing injection temperature. As the injection temperature increases, more heat is transferred to the existing chimney gas, and therefore, buoyancy is enhanced. Therefore, for sufficiently high injection temperatures, the performance of a tower will improve over and above its performance with no flue gas injection. It is worth noting from Figs. 6(*a*) and 6(*b*) that approximately 1200 kg/s change in the tower air flow rate is required to produce a 0.9°C change in the average cold water temperature.

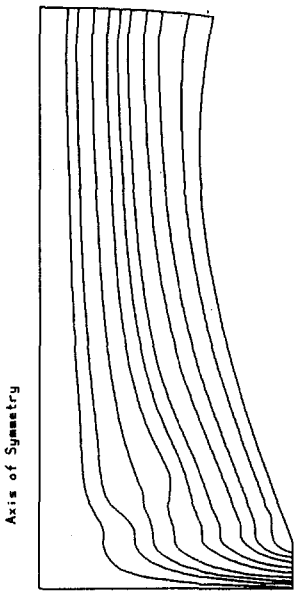


Fig. 7(*a*) Air pathlines for laterally downward flue gas injection at 65.6°C

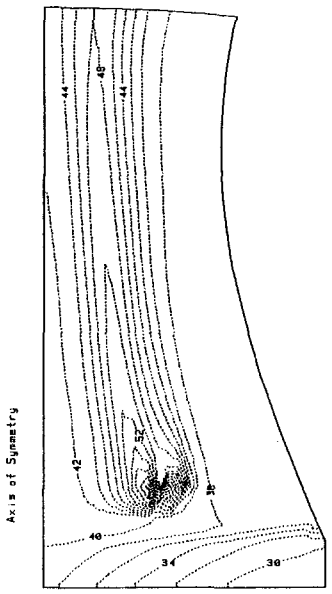


Fig. 7(*b*) Air temperature contours for laterally downward flue gas injection at 65.6°C

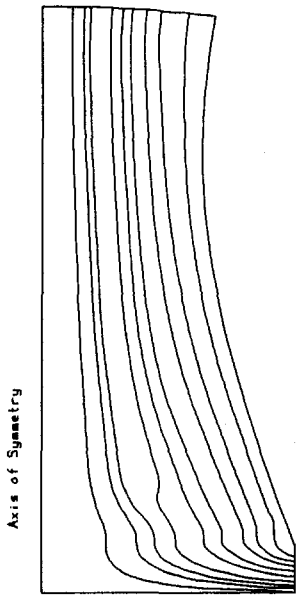


Fig. 8(*a*) Air pathlines for vertically upward flue gas injection at 65.6°C

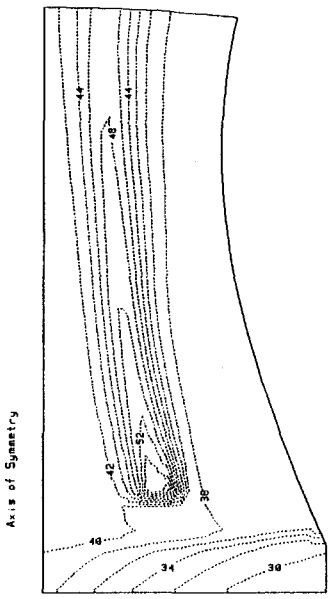


Fig. 8(*b*) Air temperature contours for vertically upward flue gas injection at 65.6°C

Figures 7(*a*) and 7(*b*) show air pathlines and air temperature contours for injecting laterally downward at the maximum injection temperature of 65.6°C. Figures 8(*a*) and 8(*b*) show air pathlines and air temperature contours for injecting vertically upward at the maximum injection temperature of 65.6°C. Figures 9(*a*), 9(*b*), 10(*a*), and 10(*b*) are similar to Figs. 7(*a*)–8(*b*), with the difference being an injection temperature of 32.2°C. The pathlines for injecting laterally downward reveal more of an obstruction to the flow field, as compared to injecting vertically upward. As expected, the obstruction becomes more significant as the injection temperature is lowered (Fig. 9(*a*)). The obstruction for the cases with laterally downward injection results in more flow stagnation in the immediate vicinity of the injection locations. The effect of this can be seen by comparing

Downloaded 02 Jun 2010 to 171.66.16.105. Redistribution subject to ASME license or copyright; see http://www.asme.org/terms/Terms_Use.cfm

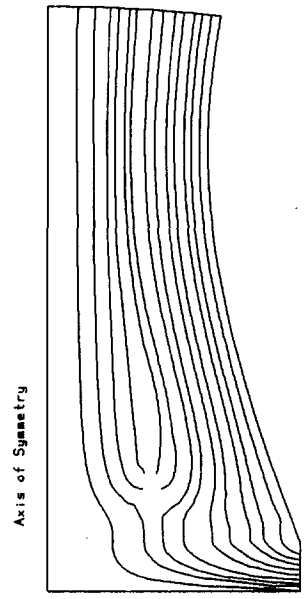


Fig. 9(*a*) Air pathlines for laterally downward flue gas injection at 32.2°C

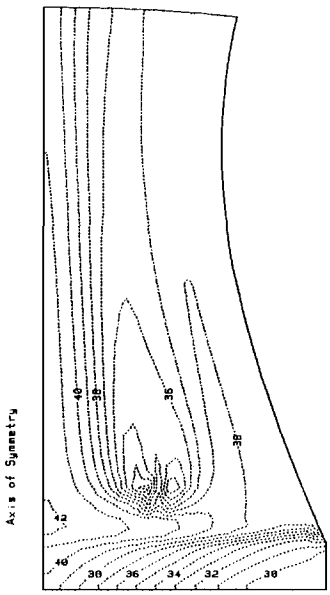


Fig. 9(*b*) Air temperature contours for laterally downward flue gas injection at 32.2°C

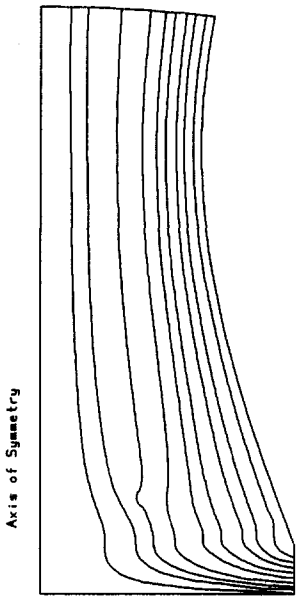


Fig. 10(*a*) Air pathlines for vertically upward flue gas injection at 32.2°C

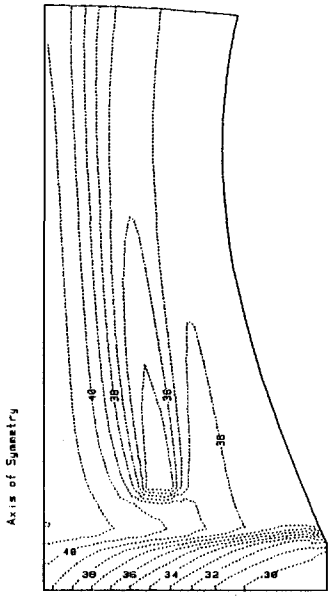


Fig. 10(*b*) Air temperature contours for vertically upward flue gas injection at 32.2°C

Figs. 7(*b*) and 8(*b*) and by comparing Figs. 9(*b*) and 10(*b*). Because of the increased flow stagnation, the temperatures in the vicinity of the injection locations are more extreme for the laterally downward injection cases.

The results given above were computed using 999 nodes and are considered to be essentially grid independent. Additional runs of the base case were computed with 1715 and 2255 nodes, and these results indicate that the cold water changed only 0.07°C for increased resolution.

Conclusions

The mechanism by which flue gas injection affects natural draft cooling tower performance is by either enhancing or restricting air flow through the tower. There are three primary mechanisms by which flue gas injection affects the air flow through a tower. The additional mass introduced by the injection presents a blockage to the existing flow field in the tower. This blockage incurs some pressure loss as the existing flow has to change directions to go around it. Also, the additional mass effectively reduces the cross-sectional flow area. Secondly, the existing flow field may experience a momentum source or sink depending on the relative magnitude and direction of the momentum of the injected flue gas. Finally, the buoyancy of the existing chimney flow may be increased or decreased, depending on the temperature and moisture content of the injected flue gas.

For this study, the buoyancy effect was found to be significantly larger than the effects of blockage and momentum trans-

Table 4 Definition of the operating point

Flue Gas Flow Rate (kg/s)	Flue Gas Temperature (°C)	Liquid Entrainment (kg/s)	Radial Injection Location (m)
1710	39.2	0.0	18.6

Downloaded 02 Jun 2010 to 171.66.16.105. Redistribution subject to ASME license or copyright; see http://www.asme.org/terms/Terms_Use.cfm

fer from the flue gas (including liquid entrainment). As a result, of the five independent variables addressed in this study, flue gas flow, flue gas temperature, radial injection location, injection orientation, and liquid entrainment, the flue gas temperature was found to have the most significant effect on tower performance (cold water temperature).

References

Anderson, D. A., Tannehill, J. C., and Pletcher, R. H., 1984, *Computational Fluid Mechanics and Heat Transfer,* Hemisphere, New York, pp. 225–226

Barbin, A. R., and Jones, J. B., 1963, "Turbulent Flow in the Inlet Region of a Smooth Pipe," ASME *Journal of Basic Engineering,* Vol. 85, No. 1, p. 29.

Benton, D. J., and Waldrop, W. R., 1988, "Computer Simulation of Transport Phenomena in Evaporative Cooling Towers," ASME JOURNAL OF ENGINEERING FOR GAS TURBINES AND POWER, Vol. 110, p. 190.

Eldredge, T. V., 1993, "An Investigation of the Effects of Flue Gas Injection on Natural Draft Cooling Tower Performance," Ph.D. Thesis, The University of Tennessee, Knoxville, TN.

Kusuda, T., 1965, "Calculation of the Temperature of a Flat-Plate Wet Surface Under Adiabatic Conditions With Respect to the Lewis Relation," *Humidity and Moisture, Vol. 1: Principles and Methods of Measuring Humidity in Gases,* R. E. Ruskin, ed., p. 16.

Lee, D. W., 1981, "Analytical Model of the Round Buoyant Jet," *Proc. Joint ASME/ASCE Bioengineering, Fluids Engineering and Applied Mechanics Conference,* Paper No. 81-FE-10.

Lowe, H. J., and Christie, D. G., 1961, "Heat Transfer and Pressure Drop Data on Cooling Tower Packings, and Model Studies of the Resistance of Natural-Draught Towers to Airflow," *Proc. International Heat Transfer Conference,* Vol. 5, pp. 933–950.

McIlvaine, R. W., 1989, "New Developments in European Power Plant Air Pollution Control," *Power Engineering,* Vol. 93, No. 2, p. 33.

Ranz, W. E., and Marshall, W. R., 1952, "Evaporation From Drops," *Chemical Engineering Progress,* Vol. 48, part 1: pp. 141–146, part 2: pp. 173–180.

Rittenhouse, R. C., 1992, "Action Builds on 1990 Clean Air Act Compliance," *Power Engineering,* Vol. 96, No. 5, p. 21–27.

Ryskin, G., and Leal, L. G., 1983, "Orthogonal Mapping," *Journal of Computational Physics,* Vol. 50, p. 71.

Shivaprasad, B. G., and Ramaprian, B. R., 1978, "Turbulence Measurements in Boundary Layers Along Mildly Curved Surfaces," ASME *Journal of Fluids Engineering,* Vol. 100, pp. 37–46.

Wark, K., and Warner, C. F., 1981, *Air Pollution: Its Origin and Control,* 2nd ed., Harper and Row Publishers.

Whitaker, S., 1972, "Forced Convection Heat Transfer Correlations for Flow in Pipes, Past Flat Plates, Single Cylinders, Single Spheres, and for Flow in Packed Beds and Tube Bundles," *AIChE Journal,* Vol. 18, p. 361.

Yao, S., and Schrock, V. E., 1976, "Heat and Mass Transfer From Freely Falling Drops," ASME *Journal of Heat Transfer,* Vol. 98, pp. 120–126.

Downloaded 02 Jun 2010 to 171.66.16.105. Redistribution subject to ASME license or copyright; see http://www.asme.org/terms/Terms_Use.cfm

A Tabular Taylor Series Expansion Method for Fast Calculation of Steam Properties

K. Miyagawa

P. G. Hill

University of British Columbia,
Vancouver, British Columbia, Canada

A new method is proposed for rapid and accurate calculation of steam properties in the regions of the state plane of greatest importance to the steam power industry. The method makes direct use of the derivatives of that Helmholtz function that is the best available wide-ranging scientific formulation of the properties of steam. It is rapid because, with a six-term Taylor series expansion, it uses property values and derivatives evaluated once and for all from the Helmholtz function and stored in tables pertaining to an optimized state plane grid configuration. The method eliminates the need for iterative property calculations and is amenable to any region of the state plane. For properties in the ranges of temperature from 0 to 800°C and pressure from 0 to 100 MPa the core memory requirement for three functions of any given pair of independent properties is less than 1 Mb. With this memory allocation it is possible everywhere in the stated range to satisfy the specific volume and enthalpy tolerances specified by the International Association for the Properties of Water and Steam. An optimized formulation of the method is demonstrated in this paper for enthalpy, entropy, and volume functions of pressure and temperature in the superheat region.

Introduction

In steam power plant design as many as 10^6 or 10^7 calls on steam routines can be made in the design of a single power plant. The cost of acquisition of the steam property information can be a substantial part of the total design cost. Though computer cycle frequency has increased greatly, the demands for analysis and optimization have risen perhaps even more impressively; substantial improvements in flow analysis call for ever more detailed numerical simulation. The 1967 IFC Formulation for Industrial Use [1] has required massive effort to adapt it [2] to modern needs. Substantial economic benefit could be had from a still faster formulation. Thus despite great improvements in computer speed, the first requirement for a steam property evaluation method is speed of execution.

The second requirement is sufficient accuracy. In the Skeleton Tables [3] the International Association for the properties of Water and Steam (IAPWS) has evaluated the experimental uncertainties in volumes and enthalpies in single-phase regions and the corresponding uncertainties in the saturation enthalpies and volumes. These constitute our principal accuracy criterion for agreement with the underlying scientific equation.

The third requirement is internal consistency with repeated sequential use of different property functions. As an example, one may consider the need for sufficient consistency of enthalpy function $h(P, s)$ and entropy function $s(P, h)$ used successively and repetitively in steam flow path calculations. The consistency problem could of course be avoided by using only the first of these functions and adopting an iterative procedure to solve for $s(P, h)$; unfortunately, iterations are quite time-consuming and must be avoided if calculation speed is to be maximized. But to prevent serious error accumulation in lengthy calculations with the two independent functions, tight restrictions must be placed on their consistency.

In addition to these requirements, it is desirable that the method be adaptable to user needs in any region of the state plane, and that its memory requirements fall within the capability of the modern personal computer.

The multi-regression optimization technique of Setzmann and Wagner [4] provides accurate short-range equations, optimized with respect to functional form, within a specified data range. However, the consistency condition between related functions may not be easy to meet. For high calculation speed, exponential and noninteger powers should be avoided. This tends to limit the range of the optimized fast equations that can be obtained by this technique.

Miyagawa [5] and Schiebener and Straub [6] used very simple piecewise continuous functions and found that large increases in speed were possible relative to the IFC 67 procedures of [2]. The general difficulty, however, of the piecewise continuous function method is in assuring consistency of values at the boundary of two neighboring functions.

Interpolation or "table look-up" methods can be fast and accurate and have acceptable storage requirements. Campbell [7] found, using a grid with pressure and enthalpy as independent variables (and with grid spacings of 5 MPa and 100 kg/kg) and bicubic interpolation, that only 20 percent of the multiplications of the IFC 67 were needed, while providing equivalent accuracy. For this function only 20 kB of storage were needed. There is a computer time cost in locating the appropriate cell, for given input coordinates, but as will be shown this can be reduced to a quite small quantity with appropriate logic. The disadvantages of the conventional interpolation methods are however that:

(*i*) the ability of the scientific formulation to provide highly accurate first and second derivatives is not utilized; instead these derivatives are in effect estimated from the stored primitives.

(*ii*) the number of multiplication operations is unnecessarily large; for even a one-dimensional interpolation the cubic spline, for example, requires 16 multiplications.

The objectives of this work have been to develop a general formulation of the tabular Taylor series expansion (TTSE) method and to demonstrate an optimization of it for enthalpy, entropy, and volume property determinations, given pressure

Contributed by the Power Division for publication in the JOURNAL OF ENGINEERING FOR GAS TURBINES AND POWER. Manuscript received at ASME Headquarters August 22, 1996. Associate Technical Editor: D. Lou.

Copyright © 1997 by ASME

Downloaded 02 Jun 2010 to 171.66.16.105. Redistribution subject to ASME license or copyright; see http://www.asme.org/terms/Terms_Use.cfm

and temperature in the steam superheat region. The method is being further developed for liquid and supercritical states with the same independent variables, and for steam states with internal energy and density as independent variables.

The Tabular Taylor Series Expansion (TTSE) Method

By using derivatives produced from the scientific formulation, Hill [8] showed that the Taylor series expansion method can achieve high accuracy with a small number of mathematical operations. The method can be demonstrated in a simple way for the saturation pressure function $P_{sat}(T)$. Using 100 equal temperature increments between triple point and critical point pressures to define a set of 101 node points T_i, and defining $x = T$ and $y = P_{sat}$, that saturation pressure can be found from

$$y = y_i + (x - x_i)[y_i' + 1/2(x - x_i)y_i'']$$

in which y_i' and y_i'' are the first and second derivatives of saturation pressure with respect to temperature; these with y are the quantities stored at each node along with the value of the temperature. The values of y and the derivatives were obtained from the algebraic formulation of Pruss and Wagner [9]. For a given value of the temperature T the nearest node point i is found from

$$i = 1 + \text{integer}[(T - T_{tp})/\Delta T]$$

in which "integer" is the Fortran rounding function NINT, T_{tp} is the triple point temperature, and ΔT is the temperature difference between neighboring nodes. With such a method and 101 nodes the relative pressure discrepancy at cell midpoints between TTSE and the scientific formulation is less than 0.0001, and the average calculation time is only 34 percent of the calculation time for the IFC 67 saturation formula given in [2].

For TTSE calculations of functions of two variables, the Taylor series expansion may be expressed as

$$Z = Z_{i,j} + (X - X_i)\left(\frac{\partial Z}{\partial X}\right)_{i,j} + \tfrac{1}{2}(X - X_i)^2\left(\frac{\partial^2 Z}{\partial X^2}\right)_{i,j} + (Y - Y_j)\left(\frac{\partial Z}{\partial Y}\right)_{i,j} + \tfrac{1}{2}(Y - Y_j)^2\left(\frac{\partial^2 Z}{\partial Y^2}\right)_{i,j} + (X - X_i)(Y - Y_j)\left(\frac{\partial^2 Z}{\partial X \partial Y}\right)_{i,j}$$

$$\left(\frac{\partial Z}{\partial X}\right)_Y = \left(\frac{\partial Z}{\partial X}\right)_{i,j} + (X - X_i)\left(\frac{\partial^2 Z}{\partial X^2}\right)_{i,j} + (Y - Y_j)\left(\frac{\partial^2 Z}{\partial X \partial Y}\right)_{i,j}$$

$$\left(\frac{\partial Z}{\partial Y}\right)_X = \left(\frac{\partial Z}{\partial Y}\right)_{i,j} + (Y - Y_j)\left(\frac{\partial^2 Z}{\partial Y^2}\right)_{i,j} + (X - X_i)\left(\frac{\partial^2 Z}{\partial X \partial Y}\right)_{i,j}$$

We now consider using the method for the functions

$$v, h, s = f(P, T)$$

in which v is specific volume, h is specific enthalpy, and s is specific entropy. To avoid infinite values for the v and s quantities as pressure goes to zero, the relationship was revised to read

$$Pv, h, Ps = f(P, T).$$

(While it would have been natural to use $[s - R \ln (P)]$ instead of s for this purpose, the logarithmic term was avoided to save computation time and because testing indicated that the product Ps provided a reasonable substitute.)

With, for example, $Z(X, Y)$ defined as $Z = Pv$ and with $X = T$ and $Y = P$, the first derivatives of Z with respect to X and Y can be found by evaluating pressure derivatives with respect to temperature and density from the Helmholtz equation. Thus

$$\frac{\partial Z}{\partial X} = \frac{P}{\rho^2}\frac{\dfrac{\partial P}{\partial T}}{\dfrac{\partial P}{\partial \rho}}$$

and

$$\frac{\partial Z}{\partial Y} = \frac{1}{\rho}\left[1 - \frac{P}{\rho\dfrac{\partial P}{\partial \rho}}\right].$$

Then by numerical differentiation with small increments of T and P (say 0.001 K and 0.001 MPa), accurate values of $\partial^2 Z/\partial X^2$, $\partial^2 Z/\partial Y^2$, and $\partial^2 Z/\partial X \partial Y$ can be obtained and stored at each node point (i, j). Thus, in the immediate vicinity of the node point, the compressibility Z can be readily obtained from the six-term Taylor series expansion.

The previously mentioned consistency requirement on "forward" and "backward" functions $h(P, T)$ and $T(P, h)$ is in principle fully satisfied; the six-term expansion can be regarded as a quadratic in T and thus the inverse function $T(P, h)$ uses exactly the same nodal information as the function $h(P, T)$. Though this may seem to guarantee exact consistency, there is nonetheless possible inconsistency at the cell boundary where there may be some discrepancy between properties of adjoining cells. Such a discrepancy will not cause a cumulative error in repeated calls of forward and backward functions, so the consistency requirement between backward and forward functions in TTSE can be much less restrictive than with independent functions.

To demonstrate the performance of the TTSE a trial grid with 40 temperatures and 80 pressure nodes in superheated steam was tested. The TTSE equation consists of only a few addition and multiplication operations and requires only single precision (4 bytes) for coefficients. The memory size on a 40 by 80 grid is $40 \times 80 \times 6 \times 4$ or approximately 77 kB for one property or about 270 for the independent properties specific volume, enthalpy and entropy.

For the large grid of a large superheat region in which the pressure changes by five orders of magnitude (between the triple point pressure and the maximum pressure [100 MPa]), cell design and the method of locating the appropriate node for a given pair of independent variables call for special consideration.

Cell Design and Optimization

Figures 1 and 2 show typical cells close to, and not close to, the saturation boundary on the $P-T$ plane. Here not only the cell size T_{size} and P_{size} are to be optimized, but also the coordinates of the location of the node N, and P_{off} are to be examined. In testing, the discrepancy between the scientific formulation and the TTSE is examined at each of the four cell corners surrounding the node N.

The principal criteria used in optimization of the method for the steam superheat region are:

1 the volumes and enthalpies of the Helmholtz equation [8] are to be reproduced within the tolerances specified by the International Skeleton Tables [3].

Downloaded 02 Jun 2010 to 171.66.16.105. Redistribution subject to ASME license or copyright; see http://www.asme.org/terms/Terms_Use.cfm

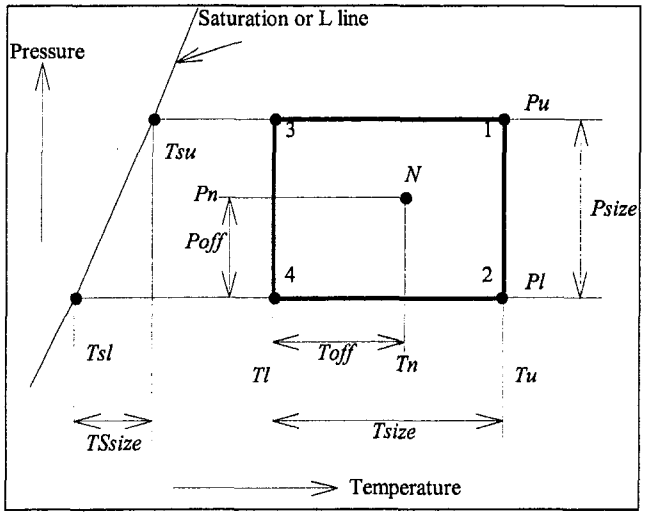


Fig. 1 Cell coordinates on the pressure-temperature plane

2 the temperature discrepancy between backward and forward functions for both enthalpy and entropy shall be no more than 50 mk in the region $s > 5.58$ kJ/kg · K.

It was found that the first criterion could be satisfied by using T_{size} values not less than 4 K. Within the selected grid size and while satisfying both of the above criteria, it was found that the temperature discrepancies could be reduced to about 15 mK for the enthalpy function and 50 mK for the entropy function. The concluding section of the paper provides a demonstration of the use of the TTSE method for turbine flow path calculations and shows that such discrepancies will be fully acceptable in practice.

Three kinds of systematic testing were conducted to determine the rms discrepancies in volume, enthalpy, and entropy for each cell size and node location:

(*i*) T_{size} and P_{size} were varied, keeping the ratio T_{size}/P_{size} constant

(*ii*) T_{size} was varied, keeping the product $T_{size}P_{size}$ constant

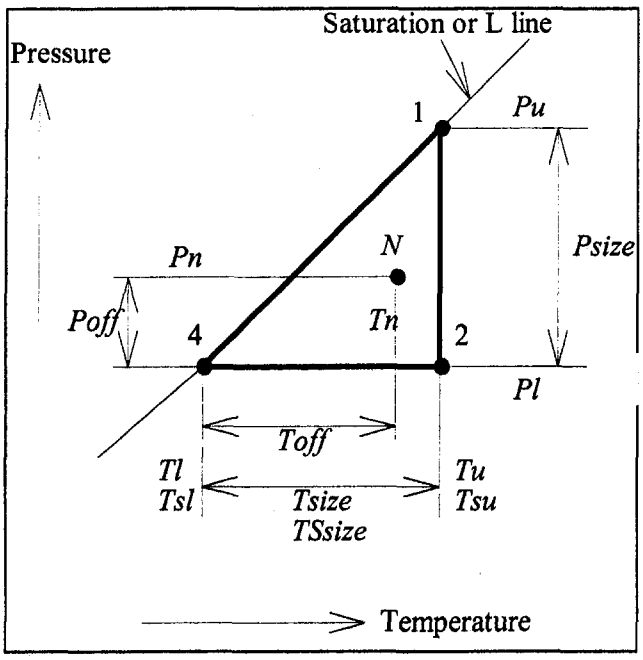


Fig. 2 Cell configuration and coordinates at the saturation boundary

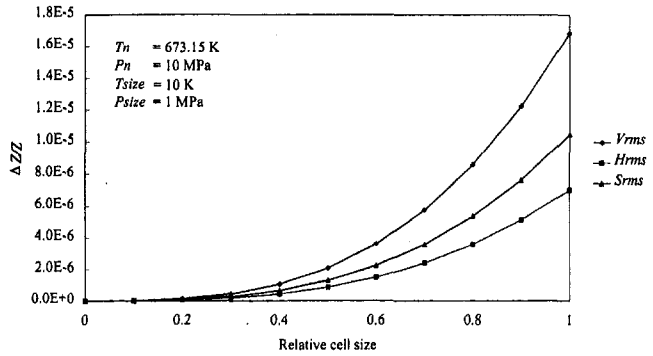


Fig. 3 The rms of $\Delta Z/Z$ with T_{size} and P_{size} varied, keeping the ratio T_{size}/P_{size} constant

(*iii*) T_n was varied along a given isobar with fixed P_{size} and T_{size}

Figure 3 shows, for one cell node (673.15 K and 10 MPa) not located near the saturation line, results of the first kind of test for the rms relative deviations of volume, enthalpy, and entropy from the Helmholtz equation [8]. The reference cell widths are 10 MPa and 1 K and cell size was changed while maintaining a constant cell size ratio of 10 MPa/K. Though only the rms values are shown, it should be noted that the deviations depend significantly on which cell corner is being tested as well as on cell size. The deviations are rapidly reduced by reducing cell size.

For the same state plane location and the same reference cell widths, Fig. 4 shows the results of the second kind of test, i.e., varying T_{size} while keeping the cell area constant. Again the deviations are dependent on testing location as well as on cell size, but the rms deviation is a good indication of the maximum deviation. We see that there is an optimum ratio of P_{size} and T_{size}, which, as Fig. 4 shows, is not the same, but not radically different, for volume, enthalpy, and entropy deviations.

Figure 5 illustrates the desirability of distributing cell size differently in different regions of the state plane. At 70 MPa, as an example, the volume deviations are very much larger in the temperature range 650 to 850 K than elsewhere; in this "critical" region where $[\partial P/\partial \rho]_T$ is minimum and the isobaric specific heat tends to be maximized, very small cell size is needed for high accuracy. Elsewhere, and in much of the state plane, the required cell size may quite large. Thus, to minimize the required memory capacity while retaining high accuracy for a wide-ranging grid, it is necessary to have cell size that is variable in two dimensions.

A wide-ranging calculation of the volume, enthalpy, and entropy deviations of the kind shown in Figs. 3, 4, and 5 has been performed for the entire superheat region to determine the cell

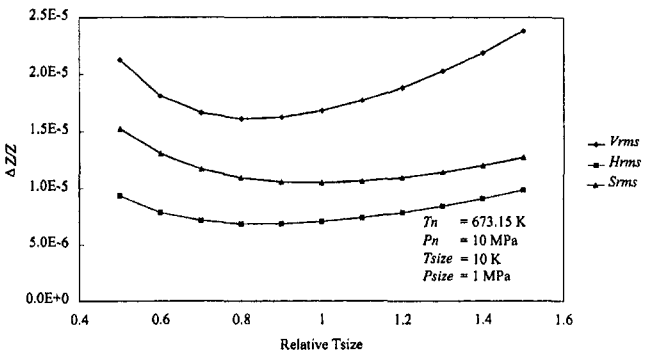


Fig. 4 The rms of $\Delta Z/Z$ with T_{size} varied, keeping the product $T_{size}P_{size}$ constant

Downloaded 02 Jun 2010 to 171.66.16.105. Redistribution subject to ASME license or copyright; see http://www.asme.org/terms/Terms_Use.cfm

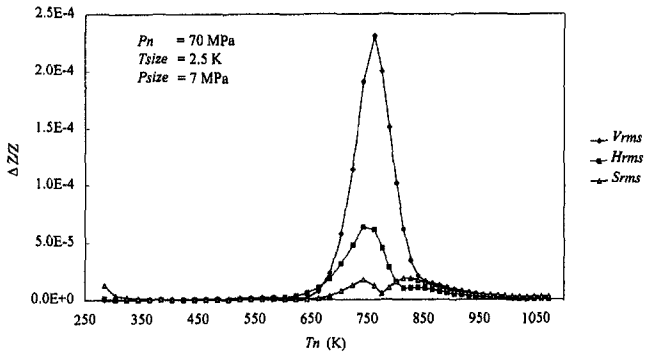


Fig. 5 The rms of $\Delta Z/Z$ with given T_{size} and P_{size} along a given isobar

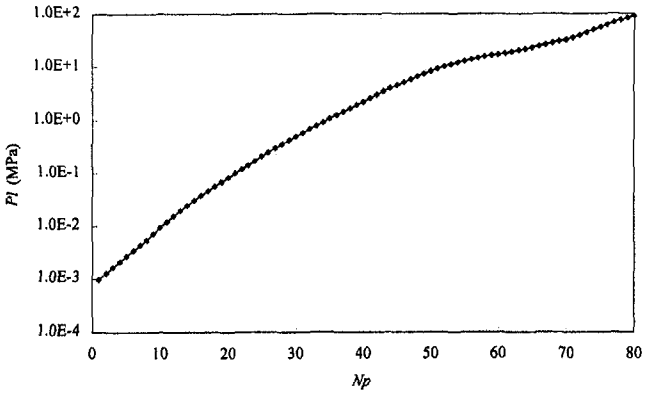


Fig. 6 Distribution of *Pl* in 80 pressure sections

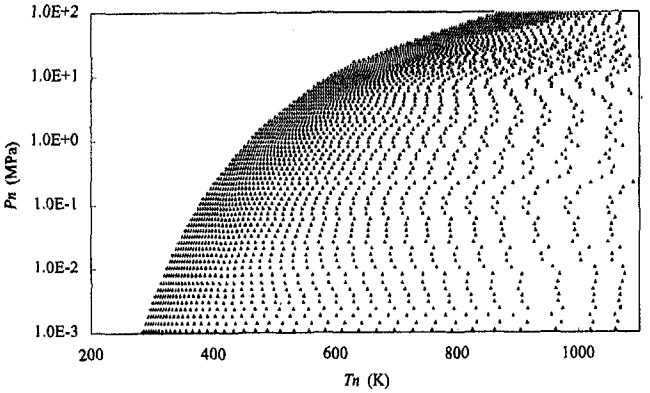


Fig. 7 Distribution of nodes in 40 × 80 grid

size distribution necessary to satisfy the volume and enthalpy tolerances of the International Skeleton Tables [3]. Here the superheat region is defined as including temperatures between saturation and 800°C and pressures up to saturation or at temperatures above 350°C, below pressures calculated from a function $P_{23}(T)$; this function is a three-term polynomial passing through the three state points defined as: (350°C, saturation), (425°C, 30 MPa), and (590°C, 100 MPa). The results of this investigation are in the form of a set of cell size distributions such that P_{size} depends on P_n only while T_{size} depends on both P_n and T_n. Figure 6 shows the distribution of pressures with cell number Np, the symbol $P1$ being defined by Fig. 1.

Figure 7 shows the optimized locations of the cells. The magnitude T_{size} varies from 4 K to 86 K, an indication of the importance of optimizing the locations of the cells. The best arrangement for T_{off} and P_{off} dimensions defined in Figs. 1 and 2 turned out to be quite simple. Setting P_{off} equal to $1/2P_{size}$ is

Table 1 Cell location and calculation times

Operation in locating cell coordinate integers i and j or in direct calculation of TTSE formula	Time (μs)
Given pressure, call subroutine	6
Perform multiple-if procedure within subroutine for determining integer j	9
Given temperature and integer j, call subroutine	6
Perform multiple-if procedure within subroutine for determining integer i	13
Calculate TTSE formula	18
Total	52

nearly optimum everywhere; setting T_{off} equal to $1/2T_{size}$ is nearly optimum except at the saturation boundary where T_{off} equal to T_{size} is best). The results reported below on accuracy of computation have used these cell size distributions.

Speed

Table 1 shows typical cell location and property calculation times using the TTSE method. These times were measured using a 486DX/33 MHz PC with hard disk drive and 256 kB cache. The operating system and compiler were MS-DOS and Microsoft-Fortran compiler version 5.1. Using the same measurement procedure, the computing times for region 2 for the IFC 67 functions $v(P, T)$, $h(P, T)$, $s(P, T)$, $T(P, h)$, and $T(P, s)$ were 144.5, 200.8, 198.5, 542.9, and 553.7 μs, respectively.

In the cell location process, calculations are entirely avoided by performing what is a half-interval search with relative magnitude decisions only. The cell location times for such a process are given in Table 1. The cell location routines are lengthy and conveniently located in subroutines. However still faster location operations may be possible if the subroutine calls are eliminated.

Accuracy

Figures 8, 9, and 10 show the accuracies typically obtained by the TTSE procedure for volume, enthalpy, and entropy calculations, respectively. In each case the calculations satisfy, or very nearly satisfy, the tolerances of the International Skeleton Tables [3]. There are only three cells (out of a total of 2573) for which the maximum relative volume deviation exceeds the tolerances of IST85 [3], and only one cell for which the enthalpy tolerance is exceeded. Much greater accuracy could be achieved at the expense of a larger grid and memory capacity, which would still be within the limits of a modern PC.

Figures 11 and 12 indicate the temperature discrepancies of the cell corners obtained by enthalpy and entropy calculations, respectively. In the first of these is shown the temperature equivalent of the maximum difference of the cell boundary, between the entropy calculated by the TTSE and that provided by the scientific equation. Figure 11 shows the corresponding tempera-

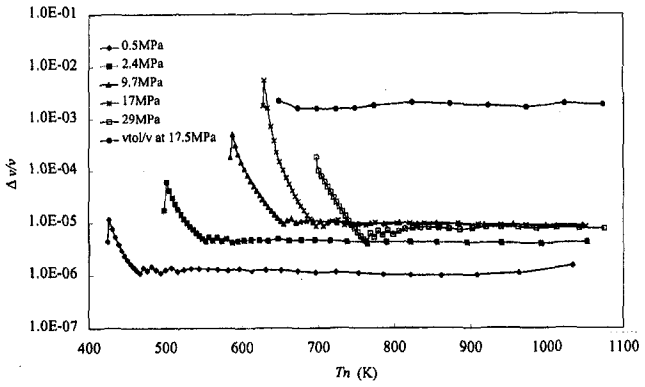


Fig. 8 $\Delta v/v$ versus *T* for several pressures and IST85 tolerance at 17.5 MPa

Downloaded 02 Jun 2010 to 171.66.16.105. Redistribution subject to ASME license or copyright; see http://www.asme.org/terms/Terms_Use.cfm

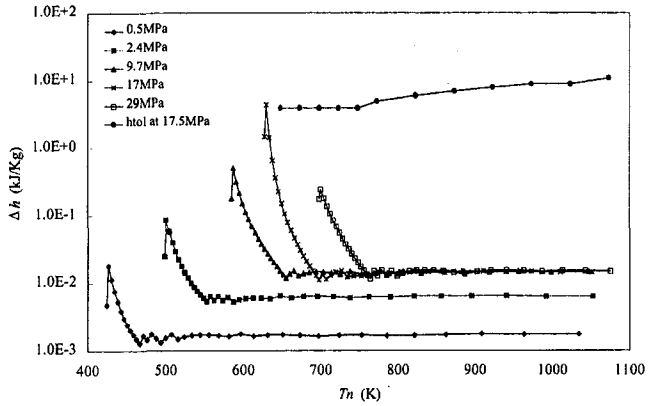


Fig. 9 Δh versus T for several pressures and IST85 tolerance at 17.5 MPa

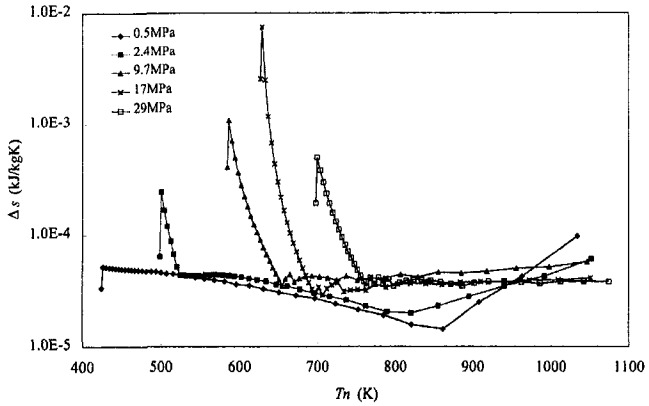


Fig. 10 Δs versus T for several pressures

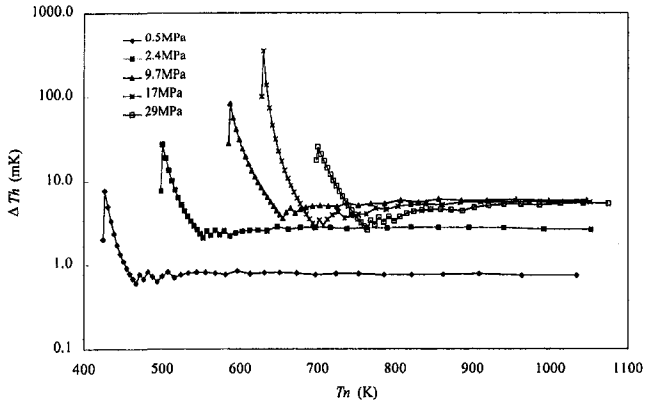


Fig. 11 Maximum enthalpy deviation from scientific formulation in temperature versus *Tn* for several pressures

ture difference for the entropy. There are 2573 cells in the region $s > 5.85$ kJ/kg · K. Tables 2 and 3 show the distribution of the errors.

Applying the method to typical turbine expansion calculations, a first task in this test was to determine the accuracy of the TTSE procedures $v(P, T)$, $h(P, T)$, and $s(P, T)$ with input values of P and T randomly selected from uniform distributions of ln (P) and T within the range $0.005 < P/\text{MPa} < 50$, $303.15 < T/K < 973.15$, and $5.85 < s/(\text{kJ/kg} \cdot \text{K}) < 8.5$, all states being superheated or on the saturation line. This range covers all steam conditions now used in steam power plants and those considered for future applications.

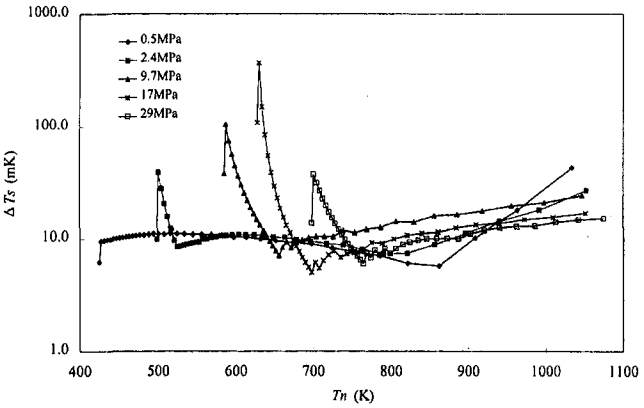


Fig. 12 Maximum entropy deviation from scientific formulation in temperature versus *Tn* for several pressures

The purpose of this test was to determine, by comparing rms and maximum errors, the relative importance of errors generated at or near cell boundaries. Table 4, in which N_{repeat} means the number of random calls, shows the result of this test of accuracy with respect to the scientific equation. That the largest error appeared only with N_{repeat} as large as 100,000 indicates that maximum errors are confined to a very small region near the cell corner.

Table 2 Statistics of errors in enthalpy at cell boundaries ($S > 5.85$ kJ/kg · K)

P_n/MPa	No. of Cells	Avg Error/mK	Max Error/mK	Cells Exceeding 15 mK
$P_n < 0.01$	360	0.2	17	7
$0.01 < P_n < 1$	1000	0.8	16	1
$P_n > 1$	1213	5.0	44	28
Total	2573	2.7	44	36

Table 3 Statistics of errors in entropy at cell boundaries ($S > 5.85$ kJ/kg · K)

P_n/MPa	No. of Cells	Avg Error/mK	Max Error/mK	Cells Exceeding 50 mK
$P_n < 0.01$	360	38	90	54
$0.01 < P_n < 1$	1000	17	66	5
$P_n > 1$	1213	12	63	4
Total	2573	18	90	63

Table 4 Deviations of volumes, enthalpies, and entropies from scientific equation for random pressure-temperature pairs

(i) Maximum errors

Nrepeat	dv/v	dh(kJ/kg)	ds(kJ/kg.K)
100	0.0000069	0.0101	0.000177
1000	0.0000184	0.0213	0.000219
10000	0.0000595	0.0713	0.000236
100000	0.0002035	0.2327	0.000616
1000000	0.0001445	0.1688	0.000437

(ii) RMS errors

Nrepeat	dv/v	dh(kJ/kg)	ds(kJ/kg.K)
100	0.0000010	0.0015	0.000030
1000	0.0000012	0.0018	0.000028
10000	0.0000016	0.0021	0.000029
100000	0.0000019	0.0024	0.000029
1000000	0.0000017	0.0023	0.000029

Downloaded 02 Jun 2010 to 171.66.16.105. Redistribution subject to ASME license or copyright; see http://www.asme.org/terms/Terms_Use.cfm

Table 5 Deviations of volume and enthalpy derivatives from scientific equation for random pressure-temperature pairs

(i) Maximum errors (relative)

Nrepeat	dv/dP	dv/dT	Cp
100	0.0002	0.0011	0.0012
1000	0.0007	0.0031	0.0037
10000	0.0020	0.0080	0.0107
100000	0.0050	0.0188	0.0237
1000000	0.0040	0.0145	0.0192

(ii) RMS (relative)

Nrepeat	dv/dP	dv/dT	dh/dT
100	0.00004	0.00023	0.00024
1000	0.00005	0.00025	0.00032
10000	0.00006	0.00030	0.00038
100000	0.00006	0.00031	0.00040
1000000	0.00006	0.00030	0.00039

A second task was to determine the corresponding accuracies of derivative quantities commonly used in steam flow calculations. In each case these derivatives were obtained directly from tables already formulated for determination of volumes and enthalpies, on the assumption of linear variation of the derivative in question over the cell space; numerical approximation of derivatives was avoided. Table 5 shows accuracies of the derivatives dv/dP, dv/dT, and dh/dT obtained in this way. Similar results were obtained for the isochoric specific heat Cv.

In general these results indicate that small errors result from using a moderately sized grid (40 temperature and 80 pressures). Reducing grid size is a powerful means of reducing error still further.

Consistency

A third task, of particular importance for turbine stage calculations, was to determine—again for random input pairs of temperature and pressure—the consistency with respect to temperature of the TTSE procedures for $h(p, T)$ and $T(p, h)$. Table 6 shows the result of that test; the high degree of consistency realized is due to the use of common derivatives in the two calculations.

Table 6 Consistency with respect to temperature of calculations using TTSE procedures for $H(P, T)$ and $T(P, H)$

Maximum Deviation

Nrepeat	dTh(mK)	dTs(mK)
100	0.030	0.030
1000	0.030	0.030
10000	0.030	0.030
100000	0.030	0.030
1000000	5.059	5.085

RMS of Deviation

Nrepeat	dTh(mK)	dTs(mK)
100	0.016	0.016
1000	0.015	0.015
10000	0.015	0.015
100000	0.015	0.015
1000000	0.016	0.016

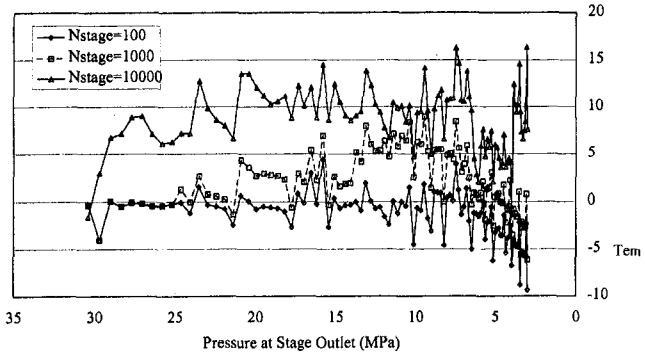


Fig. 13 Temperature difference on expansion line

The largest discrepancy that occurred (after 1,000,000 attempts) was due to a discrepancy in cell selection in which the cell selected for the forward case $[h(P, T)]$ was next to, rather than identical to, the cell selected for the backward case $[T(P, h)]$. Clearly, consistency of these procedures is not a problem for turbine stage calculations.

A fourth task was to consider a specific turbine expansion case with variable stage number and fixed inlet pressure and temperature. The chosen inlet pressure and temperature (31.12469051 MPa and 875.15K) occur at the center of a cell so that at the start of the calculation there is exact agreement between the TTSE and the scientific equation. The outlet pressure was fixed at 3 MPa and the stage adiabatic efficiency at 0.85. The objective was to determine the difference in outlet temperature obtained from the TTSE procedure from the value produced by the scientific equation. Figure 13 shows the results for stage numbers 100, 1000, and 100,000; these large stage numbers were chosen simply to emphasize the effects of repeated calculation. The deviations from the scientific equation remain within 15 mK for all cases. They seem not to be accumulated by repeated sequential use of the $h(P, T)$, $s(P, T)$, $h(P, s)$, and $T(P, h)$ procedures inherent in the turbine stage calculation. Instead, the deviations seem to be consequence of highly improbable "collisions" with cell boundaries.

Similar calculations were carried out with stage number 1000 for 25 pairs of inlet pressure and temperature. The data set is as follows: each P, T pair corresponds to a point on the straight line shown on Fig. 14, which connects cell corners with largest discrepancy between the TTSE and the scientific equation. As Fig. 14 shows, the difference between final temperatures produced by the scientific equation and the TTSE is everywhere less than 15 mK.

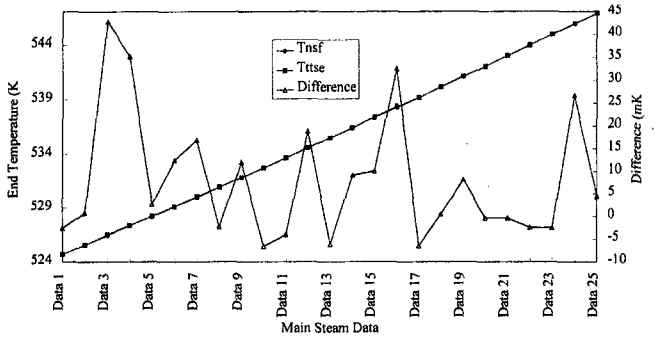


Fig. 14 Locus of end point temperature (wide sweep)

Downloaded 02 Jun 2010 to 171.66.16.105. Redistribution subject to ASME license or copyright; see http://www.asme.org/terms/Terms_Use.cfm

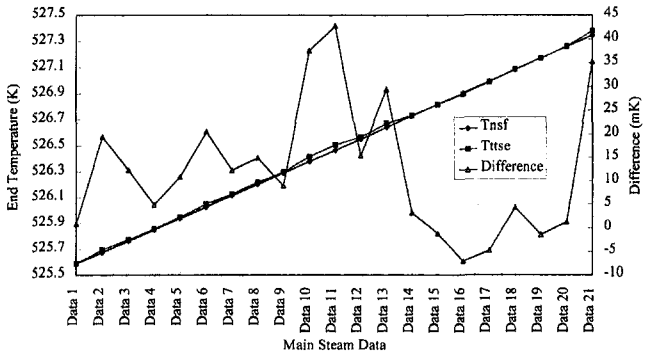


Fig. 15 Locus of end point temperature (short sweep)

Though in general the TTSE method does not require iterative procedures in determining steam properties, iterative procedures may be required for other reasons. If, for example, one starts with the end point of a given turbine expansion and requires determination of the initial temperature, iteration will be required, not because of the need to solve for T, with known h and P, from a given function $h(P, T)$, but rather because of the way adiabatic efficiency is defined. In this case the need arises for the numerical derivative of outlet temperature with respect to inlet temperature, given the inlet and outlet pressures. If too small a differential is employed, fluctuations may arise in forming such a derivative. To illustrate, we modify the preceding example by considering input data pairs along the same temperature-pressure line but reduce the temperature interval between points by a factor of 10, to 65 mK.

The fluctuations in the ratios of the outlet temperature differentials shown in Fig. 15 to the 65 mK inlet temperature differential are large enough that convergence failure of the iteration process is possible. However, this problem is readily avoided by using a sufficiently large inlet temperature differential in numerical formation of the appropriate derivative.

Conclusions

1 A Tabular Taylor series expansion (TTSE) procedure can provide determinations of the thermodynamic properties of steam, which are based directly on the best available scientific formulation, and fully satisfy the speed and accuracy requirements of the steam power industry. The method does not require iterative procedures nor the estimation of derivatives from numerical methods

2 The TTSE memory requirements for determination of three independent properties as functions of any pair of independent variables are less than 1 Mb, which is well within the capacity of the modern personal computer.

3 For the steam superheat region, the speed of calculation of properties is nearly a factor of three faster than that of the IFC 67 formulation for Industrial Use [2]. This speed advantage was made possible by the simplicity of the TTSE equations and by development of a new algorithm for cell location.

4 For the steam superheat region, it has been shown that an optimizing strategy for determination of cell size can greatly reduce the memory requirement.

5 The requirements of consistency in steam flow calculations are met by use, within the same cell of the same information for determining, e.g., $h(P, T)$ and $T(P, h)$, or $s(P, T)$ and $T(P, s)$.

6 The method is versatile. It is readily adaptable to any region of the state plane, except possibly very close to the critical point, where, if pressure is one of the independent variables and high accuracy is required, storage capacity might become excessive. Otherwise the method appears adaptable to any pair of independent variables, and to any accuracy requirement. It can be readily adapted to any scientific formulation for the properties of water and steam.

Acknowledgments

Thanks are due to Mr. J. W. E. Campbell for valuable critical suggestions and to the National Science and Engineering Research Council of Canada for financial support of one of us (PGH).

References

1 *The 1967 IFC Formulation for Industrial Use,* edited by the International Formulation Committee of the 6th International Conference of the Properties of Steam, ASME, New York.

2 *Properties of Water and Steam Using the 1967 IFC Formulation for Industrial Use* and other IAPWS Releases (a computer program package), ASME 1990, 1991, New York.

3 *Skeleton Tables of Thermodynamic Properties of Single-Fluid Phase of Ordinary Water Substance:* Table 1: The most probable specific volumes with their associated tolerances, Table 2: The most probable specific enthalpies with their associated tolerances. International Association for the Properties of Water and Steam, 1985.

4 Setzmann, V., and Wagner, W., *Int. J. Thermophysics,* Vol. 10, 1989, p. 1103.

5 Miyagawa, K., "Simplified Functions for Quick Calculations of Steam and Water Properties," in: *Physical Chemistry of Aqueous Solutions, Proc. 12th International Conference on the Properties of Water and Steam,* Orlando, FL, Sept 12–16, 1994, New York, Begell House.

6 Schiebener, P., and Straub, J., "Fast Evaluation Algorithms for Properties of State Exemplified With Ordinary Water Substance," *Proc. 11th International Conference on the Properties of Steam,* Sept 11–17, 1989, Prague, M. Pichal and O. Sifner, eds., Hemisphere, New York, 1990.

7 Campbell, J. W. E., "Review of the Present Status of the 1967 IFC Formulation for Industrial Use and the Need for Its Replacement in the United Kingdom," 1981; letter communicated to the IAPWS Subcommittee on Industrial Calculations, 1992.

8 Hill, P. G., "Integration of Industrial and Scientific Formulation: for the Thermodynamic Properties of Water and Steam," in: *Physical Chemistry of Aqueous Solutions, Proc. 12th Int. Conference on Properties of Water and Steam,* Orlando, FL, Sept. 1994, New York, Begell House.

9 Pruss, A., and Wagner, W., *A New Fundamental Equation for Water,* Bochum, Dec. 1994.

10 Miyagawa, K., Oguchi, K., Ohta, M., Okita, N., Sato, T., and Tsumita, Y., "Required Accuracies of the Inverse Equations, $T(h, P)$ and $T(s, P)$ for Superheated Steam, Determined by Power Cycle Calculations," in: *Physical Chemistry of Aqueous Solutions, Proc. 12th International Conference on the Properties of Water and Steam,* Orlando, FL, Sept. 12–16, 1994, New York, Begell House.

Downloaded 02 Jun 2010 to 171.66.16.105. Redistribution subject to ASME license or copyright; see http://www.asme.org/terms/Terms_Use.cfm